PROCEEDINGS

28TH INTERNATIONAL WORKSHOP ON WATER WAVES AND FLOATING BODIES

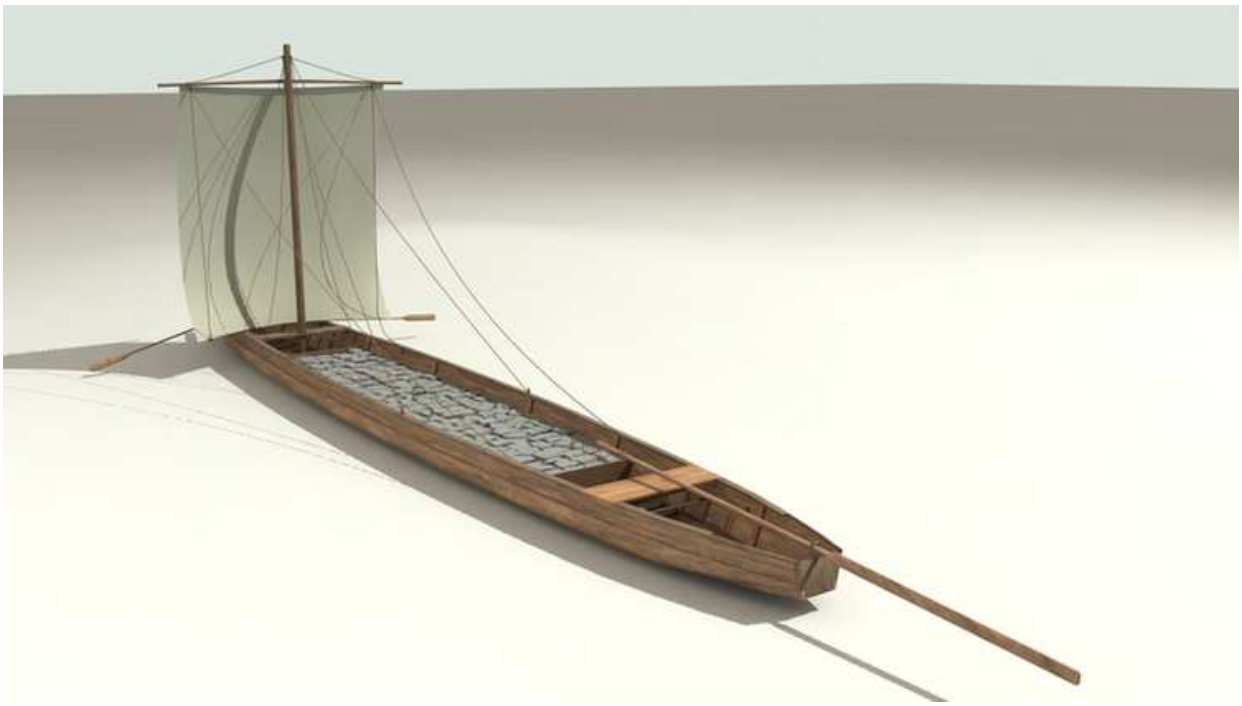

EDITORS:
BERNARD MOLIN, OLIVIER KIMMOUN, FABIEN REMY

APRIL 7-10, 2013
DOMAINE DE MOUSQUETY
L'ISLE SUR LA SORGUE, FRANCE

PROCEEDINGS

28TH INTERNATIONAL WORKSHOP ON WATER WAVES AND FLOATING BODIES

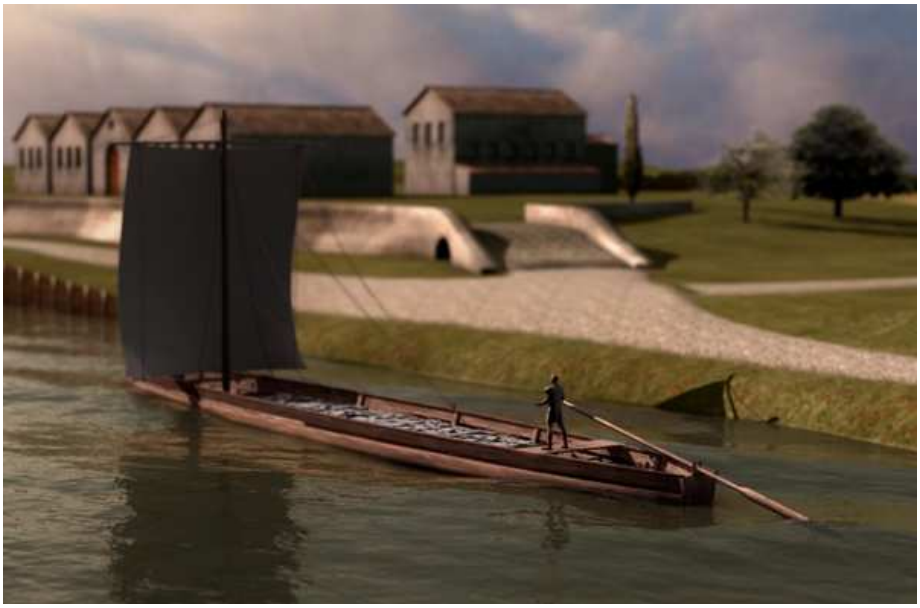

EDITORS:
BERNARD MOLIN, OLIVIER KIMMOUN, FABIEN REMY

APRIL 7-10, 2013
DOMAINE DE MOUSQUETY
L'ISLE SUR LA SORGUE, FRANCE

Recovery of a barge section with the city of Arles in the background

Cover picture

The remains of a Roman river barge, 31 m long and 3 m wide, nearly intact, were recently discovered at the bottom of the Rhône river, next to Arles which was a major port in Roman times. The barge is believed to have sunk in a flood event, by the first century after Christ. It was built of oak- and pine-wood, and carried a cargo of construction stones from Saint-Gabriel quarry, upriver near Tarascon. The shipwreck has conserved its galley gear with the glazed ceramic, and one *dolium* reused as a brasero for cooking as well as other tools.

To ease its recovery, the wreck was cut into ten sections. After restoration it will be exhibited, from the fall of 2013, at the Arles Museum.

Recently many remains from Roman times have been recovered from the bottom of the Rhône river. Most famous (but not very cheerful) is the Cesar bust (below), also to be seen at the Arles Museum.

Credits: Arles Museum of Antiquity / General Council of Bouches-du-Rhône.

SPONSORS OF THE 28TH IWWWFB

HOSTED BY

www.centrale-marseille.fr/en/home

SCIENTIFIC COMMITTEE

Bernard MOLIN, École Centrale Marseille & IRPHÉ, France
Harry BINGHAM, Technical University of Denmark, Denmark
Spyros MAVRAKOS, National Technical University of Athens, Greece
Yannis CHATJIGEORGIOU, National Technical University of Athens, Greece

LOCAL ORGANIZING COMMITTEE

Bernard MOLIN, Fabien REMY, Olivier KIMMOUN
Guillaume DUPONT, Sylvain VIROULET, Jean-Baptiste LACAZE, Yan SU

PREFACE

The International Workshop on Water Waves and Floating Bodies is an annual meeting of engineers and scientists with a particular interest in water waves and their effects on floating and submerged marine structures. The IWWWFB was initiated by Professor D. V. Evans (University of Bristol) and Professor J. N. Newman (MIT) following informal meetings between their research groups in 1984. First intended to promote communications between workers in the UK and the USA, the interest and participation quickly spread to include researchers from many other countries around the world. The workshop places particular emphasis on the participation of younger researchers, on the stimulation of discussions between engineers and scientists, and to the presentation of preliminary basic scientific work before its publication elsewhere. The workshop is an important reference point for organizing and spreading knowledge in this area. In particular, the workshop proceedings are freely accessible through the dedicated internet address www.iwwwfb.org where all contributions from 1986 on can be found.

Close to 80 abstracts were submitted to this year's workshop, out of which 60 have been retained for presentation and are included in the proceedings. The contributions cover a wide range of topics related to the interaction between ocean waves and marine structures, while the authors cover all career stages from PhD students to the most senior and distinguished researchers.

This is the fourth year since the establishment of the Tuck Fellowship which, in memory of Prof. Ernie Tuck, supports the participation of one PhD student, or young researcher, each year. Nine applications for the Tuck Fellowship were received this time and the prize was awarded to Dimitrios N. Konispoliatis, a PhD student at the National Technical University of Athens, while Hugh Wolgamot, a PhD student at the University of Oxford, was selected as the runner-up.

This year's workshop is dedicated to the memories of Fritz Ursell and Enok Palm, deceased in 2012, both of them regular participants to the IWWWFB since its early years.

FRITZ JOSEPH URSELL 1923-2012

by David Evans

Fritz Ursell was one of the most distinguished applied mathematicians of his generation. He made fundamental contributions in the theory of linear water waves in a research career spanning over sixty years which inspired successive generations of researchers in the field. Perhaps less well-known to colleagues are his major contributions to other fields including aerodynamics, acoustics, mathematical methods and oceanography, these being the topics covered in the second volume of his collected papers up to 1992.

He was born in Düsseldorf and the change of government in 1933 and his Jewish ancestry prompted his parents to send him to England in 1937 for his education. Within a few months he had learned enough English to pass the Common Entrance examination into the prestigious Clifton College in Bristol. In May 1940 he moved briefly to Marlborough College which was rated highly for mathematics and in December of that year he applied for and won a Trinity College Major Scholarship at Cambridge. After obtaining first class marks in Parts I and II of the Mathematical Tripos he went on to study Part III where he attended lectures by, amongst others, Besicovich, Hardy, Littlewood, and Dirac, and obtained a distinction in the examinations. Keen to support the war effort he was recommended for a post at the Royal Aircraft Establishment but was turned down due to being classified an enemy alien. Instead, in 1943, he was posted to the Admiralty Research Laboratory in south west London and his subsequent career was determined.

After the war he stayed on at ARL working on ships in waves. He re-discovered Havelock's wavemaker theory and applied it to find the reflection from a fixed thin vertical barrier in waves and the velocity potential everywhere. This paper remains one of the few explicit solutions to the boundary-value problem for linear water waves. He then turned his attention to a half-immersed circular cylinder oscillating vertically with constant frequency. His novel approach involved expanding the velocity potential in terms of a wave

source and a set of higher-order *wave-free* harmonic potentials each satisfying the free surface condition. He showed that the resulting infinite system of equations was convergent for sufficiently small wavenumbers Ka and produced the first rigorous computations for the added mass and damping for the cylinder.

The method of multipoles is now an established analytic tool in solving problems involving radiation and scattering by circular or spherical geometries and has been used in many papers presented at the Workshop over the years. Less well-known is his next paper which showed that the method could be extended to non-circular geometries by using an initial transformation. Its utility was illustrated in the paper by Choi *et al* at last year's Workshop.

In 1947 he was appointed to an ICI Research Fellowship in Manchester. Shortly afterwards he was elected to a Prize Fellowship at Trinity College for four years which Fritz regarded as the proudest day of his academic life. He was granted leave to postpone the Fellowship in order to work in the Manchester Mathematics Department whose Applied staff included Sydney Goldstein, Richard Meyer, Douglas Jones and James Lighthill.

During his time in Manchester he produced three remarkable papers on submerged circular cylinders. The first confirmed rigorously the result suggested by Dean, that the reflection of a normally incident wave by the cylinder was identically zero for all geometries and wave frequencies. He then showed, in a short but dense paper that the solution was unique. Finally he showed that if motion along the cylinder axis was allowed, there existed a trapped mode of finite energy, the first such example in water waves.

The period 1950-1961 was spent as a Lecturer in Cambridge where he met G.I.Taylor. Fritz had extended the well-known Stokes result for an edge wave travelling along the shoreline of a uniform sloping beach to show that this was just one of a family of bounded solutions of exponential type. On more than one occasion I pressed Fritz to explain how he derived these but to no avail. He just wrote the solution down. G.I. encouraged him to check the theory by doing an experiment and helped provide the equipment. The theory was confirmed.

He spent the academic year 1957-8 in the Hydrodynamics Laboratory at MIT where he met a young doctoral student Nick Newman who accompanied him back to Cambridge for the following year. In 1961 he accepted the Beyer Chair of Applied Mathematics at Manchester in succession to Lighthill. One of Fritz's students at Cambridge was a young Australian, Ernie Tuck who chose to stay on and work with him for a second year and spend his third year in Manchester. Fritz was elected to the Royal Society in 1972 and remained at Manchester until his retirement in 1990 during which time he graduated thirteen doctoral students and continued to produce a steady stream of high-quality papers on water waves. Amongst these was his 1964 paper on the decay of the free motion of a half-immersed cylinder, in which he proved the remarkable result that the cylinder ultimately came to rest monotonically in time rather than being sinusoidally damped. This paper continues to attract interest and discussion as the paper by Meylan & Ralph in last year's Workshop illustrates.

It was my good fortune to be taught by Fritz as a final year undergraduate, to be supervised by him as a PhD student and to work with him for three years as a colleague on the staff at Manchester. His lectures, just like his research papers were models of clarity and precision, but again, like his papers, they contained a depth of detail only revealed on closer study.

He was very much a 'hands-off ' research supervisor, allowing me to wrestle with

difficulties for up to six weeks or more before gently inquiring of me, during the morning coffee break, 'and how are we getting on?' On one occasion I went to see him with a problem I had which he was unable to resolve but which I finally sorted out on my own a week later. When I told him, he smiled and said that he had realised the answer just after I had left but thought it best that I work it out for myself. He gave me advice over getting one's work published which included writing at least four drafts before submitting to a journal. I was somewhat bemused therefore to be handed a draft manuscript of his 1964 paper mentioned above, full of corrections and insertions in the margins which was clearly the only version he wrote.

As a junior colleague I was very much in awe of him because of his reputation and position and it was many years later before I plucked up the courage to address him as Fritz. In fact I needn't have worried. He was a kind and gentle man, not one to stand on ceremony and wholly supportive of his former students, myself included, throughout their careers.

Aside from his consummate skills as a mathematician, Fritz was a true renaissance man, capable of conversing knowledgeably yet modestly, on a wide range of subjects including European history, politics, music, and literature, especially Shakespeare.

There can be little doubt that Fritz's clear open style and rigorous approach to research, as well as his encouragement of younger researchers influenced Nick and myself when we met with our own students and research assistants at the Hamburg ONR Symposium to plan the idea and the format of the Workshop. That Fritz was an enthusiastic and regular participant at all but the later Workshops, suggests that we may have had some success in promoting these ideals.

Ship hydrodynamics, water waves and asymptotics, Collected papers of F Ursell 1946-1992, Volumes 1 & 2, Advanced Series on Fluid Mechanics, 1994, World Scientific Publishing.

ENOK JOHANNES PALM 1924-2012

by John Grue

Enok Palm is mostly recognized within the natural science for his contributions to the understanding of mean flow fluxes in the atmosphere. In a joint work with his contemporary, the meteorologist Arnt Eliassen, they explained mathematically the formation of lee waves and particular cloud patterns driven by air-flow over mountains. They showed that the vertical flux of horizontal momentum does not change with height, a fundamental property and of importance in the study of fine scale atmospheric flow. They proved this for both short and long waves. Their findings have provided a basis for quite wide generalizations within the research fields of meteorology and numerical weather forecasting, and one is referring to Eliassen-Palm theory, the Eliassen-Palm theorem, EP-fluxes, Eliassen-Palm diagnostics, etc.

Enok Palm was educated and had his scientific break-through in a dedicated research group within mathematical meteorology and hydrodynamics at the University of Oslo, Norway. Developing from what is referred to as the *Bergen School of Meteorology* – this has provided the basis for much of modern weather forecasting; it was founded by the meteorologist Vilhelm Bjerknes and his younger co-workers almost 100 years ago – this was a vital scientific environment that over the years attracted many talented students. Mathematical problems relating to fronts, stability, waves and transition to turbulence in atmospheric motion occupied this lively group. It was led by the hydrodynamicist Einar Høiland, Vilhelm Bjerknes' last Carnegie assistant. For a few years in the 1950s the group was one among a few leading centers within international meteorology. The Oslo-environment attracted longer and shorter visits by leaders like Carl-Gustaf Rossby, Erik H. Palmén, Jule G. Charney, Eric Eady, Norman A. Phillips and others. Many of the young Norwegian members were invited to work as specialists in dedicated research groups in the United States (including Ragnar Fjørtoft and Arnt Eliassen who with John von Neumann at Princeton pioneered on numerical weather forecasting), and Enok Palm

was invited to give lectures on mountain waves at Department of Meteorology, University of California, Los Angeles, in the academic year 1954-1955, a lecture series that was motivated by several airplane accidents that had occurred in the mountain driven wavy flows.

After the mountain waves, Enok Palm worked on various problems relating to stability of flow. One of them was pattern formation in supercritical Rayleigh-Bénard convection which he analysed by a set of truncated Fourier series including terms up to cubic interaction. In the analysis he derived a coupled set of amplitude equations for the two preferred waves where the instability caused both modes to grow (the solution to bifurcate). The combination of the modes gave the supercritical hexagon pattern. The derivations of the amplitude equations were a key-point in his analysis. Equally essential is the physical modeling where he incorporated the kinematic viscosity's variation with temperature, a feature that was known from experiments to be important in cellular convection. With the mathematical model he was, for the first time, able to obtain theoretically the formation of hexagons in Rayleigh-Bénard convection (published in JFM in 1960).

It is noted that P.G. Drazin and P.H. Reid in their textbook *Hydrodynamic stability* write that the first to derive the 'Landau equation' (referring to Lev D. Landau's work from 1944) from the system of partial differential equations were Enok Palm (on thermal convection), and J. Trevor Stuart and J. Watson (on plane parallel flows) (all publications in 1960). Regarding Enok Palm's work that is not true; he worked with a set of equations for two amplitudes with initial conditions for both. Enok Palm's analysis is similar to the now famous model Ed. Lorentz was working on (they knew each other well), developing a flow model with a truncated set of three equations, and a corresponding set of three initial amplitudes. To include several initial amplitudes in a Landau equation is not straight forward.

Theoretical studies of nonlinear instability and pattern formation developed from the early sixties and have become important research topics within several branches of the natural science and applied mathematics. Enok Palm expanded on his 1960-work in the years that followed. Derivation of a set of nonlinear amplitude equations (later he began working with Landau equations) for analysis of various fluid processes with coefficients obtained from perturbation analysis was the main angle of attack. Some of the processes he and his students investigated were linearly stable but unstable to finite amplitude perturbations. Thermal convection, perturbation methods and subjects in nonlinear mechanics entered in the regular teaching in hydrodynamics at the University of Oslo from the 1960s.

In 1960 Enok Palm was appointed Professor of Mechanics at the Norwegian Institute of Technology in Trondheim, now the Norwegian University of Science and Technology. In 1963 he was back in Oslo, appointed as Professor of Applied Mathematics, a chair that dates back to 1814 and the time when the University was founded (in 1811). His research group continued the work on stability problems including pioneering work on algebraic instability, lift-up effect and transition to turbulence in plane shear flows.

Enok Palm and the IWWWFB

One may say that the oil-age in Norway began in 1971 with the successful production start on the Ekofisk field of ConocoPhillips in the North Sea. With this followed a considerable need to train candidates for the new industry. Enok Palm quickly realized that students with a background in theoretical mechanics would be highly useful to the

various jobs that came with offshore engineering. Moreover the industry expressed new research needs, particularly within the natural sciences. At Department of Mathematics of University of Oslo which hosts the research group in fluid mechanics (Mechanics Division) Enok Palm met with the Manager, Jan Erlvang. They together decided that Enok takes up research and training in relation to the new industrial needs, and the Department gives priority and funds the activity. This was the start of marine hydrodynamics at the University of Oslo.

As a first year student at the University the academic year 1976/77 I took the introductory course in mechanics, lectured by Professor Palm. Besides the classical subjects like Newton's laws, conservation of momentum, planetary motion etc., he described glimpses of his new research on wave analysis of ships and offshore structures. Where I sat listening in the lecture room, I asked myself, what could be more useful than applying mathematics skills to such an important dimension, calculating the safety within the new offshore industry? That was my first encounter with the subject of marine hydrodynamics. Later I became his student, close colleague and friend.

To take up research on marine hydrodynamics was a start from scratch; Enok really did a serious job. One of the first things he did was to visit leading research groups in the field. One such visit was to Netherlands Ship Model Basin where he learned about the measurements by Johan Wichers, finding that the slow drift motion of a moored ship had a stronger damping when there were incoming waves than when the sea was calm (published by J.E.W. Wichers and M.F. van Sluijs in 1979). This problem motivated the research in marine hydrodynamics at the University of Oslo. He organized colloquia on: integral equations, second-order radiation and diffraction, slender body theory, nonlinear waves, Green functions. Another subject was Fritz Ursell's work on wave reflection from a submerged cylinder. Enok's method was the same as he had experienced himself as a young student; the students were put at work! We all had to present (many!) seminar lectures, and the rule was, that those students who worked hardest and presented the most, also benefitted most. Our teacher was always attending the seminar lectures and he performed a keen, detailed examination of the presenter's lay-out. When the new course in *marine hydrodynamics* was introduced in Oslo the academic year 1980/81, I – as the youngest in the group of master students – was put to lecture Nick Newman's book. Our education was very well taken care of.

What came out as research in marine hydrodynamics from Oslo, after all, is a mathematical formulation of the complete slow drift damping problem with a numerical implementation in the code WAMIT (we denote this version by WAMITUIO). The program is in use by Det Norske Veritas and other companies in the world wide offshore industry. Problems on wave and current interaction of floating geometries in two and three dimensions occupied the research group, first with me as Enok's student, and later with Enok and me together with new students. Enok and I began working on internal waves, also motivated by industrial needs. Enok contributed regularly to the Workshop from 1987 and co-chaired the 4th. His last was the Spitzbergen-Workshop in 2005.

P.G. DRAZIN & W.H. REID *Hydrodynamic stability*, Cambridge University Press, 1981.

28TH IWWWFB PROGRAM

SUNDAY, APRIL 07, 2013

9:00-12:00	Registration	
9:30-11:30	Tour to Fontaine de Vaucluse	
12:15-13:15	**Lunch**	
13:30-13:45	Welcome - Opening remarks	
SESSION 1	CHAIR J.N. NEWMAN	
13:45-14:07	A second order ordinary differential equation for the frequency domain Green function	Clément A.H.
14:07-14:30	Evaluation of time-domain capillary-gravity Green function	Dai Y., Chen X.-B.
14:30-14:52	Expansion formula for velocity potential for wave interaction with floating and submerged structures	Mohapatra S.C., Sahoo T.
14:52-15:15	A novel connection between the Ursell and Dean vertical barrier potentials	Porter R., Evans D.V.
15:15-15:40	**Coffee break**	
SESSION 2	CHAIR A. HERMANS	
15:40-16:02	A note on added resistance for slow ships	Bingham H.B., Afshar M.A.
16:02-16:25	Illustrative applications of the Neumann-Michell theory of ship wave	Huang F., Li X., Noblesse F., Yang C., Duan W.-Y.
16:25-16:47	The limits of applicability of shallow-water wave theory	Doctors L.J.
16:47-17:10	A nonlinear calculations of interfacial waves generated by a moving ship and evaluation of the forces in the dead water problem	Grue J.
17:10-17:35	**Break**	
SESSION 3	CHAIR W.-Y. DUAN	
17:35-17:57	Semi analytical solution for second order hydroelastic response of the vertical circular cylinder in monochromatic water waves	Choi Y.M., Malenica S.
17:57-18:20	Time-domain hydro-elastic dynamic analysis of a large floating body including second-order wave loads	Kang H.Y., Kim M.H.
18:20-18:42	Whipping response of a box barge in oblique seas	Piro D.J., Maki K.J.
19:00-20:00	**Welcome party**	
20:00-21:30	**Dinner**	

MONDAY, APRIL 08, 2013

SESSION 4	CHAIR O.M. FALTINSEN	
8:15-8:37	Hydrodynamic impact of three-dimensional bodies on waves	Scolan Y.-M., Korobkin A.A.
8:37-9:00	Numerical and experimental studies of plate ditching	Iafrati A., Calcagni D.
9:00-9:22	Wagner-type models of water impact with separation for a finite wedge	Korobkin A.A.
9:22-9:45	The impact of a fractionally (viscoelastic) damped system onto the water free surface	Casetta L., Franzini G.R., Pesce C.P.
9:45-10:07	Multiple oblique impacts on thin liquid layer with restoring forces	Khabakhpasheva T.I., Korobkin A.A.
10:07-10:30	**Coffee break**	
SESSION 5	CHAIR H.B. BINGHAM	
10:30-10:52	A model test for the wave interaction with a four-cylinder structure	Cong P.W., Teng B., Zhang K., Huang Y.F.
10:52-11:15	Second-order resonance among an array of two rows of vertical circular cylinders	Kagemoto H., Murai M., Fujii T.
11:15-11:37	Cloaking a circular cylinder in deep water	Newman J.N.
11:37-12:00	An experimental study of near-cloaking	Dupont G., Kimmoun O., Molin B., Guenneau S., Enoch S.
12:00-12:22	Radiation and trapping behaviour of arrays of truncated cylinders	Wolgamot H., Eatock Taylor R., Taylor P.H.
12:30-13:30	**Lunch**	
SESSION 6	CHAIR J. GRUE	
13:45-14:07	On the dispersive modeling of the 2011 Tohoku tsunami generation by coseismic/SMF processes, and near- and far-field impact	Grilli S., Harris J.C., Kirby J.T., Shi F., Ma G., Masterlark T., Tappin D., Tajalli Bakhsh T.S.
14:07-14:30	A comparison of simulation approaches based on the Zakharov equations for nonlinear waves in the coastal zone	Benoit M., Yates M.L., Chazel F.
14:30-14:52	Extreme wave run-up on a vertical cliff	Carbone F., Dutykh D., Dudley J.M., Dias F.
14:52-15:15	Free surface determination from pressure measurements at the sea bed	Clamond D.
15:15-15:40	**Coffee break**	
SESSION 7	CHAIR R. EATOCK TAYLOR	
15:40-16:02	Lagrangian modelling of extreme wave groups	Buldakov E.V.
16:02-16:25	Stokes drift and net transport for two-dimensional wave groups in deep water	Van den Bremer T.S., Taylor P.H.
16:25-16:47	Wave simulation in a 3D coupled numerical and physical wave basin	Yang Z.W., Bingham H.B., Liu S.X.
16:47-17:15	**Break**	
SESSION 8	CHAIR D.V. EVANS	
17:15-17:37	Trapping of time-harmonic waves by freely floating structures consisting of multiple bodies (motionless and/or heaving)	Kuznetsov N., Motygin O.
17:37-18:00	Shapes of zero wave resistance and trapped modes	Makasyeyev M.V.
18:00-18:22	Near trapping and the singularity expansion method	Meylan M.H., Fitzgerald C.
18:22-18:45	Physics of sloshing impacts in tanks of membrane LNG carriers	Brosset L. (GTT)
19:00-19:45	**IWWWFB Steering Committe Meeting**	
20:00-21:30	**Dinner**	

TUESDAY, APRIL 09, 2013

SESSION 9	CHAIR A. IAFRATI	
8:15-8:37	Numerical simulation of fluid-structure interaction using a level-set immersed boundary method	Bai W., Huo C.
8:37-9:00	Two-dimensional and three-dimensional simulation of wave interaction with an oscillating wave surge converter	Rafiee A., Dias F.
9:00-9:22	A numerical strategy for gas cavity-body interactions from acoustic to incompressible liquid phases	Colicchio G., Greco M., Faltinsen O.M.
9:22-9:45	Fluid-structure interaction during wave-impact with air-entrapment in a sloshing tank	Lugni C., Bardazzi A., Faltinsen O.M., Graziani G.
9:45-10:07	Collision of two liquid wedges	Semenov Y.A., Wu G.X., Oliver J.M.
10:07-10:30	**Coffee break**	
SESSION 10	CHAIR F. NOBLESSE	
10:30-10:52	Hyper-singular integral-equation for a finite-draft surface piercing cylindrical shell at high and low-frequency	Yeung R.W., Nokob M.H.
10:52-11:15	Numerical analysis of floating-body motions in arbitrary bathymetric domain	Kim T., Kim Y.
11:15-11:37	Towards real time simulation of ship-ship interaction. Part II: double body flow linearization and GPU implementation	Lindberg O., Glimberg S.L., Bingham H.B., Engsig-Karup A.P., Schjeldahl P.J.
11:37-12:00	A real-time simulation technique for ship-ship and ship-port interactions	Pinkster J.A., Bhawsinka K.
12:00-12:22	Simplified formulation for parametric roll in regular and irregular waves	Song K.-H., Kim Y., Park D.-M.
12:30-13:30	**Lunch**	
SESSION 11	CHAIR J.A. PINKSTER	
13:45-14:07	Hydrodynamic interaction among multiple cylindrical OWC devices restrained in regular waves	Konispoliatis D.N., Mavrakos S.A.
14:07-14:30	Capture width for arrays of wave energy converters	Farley F.J.M.
14:30-14:52	External dynamics system of twin floating bodies for perfect wave absorption	Minoura M., Hirao C., Miyazaki Y., Kashiwagi M.
14:52-15:15	Wave-power extraction from a finite array of oscillating wave surge converters	Renzi E., Dias F.
15:15-15:37	Demonstrating the feasibility of a distensible-tube WEC with a distributed power take-off	Rainey R.C.T., Chaplin J.R.
15:37-16:05	**Coffee break**	
SESSION 12	CHAIR A.A. KOROBKIN	
16:05-16:27	Evolution of water waves generated by sub-aerial deformable landslide	Viroulet S., Kimmoun O., Kharif C.
16:27-16:50	Modelling wave interaction with a surface-piercing vertical cylinder using Open-FOAM	Chen L.F., Morgan G.C.J., Zang J., Hillis A., Taylor P.H.
16:50-17:12	Focused wave impact on a vertical cylinder: Experiment, numerical reproduction and a note on higher harmonics	Paulsen B.T., Bredmose H., Bingham H.B.
17:12-17:35	Dissipation around rolling boxes	Lu L., Chen X.-B., Teng B., Gou Y., Jiang S., Guo X.
17:35-17:57	The application of velocity decomposition to airfoil problems	Rosemurgy W.J., Maki K.J., Beck R.F.
18:00-18:15	ONRG and the associated hydrodynamics related programs	Lin W.-M.
19:00-	**Banquet dinner**	

WEDNESDAY, APRIL 10, 2013

SESSION 13	CHAIR N. KUZNETSOV	
8:30-8:52	The wave radiation problem in a two-layer fluid by time-domain method	Gou Y., Chen X.J., Wang G.B., Teng B., Ning D.Z.
8:52-9:15	GN equations to describe internal solitary waves in two-layer fluid	Zhao B.B., Duan W.Y.
9:15-9:37	Wave forces on oscillating horizontal cylinder submerged under non-homogeneous surface	Sturova I.V.
9:37-10:00	On the wave resistance of an immersed prolate spheroid in infinite water depth	Chatjigeorgiou I.K., Mavrakos S.A., Miloh T.
10:00-10:20	**Coffee break**	
SESSION 14	CHAIR M. KASHIWAGI	
10:20-10:42	Time dependent flexural gravity wavemaker problem	Mohanty S.K. , Mondal R., Sahoo T.
10:42-11:05	The effect of a vertically sheared current on rogue wave properties	Kharif C., Viroulet S., Thomas R.
11:05-11:27	Current effects on higher harmonic waves	Ning D.Z., Lin H.-X., Teng B.
11:27-11:50	Hybrid-spectral model for fully nonlinear numerical wave tank	Christiansen T.B., Engsig-Karup A.P., Bingham H.B.
11:50-12:00	Closure	
12:30-13:30	**Lunch**	

CONTENTS

Numerical simulation of fluid-structure interaction using a Level-Set Immersed Boundary Method

Author Names: Wei Bai, Chengzhong Huo
Department of Civil and Environmental Engineering, National University of Singapore, Singapore, (w.bai@nus.edu.sg, ceehc@nus.edu.sg)

1 Introduction

Investigation of the interaction between free surface flows and marine structures is a classical hydrodynamic problem and has a wide range of applications in many offshore engineering problems. It is difficult to study numerically complex free-surface evolutions and irregular boundaries. The challenge is even harsher if the structure is in motion. For example, a flow singularity occurs when a body impacts the free surface which gives rise to a high pressure peak localized at the spray root and makes water entry and exit problems difficult. In recent years, the Level-Set Method (LSM) has become a popular tool for the modeling of two-phase fluid flows due to its simple representation of the surface curvature and the ease of its implementation, See Osher and Fedkiw (2001) for a review. Due to its standard form does not guarantee the overall conservation of fluid, especially in regions of high curvature, the Hybrid Partical Level Set Method (HPLS) of Enright etal. (2002) has been proposed to improve its conservation properties and accuracy. On the other hand, the Immersed Boundary Method (IBM) is popularly used to mimic the boundary immersed in the fluid flow. In the IBM, a body force is introduced to the momentum equations to enforce the boundary condition of the structure in the fluid (Fadlun et al. 2000). The IBM has the advantage of simplifying the grid generation and its inherent simplicity to study moving body (Mittal et al. 2005) on fixed Cartesian grids. Furthermore, it is very convenient to compute forces acting on a body namely lift and drag force, because of its appropriate treatment in the IBM. These advantages suggest that it is well suited to study problems involving a moving body with the free surface flow.

Here, we investigate the applicability of the particle Level-Set Immersed Boundary Method (LS-IBM) for the simulation of breaking waves with obstacle and water entry problem. The incorporation of an immersed boundary method with a free surface capture scheme implemented in a Navier-Stokes solver allows the interaction between fluid flow with free surface and moving bodies of almost arbitrary shape to be modeled. Dam break past a rectangular obstacle is modeled using the present model and the simulation results using LS-IBM agree well with the experimental results in the literature. The LS-IBM is also applied to study breaking waves with obstacle of different shape for different purpose. In this paper only the dam break past a circle obstacle is shown for the purpose of demonstration.

2 Mathematical Model

2.1 Governing equations

In the study of 2D wave-structure interactions, the incompressible viscous fluid flow is governed by the Navier-Stokes equations:

$$\frac{\partial u_i}{\partial t} + u_j \frac{\partial u_i}{\partial x_j} = \frac{1}{\rho(\varphi)}\left(-\frac{\partial p}{\partial x_i} + \frac{\partial \tau_{ij}}{\partial x_j} \right) + f_i \qquad (2.1)$$

and the continuity equation:

$$\frac{\partial u_i}{\partial x_i} = 0 \qquad (2.2)$$

where Cartesian tensor notation is used, (i = 1, 2), u_j, p and x_j are the velocities, pressure and spatial coordinates respectively, f_i represents momentum forcing components, ρ is the fluid density and τ_{ij} are the viscous stress components given by

$$\tau_{ij} = \mu(\phi)\left(\frac{\partial u_i}{\partial x_j} + \frac{\partial u_j}{\partial x_i} \right) \qquad (2.3)$$

where μ is the fluid viscosity.

2.2 Free surface equations

We investigate the motion of two incompressible fluids and track the movement of the free surface implicitly by the Level Set Method (LSM). In LSM a scalar quantity φ, known as the level set function, is specified throughout the domain to represent the location of grid cells relative to the surface. Here, we define φ to be a signed distance function, which measures the shortest distance from the grid cell to the free surface (*i.e.* $|\nabla\varphi| = 1$) and is positive in one fluid phase and negative in the other. The evolution of the level set function φ is governed by

$$\frac{\partial\phi}{\partial t} + u_i \frac{\partial\phi}{\partial x_i} = 0 \tag{2.4}$$

In the governing equations, both ρ and μ vary dependant on the local fluid phase properties and are smoothed over a small distance $\varepsilon = 2\Delta x$ across the surface by use of a Heaviside function H to avoid numerical instabilities caused by the sharp gradients present. We calculate ρ and μ by

$$\begin{aligned} \rho(\phi) &= \rho_{air} + H(\phi)(\rho_{water} - \rho_{air}) \\ \mu(\phi) &= \mu_{air} + H(\phi)(\mu_{water} - \mu_{air}) \end{aligned} \tag{2.5}$$

where,

$$H(\phi) = \begin{cases} 0 & \phi < \phi \\ \frac{1}{2} + \frac{\phi}{2\varepsilon} + \frac{1}{2\pi}\left(\frac{\pi\phi}{\varepsilon}\right) & -\varepsilon \le \phi \le \varepsilon \\ 1 & \phi > \varepsilon \end{cases} \tag{2.6}$$

At present, we neglect the influence of surface tension since we are currently interested in the large scale dynamics of gravity waves.

3 Numerical Approach

3.1 Navier-Stokes solver

The Navier-Stokes equations are discretized on a staggered grid with p, ρ and μ defined at grid cell centers and the velocity components at cell faces. We discretize the temporal gradient with a second order Runge Kutta Total Variation Diminishing (RK-TVD) scheme. Eqs. (2.1) and (2.2) are discretized using a fractional step method.

$$u_i^{**} = u_i^n + \Delta t\left(\frac{1}{\rho^n(\varphi)}\left(\frac{\partial\tau_{ij}^n}{\partial x_j}\right) - u_j^n \frac{\partial u_i^n}{\partial x_j} + g_i + f_i\right) \tag{3.1}$$

$$\frac{\partial}{\partial x_i}\left(\frac{1}{\rho^n(\varphi)}\frac{\partial p^n}{\partial x_i}\right) = \frac{1}{\Delta t}\left(\frac{\partial u_i^{**}}{\partial x_i}\right) \tag{3.2}$$

$$u_i^{n+1} = u_i^{**} - \frac{\Delta t}{\rho^n(\varphi)}\frac{\partial p^n}{\partial x_i} \tag{3.3}$$

where u^{**} is the predicted velocity, f_i is the momentum forcing used to enforce the desired boundary conditions on an immersed boundary interface and $\triangle t$ is the time step. In discretizing the convective term in (Eq. 2.1) it is essential to avoid the introduction of numerical instabilities due to the sharp density gradient at the surface. We employ first order upwinding to ensure stability. The diffusive term in (Eq. 2.1) is discretized with a second order central difference. The time step is restricted by the CFL condition and gravity as discussed in Kang et al. (2000). The CFL number for our simulations is kept below 0.5.

3.2 Free surface solver

Accurate solution of the level set equation (Eq. 2.4) is crucial to capture the correct surface physics. Here, we discretize φ at cell centers and calculate velocity gradients with a fifth order HJ-WENO scheme (Jiang and Peng, 2000). Temporal gradients are resolved with a third order RK-TVD scheme. Since only the location of the surface is of interest, φ can be solved in a narrow band close to the interface. For the HJ-WENO scheme the narrow band occupies six cell widths either side of the surface in all directions (Peng *et al.*1999). As φ is evolved in time it may deviate away from being a signed distance function (*i.e.* $|\nabla\varphi \mid \neq 1$) requiring reinitialisation. Here, we reinitialize φ with an efficient fast marching technique at every time step, see Sethian (1996) for details.

3.3 Immersed boundary treatment

It is noted that the term f_i must be determined prior to the computation of the predicted velocities u^{**}. This term is prescribed at each time step to establish the desired boundary moving velocity V_{ib}. For a time –stepping scheme, this force can be expressed as

$$\frac{u_i^{n+1} - u_i^n}{\Delta t} = RSH_i + f_i \tag{3.4}$$

where RSH_i includes the convective, viscous, pressure gradient and body force of the governing equations. If the forcing f_i must yield $u_i^{n+1} = V_{ib}^{n+1}$ on

the immersed boundary where V_{ib}^{n+1} is the Dirichlet boundary condition at the immersed boundary, the forcing is given from the equation below,

$$f_i = \frac{V_{ib} - u_i^n}{\Delta t} - RSH_i \tag{3.5}$$

This forcing is direct in the sense that the desired boundary condition can be satisfied at every time step but only holds when the immersed boundary coincides with the grid. In general, Eulerian grid nodes almost never coincide with the immersed boundary in practical applications. f_i needs to be computed at grid points near and not exactly on the interface. The value of u_f at the forcing points is not known and has to be reconstructed using the information from the interface and surrounding field. In terms of u_f that has been predicted by the reconstruction, the force on the forcing points can be expressed as

$$f_i = \frac{u_f - u_i^n}{\Delta t} - RSH_i \tag{3.6}$$

4 Results

4.1 Dam break past a rectangular obstacle

Fluid flow past a fixed rectangular obstacle is simulated to verify that the present LS-IBM accurately predicts flow phenomena such as separation and wave breaking. In order to compare our results directly with the experiments of Koshizuka at al. (1995) and numerical simulations of Larese at al. (2008) and Gao Mimi (2011), we consider a rectangular column of water of initial height $2L$ and width L within a computational domain of $4L \times 4L$ (height × length) where L = 0.072m. An obstacle block with geometry $h \times 2h$, where h = 0.024m is used in the experiment and numerical simulation, is located at the middle of the tank. A schematic view of the problem is shown in Figure 1. In this case, we set the immersed boundary coincide with the grid line. So the momentum forcing term is specified in a way to make the velocity magnitude to be equal to the immersed boundary velocity at these points. Base on the no-slip condition on immersed boundary, the velocity on these points should be zero. And then we can obtain the forcing term which satisfy the desired boundary conditions on the immersed boundary.

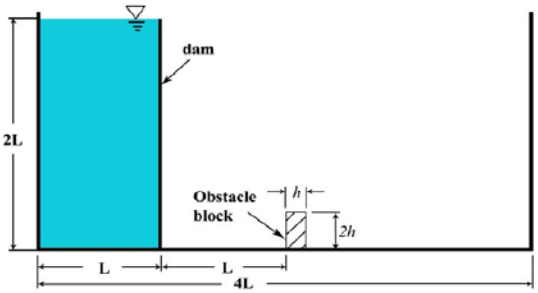

Figure 1 Sketch of dam break with a rectangular obstacle

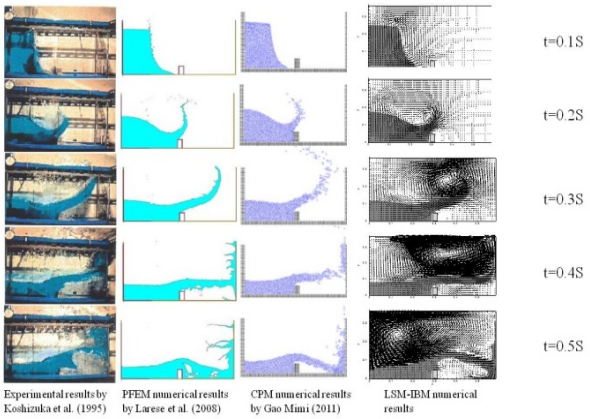

Figure 2 comparison of snapshot for the dam break with a rectangular obstacle

Figure 2 shows the water profiles at several time instants after dam breaks. The numerical results using LS-IBM agree well with the experimental results and look better than the other two numerical simulations.

4.2 Dam break past a circular obstacle

To further demonstrate the capability of LS-IBM in simulation of arbitrary bodies, another dam break example is presented in this section. We choose a circular obstacle that consists of many line segments of different slopes to verify the capability of the interpolation method. The computational domain is $4L \times 4L$ (height × length) and dam dimension is $2L \times L$ (height × width) where L = 0.6m. The radius of the circle is 0.19m and the position of the center is 0.6m away from the right side boundary and 0.26m above the bottom. A schematic view of the problem is shown in Figure 3.

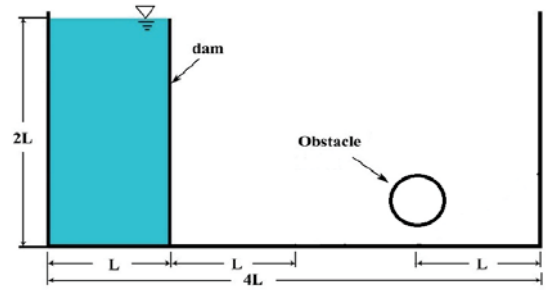

Figure 3 Sketch of dam break with a circular obstacle

In this case, the immersed boundary is not aligned with the grid plane which makes the problem more complicated. The momentum forcing term will act only on the points nearest to the immersed boundary. In order to render a velocity that is approximately equal to immersed boundary velocity for the forcing term, an interpolation for the momentum forcing is therefore required.

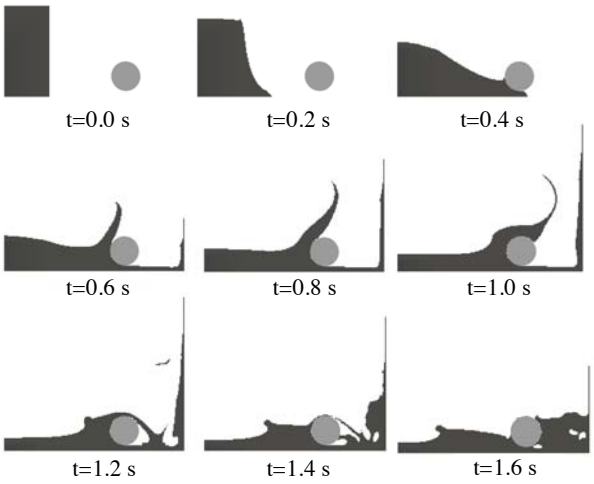

Figure 4 Water profiles at several time instants for dam breaking with a circle obstacle

Snapshots of this case are shown in Figure 4. Good performance can be seen. The results indicate that the interpolation method is correct and it can be implemented successfully for the fluid-structure interaction problem.

5 Conclusions

The Level-Set Immersed Boundary Method (LS-IBM) technique has been successfully implemented to simulate dam breaking with complex-shape obstacles. The results perform well and are in good agreement with the available experimental results, which show that the IBM is very robust for complicated geometries. Now, water entry of a moving body is being investigated, and some preliminary results have been obtained.

6 References

Enright, D, Fedkiw, R, Ferziger, J, Mitchell, I (2002). "A Hybrid Particle Level Set Method for Improve Interface Capturing," *J. Comput. Phys.*Vol 183, pp 83-116.

Fadlun E.A., Verzicco R., Orlandi P., Mohd-Yusof J., 2000. Combined immersed-boundary finite-difference methods for three-dimensional complex flow simulations. *J. Comput. Phys.* 61, 35-60.

Jiang, G-S, and Peng, D (2000). "Weighted ENO schemes for Hamilton-Jacobi Equations," *SIAM J. Sci. Comput.* Vol 21, No 6, pp 2216-2143.

Kang, M, Fedkiw, R.P. and Liu, X-D (2000). "A boundary condition capturing method for multiphase incompressible flow," *J. Sci. Comput.* Vol 15, pp 323-360.

Koshizuka, S., Tamako, H. and Oka, Y. (1995). A particle method for incompressible viscous flow with fluid fragmentation, *Computational Fluid Dynamic Journal*, 4(1), 29-46.

Larese, A., Rossi, R., Onate, E. and Idelsohn, S.R. (2008).Validation of the particle finite element method (PFEM) for simulation of free surface flows, *Engineering Computations*, 25, 385-425.

Mittal R. and Iaccarino G., 2005. Immersed boundary methods. Annual Review of Fluid Mechanics 37, 239-261.

Osher, S, and Fedkiw, R.P (2001). "Level set methods: An overview and some recent results," *J. Comput. Phys.* Vol 169, pp 463-502.

Peng, D, Merriman, B, Osher S, Zhao, H, Kang, M (1999). "A PDE-Based Fast Local Level Set Method," *J. Comput. Phys.*Vol 155, pp 410-438.

Sethian, J.A. (1996). A fast marching level set method for monotonically advancing fronts. *Proceedings of the National Academy of Science USA*. **93**: 1591-1595.

A comparaison of simulation approaches based on the Zakharov equations for nonlinear waves in the coastal zone

Michel Benoit[1], Marissa L. Yates[1], Florent Chazel[2]
[1]Université Paris-Est, Saint-Venant Laboratory for Hydraulics
ENPC, EDF R&D, CETMEF, 78400 Chatou, France
michel.benoit@saint-venant-lab.fr, marissa.yates-michelin@developpement-durable.gouv.fr

[2]INSA Toulouse
Institut de Mathématiques de Toulouse, 31077 Toulouse, France
florent.chazel@insa-toulouse.fr

Introduction

To model the propagation of nearshore waves, scientists and engineers have a need for accurate, rapid wave models that are capable of simulating wave fields over large spatial domains. Accurate models must also be capable of taking into account the nonlinear and dispersive effects of propagating waves, which are particularly important in the nearshore region.

A variety of models have been developed to address this need, ranging from models based on the mild slope equation for linear monochromatic waves to CFD approaches based on the Navier-Stokes equations for incompressible and turbulent flows, including models based on Boussinesq, Korteweg-DeVries, Serre, Green-Naghdi equations among others. The application of CFD models for modeling the nearshore zone is still largely limited by the size of the spatial domain due to the computational cost. Although these models are well-adapted to simulating wave-structure interactions at a local scale and wave breaking processes, alternative approaches are needed to model nearshore waves on larger spatial scales.

Potential wave models, based on the assumption of inviscid and irrotational flow, require the resolution of the Laplace equation in the fluid domain, with the correct specification of the boundary conditions. Fully nonlinear potential flow models have been developed following this approach, using boundary integral methods (e.g. [Grilli and Horrillo, 1999]) or finite differences (e.g. [Bingham and Zhang, 2007]) to obtain highly accurate results. The problem may be further simplified by assuming a form of the vertical structure of the flow, as in Boussinesq or Serre models, in which the computational domain has thus been reduced by one dimension. Boussinesq-type models were originally based on the assumptions of weak nonlinearity (ratio of wave height to wave length) and weak dispersive effects, limiting their range of application. However, significant developments in the last 25 years have allowed the extension of Boussinesq-type models to a include the effects of nonlinearity and dispersion to varying degrees.

Here, three different approaches for resolving the so-called Zakharov equations [Zakharov, 1968] in the case of variable bathymetry are compared for several test cases, two of them being presented hereafter: (i) the propagation and reflection from a wall of a solitary wave [Cooker et al., 1997] and (ii) the shoaling of a series of waves on a beach [Kennedy et al., 2001].

Overview of mathematical and numerical models

A three-dimensional domain $(\underline{x}, z)$ is considered, with a free surface elevation $z = \eta(\underline{x}, t)$ and a bottom boundary $z = -h(\underline{x})$, which are single-valued functions of $\underline{x}$. Assuming irrotational flow, the velocity potential $\phi(\underline{x}, z, t)$ satisfies the Laplace equation in the fluid domain:

$$\nabla^2 \phi = 0, \qquad -h(\underline{x}) \leq z \leq \eta(\underline{x}, t) \tag{1}$$

Following Zakharov [1968], the kinematic and dynamic surface nonlinear boundary conditions are formulated as:

$$\eta_t = -\nabla\eta \cdot \nabla\tilde{\phi} + \tilde{w}(1 + \nabla\eta \cdot \nabla\eta) \tag{2}$$

$$\tilde{\phi}_t = -g\eta - \frac{1}{2}\nabla\tilde{\phi} \cdot \nabla\tilde{\phi} + \frac{1}{2}\tilde{w}^2(1 + \nabla\eta \cdot \nabla\eta), \tag{3}$$

where $\tilde{\phi}(\underline{x},t) = \phi(\underline{x},\eta(\underline{x},t),t)$, and $\tilde{w}(\underline{x},t) = \frac{\partial\phi}{\partial z}|_{z=\eta}$ is the vertical velocity at the surface. By specifying lateral boundary conditions and choosing a method to calculate the gradients of ϕ and η, these two equations can be integrated in time once the vertical velocity at the surface $\tilde{w}(\underline{x},t)$ has been determined. The problem requiring attention is the method used to calculate $\tilde{w}(\underline{x},t)$, typically called Dirichlet-to-Neumann (DtN), and three different approaches are described here.

1. **Model A.** The first method requires discretizing the vertical (with NZ points to form $NL = NZ-1$ layers) to calculate ϕ in the entire domain using finite differences, following the approach of Bingham and Zhang [2007] and Engsig-Karup et al. [2009]. The vertical distribution of the points is defined by the zeros of Chebyshev-Gauss-Lobatto polynomials.
2. **Model B.** The second method is based on the spectral approach of Tian and Sato [2008], which expresses the vertical profile of ϕ as a linear combination of base functions (with NL being the maximum order of the polynomial), here defined to be the Chebyshev orthogonal polynomials of the first kind.
3. **Two-layer model.** The third approach is a two-layer Boussinesq-type model, developed by Chazel et al. [2009], with the vertical domain divided into two layers at the level $z = -\sigma h(\underline{x})$, with σ defined to be a constant. A DtN operator is defined at the still water level, $z = 0$, and two closure relations are determined via truncated Taylor expansions of the velocity potential and vertical velocity between the still water level and the free surface. The generalized Boussinesq procedure is followed by searching for a solution to the Laplace equation in each layer in the form of a truncated Taylor series expansion in the vertical, in which Padé approximants are used to lower the order of derivatives in the truncated series.

All spatial derivatives are calculated using fourth-order finite difference schemes, and all simulations are completed using a fourth-order Runge-Kutta integration scheme.

Results on two selected test cases

Propagation and reflection from a wall of a solitary wave

The first test case is based on the work of Cooker et al. [1997] and Grilli and Svendsen [1991], who simulated the run-up and reflection from a wall of solitary waves with relative wave heights of H/h (H=wave height) ranging from 0.075 to 0.7. The initial conditions of the simulations are given by the iterative method of Tanaka [1986] for a water depth of $h = 1$ m. The non-dimensional maximum run-up η_{max}/h and the time of maximum run-up $t_{\eta_{max}}/\tau$ (with $\tau = (h/g)^{1/2}$) for each run are compared with the results of Cooker et al. [1997] (Figure 1).

The values of maximum run-up simulated by the three models agree well with each other and with the reference data until a relative wave height of 0.4 (Figure 1a). With more highly nonlinear waves, the simulations with the two-layer model begin to diverge from the reference data, underestimating the maximum level of run-up. Models A and B continue to show similar results until the relative wave height reaches 0.65 and 0.6, respectively. Above these limits, the simulations diverge before the waves reach η_{max}. The simulated times of maximum run-up (Figure 1b) agree well with the reference data except for the most extreme values of relative wave height, indicating that the models are able to simulate well the phase speed of the waves, except for the most nonlinear cases at the limit at which the simulations diverge.

Shoaling of a series of waves on a beach

The second test case is based on the work of Kennedy et al. [2001], who modeled the shoaling of a series of waves up a beach until the breaking point. The initial condition at the free surface

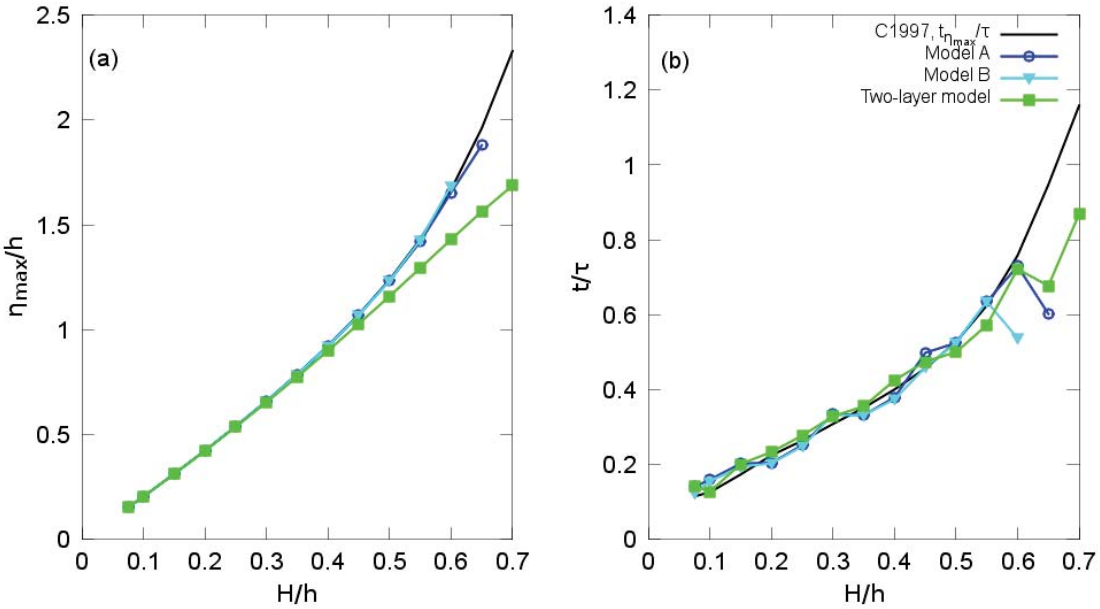

Figure 1: Comparison of (a) the maximum elevation of wave run-up and (b) the time that the wave reached the maximum run-up with the results of Cooker et al. [1997].

is defined by 10 sine waves of decreasing amplitude in the first half of the domain, with no initial velocity. When the simulations start, the waves begin propagating up the beach, and the simulations are stopped at a pre-defined time before wave breaking begins. Of the three cases evaluated by Kennedy et al. [2001], the results of the simulations with the most nonlinear waves, with a relative wave amplitude a/h=0.125 (a=wave amplitude), are presented here (Figure 2). The most difficult region to accurately simulate is the region of wave shoaling, from $x = 40$ m to $x = 60$ m, and the elevation of the maximum wave crests and minimum wave troughs is compared with the reference data of Kennedy et al. [2001].

For all three models, the simulation results depend highly on the horizontal resolution of the domain (Figure 2). Models A and B have nearly identical results, and an increase in the horizontal resolution from a constant $\Delta x = 0.1$ m to a variable $\Delta x = 0.025 - 0.1$ m enables both models to significantly improve the agreement with the reference data set. The two-layer Boussinesq model significantly underpredicts the maximum wave crest elevation with low horizontal resolution ($\Delta x = 0.2$ m). However, when the horizontal resolution is increased, instabilities develop and rapidly grow, causing the divergence of the model. It is necessary to apply a filter [Savitzky and Golay, 1964] for $\Delta x < 0.2$ m. Decreasing the resolution to $\Delta x = 0.11$ m does not improve the results as the application of the filter reduces the maximum crest heights.

These two test cases demonstrate the differences between the three strategies for resolving the Zakharov equations. Current work includes comparing the model simulations to laboratory observations of the propagation and shoaling of waves over a bar, and the result of additional cases will be presented during the Workshop.

References

H.B. Bingham and H. Zhang. On the accuracy of finite-difference solutions for nonlinear water waves. *J. Eng. Math*, 58:211–228, 2007.

F. Chazel, M. Benoit, A. Ern, and S. Piperno. A double-layer boussinesq-type model for highly nonlinear and dispersive waves. *Proc. Roy. Soc. London*, 2009.

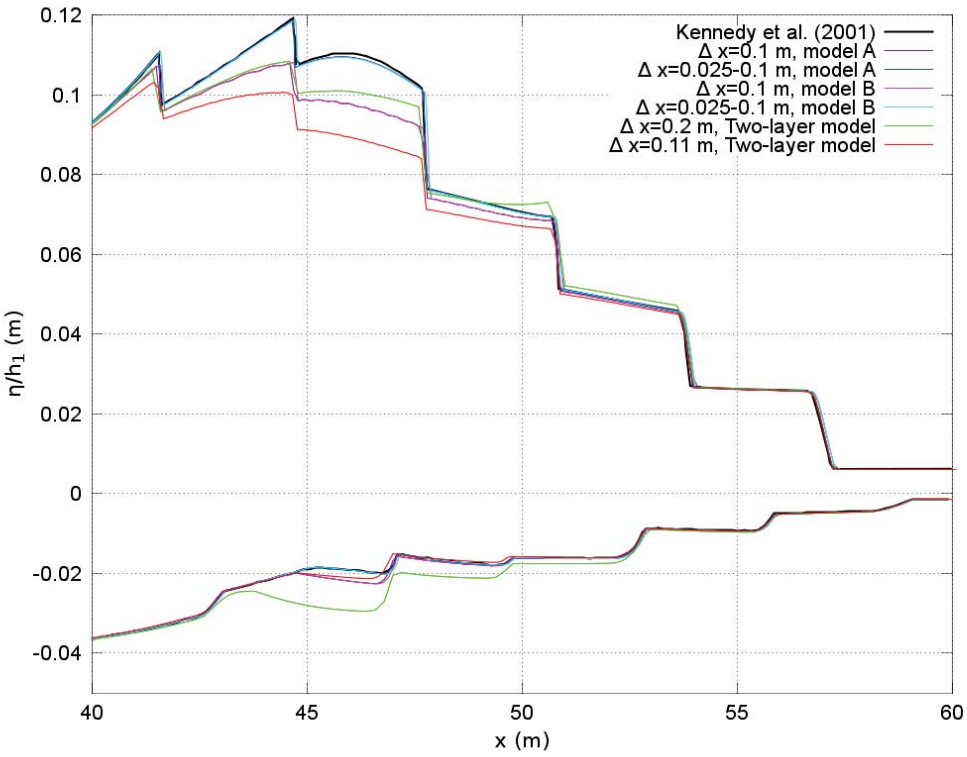

Figure 2: Comparison of the envelope of wave crests and wave troughs for the test case with a/h=0.125 with the results of Kennedy et al. [2001].

M.J. Cooker, P.D. Weidman, and D.S. Bale. Reflection of a high-amplitude solitary wave at a vertical wall. *J. Fluid Mech.*, 342:141–158, 1997.

A.P. Engsig-Karup, H. B. Bingham, and O. Lindberg. An efficient flexible-order model for 3D nonlinear water waves. *J. Comp.l Phys.*, 228:2100–2118, 2009.

S. T. Grilli and I. A. Svendsen. Long wave interaction with steeply sloping structures. In ASCE edition, editor, *Proc. 22nd Intl. Conf. on Coastal Engineering*, volume 2, pages 1200–1213, Delft, The Netherlands, 1991.

S.T. Grilli and J. Horrillo. Shoaling of periodic waves over barred-beaches in a fully nonlinear numerical wave tank. *Int. J. Offshore Polar Eng*, 9(4):257–263, 1999.

A.B. Kennedy, J.T. Kirby, Q. Chen, and R.A. Dalrymple. Boussinesq-type equations with improved nonlinear performance. *Wave Motion*, 33:225–243, 2001.

A. Savitzky and M.J.E. Golay. Smoothing and differentiation of data by simplified least squares procedures. *Anal. Chem.*, 36:1627–1639, 1964.

M. Tanaka. The stability of solitary waves. *Phys. Fluids*, 29(3):650–655, 1986.

Y. Tian and S. Sato. A numerical model on the interaction between nearshore nonlinear waves and strong currents. *Coast. Eng. Journal*, 50(4):369–395, 2008.

V.E. Zakharov. Stability of periodic waves of finite amplitude on the surface of a deep fluid. *J. Appl. Mech. Tech. Phys.*, 9(2):190–194, 1968.

A note on added resistance for slow ships *

Harry B. Bingham and Mostafa Amini Afshar†
Mech. Engineering, Tech. Univ. of Denmark
E-mail: hbb@mek.dtu.dk, maaf@mek.dtu.dk

Introduction

Rising fuel costs and increased environmental regulation of emissions, combined with a current over-capacity in the global shipping fleet, have provided a strong incentive for a dramatic reduction in the operating speed of cargo ships. In particular, many ships are routinely sailing at 10 knots and under these days, which translates to an engine load of as little as 10 to 20% of the design operating load. This trend towards slow and ultra-slow steaming is expected to continue, and thus lead to new ship designs with smaller engines and possibly auxiliary wind-propulsion systems. One consequence of slower design speeds and a reduction in installed engine power is an increased concern about the ship's ability to maintain maneuverability and escape a lee shore under heavy weather conditions. While the calm water resistance of a ship tends to increase at a rate proportional to ship speed raised to a high power (typically somewhere from 4 to 6), the added resistance due to waves generally increases only linearly with increasing ship speed. Thus the lower the design speed the more important an accurate prediction of the added-resistance becomes.

This abstract reviews the existing methods for predicting the added resistance of a sailing ship, and highlights the large uncertainties involved in both calculating and measuring this sensitive quantity. This serves to motivate a recently begun PhD project with the goal of an improved added resistance tool based on the high-order finite difference approach described by [9, 10], and references therein.

Methods for Computing Added Resistance

We adopt a Cartesian coordinate system $x_i = [x_1, x_2, x_3]$ with origin on the still water level and the x_3 axis vertically upwards. When a ship sails along the x_1 axis at a given speed U through calm water it experiences a constant force

$$F_1 = -R \tag{1}$$

where R is the calm water resistance. If the ship now sails through a seaway, it will experience an unsteady force in the x_1-direction $F_1(t)$. The mean value of this unsteady force over some time-period T is

$$\overline{F_1} = \frac{1}{T}\int_0^T F_1(t)\, dt = -(R + R_w + R_a) \tag{2}$$

where R_w is the added resistance due to waves and R_a is the added resistance due to wind which is typically at least an order of magnitude smaller than R_w.

There are basically three methods for predicting F_1:

1. **Near-Field Pressure integration:**

$$F_1 = \int_{S_b} p\, n_1\, dS \tag{3}$$

where p is the fluid pressure and n_1 is the x_1-component of the unit normal vector to the body surface S_b.

*The authors wish to thank the EU 7th Framework Programme (grant # 266030, ULYSSES) for funding, and the Danish Center for Scientific Computing for supercomputing resources.

†Presenting author

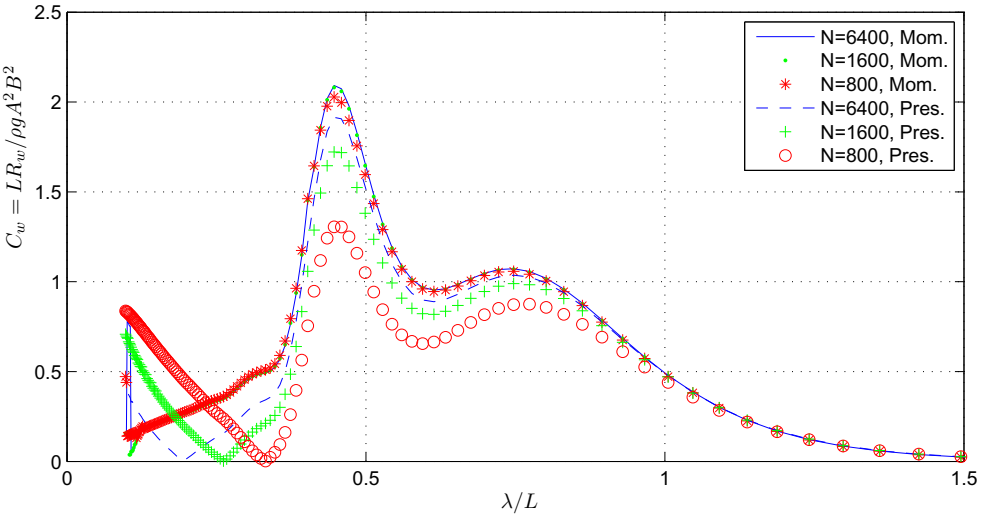

Figure 1: Convergence for calculations of the added resistance of a Wigley hull at zero forward speed using WAMIT and both near-field pressure integration and far-field momentum conservation.

2. **Momentum Conservation:**

$$F_1 = \int_{S_c} (p\, n_1 + \rho u_1\, n_i u_i)\, dS \tag{4}$$

where u_i is the fluid velocity vector and S_c is a control surface away from the body. Here the summation convention applies to repeated indices.

3. **Energy Conservation:** The work done by the ship on the undisturbed waves (per wave period) equals the average energy flux removed from the wave propagation direction and sent in other directions.

$$F_1[c + U\cos(\beta)] = \text{Ave. energy flux sent sideways.} \tag{5}$$

where c is the wave phase speed and β the wave heading angle measured from the x_1-axis.

Many particular forms for these relations have been derived over the years depending on the approximations and assumptions made, and on the numerical methods applied. Common to all forms however, is the assumption that higher-order potentials do not contribute to the mean force which can therefore be computed from the first-order solution alone. Most existing solutions are based either on the strip theory of Salvesen, Tuck & Faltinsen [12] or on 3D Boundary Element Methods (BEMs).

At zero forward speed, the added resistance (or drift force) can be robustly computed using 3D panel methods and either near-field pressure integration or far-field momentum conservation. However, much finer resolutions are required to show convergence for drift forces than are necessary for strictly linear quantities, at least when using near-field pressure integration methods. An example is shown in Figure 1 which shows the convergence of the drift force on a Wigley hull computed using the 3D BEM code WAMIT [8] and both near-field pressure integration and far-field momentum conservation. Here quantities have been non-dimensionalized using the fluid density ρ, the gravitational acceleration constant g, the ship length L and beam B, and the incident wave length λ and amplitude A. These results have been computed using the low-order (constant-strength flat panel) version of the code and N indicates the total number of panels on the hull. From this plot it is clear that the two methods are converging towards the same result

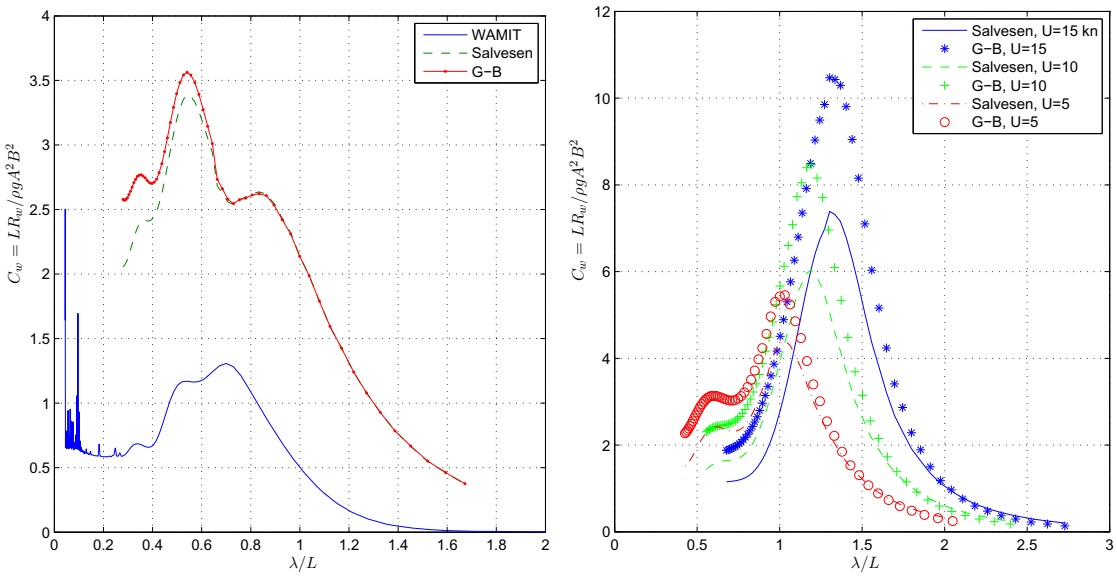

Figure 2: Added resistance calculations for a tanker hull at various forward speeds using strip theory methods.

for all relative wave lengths, but the momentum conservation method does so much faster than the pressure integration method.

At non-zero forward speed the situation is less satisfying. Two methods are widely applied to strip theory calculations: Salvesen's method based on near-field pressure integration [11]; and the energy conservation method first suggested by Gerritsma & Beukelmann [4]. Figure 2 shows an example of some converged strip theory calculations for a modern tanker hull at $U = 0, 5, 10$ and 15 knots calculated using these two methods. WAMIT results for $U = 0$ are also shown for reference. Clearly both methods fail completely when $U = 0$, which is not surprising since the main assumptions of strip theory are violated in this case. At non-zero forward speed, there is good agreement between the methods for where the peak response lies but the predicted magnitude of the force differs dramatically for all but the longest waves and can be almost a factor of two near the peak.

3D BEM methods are also available for computing added resistance at forward speed; based either on the time-domain free-surface Green function *e.g.* [6, 1] or on the Rankine Green function *e.g.* [7, 5]. These calculations show a reasonable agreement with experiments in the sense that uncertainties in the measurements can easily be a factor of two or more; but convergence of the calculations has so far not been demonstrated. Presumably the quadratic scaling of the solution effort with increasing resolution associated with BEM methods prevents a true demonstration of convergence for this sensitive quantity.

A High-Order Finite Difference Method for Added Resistance

Building on ongoing work discussed in [9, 10, 3, 2] we are developing a high-order finite difference solver for the linear forward speed problem, using both Neumann-Kelvin and double-body linearizations, which will also give predictions of added resistance. Due to the combination of high-order numerical accuracy and a linear scaling of the solution effort with increasing resolution, we hope to be able to show convergence for both pressure integration and momentum conservation methods. At this point we have validated the double-body flow solution and are currently implementing the radiation and diffraction solutions. Figure 3 shows the convergence of the double-body m-terms on a translating hemisphere along with a snapshot of the double-body surface elevation. The slopes of these convergence curves are approximately 4, consistent with the

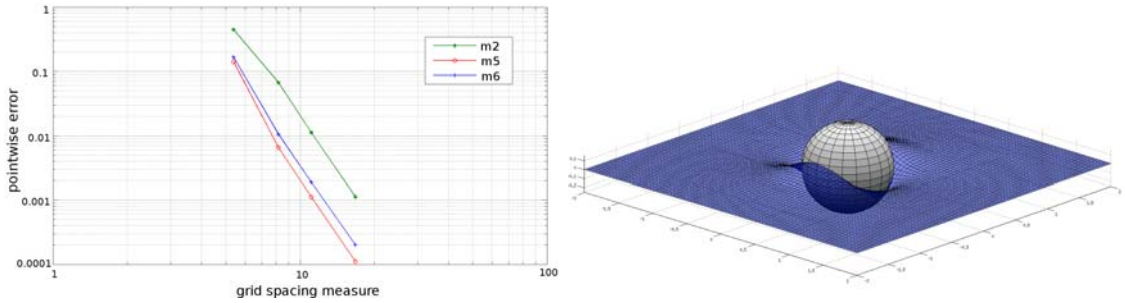

Figure 3: Convergence of the double-body m-terms on a sphere and a snapshot of the double-body free-surface elevation.

fourth-order finite-difference schemes used in this test case. Further results will be presented at the workshop.

References

[1] H. B. Bingham, F. T. Korsmeyer, and J. N. Newman. Predicting the seakeeping characteristics of ships. In 20^{th} *Symp. on Naval Hydrodynamics*, Santa Barbara, Ca, 1994. Office of Naval Res.

[2] H. B. Bingham and H. Zhang. On the accuracy of finite difference solutions for nonlinear water waves. *J. Engineering Math.*, 58:211–228, 2007.

[3] A. P. Engsig-Karup, H. B. Bingham, and O. Lindberg. An efficient flexible-order model for 3D nonlinear water waves. *J. Comput. Phys.*, 228:2100–2118, 2009.

[4] J. Gerritsma and W. Beukelman. Analysis of the resistance increase in waves of a fast cargo ship. Technical Report 334, Shipbuilding laboratory, Technological University - Delft, Delft, The Netherlands, 1971.

[5] S. A. Joncquez, P. Andersen, and H. B. Bingham. A comparison of methods for computing the added resistance. *J. Ship Res.*, 56(2):106–119, 2012.

[6] F. Kara. Time domain prediction of added resistance of ships. *J. Ship Res.*, 55(3):163–184, 2011.

[7] K.-H. Kim and Y. Kim. Numerical study on added resistance of ships by using a time-domain rankine panel method. *Ocean Engineering*, 38:1357–1367, 2011.

[8] J. N. Newman and C.-H. Lee. *WAMIT; A radiation-diffraction panel program for wave-body interactions*. WAMIT, Inc, Chestnut Hill, MA, U.S.A, 2009. http://www.wamit.com.

[9] R. Read and H. B. Bingham. An overset grid approach to linear wave-structure interaction. In 31^{st} *Intl. Conf. on Offshore Mech. and Arctic Eng.*, Rio di Janiero, Brazil, 2012.

[10] R. Read and H. B. Bingham. Solving the linear radiation problem using a volume method on an overset grid. In 27^{th} *Intl. Wrkshp. Water Waves and Floating Bodies*, Copenhagen, Denmark, 2012.

[11] N. Salvesen. Added resistance of ships in waves. *J. Hydronautics*, 12(1):21–34, 1978.

[12] N. Salvesen, E. O. Tuck, and O. Faltinsen. Ship motions and sea loads. *Soc. Nav. Arch. Mar. Eng., Trans.*, 78:250–287, 1970.

LAGRANGIAN MODELLING OF EXTREME WAVE GROUPS

E. V. Buldakov; Department of Civil Engineering, UCL, Gower Street, LONDON, WC1E 6BT, UK

SUMMARY

A 2D Lagrangian numerical wave model is presented and validated against a set of physical wave-flume experiments on focussed wave groups. The Lagrangian calculations demonstrate good agreement with experimental results. The model proves to be efficient in modelling both long-term wave propagation along the flume and strongly-nonlinear waves including initial stages of wave breaking.

1 INTRODUCTION

Numerical simulation of extreme ocean waves implies contradicting requirements to a model. It should be capable of both accurate modelling of long-term propagation of a dispersive wave and adequate representation of behaviour of strongly-nonlinear waves including wave breaking. The main difficulty of numerical solvers for modelling of extreme waves is strong deformation the computational domain. There are different ways of dealing with this problem. The most powerful models for simulation of strongly-nonlinear and breaking waves are based on a volume of fluid (VoF) method (e.g. de Jouëtte *et al.*, 1996). These models use a larger computational domain with cells not occupied by the fluid and introduce an artificial variable describing occupation of a cell. The boundary between fluid and air domains is not specified exactly but smoothed over several grid cells, which leads to considerable errors in the dispersion relation. Together with high requirements for computational resources this makes using VoF methods for modelling long-term processes impractical. The natural way of modelling strong deformations of a fluid domain is using equations of fluid motion in the Lagrangian form which though in some cases are more complicated than the Eulerian counterparts, to be solved in a fixed domain of Lagrangian labels. Lagrangian models are capable of efficient modelling of very steep and overturning waves and still have advantages for long-term runs since they follow water surface and produce smaller error in the dispersion relation. Some of the contemporary solvers use mixed approaches utilising certain elements of the Lagrangian description but they still do not exploit all its advantages. Mixed-Eulerian-Lagrangian (MEL) boundary-integral Boundary-integral methods (Longuet-Higgins & Cokelet, 1976; Tsai & Yue, 1996) use the linearity of inviscid irrotational Eulerian formulation and can not be used for flows with arbitrary vorticity. The smooth particle hydrodynamics (SPH) approach (e.g. Monaghan, 1994) though can be considered as fully Lagrangian is based on the artificial physical models and has no such a firm theoretical background as the straightforward numerical solution of Lagrangian equations. Surprisingly, the author could not find many published works where the fully-Lagrangian formulation would be used for solving water-waves problems. The rare example is the work of Protopopov (2007) who uses the formal transformation to Lagrangian coordinates for 2D Euler equations, suggests a numerical method for solving the resulting problem and applies it to selected free surface flows. In this paper the finite-difference technique is applied directly to Lagrangian equations of fluid motion. A 2D version of the inviscid finite difference Lagrangian numerical solver is introduced and applied for modelling of wave groups generated in a wave flume. By the complexity level the considered technique is comparable with potential Eulerian solvers and far simpler then SPH or VoF methods.

2 LAGRANGIAN 2D WATER-WAVE FORMULATION

We use a 2D inviscid fully-Lagrangian water-wave formulation presented in Buldakov *et al.* (2006) describing time evolution of Cartesian coordinates of fluid particles $x(a,c,t)$ and $z(a,c,t)$ as functions of Lagrangian labels (a,c). The formulation includes the Lagrangian continuity equation and the Lagrangian form of vorticity conservation

$$\frac{\partial(x,z)}{\partial(a,c)} = J(a,c)\,; \quad \frac{\partial(x_t,x)}{\partial(a,c)} + \frac{\partial(z_t,z)}{\partial(a,c)} = \Omega(a,c)\,, \tag{1}$$

and the dynamic free-surface condition

$$x_{tt}x_a + z_{tt}z_a + g\,z_a\,\big|_{c=0} = 0\,. \tag{2}$$

Functions $J(a,c)$ and $\Omega(a,c)$ are given functions of Lagrangian coordinates. $J(a,c)$ is defined by initial positions of fluid particles associated with labels (a,c). If initial positions of fluid particles are used as Lagrangian labels then $J=1$. $\Omega(a,c)$ gives the vorticity distribution and for an irrotational flow $\Omega=0$. Lagrangian formulation does not require the kinematic free-surface condition which is satisfied by specifying a fixed curve in the Lagrangian coordinates corresponding to the free surface, e.g. $c=0$. A specific problem within the general formulation is defined by boundary and initial conditions. Conditions describing a wave flume used in this paper are specified as follows. We use the rectangular Lagrangian domain with $c=0$ being the free surface and $c=-h$ being the bottom. The known shape of the bottom provides the condition on the lower boundary of the Lagrangian domain For the case of a flat bed of depth h we have $z=-h$. On the right boundary of the

Lagrangian domain $a = a_{\max}$ a given motion of a vertical wall represents the motion of a piston wavemaker: $x(a_{\max}, c, t) = a_{\max} + X_{\rm wm}(t)$, where $X_{\rm wm}(t)$ is a prescribed motion of the paddle, and we have a solid vertical wall on the left boundary $x(a_{\min}) = a_{\min}$. Positions and velocities of fluid particles must be supplied as initial conditions, e.g. still water conditions.

3 NUMERICAL MODEL

The problem formulated in the previous section is solved numerically using a finite-difference technique. Since equations (1) for internal points of the domain include only first order spatial derivatives a compact four-point Keller box scheme can be used for finite-difference approximation of these equations. Values of unknown functions x and z on the sides of the stencil box are calculated as averages of values at adjacent points and then used to approximate derivatives across the box by first-order differences. The scheme provides the second-order approximation for the central point and uses only 4 mesh points in the corners of the box which makes the resulting solver less demanding for memory resources. Time derivatives in (1) are approximated by second-order backward differences. Spatial derivatives in the free-surface boundary condition (2) are approximated by second-order central differences and special attention must be paid to approximation of second time derivatives since it defines the form of the numerical dispersion relation and is crucial for the overall stability of the scheme. For simplicity let us consider a case of continuous spatial field in (1-2) combined with discrete time approximation in (2). Let us approximate second derivatives by 3-point backward differences and expand this approximation to Taylor series with respect to a small time step τ. We get

$$(f(t-2\,\tau) - 2\,f(t-\tau) + f(t))/\tau^2 = f''(t) - \tau\,f'''(t) + O(\tau^2)\,. \tag{3}$$

The approximation is of the first order with the leading term of the error proportional to the third derivative of a function, which gives the main contribution to the error of the dispersion relation. Under an assumption of small perturbations we represent unknown functions in the form $x = a + \varepsilon\,\xi(a,c,t)$; $\quad z = c + \varepsilon\,\zeta(a,c,t)$ and keep only linear terms of expansions with respect to the small displacement amplitude $\varepsilon \to 0$. Introducing a displacement potential ϕ: $\eta = \partial\phi/\partial a$; $\quad \zeta = \partial\phi/\partial c$ we satisfy the vorticity conservation to the first order and the corresponding approximation of the continuity equation is the Laplace equation for ϕ. The dynamic surface condition (2) becomes

$$\phi_a'' + g\,\phi_{ac} - \tau\,\phi_a{}''' = O(\tau^2)\,, \tag{4}$$

where dashes denote time derivatives and only the leading term of the approximation error from (3) is taken into account. To derive the numerical dispersion relation we are looking for a solution in the form of a regular wave in deep water: $\phi = e^{i\,k\,a}\,e^{k\,c}\,e^{i\,\omega\,t}$, which satisfy the Laplace equation. The dynamic condition (4) is satisfied when a dispersion relation connecting ω and k is valid. Similar analysis can be performed for higher orders of approximation of the derivatives. Below is the summary of dispersion relations obtained for orders $n = 1 \ldots 4$:

$$\omega = \sqrt{gk}\,(\,\pm 1 + \tfrac{1}{2}\,i\,\hat\tau + O(\hat\tau^2)\,)\,; \qquad \omega = \sqrt{gk}\,(\pm 1 \mp \tfrac{11}{24}\,\hat\tau^2 + \tfrac{1}{2}\,i\,\hat\tau^3 + O(\hat\tau^4)\,)\,;$$
$$\omega = \sqrt{gk}\,(\,\pm 1 - \tfrac{5}{12}\,i\,\hat\tau^3 + O(\hat\tau^4)\,)\,; \quad \omega = \sqrt{gk}\,(\,\pm 1 \pm \tfrac{137}{360}\,\hat\tau^4 - \tfrac{19}{24}\,i\,\hat\tau^5 + O(\hat\tau^6)\,)\,.$$

Here we use a non-dimensional expansion parameter $\hat\tau = \sqrt{gk}\,\tau$. As can be seen, the first-order scheme (top left) introduces numerical viscosity proportional to $\hat\tau$ which leads to fast decay of perturbations and is not acceptable for long-term modelling. The higher-order schemes (second row) include terms proportional to $-i$, leading to grows of perturbations and making the numerical scheme unstable. We therefore use the second-order scheme (top right), which incorporates a numerical error to dispersion at the second order $\hat\tau^2$ and weak dissipation at the third order $\hat\tau^3$. The overall numerical scheme is therefore of the second order in both time and space.

A fully-implicit time marching is applied, and Newton iterations are used on each time step to solve nonlinear algebraic difference equations. To reduce calculation time the inversion of a Jacobi matrix during Newton iterations is made at a first iteration and when iterations start to diverge. Otherwise the previously calculated inverse Jacobi matrix is used. Usually only one inversion per each time step is required. An adaptive mesh is used in the horizontal direction with an algorithm based on the shape of the free surface in Lagrangian coordinates $z(a,0,t)$ to refine mesh at each time step in regions of high surface gradients and curvatures. Constant mesh refinement near the free surface is used in the vertical direction Convergence tests were performed for some of the cases. The scheme demonstrate convergence for all parameters: number of computational points in horizontal and vertical directions and time step. Compromising between accuracy and computational resources we use 201×21 computational mesh and 0.002 sec time step for most calculations in the paper, which required about 5 sec of computational time of a standard PC for each time step. For highly-nonlinear stages of flow with development of wave breaking a higher number of spacial points and a smaller time step were used.

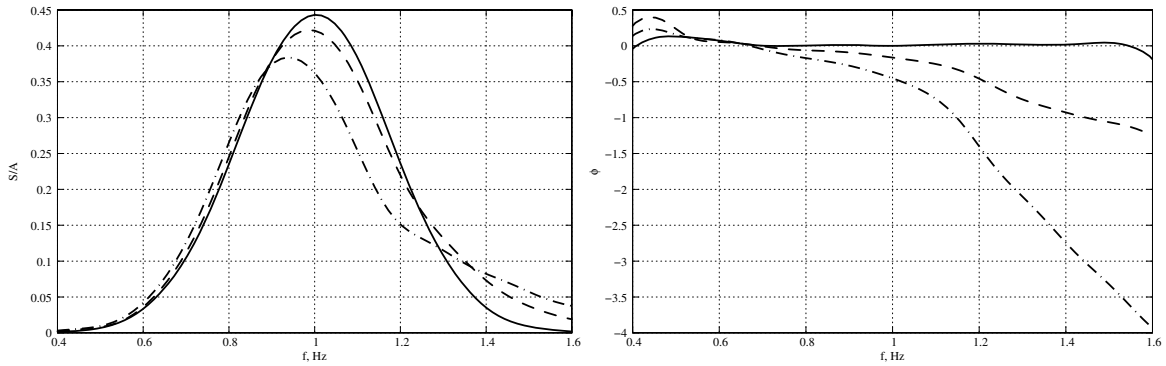

Figure 1: Linearised spectra of experimental wave groups at a focus point. Amplitude (left) and phase (right). Solid– $A = 2.5\,cm$; dashed– $A = 5\,cm$; dash-dotted– $A = 7.5\,cm$.

4 EXPERIMENTS

Experiments on generation and propagation of focussed wave groups were performed in a coastal wave flume of the Civil Engineering department at UCL. The flume has the width of $45\,cm$ and the length of the working section between two piston wavemakers is $12.5\,m$. A paddle on the right end of the flume is used as a wave generator and the opposite paddle as an absorber. Center of the flume is used as an origin of the coordinate system with the x-axis directed towards the wave generator positioned at $x = 6.25\,m$. Water depth over a horizontal bed of the flume was set to $h = 40\,cm$. The flume paddle uses a control system operating in frequency domain with force feedback which allows precise control and partial absorption of reflected waves. Input of the control system is the linearised amplitude spectrum of the generated wave at the center of the flume. The control system uses discrete spectrum and generates periodic paddle motions. For our experiments we use an overall return period of $64\,sec$, which is the time between repeating identical events produced by the paddle. Wave propagation was monitored by a series of resistance wave probes measuring surface elevation. Motion of the paddle had also been recorded. Each of experimental runs included 6 return periods. It was assumed that the periodic wave system with the return period of $64\,sec$ is established in the flume after the first period. The data for the first return period was neglected and the rest of the data was averaged between the following 5 periods. Each of the runs was repeated at least 3 times at and high level of repeatability was demonstrated. For each spectrum two waves with constant phase shift of π were generated: peak and through focussed waves. The corresponding data records were used for harmonic analysis of signals. Even harmonics were found as a half-sum of peak and trough focussed signals, and odd harmonics as their half difference (Taylor *et al.*, 2004). The dominating part of the odd-harmonic signal is due to a linear part of the spectrum. The form and the amplitude of the linearised spectrum completely define the wave. Our aim is therefore generating wave groups with a prescribed linearised spectrum focussed at $x = 0$. Paddle control does not account for dissipative and nonlinear effects, and a spectrum of an actually generated wave group differs from an input spectrum of the control system. We use the following iterative procedure to generate waves of desired spectrum focussed at the center of the flume:

$$a^n_{\rm in}(\omega) = a^{n-1}_{\rm in}(\omega)\, a_{\rm tgt}(\omega)/a^{n-1}_{\rm out}(\omega); \quad \phi^n_{\rm in}(\omega) = \phi^{n-1}_{\rm in}(\omega) + (\,\phi_{\rm tgt}(\omega) - \phi^{n-1}_{\rm out}(\omega)\,)\,, \tag{5}$$

where $a^n_{\rm in}(\omega)$ and $\phi^n_{\rm in}(\omega)$ are input amplitude and phase of the spectral component at frequency ω for iteration n; $a^n_{\rm out}(\omega)$, $\phi^n_{\rm out}(\omega)$ are amplitudes and phases of the corresponding spectral components of a linearised spectrum of a generated wave at the center of the flume (focus point), and $a_{\rm tgt}(\omega)$, $\phi_{\rm tgt}(\omega)$ are target spectral components. We applied the iterative procedure (5) to generate a Gaussian wave group with peak frequency of $1\,Hz$ focussed at the center of the flume and having linear focus amplitude of $2.5\,cm$. Then we use the same input spectrum to generate higher amplitude waves with linear focus amplitudes A of 5 and $7.5\,cm$. The resulting waves are of tree distinct types: weakly non-linear, moderately non-linear and strongly non-linear breaking waves. Their linearised spectra at $x = 0$ are shown on figure 1. As can be expected, non-linear defocussing and transformation of linear spectrum can be observed for higher amplitude waves.

5 RESULTS

The numerical Lagrangian model introduced in Sections 2,3 have been used to simulate wave flume experiments described in the previous section. Parameters of calculations correspond to experimental parameters and linearised experimental records of motion of a wave generator had been used to generate waves in the numerical wave flume. Figure 2 demonstrates the excellent comparison between experimental and computational results for amplitude spectrum and time history of surface elevation at the focus point $x = 0$ for a moderately steep

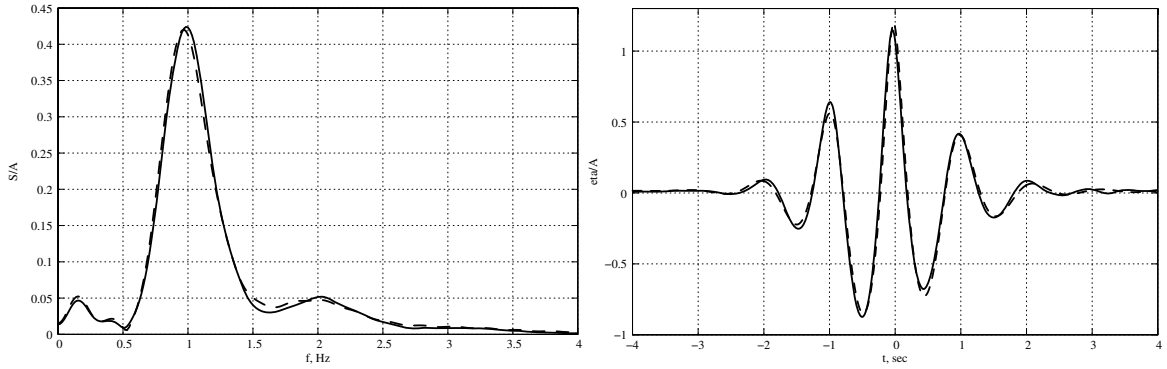

Figure 2: Comparison of experimental (solid) and calculated (dashed) results for surface elevation at $x = 0$ for a wave group with $A = 5\,cm$. Left– full amplitude spectrum; right– time history.

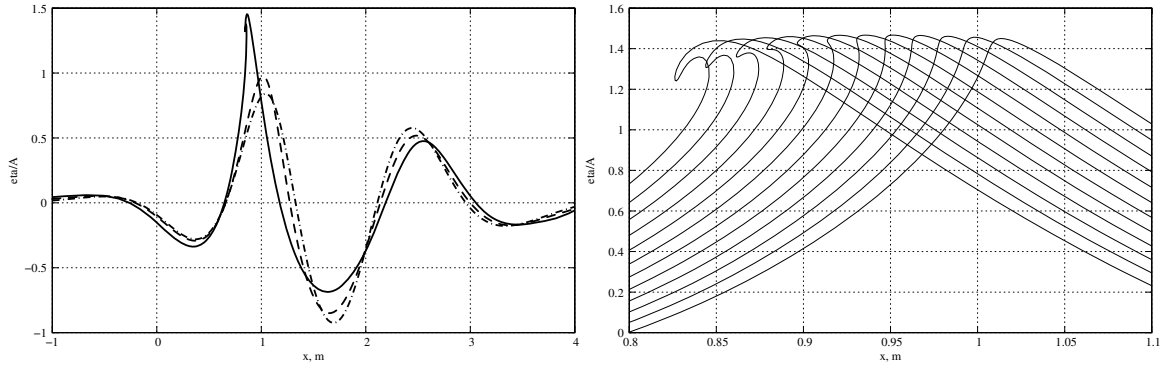

Figure 3: Left: wave profiles for wave groups of different amplitudes at $t = -1.7\,sec$. Right: development of a micro-plunger at the crest of a breaking wave starting from $t = -1.8\,sec$, time between profiles is $0.01\,sec$.

wave of $A = 5\,cm$. Wave generation process starts approximately $10\,sec$ before the linear focus time $t = 0$ and the distance between the focus point and the wave generator is $6.25\,m$. We therefore can see that the model is capable of adequate modelling of propagation of nonlinear dispersive waves for time scales of several periods and length scales of several wave lengths. For a high amplitude wave ($A = 7.5\,cm$) wave breaking was observed in the experiment. Modelling of spilling breaking is beyond the capability of the current version of the Lagrangian solver and the computational process for this wave breaks down at $t \approx -1.7\,sec$. However, as can be seen from Figure 3 the model generates a realistic near-breaking profile with developing a micro-plunger at the wave crest. These results can give valuable information on kinematics of pre-breaking wave which can be used for calculating loads of such waves on structures. To conclude, the Lagrangian numerical model provides a powerful and effective tool for modelling strongly-nonlinear waves. The model demonstrates good agreement with experiments. It is efficient in modelling both long-term wave propagation along the flume and developing of extreme waves including initial stages of wave breaking.

References

Buldakov, E. V., Eatock Taylor, R. & Taylor, P. H. 2006 New asymptotic description of nonlinear water waves in Lagrangian coordinates. *J. Fluid Mech.* **562**, 431–444.

Longuet-Higgins, M. S. & Cokelet, E. D. 1976 The deformation of steep surface waves on water. I. A numerical method of computation. *Proc. R. Soc. Lond. A.* **350**, 1–26.

de Jouëtte, C., Gouez, J. M. L., Put, O. & Rigaud, S. 1996 Volume of fluid method (VOF) applied to non-linear wave problems on body-fitted grids. In *11th International Workshop on Water Waves and Floating Bodies*. Hamburg, Germany.

Monaghan, J. J. 1994 Simulating free surface flows with SPH. *Journal of Computational Physics* **110**, 399–406.

Protopopov, B. E. 2007 Computation of wave motions of fluid using euler's equations. *Computational Technologies* **12** (1), 82–92, (in Russian).

Taylor, P., Hunt, A., Borthwick, A. & P.K.Stansby 2004 Phase inversion and the identification of harmonic structure in costal engineering experiments. In *29th International Conference on Coastal Engineering*. Lisbon, Portugal.

Tsai, W. & Yue, D. K. P. 1996 Computation of nonlinear free-surface flows. *Ann. Rev. Fluid Mech.* **28**, 249–278.

Extreme wave run-up on a vertical cliff

Francesco Carbone[1], Denys Dutykh[1], John M. Dudley[2], Frédéric Dias[1]

[1] *School of Mathematical Sciences, University College of Dublin, Ireland,*

[3] *Institut FEMTO-ST, UMR 6174 CNRS-Université de Franche-Comté, Besançon, France*

The notion of *design wave* is usually used by engineers to dimension various coastal structures[7], even if there is a difficulty in determining the wave height to be used in semi-empirical formulas for the pressure field. In general, by considering an idealized simple monochromatic wave component with amplitude a_0, its wave height can be trivially computed to be $H_0 \sim 2a_0$, and consequently the design wave. Here we show that even a simple monochromatic sea state, subject to nonlinear dynamics on the flat bottom, can produce much higher amplitudes on a vertical wall. This suggests that the concept of design wave has to be revisited. Moreover, recalling that 89% of reported past freak wave events happened in shallow waters or coastal areas[9], our work can shed some light onto the extreme wave events in the shallow water regime.

One of the most important questions in water wave theory is the understanding of wave interaction and reflection. We describe the wave propagation of the free surface of an incompressible homogeneous inviscid fluid, through the fully nonlinear Serre–Green–Naghdi (SGN) equations[8,12]. We consider a two-dimensional wave tank with a flat impermeable bottom of uniform depth $d = \text{const}$, which is filled with an incompressible, inviscid fluid. The Cartesian coordinate system Oxy is chosen such that the axis Oy points vertically upwards and the horizontal axis Ox coincides with the undisturbed water level $y = 0$.

The SGN system reads[2,4]:

$$h_t + (hu)_x = 0, \tag{1}$$

$$u_t + \left(\tfrac{1}{2}u^2 + gh\right)_x = \tfrac{1}{3}h^{-1}\Big[h^3\big(u_{xt} + uu_{xx} - u_x^2\big)\Big]_x, \tag{2}$$

where $h(x,t) := d + \eta(x,t)$ is the total water depth ($\eta(x,t)$ being the free surface elevation with respect to the water level), while $u(x,t)$ is the depth-averaged horizontal velocity, g is the gravity acceleration. The model has been previously validated by extensive comparisons with experimental data for wave propagation and run-up[5].

In our numerical experiments we consider a flat channel of length ℓ, bounded on the right by a rigid vertical wall and by a wavemaker on the left. Hereinbelow we will use the dimensionless variables in which all the lengths are normalized with d, speeds with $\sqrt{gd}$ and time with $\sqrt{d/g}$. This scaling is equivalent to setting $g = 1$ $\mathsf{m/s^2}$, $d = 1$ m in the governing equations (1), (2).

In order to solve numerically the SGN equations we use a high-order finite-volume scheme[5], while for time integration we use the fourth-order Runge–Kutta scheme. The computational domain is divided into equal intervals (i.e. control volumes) such that we have $N = 1000$ control volumes per wavelength. The initial conditions are the state of rest $\eta(x, t = 0) \equiv 0$, $u(x, t = 0) \equiv 0$. On the wavemaker we generate a monochromatic incident wave $\eta(x = 0, t) = \eta_0(t) = a_0 \sin(\omega t)\mathcal{H}(T - t)$, where T represent the final generation time and the amplitude is fixed to the value $a_0 = 0.05$, $\omega \in [0.01,\ 0.25]$, and $\mathcal{H}(t)$ is the Heaviside function. We generate only a finite number N_w of waves with period $T_0 = 2\pi/\omega$, say $T := N_w T_0$. The length ℓ of the computational domain and the final simulation time T_f are

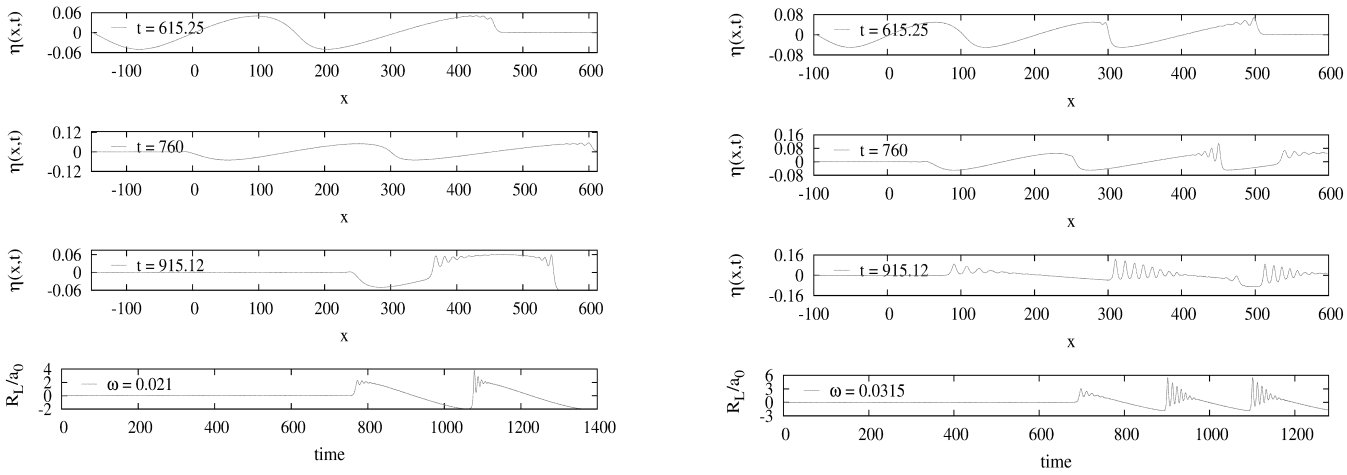

FIG. 1. Time evolution of the free surface elevation as a function of space, at three different times, left column two-wave case, right column three-wave case. The lower panel reports the maximal elevation at the wall $\mathcal{R}_\ell/a_0$ as a function of time.

chosen adaptively in order to allow all important interactions and to prevent any kind of reflections with the left generating boundary:

$$\ell = (N_w + \tfrac{1}{2})\lambda_0, \quad T_f = \frac{\ell}{\sqrt{g(d+a_0)}} + T, \tag{3}$$

λ_0 being the wavelength corresponding to the frequency ω.

We begin our experiments by considering a single sinusoidal wave interacting with the solid wall. The maximal wave elevation $\mathcal{R}_{\max} \simeq 0.10245$ on the wall reaches roughly twice the incident wave amplitude $a_0 = 0.05$ (at $t \simeq 70$). This result is in a good agreement with previous numerical studies on solitary waves interactions[1,3,10] even if the incident shape is not exactly the same. The maximal relative run-up $\mathcal{R}_{\max}/a_0 \simeq 2.34$ is achieved for $\omega_{\max} = 0.145$. The value of $\mathcal{R}_{\max}$ is slowly decreasing for $\omega > \omega_{\max}$.

The dynamics of two waves injected into the domain is similar to the single wave case, but the nonlinear effects become even more apparent (see Figure 1). In a certain range of wave periods ($\omega \in (0.01, 0.05)$), when the second wave impinges on the first reflected wave, a so called dispersive shock wave forms and propagates towards the wall[6,11]. The maximal amplification is achieved when the second wave hits the wall (cfr. last panel of Figure 1), an effect due to nonlinear interactions between two counter-propagating waves:

$$\mathcal{R}_{\max}/a_0 \simeq 3.8, \quad \text{for} \quad \omega = 0.021. \tag{4}$$

High run-up values are possible due to the energy transfer between the first reflected wave and the second incoming wave.

The three regimes (hyperbolic, equilibrium and dispersive) are described on Figure 2, where we show the space-time dynamics of the three-wave system. The left panel shows the hyperbolic regime, on the central panel strong dispersive shocks can be observed, while on the right panel the dynamics is smooth due the dispersion. In the last case the amplification is mainly produced by the linear superposition of the incident and reflected waves. The reflection and interaction are clearly observed by smooth secondary peaks in the space time plots (see Figure 2). Wave interactions described above depend strongly on the frequency

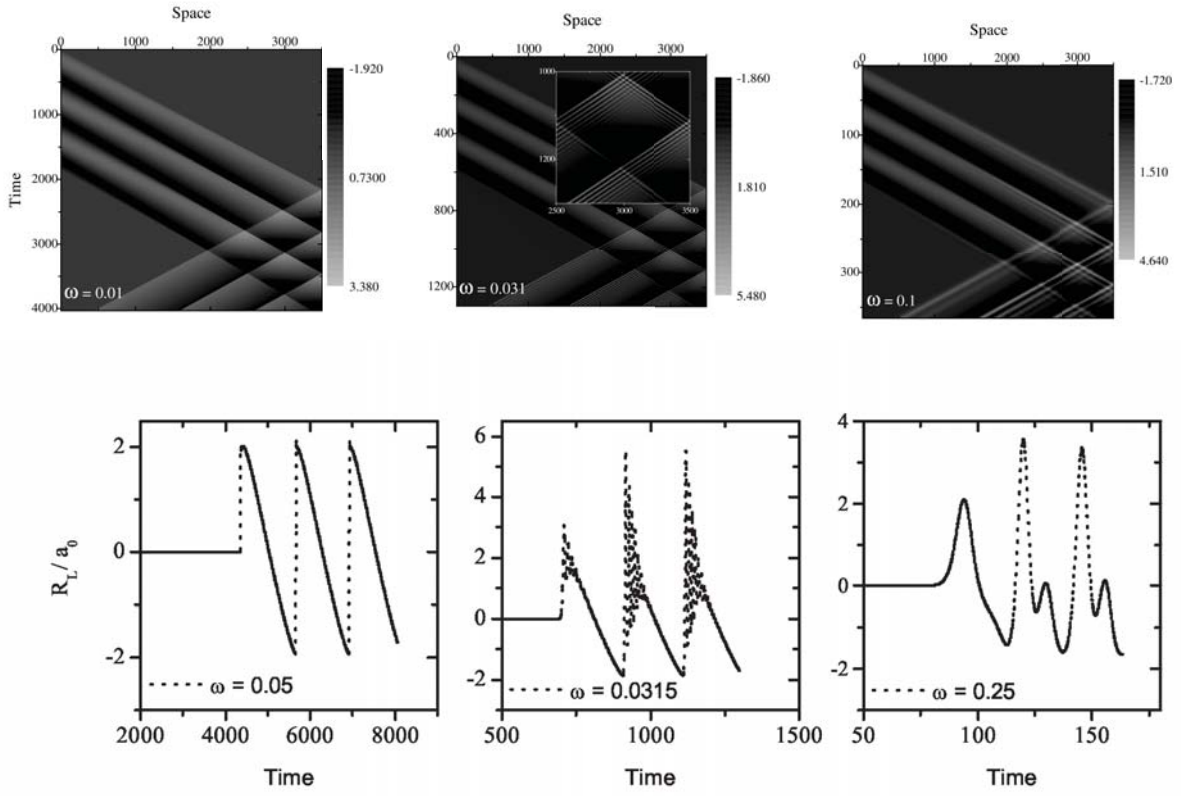

FIG. 2. Upper row space-time evolution plots for three incident waves case shown for three particular values of the wave frequency ω, lower row Time evolution of the wave run-up on the vertical wall for the three incident waves case recorded for several values of the incoming frequency ω. The maximum run-up is achieved for $\omega_{\max} \approx 0.0315$.

ω of the impinging waves. The dependence of the maximal run-up $\mathcal{R}_{\max}$ on the incident wave frequency ω and the number N_w of incident waves is shown on Figure 3, the optimal energy transfer due to dispersive shocks happens for three incident waves. In this case the maximal run-up is observed around $\omega_{\max} = 0.035$ and the amplification is equal to ${}^{R_{\max}}/_{a_0} \simeq 5.43$. However, the energy transfer process is saturated for three waves. As the wave frequency increases, the wavelength shortens and the dispersive effects become gradually more important. Around $\omega_{\max}$ the dispersive effects are balanced with nonlinearities to produce the most pronounced dispersive shock waves. Starting from $\omega \simeq 0.11$ waves become smooth due to dispersive regularization.

More general wave groups have to be studied in future investigations to unveil their potential for focussing on the walls. In addition, we are going to investigate the effect of the forces exerted by incident waves on vertical obstacles, which can be different from the purely kinematic amplitude focussing presented in this study. In other words, it is not clear whether the highest wave will produce the highest dynamic pressure spike on the wall. The effect of the wave amplitude is to be investigated as well since all the processes under consideration are highly nonlinear. Some theoretical explanation of these phenomena is also desireable. However, the difficulty is rather high because of important nonlinearities

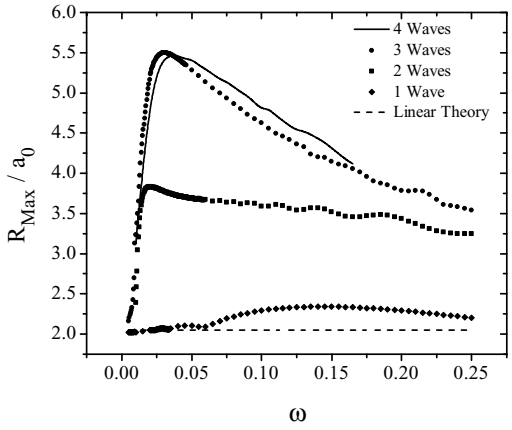

FIG. 3. Maximum wave run-up $\mathcal{R}_{\max}/a_0$ on the right vertical wall as a function of incoming wave frequency for different numbers of incident pulses: 1 (squares), 2 (circles), 3 (triangles) and 4 (solid line). The dashed line represents the linear limit where $\mathcal{R}_{\max}/a_0 \equiv 2$.

mentioned hereinabove. We claim that no linear theory is sufficient to provide a satisfactory explanation of the reported phenomenon.

[1]Chambarel, J., C. Kharif, and J. Touboul, Head-on collision of two solitary waves and residual falling jet formation, *Nonlin. Processes Geophys.*, *16*, 111–122, 2009.

[2]Clamond, D., and D. Dutykh, Practical use of variational principles for modeling water waves, *Physica D: Nonlinear Phenomena*, *241*(1), 25–36, doi:10.1016/j.physd.2011.09.015, 2012.

[3]Cooker, M. J., P. D. Weidman, and D. S. Bale, Reflection of a high-amplitude solitary wave at a vertical wall, *J. Fluid Mech.*, *342*, 141–158, 1997.

[4]Dias, F., and P. Milewski, On the fully-nonlinear shallow-water generalized Serre equations, *Physics Letters A*, *374(8)*, 1049–1053, 2010.

[5]Dutykh, D., D. Clamond, P. Milewski, and D. Mitsotakis, An implicit-explicit finite volume scheme for fully nonlinear Serre equations, *Submitted*, 2011.

[6]El, G. A., R. H. J. Grimshaw, and N. F. Smyth, Unsteady undular bores in fully nonlinear shallow-water theory, *Phys. Fluids*, *18*, 27,104, 2006.

[7]Goda, Y., New wave pressure formulae for composite breakers, in *Proc. 14th Int. Conf. Coastal Eng.*, pp. 1702–1720, 1974.

[8]Green, A. E., and P. M. Naghdi, A derivation of equations for wave propagation in water of variable depth, *J. Fluid Mech.*, *78*, 237–246, 1976.

[9]Nikolkina, I., and I. Didenkulova, Rogue waves in 2006 - 2010, *Nat. Hazards Earth Syst. Sci.*, *11*, 2913–2924, doi:10.5194/nhess-11-2913-2011, 2011.

[10]Pelinovsky, E. N., E. Troshina, V. Golinko, N. Osipenko, and N. Petrukhin, Runup of tsunami waves on a vertical wall in a basin of complex topography, *Phys. Chem. Earth. (B)*, *24*(5), 431–436, 1999.

[11]Wei, G., J. T. Kirby, S. T. Grilli, and R. Subramanya, A fully nonlinear Boussinesq model for surface waves. Part 1. Highly nonlinear unsteady waves, *J. Fluid Mech.*, *294*, 71–92, 1995.

[12]Zheleznyak, M. I., and E. N. Pelinovsky, Physical and mathematical models of the tsunami climbing a beach, in *Tsunami Climbing a Beach*, edited by E. N. Pelinovsky, pp. 8–34, Applied Physics Institute Press, Gorky, 1985.

The impact of a fractionally (viscoelastic) damped system onto the water free surface

Leonardo Casetta*, Guilherme R. Franzini, and Celso P. Pesce
lecasetta@gmail.com, gfranzini@usp.br, ceppesce@usp.br

Offshore Mechanics Laboratory - LMO, Escola Politécnica, University of São Paulo, Brazil

1 Introduction

Since the pioneering works of von Karmán [1] and Wagner [2], who were originally motivated by the landing of seaplanes, considerable effort has been made toward the comprehension and formulation of the physical phenomena which govern the impact of structures onto a liquid surface. It is well-known that the formal treatment of this problem is embedded in a great variety of difficulties which appear in both theoretical and experimental approaches. From a practical point of view, the water impact can be seen as the cornerstone for the analysis of important problems in ship dynamics and offshore engineering (see [3]). For this reason, interests on the subject are recursively renewed in accordance with the current necessities of technology and industry. From sixties to present, for instance, the hydroelastic behaviour of impacting marine structures has received a special attention when regarding design and safety (see [3], [4], [5]). Likewise, recent advances in modern engineering have revealed that viscoelastic materials play an important role on dissipation of vibration, active noise control and stability, particularly of fast boats and floating structures (see [6], [7]). In this sense, the present work aims at theoretically addressing the impact of a viscoelastic damped system onto a liquid surface. As analogously pointed out for the elastic case (see [5]), it is believed that the upcoming discussion might help with the understanding of important features of the structural water impact response when taking a viscoelastic damper. In this sense, fractional calculus is evoked to model viscoelastic effects (see [8], [9]). Additionally, physical insights from such coupled dynamics, which appears from the combination of the hydrodynamic impact force with the fractional-order dissipation term, are to be exposed. This article presents the preliminary results of an ongoing research which aims at bridging the water impact problem, as well as the following fluid-structure interaction, to the advances of fractional-order mechanics of the twentieth century. It was originally motivated by the current studies on the impact of an elastic system onto the water free surface (see [3], [4], [5]).

2 Fractional-order derivatives and viscoelastic theory

Fractional calculus deals with the uncustomary derivatives of non-integer order, which are named fractional derivatives (see [8]). In the treatment of mechanical systems, Caputo's definition is rather preferable for physical reasons, that is, if $0 < \alpha < 1$, the α- order derivative of $f = f(t)$, named $D^\alpha f$, is given as

$$D^\alpha f(t) = \frac{1}{\Gamma(1-\alpha)} \int_0^t \frac{df(\tau)}{d\tau} \frac{d\tau}{(t-\tau)^\alpha} \tag{1}$$

where Γ is the gamma function.

Eq. 1 can be used to model the viscoelastic damping force F_v by means of the constitutive relation

$$F_v = cD^\alpha \delta \tag{2}$$

where δ is the displacement, and c and α are constants which depend on the viscoelastic material.

3 Mathematical formulation

Let us consider the vertical water entry of two rigid spheres of radius R that are connect by a viscoelastic material; that is, $0 < \alpha < 1$ applies on Eq. 2 (see Fig. 1(a)). Analogously to [4], [5], the equations of motion[1] follow from Newton's law:

$$m_1 \ddot{z_1} + cD^\alpha \delta + F_h = 0 \tag{3}$$

$$m_2(\ddot{z_1} - \ddot{\delta}) - cD^\alpha \delta = 0 \tag{4}$$

*Corresponding author.

[1] Note that the mass matrix renders non symmetric due to the adoption of the relative motion as generalized coordinate.

For the sake of simplicity of such preliminary analysis, the hydrodynamic impact force F_h, which acts on the sphere that touches water free surface, is written from the linearized Wagner's approach,

$$F_h(z_1, \dot{z_1}) = \frac{d}{dt}(M(z_1)\dot{z_1}), \quad M(z_1) = 4\sqrt{3}\rho(Rz_1)^{3/2} \tag{5}$$

where ρ is the density of the water and $M(z_1)$ is the added mass of the impacting body; see discussions on its proper definition in [10].

4 On energy distribution

As it has been addressed, the distribution of energy during water entry is an important point to be discussed. The initial kinetic energy of the solid system, that is, $T_s(0) = \frac{1}{2}(m_1 + m_2)v_0^2$, where v_0 is the velocity at the instant of impact, is not entirely transmitted to the bulk of liquid, once it is partially drained to spray jets and partially dissipated due to the viscoelastic damping. This implies the following energy balance $T_s(t) + T_b(t) + T_j(t) + \Im(t) = T_s(0)$, where $T_b(t) = \frac{1}{2}M(z_1(t))\dot{z_1}^2(t)$ is the kinetic energy of the bulk of liquid, $T_j(t) = \int_0^t \frac{1}{2}\frac{dM(z_1(\tau))}{d\tau}\dot{z_1}^2(\tau)d\tau$ is the kinetic energy that is drained to spray jets (see [10]), and $\Im(t) = \frac{1}{2}c(D^{\alpha/2}\delta(t))^2$ is the energy that is dissipated by the viscoelastic connection (see [8]).

5 Numerical simulations

A simple Euler's numerical scheme was found to be suitable to integrate the system of ordinary fractional differential equations, which is given by Eqs. (3) and (4), and so to furnish the time history of the physical quantities in in the energy balance (see Figs. 1(b) - 1(f)). In nondimensional form, Eqs. (3), (4) and the energy balance are respectively written as

$$\ddot{\bar{z_1}} + \frac{\gamma}{1+\lambda(\bar{z_1})}\bar{D}^{\alpha}\bar{\delta} + \frac{1}{\beta+\mu(\bar{z_1})}\frac{d\mu(\bar{z_1})}{d\bar{z_1}}\dot{\bar{z_1}}^2 = 0 \tag{6}$$

$$(\ddot{\bar{z_1}} - \ddot{\bar{\delta}}) - \kappa\gamma\bar{D}^{\alpha}\bar{\delta} = 0 \tag{7}$$

$$\phi_s + \phi_b + \phi_s + \psi = 1 \tag{8}$$

with the following nondimensional variables and parameters: $\mu(\bar{z_1}) = (3\sqrt{3}/\pi)\bar{z_1}^{3/2}$, $\lambda(\bar{z_1}) = \mu(\bar{z_1})/\beta$,
$\phi_s = T_s/T_s(0) = \frac{\kappa\ddot{z_1}^2 + (\dot{z_1} - \dot{\bar{\delta}})^2}{(\kappa+1)}$, $\phi_b = T_b/T_s(0) = \frac{3\kappa\sqrt{3}}{\pi\beta(\kappa+1)}\bar{z_1}^{3/2}\dot{\bar{z_1}}^2$,
$\phi_j = T_j/T_s(0) = \frac{9\kappa\sqrt{3}}{2\pi(1+\kappa)}\int_0^t \dddot{\bar{z_1}}(\tau)\sqrt{\bar{z_1}(\tau)}d\tau$, $\psi = \Im/T_s(0) = \frac{\kappa\gamma}{\kappa+1}(\bar{D}^{\alpha/2}\bar{\delta})^2$

$\beta = \rho_1/\rho$, $\gamma = (cv_0^{\alpha-2})/(m_1R^{\alpha-2})$, $\kappa = m_1/m_2 = \rho_1/\rho_2$, $\bar{z_1} = z_1/R$, $\bar{\delta} = \delta/R$, $\dot{z_1} = d\bar{z_1}/d\bar{t} = (dz_1/dt)/v_0$, $\ddot{\bar{z_1}} = d^2\bar{z_1}/d\bar{t}^2 = R/v_0^2(d^2z_1/dt^2)$, $\ddot{\bar{\delta}} = d^2\bar{\delta}/d\bar{t}^2 = R/v_0^2(d^2\delta/dt^2)$, $\bar{D}^{\alpha}\bar{\delta} = R^{\alpha-1}/v_0^{\alpha}(D^{\alpha}\delta)$.

ρ_1 and ρ_2 are respectively the density of spheres 1 and 2.

6 Discussion

This paper presented some initial considerations concerning the inclusion of fractional-order effects within the study of the water impact problem. A preliminary parametric study was carried out by varying α, the fractional-order of the derivative, in the range of $[0, 1[$, keeping $\kappa = 1$, $\beta = 0.1$ and $\gamma = 10$ as fixed. Fig 1(b) shows the acceleration time history of the impacting sphere, penetrating the water surface, for six distinct values of α. It is interesting to notice that, despite the nonlinear nature of Eqs. (6) - (7), the acceleration peak exhibits a weak dependence on α, yet decreasing in intensity as α increases. This is clearer presented in Fig. 1(c), where the acceleration peak is plotted as function of α. However, the oscillatory character of the dynamic response, which occurs just after the acceleration peak, strongly depends on α. This is physically reasonable since the fractional-order dissipation can be seen as lying in the transition region from the purely elastic case, $\alpha = 0$ - strongest oscillatory character, to the purely viscous case, $\alpha = 1$ - non-oscillatory character. Likewise, Figs.

1(c) and 1(d) show that the peak of the relative acceleration between the connected bodies is weakly dependent on α. On the other hand, the amplitude of the oscillatory *relative* motion, which takes place after the acceleration peak, is greatly affected by the choice of α. In fact, the amplitude of the oscillatory relative motion for $\alpha = 0.1$ is approximately twice the amplitude of the oscillatory motion for $\alpha = 0.8$. This may play an important role for design and safety as well as for further analysis of the structural response of boat hulls and floating structures. Fig. 1(e) shows the ratio between the viscoleastic connecting force and the hydrodynamic impacting force. As it can be seen, the ratio is always much lower than unity, and its peak is attained much after the acceleration peak occurs. Finally, Fig. 1(f) presents the energy balance during the water impact of this fractionally damped system, taking $\alpha = 0.75$. Although taking into account a viscoelastic damper, energy is mostly drained through the spray jets. In fact, the energy contained in the bulk of the liquid and that dissipated due to the viscoelastic connection are much smaller. Moreover, the time history of the energy dissipated to spray jets exhibits, to a very good extent, the opposite behavior of the time history of kinetic energy of the solid system. Future investigations aim at addressing a more comprehensive parametric analysis, regarding κ, β, γ and α. Other nonlinear effects following from the coupling between the hydrodynamic impact force and the fractional-order dissipation term are to be studied. Possible generalizations to consider the water impact of a fractionally damped plate can also be taken into account.

7 Acknowledgments

The authors acknowledge FAPESP, the State of São Paulo Research Foundation, for the Postdoctoral Research Grant no 2012/10848−4 (L.C.) and PhD scholarship no 2008/00688−4 (G.R.F.), and CNPq, the Brazilian National Research Council, for the Research Grant no 303838/2008-6 (C.P.P.). The first author specially thanks his daughter, Clara C. C. Casetta, for having helped with the typewriting of this manuscript.

8 References

[1] Von Kármán, T.: The impact on seaplane floats during landing. Technical note 321. NACA/NASA Langley Research Center (1929)

[2] Wagner, H. : Landing of seaplanes. Technical memorandum 622. NACA/NASA Langley Research Center (1931)

[3] Khabakhpasheva, T.I., Korobkin, A.A.: Elastic wedge impact onto a liquid surface: Wagner's solution and approximate models. J. Fluids Struct. http://dx.doi.org/10.1016/j.jfluidstructs.2012.08.004 (2012)

[4] Carcaterra, A., Ciappi, E., Iafrati, A., Campana, E.F.: Shock spectral analysis of elastic systems impacting on the water surface. J. Sound Vib. 229(3), 579- 605 (2000)

[5] Carcaterra, A., Ciappi, E.: Hydrodynamic shock of elastic structures impacting on the water: theory and experiments. J. Sound Vib. 271, 411-439 (2004)

[6] Kurano, S.: Experimental study on effects of elastomer coating on the vibration-damping property of steel and CFRP plates for ship's hull. Trans. Japan Soc. Mech. Eng. A. 71(706), 982-989 (2005)

[7] Olunloyo, V.O.S., Osheku, C.A., Agboola, F.: Application of sandwich visco elastic beam-plate smart structures dampers in ship structures. Proceedings of the 10th International Symposium on Practical Design of Ships and others Floating Structures (PRADS), Texas (2007)

[8] Riewe, F.: Nonconservative Lagrangian and Hamiltonian mechanics. Phys. Rev. E. 53(2), 1890-1899 (1996)

[9] Koeller, R.C.: Applications of fractional calculus to the theory of viscoelasticity. J. Appl. Mech. 51, 299-307 (1984)

[10] Casetta, L., Pesce, C.P.: The proper definition of the added mass for the water entry problem. Proceedings of the 21st International Workshop on Water Waves and Floating Bodies (IWWWFB), Loughborough (2006)

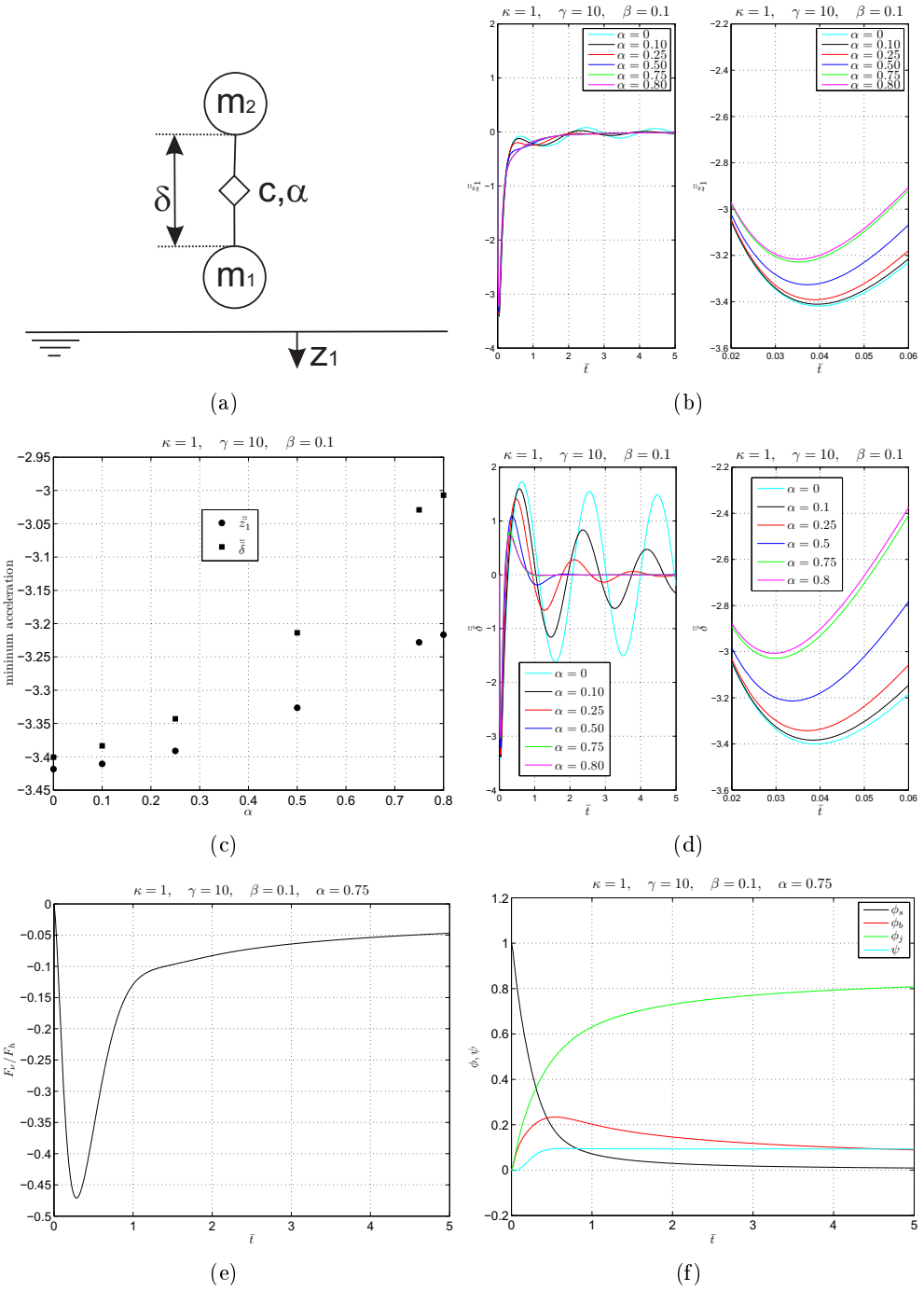

Figure 1: 1(a) - Schematic representation; 1(b) - Nondimensional acceleration of the impacting sphere vs time; 1(c) - Peak of nondimensional acceleration (impact and relative) vs α; 1(d) - Nondimensional relative acceleration vs time; 1(e) - Ratio between viscoelastic and impact force versus time; 1(f) - Energy balance vs time.

On the wave resistance of an immersed prolate spheroid in infinite water depth

by

Ioannis K. Chatjigeorgiou[1] chatzi@naval.ntua.gr

Spyros A. Mavrakos[1] mavrakos@naval.ntua.gr

Touvia Miloh[2] miloh@eng.tau.ac.il

[1]School of Naval Architecture and Marine Engineering, National Technical University of Athens, Greece

[2]Faculty of Engineering, Tel-Aviv University, Israel

1 Introduction

It is the purpose of this study to present a newly developed robust and efficient solution of the wave resistance problem of immersed prolate spheroids moving under regular waves with constant forward speed. Here the term "wave resistance" is associated with the coupled forward speed and wave impact problem, the latter being directed to the spheroid under arbitrary heading angle. Parts of the investigated subject were partly treated in the past by several authors who, however, isolated the two major contributions, namely the forward speed and the wave effects. In this context Havelock [1] approximated the wave resistance of prolate and oblate spheroids using Lagally's [2] theorem (without mentioning Lagally in this connection) using the axial source distribution corresponding to the motion of the spheroid in an infinite mass of liquid. Farell [3] expanded the sources distributed on the surface of the spheroid into series of spheroidal harmonics and reported significant differentiations compared to Havelock's [1] predictions. Wu and Eatock Taylor [4-5] used Farell's [3] approach to tackle the diffraction (only) problem assuming (only) frontal wave heading.

Here a solution to the complete problem is presented (waves and forward speed) which we achieved by employing Miloh's [6] image singularities.

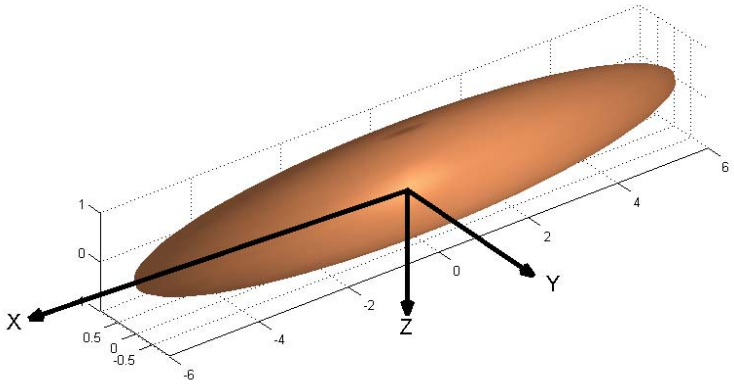

Fig. 1 3D image of a prolate spheroid below the free surface (non-axisymmetric case) with *a/b*=6.

2 Multipole expansions in curvilinear coordinates for surface waves

The concerned spheroidal body is considered immersed at a distance *f* below the undisturbed free surface (Fig. 1). The non-axisymmetric case is considered meaning that symmetrical axis (*x*-axis) is parallel to the free surface. Using left-handed Cartesian (*x*, *y*, *z*) coordinates, fixed on the free surface with *z* pointing downwards we start with the following well known Fourier expansion for the fundamental Green's function of the Laplace equation

$$\frac{1}{\sqrt{x^2+y^2+(z-f)^2}}=\frac{1}{2\pi}\int_0^{\infty}\int_{-\pi}^{\pi}e^{-k|z-f|+ik(x\cos a+y\sin a)}\,\mathrm{d}a\,\mathrm{d}k \qquad (1)$$

The common linearized free-surface boundary condition for the velocity potential, in the case of time-harmonic oscillations with frequency ω, including a forward motion with constant velocity U along the x direction, is

$$\left(-i\omega + U\frac{\partial}{\partial x}\right)^2 \phi - g\frac{\partial \phi}{\partial z} = 0\,, \tag{2}$$

to be applied at z=0 with g being the gravitational acceleration. Eq. (2) can also be cast to

$$\left(\sqrt{K} - k\sqrt{\tau}\cos a\right)^2 \phi + \frac{\partial \phi}{\partial z} = 0\,, \tag{3}$$

where $\tau = U^2/g$ and $K = \omega^2/g$. Hence the Green's function can be written as

$$G(x,y,z) = \frac{1}{\sqrt{x^2+y^2+(z-f)^2}} - \frac{1}{2\pi}\int_0^{\infty}\int_{-\pi}^{\pi} Q(k,a)e^{-k(z+f)+ik(x\cos a + y\sin a)}\mathrm{d}a\mathrm{d}k\,, \tag{4}$$

where

$$Q(k,a) = \frac{\left(\sqrt{K}-k\sqrt{\tau}\cos a\right)^2 + k}{\left(\sqrt{K}-k\sqrt{\tau}\cos a\right)^2 - k} \tag{5}$$

Clearly for τ=0 (U=0) we recover the diffraction problem whereas for K=0 (ω=0) we get the forward speed (wave resistance) problem. The former case applies directly to the radiation problem as well by replacing the Neumann boundary condition on the spheroid by

$$\frac{\partial \phi_R^{(i)}}{\partial n} = n_i\,;\ \frac{\partial \phi_R^{(i+3)}}{\partial n} = \left(\vec{r}\times\vec{n}\right)_i\,,\ \text{for } i=1,2,3, \tag{6}$$

where the index R is used to denote the radiation potential, $\vec{r}$ is the position vector (with respect to the origin) and n_i denotes the unit vector in the direction i. The boundary conditions involved in (6) describe all six radiation problems. Finally, in order to satisfy the far-field Sommerfeld radiation condition, the following notation is used in (4) and in the sequel,

$$\int_0^{\infty}\frac{F(k)}{\sigma-k}\mathrm{d}k = PV\int_0^{\infty}\frac{F(k)}{\sigma-k}\mathrm{d}k - i\pi F(\sigma)\,, \tag{7}$$

where the acronym PV is used to denote Cauchy's Principal Value Integral.

3 Prolate spheroidal coordinates – non axisymmetric case

A prolate spheroidal (ζ, μ, ψ) coordinate system is defined, with an origin at a depth f below the undisturbed free surface such that the spheroid is assumed to be fully submerged. We also define ζ=cosh$u$, μ=cosϑ, where $0\le u\le\infty$, $0\le\vartheta\le\pi$ and $0\le\psi\le 2\pi$. The transformation from prolate spheroidal to Cartesian coordinates is $x=c\cosh u\cos\vartheta$, $y=c\sinh u\sin\vartheta\sin\psi$, $z=c\sinh u\sin\vartheta\cos\psi$. Hence, $x=c\mu\zeta$ and $z+iy=c(\zeta^2-1)^{1/2}(1-\mu^2)^{1/2}e^{i\psi}$, where c represents half the distance between the two foci of the spheroid. In terms of the semi-major a and semi-minor b axes of the spheroid, c is expressed as $c=ae$ where $e=(1-(b/a)^2)^{1/2}$ denotes the eccentricity. It is noted that in the following analysis c was taken equal to unity and thus it is used as a reference length scale. For manipulating the original Green's function (see Eq. (4)) in prolate spheroidal coordinates we use a most useful relation which was originally suggested without proof by Havelock [7] and later rigorously obtained by Miloh [6]. The concerned relation expresses any exterior spheroidal harmonic in terms of prescribed singularities disturbed on the major axis of the spheroid between the two foci. In particular Havelock's formula for the present case may be written as

$$P_n^m(\mu)Q_n^m(\zeta)e^{im\psi} = \frac{1}{2}\left(\frac{\partial}{\partial z} + i\frac{\partial}{\partial y}\right)^m \int_{-1}^{1}\frac{(1-\lambda^2)^{m/2}P_n^m(\lambda)}{\sqrt{(x-\lambda)^2+y^2+z^2}}\mathrm{d}\lambda \tag{8}$$

where P_n^m, Q_n^m denote the associate Legendre functions of the first and the second kind with order m and degree n. Accordingly, using the proposed approach one can readily express the Green's function as

$$G_n^m(x,y,z) = P_n^m(\mu)Q_n^m(\zeta)e^{im\psi} - \frac{(-1)^m}{4\pi}\int_0^\infty \mathrm{f}_m^n(x,y;k)k^m Q(k,a)e^{-k(f-z)}\mathrm{d}k \tag{9}$$

where

$$\mathrm{f}_m^n(x,y;k) = \int_{-\pi}^{\pi}\int_{-1}^{1}(1-\lambda^2)^{m/2}P_n^m(\lambda)e^{-ik\lambda\cos a}(\sin a - 1)^m e^{ik(x\cos a + y\sin a)}\mathrm{d}\lambda\mathrm{d}a \tag{10}$$

It should be noted that the above relations assume that the direction of the vertical coordinate has been reversed showing upward. To enable feasibility of numerical computations Eqs. (9)-(10) should be further manipulated. To this end exp(-*ik*λcos*a*) is expanded into a Taylor series and a most useful relation that can be found in Gradshteyn and Ryzhik [8, p. 772] is employed. Hence the next representation of Green's function reads

$$G_n^m(x,y,z) = P_n^m(\mu)Q_n^m(\zeta)e^{im\psi} - \frac{(-1)^m}{4\pi}\sum_{q=0}^{\infty}(-i)^q I_n^m(q)\int_0^\infty k^{m+q}e^{-2kf} \times \int_{-\pi}^{\pi}Q(k,a)(\cos a)^q(\sin a - 1)^m e^{kz^*+ik(x\cos a + y\sin a)}\mathrm{d}a\mathrm{d}k \tag{11}$$

where

$$I_n^m(q) = \frac{(1-(-1)^{n+q})(-1)^m 2^{-m-1}\Gamma(1/2+q/2)\Gamma(1+q/2)\Gamma(1+m+n)}{q!\Gamma(1-m+n)\Gamma(1+m/2-n/2+q/2)\Gamma(3/2+m/2+n/2+q/2)} \tag{12}$$

Note that the dependence on the vertical coordinate was transformed to be expressed in terms of the *z** axis fixed on the center of the body.

In order to allow the employment of the zero velocity condition on body's surface the exponential term in Eq. (11) must be cast to spheroidal harmonics. To this end a most useful relation shown by Havelock [9] will be applied. This is

$$e^{kz^*+ik(x\cos a + y\sin a)} = \sum_{s=0}^{\infty}\sum_{t=0}^{s}\frac{\varepsilon_t}{2}i^{s-t}(2s+1)\frac{(s-t)!}{(s+t)!}j_s(kc\cos a)P_s^t(\mu)P_s^t(\zeta)\left[N_t(a)\cos t\psi + i\tilde{N}_t(a)\sin t\psi\right] \tag{13}$$

where j_s is the spherical Bessel function of the first kind and

$$N_t(a) = \left[\left(\frac{1+\sin a}{\cos a}\right)^t + \left(\frac{1-\sin a}{\cos a}\right)^t\right],\ \tilde{N}_t(a) = \left[\left(\frac{1-\sin a}{\cos a}\right)^t - \left(\frac{1+\sin a}{\cos a}\right)^t\right] \tag{14}$$

The final form of Green's function now becomes

$$G_n^m(x,y,z) = P_n^m(\mu)Q_n^m(\zeta)e^{im\psi} + \sum_{s=0}^{\infty}\sum_{t=0}^{s}\left(C_{ns}^{mt}\cos t\psi + i\tilde{C}_{ns}^{mt}\sin t\psi\right)P_s^t(\mu)P_s^t(\zeta) \tag{15}$$

where

$$C_{ns}^{mt} = -\frac{(-1)^m}{4\pi}\frac{\varepsilon_t}{2}i^{s-t}(2s+1)\frac{(s-t)!}{(s+t)!}\sum_{q=0}^{\infty}(-i)^q I_n^m(q)\int_{-\pi}^{\pi}(\cos a)^q(\sin a - 1)^m N_t(a) \times \int_0^\infty k^{m+q}e^{-2kf}Q(k,a)j_s(kc\cos a)\mathrm{d}k\mathrm{d}a \tag{16}$$

and $\tilde{C}_{ns}^{mt}$ is obtained through the former after replacing $N_t(a)$ by $\tilde{N}_t(a)$. The calculation of C_{ns}^{mt} and $\tilde{C}_{ns}^{mt}$ coefficients virtually completes the solution to the problem and the scattered potential is obtained by the following multipole expansion in prolate spheroidal coordinates

$$\phi(\mu,\zeta,\psi) = \sum_{n=0}^{\infty}\sum_{m=0}^{n}A_n^m\left\{P_n^m(\mu)Q_n^m(\zeta)e^{im\psi} + \sum_{s=0}^{\infty}\sum_{t=0}^{s}\left(C_{ns}^{mt}\cos t\psi + i\tilde{C}_{ns}^{mt}\sin t\psi\right)P_s^t(\mu)P_s^t(\zeta)\right\} \tag{17}$$

The unknown expansion coefficients A_n^m are derived by employing the zero velocity condition on the wetted surface of the spheroid. Eq. (17) represents a global formulation that covers all possible cases, namely the diffraction problem (U=0), the wave resistance problem (ω=0) and the complete forward speed and wave impact problem ($U\neq0$, $\omega\neq0$). In fact only $Q(k,a)$ need to be changed whilst for the diffraction and the wave resistance problems is reduced respectively to

$$Q(k,a)=\frac{K+k}{K-k},\ Q(k,a)=\frac{k+1/\tau\cos^2 a}{k-1/\tau\cos^2 a} \tag{18}$$

The most challenging part as regards the computation of C_{ns}^{mt} and $\tilde{C}_{ns}^{mt}$ is the numerical evaluation of Cauchy's Principal Value Integral involved in the infinite series of Eq. (16). However special attention must be given to the singularity that occurs at $a=\pm\pi/2$. For the diffraction problem this can be easily avoided adopting the ascending series of Bessel function. This however will make the expressions that provide C_{ns}^{mt} and $\tilde{C}_{ns}^{mt}$ much more complicated. In particular the former will be given by

$$C_{ns}^{mt}=\frac{(-1)^m i^{s-t}}{4\pi}\pi^{1/2}\frac{\varepsilon_t}{2}(2s+1)\frac{(s-t)!}{(s+t)!}\sum_{q=0}^{\infty}\sum_{p=0}^{\infty}\frac{(-1)^{p+q}i^q(1/2)^{2p+s+1}}{q!\,p!\,\Gamma(s+p+3/2)}I_n^m(q)$$
$$\times\int_0^{\infty}k^{m+q+2p+s}\frac{K+k}{K-k}e^{-2kf}\,\mathrm{d}k\int_{-\pi}^{\pi}(\sin a-1)^m(\cos a)^{q+2p+s-t}\left[(1+\sin a)^t+(1-\sin a)^t\right]\mathrm{d}a \tag{19}$$

that allows separate integrations oven a and k. For the coupled forward speed and wave heading problem one must find the roots of the denominator in Eq. (5). In that case the numerical implementation requires the calculation of two Cauchy PV integrals in terms of the roots

$$\rho_{1,2}=\frac{2\sqrt{K\tau}\cos a+1\pm\left(1+4\sqrt{K\tau}\cos a\right)^{1/2}}{2\tau\cos^2 a} \tag{20}$$

The roots $\rho_{1,2}$ must be real regardless a. This condition is always satisfied if $\omega U/g<1/4$ and that finding is in compliance with the requirement for the existence of an upper bound for the critical frequency $\omega_c=0.25g/U$ of oscillating singularities [10] where the classical linearized solution yields infinitely large wave amplitude.

Some numerical examples for prolate spheroids of different submergence depth and slenderness ratio will be presented at the Workshop together with a comparison against Farell's [3] and Havelock's [1] approximations.

4 References

[1] Havelock TH (1931) The wave resistance of a spheroid. Proc Royal Soc London, A131: 275-285

[2] Lagally M (1922) Berechnung der Kräfte und Momente, die strömende Fliassigkeiten auf ihre Begrenzung Ausiiben. Z Angew Math Mech, 2: 409-422

[3] Farell C (1973) On the wave resistance of a submerged spheroid. J Ship Res, 17: 1-11

[4] Wu GX, Eatock Taylor R (1987) The exciting force on a submerged spheroid in regular waves. J Fluid Mech, 182: 411-426

[5] Wu GX, Eatock Taylor R (1989) On radiation and diffraction of surface waves by submerged spheroids. J Ship Res, 33: 84-92

[6] Miloh T (1974) The ultimate image singularities for external ellipsoidal harmonics. SIAM J Appl Math 26: 334-344

[7] Havelock TH (1952) The moment on a submerged solid of revolution moving horizontally. Quart. J. Mech Appl Math, 5: 129-136

[8] Gradshteyn IS, Ryzhik IM (2007) Tables of integrals, series and products (seventh edition). Elsevier Academic Press, London

[9] Havelock TH (1954) The forces on a submerged body moving under waves. Transactions Institution of Naval Architects 96: 77-88

[10] Dagan G, Miloh T (1982) Free surface flow past oscillating singularities at resonance frequency. J Fluid Mech, 120, 139-154.

MODELLING WAVE INTERACTIONS WITH A SURFACE-PIERCING VERTICAL CYLINDER USING OpenFOAM

L.F. Chen[1], G.C.J. Morgan[1], J. Zang[1], A. Hillis[1] and P.H. Taylor[2]

[1]Department of Architecture and Civil Engineering, University of Bath
[2] Department of Engineering Science, University of Oxford
lc499@bath.ac.uk g.c.j.Morgan@bath.ac.uk j.zang@bath.ac.uk
a,hillis@bath.ac.uk paul.taylor@eng.ox.ac.uk

INTRODUCTION

With the intensification of the global energy crisis, the development of marine renewable energy is attracting increasing attention. To achieve the renewable energy targets, a rigorous approach is required leading to the better design of wave energy converters with increased efficiency. Wave loading is a key factor to be considered for structural design. Either over-predicted or under-predicted loading would cause severe consequences. Over-predicting the loading will lead to overdesign and then very expensive structures. The consequence of under-prediction may even more dangerous and expensive - leading to under-design and structural failure.

The use of Computational Fluid Dynamics (CFD) codes is becoming increasing important in engineering design work. The free, open-source library for continuum-mechanics problems known as OpenFOAM is suitable for solving complex free-surface motions (Weller et al., 1998). It has been applied to coastal engineering successfully by Morgan et al. (2010, 2011). The experimental results for the propagation of monochromatic waves over a submerged bar have been reproduced in his numerical simulations, with up to 6^{th} order harmonics correctly modelled.

This research is focussed on the assessment of how OpenFOAM performs when applied to non-linear wave interaction with a vertical surface piercing cylinder, a typical representation of an offshore wind turbine foundation. A few new functions have been developed to advance wave generation and wave absorbing capabilities of the model. A series of experiments performed in the Danish Hydraulic Institute's shallow water basin in 2009 have been reproduced using OpenFOAM to test the accuracy of the model predicting wave-structure interaction problems. The decomposition of the measured signals into harmonics has also been carried out to examine the effects of wave and loading nonlinearity.

VALIDATION AND RESULT DISCUSSIONS

The experiments were performed at the Danish Hydraulic Institute, details were given in Zang et al (2010). The shallow water basin (35m x 25m) was used for the tests with a water depth of 0.505m. A cylinder of diameter 0.25m was suspended from a rigid frame, leaving only a 1mm gap beneath to the bed of the basin. The total horizontal hydrodynamic force on the cylinder was measured via a load cell, and 19 wave gauges were placed to monitor the wave-field around the cylinder. The layout for the wave gauges can be seen in Figure 1. The numerical results for the free surface elevations at wave gauges of 1, 5, 9, 13, 17 and 19, and the horizontal force on the cylinder have been compared with experimental measurements for

several cases, of which two cases will be discussed in this paper. These two cases correspond to the same slenderness (ka=0.37) and same kD (1.39) for the cylinder, but have different steepness (kA_1=0.1, and kA_2=0.2). Here k is wave number, a is cylinder radius, D is water depth and A is wave crest with A_1=0.035m, A_2=0.07m. For both cases, wave period is 1.22s.

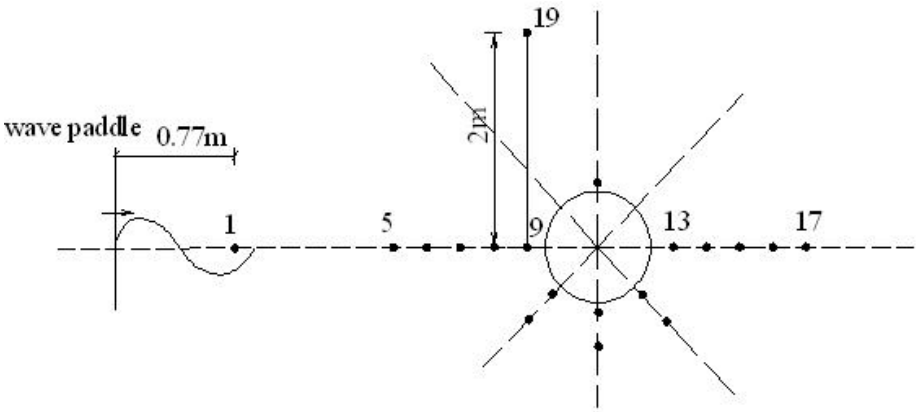

Figure 1: The arrangement of wave gauges in the wave tank

In the numerical simulations, a few key factors have been examined to ensure accurate reproduction of the experiments. As the wave generation in the numerical model is via the flux into the computational domain through a fixed vertical wall, different from wave generation by piston paddles in the experiments, a careful match between experiments and numerical models for the first wave gauge (0.77m from the paddle) was made to ensure the incoming waves in the numerical tank are very close to the waves generated in the experiments. Wave focus time, focus distance and phase angle are all carefully chosen to match the experiments. A damping zone is also added in the computational domain to avoid reflection at the downstream end of the numerical tank.

Time series of experimental and numerical free surface elevations at a few locations along the central line for the cases with cylinder in place are given in Figure 2. Note that the wave gauge 19 is placed close to the side wall of the numerical tank for a second check of the incoming waves. At location of wave gauge 9, which is 2mm in front of the upstream stagnation point of the cylinder, all wave components are in phase and the wave group produces a large energetic events. Wave breaking at wave gauge 13, which was observed in experiments, may lead to a relatively larger discrepancy between the predicted and measured values of the free surface elevations. A finer mesh would be required to obtain a better match. Apart from gauge 13, the numerical model appears to have captured all the main physical features of the nonlinear focused wave interaction with the vertical cylinder, with close matching of both crest values of the free surface and horizontal forces, and the wave shapes.

In order to extract the harmonic structure of the free surface and wave loading on the cylinder, both crest focused waves and trough focused waves were performed, both in the experiments and the numerical simulations. Following Zang et al. (2006), Zang et al. (2010) and Fitzgerald et al. (2012), our simple phase-based separation method has been applied to decompose higher order harmonics cleanly without cross-contamination between adjacent

harmonics. Table 1 shows the comparisons of the crest values of each harmonic of free surface elevations and horizontal forces for wave amplitudes with the cylinder in place. This is clear that the 2nd order components for case 2 are much larger than case 1, about 4-5 times larger than the values in case 1, which is consistent with the expected Stokes-type behavior.

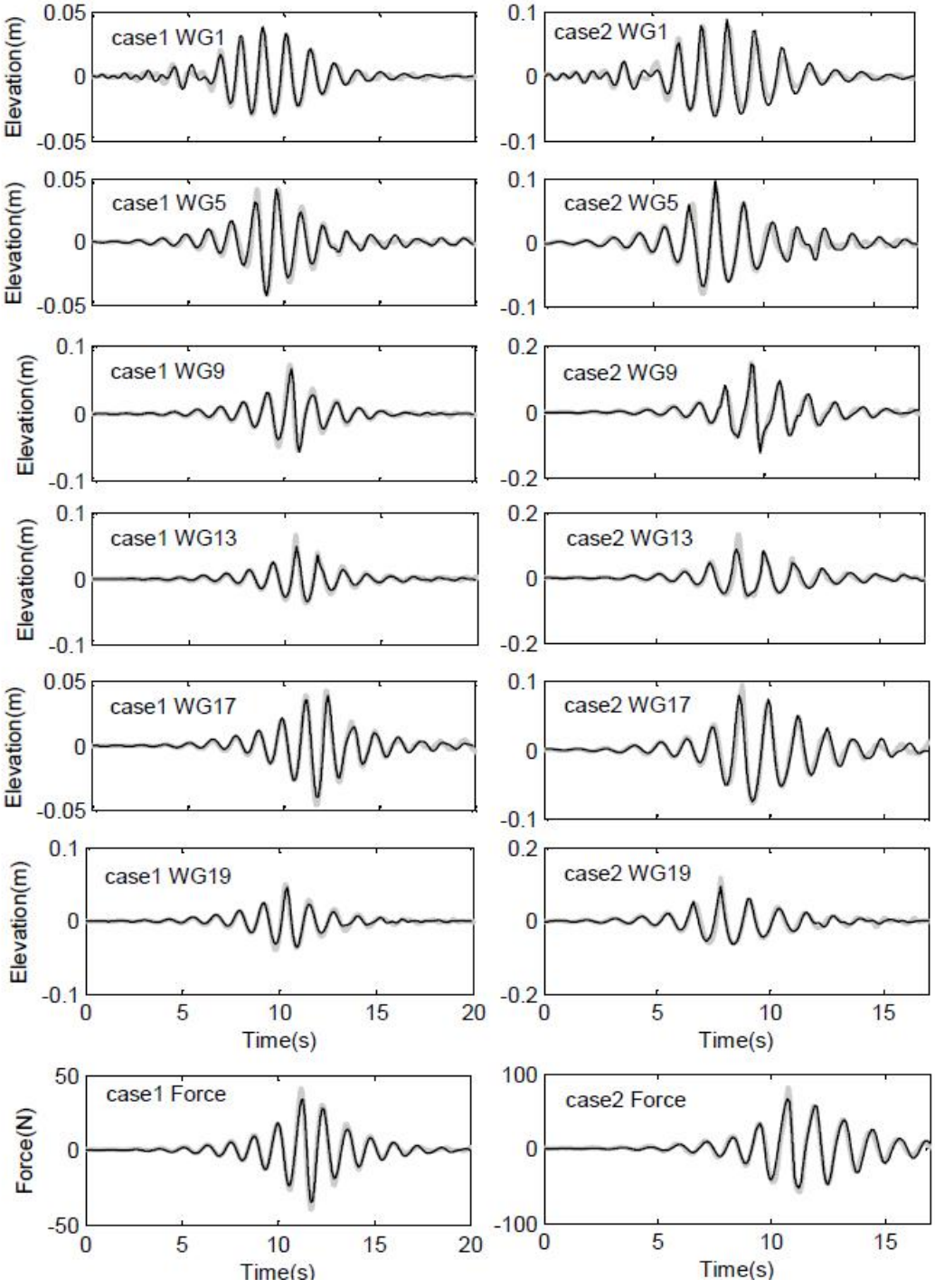

Figure 2: Time series of free surface elevations and horizontal forces for both cases with cylinder in place. The experimental data is in thick grey line and the numerical results are in thin black line.

Given the good match for all the components, we are confident that accurate predictions of the free surface elevations in the wave-field and the horizontal force on the cylinder can be made by using the present model based on OpenFOAM.

harmonics	Peak free surface elevations (m)				Peak horizontal forces (N)			
	case 1		case 2		case 1		case 2	
	kA_1=0.1		kA_2=0.2		kA_1=0.1		kA_2=0.2	
	Exp	Num	Exp	Num	Exp	Num	Exp	Num
long wave	0.0016	0.0017	0.0050	0.0130	1.91	1.80	7.50	7.50
linear	0.0530	0.0560	0.0930	0.1050	40.0	32.0	67.0	57.0
2nd	0.0105	0.0104	0.0370	0.0430	2.20	3.20	9.50	12
3rd	0.0020	0.0020	0.0080	0.0130	1.30	0.70	9.50	4.50
4th	0.0055	0.0075	0.0057	0.0034	1.00	0.20	1.70	2.70

Table 1: Each harmonic of free surface elevations at the location of WG9 and horizontal forces for both cases with cylinder in place. Exp means Experimental data and Num means Numerical results.

From the preliminary results, we conclude that the present model based on OpenFOAM can accurately predict the non-linear wave interaction with a vertical cylinder up to at least the 4th frequency harmonic. By using the crest-trough phase-based separation method, we can reproduce harmonic structure in both the free surface and the wave loading on the structure. Further examples of the validation and the harmonic structure of the free surface and hydrodynamic loading on a surface-piercing column will be presented at the workshop.

ACKNOWLEDGEMENTS

The first author acknowledges the financial support of the University of Bath for her PhD study. The second author thanks the Great Western Research, Edenvale Young Associates Ltd and the University of Bath for the support of his PhD study.

REFERENCES

1. Weller, H. G.; Tabor, G.; Jasak, H. & Fureby, C. (1998) *A tensorial approach to computational continuum mechanics using objectoriented techniques*. Computers in Physics, 12(6): 620–631.
2. Morgan, G. and Zang, J. et al. (2010) *Using the rasInterFoam CFD model for wave transformation and coastal modelling*. The 32nd international Conference on Coastal Engineering (ICCE 2010).
3. Morgan, G. and Zang, J. (2011). Application of OpenFOAM to Coastal and Offshore Modelling. *In*: *The 26th International Workshop on Water Waves and Floating Bodies*, Greece.
4. Futzgerakd, C. Grice, J. and Taylor, P.H. et al.(2012) *Phase manipulation and the harmonic components of ringing forces on a surface-piercing column*. Proc. 27th IWWWFB, Denmark.
5. Zang, J., Taylor, P.H. and Tello, M. et al. (2010). *Steep Wave and Breaking Wave Impact On Offshore Wind Turbine Foundations -- Ringing Revisited.* Proc. 25th IWWWFB, China.
6. Zang, J., Gibson, R., Taylor, P. H., Eatock Taylor, R. and Swan, C. (2006). *Second order wave diffraction around a fixed ship-shaped body in unidirectional steep waves*. Journal of Offshore Mechanics and Arctic Engineering, 128 (2), pp. 89-99.

Semi analyticial soultion for second order hydroelastic response of the vertical circular cylinder in monochromatic water waves

Choi Y.M.[(1)] **& Malenica Š**[(2)]

[(1)] *PNU, Busan, Korea*
[(2)] *BUREAU VERITAS, Paris, France*

Theory

The body motion is described by the following displacement vector field:

$$\boldsymbol{H}(\boldsymbol{x},t) = \varepsilon \boldsymbol{H}^{(1)}(\boldsymbol{x},t) + \varepsilon^2 \boldsymbol{H}^{(2)}(\boldsymbol{x},t) = \sum_{i=1}^{N} \left\{ \varepsilon \xi_i^{(1)}(t) + \varepsilon^2 \xi_i^{(2)}(t) \right\} \boldsymbol{h}_i(\boldsymbol{x}) \tag{1}$$

where $\boldsymbol{h}_i(\boldsymbol{x})$ is the i-th mode shape function vector and ξ_i is its amplitude and N is the number of modes. The problem is formulated within the classical assumptions of the potential flow theory leading to the definition of the velocity potential $\Phi(\boldsymbol{x},t)$ for which the corresponding Boundary Value Problem (BVP) is built. Within the second order theory, which is of concern here, the fully non linear potential is formally written in the form:

$$\Phi(\boldsymbol{x},t) = \varepsilon \Phi^{(1)}(\boldsymbol{x},t) + \varepsilon^2 \Phi^{(2)}(\boldsymbol{x},t) \tag{2}$$

The use of the classical perturbation theory leads to the BVP's for different potentials. At first two orders, these BVP's are composed of the Laplace equation in the fluid domain, zero normal velocity at the fixed boundaries, radiation condition at infinity and the following free surface boundary conditions:

$$\frac{\partial^2 \Phi^{(1)}}{\partial t^2} + g \frac{\partial \Phi^{(1)}}{\partial z} = 0 \tag{3}$$

$$\frac{\partial^2 \Phi^{(2)}}{\partial t^2} + g \frac{\partial \Phi^{(2)}}{\partial z} = \frac{1}{g} \frac{\partial \Phi^{(1)}}{\partial t} \left[\frac{\partial^{(3)} \Phi^{(1)}}{\partial t^2 \partial z} + g \frac{\partial^2 \Phi^{(1)}}{\partial z^2} \right] - 2 \nabla \Phi^{(1)} \nabla \frac{\partial \Phi^{(1)}}{\partial t} \tag{4}$$

The corresponding body boundary condition is obtained after careful investigation of the body kinematics:

$$\nabla \Phi^{(1)} \boldsymbol{n} = \dot{\boldsymbol{H}}^{(1)} \boldsymbol{n} \tag{5}$$

$$\nabla \Phi^{(2)} \boldsymbol{n} = \dot{\boldsymbol{H}}^{(2)} \boldsymbol{n} - [(\boldsymbol{H}^{(1)} \nabla) \nabla \Phi^{(1)}] \boldsymbol{n} + (\dot{\boldsymbol{H}}^{(1)} - \nabla \Phi^{(1)}) \boldsymbol{n}^{(1)} \tag{6}$$

where overdot denotes the time derivative, $\boldsymbol{n}$ is the normal vector at rest and $\boldsymbol{n}^{(1)}$ its first order correction:

$$\boldsymbol{n}^{(1)} = (\nabla \boldsymbol{H}^{(1)}) \boldsymbol{n} - (\underline{\underline{\nabla \boldsymbol{H}^{(1)}}})^T \boldsymbol{n} \tag{7}$$

Finally, the total potential at each order is composed of the incident wave potential Φ_I and the perturbaion potential Φ_B which results from the interaction of the incident potential and the body:

$$\Phi(\boldsymbol{x},t) = \Phi_I(\boldsymbol{x},t) + \Phi_B(\boldsymbol{x},t) = \varepsilon [\Phi_I^{(1)}(\boldsymbol{x},t) + \Phi_B^{(1)}(\boldsymbol{x},t)] + \varepsilon^2 [\Phi_I^{(2)}(\boldsymbol{x},t) + \Phi_B^{(2)}(\boldsymbol{x},t)] \tag{8}$$

The incident potential represents the excitation of the system and does not depends on the presence of the body. This means that it satisfies the Laplace equation in the fluid domain, zero flux condition at the bottom and the free surface conditions (3) and (4) where only the incident velocity potential is included. In order to solve for the amplitudes of the body deformations at each order, we need to further decompose the interaction potential Φ_B into the part Φ_R which depends directly on the body motion and the part Φ_D which is independent of the body motion at the corresponding order. In that respect, the radiation potentials are chosen to satisfy the homogeneous free surface boundary condition and the following body boundary conditions:

$$\nabla \Phi_R^{(1)} \boldsymbol{n} = \dot{\boldsymbol{H}}^{(1)} \boldsymbol{n} \quad , \quad \nabla \Phi_R^{(2)} \boldsymbol{n} = \dot{\boldsymbol{H}}^{(2)} \boldsymbol{n} \tag{9}$$

On the other side the potential Φ_D is chosen to satisfy all the remaining boundary conditions i.e. the non-homogeneous free surface condition and the remaining part of the body boundary condition. This leads to the following decomposition of the interaction potential Φ_B:

$$\Phi_B^{(1)}(\boldsymbol{x},t) = \phi_D^{(1)}(\boldsymbol{x},t) + \sum_{j=1}^{N} \dot{\xi}_j^{(1)} \Phi_{Rj}^{(1)} \qquad , \qquad \Phi_B^{(2)}(\boldsymbol{x},t) = \phi_D^{(2)}(\boldsymbol{x},t) + \sum_{j=1}^{N} \dot{\xi}_j^{(2)} \Phi_{Rj}^{(2)} \tag{10}$$

where Φ_D is usually called the diffraction potential and Φ_{Rj} the radiation potentials.
Let us also note that the diffraction potential is usually decomposed into two parts: ϕ_{DB} satisfying the homogeneous condition on the free surface and non-homogeneous condition on the body, and Φ_{DD} satisfying the non-homogeneous condition on the free surface and homogeneous on the body.
Once the different potentials evaluated, the pressure is calculated from Bernoulli equation:

$$p = -\varrho[gz + \frac{\partial \Phi}{\partial t} + \frac{1}{2}(\nabla\Phi)^2] = -\varrho\{gz + \varepsilon\frac{\partial \Phi^{(1)}}{\partial t} + \varepsilon^2[\frac{\partial \Phi^{(2)}}{\partial t} + \frac{1}{2}(\nabla\Phi^{(1)})^2 + (\boldsymbol{H}^{(1)}\nabla)\frac{\partial \Phi^{(1)}}{\partial t}]\} \tag{11}$$

Frequency domain

The above defined problem is now formulated in frequency domain. We start by defining the incident wave potential:

$$\Phi_I(\boldsymbol{x},t) = \Re\{\varphi_I^{(1)}(\boldsymbol{x})e^{-i\omega t}\} + \Re\{\varphi_I^{(2)}(\boldsymbol{x})e^{-2i\omega t}\} \tag{12}$$

where:

$$\varphi_I^{(1)} = -\frac{igA}{\omega}\frac{\cosh k_0(z+D)}{\cosh k_0 D}e^{ik_0 x} \qquad , \qquad \varphi_I^{(2)} = -\frac{3i\omega\nu A^2}{2\sinh^2 k_0 D}\frac{\cosh 2k_0(z+D)}{4\nu\sinh^2 k_0 D}e^{ik_0 x} \tag{13}$$

The boundary conditions for other potentials follow straightforwardly and we end up with the fact taht all the potentals, at any order, satisfy one of the two types of the BVP defined below:

$$\left.\begin{array}{lll} \Delta\psi_B = 0 & \Delta\psi_Q = 0 & r > a \ , \ -D < z < 0 \\ -\alpha\psi_B + \dfrac{\partial\psi_B}{\partial z} = 0 & -\alpha\psi_Q + \dfrac{\partial\psi_Q}{\partial z} = Q(r,\theta) & z = 0 \\ \dfrac{\partial\psi_B}{\partial n} = v(z,\theta) & \dfrac{\partial\psi_Q}{\partial n} = 0 & r = a \\ \dfrac{\partial\psi_B}{\partial z} = 0 & \dfrac{\partial\psi_Q}{\partial z} = 0 & z = -D \\ \psi_B \to 0 & \psi_Q \to 0 & r \to \infty \end{array}\right\} \tag{14}$$

The potential ψ_B is called body perturbation potential and ψ_Q free surface perturbation potential and they can be calculated either numerically or semi-analytically for vertical circular cylinder (e.g. see [1]).

Hydrodynamic forces and body motions

The forces are obtained by integration of the pressure over the wetted body surface:

$$\boldsymbol{F} = \int\int_{\tilde{S}_b} p\boldsymbol{H}\tilde{\boldsymbol{n}}dS \tag{15}$$

where p is the pressure calculated from Bernoulli equation (11), $\tilde{S}_b$ is the instantaneous body surface and $\tilde{\boldsymbol{n}}$ is the instantaneous normal vector. Special attention should be given to the proper separation of different terms in order to write the final motion equation:

$$\{-\omega^2([\boldsymbol{M}] + [\boldsymbol{A}(\omega)]) - i\omega[\boldsymbol{B}(\omega)] + [\mathbf{C}]\}\{\xi^{(1)}\} = \{\boldsymbol{F}_E^{(1)}\} \tag{16}$$

$$\{-4\omega^2([\boldsymbol{M}] + [\boldsymbol{A}(2\omega)]) - 2i\omega[\boldsymbol{B}(2\omega)] + [\mathbf{C}]\}\{\xi^{(2)}\} = \{\boldsymbol{F}_E^{(2)}\} \tag{17}$$

where $[\boldsymbol{M}]$ is the modal mass matrix, $[\boldsymbol{A}]$ is the associated added mass matrix, $[\boldsymbol{B}]$ is the damping matrix, $[\mathbf{C}]$ is the stiffnes matrix (including both hydrostatic and structural parts) and $\{\boldsymbol{F}_E^{(1)}\}$ and $\{\boldsymbol{F}_E^{(2)}\}$ are the first and second order excitation forces. Note that the added mass and damping matrices are obtained by integrating the pressure associated with the radiation potential φ_{Rj} while the excitation forces are obtained after integration of all the remaining pressure components.

Vertical circular cylinder

General solution for ψ_B and ψ_Q can be written in the following form [1]:

$$\psi_B(r,z,\theta) = \sum_{m=-\infty}^{\infty}\left[f_0(z)\beta_{m0}H_m(k_0r)+\sum_{n=1}^{\infty}f_n(z)\beta_{mn}K_m(k_nr)\right]e^{im\theta} \tag{18}$$

$$\psi_Q(r,z,\theta) = \sum_{m=-\infty}^{\infty}\left[f_0(z)A_{m0}+\sum_{n=1}^{\infty}f_n(z)A_{mn}\right]e^{im\theta} \tag{19}$$

where the most complex terms which invloves the infinite integration over the free surface are given by:

$$A_{m0} = -\frac{2C_0\int_a^{\infty}H_m(k_0\rho)Q_m(\rho)\rho d\rho}{k_0aH'_m(k_0a)} \quad , \quad A_{mn} = -\frac{2C_0\int_a^{\infty}K_m(k_n\rho)Q_m(\rho)\rho d\rho}{k_naK'_m(k_na)} \tag{20}$$

and the detailed expressions for all the other terms can be found in [1].
In order to solve for ψ_B and ψ_Q we need to express the boundary conditions in cylindrical coordinates. First we assume that the column is free to bend only and we define the deformation modes:

$$\boldsymbol{h}_i = h_{ix}(z)\boldsymbol{i}+0\boldsymbol{j}+0\boldsymbol{k} \quad , \quad \boldsymbol{h}_i\nabla = h_{ix}(z)\frac{\partial}{\partial x} = h_{ix}(z)(\cos\theta\frac{\partial}{\partial r}-\frac{\sin\theta}{r}\frac{\partial}{\partial\theta}) \tag{21}$$

We also assume that the normal vector is pointing out of the fluid domain and we write:

$$\boldsymbol{n} = -\cos\theta\boldsymbol{i}-\sin\theta\boldsymbol{j}+0\boldsymbol{k} = -\boldsymbol{e}_r+0\boldsymbol{e}_\theta+0\boldsymbol{k} \quad , \quad \boldsymbol{n}^{(1)} = \sum_{i=1}^{N}\xi_i^{(1)}\frac{\partial h_{ix}}{\partial z}\cos\theta\boldsymbol{k} \tag{22}$$

where $(\boldsymbol{e}_r,\boldsymbol{e}_\theta,\boldsymbol{k})$ are the unit vectors of the cylindrical coordinate system.

Body boundary conditions

After applying the described theory we end up with the following body boundary conditions (only non-zero terms are presented):

$$\frac{\partial\varphi_{DB}^{(1)}}{\partial n} = -\frac{\partial\varphi_I^{(1)}}{\partial n} \quad , \quad \frac{\partial\varphi_{Rj}^{(1)}}{\partial n} = \boldsymbol{h}_j\boldsymbol{n} = -h_{jx}\cos\theta \tag{23}$$

$$\frac{\partial\varphi_{DB}^{(2)}}{\partial n} = -\frac{\partial\varphi_I^{(2)}}{\partial n} \tag{24}$$

$$+\frac{1}{2}\sum_{i=1}^{N}\xi_i^{(1)}h_{ix}(z)(\frac{\partial^2\varphi^{(1)}}{\partial r^2}\cos\theta-\frac{1}{r}\frac{\partial^2\varphi^{(1)}}{\partial\theta\partial r}\sin\theta)-\frac{1}{2}\sum_{i=1}^{N}\xi_i^{(1)}\frac{\partial h_{ix}}{\partial z}\frac{\partial\varphi^{(1)}}{\partial z}\cos\theta \tag{25}$$

$$\frac{\partial\varphi_{Rj}^{(2)}}{\partial n} = \boldsymbol{h}_j\boldsymbol{n} = -h_{jx}\cos\theta \tag{26}$$

Free surace boundary conditions

All the free surface conditions are homogeneous except the one for $\varphi_{DD}^{(2)}$. The non-homogeneous term $Q_{DD}^{(2)}$ can be written as follows:

$$Q_{DD}^{(2)} = \frac{i\omega}{g}\{(\nabla\varphi_B^{(1)}\nabla\varphi_B^{(1)}+2\nabla\varphi_I^{(1)}\nabla\varphi_B^{(1)})-\frac{1}{2}[(\varphi_B^{(1)}+\varphi_I^{(1)})(\frac{\partial^2\varphi_B^{(1)}}{\partial z^2}-\nu^2\varphi_B^{(1)})+\varphi_B^{(1)}(\frac{\partial^2\varphi_I^{(1)}}{\partial z^2}-\nu^2\varphi_I^{(1)})]\} \tag{27}$$

In the case of the vertical circular cylinder, the first order interaction potential $\varphi_B^{(1)}$ can be written in the following form:

$$\varphi_B^{(1)} = \sum_{m=-\infty}^{\infty}\left[f_0(z)\gamma_{m0}H_m(k_0r)+\sum_{n=1}^{\infty}f_n(z)\gamma_{mn}K_m(k_nr)\right]e^{im\theta} = \sum_{m=-\infty}^{\infty}f_0(z)\gamma_{m0}H_m(k_0R)e^{im\theta} \tag{28}$$

where the second expression is valid at large radial distance R only.
With this in mind, we can calculate $Q_{DDm}^{(2)}$ and subsequently the second order diffraction potential $\varphi_{DD}^{(2)}$. Special attention should be given to the evaluation of the free surface integrals in (20) which are highly oscillatory and extend to infinity. In this work we use the numerical integration close to the cylinder and the semi-analytical method [1] in the far field.

Numerical example

We chose the example proposed in [2]. The following modes of deformation are defined:

$$h_{ix}(z) = q^2 P_{i-1}(q) \ , \ q = 1 + z/D \ , \ P_n(q) = \sum_{m=0}^{n} (-1)^m \frac{(4+2n-m)!}{m!(n-m)!(4+n-m)!} q^{n-m} \tag{29}$$

The deformation modes and the linear RAO results are shown in Figure 1. These results are the same as the numerical results given in [2]. This validates the present approach for linear case.
The preliminary second order results are shown in Figure 2. They concern the non-homogeneous term in the second order free surface condition and the difference in between the results, when full and asymptotic expressions for first order potential are used, is shown. We can see that the results converge quickly to asymptotic solution which is good point which means that the classical procedure for second order diffraction [1] can be used very quickly. Knowing that the pure second order diffraction problem for vertical circular cylinder is already solved [1], this ensures the efficiency of the proposed method. More detailed results will be presented at the Workshop.

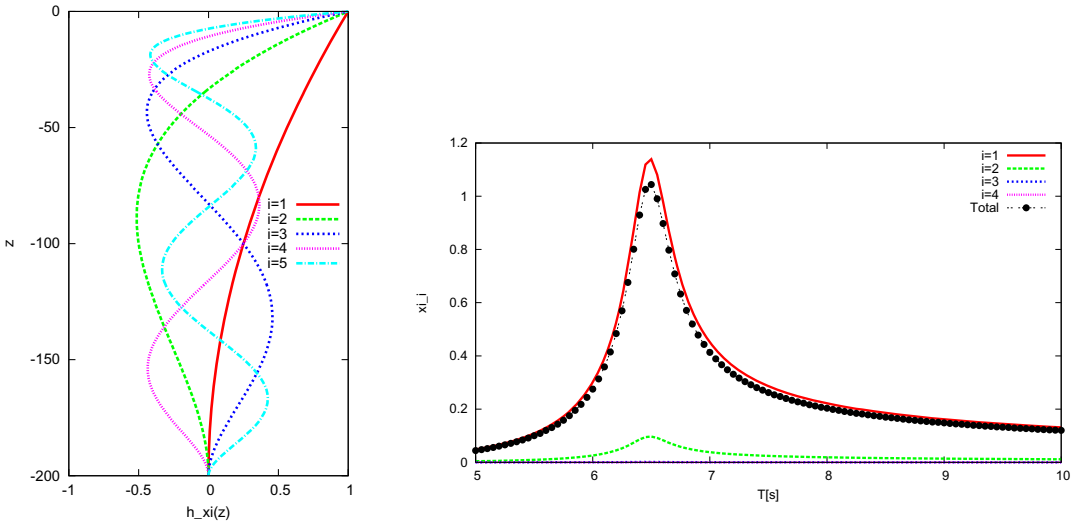

Figure 1: Deformation modes and linear RAO of the motion of the column top.

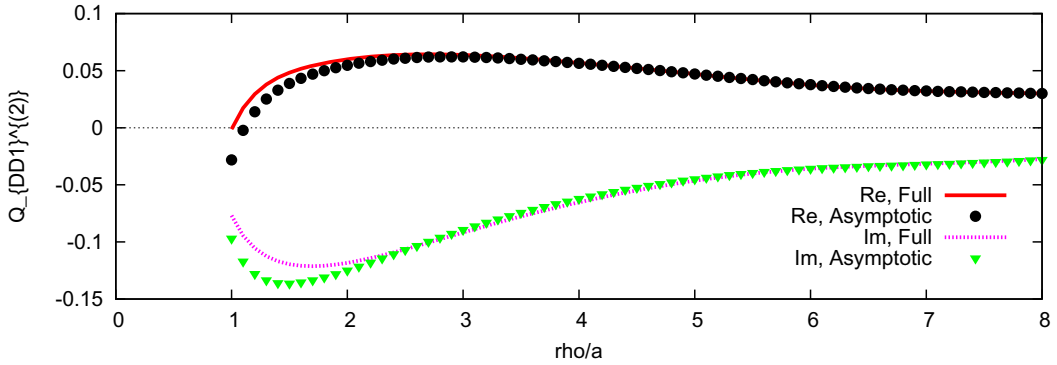

Figure 2: Original and asymptotic second order forcing term on the free surface.

Acknowledgements

The authors acknowledge the support of the National Research Foundation of Korea (NRF) grant funded by the Korea Government (MEST) through GCRC-SOP.

References

[1] Malenica S. & Molin B. 1995. : "Third harmonic wave diffraction by a vertical cylinder", Journal of Fluid Mechanics, vol. 302, pp.203-229.

[2] Newman J.N. 1994. : "Wave effects on deformable bodies", Applied Ocean Research, Vol. 16

(Abstract submitted to the 28th IWWWFB, Marseille, France, 2013)

Hybrid-Spectral Model for Fully Nonlinear Numerical Wave Tank*

Torben B. Christiansen[(1),†], Allan P. Engsig-Karup[(2)], Harry B. Bingham[(1)]
[(1)]DTU Mechanics, [(2)]DTU Informatics, Technical University of Denmark
E-mail: tobc@mek.dtu.dk, apek@imm.dtu.dk, hbb@mek.dtu.dk

Introduction

This abstract is concerned with the development of an efficient and scalable hybrid-spectral model for a fully nonlinear numerical wave tank with finite dimensions, which is used for simulation of nonlinear free surface waves generated by a moving wavemaker.

The approach pursued here is based on the OceanWave3D strategy established in [1, 6, 7], replacing the horisontal high order finite difference approximations used in OceanWave3D with a Fourier Collocation method based on cosine modes. This is combined with a modal Chebyshev Tau method for the potential in the vertical, which by applying an efficient strategy for solving the discrete Laplace equation yields a new attractive and accurate Dirichlet-to-Neumann operator, recently established in [4].

The application of hybrid-spectral methods in the context of the OceanWave3D strategy is motivated by the comparative study of two serial implementations of nonlinear water wave models carried out in [5], which demonstrated that the high-order finite difference model (OceanWave3D) requires approximately an order of magnitude larger computational effort than the high order spectral model (HOS) in order to solve highly nonlinear water wave problems to the same level of accuracy. Compared to the HOS model, the main advantage of OceanWave3D is a relatively straight-forward introduction of non-rectangular geometry, in particular varying bottom bathymetry and the generation of waves by a moving wavemaker. These attractive properties, associated with the OceanWave3D solution strategy, are retained in the presented hybrid-spectral method.

In this abstract the governing equations for the fully nonlinear free surface potential wave problem are derived in curvlinear coordinates on a fixed computational domain, which allows the fully nonlinear wavemaker condition to be satisfied directly. The hybrid-spectral discretization strategy and iterative solution of the resulting discrete Laplace problem are detailed, and it is described how the wavemaker can be modelled by the introduction of additional potentials following the line of [2], which with the present discretization strategy can be obtained essentially free of cost.

*The authors wish to thank the Danish Agency for Science, Technology and Innovation (grant # 09-067257) for funding, and the Danish Center for Scientific Computing for supercomputing resources.

†Presenting author

Problem Formulation

A Cartesian coordinate system $x_i = (x_1, x_2, x_3)$ is adopted with the x_1x_2-plane located at the still water level and the x_3-axis pointing vertically upwards. Indicial notation is invoked and the summation convention applies to repeated indices, with latin indicies $i = 1, 2, 3$ accounting for all spatial dimensions, while greek indicies $\alpha = 1, 2$ only apply to the horisontal dimensions. The still water depth is given by $x_3 = -h(x_\alpha)$ and the position of the free surface is defined by $x_3 = \zeta(x_\alpha, t)$. The wave tank is assumed rectangular in the horisontal plane with dimensions L_1, L_2 and vertical walls, and the gravitational acceleration g is assumed to be constant. Assuming an inviscid fluid and in irrotational flow, the fluid velocity $u_i = \partial_{x_i}\phi$ is defined by the gradient of a scalar velocity potential $\phi(x_i, t)$. The position of the free surface in an Eulerian frame of reference is captured by the usual kinematic boundary condition, while the dynamic free surface boundary condition follows from Bernoulli's equation,

$$\partial_t\zeta = \partial_{x_3}\phi - \partial_{x_\alpha}\phi\,\partial_{x_\alpha}\zeta, \tag{1a}$$

$$\partial_t\phi = -g\zeta - \tfrac{1}{2}\partial_{x_i}\phi\,\partial_{x_i}\phi. \tag{1b}$$

To evolve these equations in time requires solving the Laplace equation for ϕ in the fluid volume Ω. A well-posed Laplace problem is achieved by specifying a known ϕ at the free surface ζ, together with kinematic boundary conditions at the solid boundaries to the domain, i.e. the wave maker, walls and seabed,

$$\partial_{x_ix_i}\phi = 0, \quad x_i \in \Omega, \tag{2a}$$

$$n_i(\partial_{x_i}\phi - v_i^{solid}) = 0, \quad x_i \in \partial\Omega^{solid}, \tag{2b}$$

The free surface is a time-dependent moving boundary with an a priori unknown position, practically resulting in a time-dependent domain which may handled efficiently using the well-known σ-transformation in the vertical [1]. Further introducing a wavemaker as a moving solid boundary, with an a priori known position $x_1 = F(x_2, x_3, t)$ provided by a paddle signal, yields the requirement for a more general mapping between the physical domain Ω and a fixed, time-independent computational domain Ω_C,

$$x_i = x_i(\xi^j, t) \quad \Leftrightarrow \quad \xi^j = \xi^j(x_i, t), \quad \xi^j \in \Omega_C \tag{3}$$

where $\xi^j = (\xi^1, \xi^2, \xi^3)$ is a set of general curvlinear coordinates. The mapping $x_i = x_i(\xi^j, t)$ from computational to physical space is done using transfinite interpolation with linear blending of the boundary

faces, i.e. the free surface, seabed, wavemaker and the fixed walls of the domain [8], while the inverse mapping $\xi^j = \xi^j(x_i,t)$ is not established explicitly though it formally indeed does exist. Taking the derivatives of the mappings $\partial_{\xi^j} x_j$ and $\partial_{x_i}\xi^j$ yield the Cartesian components of the covariant and contravariant basis vectors $\boldsymbol{g}_j$ and $\boldsymbol{g}^j$, which also defines the co- and contravariant metric tensors g_{ij} and g^{ij},

$$(\boldsymbol{g}_j)_i = \partial_{\xi^j} x_i, \qquad \left(\boldsymbol{g}^j\right)_i = \partial_{x_i}\xi^j, \tag{4a}$$

$$g_{ij} = \boldsymbol{g}_i \cdot \boldsymbol{g}_j, \qquad g^{ij} = \boldsymbol{g}^i \cdot \boldsymbol{g}^j. \tag{4b}$$

Via the chain rule, these co- and contravariant basis vectors provide the relationship between spatial derivatives in the physical and computational spaces. For example, derivatives of ζ and ϕ with respect to x_i and ξ^j are related by

$$\partial_{x_\alpha}\zeta = \partial_{x_\alpha}\xi^j\,\partial_{\xi^j}\zeta \;= (\boldsymbol{g}^j)_\alpha\,\partial_{\xi^j}\zeta, \tag{5a}$$

$$\partial_{x_i}\phi = \partial_{x_i}\xi^j\,\partial_{\xi^j}\phi \;= (\boldsymbol{g}^j)_i\,\partial_{\xi^j}\phi. \tag{5b}$$

Note that $\partial_{x_3}\zeta = 0$ and hence only $\partial_{x_\alpha}\zeta$ are evaluated. Similarly the temporal derivatives of ζ, ϕ in physical and computational spaces are related as follows, due to [8],

$$\begin{aligned}(\partial_t\zeta)_{x_i} &= (\partial_t\zeta)_{\xi^j} - (\partial_t x_\alpha)_{\xi^j}\;\partial_{x_\alpha}\zeta \\ &= (\partial_t\zeta)_{\xi^j} - w_\alpha(\boldsymbol{g}^j)_\alpha\,\partial_{\xi^j}\zeta,\end{aligned} \tag{6a}$$

$$\begin{aligned}(\partial_t\phi)_{x_i} &= ((\partial_t\phi)_{\xi^j} - (\partial_t x_i)_{\xi^j}\;\partial_{x_i}\phi \\ &= (\partial_t\phi)_{\xi^j} - w_i(\boldsymbol{g}^j)_i\,\partial_{\xi^j}\phi,\end{aligned} \tag{6b}$$

where $()_{\xi^j}, ()_{x_i}$ indicates the spatial coordinates being kept fixed under partial time differentiation, while $w_i = (\partial_t x_i)_{\xi^j}$ denotes the transport velocity of the transient physical reference frame due to the motion of the boundaries.

The covariant basis vectors $\boldsymbol{g}_j$ are immediately evaluated from the mapping function $x_i = x_i(\xi^j,t)$ at any instance in time by application of the differential operators ∂_{ξ^i} in computational space. From these the contravariant basis vectors $\boldsymbol{g}^j$, which are required to evaluate (5)-(6), are computed by cross products of $\boldsymbol{g}_j$ as,

$$\boldsymbol{g}^k = (\sqrt{g})^{-1}\,\varepsilon_{ijk}\,\boldsymbol{g}_i \times \boldsymbol{g}_j, \quad \sqrt{g} = \sqrt{\det(g_{ij})}. \tag{7}$$

in which $\sqrt{g}$ has been introduced as the Jacobian of the mapping and ε_{ijk} is the permutation operator. Similarly the contravariant metric tensor g^{ij} follows from the covariant tensor g_{ij} as its inverse,

$$g^{ij}g_{ij} = \delta_i^j \quad \Rightarrow \quad \left(g^{ij}\right) = (g_{ij})^{-1}, \tag{8}$$

where δ_i^j denotes the Kronecker delta.

Inserting (5)-(6), the free surface evolution equations (1) may be cast in computational space as,

$$\begin{aligned}\partial_t\zeta &= w_\alpha(\boldsymbol{g}^j)_\alpha\,\partial_{\xi^j}\zeta + (\boldsymbol{g}^j)_3\,\partial_{\xi^j}\phi \\ &\quad - \left((\boldsymbol{g}^j)_\alpha\,\partial_{\xi^j}\phi\right)\left((\boldsymbol{g}^k)_\alpha\,\partial_{\xi^k}\zeta\right), \\ &= (\boldsymbol{g}^j)_3\,\partial_{\xi^j}\phi - \left((\boldsymbol{g}^j)_\alpha\,\partial_{\xi^j}\phi - w_\alpha\right)\left((\boldsymbol{g}^k)_\alpha\,\partial_{\xi^k}\zeta\right),\end{aligned} \tag{9a}$$

$$\begin{aligned}\partial_t\phi &= w_i(\boldsymbol{g}^j)_i\,\partial_{\xi^j}\phi - g\zeta \\ &\quad - \tfrac{1}{2}\left((\boldsymbol{g}^j)_i\,\partial_{\xi^j}\phi\right)\left((\boldsymbol{g}^k)_i\,\partial_{\xi^k}\phi\right), \\ &= -g\zeta - \tfrac{1}{2}\left((\boldsymbol{g}^j)_i\,\partial_{\xi^j}\phi - w_i\right)\left((\boldsymbol{g}^k)_i\,\partial_{\xi^k}\phi\right),\end{aligned} \tag{9b}$$

which shows that the transient physical domain is captured by recasting the free surface equations in arbitrary Eulerian-Lagrangian form in computational space. As a remark the widely used Zakharow form of the free surface equations, applied e.g. in [1], may be derived from (9) simply by taking the mapping $x_i = x_i(\xi^j,t)$ to be the inverse of the σ-transform.

The Laplace equation and the kinematic solid boundary condition (2) are similarily expressed in curvlinear coordinates as follows, due to [8],

$$(\sqrt{g})^{-1}\partial_{\xi^i}\left(\sqrt{g}g^{ij}\partial_{\xi^j}\phi\right) = 0 \qquad \xi^j \in \Omega_C, \tag{10a}$$

$$n_i\left((\boldsymbol{g}^j)_i\,\partial_{\xi^j}\phi - v_i^{solid}\right) = 0, \quad \xi^j \in \partial\Omega_C^{solid}, \tag{10b}$$

in which it is assumed that the normal vector n_i to the physical solid boundaries and the solid boundary velocity v_i^{solid} are expressed in computational space.

Numerical Methods

A method of lines approach is adopted for the discretization of the governing equations stated above. For the time-integration of the free-surface equations (9), the classic four-stage, fourth-order Runge-Kutta scheme is employed as it is not subject to any severe stability constraint on the choice of time steps.

The governing equations are discretized in the computational space using a hybrid-spectral collocation method detailed in [4], combining a nodal Fourier collocation method on a horisontal grid of $\boldsymbol{M} = (N_1, N_2)$ grid points with a modal Chebyshev Tau method in the vertical truncated to the first $N_3 = N + 1$ Chebyshev polynomials, where N is the polynomial order. Due to the finite dimensions and rectangular shape of the numerical wave tank (with the wavemaker at neutral position), it was suggested by [2] to employ a tensor product of cosine modes, i.e. real-and-even Fourier modes, as the basis for the horisontal Fourier collocation method, since they are the natural modes of the tank. Hence ζ, ϕ have the global representation in the computational domain,

$$\zeta(\xi^\alpha,t) = \sum_{\boldsymbol{m}=0}^{\boldsymbol{M}-1} \zeta_{\boldsymbol{m}}(t)\,l_{\boldsymbol{m}}(\xi^\alpha), \tag{11a}$$

$$\phi(\xi^j,t) = \sum_{\boldsymbol{m}=0}^{\boldsymbol{M}-1}\sum_{n=0}^{N} \hat{\phi}_{\boldsymbol{m}n}(t)\,l_{\boldsymbol{m}}(\xi^\alpha)\;T_n\left(\xi^3\right), \tag{11b}$$

where $\zeta_{\boldsymbol{m}}(t) = \zeta(\boldsymbol{\xi}_{\boldsymbol{m}},t)$ and $\hat{\phi}_{\boldsymbol{m}n}(t) = \hat{\phi}_n(\boldsymbol{\xi}_{\boldsymbol{m}},t)$ are the solutions at the collocation nodes $\boldsymbol{\xi}_{\boldsymbol{m}} =$

$(\boldsymbol{m} + \frac{1}{2})/\boldsymbol{M}\pi$, while $T_n(\xi^3) = \cos\left(n \arccos\left(\xi^3\right)\right)$ are the Chebyshev polynomials and $l_{\boldsymbol{m}}(\xi^\alpha)$ are globally defined nodal Lagrange interpolation polynomials, which may be formally derived from the cosine modes $\psi_{\boldsymbol{m}}(\xi^\alpha) = \cos\left(m_1\xi^1\right)\cos\left(m_2\xi^2\right)$. Finally $\boldsymbol{m} = (m_1, m_2)$ is a multi-index where the two components of $\boldsymbol{m}$ are allowed to vary independently.

The horisontal derivatives ∂_{ξ^α} are approximated by their discrete counterparts in computational space using the Fast Fourier/Cosine Transform (FFT/FCT) to evaluate the derivatives in the collocation nodes. The Chebyshev Tau method provides an efficient, spectrally accurate Dirichlet-to-Neumann operator for the evaluation of the gradient of the velocity potential at the free surface. Based on orthogonal truncation rather than interpolation (as used e.g. in finite difference methods), the Chebyshev Tau method seeks to satisfy the Laplace equation (10a) over the depth for each vertical set of collocation nodes in weak form by requiring the residual to be orthogonal to a set of test functions $T_q\left(\xi^3\right)$ for $q = 0, \ldots, N-2$. The remaining two equations, required to obtain a square system of N_z equations with the N_z unknowns $\hat{\phi}_{\boldsymbol{m}n}$ for each vertical set of collocation nodes, arise by imposing additional constraints on the coefficients in order to satisfy the free surface and bottom boundary conditions. For further details on the Chebyshev Tau method see e.g. [3].

Applied to the Laplace equation (10a) the Chebyshev Tau method yields a set of convolution sums, which for relatively simple mappings between the physical and the computational domain, such as the σ-transform, may be evaluated efficiently in modal space. The costs associated with the evaluation of the Laplacian in such cases by direct convolution sums are comparable to those of applying a sixth order finite difference method. However, as demonstrated in [4] the Chebyshev Tau method introduces significantly lower dispersion errors than comparable finite difference methods. For more general mappings it may be advantageous to evaluate the convolution sums by pseudo-spectral products in the corresponding nodal space trough application of the FCT, which applies to Chebyshev polynomials.

The resulting discrete Laplace problem can be stated as a rank $n = N_1N_2N_3$ linear system of equations $\mathcal{A}\Phi = b$, where $\mathcal{A}$ is a large dense, non-symmetric matrix (in case the FFTs are replaced with matrix-based discrete Fourier transforms), Φ is a vector of values for the unknown scalar velocity potential, while b is a vector accounting for the inhomogeneous boundary conditions. Since the discrete Laplace problem is one spatial dimension $\mathcal{O}(N_z)$ larger than the free surface problem, the solution of this linear system at every time step is consequently the computational bottleneck of the model.

The discrete Laplace problem can be solved efficiently (i.e. with optimal scaling of the computational effort and memory footprint) by a iterative left preconditioned defect correction (PDC) method, as detailed in [4]. Evaluation of the residual $r = b - \mathcal{A}\phi$ and hence the matrix-vector product $\mathcal{A}\phi$ does not require $\mathcal{A}$ to be formed explicitly and may be evaluated in $\mathcal{O}(n \log N_1)$ and $\mathcal{O}(n \log N_2)$ operators by application of the FCT horisontally.

The action of the preconditioning problem in the PDC method is to compute the correction δ to the current solution by solving the linear system of equations $\mathcal{M}\delta = r$, where $\mathcal{M} \approx \mathcal{A}$ is the preconditioning matrix. For the present problem and hybrid-spectral discretization method, the corresponding constant coefficient Laplace problem (i.e. neglecting bottom variations, free surface elevation and wavemaker motion) provides an attractive efficient and sparse preconditioning strategy. In order to avoid assembling and factorizing the full dense preconditioning matrix, the residual r is first transformed to a modal cosine representation horizontally by use of the FCT, while the modal Chebyshev representation is retained in the vertical. This decouples the preconditioning step into a inhomogeneous constant coefficient Helmholz equation in the vertical for each horizontal cosine mode, since $r \neq 0$ and $\nabla^2\psi_{\boldsymbol{m}}(\xi^\alpha) = -\boldsymbol{m}\cdot\boldsymbol{m}\,\psi_{\boldsymbol{m}}(\xi^\alpha)$.

Applying the Chebyshev Tau method in the vertical to each of the Helmholz equations yields N_1N_2 sparse systems of N_3 equations at each horisontal collocation point. These systems are primarily quasi-pentadiagonal as each row contains only three non-zero entries in diagonals $(-2, 0, +2)$ in addition to two dense rows enforcing the boundary conditions, see [3]. Using a tailored Gaussian elimination solution strategy, each of these systems is solved in just $18N_3$ operations, only around twice the cost of the classic tridiagonal matrix algorithm, and with the same $2p$ memory footprint, making this preconditioning strategy well suited for parallel implementation.

Wave Generation by Additional Potentials

The wavemaker is modelled as a solid moving boundary with a known position $x_1 = F(x_2, x_3, t)$, which gives rise to the following free slip condition,

$$\partial_t F = \partial_{x_1}\phi - \partial_{x_2}F\partial_{x_2}\phi - \partial_{x_3}F\partial_{x_3}\phi = \partial_n\phi, \quad (12)$$

where ∂_n denotes the derivative normal to the wavemaker with normal vector $n_i^{gen} = (1, -\partial_{x_2}F, -\partial_{x_3}F)$. The velocity potential (11b) defined in terms of cosine modes implicitly satisfies homogeneous Neumann boundary conditions, hence it cannot account for the inhomogeneous Neumann boundary condition introduced by the wavemaker motion. This was also noted by [2], who suggested the use of additional potentials to account for the inhomogeneous Neumann condition by splitting the potential into two,

$$\phi = \phi_P + \phi_G, \quad (13)$$

where ϕ_P is the propagating spectral potential defined in (11b) and ϕ_G is the generation potential accounting for the inhomogeneous Neumann condition (12) at the wavemaker, while the total potential ϕ is advanced by the free surface equations (9).

In this work we seek to establish the generation potential ϕ_G by exploiting that the Laplace equation and boundary conditions (10a) are solved directly in discrete form in the fluid domain, and not—as was done in [2]—by constructing the velocity potential such that satisfies the governing equations identically in the domain. Casting the Laplace problem in physical space for clarity, this approach can be illustrated by considering a piston type wavemaker with position $x_1 = F(t)$, i.e. a translation of the wall. The inhomogeneous Neumann condition at the wavemaker (12) must be satisfied by the generation potential,

$$\partial_t F = \partial x_1 \phi_G, \quad x_1 = F, \tag{14}$$

while ϕ_G at the same time may not introduce inhomogeneous Neumann terms on the other walls of the domain. However, ϕ_G is not required to satisfy the Laplace equation, bottom or free surface boundary conditions, suggesting that ϕ_G can be expressed as,

$$\phi_G(x_i, t) = \partial_t F(x_2, x_3, t)\, \varphi_G(x_1, t), \tag{15}$$

where the function $\varphi_G(x_1, t)$ must satisfy $\partial_{x_1}\varphi_G|_{x_1=F(t)} = 1$ and $\partial_{x_1}\varphi_G|_{x_1=L_1} = 0$ in order to reflect the Neumann conditions at these locations. These conditions may be satisfied by the third order Hermite polynomial,

$$\varphi_G(x_1, t) = (L_1 - F(t))^{-2}\,(x_1 - F(t))\,(L_1 - x_1)^2, \tag{16}$$

which further satisfies $\varphi_G|_{x_1=F(t)} = \varphi_G|_{x_1=L_1} = 0$. Inserting the splitting of the velocity potential (13) in (2) yields a Poisson equation for the propagation potential ϕ_P with homogeneous Neumann boundary conditions at the wavemaker and all fixed walls,

$$\phi_P = \phi - \phi_G, \qquad x_3 = \zeta, \tag{17a}$$
$$\partial_{x_i x_i}\phi_P = -\partial_{x_i x_i}\phi_G, \qquad x_i \in \Omega, \tag{17b}$$
$$\partial_{x_1}\phi_P = 0, \qquad x_1 = F, \tag{17c}$$
$$n_i^{wall}\partial_{x_i}\phi_P = 0, \qquad x_i \in \partial\Omega^{wall}, \tag{17d}$$
$$n_i^{bot}\partial_{x_i}\phi_P = -n_i^{bot}\partial_{x_i}\phi_G, \qquad x_i \in \partial\Omega^{bot}, \tag{17e}$$

This Poisson equation may be discretized using the presented hybrid-spectral method and solved efficiently with the PDC method. The generation potential is thus essentially obtained free of cost, as only the action of the discrete Laplace operator on the generation potential must be evaluated in order to form the right-hand-side vector to the Poisson problem. The approach generalises to other types of wavemakers such as flaps, in which case it is necessary to express the generation potential and Poisson equation for the propagation potential in computational space. Further the idea of additional potentials may be used to introduce Sommerfeld type, radiation outflow conditions at the opposite end of the wave tank.

Results & Future Work

The presented hybrid-spectral model provides an efficient and accurate tool for simulation of fully nonlinear free surface waves. Compared to the OceanWave3D finite difference based model, preliminary studies considering highly nonlinear propagating waves indicate both improved accuracy and a 50% reduction of the computational costs for identical problem sizes, see [4].

At the 28$^{\text{th}}$ IWWWFB we will present results obtained with the fully nonlinear numerical wave tank, including the wavemaker model by introduction of additional potentials essentially free of cost.

References

[1] H. B. Bingham and H. Zhang. On the accuracy of finite difference solutions for nonlinear water waves. *J. Engineering Math.*, 58:211–228, 2007.

[2] F. Bonnefoy, D. Le Touzé, and P. Ferrant. A fully-spectral 3d time-domain model for second-order simulation of wavetank experiments. part a: Formulation, implementation and numerical properties. *Applied Ocean Research*, 28:33–43, 2016.

[3] C. Canuto, M.Y. Hussaini, A. Quarteroni, and T.A. Zang. *Spectral Methods – Fundamentals in Single Domains*. Spring, 2006.

[4] T.B. Christiansen, A.P. Engsig-Karup, H.B. Bingham, G. Ducrozet, and P. Ferrant. Efficient hybrid-spectral model for fully nonlinear numerical wave tank. In *OMAE'13-10861: 21st International Conference on Offshore Mechanics and Arctic Engineering*, Nantes, France, 2013.

[5] G. Ducrozet, H. B. Bingham, A. P. Engsig-Karup, F. Bonnefoy 1, and P. Ferrant. A comparative study of two fast nonlinear free-surface water wave models. *Int. J. Num. Methods in Fluids (published online)*, 2011.

[6] A. P. Engsig-Karup, H. B. Bingham, and O. Lindberg. An efficient flexible-order model for 3D nonlinear water waves. *J. Comput. Phys.*, 228:2100–2118, 2009.

[7] A. P. Engsig-Karup, M. G. Madsen, and S. L. Glimberg. A massively parallel gpu-accelerated model for analysis of fully nonlinear free surface waves. *Int. J. Num. Methods in Fluids (published online)*, 2011.

[8] M. Farrashkhalvat and J.P. Miles. *Basic Structured Grid Generation*. Butterworth Heinemann, 2003.

Extended abstract for the 28th International Workshop on Water Waves and Floating Bodies, 7-10 April 2013, Marseille, France

Free surface determination from pressure measurements at the sea bed

Didier CLAMOND

Laboratoire J.-A. Dieudonné, University of Nice – Sophia Antipolis, France.
E-Mail: didierc@unice.fr

1 Introduction

Within the framework of incompressible, homogeneous and inviscid flow modelling of water waves, the pressure plays an important role in establishing various qualitative properties of traveling waves. The pressure is also essential in quantitative studies because often in practice the elevation of a surface water-wave is determined from pressure data obtained at the sea bed, see e.g. [6]. Indeed, measuring a free surface wave motion without intrusive probes is of most importance for practical applications, and one way to achieve this is to use pressure gauges at the sea bed. From these pressure measurements, the question is how one can reconstruct the free surface.

A standard approach consists in assuming that the hydrostatic approximation is sufficiently accurate. However, already for waves of moderate amplitude, prediction errors exceeding 15% frequently occur [1]. These inaccuracies are due to the fact that the hydrostatic approximation ignores even linear wave effects. Within the linear regime of water waves of small amplitude in finite depth, one can derive a better approximation [4], but its benefit is offset by the fact that, for waves of moderate amplitude, it often overestimates the wave height by more than 10% [6]. These considerations motivated the quest for a reconstruction formula that accounts for nonlinear effects and that is thus applicable to waves of moderate and large amplitude. Nonlinear nonlocal equations relating the dynamic pressure on the bed and the wave profile were obtained without approximation from the governing equations [3, 5]. The entangled character of these equations is a considerable impediment in the pursuit of an in-depth analysis and for practical applications.

Very recently, new exact tractable relations have been obtained [2], allowing mathematical analysis and a straightforward numerical procedure for deriving the free surface from the pressure at the bed. However, in [2], only relations leading to procedures where convergence and unicity could be rigorously proven were included. It is nonetheless possible to derive several other exact relations that are of major practical interest, though the efficiency of the procedures based on these relations have not yet be proven (i.e. convergence and unicity is theoretically unknown). The present paper is devoted to the derivation of these new relations and to the numerical illustration of heir efficiency.

In section 2, the hypothesis and notations are introduced for steady irrotational surface waves on constant depth. In order to make the present paper self-contained, the main results of [2] are given in section 3. A new, purely local, expression for the free surface is then derived in section 4, which is the main result of the present paper.

2 Hypothesis and notations

In a frame of reference moving at the constant wave speed c, the flow beneath a traveling wave reduces to a steady motion with respect to the moving coordinate system. Let (x, y) be a Cartesian coordinate system moving with the wave, x being the horizontal coordinate and y the upward vertical coordinate. Let $\{u(x, y),\, v(x, y)\}$ be the velocity field in the moving frame. The wave is

$(2\pi/k)$-periodic in the x-direction, and we denote by $y = -d$, $y = \eta(x)$ and $y = 0$ the equations of the horizontal bottom, of the free surface and of the mean water level, respectively. The latter equation expresses the fact that $\langle \eta \rangle = 0$ for the smooth $(2\pi/k)$-periodic wave profile η, where $\langle \cdot \rangle$ is the Eulerian average operator over one wavelength,

$$\langle\, \eta \,\rangle \;\equiv\; \frac{k}{2\,\pi} \int_{-\pi/k}^{\pi/k} \eta(x)\; \mathrm{d}x \;=\; 0. \tag{1}$$

Let ϕ and ψ be the velocity potential and the stream function, respectively, such that $u = \phi_x = \psi_y$ and $v = \phi_y = -\psi_x$. It is convenient to introduce the complex potential and the complex velocity $f = \phi + \mathrm{i}\psi$ and $w = u - \mathrm{i}v$, respectively, that are holomorphic functions of the complex variable $z = x + \mathrm{i}y$, with $f = f(z)$ and $w = \mathrm{d}f/\mathrm{d}z$. The equation of mass conservation for a homogeneous fluid and the irrotational character of the flow are identically fulfilled with the requirement that f and w are holomorphic functions throughout the fluid domain. The Euler equation can be expressed by means of the Bernoulli condition

$$2\,p \;+\; 2\,g\,y \;+\; u^2 \;+\; v^2 \;=\; B, \qquad x \in \mathbb{R},\; -d \leqslant y \leqslant \eta(x), \tag{2}$$

for some Bernoulli constant B, where $p = p(x, y)$ is the pressure divided by the density. From (1) and (2), we get

$$B \;=\; \big\langle\, {u_{\mathrm{s}}}^2 \;+\; {v_{\mathrm{s}}}^2 \,\big\rangle \;=\; \big\langle\, {u_{\mathrm{b}}}^2 \,\big\rangle\,, \tag{3}$$

where u_{s} and v_{s} denote the restrictions of u and v to the free surface, respectively, while u_{b} denotes the restrictions of u at the bed. (The second equality in (3) derives from the irrotationality.) The relations (2) and (3) yield

$$\langle\, p_{\mathrm{b}} \,\rangle \;=\; g\,d, \tag{4}$$

where $p_{\mathrm{b}}(x) = p(x, -d)$ is the normalized relative pressure at the bed.

Finally, we define the wave phase velocity c such that $c = -\langle u_{\mathrm{b}} \rangle$, so that the wave travels with phase speed c in the frame of reference where the mean horizontal velocity is zero at the bed, and where $c > 0$ if the wave travels toward the increasing x-direction.

3 Equations for the surface recovery

Instead of dealing with the complex potential f or with the complex velocity w, it is advantageous to use the holomorphic function w^2. Indeed, the function $\mathcal{P}$ defined by

$$\mathcal{P}(z) \;\equiv\; \tfrac{1}{2}\,B \;+\; g\,d \;-\; \tfrac{1}{2}\,w^2(z) \;=\; \tfrac{1}{2}\,B \;+\; g\,d \;-\; \tfrac{1}{2}\,(u^2 - v^2) \;+\; \mathrm{i}\,u\,v, \tag{5}$$

is holomorphic in the fluid domain and its restriction to the flat bed $y = -d$ has zero imaginary part and real part p_{b}, i.e., $p_{\mathrm{b}}(x) = \mathcal{P}(x - \mathrm{i}d) = gd + \frac{1}{2}(B - u_{\mathrm{b}}^2)$. Thus p_{b} determines $\mathcal{P}$ uniquely throughout the fluid domain, i.e., $\mathcal{P}(z) = p_{\mathrm{b}}(x + \mathrm{i}y + \mathrm{i}d)$. Note that p coincides with the real function $\mathrm{Re}\{\mathcal{P}\}$ only on $y = -d$ because p is not a harmonic function in the fluid domain.

Using the surface impermeability and (2) on the free surface $y = \eta(x)$ where $p = 0$, we have

$$\begin{aligned}(u_{\mathrm{s}} - \mathrm{i}v_{\mathrm{s}})^2 \;&=\; (1 - \mathrm{i}\eta_x)^2\, u_{\mathrm{s}}^2 \;=\; (1 + \eta_x^2)\, u_{\mathrm{s}}^2\, (1 - \mathrm{i}\eta_x) \,/\, (1 + \mathrm{i}\eta_x) \\ &=\; (u_{\mathrm{s}}^2 + v_{\mathrm{s}}^2)\, (1 - \mathrm{i}\eta_x) \,/\, (1 \;+\; \mathrm{i}\eta_x) \;=\; (B - 2g\eta)\, (1 - \mathrm{i}\eta_x) \,/\, (1 + \mathrm{i}\eta_x).\end{aligned}$$

Multiplying this relation by $(1 + \mathrm{i}\eta_x)$ and using (5), we obtain at once

$$g\eta\,(1 - \mathrm{i}\eta_x) \;+\; \mathrm{i}B\eta_x \;=\; [\,\mathcal{P}(x + \mathrm{i}\eta) \;-\; g\,d\,]\,(1 + \mathrm{i}\eta_x). \tag{6}$$

The real and imaginary parts of (6) give two equations for η:

$$g\,\eta \;=\; \mathrm{Re}\{\mathcal{P}_\mathrm{s}\} \;-\; g\,d \;-\; \eta_x\,\mathrm{Im}\{\mathcal{P}_\mathrm{s}\}, \qquad (B \,-\, g\,\eta)\,\eta_x \;=\; [\,\mathrm{Re}\{\mathcal{P}_\mathrm{s}\} \,-\, gd\,]\,\eta_x \;+\; \mathrm{Im}\{\mathcal{P}_\mathrm{s}\}, \quad (7)$$

where, as above, the subscript 's' denotes the evaluation at the free surface $y = \eta(x)$. Using (5), we can see that equations (7) are precisely

$$g\,\eta \;=\; \tfrac{1}{2}\,[\,B \,-\, u_\mathrm{s}^2 \,-\, v_\mathrm{s}^2\,], \qquad (B \,-\, g\eta)\,\eta_x \;=\; \tfrac{1}{2}\,[\,B \,+\, u_\mathrm{s}^2 \,+\, v_\mathrm{s}^2\,]\,\eta_x. \quad (8)$$

Thus, both are ensured by the validity of the Bernoulli condition (2) on the free surface. Since $\eta_x \neq 0$ between consecutive crests and troughs, not only does $(8a)$ imply $(8b)$, but also $(8b)$ ensures the validity of $(8a)$ between consecutive crests and troughs, and by continuous extension everywhere.

For the recovery of the surface wave profile η, given the function p_b, one can proceed as follows. For periodic waves, the pressure p at the bed $y = -d$ can be approximated, e.g., by a N-th order Fourier polynomial and the function $\mathcal{P}$ is obtained at once, i.e.,

$$p_\mathrm{b}(x) \;\approx\; \sum_{n=-N}^{N} \mathfrak{p}_n\,\exp(\mathrm{i}nkx) \qquad \Rightarrow \qquad \mathcal{P}(z) \;\approx\; \sum_{n=-N}^{N} \mathfrak{p}_n\,\exp(\mathrm{i}nk[x+\mathrm{i}(y+d)]), \quad (9)$$

with $\mathfrak{p}_{-n} = \overline{\mathfrak{p}}_n$ since p_b is real, and $\mathfrak{p}_0 = gd$. Note that (9) is not the only possible approximation and, e.g., elliptic functions could also be used, specially in shallow water.

The wave amplitude η_0 is obtained evaluating $(7a)$ at the wave crest located at $x = 0$ (where $\eta_x = 0$ and $\eta = \eta_0$) leading to the implicit equation

$$\eta_0 \;=\; \mathrm{Re}\{\mathcal{P}(\mathrm{i}\eta_0)\}\,/\,g \;-\; d. \quad (10)$$

The crest height η_0 is obtained as the unique solution to (10), as proven in [2] and where numerical examples are provided. With η_0 determined by solving (10) iteratively, η is subsequently obtained re-expressing $(7b)$ as the ordinary differential equation

$$\eta_x \;=\; \mathrm{Im}\{\mathcal{P}_\mathrm{s}\}\,/\,[\,B \,-\, g\eta \,-\, \mathrm{Re}\{\mathcal{P}_\mathrm{s}\} \,+\, gd\,], \quad (11)$$

with initial data $\eta(0) = \eta_0$. The right-hand side of (11) being smooth, the solution can be obtained by a standard iterative procedure, as proven and illustrated in [2]. It is however possible to derive a local simpler expression which does not require the resolution of a differential equation.

Note that the surface reconstruction procedure described here is valid for all waves, except perhaps for the highest ones with an angular crest and for waves with different crests, as demonstrated in [2]. Note also that the inclusion of surface tensions is straightforward, but this generalisation has little practical interest.

4 New equation for the surface recovery

Let be yet another holomorphic function $\mathcal{Q}$ such that

$$\mathcal{Q}(z) \;\equiv\; \int_{z_0}^{z} \big[\,\mathcal{P}(z') \,-\, g\,d\,\big]\,\mathrm{d}z' \;=\; \int_{z_0}^{z} \tfrac{1}{2}\,\big[\,B \,-\, w(z')^2\,\big]\,\mathrm{d}z', \quad (12)$$

where z_0 is an arbitrary constant. Taking z_0 at the origin of the free surface — i.e., $x = 0$, $y = \eta_0$ thence $z_0 = \mathrm{i}\eta_0$ — and choosing the surface as integration path, the definition (12) yields

$$\mathcal{Q}_\mathrm{s}(x) \;=\; \int_0^x \big[\,\mathcal{P}(x' + \mathrm{i}\eta(x')) \,-\, g\,d\,\big]\,[\,1 \,+\, \mathrm{i}\,\eta_x(x')\,]\,\mathrm{d}x', \quad (13)$$

thence, substituting (6), after some elementary algebra

$$\mathcal{Q}_{\rm s}(x) \;=\; \int_0^x g\,\eta(x')\,{\rm d}x' \;+\; {\rm i}\,[\,\eta(x) \,-\, \eta_0\,]\,\big[\,B \,-\, \tfrac{1}{2}\,g\,\eta_0 \,-\, \tfrac{1}{2}\,g\,\eta(x)\,\big]\,. \tag{14}$$

The imaginary part of this relation yields an implicit equation for η:

$$\kappa\,\eta \;=\; 1 \;-\; \sqrt{(1-\kappa\eta_0)^2 \,-\, (2\kappa/B)\;{\rm Im}\{\mathcal{Q}_{\rm s}\}}\,, \tag{15}$$

where $\kappa \equiv g/B$ is a parameter introduced for convenience. The relation (15) is algebraic (i.e., neither differential nor integral) and local. η can be obtained via functional iterations once $\mathcal{Q}$ is known. Once the pressure at the bottom is known, it is trivial to obtain $\mathcal{P}$ as indicated above and, subsequently, $\mathcal{Q}$ is easily obtained too, for example from the approximation (9)

$$\mathcal{Q}(z) \;\approx\; \sum_{n\neq 0} \frac{\mathfrak{p}_n}{{\rm i}nk}\,[\,\exp({\rm i}nkz) \,-\, \exp(-nk\eta_0)\,]\exp(-nkd). \tag{16}$$

The remaining open question is whether or not the iterations of (15) converge. Preliminary numerical investigations suggest that converge occurs, but a more thorough analysis is required as formula (15) is potentially very useful for practical applications.

Note that solutions of (15) are also solutions of (11). Indeed, using (13), the derivative of (15) gives

$$\eta_x \;=\; \frac{(1/B)\,[\,{\rm Im}\{\mathcal{Q}_{\rm s}\,]_x}{\sqrt{(1-\kappa\eta_0)^2 \,-\, (2\kappa/B)\;{\rm Im}\{\mathcal{Q}_{\rm s}\}}} \;=\; \frac{{\rm Im}\{\mathcal{P}_{\rm s}\} \;+\; (\,{\rm Re}\{\mathcal{P}_{\rm s}\} \,-\, g\,d\,)\,\eta_x}{B \;-\; g\,\eta}, \tag{17}$$

and solving this equation for η_x yields equation (11) precisely, of course.

5 Conclusion

We have derived some exact relations for the reconstruction of the free surface wave profile from pressure measurements at the bed. In particular, we obtained a new local relation for the free surface that is potentially very attractive for practical applications.

More insights of the method, including mathematical proofs and numerical examples will be presented at the workshop.

References

[1] Bishop, C. T. & Donelan, M. A. 1987. Measuring waves with pressure transducers. *Coastal Eng.* **11**, 309–328.

[2] Clamond, D. & Constantin, A. 2013. Recovery of steady periodic wave profiles from pressure measurements at the bed. *J. Fluid Mech.* **714**, 463–475.

[3] Constantin, A. 2012. On the recovery of solitary wave profiles from pressure measurements. *J. Fluid Mech.* **699**, 373–384.

[4] Escher, J. & Schlurmann, T. 2008. On the recovery of the free surface from the pressure within periodic traveling water waves. *J. Nonlinear Math. Phys.* **15**, 50–57.

[5] Oliveras, K. L., Vasan, V., Deconinck, B. & Henderson, D. 2012. Recovering surface elevation from pressure data. *SIAM J. Appl. Math.* **72**, **3**, 897–918.

[6] Tsai, C. H., Huang, M. C., Young, F. J., Lin, Y. C. & Li, H. W. 2005. On the recovery of surface wave by pressure transfer function. *Ocean Eng.* **32**, 1247–1259.

A second order Ordinary Differential Equation for the frequency domain Green function.

by Alain H. Clément
alain.clement@ec-nantes.fr

LUNAM Université, Ecole Centrale de Nantes,
LHEEA CNRS UMR6598, 1, Rue de la Noë, 44300 Nantes, FRANCE

The present work is developped under the usual assumptions of linear potential flow theory. We consider a source point $Q^{'}(x^{'}, y^{'}, z^{'})$, and a field point $Q(x, y, z)$ both lying in the lower half-plane $(z < 0, z^{'} < 0)$. r is the relative horizontal distance, $Z = z + z'$ the vertical distance between the field point and $Q'_1$the image of the source point relative to the free surface (fig.1). R is the distance $|QQ'|$ and $R_1 = \sqrt{r^2 + Z^2}$ the distance $|QQ'_1|$.

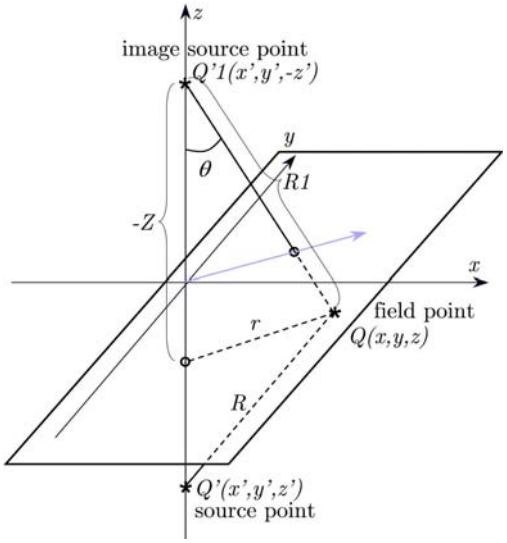

Figure 1: source and field point - layout and notations

1 Time and Frequency domain Green functions

Frequency-domain - Let us first recall the expression of the complex Green function of the diffraction-radiation problem in water of infinite depth in non-dimensionalized variables.

$$G_\infty(r, Z, i\omega) = \left(\frac{1}{R} - \frac{1}{R_1}\right) + 2\mathrm{PV}\int_0^\infty \frac{k}{k - k_0} e^{kZ} J_0(kr)dk - 2i\pi sgn(\omega) k_0 e^{k_0 Z} J_0(k_0 r) \tag{1}$$

or

$$G_\infty(r, Z, i\omega) = G_0(Q, Q') + \ G(r, Z, i\omega)$$

where $k_0 = \omega^2$, and $\mathrm{PV}\int$ means principal value of the integral.

This expression can be shown to be equivalent to Wehausen [6] formulation:

$$G_\infty(r, Z, i\omega) = \frac{1}{R} + \mathrm{PV}\int_0^\infty \frac{k + k_0}{k - k_0} e^{kZ} J_0(kr)dk - 2i\pi sgn(\omega) k_0 e^{k_0 Z} J_0(k_0 r) \tag{2}$$

by using the identity :$(R_1)^{-1} = \left(r^2+Z^2\right)^{-\frac{1}{2}} = \int_0^\infty e^{kZ}J_0(kr)dk$ [4]. Eq (1) gives the velocity potential at point Q generated by a pulsating source of unit strenght located at point Q'. The G_∞ function (1) is the basic mathematical tool used to solve diffraction-radiation problems in regular waves of frequency ω, and period $T = 2\pi/\omega$.

Time-domain - when the source strength is no longer a cosine function of time but a simple impulse, namely $q(t) = \delta(t)$ a Dirac function, then the Green function is given by

$$F_\infty(r,Z,t) = \left(\frac{1}{R} - \frac{1}{R_1}\right)\delta(t) + 2\mathbb{H}(t)\int_0^\infty \sqrt{k}e^{kZ}J_0(kr)\sin(t\sqrt{k})dk \tag{3}$$

or

$$F_\infty(r,Z,t) = G_0(Q,Q')\delta(t) + \mathbb{H}(t)F(r,Z,t)$$

with $\mathbb{H}(t)$ the Heaviside step function. Considering the velocity potential as the output of the fluid *system* with source strength as the input, it is established that the Green function of frequency domain eq.(1) can be derived as the Fourier transform of the time-domain Green function eq.(3), with the following convention and notations:

$$G_\infty(r,Z,i\omega) = \hat{F}_\infty(r,Z,i\omega) = \mathcal{F}\left\{F_\infty(r,Z,t)\right\} = \int_{-\infty}^{\infty} F_\infty(r,Z,t)e^{-i\omega t}dt \tag{4}$$

In [2] [1], we have shown the integral part $F(r,Z,t)$ of the above time-domain Green function to be the solution of an exact fourth order linear ordinary differential equation with polynomial coefficient,

$$\left(r^2+Z^2\right)F^{(4)} - ZtF^{(3)} + \left(\frac{1}{4}t^2 - 4Z\right)F^{(2)} + \frac{7}{4}tF^{(1)} + \frac{9}{4}F = 0 \tag{5}$$

where the notation $F^{(n)}$ holds for the n^{th} derivative of F with respect to the time variable t. Among other applications, this ODE has been shown [3] to provide a good mean to speed up the inline computations of the Green function in time-domain BEM computational codes.

In this paper, we will show how to derive from eq.5 a similar ODE, but in the frequency variable, for the frequency domain Green function $G(r,Z,i\omega)$.

2 Fourier transform of the time-domain ODE

Let us first introduce the auxiliary function $S(r,Z,t) = \mathbb{H}(t)F(r,Z,t)$ with $\mathbb{H}$ the Heaviside step function.

Taking into account the differential relation between the Heaviside and Dirac functions, i.e $\delta(t) = d\mathbb{H}(t)/dt = \mathbb{H}^{(1)}(t)$, we establish the following relations by successive differentiation

$$\begin{aligned}
S &= \mathbb{H}F\\
S^{(1)} &= \delta F + \mathbb{H}F^{(1)}\\
S^{(2)} &= \delta^{(1)}F + 2\delta F^{(1)} + \mathbb{H}F^{(2)}\\
S^{(3)} &= \delta^{(2)}F + 3\delta^{(1)}F^{(1)} + 3\delta F^{(2)} + \mathbb{H}F^{(3)}\\
S^{(4)} &= \delta^{(3)}F + 4\delta^{(2)}F^{(1)} + 6\delta^{(1)}F^{(2)} + 4\delta F^{(3)} + \mathbb{H}F^{(4)}
\end{aligned}$$

The time domain homogeneous ODE (5) obviously still holds when both sides are multiplied by $\mathbb{H}(t)$, leading to:

$$\begin{aligned}
\left(r^2+Z^2\right)S^{(4)} - ZtS^{(3)} + \left(\frac{1}{4}t^2 - 4Z\right)S^{(2)} + \frac{7}{4}tS^{(1)} + \frac{9}{4}S = \\
+\delta\left[\left(r^2+Z^2\right)F^{(3)} - 3ZtF^{(2)} + 2\left(\tfrac{1}{4}t^2 - 4Z\right)F^{(1)} + \tfrac{7}{4}tF\right]\\
+\delta^{(1)}\left[6\left(r^2+Z^2\right)F^{(2)} - 3ZtF^{(1)} + \left(\tfrac{1}{4}t^2 - 4Z\right)F\right]\\
+\delta^{(2)}\left[4\left(r^2+Z^2\right)F - ZtF\right]\\
+\delta^{(3)}\left(r^2+Z^2\right)F
\end{aligned} \tag{6}$$

2.1 Left-hand side

As expected, the left hanfd side of (6) is the same as eq.5. Let's now take its Fourier transform

$$\mathcal{L} = \mathcal{F}\left\{\left(r^2+Z^2\right)S^{(4)} - ZtS^{(3)} + \left(\frac{1}{4}t^2 - 4Z\right)S^{(2)} + \frac{7}{4}tS^{(1)} + \frac{9}{4}S\right\} \tag{7}$$

By using the basic rules of Fourier transform for a derivative $F\left\{f^{(n)}(t)\right\} = (i\omega)^n \hat{f}(i\omega)$, and for the product by a polynomial $F\left\{t^m f(t)\right\} = i^m \frac{d^m}{d\omega^m}\hat{f}(i\omega)$ [5], and after re-ordering we get:

$$\mathcal{L} = \frac{\omega^2}{4}\hat{S}^{(2)} - \omega\left(\omega^2 Z + \frac{3}{4}\right)\hat{S}^{(1)} + \left(\omega^4\left(r^2+Z^2\right) + \omega^2 Z + 1\right)\hat{S} \tag{8}$$

2.2 Right-hand side

For developping the Fourier transform of the right hand side of (6), we then apply the following relations derived from the fundamental property of the Dirac delta function, and integration by parts:

$$\begin{aligned}
\mathcal{F}\left\{\delta(t)f(t)\right\} &= \int_{-\infty}^{+\infty}\delta(t)f(t)e^{-i\omega t} = f(0) \qquad (9)\\
\mathcal{F}\left\{\delta^{(1)}(t)f(t)\right\} &= \int_{-\infty}^{+\infty}\delta^{(1)}(t)f(t)e^{-i\omega t} = -f^{(1)}(0) + i\omega f(0)\\
\mathcal{F}\left\{\delta^{(2)}(t)f(t)\right\} &= \int_{-\infty}^{+\infty}\delta^{(2)}(t)f(t)e^{-i\omega t} = f^{(2)}(0) - 2i\omega f^{(1)}(0) - \omega^2 f(0)\\
\mathcal{F}\left\{\delta^{(3)}(t)f(t)\right\} &= \int_{-\infty}^{+\infty}\delta^{(3)}(t)f(t)e^{-i\omega t} = -f^{(3)}(0) + 3i\omega f^{(2)}(0) + 3\omega^2 f^{(1)}(0) - i\omega^3 f(0)
\end{aligned}$$

Then, after simple calculations and simplifications, the Fourier transform of the right-hand side $\mathcal{R}$, is found to be expressed simply as:

$$\mathcal{R} = \frac{2\left(1+Z\omega^2\right)}{\sqrt{\left(r^2+Z^2\right)}} \tag{10}$$

2.3 The complete frequency-domain ODE

From (1) and (3) is is clear that $\hat{S}(r,Z,i\omega)$ is nothing but the frequency dependent part G of $G_\infty(r,Z,i\omega)$. The ODE for $G(r,Z,i\omega)$ can thus be formed now from its left hand and right hand sides, derived above, giving:

$$\boxed{\frac{\omega^2}{4}G^{(2)} - \omega\left(\omega^2 Z + \frac{3}{4}\right)G^{(1)} + \left(\omega^4\left(r^2+Z^2\right) + \omega^2 Z + 1\right)G = \frac{2\left(1+Z\omega^2\right)}{\sqrt{\left(r^2+Z^2\right)}}} \tag{11}$$

So, for the frequency domain complex Green function $G(r,Z,i\omega)$, the ODE is of order 2, logically, due to the maximum order 2 of the polynomial coefficients of the time domain ODE (5). Similar 2nd order ODE can be derived for the gradient $\frac{\partial G}{\partial r}$ and $\frac{\partial G}{\partial Z}$ by applying straightforwardly the same method to the time domain ODE derived in [1] respectively for the gradient $\frac{\partial F}{\partial r}$and $\frac{\partial F}{\partial Z}$of the time domain Green function.

The initial conditions for the ODE eq.11 can be easily deduced from the developped expression of G in (1), leading to:

$$\begin{cases} G(r,Z,0) = \frac{2}{\sqrt{\left(r^2+Z^2\right)}} - i(0) \\ \lim\limits_{\omega\to 0}\left\{\frac{\partial}{\partial\omega}G(r,Z,i\omega)\right\} = 0 + i(0) \end{cases} \tag{12}$$

The results of a numerical check of this ODE (11) are shown on fig:2 and fig:3 were we have integrated it by a standard Runge-Kutta algorithm from $\omega = 0$ to 4. (test case parmeters: r=2, Z=-1). Here all

3 terms of the differential equation are plotted independently, together with their sum, real part on the left, imaginary part on the right. The isolated dots show the same quantities (real and imaginary parts of the LHS of eq:11) calculated from the usual Green function routines of the BEM code AQUAPLUS [8] based on the classical series and asymptotic expansions for this function [7]. An excellent agreement is observed for both real and imaginary parts.

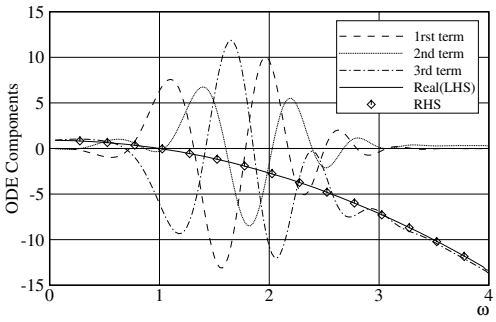

Figure 2: components of the ODE - Real part

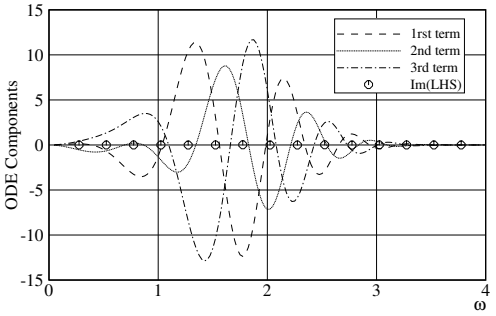

Figure 3: components of the ODE - imaginary part

3 conclusion

The Green functions of free surface hydrodynamics were shown to be solution of exact linear ordinary differential equations. This result, uncovered at the IWWWFB in Marseille (1997) for the time-domain Green function, is extended here for it's sister function in the frequency-domain. In both cases, theses results can be exploited to speed-up the computations of BEM based seakeeping codes. A lot of other applications will probably be discovered in further research works. The extension of these results to the case of finite water depth is still an open challenge.

References

[1] Clément, A.H., (1998) An Ordinary Differential Equation for the Green Function of Time-Domain Free-Surface Hydrodynamics. *J. Engng. Math.*, **33**: 201-217.

[2] Clément, A.H., (1997) A shortcut to compute time-domain free-surface potentials avoiding Green function evaluation. in Proc. IWWWFB97, Carry-le-Rouet.

[3] Clément, A.H., (1999): Using differential properties of the Green function in seakeeping computational codes. In *Proc. 7th Intern. Conf. Numer. Ship Hydrod.* Nantes. pp.6.5-1 à 6.5-15.

[4] Abramowitz, M. and Stegun, I., (1970) *Handbook of Mathematical Functions with Formulas, Graphs and Mathematical Tables*. New York: Dover Publications 1045 pp.

[5] Debnath, L., (1995) *Integral transforms and their applications*. CRC Press.

[6] Wehausen, J.V and Laitone, E.V, (1960) Surface waves, in S Flugge (eds) *Handbuch des Physik Vol.9*, Springer-Verlag New-York pp. 446-778.

[7] Newman, J.N., (1985) Algorithms for the free-surface Green function, *Journal of Engineering Mathematics*, Vol.19-1, pp.57-67.

[8] Delhommeau G. (1989) Amélioration des performances des codes de calcul de diffraction-radiation au premier ordre, in *Proc. Deuxièmes Journées de l'Hydrodynamique*, Nantes.

A numerical strategy for gas cavity-body interactions from acoustic to incompressible liquid phases.

G. Colicchio[1,2] **giuseppina.colicchio@cnr.it**
M. Greco[1,2,3] **marilena.greco@cnr.it**
O.M. Faltinsen[2,3] **odd.faltinsen@ntnu.no**

1 **CNR-INSEAN, Italian Ship Model Basin, Roma – Italy.**
2 **CeSOS and AMOS, NTNU, Trondheim – Norway.**
3 **Dept. of Marine Technology, NTNU, Trondheim – Norway.**

The gas-cavity problem with initially high pressure, evolving in a surrounding liquid, and interacting with a near body, is a very interesting research topic because it involves several physical phenomena and is of practical interest in different contexts. For instance, underwater explosions represent an important issue for ships and offshore structures. Therefore it is necessary to predict structural effects and try to improve vessel design. To this purpose, physical tests were performed along the years and theories were developed (Cole 1948). Another important application is in medical field. Implosion of micro-bubbles with ultrasound in biological flows is used within a noninvasive technique to remove calculi in human bodies (Lingeman *et al*. 2009).

Here we first focus on the first application. When an underwater explosion occurs, a chemical reaction and a detonation process cause the formation of a hot gas with high pressure and the release of a shock wave traveling in the surrounding fluid. Then a superheated, spherical, bubble is formed which will first expand while the high pressure reduces in time and propagates in the surrounding liquid. Eventually the bubble starts to oscillate and affect the local pressure. In the first stage (shock wave) both the gas and the surrounding liquid behave as compressible, in the later stages (gas bubble) the acoustic wave will disappear and the water can be considered incompressible. The interaction of this two-phase fluid with a body will then depend on the vicinity of the body from the explosion zone and by the presence or not of other boundaries, *e.g.* the sea floor, the free surface.

The solution strategy: a time-space domain decomposition

We first assume that the explosion occurs very far from other boundaries and that hydrostatic pressure does not affect the explosion phenomenon leading to a radial symmetry of the bubble evolution. Initial values of bubble radius, density and pressure, can be obtained from physical tests. A compressible '1D' solver along the radial direction r is then used to simulate the flow evolution until the first shock wave from the explosion becomes close to the bottom of a vessel assumed infinitely extended within the local analysis. This can be done because the problem equations are hyperbolic and so the presence of the structure will not affect the fluid behind the shock wave. As the shock wave becomes close to the body, a time-space Domain-Decomposition (DD) strategy is switched on, where a compressible 3D solver is initiated by the simplified '1D' solution in an inner region affected by the body and used to investigate the fluid-body interactions. The '1D' solution is still applied far from the structure and provides the boundary conditions to the 3D solver along a control surface bounding the inner domain. This implies a one-way coupling. The DD limits the computational costs which are quite high if a compressible 3D solver is used for the whole simulation and everywhere due to the limits in the time step connected with the local speed of sound in the fluid. In case of an explosion very close to boundaries, this DD cannot be applied. The main features of the methods involved in the DD are briefly described next.

'1D' compressible solver for multi-phase flows Assuming radial symmetry, the problem (in general governed by the later equation (3)) can be studied as one-dimensional in the r direction with formal Euler equation

$$\frac{\partial \boldsymbol{U}}{\partial t} + \frac{\partial \boldsymbol{F}}{\partial r} = \boldsymbol{S}\,, \tag{1}$$

with $\boldsymbol{U} = [\rho, \rho u, E]^T$, $\boldsymbol{F} = [\rho u, \rho u^2, (E+p)u]^T$ and $\boldsymbol{S} = 2[\rho u/r, \rho u^2/r, u(E+p)/r]^T$. Here u is the radial velocity, p the pressure and E the total energy $\rho(e+u^2/2)$. For the closure of the problem we need an equation of state (EOS) for the specific internal energy e. Here this is assumed of the form $\rho e = f_f(\rho)p + g_f(\rho)$, with the functions f_f and g_f depending on the fluid properties. In particular, the JonesWilkinsLee EOS is used for the gas (Dobratz and Crawford 1985) and an isentropic Tait relation for the water (Cole 1948), *i.e.*

$$\begin{array}{ll} f_g = 1/\omega & g_g = [-A_g(1-\omega\rho_g/(R_1\rho_{0g}))e^{-R_1\rho_{0g}/\rho} - B_g(1-\omega\rho_g/(R_2\rho_{0g}))e^{-R_2\rho_{0g}/\rho_g}]/\omega \\ f_w = 1/\gamma_w & g_w = (B_w - A_w)\gamma_w/(\gamma_w - 1) \end{array} \tag{2}$$

Here the subscripts g and w stand for gas and water, respectively, ρ_{0g} is the initial gas density, γ_w is the ratio of specific heats for water and the other parameters are given later. The problem is solved in time with a first order scheme using the HLL approximate Riemann solver (Toro 1999) to estimate the fluxes $\boldsymbol{F}$ in each fluid and enforcing a two-shock

approximation to the Riemann problem at the interface as proposed by Liu *et al.* (2003). The latter provides an exact solution when a shock wave is reflected and is reliable for gas-gas or gas-water flow. The related equation system is nonlinear and is solved iteratively with a Newton-Raphson method giving u_i, p_i, ρ_i^L and ρ_i^R, respectively, the radial velocity and pressure at the interface and the left and right density. To avoid possible instability of the solution, the left and right densities are corrected by enforcing an isobaric condition across the interface. This interface algorithm is inserted into a ghost fluid method (Liu *et al.* 2003) providing the conditions across the interface to each fluid. In particular, say that the interface is between node i and i+1 of the computational grid and that we need to solve for the fluid on the left. Here we consider that for nodes $\geq$ i the density, velocity and pressure are, respectively, ρ_i^L , u_i and p_i, and the other needed quantities are obtained subsequently. Similarly is done for the fluid on the right. At this stage the fluxes $\boldsymbol{F}$ can be calculated in each fluid and the problem can be stepped forward in time. The location of the interface is updated using the velocity u_i. The solver has been satisfactorily verified against several numerical solutions, for fully 1D problems (in this case $\boldsymbol{S} = 0$ in equation (1)) and problems with radial symmetry.

3D compressible multi-phase solver In 3D, the compressible inviscid flow is represented by the equation

$$\frac{\partial \boldsymbol{U}}{\partial t} + \frac{\partial \boldsymbol{F}_x}{\partial x} + \frac{\partial \boldsymbol{F}_y}{\partial y} + \frac{\partial \boldsymbol{F}_z}{\partial z} = 0, \tag{3}$$

with $\boldsymbol{U} = [\rho, \rho u, \rho v, \rho w, E]^T$, $\boldsymbol{F}_x = [\rho u, \rho u^2 + p, \rho uv, \rho uw, (E + p)u]^T$, $\boldsymbol{F}_y = [\rho v, \rho uv, \rho v^2 + p, \rho vw, (E + p)u]^T$, $\boldsymbol{F}_z = [\rho w, \rho uw, \rho wv, \rho w^2 + p, (E + p)u]^T$. Here u, v, w are the velocity components. As in '1D', these equations are completed by the equations of state described in the previous paragraph. The equations are integrated with a 3^{rd} order Runge-Kutta scheme in time and they are discretized with a 2^{nd} order finite differences scheme in space. A level set function ϕ is used to represent implicitly the interface between the two fluids and it is advected in time using the equation

$$\frac{\partial \phi}{\partial t} + \boldsymbol{V}_i \cdot \nabla \phi = 0 \tag{4}$$

where $\boldsymbol{V}_i$ is the interface velocity calculated as in Liu *et al.* (2003). To make the solution efficient in time, an adaptive mesh refinement is used according to MacNeice *et al.* (2000). The grid is halved either close to the interface between the two fluids or in proximity of high gradients of the fluid variables $\boldsymbol{U}$. An example of mesh refinement is shown in figure 1, at the starting time of the explosion, close to the interface, the grid size is extremely refined. The refinement grades to a coarse mesh far from the interesting region.

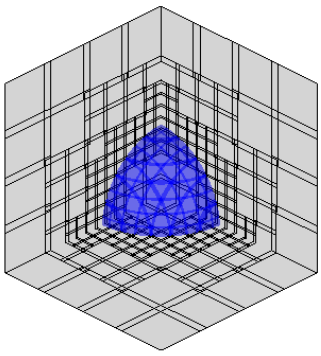

Figure 1: Example of adaptive mesh refinement close to the gas-water interface.

Fluid-structure interaction problem To estimate the local effects on the bottom of a vessel, as first attempt this has been modelled as an infinitely extended orthotropic plate, see *e.g.* Faltinsen (1999). The stresses and strains will be first evaluated using a quasi-static approach, then the structural and hydrodynamic problems will be coupled to assess excitation of hydroelasticity.

Preliminary results

The underwater explosion documented by Smith (1999) has been used as a test case to develop and assess the DD approach. The initial radius of the gas cavity is $r_0 = 0.16$ m and the parameters for the EOS of the fluids, using SI system, are: $\rho_{0g} = 1630.0$, $p_{0g} = 8.381 \cdot 10^9$, $A_g = 3.712 \cdot 10^{11}$, $B_g = 3.23 \cdot 10^9$, $R_1 = 4.15$, $R_2 = 0.95$, $\omega = 0.30$,

$\rho_{0w} = 1025.0$, $p_{0w} = 1.0 \cdot 10^6$, $A_w = 1.0 \cdot 10^6$, $B_w = 3.31E8$ and $\gamma_w = 7.5$. First the problem has been studied fully by the '1D' solver within the radial-symmetry assumption. A convergence analysis has been performed using a compu-

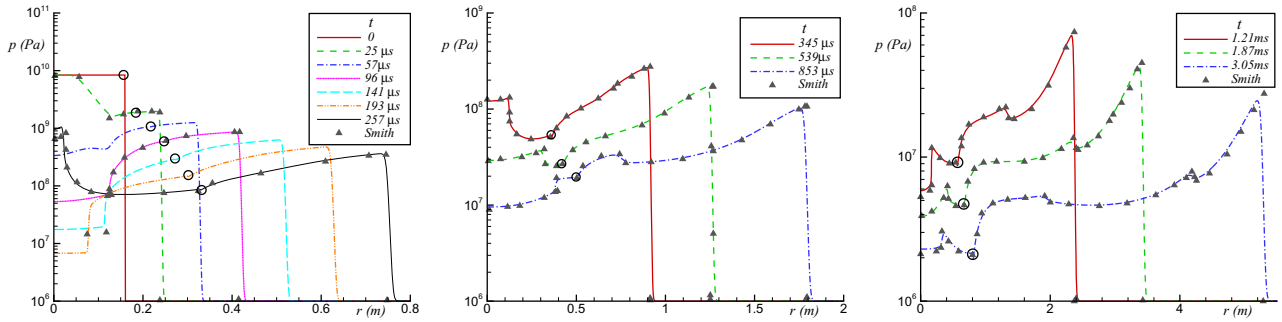

Figure 2: '1D' solution in the radial direction for the studied underwater explosion: pressure distributions at different time instants. The empty circles indicate the instantaneous radial location of the interface. The triangles are the numerical results by Smith (1999). For sake of clarity, in the left plot only the Smith's solutions at 25, 96 and 257μs, are shown.

tational domain long 10 m and a uniform discretization Δr. The order of accuracy OA (Colicchio 2004) was adopted as measure, which involves the time integral of the selected variable calculated with three discretizations and should be one for a solver accurate to the first order. In our case, using $\Delta r = 0.00125$ m, $1.5\Delta r$ ant $2.25\Delta r$ and studying the evolution up to 0.05 s, at a location $r \simeq 44r_0$, OA was found 1.45, 1.44, 1.32 and 1.56, respectively for u, p, ρ and E. At the interface, where very complicated phenomena occur, OA is more limited and was found 0.39, 0.80 and 1.10, for the position of the interface, r_i, and for u_i and p_i, respectively. The evolution for the finest grid is shown in figure 2 in terms of pressure distribution and interface location at different time instants during the initial shock-wave phase. This stage involves a cavity expansion and is typically associated with a release of more than 50% of the energy from the explosion (Keil 1961). In this example, at first (left) a primary shock wave is caused by the detonation and moves rightwards while an expansion wave moves toward the bubble center and is later reflected from it leading to a low pressure at the core of the cavity. Later on the inner pressure rises and moves as a shock wave towards the interface. There, it is partially reflected and partially transmitted into the liquid phase (center). As a consequence of these repeated reflections, the intensity of the involved shock waves is reduced bringing toward an incompressible behavior (right). The described results fit well those by Smith (1999), based on an arbitrary Lagrangian-Eulerian version of the advective upstream-splitting shock-capturing scheme, also given in the figure. On a longer time scale the cavity reaches a maximum radius of about 2.2 m ($\simeq 13.8r_0$) at about 0.066 s, this is consistent with the values reported by Smith (1999). Then, within the gas-bubble phase, the cavity starts to oscillate with smaller amplitudes as shown in the left of figure 3. Both pressure and velocity at the interface (center and right plots) are highest at the beginning. When the bubble is compressed the pressure tends to a peak and the velocity becomes negative, the magnitude of both of them decreases in time. According to studies by Keil (1961), most of the remaining energy from the explosion is released during the first bubble pulsation.

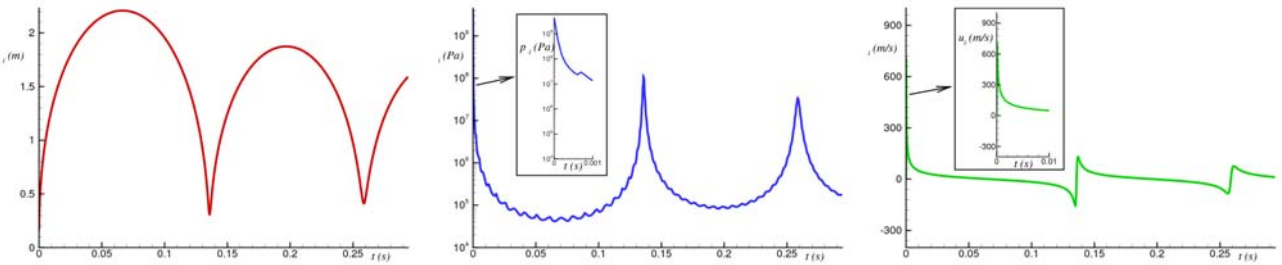

Figure 3: '1D' solution in the radial direction for the studied underwater explosion: location (left), pressure (center) and radial velocity (right) of the interface as a function of time. The results were obtained using a computational domain long 100 m, with constant $\Delta r = 0.00125$ m within 10 m and then stretching exponentially outwards.

The positive verification of the '1D' solver represents the first step of the solution strategy. The 3D method has also been built as compressible solver with one fluid and the exchange of information from the '1D' domain with the evolving cavity to the 3D domain with the compressible water is presently under assessment. This part of the research activity and the further developments, including the possibility to have the gas-water interface in the 3D solver sub-domain and the structural analysis, will be discussed at the workshop.

This research activity is supported by the Centre for Ships and Ocean Structures (CeSOS), NTNU, Trondheim, within the ”Violent Water-Vessel Interactions and Related Structural Loads” project and presently ongoing also within the Centre for Autonomous Marine Operations and Systems (AMOS), NTNU, Trondheim.

References

COLE, R. H. (1948). *Underwater Explosions*. Princeton, New Jersey: Princeton University Press.

COLICCHIO, G. (2004). *Violent disturbance and fragmentation of free surfaces*. Ph. D. thesis, University of Southampton, Southampton, UK.

DOBRATZ, B. M. AND P. C. CRAWFORD (1985). *LLNL Explosives HandbookProperties of Chemical Explosives and Explosive Simulants*. Lawrence Livermore National Laboratory.

FALTINSEN, O. (1999). Water entry of a wedge by hydroelastic orthotropic plate theory. *J. Ship Research 43*(3), 180–193.

KEIL, A. (1961). The response of ships to underwater explosions. Technical Report 1576, David Taylor Model Basin.

LINGEMAN, J., J. MCATEER, E. GNESSIN, AND A. EVAN (2009). Shock wave lithotripsy: advances in technology and technique. *Nat. Rev. Urol. 6*, 660–670.

LIU, T., B. KHOO, AND K. YEO (2003). Ghost fluid method for strong shock impacting on material interface. *J. Comput. Phys. 190*, 651–680.

MACNEICE, P., K. M. OLSON, C. MOBARRY, R. DEFAINCHTEIN, AND C. PACKER (2000). PARAMESH : A parallel adaptive mesh refinement community toolkit. *Computer Physics Communications 126*, 330–354.

SMITH, R. (1999). AUSM(ALE): A Geometrically Conservative Arbitrary LagrangianEulerian Flux Splitting Scheme. *J. of Computational Physics 150*, 268–286.

TORO, E. (1999). *Riemann Solvers and Numerical Methods for Fluid Dynamics*. Springer-Verlag.

A model test for the wave interaction with a four-cylinder structure

P. W. Cong, B. Teng, K. Zhang and Y.F. Huang
State Key Laboratory of Coastal and Offshore Engineering
Dalian University of Technology
Dalian 116024, Liaoning, China
E-mail: bteng@dlut.edu.cn

1. INTRODUCTION

The prediction of the runup and free surface elevation is of great interest for the offshore industry, e.g. to determine the air gap. Air gap is the vertical distance from the underside of the platform deck to the wave crest. This clearance must be sufficient that the wave does not strike the lower deck. At the same time, it must also be minimized in order to avoid raising the centre of gravity and exposed vertical surface area of the platform, which may affect the wind loading and will increase the wind overturning moments.

An important influence on the determination of air gap is the phenomenon known as near-trapping. For a multi-column structure this has been shown theoretically to occur at critical frequencies dependent upon the geometry of the structure. These phenomena can cause the local wave elevations to be significantly greater than that of the undisturbed incident wave. Considering arrays of vertical bottom mounted circular columns, the scattering of water waves by arrays of columns was solved exactly by Linton and Evans (1990). Subsequently Evans & Porter (1997) made a detailed investigation of near-trapping by circular arrays of vertical cylinders. Malenica et al. (1999) extended the studies of near-trapping in an array to the second-order and suggest that second-order near-trapping occurs when the frequency of the second-order components is equal to the frequency of first-order near-trapping. However predicted by theoretical study, the near-trapping phenomenon has rarely been experimentally verified.

In the present study the diffraction of regular waves by an array of four vertical cylinders is investigated by a model test. The test was undertaken in a wave basin at Dalian University of Technology and designed to measure the free surface elevation η at multiple locations close to the body surface subjected to regular waves of the steepness kA varies from 0.06 to 0.10, where k is the wave number, A is the incident wave amplitude. Ohl *et al.* (2001) has carried out a similar experiment and outstanding results are obtained from the experiment. Due to model and facility constraints the experiment was conducted for 6 frequencies in the range $0.449<ka<0.555$, where a is the cylinder radius. In the present test, a wider range of frequencies $0.408<ka<1.966$ were employed and over this frequency range the near-trapping phenomenon both at the first- and the second-order can be investigated. As the near-trapping phenomenon is sensitive to the change in ka, tests were conducted for totally 30 frequencies and the frequencies are distributed densely in the range where near-trapping phenomena are theoretically predicted to occur.

First- and second-order terms of wave elevations are computed from the measured time series. It can be found that high localized wave elevations were observed at both the first- and second-order. The large increases in free surface elevations are found to occur over a range of frequencies, close to the near-trapping frequency. The results are then compared with those obtained by QTFDUT, a hydrodynamic analysis program developed in the frame of potential flow theory. It's found that the potential flow theory can be effective at predicting the first- and second-order qualities. At most frequencies satisfying results can be obtained by using the linear diffraction theory alone. However, at some crucial frequencies, the magnitude of local free surface is affected by significant nonlinear interactions, and the second-order qualities make a considerable contribution.

2. SET-UP OF THE EXPERIMENT

Test was undertaken in a wave basin at Dalian University of Technology. The basin has a plan area of 55m×34m. The water depth for testing is 0.5m. A wave generator with 70 computer controlled individual paddles is arranged at the basin's upstream end. In the procedure of the experiment these paddles generated unidirectional regular

waves, with the wave crests parallel to the wave paddles. At the downstream end of the basin, a wave absorbing beach is arranged, which can prevent significant reflection of wave energy. Along the side walls wave absorbers are placed. To obtain a sufficient long period for data acquisition without spurious harmonics all these precautions are necessary.

Fig.1 is a plan view of the model placement in the basin. The four cylinders are arranged at the corners of a square. The diameter of each cylinder is 400mm and the gap between cylinders is one diameter. The origin of the coordinate system is at the center of the cylinders and on the undisturbed free surface. The *z*-axis points vertically upwards, the *x*-axis is in the direction of incident wave propagation and the *y*-axis is parallel to the wave paddles. Four wave gauges are placed in the vicinity of the four cylinders as described in Fig.1. All gauges are 18mm away from the cylinder surface and the wave gauge positions are shown in Table 1.

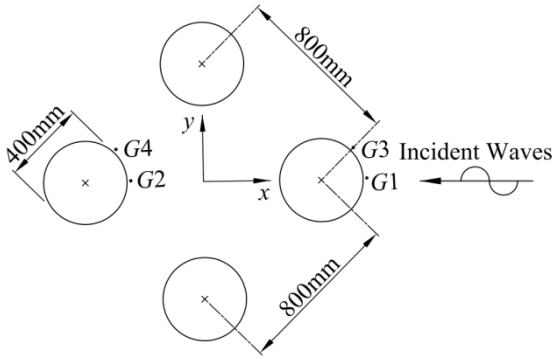

Fig.1 plan view of the model placement in the basin

Table.1 The wave gauge positions

Gauge	*x*(mm)	*y*(mm)
*G*1	618.00	0.00
*G*2	-182.00	0.00
*G*3	554.15	154.15
*G*4	-245.85	154.15

Tests were conducted for 30 regular wave periods. For each wave period, three waves with steepness *kA* of 0.06, 0.08 and 0.10 were chosen. Minor difference was found during the experiment between the measured incident amplitude *A* and the target value.

3. NUMERICAL PROGRAM

The hydrodynamic analysis program QTFDUT is used to compare with the experimental results. This program is developed in the frame of potential flow theory and utilizes the higher order boundary element method to solve the diffraction and radiation problem. First- and second-order velocity potentials can be computed for wave incident upon fixed and floating bodies of arbitrary shape.

Prior to the present study, the program has been used to investigate wave diffraction for various geometries. Through comparisons with analytical solutions, semi-analytical solutions and published data, the validation of the program has been rigorously verified. Teng *et al*. (2012) has verified the program in a study, which considered the wave interaction with fixed arrays of bottom mounted cylinders. The second-order wave elevations generated by QTFDUT agree remarkably well with the Malenica *et al.*'s (1999) semi-analytical solutions.

4. SOME RESULTS OF THE EXPERIMENT

The results from the regular wave tests are presented in this section. Firstly, the time history of measured data is shown for two typical conditions. From Fig.2 it can be observed that the measured data is stable and reaches their intended height. It also can be seen that the data used to be analyzed contains more than 15 steady-state waves, is of sufficient length to fully capture subtle features in the test. At T=0.68, the contribution from the nonlinear quantities is insignificant which implies that the results can be well predicted by linear wave theory. At T=1.36, nonlinear interactions have a strong effect on the local free surface ($\eta^{(1)}$=5.742cm and $\eta^{(2)}$=6.627cm) and can't be accurately predicted by using linear wave theory alone. Band pass filtering method is used to analyze the measured data series and the measured data are decomposed into the first- and the second-order quantities.

The results are then discussed with reference to linear and second-order wave theory. The results for the 4 gauge positions are presented in Figs. 3~4. For each gauge position, amplitude versus test wave period T is plotted. The validation of higher-order diffraction theories has primarily conducted on forces or moments which are integrated quantities. In present study, more rigorous comparison is carried out based on the free surface elevation.

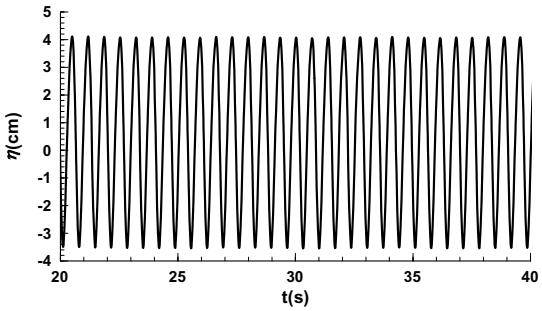

(*a*) A=1.184cm, T=0.68s, kA=0.103

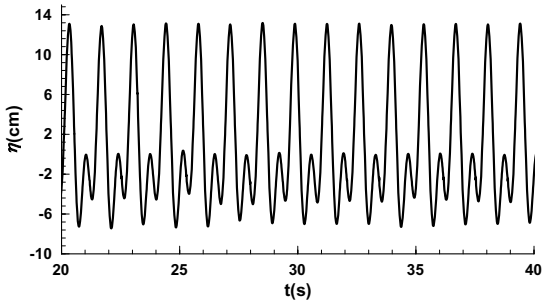

(*b*) A=3.890cm, T=1.36s, kA=0.099

Fig. 2 Measured time history of the free surface elevation at $G1$ for two conditions

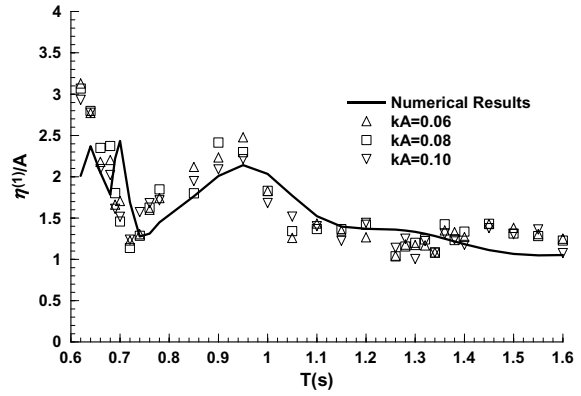

(*a*) at $G1$

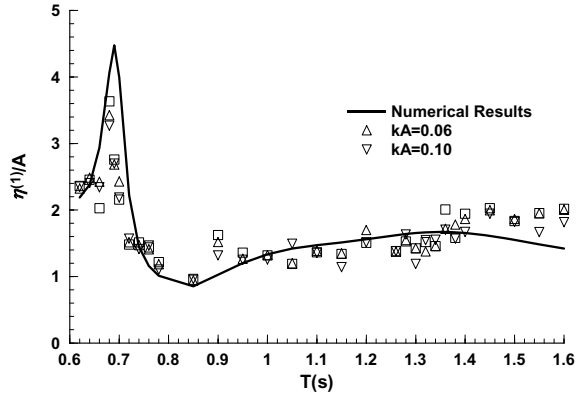

(*b*) at $G2$

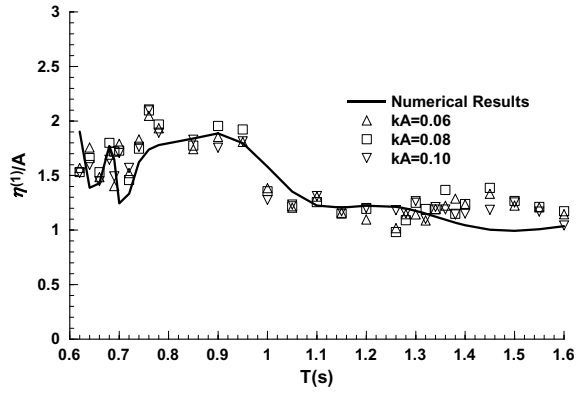

(*c*) at $G3$

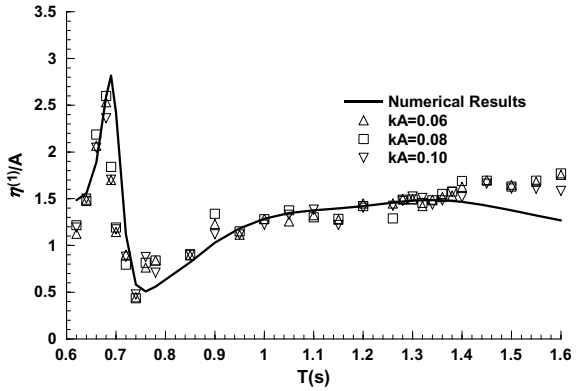

(*d*) at $G4$

Fig. 3 The first-order wave elevation at gauge positions

Fig.3 shows the numerical and experimental first-order quantities. The plotted quantities are non-dimensionalized with A. It can be seen that the experimental results and theoretical results are in good agreement. There is also little difference between the results with different wave steepness. Above observations indicate that the potential flow theory can be effective at predicting the first-order elevation. Then at $G2$ large increases in free surface elevations occur over a narrow range of frequencies can be observed. The behavior of the experimental results in the range is close to the corresponding behavior described by the numerical results. Which implies that the near-trapping phenomenon indeed exist in the practice. While the match between experiment and theory is close, there are discernible differences in the magnitude and wave period of the maximum amplitude. The highest first-order elevation $\eta^{(1)}/A$ is equal to 3.63 and occurs at T=0.68s at $G2$. At the same time the corresponding highest numerical value occurs at about T=0.69s and is greater than the maximum experimental value. The reason for the shift of the period corresponding to the maximum value needs further investigation. It is also meaningful to note that the magnitude of the diffracted first-order amplitude at $G2$ never drops below that of the incident wave amplitude.

Fig.4 shows the numerical and experimental second-order quantities. The plotted quantities are non-dimensionalized with kA^2. It can be seen that overall trends of the experimental results are similar and all experimental results seem to correspond to the numerical prediction in general. The highest second order elevations $\eta^{(2)}/kA^2$ is equal to 14.90 and occurs at the gauge $G2$ when T=1.36s. As wave period approaching 1.36s, the magnitude increases rapidly and the resonance like phenomenon occurs over a broader range than that of the first-order. Shift of the period corresponding to the maximum value is also observed at the second-order. The

geometry used in the present test is identical to the case studied by Evans & Porter (1997) and Malenica *et al*. (1999). Malenica *et al.* (1999) found that near-trapping of the second-order wave occurs when its frequency coincides with the linear near-trapping frequency. In the present study, for the first-order component high localized wave elevations are observed at T=0.68s and for the second-order component the corresponding phenomenon occurs at T=1.36s. This finding coincides with the conclusion of Malenica *et al*. (1999).

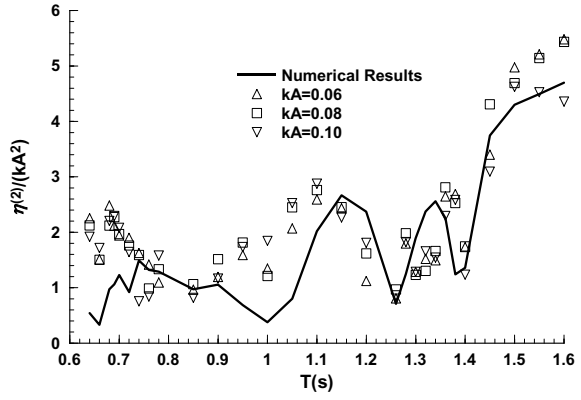

(*a*) at *G*1

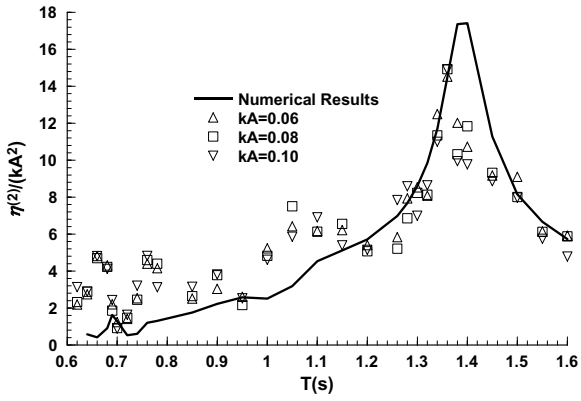

(*b*) at *G*2

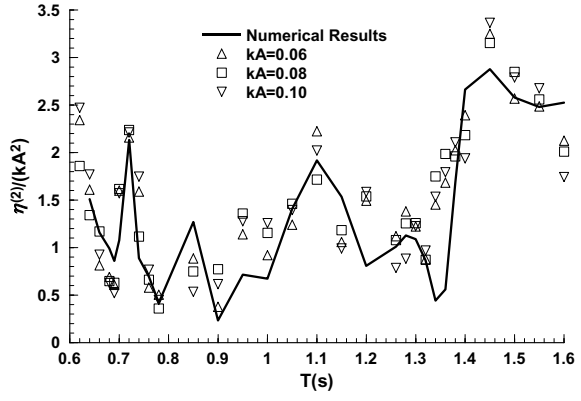

(*c*) at *G*3

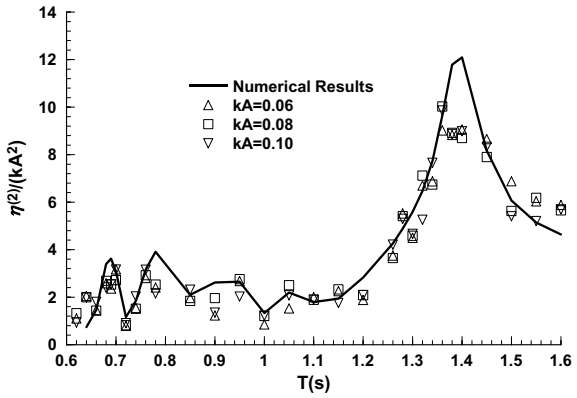

(*d*) at *G*4

Fig. 4 The second-order wave elevation at gauge positions

5. CONCLUSION

Though analyzing the results of a model test it is found that the potential flow theory can be effective at predicting both the first- and the second-order qualities. The resonant like phenomena were observed in the model test. When the important phenomenon occurs at the second-order, significant nonlinear interactions can be observed and it makes a considerable contribution to the free surface elevation.

ACKNOWLEDGEMENTS

The work is financial supported by the National Basic Research Program of China (973-Program) (Grant No. 2011CB013703).

REFERENCES

[1] Evans, D.V., Linton, C.M., 1997. Near-trapping of waves by circular arrays of vertical cylinders. *App. Ocean Res*., 19: 83~99.

[2] Linton, C. M., Evans, D.V., 1990. The interaction of waves with arrays of vertical circular cylinders. *J. Fluid Mechanics*.215: 549-569.

[3] Malenica, S., Eatock Taylor, R., Huang JB. 1999. Second-order wave diffraction by an array of vertical cylinders. *J. Fluid Mechanics*, 390: 349~373.

[4] Ohl, C.O.G., Eatock Taylor, R., Taylor, P. H., *et al*., 2001. Water wave diffraction by a cylinder array. Part 1. Regular waves. *J. Fluid Mechanics*, 442: 1~32.

[5] Teng, B., Cong, P.W., 2012. Nonlinear free surface by a square array of truncated cylinders, 27th *IWWWFB*, Copenhagen.

Evaluation of Time-Domain Capillary-Gravity Green Function

Yuzhi Dai[1] and **Xiaobo Chen**[2]

[1]Shipbuilding Engineering College, Harbin Institute of Technology, 264209 Weihai, China
[2]Research Department, Bureau Veritas, 92571 Neuilly-Sur-Seine, France

We present this paper, in memory of Professor Fritz Ursell, which contains an exercise following his work on the generalization of steepest descent method in 1960, 1964 and 1968. The potential flow generated by an impulsive point source at the free surface with surface tension is analyzed and different asymptotic expressions have been obtained. They include a series expansion for small time, asymptotic expansion for very large time and uniform asymptotic expansions including Airy function and its derivative for intermediate and large time.

1 Introduction

The surface tension and fluid viscosity are neglected in the classical potential theory. Green function representing the velocity potential due to an impulsive disturbance presents a perplexing peculiarity - the surface elevation in a region approaching to the disturbance is found to oscillate with indefinitely increasing amplitude and indefinitely decreasing wavelength as pointed out in Lamb (1932), Ursell (1960), Clement (1998) and Chen & Wu (2001). The investigation of Chen (2002) and Chen & Duan (2003) shows that the introduction of surface tension in the formulation of ship waves eliminates the singularity of ship waves in the region near the track of the source point at the free surface. This stimulates our study on numerical evaluation of time-domain capillary-gravity Green function.

We study the potential at the point $P(x, y, z)$ and time instant t', generated at the point $Q(\xi, \eta, \zeta)$ and time t by a source of unit impulsive strength $\delta(t)$. The time-domain capillary-gravity Green function is the sum of an impulsive term and a memory part. The memory part is given by Wehausen & Laitone (1964, eq.24.28) and expressed by a wavenumber integral :

$$G(P, t', Q, t) = 2\int_0^\infty e^{k(z+\zeta)}\mathbf{J}_0(kR)\sqrt{gk + (T/\rho)k^3}\sin[\sqrt{gk + (T/\rho)k^3}(t - t')]dk \tag{1}$$

where $R = \sqrt{(x-\xi)^2 + (y-\eta)^2}$ is the horizontal distance between the two points P and Q, g is the acceleration due to gravity, ρ water density and T surface tension on the air-water interface. $\mathbf{J}_0(\cdot)$ is the zeroth-order Bessel function of the first kind. If we use L as a reference length to write the non-dimensional quantities as

$$\tau = (t - t')\sqrt{g/L}; \quad (c, h) = (z + \zeta, R)/L; \quad \sigma = \sqrt{T/(\rho g L^2)}$$

the memory part G is written as

$$G(P, t', Q, t) = 2\sqrt{g/L^3}F(c, h, \tau) \tag{2}$$

such that the Green function is written in its dimensionless form :

$$F(c, h, \tau) = \int_0^\infty e^{kc}\mathbf{J}_0(kh)\omega(k)\sin[\omega(k)\tau]dk \quad \text{with} \quad \omega(k) = \sqrt{k + \sigma^2 k^3} \tag{3}$$

If we take $\sigma = 0$, the expression (3) keeps the same form as that of pure-gravity waves.

2 Contour integrals passing through the saddle points

By using the identity $\mathbf{J}_0(kh) = \mathbf{H}_0^+(kh) + \mathbf{H}_0^-(kh)$ with the Hankel function $\mathbf{H}_0^\pm(kh) = \mathbf{J}_0(kh) \pm i\mathbf{Y}_0(kh)$ in (3), we may decompose $F = F^+ + F^-$ with F^+ and F^- associated with $\mathbf{H}_0^+$ and $\mathbf{H}_0^-$, respectively. At large values of $\omega(k)\tau$ and kh, the integrand of F^+ and F^- is of highly oscillatory. The phase function in the integrand of F^+ is $\psi^+ = \omega(k)\tau + kh$ while that of F^- is $\psi^- = \omega(k)\tau - kh$, identified by using the asymptotic expression of $\mathbf{H}_0^\pm(kh)$ for large kh.

The phase function $\psi^+ = \omega(k)\tau + kh$ does not present any saddle point for $\Re\{k\} > 0$. The integration path along the real axis of k for F^+ can then be deformed to the path along the imaginary axis of k since the arc integral linking both axis at infinity can be shown to be nil.

Following the work by Chen & Duan (2003) there are two saddle points k_g and k_T associated with the phase function $\psi^- = \omega(k)\tau - kh$ in the integrand of F^- :

$$k_g = 1/(4v^2) + O(\sigma/v^2) \quad \text{and} \quad k_T = 4v^2/(9\sigma^2) + O(\sigma/v^2) \quad \text{for} \quad v \gg \sqrt{\sigma} \tag{4}$$

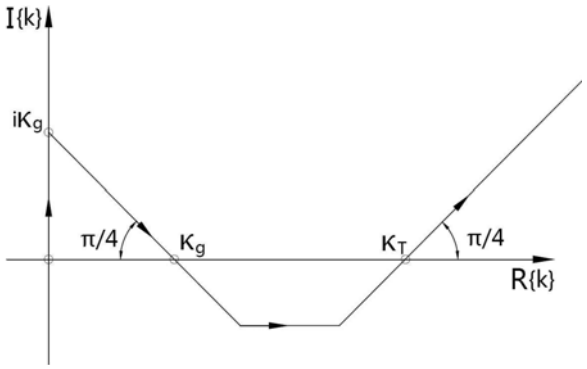

Figure 1: Integral contour for $v > v_0$

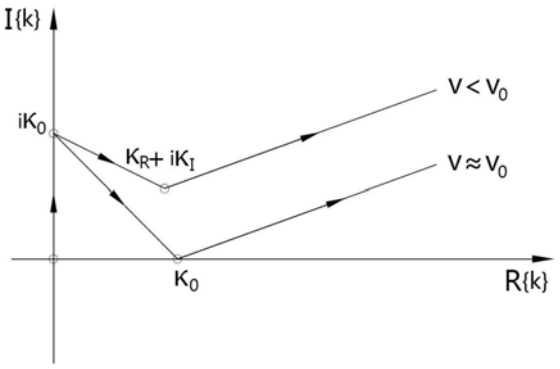

Figure 2: Integral contour for $v \leq v_0$

where $v = h/\tau$ is the wave velocity. When v is of the same order as $\sqrt{\sigma}$, the wavenumbers k_g and k_T become close and in particular, $k_g = k_T = k_0 \approx 0.393/\sigma$ for $v = v_0 \approx 1.086\sqrt{\sigma}$. When $v < v_0$, the wavenumbers k_g and k_T are complex. At the limit $v = 0$, we have $k_g = -i0.577/\sigma = -k_T$.

For $v > v_0$, the double derivatives $\partial^2\psi^-/\partial k^2(k = k_g) < 0$ and $\partial^2\psi^-/\partial k^2(k = k_T) > 0$ so that the steepest paths through $k = k_g$ and $k = k_T$ should be those with increments $\Delta k = |\Delta k|e^{-i\pi/4}$ and $\Delta k = |\Delta k|e^{+i\pi/4}$ assuming $|c| \ll 1$, respectively. At very large $k > k_T$, any path in the first quadrant is good although the best is that with increment $\Delta k = |\Delta k|e^{+i\pi/3}$ for $k \to \infty$. Furthermore, the contribution from the end point at $k = 0$ is taken account by an integration on a limited segment along the imaginary axis. The integration paths are depicted on Figure 1 and Figure 2 for $v > v_0$ and $v \leq v_0$, respectively. The Green function computed along the paths defined above is used to compare the asymptotic expansions in the following.

3 Series expansions for small τ

By expanding the sine function and $\sqrt{k + \sigma^2 k^3}$ for small τ and σ, we obtain

$$\begin{aligned} F(c,h,\tau) &= \int_0^\infty e^{kc}\mathbf{J}_0(kh)\sqrt{k+\sigma^2k^3}\sin(\tau\sqrt{k+\sigma^2k^3})dk \\ &= \sum_{m=0}^{\infty}\sum_{n=0}^{m+1}\frac{(-1)^m\tau^{2m+1}}{(2m+1)!}\frac{(m+1)!}{n!(m+1-n)!}\sigma^{2m+2-2n}\int_0^\infty e^{kc}\mathbf{J}_0(kh)k^{3m+3-2n}dk \end{aligned}$$

Using the identity (6.621) in Gradshteyn & Ryzhik (2007) :

$$\int_0^\infty e^{kc}\mathbf{J}_0(kh)k^{3m+3-2n}dk = (3m+3-2n)!P_{3m+3-2n}(\cos\theta)\,r^{-(3m+4-2n)} \tag{5}$$

where

$$r = \sqrt{h^2+c^2} \quad \text{and} \quad \cos\theta = -c/r$$

we find that $F(c,h,\tau)$ is expressed in the form

$$F(c,h,\tau) = \sum_{m=0}^{\infty}\sum_{n=0}^{m+1}\frac{(-1)^m\tau^{2m+1}}{(2m+1)!}\frac{(m+1)!(3m+3-2n)!}{n!(m+1-n)!}\sigma^{2m+2-2n}P_{3m+3-2n}(\cos\theta)\,r^{-(3m+4-2n)} \tag{6}$$

which can be used for small τ.

4 Expansions for very large τ

At very large time of τ, the behaviors of $F(c,h,\tau)$ depend on the contributions of integration in the vicinity of end points and saddle points. To estimate the contribution from the end points, we change the integral variable k to ω and rewrite $F(c,h,\tau)$ as

$$F(c,h,\tau) = 2\int_0^\infty e^{kc}\mathbf{J}_0(kh)\omega^2/(1+3\sigma^2k^2)\sin(\omega\tau)d\omega \quad \text{with} \quad \varphi = \psi^-/\tau = \omega(k) - kv \tag{7}$$

in which the amplitude function of the integrand is expanded at $\omega \to 0$ as

$$e^{kc}\mathbf{J}_0(kh)\omega^2/(1+3\sigma^2k^2) = \omega^2 + c\omega^4 + (-3\sigma^2 - h^2/4 + c^2/2)\omega^6 + O(\omega^8) \tag{8}$$

Introducing (8) into (7) and using the identity

$$\int_0^\infty \omega^n \sin(\omega\tau)d\omega = \cos(n\pi/2)n!/\tau^{n+1} \tag{9}$$

we have

$$F(c,h,\tau) \approx -4/\tau^3 + 48c/\tau^5 + 5!(36\sigma^2 + 3h^2 - 6c^2)/\tau^7 + O(\tau^{-9}) \tag{10}$$

The expression (10) representing the contribution from the end point at $k = 0$ for very large τ should be added to the contributions from saddle points which are now developed below.

5 Uniform asymptotic expansions

For the large value of h and τ, the dominant contribution comes from the saddle points in the integrand of $F^-(c,h,\tau)$ and we write (3) in the complex form :

$$F(c,h,\tau) \approx F^- = \Im\left\{\int_0^\infty \frac{\omega e^{kc+\pi i/4}}{\sqrt{2\pi kh}} e^{i\tau\varphi(k,v)}dk\right\} \quad \text{with} \quad \tau\varphi(k,v) = \psi^-(\tau,h,k) \tag{11}$$

To develop an uniform asymptotic expansion, we use the method of Chester, Friedman & Ursell (1957) and define a cubic transform of the variable of integration k to u

$$i\varphi(k,v) = i(\omega - kv) = -(u^3/3 - \gamma^2 u) + \rho \tag{12}$$

it follows that

$$F(c,h,\tau) \approx \Im\left\{e^{\tau\rho}\int_{\infty e^{2\pi i/3}}^{\infty e^{4\pi i/3}} G_0(u,v)e^{-\tau(u^3/3-\gamma^2 u)}du\right\} \tag{13}$$

where

$$G_0(u,v) = \sqrt{(1+\sigma^2k^2)/(2\pi h)}e^{kc+\pi i/4}(dk/du) \tag{14}$$

We then construct a Bleistein sequence to replace the integrand $G_0(u,v)$

$$G_0(u,v) = b_0 + b_1 u + (u^2 - \gamma^2)H_0(u,v) \tag{15}$$

We obtain the uniform asymptotic expansions of $F(c,h,\tau)$ for large τ

$$F(c,h,\tau) \approx \Im\left\{2\pi i e^{\tau\rho}[\mathbf{Ai}(\tau^{2/3}\gamma^2)b_0/\tau^{1/3} + \mathbf{Ai}'(\tau^{2/3}\gamma^2)b_1/\tau^{2/3}]\right\} \tag{16}$$

where

$$\rho = i(\varphi(k_T,v) + \varphi(k_g,v))/2 \tag{17}$$

$$\gamma = \begin{cases} \exp(\pi i/2)\{[\varphi(k_g,v) - \varphi(k_T,v)]3/4\}^{1/3} & \text{for} \quad v > v_0 \\ 0 & \text{for} \quad v = v_0 \\ \exp(\pi i)\{\Im[\varphi(k_T,v) - \varphi(k_g,v)]3/4\}^{1/3} & \text{for} \quad v < v_0 \end{cases} \tag{18}$$

and

$$b_0 = \begin{cases} e^{i\pi/4}/\sqrt{8\pi h}\left(\sqrt{1+\sigma^2k_g^2}e^{k_g c}\left.(dk/du)\right|_{u=-\gamma} + \sqrt{1+\sigma^2k_T^2}e^{k_T c}\left.(dk/du)\right|_{u=\gamma}\right) & \text{for} \quad v \neq v_0 \\ e^{-i\pi/4}/\sqrt{2\pi h}\sqrt{1+\sigma^2k_0^2}\left(2/\varphi'''_{kkk}(k_0,v)\right)^{1/3} & \text{for} \quad v = v_0 \end{cases} \tag{19}$$

$$b_1 = \begin{cases} e^{i\pi/4}/(\gamma\sqrt{8\pi h})\left(\sqrt{1+\sigma^2k_T^2}e^{k_T c}\left.(dk/du)\right|_{u=\gamma} - \sqrt{1+\sigma^2k_g^2}e^{k_g c}\left.(dk/du)\right|_{u=-\gamma}\right) & \text{for} \quad v \neq v_0 \\ 0 & \text{for} \quad v = v_0 \end{cases} \tag{20}$$

with

$$\left.\frac{dk}{du}\right|_{u=\mp\gamma} = \begin{cases} e^{-i\pi/2}\sqrt{2\left|\gamma/\varphi''_{kk}(k_{g,T},v)\right|} & \text{for} \quad v > v_0 \\ e^{-i[\pi \pm \arg(i/\varphi''_{kk}(k_T,v))]/2}\sqrt{2\left|\gamma/\varphi''_{kk}(k_{g,T},v)\right|} & \text{for} \quad v < v_0 \end{cases} \tag{21}$$

The resulting expansion (16) is uniformly valid for a large zone $|v - v_0| < M_v$ independent of τ and more details can be found in Dai and Chen (2012). The pure gravity waves on finite depth due to an impulse have the similar situation and studied in Clarisse *et al.* (1995).

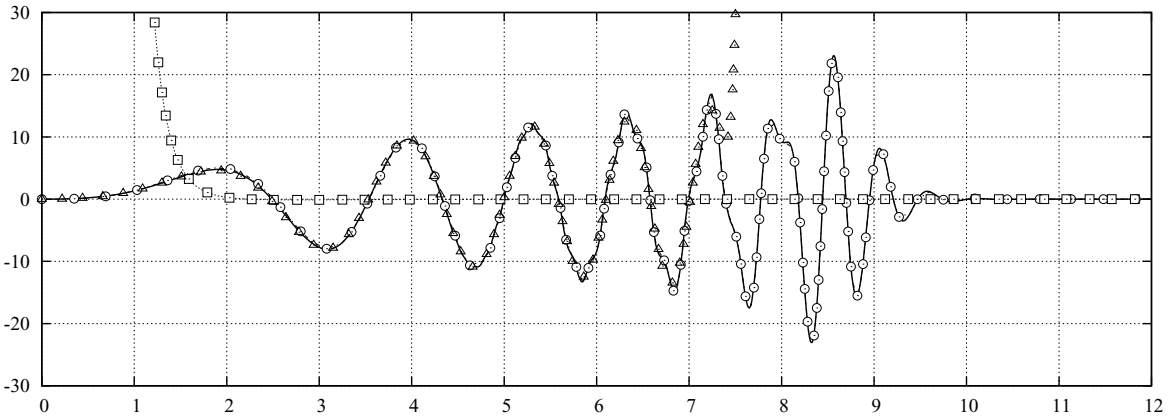

Figure 3: Comparison of asymptotic expansions with contour integrals for $(c, h) = (-0.01, 0.5)$

6 Summary and conclusions

Based on the above study, $F(c, h, \tau)$ can be evaluated by the contour integration along the steepest descent paths passing through the saddle points. The results by contour integrals are useful to check the asymptotic expansions. An example of numerical results for τ varying from 0 to 12 at (c, h)=$(-0.01, 0.5)$ is depicted on Figure 3. The results of contour integral are represented by solid lines while those of the uniform asymptotic expansions (16) by the symbol of empty circles. The results of series expansions (6) are depicted by the symbol of empty triangles and those of (10) by the symbol of empty squares. For small and moderate values of τ, the series expansion (6) gives excellent results. For large values of τ the asymptotic expansions (10) representing the contribution from the end point at $k = 0$ and the uniform asymptotic expansion (16) corresponding to the contribution of saddles points at $k = k_g$ and $k = k_T$ are very good as well. Finally, at very large values of τ, the uniform asymptotic expansion (16) is of exponentially small $O(e^{-\tau|\gamma|^3 2/3})$ so that asymptotic expansions (10) becomes dominant theoretically but the absolute value remains very small.

References

[1] Lamb H. Hydrodynamics, 6th Ed. Dover Publications, New York, 1932.

[2] Ursell F. (1960) On Kelvin's ship-wave pattern. *J. Fluid Mech.* 8, 418-31.

[3] Ursell F. (1964) The decay of the free motion of a floating body. *J. Fluid Mech.* 19, 305-19.

[4] Ursell F. (1968) The expansion of water-wave potentials at great distances. *Proc. Cambridge Philos. Soc.* 64, 811-26.

[5] Clement A. H. (1998) An ordinary differential equation for the Green function of time domain free surface hydrodynamics. *J. Eng. Math.* 33(2), 201-17.

[6] Chen X.B. & Wu G.X. (2001) On singular and highly oscillatory properties of the Green function for ship waves. *J. Fluid Mech.* 445, 77-91.

[7] Chen X.B. (2002) Role of surface tension in modeling ship waves. *Proc. 17th Int. Workshop on Water Waves and Floating Bodies.* Cambridge (UK).

[8] Chen X.B. & Duan W.Y. (2003) Capillary-gravity waves due to an impulsive disturbance. *Proc. 18th. Int. Workshop on Water Waves and Floating Bodies.* Le Croisic (France).

[9] Wehausen J.V. & Laitone E.V. (1960) Surface waves. *Handbuch des Physik pringer-Verlag.*

[10] Gradshteyn I. S. & Ryzhik I. M. (2007) Table of integrals, series, and products. Seventh edition. *Academic Press.*

[11] Chester C., Friedman B. & Ursell F. (1957) An extension of the method of steepest descents, Proc. *Cambridge Philos. Soc.*53, 599-611.

[12] Dai Y.Z. & Chen X.B. (2012) Uniform asymptotic expansion of Capillary Gravity Waves. *Proc. MMM-XIII Conference*, Shanghai (China).

[13] Clarisse J.M., Newman J.N. & Ursell F. (1995) Integrals with a large parameter: water waves on finite depth due to an impulse. *Proc. R. Soc. Lond. A*, 450, 67-87.

The Limits of Applicability of Shallow-Water Wave Theory

Lawrence J. Doctors
The University of New South Wales, Sydney, NSW 2052, Australia
Email: L.Doctors@UNSW.edu.au

Summary

The shallow-water wave theory of Tuck (1966) provides a remarkably simple set of formulas for the sinkage, trim, and wave resistance of a slender vessel traveling at a steady speed. Tuck (1967) later extended this work to include the case of a channel of finite width. In the current study, we compare these predictions of Tuck with the exact finite-channel-width finite-water-depth linearized theory based on the disturbance of the free surface, as detailed by Doctors (2008). It is shown that the shallow-water theory provides a good approximation for all three abovementioned quantities at speeds up to those corresponding to a depth Froude number of about 0.6. However, the shallow-water theory always provides underpredictions, compared to both the exact theory and with experiments in a towing tank.

1 Introduction

We consider the problem of a ship with length L, beam B, and draft T, advancing with a steady speed U in water of finite depth d in a channel of width w. Principal matters of interest are the sinkage s, trim t, and resistance R of the vessel. Of particular concern is whether the vessel will "ground" or contact the bottom in very shallow channels. Thus, it is useful to compute the keel clearance c, when the vessel is underway. Details of this geometry are shown in Figure 1(a).

Michell (1898) was the first to analyze the hydrodynamics of a ship, although his work was limited to the case of water of infinite depth and with infinite lateral extent. His essential assumption regarding the physics is that the vessel should be "thin"; that is, B/L is to be small. Many comparisons of the theory with experiments in a towing tank confirm that the predictions possess engineering validity for vessels with $B/L < 0.25$.

Regarding wave resistance, this theory has since been extended to include the case of a channel with a finite width, by Sretensky (1936). Finite water depth was considered by Lunde (1951).

If one is concerned with sinkage and trim, then it is necessary to also compute the rather more complicated *near-field* integrals, as described by Doctors (2008). Thus, it is of interest to compare the efficacy of the simpler shallow-water theory with that of the complete finite-depth theory.

2 Finite-Water-Depth Wave Theory

A summary of the inviscid linearized theory predicting near-field disturbance created by a steadily advancing ship was provided by Doctors (2008). The wave elevation is given by:

$$\begin{aligned}\zeta(x,y) &= \frac{1}{\pi^2}\int_0^\infty \mathrm{d}k_x \sum_{i=0}^{\infty} \epsilon\,\Delta k_y\, k_x^2 \exp(\mathrm{i}k_x x) \\ &\quad \cdot \cos(k_y y)\cdot(\mathcal{U}-\mathrm{i}\mathcal{V})/f \\ &\quad -\frac{\mathrm{i}}{\pi}\sum_{i=0}^{\infty}{}' \epsilon\,\Delta k_y\, k k_x \exp(\mathrm{i}k_x x) \\ &\quad \cdot \cos(k_y y)\cdot(\mathcal{U}-\mathrm{i}\mathcal{V})/\frac{\mathrm{d}f}{\mathrm{d}k}\,, \end{aligned} \tag{1}$$

where the dispersion relationship and its derivative are

$$f = k^2 - k k_0 \tanh(kd) - k_y^2\,, \tag{2}$$

$$\frac{\mathrm{d}f}{\mathrm{d}k} = 2k - k_0\tanh(kd) - k k_0 d\,\mathrm{sech}^2(kd)\,, \tag{3}$$

and the fundamental circular wave number is

$$k_0 = g/U^2\,. \tag{4}$$

Here, g is the acceleration due to gravity, k_x is the longitudinal wavenumber, k_y is the transverse wavenumber and k is the circular wavenumber. Finally, the finite-depth wave functions in Equation (1) are given by the formulas

$$\mathcal{U} = \frac{P^+ + \exp(-2kd)P^-}{1+\exp(-2kd)}\,, \tag{5}$$

$$\mathcal{V} = \frac{Q^+ + \exp(-2kd)Q^-}{1+\exp(-2kd)}\,, \tag{6}$$

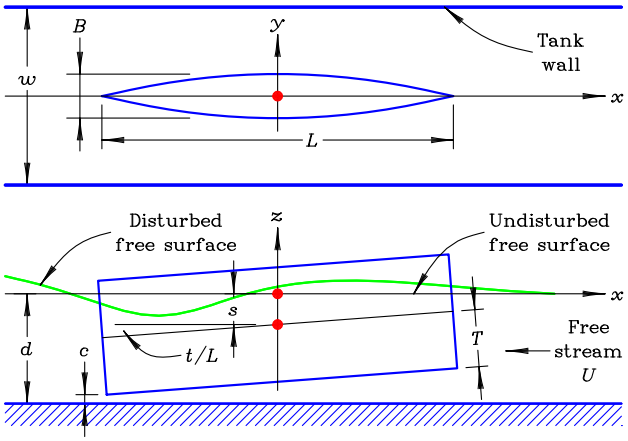

Figure 1: Definition of Problem
(a) Details of Geometry

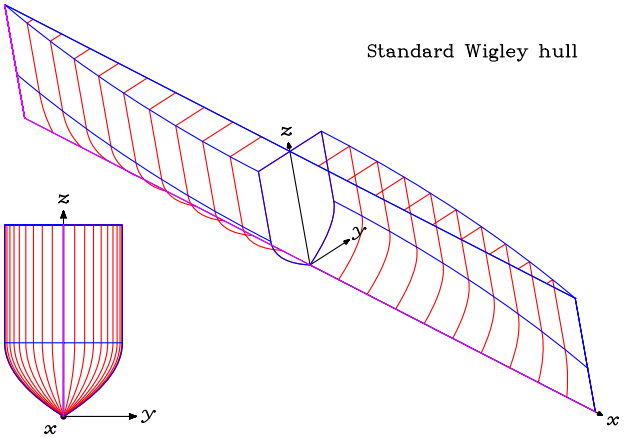

Figure 1: Definition of Problem
(b) Wireframe View

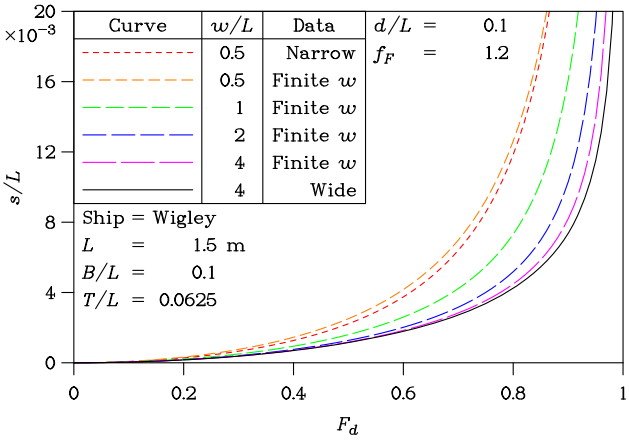

Figure 2: Three Theories for Sinkage

in which the Michell (1898) deep-water monohull functions depend on the local beam $b(x,z)$:

$$P^{\pm} + \mathrm{i}Q^{\pm} = \int_{S_0} b(x,z)\exp(\mathrm{i}k_x x \pm kz)\,\mathrm{d}S\,. \quad (7)$$

3 Shallow-Water Wave Theory

The approach here is to assume that the water-depth is sufficiently small, so that the Laplace (field) equation,

$$\phi_{xx} + \phi_{yy} + \phi_{zz} = 0\,, \quad (8)$$

can be replaced by the simpler

$$(1 - F_d^2)\phi_{xx} + \phi_{yy} = 0\,, \quad (9)$$

where the depth Froude number is

$$F_d = U/\sqrt{gd}\,. \quad (10)$$

Tuck (1967) showed, by applying the x-wise Fourier transforms to Equation (9), that the wave elevation could be expressed as

$$\zeta(x,0) = -\frac{U^2}{4\pi g d\sqrt{1-F_d^2}} \int_{-\infty}^{\infty} \exp(\mathrm{i}kx)|k| \cdot\tilde{S}(k)\coth\left(\frac{1}{2}w|k|\sqrt{1-F_d^2}\right)\mathrm{d}k\,, \quad (11)$$

where the Fourier transform of the sectional-area curve is

$$\tilde{S}(k) = \int_L S(x)\exp(-\mathrm{i}kx)\,\mathrm{d}x\,. \quad (12)$$

The pressure at the local section is directly related to the wave elevation, so that one can compute the relevant contributions to the longitudinal x force, the vertical z force, and the moment about the transverse y axis. The resistance, sinkage, and trim directly follow.

4 Sinkage

The subject of the experiments was a "simple" model possessing parabolic sections and parabolic waterlines, as suggested by Wigley (1934). The model is shown in Figure 1(b).

Figure 2 is a comparison of the theoretical dimensionless sinkage s/L for this model, plotted as a function of the depth Froude number F_d. Curve 2 through Curve 5 represent the finite-width predictions, based on Equation (11). It is seen that

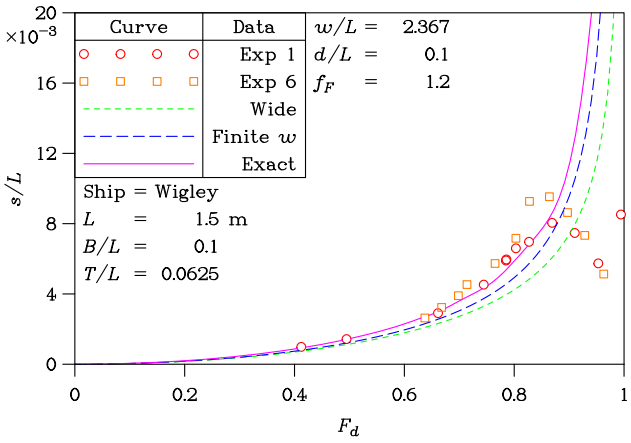

Figure 3: Sinkage
(a) $d/L = 0.1$

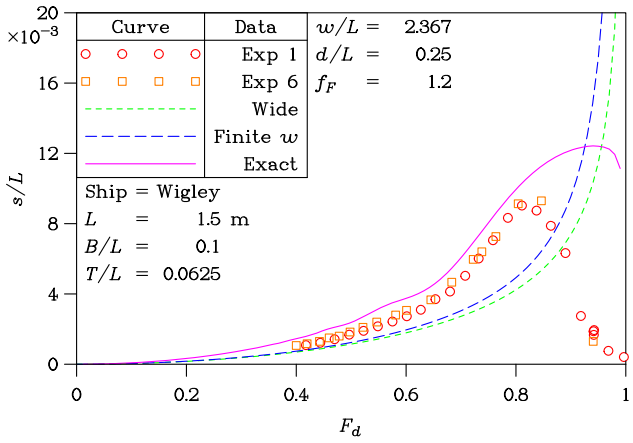

Figure 3: Sinkage
(b) $d/L = 0.25$

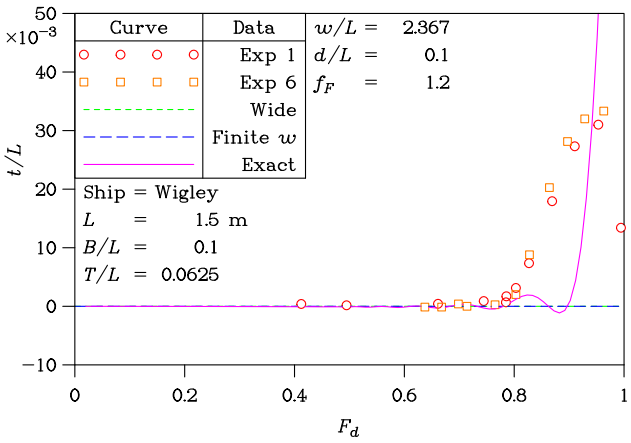

Figure 4: Trim
(a) $d/L = 0.1$

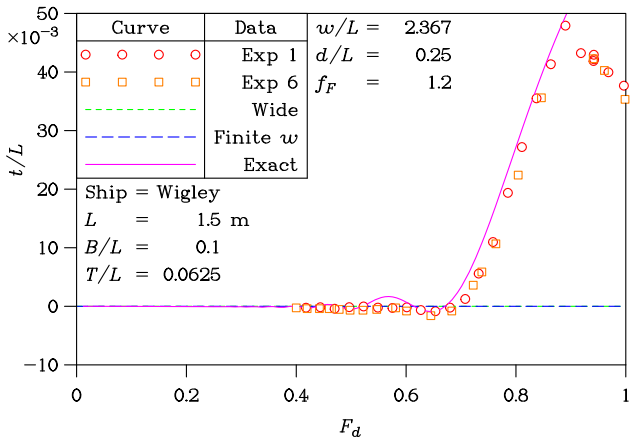

Figure 4: Trim
(b) $d/L = 0.25$

the theory approaches the expected limit of the *hydraulic theory* (Curve 1) for a narrow channel $w/L = 0.5$. Similarly, the desired limit of the *wide-channel theory* (Curve 6) of Tuck (1966) is closely achieved for the case of $w/L = 4$.

A comparison of the predicted and experimental sinkage is presented in Figure 3(a) for a relatively low depth-to-length ratio $d/L = 0.1$. Finite-width shallow-water theory represents an improvement over the wide-shallow-water theory.

Both theories are a good indication of the sinkage. Nevertheless, the more traditional finite-width finite-depth (exact theory) is better still. The case of deeper water, namely $d/L = 0.25$, in Figure 3(b) shows that the shallow-water concept is much less valid in this case.

5 Trim

The trim is depicted in the two parts of Figure 4 for the same two water depths. The shallower case in Figure 4(a) is particularly interesting, because both shallow-water theories indicate no trim, for these subcritical speeds, for this vessel with fore-aft symmetry.

This is indeed reasonably true in practice, at least up to $F_d \approx 0.8$. The exact theory does provide a positive trim at higher speeds, in keeping with observation.

At the greater depth of $d/L = 0.25$ in Figure 4(b), the trim is certainly nonzero for $F_d > 0.7$; the exact theory provides a good prediction for values of F_d up to about 0.9.

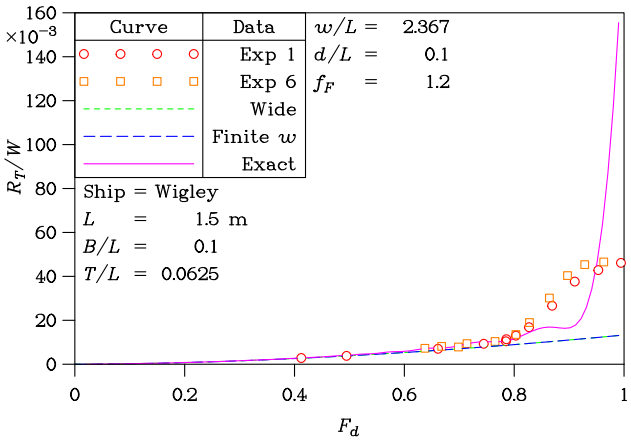

Figure 5: Total Resistance
(a) $d/L = 0.1$

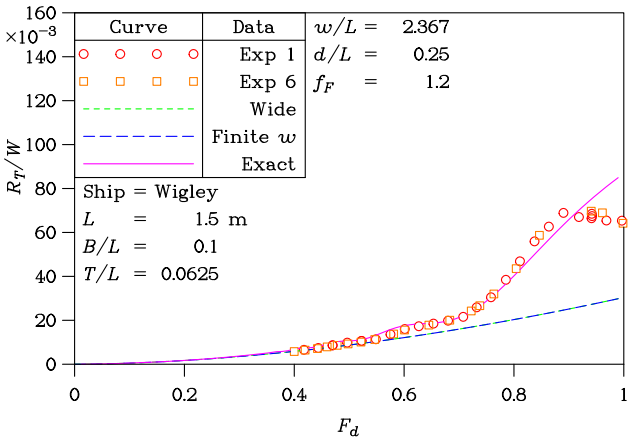

Figure 5: Total Resistance
(b) $d/L = 0.25$

6 Resistance

Finally, the resistance for the lesser of the two water depths is shown in Figure 5(a). Curiously, the shallow-water theory predicts no wave resistance, so the only contribution to the total resistance R_T is through the frictional resistance, which was computed using the 1957 International Towing Tank Committee (ITTC) formulation, together with a frictional form factor $f_F = 1.2$.

The resistance is rendered dimensionless by the vessel weight W. The exact formulation provides a nonzero wave resistance in Figure 5(a). For the greater depth in Figure 5(b), the "exact" theory gives a good indication of the total resistance at speeds corresponding to almost $F_d = 0.9$.

7 Concluding Comments

The lowest depth corresponded to a depth-to-draft ratio d/T of 1.6. It would be instructive to conduct experiments at lower depths, where the shallow-water theory will be more applicable.

This study has been confined to the subcritical-speeds. The nature of the theoretical formulations is substantially different for the supercritical case — another fruitful area of research.

The tests were performed in the Towing Tank at the Australian Maritime College (AMC) under the supervision of Mr Gregor Macfarlane.

8 References

Doctors, L.J.: "The Unsteady Growth of Ship Waves in a Towing Tank", *Proc. Twenty-Third International Workshop on Water Waves and Floating Bodies (23 IWWWFB)*, Jeju, Korea, pp 37–40 (April 2008)

Lunde, J.K.: "On the Linearized Theory of Wave Resistance for Displacement Ships in Steady and Accelerated Motion", *Trans. Society of Naval Architects and Marine Engineers*, Vol. 59, pp 25–76, Discussion: 76–85 (December 1951)

Michell, J.H.: "The Wave Resistance of a Ship", *Philosophical Magazine*, Series 5, Vol. 45, No. 272, pp 106–123 (January 1898)

Sretensky, L.N.: "On the Wave-Making Resistance of a Ship Moving along in a Canal", *Philosophical Magazine*, Series 7, Supplement, Vol. 22, No. 150, pp 1005–1013 (November 1936)

Tuck, E.O.: "Shallow-Water Flows past Slender Bodies", *J. Fluid Mechanics*, Vol. 26, Part 1, pp 81–95 (September 1966)

Tuck, E.O.: "Sinkage and Trim in Shallow Water of Finite Width", *Schiffstechnik*, Vol. 14, No. 73, pp 92–94 (1967)

Wigley, W.C.S.: "A Comparison of Experiment and Calculated Wave-Profiles and Wave-Resistances for a Form Having Parabolic Waterlines", *Proc. Royal Society of London*, Series A, Vol. 144, No. 851, pp 144–159 + 4 plates (March 1934)

An experimental study of near-cloaking

G. Dupont[1,2,4], O. Kimmoun[2,3,4], B. Molin[2,3], S. Guenneau[1,4], S. Enoch[1,4]
[1] Institut Fresnel, UMR CNRS 7249, 13 397 Marseille cedex 20
[2] IRPHÉ, UMR CNRS 7342, 13 384 Marseille cedex 13
[3] Ecole Centrale Marseille, 13 451 Marseille cedex 20
[4] Aix-Marseille Université (AMU)

In the past years there has been much research work on "cloaking", whereby some object is made "invisible". From electromagnetics the topic has been extended to other fields such as acoustics, structural mechanics and, more recently, hydrodynamics. In the water wave context, "invisibility" means that the diffracted wave field is nil in the far-field at all azimuthal angles. This can usually be achieved only at one wave frequency. At the 26th IWWWFB Porter (2011) presented an application to the case of a vertical cylinder, rendered invisible by a local modification of the bathymetry in an otherwise constant depth ocean. This case was further investigated by Newman (2012).

In this paper we report a similar study, where a vertical dihedral, at the end of the ECM wavetank, is attempted to be rendered invisible.

Experimental set-up

Our wave flume is about 15 m long and 65 cm wide. In the reported experiments the waterdepth was set at 40 cm. The beach at the end of the tank was removed and a rigid vertical plate was installed, from wall to wall, at an angle of 60 degrees, thereby achieving a dihedral. In this configuration a first series of regular wave tests was run, with wave number k mainly in the range π/b through $2\,\pi/b$ (b being the tank width), meaning the reflected wave system, in the far-field, consists of two modes: the inline mode and the first sloshing (plus progressive) mode. The two components were separated by an array of 5 wave gauges over the width of the tank, set at different inline positions (the same experimental case being run as many times as different positions were used).

In a second stage an "invisibility carpet", consisting in 18 vertical poles, with trapezoidal cross-sections, was set in front of the dihedral. The same regular wave tests were run, and the reflected inline and sloshing modes were separated from the wave gauge measurements. Successful "invisibility" implies that the sloshing modes vanish and only the inline reflected mode remains.

Numerical determination of the reflected wave system

The problem was formulated within the frame of linearized potential flow theory, and solved numerically with the COMSOL Multiphysics software. In the dihedral alone case (without the "invisibility carpet") a semi-analytical method, described below, was also used to validate COMSOL's results.

Due to the wall-sided geometry the linearized velocity potential writes

$$\Phi(x,y,z,t) = \Re\left\{-\mathrm{i}\,\frac{A_I\,g}{\omega}\,\frac{\cosh k(z+h)}{\cosh kh}\,\varphi(x,y)\,\mathrm{e}^{-\mathrm{i}\,\omega t}\right\} \tag{1}$$

where A_I is the amplitude of the incoming waves, h the waterdepth, ω the frequency and k the wave number. The reduced potential φ satisfies the Helmholtz equation $\Delta\varphi + k^2\,\varphi = 0$ in the fluid domain, no-flow conditions at the solid walls and appropriate ingoing and outgoing conditions at $x \to \infty$.

Dihedral alone

Figure 1 shows the geometry at the end of the tank. It consists in two overlapping rectangular sub-domains:
– the angular sector $0 \le R \le 2\,d$; $0 \le \theta \le \pi/3$ (inside the green contour in figure 1).
– the semi-infinite strip $d \le x < \infty$; $0 \le y \le b$ with $d = b\,\sqrt{3}/3$ (inside the red contour).

Within the first sub-domain the reduced potential φ takes the general form:

$$\varphi_1(R,\theta) = \sum_{m=0}^{\infty} A_m\,\frac{J_{3m}(kR)}{J_{3m}(2kd)}\,\cos 3m\theta \tag{2}$$

with J_{3m} the Bessel function of the first kind.

Within the second sub-domain it can be written as:

$$\varphi_2(x,y) = \mathrm{e}^{-\mathrm{i}\,kx} + \sum_{n=0}^{\infty} B_n\,\cos\lambda_n y\,\mathrm{e}^{-\alpha_n\,(x-d)} \tag{3}$$

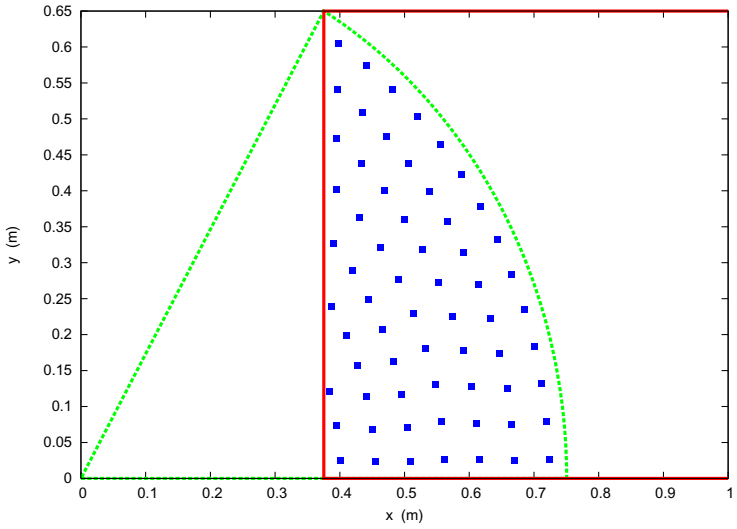

Figure 1: Sub-domains 1 and 2 and control points.

where $\lambda_n = n\,\pi/b$ and

$$\alpha_n = -\mathrm{i}\,\sqrt{k^2-\lambda_n^2} \quad \text{for} \;\; n \le N_2 \qquad\qquad \alpha_n = \sqrt{\lambda_n^2-k^2} \quad \text{for} \;\; n > N_2 \tag{4}$$

N_2 being the largest integer n such that $\lambda_n < k$.

The unknown coefficients A_m and B_n can be determined by enforcing that the two expressions coincide in the common region. To this end the series are truncated at orders M and N, $N_{\rm pt}$ (with $N_{\rm pt} \gg M+N+2$) control points (shown as blue square symbols) are distributed over the common region, and the following quantity

$$E = \sum_{i=1}^{N_{\rm pt}} \Big| \varphi_1(x_i,y_i) - \varphi_2(x_i,y_i) \Big|^2 \tag{5}$$

is minimized.

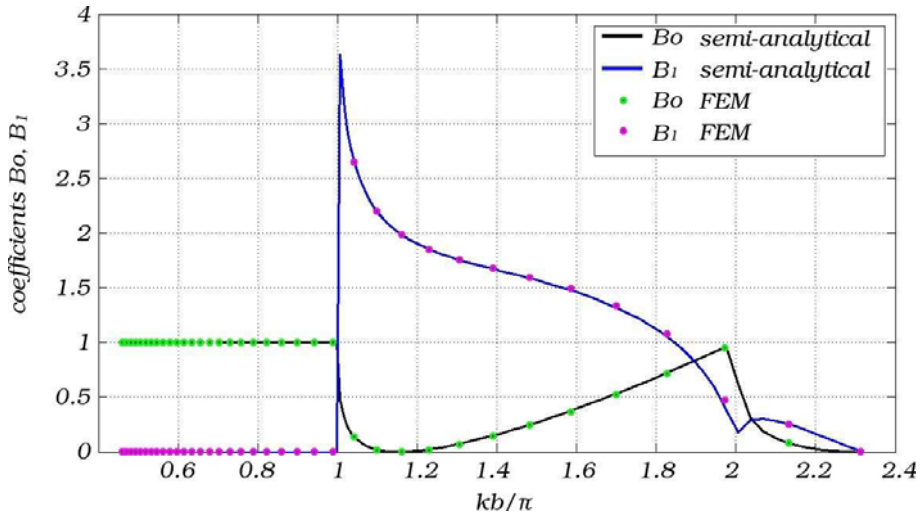

Figure 2: Coefficients $|B_0|$ and $|B_1|$ vs kb/π.

Figure 2 shows the moduli of the non-dimensional amplitudes B_0, B_1 of the propagating modes for $0.5 \le k\,b/\pi \le 2.3$, as obtained semi-analytically with this method and as obtained numerically with the Finite Element Method of COMSOL. The agreement is excellent.

Invisibility carpet

The trapezoidal end part of the wave-flume is covered with vertical poles of prismatic cross-sections, as shown in figure 4. The void fraction is close to 50 %, and the "carpet" extends 1.5 m from the end point of the tank. These choices are somewhat arbitrary. Keeping constant the void fraction and extension of the carpet, the number of inclusions in the inline and transverse directions are varied in COMSOL computations.

An efficiency function is defined from the quantity

$$F = \sum_n \int_0^b \left| \varphi(x_n, y) - \overline{\varphi(x_n, y)} \right|^2 \, \mathrm{d}y \tag{6}$$

where a number of reference abscissas x_n are taken, from the edge of the carpet toward the wavemaker. When there is no carpet F takes the value F_0. The efficiency is then defined as F/F_0. An efficiency equal to zero means that the dihedral has been made "invisible".

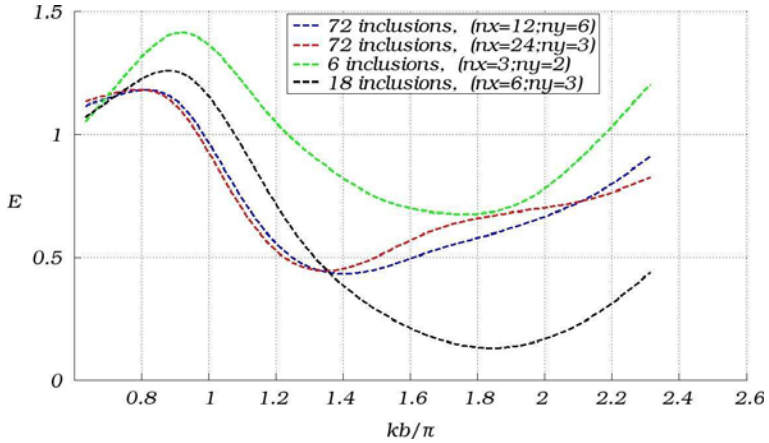

Figure 3: Efficiency function F/F_0, for different numbers of inclusions.

Figure 3 shows the obtained efficiencies for 4 different arrangements, and for $k\,b/\pi$ in the range 0.8 to 2.2. It is somewhat puzzling that the most efficient carpet, in the range $1.4 \leq k\,b/\pi < 2.2$, is the carpet with the intermediate number of inclusions (18). This is the carpet that was modeled experimentally. A photograph is shown in figure 4.

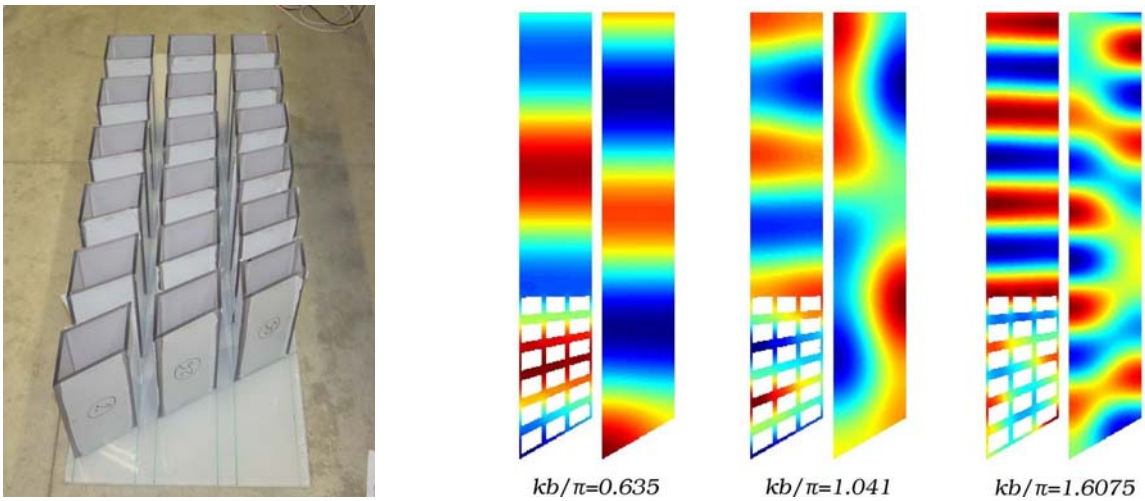

Figure 4: Photograph of the invisibility carpet (left). Calculated wave patterns in the end part of the tank for 3 kb values (right).

Figure 4 (right) shows calculated patterns of the free surface elevation, with and without the invisibility carpet, for 3 values of $k\,b/\pi$. The first value ($kb/\pi = 0.635$) is below the cut-off frequency, so the wave pattern is unidirectional in both cases.

Results for the non-dimensional amplitudes B_0 and B_1, from COMSOL computations, for the 18 inclusions arrangement, are shown in figure 5, and compared with the dihedral alone case. With the carpet the inline coefficient B_0 takes values very close to 1 all over the kb range, while the B_1 coefficient is strongly decreased.

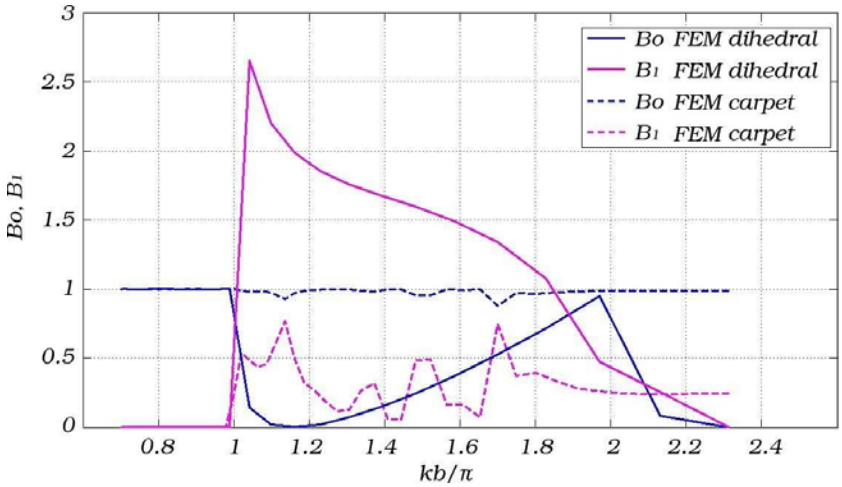

Figure 5: Results from COMSOL computations: B_0 and B_1 without (full lines) and with (dashed lines) the carpet.

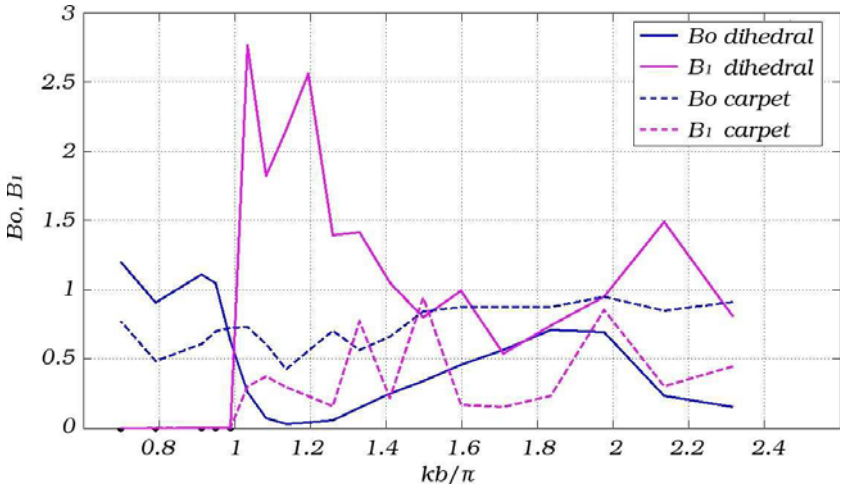

Figure 6: Results from experiments: B_0 and B_1 without (full lines) and with (dashed lines) the carpet.

Finally figure 6 shows the experimental B_0 and B_1 coefficients, as derived from the wave gauges measurements. The agreement with the results in figure 5 is fair in the dihedral alone case. In the carpet case it is only qualitative. In particular the experimental B_0 coefficient, in the low kb range, is much lower than 1, suggesting that appreciable energy dissipation takes place in the carpet, most likely through viscous effects. Another reason for discrepancies might be that at low kb values, the wave flume being only about 15 m long, with no active absorption mechanism, the steady state window is rather short.

Acknowledgement

SG wishes to thank ERC for supporting this work.

References

Porter R. 2011 Cloaking of a cylinder in waves, in *Proc. 26th Int. Workshop Water Waves & Floating Bodies*, Athens.

Newman J.N. 2012 Scattering by a cylinder with variable bathymetry, in *Proc. 27th Int. Workshop Water Waves & Floating Bodies*, Copenhagen.

Capture width for arrays of wave energy converters

F.J.M. Farley

Energy and Climate Change Division, University of Southampton, Highfield, Southampton SO17 1BJ

In this paper I use the "optical theorem for wave power" to calculate the capture width for arrays of wave energy converters. The optical theorem (in analogy with the optical theorem in atomic physics [1]) relates the capture width (CW) for a wave energy converter (WEC) to the polar diagram $f(\theta)$ of the total wave generated by the device due to its unmoving presence in the sea together with its motions and the forces it exerts,

$$CW = \lambda \frac{|\Re f(0)|^2}{\int_{-\pi}^{\pi} |f(\theta)|^2 d\theta} \tag{1}$$

Here $f(\theta)$ gives the complex amplitude of the wave generated by the device as a function of the angle θ relative to the propagation direction of the incident waves, (the forward direction). Equation (1) has been derived independently by many authors and reviewed recently by Farley [2] with references to previous work. In [2] it is established that the relevant angular distribution $f(\theta)$ is for the total wave generated by the device and the forward amplitude $f(0)$ is required in the numerator of (1) rather than the backward amplitude $f(\pi)$. (Not to be confused with the backward amplitude $f(\pi)$ required in the theorem of Newman [3] using waves from the device motions alone omitting the waves generated by the device's unmoving presence). The formula gives the capture width in the best case, when the motions of the WEC have been optimised in amplitude and phase.

It was pointed out in [2] that equation (1) can be applied not only to a single machine but also to calculate the capture by any combination of reasonably localised WEC's in any pattern or array. One only needs to compute the overall polar diagram $f(\theta)$ and then apply (1).

In an array of identical WECs there are two effects to be considered:
a) The wave generated by each WEC propagates to the neighbouring WECs and adds to the incident wave. This is important if the array is closely packed. For an array of heaving point absorbers Mei [4] shows that the radiation damping is increased and the resonance is broadened.
b) At a distance the waves generated by each WEC combine to give the overall polar diagram $f(\theta)$ which determines the capture width. If the array spacing is large compared with the size of the individual elements this is the main effect and the direct interactions (a) can be neglected, as argued for example by Garnaud and Mei [5] who consider a long linear array parallel to the direction of wave propagation.

Here I assume that the components of the array are widely spaced so the modification of the incident wave by radiation from neighbouring elements can be neglected. All effects on the capture width arise from (b). In computing the overall angular distribution the polar diagram of each element should be included. The frequency response of the array will be just the same as the frequency response of the individual elements with no broadening. If all the elements are close together the polar diagram will be the same as that of a single element and the capture width will be unchanged. As the components are moved further apart the polar diagram changes and the capture width rises.

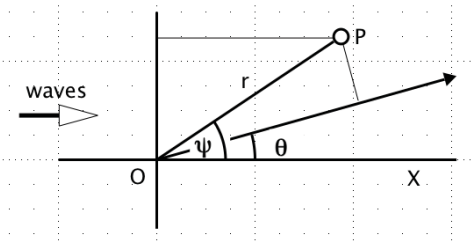

Array theory

Consider an array which is symmetric about a central point O and compute $f(\theta)$ as from this origin. The incident monochromatic waves propagate in the direction OX and θ is the angle of the generated wave relative to OX. The wave

generated by a WEC element at point P, distance r from O at angle ψ, has a relative phase advance

$$\phi = kr\{cos(\psi - \theta) - cos(\psi)\} = 2\ k\ r\ sin(\psi - \theta/2).\ sin(\theta/2) \tag{2}$$

As the array is symmetric about O, imaginary parts of the generated waves will cancel. The overall amplitude at angle θ is given by the sum over the array of

$$f(\theta) = \Sigma\ cos(\phi) \tag{3}$$

For an array symmetric about O the overall phase will be the same as that from a WEC element at O. In the forward direction with $\theta = 0$, $\phi = 0$ for all elements, so their contributions all add up.

Linear arrays

Results for heaving buoys in a linear array perpendicular to the wave direction, buoy spacing d, are shown in figure 1 for a line of 11 boys and a line of 41 buoys. The CW rises to a peak when $kd = 4.8$ followed by a steep drop when buoy spacing is one wavelength !! The best result gives a factor 2.25 improvement over the simple sum for 41 buoys, a factor 2.35 for 11 buoys. For larger array spacings, the CW continues to be periodic but is generally smaller . The average improvement factor is close to 41 for 41 buoys, close to 11 for 11 buoys, as one might naively expect. With a wide spectrum sea the result will be some average over adjoining values of kd. In 1976 Budal [6] computed the energy balance in the far field for a line of 10 buoys and obtained a graph similar to figure 1. McIver [7] found essentially the same for a line of 5 buoys.

Two parallel lines of buoys, both parallel to the wave crests, have been recommended. The same calculation gives a poor result if the line spacing is one or two wavelengths. Optimum line spacing is about 0.75 λ which gives figure 2 with an improvement factor 188 for 82 buoys, a ratio of 2.29 per buoy. Comparing with figure 1, it seems that a single line is very nearly as good.

The result for a linear array oriented parallel to the wave direction is given in figure 3, again for lines of 11 and 41 buoys. In this case there are pronounced minima when the buoy spacing is some multiple of $\lambda/2$, but on the whole the CW increases as the buoy spacing is increased. However the best results are disappointing: the improvement factors over the same number of independent buoys is only 0.7 for 11 buoys and 0.55 for 41 buoys.

Circular arrays

The polar diagram for a circular disc-shaped array can be obtained in the same way, (but in this case neglecting the hydrodynamic modifications of the incident wave [4]). The improvement ratio for a ring of 6 buoys with another at the centre, was caculated as a function of ring diameter. For very small diameters the ratio is 1, so the capture width is the same as that of a single buoy. The ratio rises to a maximum of 7.2 when the radius is 1.64 λ, hardly better than 7 separate buoys. A disc is a collection of rings, so will be no better. It seems that the compact arrays studied in [4] will have a broader resonance because of the close interactions but the peak response will hardly justify the extra expense.

A paradox

The array captures more power because on average the radiation to the far field is reduced by destructive interference. The radiation damping of each buoy will be correspondingly reduced. To capture more power each device must move more. Why should it do so when I have assumed that the incident wave at each device is unmodified? This is a mystery. Theorem (1) is valid only if the device motions have been optimised, which must imply less internal damping than for an isolated buoy. However less damping implies a narrower resonance; so in a wide-spectrum sea the gains predicted by figures 1 etc may prove illusionary.

Conclusions

1) A line of WECs perpendicular to the wave direction is the best shape for the array.
2) Spacing should be of order 3/4 times the wavelength, a bit smaller for a wide spectrum sea; one wavelength spacing is bad.
3) The total CW is then about a factor 2 more than for the individual elements deployed separately.
4) Two parallel broadside lines do not offer much improvement.

References

[1] F.J.M. Farley, (2004) *Optical theorem in atomic physics and wave power*, 19th International Workshop on Water Waves and Floating Bodies, Cortona, Italy (http://www.iwwwfb.org/)

[2] F.J.M. Farley, (2012) *Far field theory of wave power capture by oscillating systems*, Phil.Trans. A370, 278

[3] J.N. Newman, (1979) *The interaction of stationary vessels with regular waves*, Proc. 11th Symp. on Naval Hydrodynamics, London, UK, pp. 491 - 501

[4] C.C. Mei, (2012) *Hydrodynamic principles of wave power extraction*, Phil.Trans. A370, 208

[5] X. Garnaud and C.C. Mei, (2010) *Bragg scattering and wave-power extraction by an array of small buoys*, Proc. Roy. Soc. A466, 79

[6] K. Budal, (1977) *Theory for absorption of wave power by a system of interacting bodies*, Journ. Ship Research 21, 248; (and preprint 1976).

[7] P. McIver, (1995) *Arrays of wave energy devices*, 5th International Workshop on Water Waves and Floating Bodies, Oxford, UK (http://www.iwwwfb.org/)

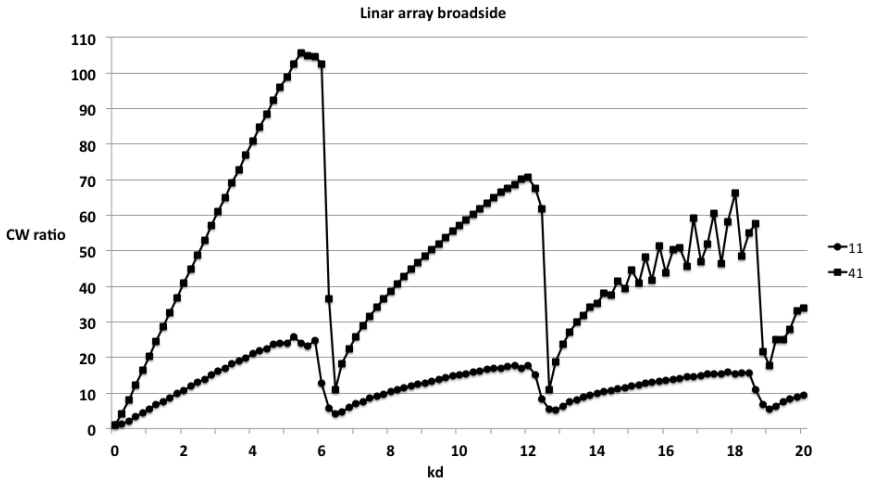

Figure 1: *Capture widths for a line of buoys perpendicular to the wave direction, spacing d. For 11 buoys and 41 buoys. Total CW compared to a single buoy*

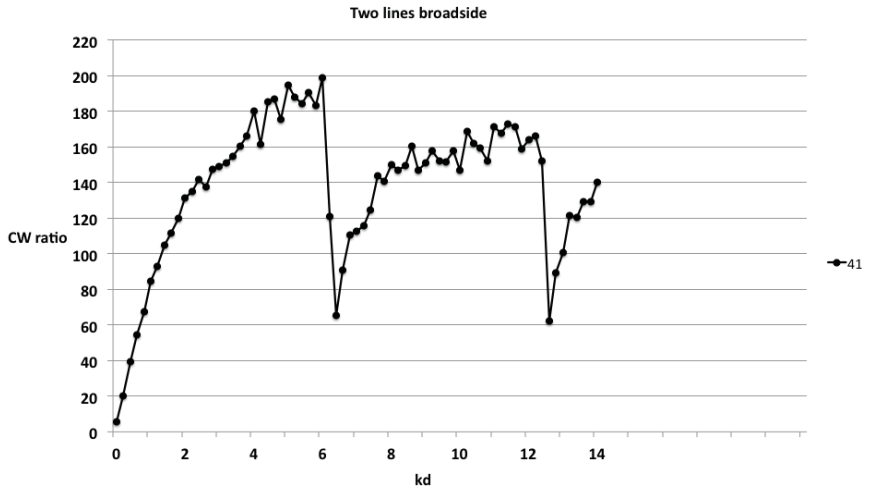

Figure 2: *Capture width ratio for two parallel lines of buoys perpendicular to the wave direction, spacing d. Each line has 41 buoys.*

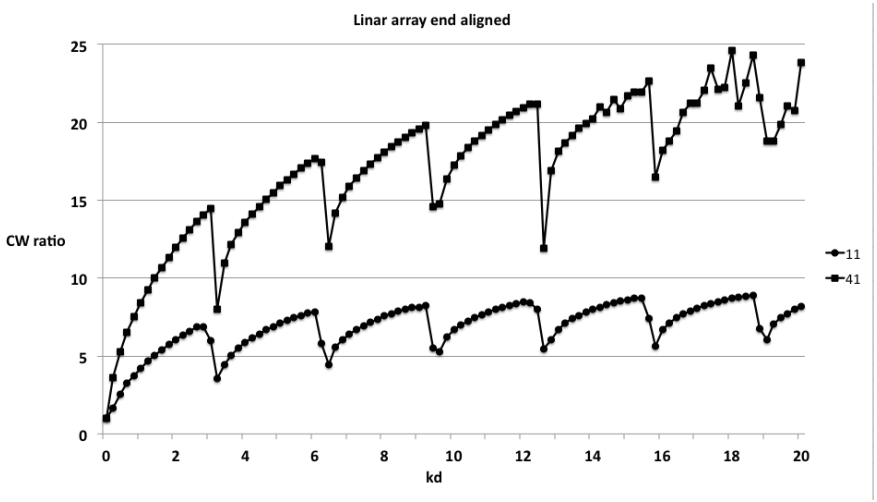

Figure 3: *Capture widths for a line of buoys parallel to the wave direction, spacing d. For 11 buoys and 41 buoys.*

The Wave Radiation Problem in A Two-layer Fluid by Time-domain Method

Y Gou, XJ Chen, GB Wang, B Teng, DZ Ning

(State Key Laboratory of Costal and Offshore Engineering, Dalian University of Technology, Dalian, China)

e-mail: gouying@dlut.edu.cn

INTRODUCTION

In the real ocean, density of sea water is actually changing with the depth due to the variations in salinity and temperature. The two-layer fluid system is the simplest model to investigate the internal wave. In this system there exists a density discontinuity at the interface between the upper and the lower layers, and the density is constant in each layer. The internal waves will be generated on the interface such as solitary wave and periodic wave. For internal solitary wave, the wave length is much longer than the characteristic length of structure. So the internal solitary wave forces acting on ocean structures can be simulated by Morison formula (Song, et al. 2011). For the harmonic internal waves, the wave length is over a wide range. The diffraction/radiation theory should be adopted when the characteristic length of structure is relative large.

The multipole expansion method is utilized by Cadby and Linton (2000) to investigate wave radiation on a submerged sphere. Ten and Kashiwagi (2004) and Kashiwagi et al. (2006) developed a linearized 2-D diffraction/radiation model, in which boundary integral-equation method is implemented in frequency-domain. In this model, the Green function which satisfied the free surface and interface boundary conditions is derived. Nguyen and Yeung (2011) derived the unsteady 3-D sources for a two-layer fluid of finite depth.

Teng and Gou(2009) and Gou et al. (2012) developed a time-domain numerical method by boundary element method to study the diffraction problem in a two-layer fluid. In this numerical model, the simple Rankine source is used, and the complicated wave Green function is avoided to be calculated. As the continued work, the wave radiation problem in a two-layer fluid is simulated by this time-domain method here. The forced oscillation of a truncated cylinder in finite depth is considered. Comparisons are made with an analytic solution derived by Shi and You (2009), which the eigenfunction expansion method is used. The examination shows that the model gives very steady results and has good agreement with the analytic solution, and some significant results can be drawn.

NUMERICAL MODEL

A Cartesian coordinate system is defined with the origin in the plane of the undisturbed free surface, and the z-axis positive upwards. The densities of the fluids in the upper and the lower layers are ρ_1 and ρ_2, respectively. Other notations are shown in Fig.1. The fluid in each layer is assumed to be inviscid and incompressible, and the flow irrotational. Furthermore, the motions of the body are relatively small so that the linear potential theory is applied.

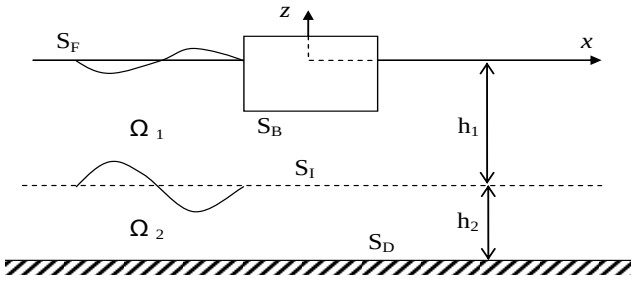

Fig.1 Definition Sketch

The radiation velocity potentials $\Phi^{(1)}$ and $\Phi^{(2)}$ in the fluid domain Ω_1 and Ω_2 satisfy Laplace equation, and the linearized boundary conditions are satisfied as follows:

$$\Phi^{(1)}{}_{tt} + g\Phi^{(1)}{}_{z} = 0, \qquad \text{on z=0} \tag{1}$$

$$\Phi^{(1)}{}_{z} = \Phi^{(2)}{}_{z}, \qquad \text{on z=-h}_1 \tag{2}$$

$$\gamma(\Phi^{(1)}{}_{tt} + g\Phi^{(1)}{}_{z}) = \Phi^{(2)}{}_{tt} + g\Phi^{(2)}{}_{z}, \text{ on z=-h}_1 \tag{3}$$

$$\frac{\partial \Phi^{(1)}}{\partial n} = V_n \tag{4}$$

$$\Phi^{(2)}{}_{z} = 0, \qquad \text{on z=-h}_1\text{-h}_2 \tag{5}$$

where $\gamma = \rho_1 / \rho_2$, V_n is the velocity of the body.

In order to avoid the reflection of scatter waves, an

artificial damping layer must be utilized to absorb the scattered wave. For the two-layer fluid system, a damping term is added to both the free surface and the internal surface boundary conditions on the outer part.

$$\frac{\partial \eta^{(m)}}{\partial t} = \frac{\partial \Phi^{(m)}}{\partial z} - \nu(r)\eta^{(m)} \qquad m = 1,2 \tag{6}$$

$$\begin{aligned} &\frac{\partial \Phi^{(m)}}{\partial t} = -g\eta^{(m)} - \nu(r)\Phi^{(m)} \qquad m = 1 \\ &\frac{\partial \varphi}{\partial t} = (1-\gamma)g\eta^{(m)} - \nu(r)\varphi \qquad m = 2 \end{aligned} \tag{7}$$

where

$$\varphi = \gamma\Phi^{(1)} - \Phi^{(2)} \tag{8}$$

$$v(r) = \begin{cases} \alpha\omega\left(\dfrac{r-r_0}{\lambda}\right)^2 & (r_0 \le r \le r_0 + \beta\lambda) \\ 0 & (r < r_0) \end{cases} \tag{9}$$

Here, damping coefficient α and beach breadth coefficient β are equal to 1.0.

The structure considered here is located in the upper fluid. Applying the Green's second identity to Green function and radiation velocity potential $\Phi^{(1)}$ and $\Phi^{(2)}$ in each layer respectively, we can obtain the integral equations:

$$\begin{aligned} &\alpha\Phi^{(1)} - \iint_{S_B} \Phi^{(1)} \frac{\partial G_1}{\partial n} \mathrm{d}s + \iint_{S_F} G_1 \frac{\partial \Phi^{(1)}}{\partial n} \mathrm{d}s + \iint_{S_I} G_1 \frac{\partial \Phi^{(1)}}{\partial n} \mathrm{d}s \\ &= -\iint_{S_B} G_1 \frac{\partial \Phi^{(1)}}{\partial n} \mathrm{d}s + \iint_{S_F} \Phi^{(1)} \frac{\partial G_1}{\partial n} \mathrm{d}s + \iint_{S_I} \Phi^{(1)} \frac{\partial G_1}{\partial n} \mathrm{d}s \end{aligned} \tag{10}$$

$$\iint_{S_I} G_2 \frac{\partial \Phi^{(2)}}{\partial n} \mathrm{d}s = \iint_{S_I} \Phi^{(2)} \frac{\partial G_2}{\partial n} \mathrm{d}s - \alpha\Phi^{(2)} \tag{11}$$

where

$$G_1 = -\frac{1}{4\pi r}, \quad G_2 = -\frac{1}{4\pi r} - \frac{1}{4\pi r_2} \tag{12}$$

Here, r is the distance between the field and the source points, and r_2 is the distance between the field point and the image of the source point about the sea bed. The direct method is used to calculate the solid angle α (Teng, et al, 2006). The computational field is divided by second order isoparametric elements, and two sets of linear equations are obtained after the discretization to Eqs.(10) and (11).

$$\begin{bmatrix} a_{11} & a_{12} & a_{13} \\ a_{21} & a_{22} & a_{23} \\ a_{31} & a_{32} & a_{33} \end{bmatrix} \begin{Bmatrix} \left\{\dfrac{\partial \Phi^{(1)}}{\partial n}\right\}_{S_F} \\ \left\{\Phi^{(1)}\right\}_{S_B} \\ \left\{\dfrac{\partial \Phi^{(1)}}{\partial n}\right\}_{S_I} \end{Bmatrix} = \begin{bmatrix} s_{11} & s_{12} & s_{13} \\ s_{21} & s_{22} & s_{23} \\ s_{31} & s_{32} & s_{33} \end{bmatrix} \begin{Bmatrix} \left\{\Phi^{(1)}\right\}_{S_F} \\ \left\{\dfrac{\partial \Phi^{(1)}}{\partial n}\right\}_{S_B} \\ \left\{\Phi^{(1)}\right\}_{S_I} \end{Bmatrix} \tag{13}$$

$$[b]\left\{\frac{\partial \Phi^{(2)}}{\partial n}\right\}_{S_I} = [t]\left\{\Phi^{(2)}\right\}_{S_I} \tag{14}$$

Applying the interface conditions Eq.(2) and the velocity potential function φ defined by Eq.(8), we can get a single set of linear equations as follows:

$$\begin{aligned} &\begin{bmatrix} a_{11} & a_{12} & a_{13} + \dfrac{1}{\gamma} s_{13} t^{-1} b \\ a_{21} & a_{22} & a_{23} + \dfrac{1}{\gamma} s_{23} t^{-1} b \\ a_{31} & a_{32} & a_{33} + \dfrac{1}{\gamma} s_{33} t^{-1} b \end{bmatrix} \begin{Bmatrix} \left\{\dfrac{\partial \Phi^{(1)}}{\partial n}\right\}_{S_F} \\ \left\{\Phi^{(1)}\right\}_{S_B} \\ \left\{\dfrac{\partial \Phi^{(1)}}{\partial n}\right\}_{S_I} \end{Bmatrix} = \\ &\begin{bmatrix} s_{11} & s_{12} & \dfrac{1}{\gamma} s_{13} \\ s_{21} & s_{22} & \dfrac{1}{\gamma} s_{23} \\ s_{31} & s_{32} & \dfrac{1}{\gamma} s_{33} \end{bmatrix} \begin{Bmatrix} \left\{\Phi^{(1)}\right\}_{S_F} \\ \left\{\dfrac{\partial \Phi^{(1)}}{\partial n}\right\}_{S_B} \\ \{\varphi\}_{S_I} \end{Bmatrix} \end{aligned} \tag{15}$$

From the above equation, we can find that the velocity potential $\Phi^{(1)}$ and $\Phi^{(2)}$ on the interface have no need to be solved in the time matching procedure, and they have been replaced by φ. It makes the time matching process easier. The 4th-order Runga-Kutta approach is used, basing on boundary conditions Eqs.(4), (6) and (7). In order to avoid the initial effect a ramping function is utilized.

$$R_m(t) = \begin{cases} \dfrac{1}{2}\left(1 - \cos\left(\dfrac{\pi t}{T_m}\right)\right) & t \le T_m \\ 1 & t \ge T_m \end{cases} \tag{16}$$

where T is the wave period, and T_m=2T in this simulation. Then, all the time histories of wave elevations on free and internal surface and wave forces acting on the body can be calculated.

NUMERICAL RESULTS

The forced oscillation of a truncated cylinder in a two layer fluid of finite depth is considered. The sketch is also shown in Fig.1. The cylinder has a radius of a=1.0m, and a draft of T =1.0m. The water depths of the upper and the lower layers are h_1 =1.4m, h_2=0.6. The densities of the fluids in the upper and the lower layers are ρ_1=998.2kg/m^3 and ρ_2=1027.2kg/m^3, respectively. That means γ=0.972.

In this numerical method, both the free surface and internal surface should be meshed. The radius of computed field is about 3λ in this case, and the length of the damping layer 1.5λ is included. Here, λ is the wave length relative to the internal wave mode. The computational meshes on the body surface, the free surface and the internal surface are shown in Fig.2

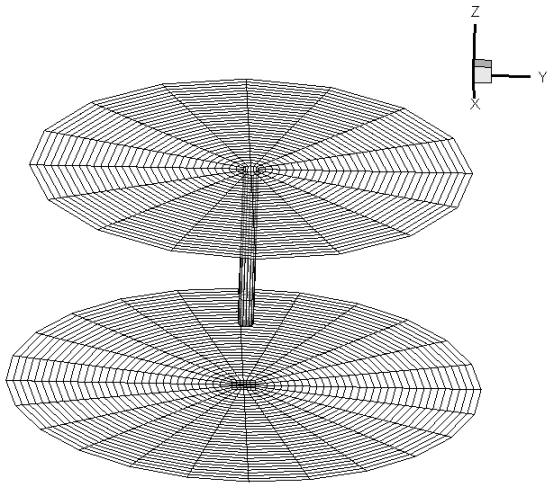

Fig.2 Mesh of the computational field.

Surge motion

The truncated cylinder is forced to oscillate in surge direction by the function of ξ_x=Asinωt. A is the amplitude of the surge oscillation, and ω is the oscillation angle frequency. So the velocity of the truncated cylinder V_x=$A\omega$ cosωt. When the unknown velocity potentials over truncated cylinder surface are obtained, the pressure can be derived from the Bernoulli equation, the forces and moments acting on the body can be calculated by integrating the pressure over the mean body surface. In order to compare with the analytical result derived by Shi and You (2009), the radiation force of unit oscillation was divided into added mass and damping coefficient. In order to investigate the hydrodynamic forces in two-layer fluid system, the results of single-layer is also shown.

Fig.3 and Fig.4 show the added mass and damping coefficient of surge oscillation. It should be note that there are two possible scatter waves with a prescribed frequency in a two-layer fluid, which so called the surface wave mode and internal wave mode. The results presented here are the total action of both the two modes. From the comparison with analytic results, we can see that the present numerical model by time-domain method have good precision. Furthermore, the results indicate that the results of two-layer fluid are significant compared with the results of single-layer in relative lower frequency range. The interface elevation at t=9T is shown in Fig.5. It can be seen that the wave profile is smooth enough, and demonstrated the steady of this numerical model.

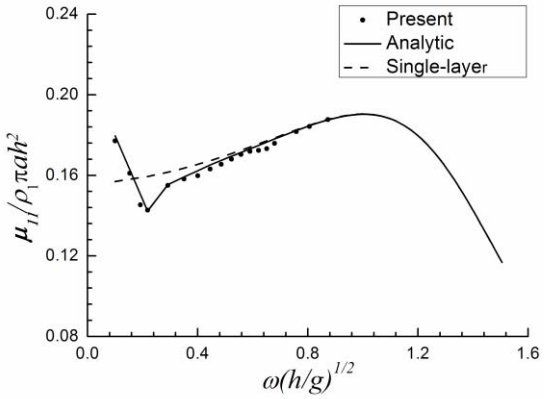

Fig.3 Added mass of surge motion

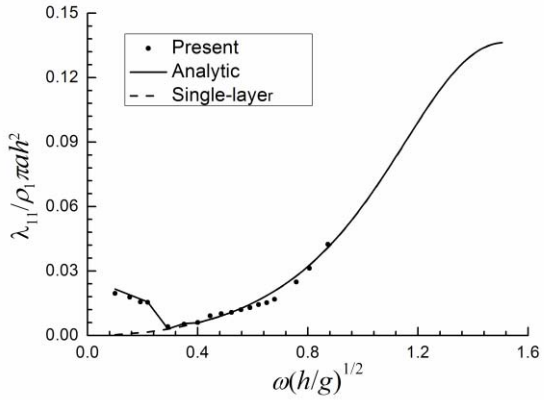

Fig.4 Damping coefficient of surge motion

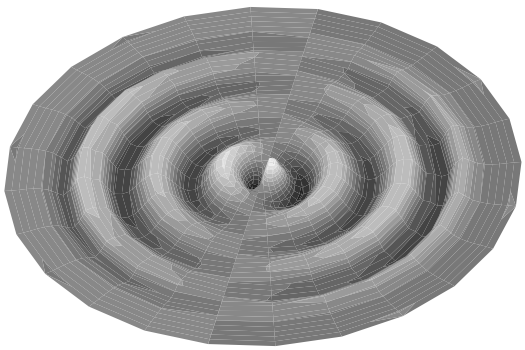

Fig.5 The interface elevation at t=9T

Pitch motion

The truncated cylinder is also forced to oscillate in pitch direction by the function of $\alpha_y = A\sin\omega t$. Here, A and ω are the amplitude and angle frequency of the pitch oscillation, respectively. The rotation center is located on the origin center.

Fig.6 and Fig.7 show the added mass and damping coefficient of pitch motion, respectively. Consistent with previous conclusions, the numerical results have good agreement with analytic solutions, and the results are significant in the relative lower frequency range compared with the sing-layer solutions.

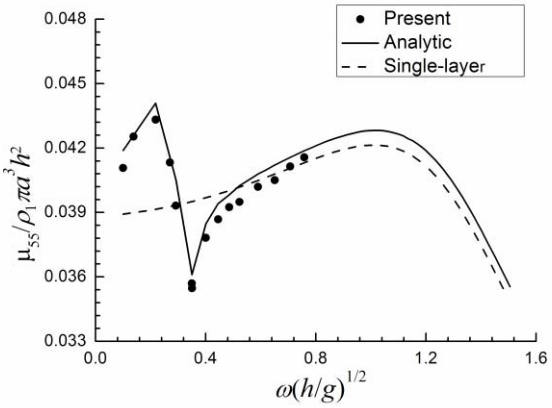

Fig.6 Added mass of pitch motion

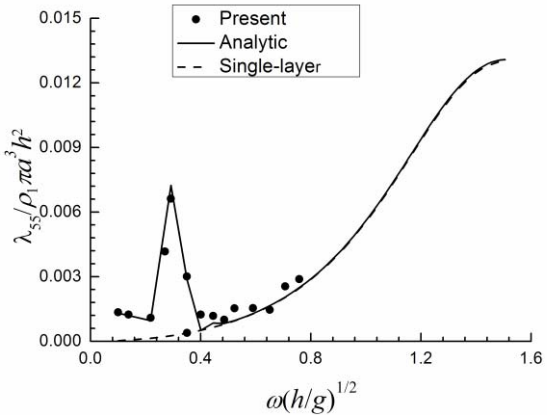

Fig.7 Damping coefficient of pitch motion

CONCLUSIONS

A boundary element method was developed to solve the linearized wave radiation problem in a two-layer fluid system. The simple Rankine source is used to form the boundary integral equation in time-domain, so the present method can be applied to study the instant wave diffraction and radiation problem. However, more computational cost is needed in this method, because of both free and internal surface must be meshed.

As an example of the computed results, the forced oscillations of a truncated cylinder in surge and pitch directions were considered, respectively. From the comparison with the analytical solutions, it was confirmed that the present numerical model can be applied to investigate the wave radiation problem in a two-layer fluid. By the comparison with single-layer fluid, the results show the significant in relative lower frequency range.

Acknowledgements

The authors gratefully acknowledge the financial support provided by the Natural Science Foundation of China (Grant No. 51009023) and the National Research Program of China (973-Program, Grant No. 2011CB013703).

References

Cadby JR, Linton CM. Three-dimensional water-wave scattering in two-layer fluids. Journal of Fluid Mechanics, 2000, 423:155-173

Gou Y, Chen XJ and Teng B. A time-domain boundary element method or wave diffraction in a two-layer fluid. Journal of applied mathematics, 2012

Igor Ten, Masashi Kashiwagi. Hydrodynamics of a body floating in a two-layer fluid of finite depth. Part 1. radiation problem. Journal of Marine Science and Technology, 2004, 9:127-141

Kashiwagi M, Ten I, and Yasunaga M. Hydrodynamics of a body floating in a two-layer fluid of finite depth. Part 2. Diffraction problem. Journal of Marine Science and Technology, 2006, 11:150-164

Nguyen TC, Yeung RW. Unsteady three-dimensional sources for a two-layer fluid of finite depth and their applications. Journal of engineering mathematics, 2011，70(1-3):67-91

Song ZJ, Teng B, Gou Y et al. Comparisons of internal solitary wave and surface wave actions on marine structures and their responses. Applied Ocean Research, 2011, 33(2):120-129

Shi Q, You YX and Miao GP. Radiation of ertically floating cylinder in a two-layer fluid. Journal of Shanghai Jiao Tong University, 2009,43(9):187-192

Teng B and Gou Y. A time-domain model of internal wave diffraction from a 3D body in a two-layer fluid. 24th International Workshop on Water Waves and Floating Bodies, Zelenogorsk, Russia, 2009.04

Teng B, Gou Y and Ning DZ A higher order BEM for wave-current action on structures - Direct computation of free-term coefficient and CPV integrals. China Ocean Engineering, 2006, 20(3):395-410

On the dispersive modeling of the 2011 Tohoku tsunami generation by coseismic/SMF processes, and near- and far-field impact

Stephan Grilli[1], Jeffrey C. Harris[1,2], James T. Kirby[3], Fengyan Shi[3], Gangfeng Ma[4], Tim Masterlark[5], David Tappin[6] and Tayebeh S. Tajalli Bakhsh[1]

1. Ocean Engng. Dpt., Univ. of Rhode Island, Narragansett, RI 02882, USA (grilli@oce.uri.edu)
2. Laboratoire St Venant, EDF Chatou, France
3. Univ. of Delaware, Center for Applied Coastal Res., Newark, DE 19716, USA
4. Dept. of Civil and Environmental Engineering, Old Dominion University, Norfolk, VA 23529, USA
5. British Geological Survey, Kingsley Dunham Centre, Keyworth, Nottingham, NG12 5GG, UK
6. Department of Geological Sciences, University of Alabama, Tuscaloosa, Alabama, USA

1 Introduction

A careful modeling of the 2011 Tohoku-oki tsunami generation and coastal impact [2,3], using the latest generation dispersive/non-hydrostatic models [6,7,10] shows that its devastating coastal impact cannot be fully explained by a co-seismic source alone, even when assimilating all available geodetic data [3,8,9]. Indeed, such tsunami simulations fail to reproduce the elevated tsunami runup heights of up to 40 m along the (Sanriku) coast of northern Honshu, and the large amplitude higher frequency dispersive waves (of 3-4 min. period) recorded at offshore buoys (both GPS and DART).

Here, we identify and parameterize an additional source of generation of the higher-frequency tsunami waves, in the form of a large rotational Submarine Mass Failure (SMF), which we source north of the main rupture, based on travel time of the higher frequency waves. Using the three-dimensional (3D) (sigma-layer) non-hydrostatic model NHWAVE [7], we simulate tsunami generation triggered by a time and space dependent seafloor motion, due to the combination of: (i) a new co-seismic source based on a detailed 3D Finite Element Modeling (FEM) of the heterogeneous subduction zone, with geodetic data assimilation, that updates our earlier source [2,3]; and (ii) the additional tsunami source from the SMF, triggered with a 2 time delay, whose kinematics is specified based on earlier scaling and modeling work [4].

After 5 min. of simulations, tsunami waves are reinterpolated onto the nonlinear and dispersive model FUNWAVE two-dimensional grid, in Cartesian coordinates for near-field simulations [10] and in spherical coordinates for far-field simulations [5]. Various levels of grid nesting are used, both in near- and far-field, with bathymetric/topographic data of commensurate accuracy. In results, briefly summarized below, we show that the multi-source tsunami simulation results agree well with all the available near-field observations, both onshore (runup/inundation) and offshore (GPS and DART buoy data), as well as far-field observations (DART buoys), as far as South America. It should be stressed that this good agreement is achieved without assimilating any of the tsunami observations in the source (which most of the models proposed to date have done). Hence, our simulations are robust.

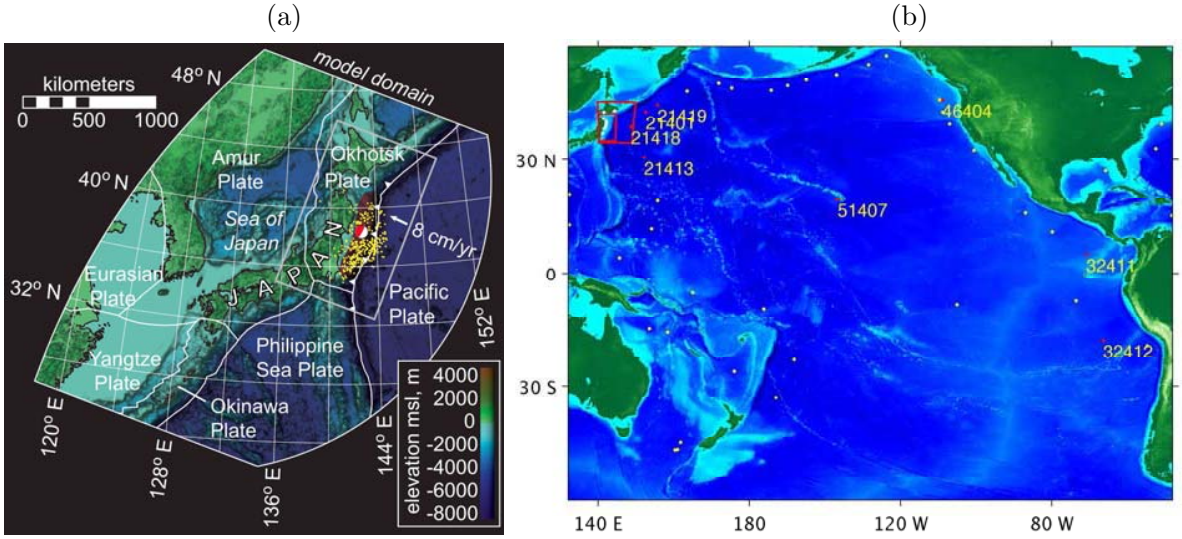

Figure 1: (a) Tohoku 2011 M9.1 earthquake seismotectonics (rupture is red polygon) and FEM domain ("model domain"); large symbol is the epicenter; yellow dots show M > 4 aftershocks (11 March – 06 May 2011); the Pacific-Okhotsk plate convergence is about 8 cm/yr. (b) Computational domains for FUNWAVE simulations: (i) near-field (regional 1000 m resolution, 800 by 1200 km, and coastal 250 m, large/small red boxes) Cartesian grid (large one also for NHWAVE); and (ii) far-field (Pacific basin scale) 2' spherical grid from 132° E to 68° W and 60° S to 60° N), with marked location of 18 DART buoys (yellow/red dots) and nearshore GPS buoys (white dots).

2 Methodology and results

Fig. 1 shows the seismotectonic context near and around the Japan trench relevant to the Tohoku-Oki tsunami as well as computational grids used in NHWAVE and FUNWAVE simulations. The co-seismic and SMF sources are first modeled for 300 s (5 min.) in a 1 km mesh regional grid, using NHWAVE, as a time- and space- varying bottom boundary condition (Fig. 1). Results are then re-interpolated into the fully nonlinear and dispersive Boussinesq model FUNWAVE for further modeling. Bathymetry/topography data bases are used, from ETOPO1 in deep water to 50 m accurate data (and model grids) nearshore and onshore. Simulations are compared to GPS and DART buoy time series (Fig. 3) and maximum runup (Fig. 4) and flow depth/inundation.

Although there are not yet any direct geological observations of the proposed SMF, its location and kinematics were identified and validated by travel-time analysis of higher-frequency waves recorded at GPS and DART buoys, and many direct SMF tsunami simulations. Additionally the proposed SMF source is justified from both the known geology of the Japan Trench, slope stability analyses, and tsunami runups and inundation limits recorded during post-tsunami field surveys [1,5]. Finally, a difference bathymetry map between post- and pre-earthquake data (not shown here for lack of space) shows large vertical seafloor deformations at the right location, consistent with our proposed SMF mechanism and kinematics.

Results in Fig. 2a show, at time t = 5min., the generation of both two long and nearly parallel leading co-seismic tsunami elevation waves to the south and a series of shorter (and hence dispersive) crescent shape SMF tsunami waves to the north. At t = 15 min., Fig. 2b shows that while the co-seismic waves do not develop a dispersive tail, the SMF waves develop into a train of

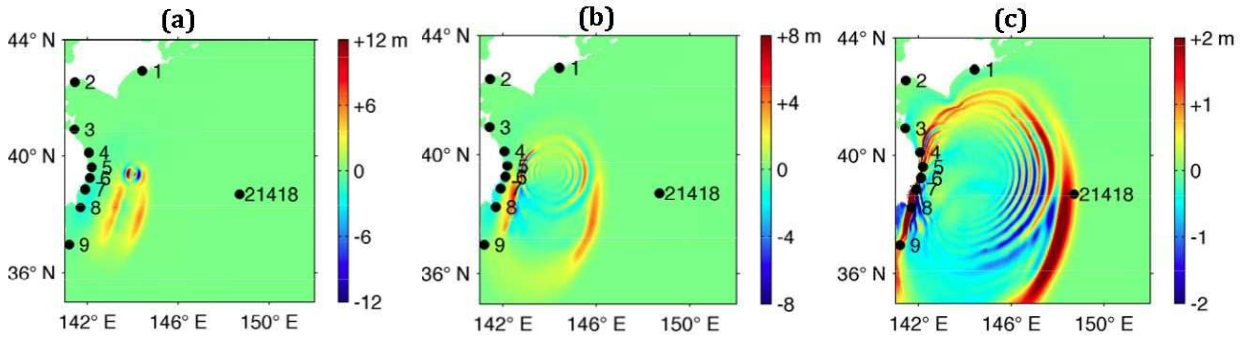

Figure 2: NHWAVE-FUNWAVE simulations using the combined co-seismic/SMF source, showing instantaneous surface elevations at t = (a) 5; (b) 15; (c) 30 min., in 1 km FUNWAVE grid (Fig. 1b). Labeled black dots mark locations of GPS buoys and of DART buoy #21418 (Fig. 3). Note the highly dispersive nature of waves generated by the SMF source triggered to the north (135 s after the co-seismic source), as compared to the longer non-dispersive co-seismic tsunami waves generated to the south.

concentric shorter waves, whose maximum elevations (both on- and offshore) are narrowly focused. Fig. 2c shows at $t = 30$ min., that the leading offshore co-seismic tsunami wave reaches the nearest DART buoy #21418, and is closely followed by at least 6 of the shorter oscillatory waves generated by the SMF. Fig. 3d shows the time series of both the simulated and observed waves at this DART buoy; their agreement is very good. Onshore, Fig. 2c shows that the same waves impact the 3 GPS buoys (Nb. 4,5,6) off of the Sanriku coast where maximum runup was measured at or slightly before the same time. Figs. 3a-c show the time series of both the simulated and observed waves at these GPS buoys; their agreement is also very good. Fig. 3 also shows that simulations of the co-seismic tsunami without the SMF waves do not reproduce the observed shorter/dispersive waves at the GPS and DART buoys.

Having been able to accurately match observations at the various buoys, with results of the simulations for the combined co-seismic/SMF tsunami source, we now compare in Fig. 4 simulated runups and inundations along the coast of northern Honshu. We see that simulations with the combined co-seismic/SMF tsunami source accurately simulate observed runups and inundations, including the 40+ m values along the Sanriku coast. By contrast, simulations with only the co-seimsic source underpredict the latter by a factor of 3. Additional results showing a comparison of far-field simulations with observations at DART buoys as well as a discussion of dispersive and Coriolis effects in the far-field tsunami will be presented during the workshop.

3 References

1. Fujiwara, T., Kodaira S., No T., Kaiho Y., Takahashi N. and Kaneda Y. (2011). Tohoku-Oki earthquake: Displacement reaching the trench axis. *Science*, **334**(6060):1240.

2. Grilli, S.T., Harris J.C., Tajali Bakhsh T.S., Kirby J.T., Shi F., Masterlark T.L. and Kyriakopoulos C. (2012a). Numerical simulation of the 2011 Tohoku tsunami: Comparison with field observations and sensitivity to model parameters. *Proc. 22nd Offshore and Polar Engng. Conf.* (Rodos, Greece, 6/17-22/2012), 6-13.

3. Grilli, S.T., Harris, J.C., Tajali Bakhsh, T.S., Masterlark, T.L., Kyriakopoulos, C., Kirby, J.T. and and Shi, F. (2012b). Numerical simulation of the 2011 Tohoku tsunami based on a new transient FEM co-seismic

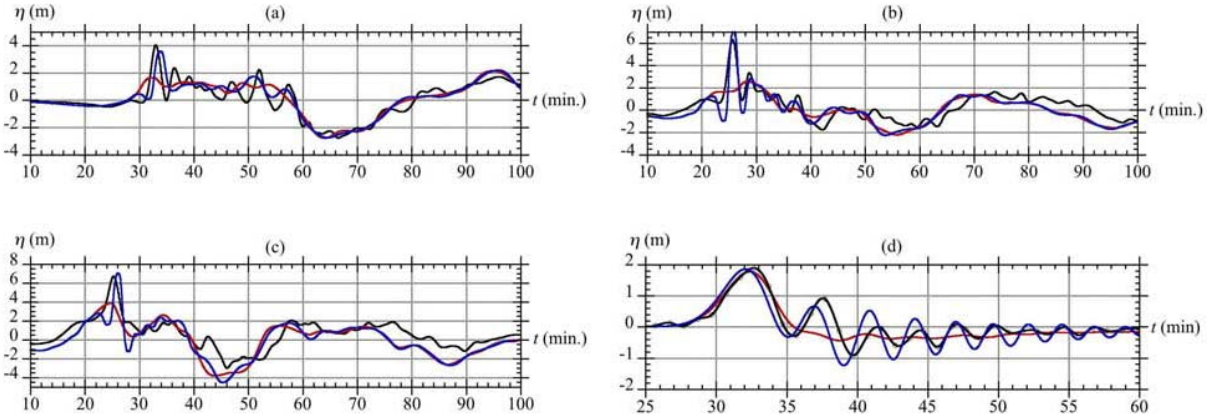

Figure 3: Surface elevations at buoys near Japan as a function of time, for 4th-6th GPS stations (marked in Figs. 1,2): (a) North Iwate; (b) Central Iwate; (c) South Iwate; and (d) DART buoy #21418. Field measurements (black), and computations for the co-seismic source alone (red), and for the latter plus the SMF source (blue). The abscissa is time t in minutes from the start of the earthquake rupture.

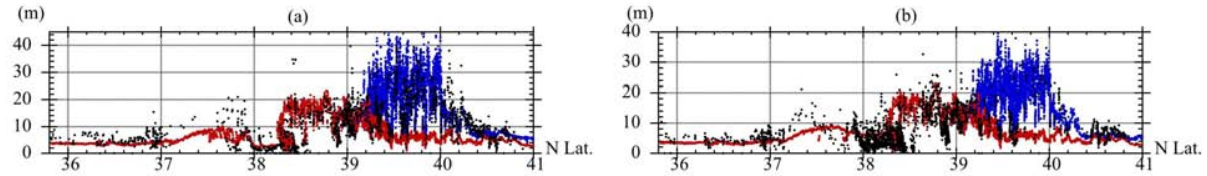

Figure 4: Comparison of simulated runup (a) and inundation (b) with measurements (black dots), for: co-seismic source alone (red), and combined co-seimsic/SMF source (blue).

source: Comparison to far- and near-field observations. *Pure and Appl. Geophys.*, DOI 10.1007/s00024-012-0528-y (published online).

4. Grilli, S.T. and P. Watts. 2005. Tsunami generation by submarine mass failure Part I : Modeling, experimental validation, and sensitivity analysis. *J. Waterw. Port Coast. and Oc. Engng.*, **131**(6), 283-297.

5. Kawamura, K., Sasaki, T., Kanamatsu, T., Sakaguchi, A., Ogawa Y. (2012). Large submarine landslides in the Japan Trench: A new scenario for additional tsunami generation. *Geophys. Res. Lett.*, **39**:L05308.

6. Kirby J.T., Shi F., Harris J.C., and Grilli S.T. (2012). Dispersive tsunami waves in the ocean: Model equations and sensitivity to dispersion and Coriolis effects. *Ocean Modell.* (in press):18 pp. http://dx.doi.org/10.1016/j.ocemod.2012.11.009.

7. Ma G., Shi F. and Kirby J.T. (2012) Shock-capturing non-hydrostatic model for fully dispersive surface wave processes. *Ocean Modell.*, **43-44**:2235.

8. Masterlark, T. (2003). Finite element model predictions of static deformation from dislocation sources in a subduction zone: Sensitivities to homogeneous, isotropic, Poisson-solid, and half-space assumptions. *J. Geophys. Res.*, **108**(B11):296.

9. Masterlark, T., and Hughes K. (2008). The next generation of deformation models for the 2004 M9 Sumatra-Andaman Earthquake. *Geophys. Res. Lett.*, **35**:L035198.

10. Shi, F., Kirby, J.T., Harris, J.C., Geiman, J.D. and Grilli, S.T. (2012) A high-order adaptive time-stepping TVD solver for Boussinesq modeling of breaking waves and coastal inundation. *Ocean Modell.*, **43-44**:3651.

28th Int. Workshop on Water Waves and Floating Bodies, L'Isle sur la Sorgue 7-10th April 2013

A nonlinear calculations of interfacial waves generated by a moving ship and evaluation of the forces in the dead water problem

John Grue
Mechanics Division, Department of Mathematics, University of Oslo, Norway

Fridtjof Nansen (1897) was the first to give a sufficiently precise, physical description of *dead water* so that the phenomenon could be given a scientific explanation. The initial systematics of the additional resistance on a ship moving in layered waters is credited to V. Wagnfrid Ekman. He was, by his supervisor Vilhelm Bjerknes, put to perform laboratory experiments on ship generated internal waves and measure the resulting force, and was able to explain the observations made by Nansen, see Ekman (1904). Recently, Ekman's experiments have been reinvestigated using modern techniques, see Mercier et al. (2011).

Linear theories of internal waves made by a moving point source have been derived, see Hudimac (1961), Crapper (1967), Keller and Munk (1970) and the references cited in these papers. They all consider the supersonic case where the source is advancing so fast, that the internal wake behind the source is a narrow v-shaped pattern. Avital and Miloh (1999) studied linear internal waves trapped by a moving vessel, basically the dispersion relation of the wake. Waves generated by a moving source in a two-layer ocean of finite depth have been studied by Yeung and Nguyen (1999). The dead water problem was also discussed in Miloh and Tulin (1988). Miloh et al. (1993) gave numerical solutions for the case of a semi-submersible slender-body (prolate spheroid) moving steadily on the free-surface.

Nonlinear calculations of dead water are scarce. What exists are calculations of the motion caused by singularities or pressure distributions. Nonlinear calculations of the wake and force on a realistic body seem to be nonexistent. We note that a nonlinear theory of interfacial waves generated by moving pressure distributions in super and subcritical conditions has been explored by Parau et al. (2007) with results presented at the 21st Workshop in 2006.

We shall here present calculations of the dead water problem using a truncated version of a fully nonlinear method of a two-layer fluid. The interfacial motion is driven by a realistic body geometry and the force on the body is evaluated. Results are obtained for subcritical, critical and supercritical motion.

Nonlinear two-layer theory

In three dimensions, we consider fully nonlinear interfacial motion of a two-layer fluid. The interfacial waves are generated by the motion of a geometry moving along the upper boundary of the upper fluid. Rigid lids are assumed at the top and bottom of the fluid layer, so there is no coupling to eventual free surface motion, which, however, can be evaluated subsequently. We assume potential flow in each of the layers. Let horizontal coordinates be denoted by $\mathbf{x} = (x_1, x_2)$ and y be vertical coordinate with $y = 0$ at the interface at rest. Let the parameters and functions describing the upper fluid be indexed by 1 and the lower fluid indexed by 0, where ρ_1, h_1, ϕ_1 denote density, layer depth at rest and velocity potential in the upper fluid, respectively, and ρ_0, h_0, ϕ_0 the corresponding quantities in the lower fluid. Thus, the upper boundary of the upper fluid is located at $y = h_1$ and the lower boundary of the lower fluid located at $y = -h_0$. The potentials are assumed to be Laplacian.

The interfacial motion is driven by a body moving horizontally along the top of the upper fluid. The geometry is given by $y - h_1 - \delta(\mathbf{x}, t) = 0$. Assuming a forward motion of the body with speed $U(t)$ along the x_1-axis the kinematic boundary condition reads

$$V_B = \frac{\partial \phi_1}{\partial n}\sqrt{1 + |\nabla \delta|^2} = U\frac{\partial \delta}{\partial x_1}$$

where n denotes the normal pointing out of the body and $\nabla = (\partial/\partial x_1, \partial/\partial x_2)$ horizontal gradient.

The interfacial elevation is determined by $y - \eta(\mathbf{x}, t) = 0$ giving as kinematic condition at the interface I: $\eta_t = V_I = \partial\phi_1/\partial n\,\sqrt{1 + |\nabla\eta|^2}$ where n is the unit normal along the interface pointing into the upper fluid 1. Balance of the pressure along the interface provides the dynamic condition obtained by $(\phi_{0,I} - \mu\phi_{1,I})_t + g'\eta + n.l.t. = 0$ where $\phi_{0,I}$ denotes the value of the potential in the lower fluid at the position of the interface I and $\phi_{1,I}$ value of the potential in the upper fluid at I. Further, $g' = g(1 - \mu)$ denotes the reduced gravity and $\mu = \rho_1/\rho_0$. With $n.l.t.$ we denote all the nonlinear terms which appear from the Bernoulli equation.

Integral equations

The Laplacian potentials are obtained by use of integral equations. In the upper layer, and for a position on the body surface B, we obtain the potential on the body surface, $\phi_B = \phi_1(\mathbf{x}, y = h_1 + \delta(\mathbf{x}, t), t)$,

$$\begin{aligned}
&\int_B \left(\frac{1}{r} + \frac{1}{r_1}\right) V_B \mathrm{d}\mathbf{x} + \int_I \left(\frac{1}{r} + \frac{1}{r_1}\right) V_I \mathrm{d}\mathbf{x} \\
&= -2\pi\phi'_B + \int_B \phi_B \frac{\partial}{\partial n}\left(\frac{1}{r} + \frac{1}{r_1}\right)\sqrt{1 + |\nabla\delta|^2}\mathrm{d}\mathbf{x} + \int_I \phi_{1,I}\frac{\partial}{\partial n}\left(\frac{1}{r} + \frac{1}{r_1}\right)\sqrt{1 + |\nabla\eta|^2}\mathrm{d}\mathbf{x}, \quad (1)
\end{aligned}$$

which connects ϕ_B, $\phi_{1,I}$, V_I and V_B where the latter is given by the body motion. In (1) a prime in ϕ'_B means $\phi_B(\mathbf{x}', y' = h_1 + \delta(\mathbf{x}', t), t)$. The distances r and r_1 are given by $r^2 = |\mathbf{x} - \mathbf{x}'|^2 + (y - y')^2$ and $r_1^2 = |\mathbf{x} - \mathbf{x}'|^2 + (y + y')^2$ where in (1) $(\mathbf{x}', y')$ is on B and $(\mathbf{x}, y)$ along I and B.

The function $1/r + 1/r_1$ is expanded in the vertical coordinate. For the integral over B we obtain $1/r + 1/r_1 = 1/R + 1/R_1 + (\delta' + \delta)(\partial/\partial(2h_1))(1/R_1) + ...$ where $R_1^2 = R^2 + (2h_1)^2$. The expanded integral equation is inverted by use of Fourier transform (Clamond and Grue, 2001, §6) where $\frac{1}{R_1} = \mathcal{F}^{-1}\left[\frac{2\pi}{k}e^{-\mathrm{i}\mathbf{k}\cdot\mathbf{x}' - 2kh_1}\right]$ is used, $\mathcal{F}$ denotes Fourier transform, $\mathcal{F}^{-1}$ inverse transform, $\mathbf{k}$ and $k = |\mathbf{k}|$ wave numbers. Following Fructus and Grue (2007) studying free surface motion we obtain the potential on the body geometry by successive approximations by $\phi_B = \phi_B^{(1)} + \phi_B^{(2)} + ...$ where

$$\begin{aligned}
\mathcal{F}(\phi_B^{(1)}) &= \frac{\mathcal{F}(\phi_{1,I})}{\cosh kh_1} - \frac{\tanh kh_1\,\mathcal{F}(V_B)}{k} \\
\mathcal{F}(\phi_B^{(2)}) &= \frac{\mathcal{F}(\eta V_I^{(1)})}{\cosh kh_1} + \frac{\mathrm{i}\mathbf{k}\tanh kh_1}{k}\cdot\mathcal{F}(\delta\nabla\phi_B) - \mathcal{F}(\delta V_B)
\end{aligned}$$

The integral equation with the evaluation point on the interface I gives similar expressions for $V_I = V_I^{(1)} + V_I^{(2)} + ...$

$$\begin{aligned}
\mathcal{F}(V_I^{(1)}) &= -k\tanh kh_1\mathcal{F}(\phi_{1,I}) - \frac{\mathcal{F}(V_B)}{\cosh kh_1} \\
\mathcal{F}(V_I^{(2)}) &= k\tanh kh_1\mathcal{F}(\eta V^{(1)}) - \mathrm{i}\mathbf{k}\cdot\mathcal{F}(\eta\nabla\phi_{1,I}) - \mathrm{i}\mathbf{k}\cdot\frac{\mathcal{F}(\delta\nabla\phi_B)}{\cosh kh_1}
\end{aligned}$$

Similar expressions are obtained for the normal velocity W_I in the lower layer along I, solving an integral equation for the potential $\phi_{0,I}$. The interfacial motion is obtained integrating the Fourier transformed kinematic and dynamic conditions at the interface, i.e. $\mathcal{F}(\eta)_t = \mathcal{F}(V_I)$ and $\mathcal{F}(\phi_{0,I} - \mu\phi_{1,I})_t + g'\mathcal{F}(\eta) = n.l.t.$ where right hand sides are obtained solving $V_I^{(1)} + V_I^{(2)} + ... = W_I^{(1)} + W_I^{(2)} + ...$ and using the Bernoulli equation. In the present calculations $\rho_1/\rho_0 = 1$ is used and all velocities are scaled by the linear long wave speed c_0.

Calculations

The body is represented by the submerged part of an ellipsoid given by $(\delta/b)^2 + (x_1/a_1)^2 + (x_2/a_2)^2 = 1$ with $\delta < 0$. Calculations of the interface are obtained with a horizontal resolution of 500 by 500 nodes in the critical condition ($U/c_0 = 1$) and 1000 by 250 when $U/c_0 = 6$ (figures 1 and 2). All computations show a region of depression ahead of the body, an uplift of the interface at the aft of the body and then a wake of waves. Calculations of the wave resistance are obtained by integrating the pressure force obtained from the Bernoulli equation over the body surface. A drag coefficient C_R is obtained dividing by $\frac{1}{2}\rho SU^2$ with $S = \pi a_1 a_2$. Figure 2 (right) shows a C_R of about 4 times the skin friction (with $Re \sim 2\times10^7$).

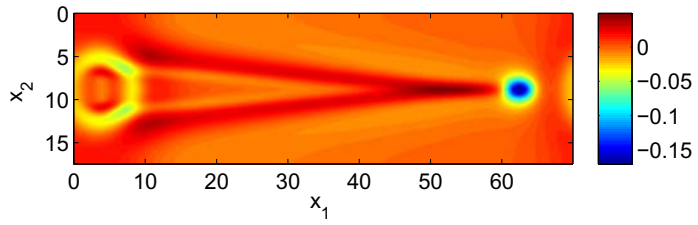

Figure 1: Interfacial elevation η/h_1 with $a_1 = 2.1h_1$, $a_2 = 0.7h_1$, $b = 0.7h_1$, $U/c_0 = 6$, $h_0/h_1 = 6$, horizontal domain of $70h_1$ by $17.5h_1$; final time $10h_1/c_0$. Final body position at $x_1/h_1 = 60.6 \pm 4$.

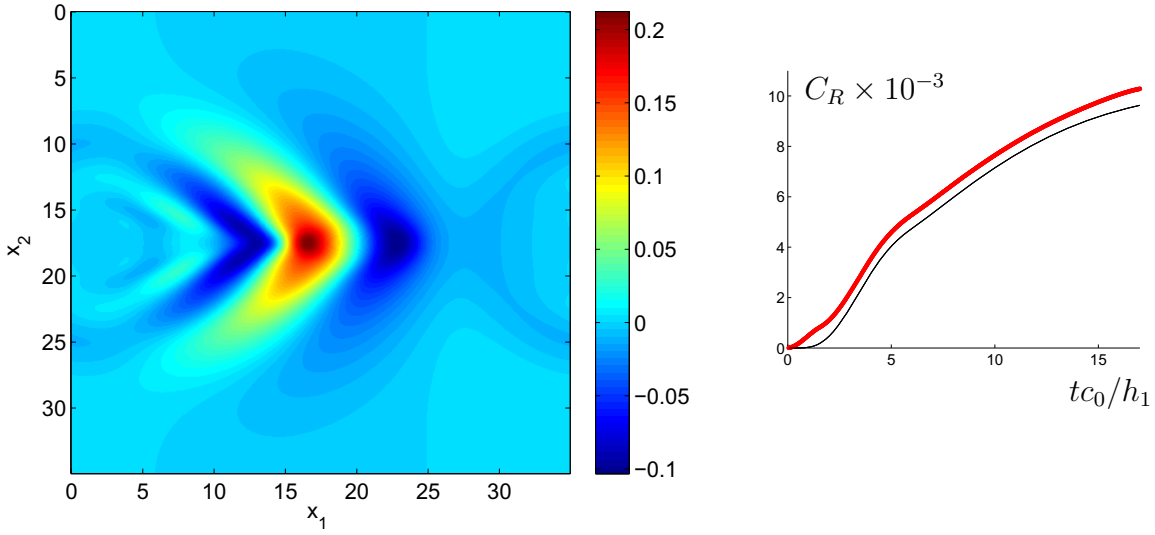

Figure 2: Interfacial elevation η/h_1 (left) and wave resistance (right) with $a_1 = 4h_1$, $a_2 = 1.5h_1$, $b = 0.3h_1$, $U/c_0 = 1$, $h_0/h_1 = 6$, horizontal domain of $35h_1$ by $35h_1$; final time $17h_1/c_0$. Final body position at $x_1/h_1 = 20.4 \pm 4$. Black curve in right plot: domain $50h_1$ by $50h_1$.

References

E. Avital and T. Miloh (1999). On an inverse problem of ship-induced internal waves. Ocean Engineering. 26:99-110.

D. Clamond and J. Grue (2001). A fast method for fully nonlinear water wave computations. J. Fluid Mech. 447:337-355.

G.D. Crapper (1967). Ship waves in a stratified ocean. J. Fluid Mech. 29:667-672.

V.W. Ekman (1904). On dead water: The Norwegian North Polar Expedition 1893-1896. Scientific results. Edited by F. Nansen. Ch. XV, A.W. Brøgger. Christiania. 152 pp. and appendix with 17 pl.

D. Fructus and J. Grue (2007). An explicit method for the nonlinear interaction between water waves and variable and moving bottom topography. J. Comp. Phys. 222:720-739.

A.A. Hudimac (1961). Ship waves in a stratified ocean. J. Fluid Mech. 11:229-243.

J.B. Keller and W.H. Munk (1970). Internal wave wakes of a body moving in a stratified fluid. Phys. Fluids 13:1425-1431.

M.J. Mercier, R. Vasseur and T. Dauxois (2011). Resurrecting Dead-water Phenomenon. Nonlin. Processes Geophys. 18:193-208.

T. Miloh, M.P. Tulin and G. Zilman (1993). Dead-water effects of a ship moving in stratified seas. J. Offshore Mech. Arctic Eng. 115:105-110.

T. Miloh and M.P. Tulin (1988) A theory of dead water phenomena. Proc. 17th Symp. Naval Hydrodynamics. National Academy Press, Washington DC, 127-142.

F. Nansen (1897). Farthest North: The epic adventure of a visionary explorer. Vol. 1. Skyhorse Publ.

E.I. Parau, J.-M. Vanden-Broeck and M.J. Cooker (2007). Nonlinear three-dimensional interfacial flows with a free surface. J. Fluid Mech. 591:481-494.

R.W. Yeung and T.C. Nguyen (1990). Waves generated by a moving source in a two-layer ocean of finite depth. J. Engng. Math. 35:85-107.

Illustrative applications of the Neumann-Michell theory of ship waves

Fuxin Huang[1], Xuhui Li[2], Francis Noblesse[3], Chi Yang[1], Wenyang Duan[2]

[1] George Mason University, Fairfax VA, USA, fhuang@gmu.edu, cyang@gmu.edu

[2] Harbin Engineering University, Harbin, China, rocklees311010062@gmail.com, duanwenyang@hrbeu.edu.cn

[3] Shanghai Jiao-Tong University, Shanghai, China, noblfranc@gmail.com

Introduction

The modification of the classic Neumann-Kelvin (NK) theory of ship waves, called Neumann-Michell (NM) theory, expounded in [1] is considered. A main difference between the NK and NM theories is that the NM theory does not involve a line integral around the ship waterline. This waterline integral, a well-known prominent feature of the NK theory, is eliminated in the NM theory by removing an inconsistency in the linearization that underlies the NK theory (which does not correspond to a consistent linear flow model) and, furthermore, by using a mathematical transformation (essentially an integration by parts).

A notable property of the NM theory is that it defines the flow around a ship hull (steadily advancing in calm water) as a correction to the classic slender-ship approximation proposed by Hogner. Specifically, the NM theory of ship waves given in [1] expresses the (nondimensional) flow potential $\widetilde{\phi}$ at a flow field point $\widetilde{\mathbf{x}}$ as the sum of the Hogner slender-ship approximation $\widetilde{\phi}_H$, which is defined explicitly in terms of the Froude number and the hull geometry, and a correction potential $\widetilde{\psi}^W$ that modifies the waves contained in the Hogner approximation $\widetilde{\phi}_H$. A main property of the NM correction $\widetilde{\psi}^W$ is that it involves the flow velocity components $\phi_d \equiv \partial\phi/\partial d$ and $\phi_t \equiv \partial\phi/\partial t$ along the two orthogonal unit vectors $\mathbf{d} \equiv (0, -\nu^z, \nu^y)$ and $\mathbf{t} \equiv (\nu, -n^x\nu^y, -n^x\nu^z)$ that are tangent to the ship hull surface Σ^H. Here, $\mathbf{n} \equiv (n^x, n^y, n^z)$ is a unit vector that is normal to Σ^H and points outside the ship (into the water), $(\nu^y, \nu^z) \equiv (n^y, n^z)/\nu$ and $\nu \equiv \sqrt{(n^y)^2 + (n^z)^2}$. Within the NM theory given in [1], the flow potential $\widetilde{\phi}$ at a point $\widetilde{\mathbf{x}}$ of the hull surface Σ^H is then determined by the solution of an integro-differential equation $\widetilde{\phi} = \widetilde{\phi}_H + \widetilde{\psi}^W(\phi_t, \phi_d)$ with $\widetilde{\mathbf{x}} \in \Sigma^H$. A straightforward iterative solution procedure $\widetilde{\phi}^{k+1} \approx \widetilde{\phi}_H + \widetilde{\psi}^W(\phi_t^k, \phi_d^k)$ with $\widetilde{\mathbf{x}} \in \Sigma^H$, $0 \leq k$ and $\phi^0 \equiv 0$ is used. The first approximation $\widetilde{\phi}^1$ in the sequence of approximations $\widetilde{\phi}^k$ to the NM potential $\widetilde{\phi} \equiv \widetilde{\phi}^\infty$ is the Hogner potential $\widetilde{\phi}_H$. Thus, the NM theory provides a way of correcting the classic Hogner approximation.

An important aspect of the NM theory is considered in [2], which gives a highly simplified analytical approximation for the local flow component in the Green function that satisfies the radiation condition and the Kelvin-Michell linearized boundary condition at the free surface. Another important element, indeed a critical one, of the NM theory is considered in [3]. There, the dual basic tasks of evaluating the wave potential $\widetilde{\phi}_H^W + \widetilde{\psi}^W$ at the free surface $\widetilde{z} = 0$ and of removing unrealistic or inconsequential short waves is considered. Briefly, within a thin layer bordering the mean free-surface plane $z = 0$, waves are evaluated in [3] using a physics-based filter, based on parabolic extrapolation in the vicinity of the free surface, that accounts for fundamental differences between a ship bow wave and waves aft of the bow wave. A third basic aspect of the NM theory, considered in [4], is the evaluation of the derivatives ϕ_t and ϕ_d that appear in the NM wave potential $\widetilde{\psi}^W(\phi_t, \phi_d)$. This issue is important because the solution of the NM integro-differential equation is significantly affected by the numerical approximation of the derivatives ϕ_t and ϕ_d, particularly within the framework of a low-order panel approach and for full hull forms. Numerical implementation of the NM theory, within the practical framework of a low-order panel method, is considered in [4], where illustrative applications to eight ship hulls are also reported.

Comparison of independent numerical predictions for the Wigley hull

Numerical predictions given by the NM theory are reported in [1,3] for the Wigley hull and the Series 60 model. Fig.1 compares these numerical predictions (obtained by the first author at GMU) for the Wigley hull and the numerical predictions (obtained by the second author at HEU) using an independent numerical implementation of the theory. The two numerical implementations are based on the same mathematical expressions. Furthermore, both use a low-order panel approach and an iterative solution procedure that iteratively improves upon the Hogner initial approximation. Thus, the numerical results can be expected to be close, but not necessarily identical due to differences in the first two authors' independent numerical implementations. Fig.1 shows good agreement between the independent numerical implementations for the sinkage, trim, and drag predicted by the NM theory for the Wigley hull. Thus, Fig.1 provides a useful verification of the numerical results given in [1,3]. However, significant discrepancies can be observed in Fig.2 for the wave profiles along the Wigley hull. These discrepancies, due to differences in the evaluation of the flow velocity $\nabla\phi$, illustrate the fact that

mathematical expressions like those given in [1-3] are not sufficient to fully determine a theory. Indeed, precise information about the numerical implementation of mathematical expressions is also required, and this important aspect of the theory is considered in [4].

Illustrative applications to four ship hulls

Numerical predictions given by the NM theory are reported in [4] for eight ship hulls. Here, we consider the four hull forms depicted in Fig.3. These hulls are the Wigley hull (top row), the Series 60 ($C_b = 0.60$) model (second row), the DTMB-5415 model (third row) and the KCS model (bottom row). Experimental measurements for these four hulls are reported in [5-8]. Fig.4 compares experimental measurements of the wave drag, reported in [5-8], and predictions of the nearfield wave drag (determined via integration of the flow pressure at the ship hull surface) and of the farfield wave drag (determined via the Havelock formula) for the hulls in fixed position (no sinkage or trim is considered in the calculations).

Conclusion

A positive and encouraging finding, at this stage of the development and application of the NM theory, is that a straightforward low-order panel implementation of the theory yields robust predictions for a broad range of ship hulls, and that these theoretical predictions are reasonable and realistic. The finding is notable in view of the remarkable simplicity of the theory, which is based on linear potential flow, does not involve a line integral around the ship waterline, amounts to the addition of a simple correction (the wave potential $\widetilde{\psi}^W$ mentioned in the introduction) that modifies the waves predicted by the classic Hogner slender-ship approximation, uses a highly-simplified Green function, and only involves staightforward Gaussian integration of elementary continuous functions. The short-wave filter and the numerical smoothing of the derivatives ϕ_d and ϕ_t given in [4] are critical elements of the theory.

Much work evidently remains to be performed before the merits and limitations of the NM theory can be fully ascertained. This work includes (i) evaluation of the flow (notably wave patterns) outside the ship hull, (ii) consideration of elementary nonlinear corrections that can be incorporated to improve the predictions given by the NM linear theory, (iii) account for sinkage and trim effects, ignored so far, which are particularly important to predict the sinkage and trim experienced by a moving ship hull, (iv) account for the viscous boundary layer and wake in accordance with the classical theory of high-Reynolds number flows around streamlined bodies, and (v) applications to a much broader set of ship hulls than the four hulls considered here and the eight hulls considered in [4]. This ongoing work will be reported as it is completed.

Acknowledgments

This work was partly funded by the Office of Naval Research. We warmly thank Ms. Kelly Cooper for her interest and support.

References

[1] Noblesse F, Huang F, Yang C (2013) The Neumann-Michell theory of ship waves, J Engineering Mathematics, in press
[2] Noblesse F, Delhommeau G, Huang F, Yang C (2011) Practical mathematical representation of the flow due to a distribution of sources on a steadily-advancing ship hull. J Engineering Mathematics 71:367-392
[3] Noblesse F, Huang F, Yang C (2013) Evaluation of ship waves at the free surface and removal of short waves, European J Mechanics B/Fluids 38:22-37
[4] Huang F, Yang C, Noblesse F (2013) Practical implementation of the Neumann-Michell theory of ship waves, in preparation
[5] McCarthy JH (1985) Collected experimental resistance and flow data for three surface ship model hulls. David W Taylor Naval Ship Research and Development Center, report DTNSRDC-85/011
[6] Experimental data for the Wigley hull are reported in Cooperative experiments on the Wigley parabolic model in Japan, prepared for the17th ITTC Resistance Committee, 2nd edition (1983)
[7] Experimental data for the Series 60 model are reported in Cooperative experiments on the Series 60 (Cb=0.6) model, prepared for the18th ITTC Resistance Committee (1986)
[8] Olivieri A, Pistani F, Avanzini A, Stern F, Penna R (2001) Towing tank experiments of resistance, sinkage and trim, boundary layer, wake, and free surface flow around a naval combatant INSEAN 2340 model.No. IIHR-TR-421. Univ of Iowa Coll of Engineering

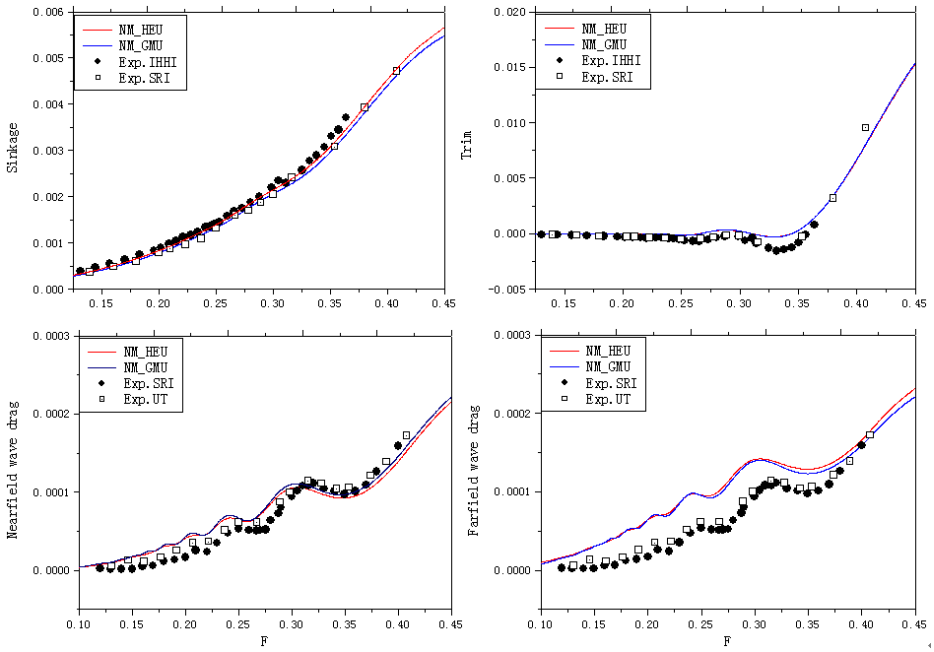

Figure 1: Experimental measurements (Exp.) and theoretical predictions, based on the NM theory (NM) and obtained at George Mason Univ. (GMU) and Harbin Engineering Univ. (HEU), of the sinkage (top left corner), trim (top right), nearfield wave drag (bottom left) and farfield wave drag (bottom right) for the Wigley hull.

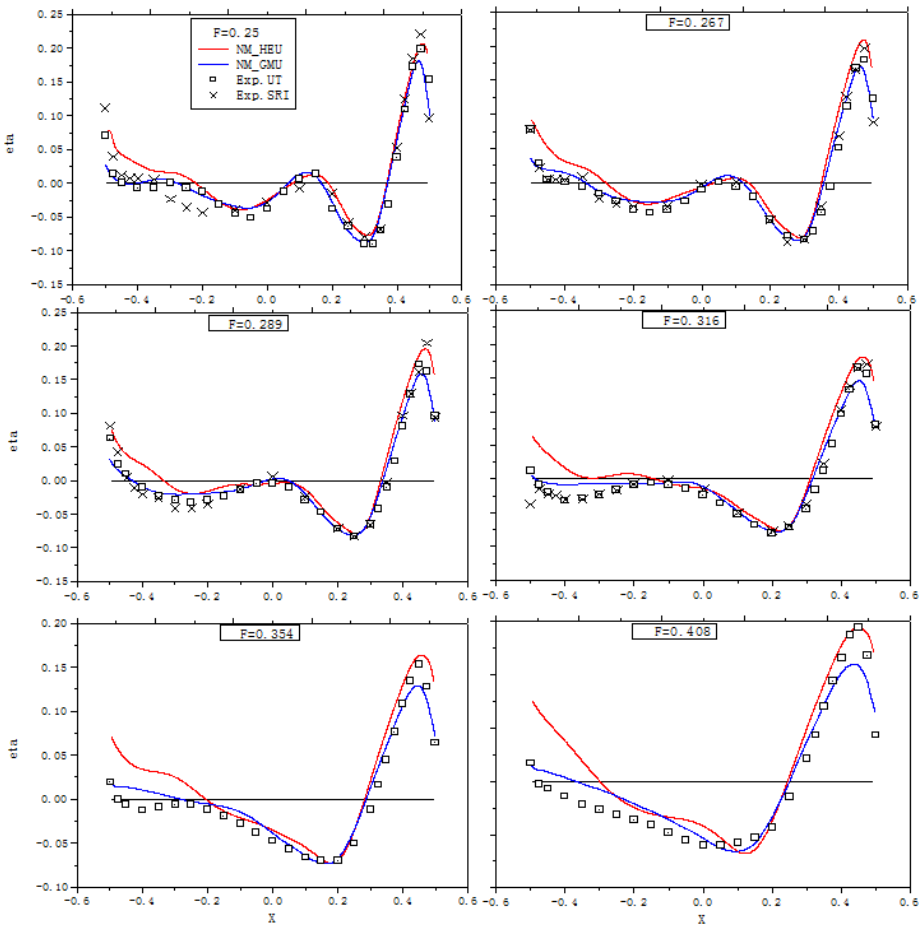

Figure 2: Experimental measurements (Exp.) and theoretical predictions, based on the NM theory (NM) and obtained at George Mason Univ. (GMU) and Harbin Engineering Univ. (HEU), of wave profiles along the Wigley hull at six Froude numbers $F = 0.25$, 0.267, 0.289, 0.316, 0.354 and 0.408.

Figure 3: Side views, with meshes over the mean wetted hull surfaces, of the Wigley hull (top row), the Series 60 $C_b = 0.60$ model (second row), the DTMB-5415 model (third row) and the KCS model (bottom row). The positive halves of these four hull surfaces are approximated using 8,000 flat triangular panels for the Wigley hull and the Series 60 model, 9,600 panels for the DTMB-5415 model, and 18,960 panels for the KCS model (fewer panels are shown in the figure for clarity).

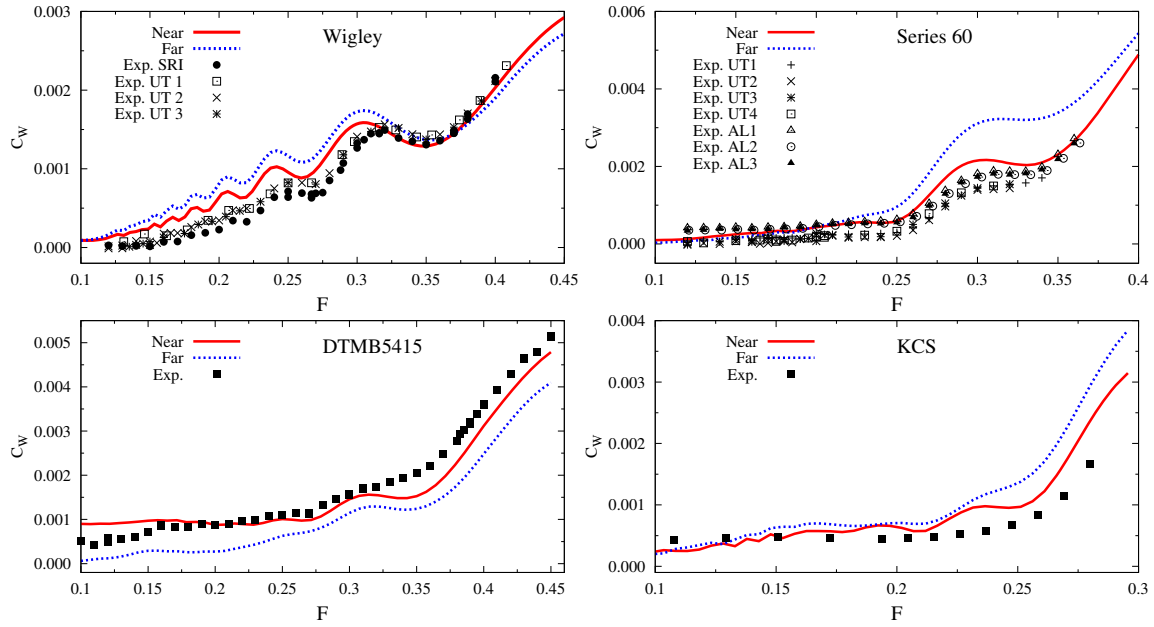

Figure 4: Experimental measurements (Exp.) of the wave drag, and nearfield (Near) and farfield (Far) wave drags predicted by the NM theory, for the Wigley hull (top left corner), the Series 60 $C_b = 0.60$ model (top right), the DTMB-5415 model (bottom left) and the KCS model (bottom right). For the experimental measurements shown here, the Wigley hull and the Series 60 model are held fixed (no sinkage or trim is allowed), but the DTMB-5415 and KCS models are unrestrained (sinkage and trim are allowed). No sinkage or trim is considered in the NM calculations.

Numerical and experimental studies of plate ditching

A. Iafrati, D. Calcagni, INSEAN-CNR (Italian Ship Model Basin- National Research Council), Rome, Italy,
E-mail: alessandro.iafrati@cnr.it

SUMMARY

The present paper deals with the water entry of a flat plate with a high horizontal speed. The activity is motivated by the need of achieving a better comprehension and more reliable simulation tools for the aircraft ditching phase. This first part of the study is focused to the ditching of a flat, rigid, plate. The problem is analyzed both numerically and experimentally. Numerically, the problem is studied in two dimensions and the self-similar solution is derived within the potential flow approximation of an ideal fluid. The problem is also addressed experimentally with the aim of building a dataset to be used for validation of computational tools. Due to the difficulties in scaling all the relevant physical parameters, experiments are performed at (almost) full scale velocity, with vertical component of 1.5 m/s and horizontal velocity in the range 30 to 50 m/s. The experimental campaign is starting soon and results will be shown at the Workshop. Here the experimental setup and the instrumentation adopted are presented. Numerical results are reported in terms of pressure distributions and free surface shape. The dependence of the pressure peak on the horizontal/vertical velocity components and on the plate inclination over the free surface is briefly discussed.

1. INTRODUCTION

In order to assess the ditching capabilities of an aircraft, the industry needs simulation tools which can model, with reduced computational effort, the fluid structure interaction taking into account the elastic/plastic structural behavior, including failure. However, simulation tools commonly adopted in the modelling of the aircraft ditching phase display strong limits in the accurate description of the complex phenomena such as highly localized pressure distributions, air cushioning, hydroelastic coupling, cavitation and ventilation (Climent et al., 2006).

For the development and validation of those simulation tools a reliable dataset is needed. Due to the difficulty in achieving a correct scaling of all the physical parameters involved, a full scale experiment is needed. Experiments of such kind are going to be performed at CNR-INSEAN under the SMAES-FP7 project. To this aim, a large high speed ditching facility has been built and installed at the end of towing tank # 1 of CNR-INSEAN. Tests will be carried out on aluminum plates 0.50 m wide, 1.00 m long. Similar experiments were already done in the early fifties (Smiley, 1951). Differently from past experiments, this experimental campaign is planned for higher horizontal components (from 30 to 50 m/s), and more detailed measurements, involving pressure, accelerations, strain and loads. The aim is to study the role played by the horizontal/vertical velocity ratio, plate incidence, shape, material and thickness on pressure distributions, acceleration and fluid structure interaction. The experimental campaign is starting soon and preliminary results for a rigid flat plate are expected by the beginning of the Workshop. In the following a description of the facility and of the experimental setup is provided only.

The design of the facility required estimates of the solution in terms of free surface shape and loads generated during the impact. As a water entry problem, a jet develops beneath the plate together with a pressure peak occurring at the root. The jet propagates along the plate until reaching the leading edge when the flow separates and the pressure and loads drops suddenly. Beside providing the loads to be used for the structural design of the guide, additional information on the time and space needed for the ditching phase to be completed can be also derived.

Due to some uncertainties in the more complex three-dimensional simulation tools, it was decided to derive those information also from a two-dimensional potential flow solution. Assuming a constant velocity and neglecting the finite length of the plate, the solution is self-similar and can be derived by using the same numerical procedure adopted in Iafrati & Korobkin, 2005. Note that the water entry problem of a wedge with a horizontal velocity component was already investigated in Faltinsen and Semenov (2008) and in Judge et al. (2004). However, in those cases the horizontal/vertical velocity ratio was much lower than that characteristic of aircraft at ditching. The incidence of the plate is also lower than that adopted in those papers.

In the following the numerical procedure is briefly recalled and results are presented in terms of free surface shape and pressure distribution. Comparisons between numerical solution and experimental results will be established as soon as the experimental results become available. Of course it is expected that load and pressures are overestimated by the two-dimensional solution as important three-dimensional effects related to the outflow at the sides are missing.

Figure 1: View of the CNR-INSEAN guided ditching facility. The guide is supported by bridges which can be varied in height in order to get the correct U/V velocity ratio. The main trolley can be also seen on the right.

2. FACILITY AND EXPERIMENTAL SETUP

In order to perform guided ditching tests, a new facility has been designed and installed at CNR-INSEAN, at the opposite end of the towing tank # 1, which is 470 m long, 13.5 m wide and 6.5 m deep.

The guide, which has a total length of about 64 m, is supported by five bridges which can be positioned at different heights, thus allowing the variation of the horizontal velocity keeping constant the vertical component, the latter being 1.5 m/s according to aircraft regulation. The model is supported by a main trolley which keeps it always attached to the guide. The main trolley is accelerated by a catapult which is designed to reach a final speed in a range 30 to 50 m/s (Fig. 1). The total mass to be accelerated is about 900 kg, whereas the mass which undergoes the impact is about 750 kg. The acceleration system is composed by a total of six elastic cords which can be elongated up to 250%.

Figure 2: Picture of the main trolley which brings the model and specimens.

The trolley run on the inner side of the beam wings (Fig. 2). In order to get a measure of the forces acting beneath the plate, the model with the specimens to be tested is connected to the trolley by four Kistler 9343 for the z components and two 9363 load cells for the x component. As the cells can only undergo forces along their axes, the installation is done in such a way that transversal components and moments do not act on the cell. Attention is also posed in avoiding possible coupling in the measurements of loads in x and z directions. The load in the y direction is not measured but it is transferred from the model to the trolley by two articulated rods (Fig. 3).

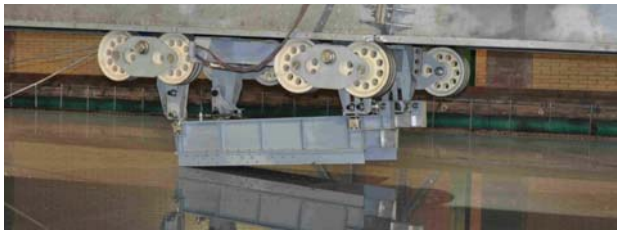

Figure 3: Picture of the trolley with model at the touch of the free surface. Note that the specimens is not installed yet.

For the first part of the test campaign, which is the one considered in this paper, a 15 mm thick, aluminum flat plate is considered. The plate is clamped to the frame which is 75 mm wide, thus leaving a free space of 350 mm by 850 mm (Fig. 4). In order to measure strains, six biaxial strain gauges are stick to the internal side of the plate. Pressures at 18 points are also measured through Kulite XTL123B pressure transducers. The position of the transducers is chosen in order to get information about the longitudinal and transversal pressure distributions, as well as about the symmetry in the impact. Velocity and displacement of the trolley are measured by a non-contact optical sensor, Correvit LFII. The acceleration components in the three directions at different positions are measured, for a total of 6 acceleration channels. Accelerations are measured by piezo-resistive Kistler M101A and M301A accelerometers.

All the data are acquired on-board by four Sirius Dewesoft modules and one Dewe 43, for a total of 40 channels. In order to correctly capture the pressure variations, data are acquired at 200 kS/s. The five acquisition systems are connected to a Sbox Dewesoft PC which communicate in wireless mode to an external PC. All the electronics is installed in a waterproof box which is positioned inside the model. Also the latter is sealed against water penetration.

Tests will be done at three different values of the horizontal component 30, 40 and 50 m/s, with the vertical component always equal to 1.5 m/s. The plate incidence with respect to the free surface will be varied from 4 to 10 degrees.

Figure 4: Instrumented aluminum plate. The strain gauges and the holes for the pressure probes can be seen. The two rows of bolts can be also recognized, which clamps the plate to the frame.

3. NUMERICAL MODEL AND RESULTS

The flow generated by the water entry of a plate with horizontal velocity component can be studied within the potential flow approximation. The fluid is assumed to be ideal and incompressible, and the action of gravity is neglected. In this conditions the problem is self-similar and the solution can be derived by using a pseudo-time stepping approach, similar to that used in Iafrati & Korobkin (2005). The problem is formulated in terms of the self-similar variables

$$\xi = \frac{x}{Ut} \quad \eta = \frac{y}{Ut} \quad \varphi = \frac{\phi}{U^2 t} \tag{1}$$

so that the initial boundary value problem in the physical variables can be transformed into the following boundary

value problem for the self-similar velocity potential:

$$\nabla^2\varphi = 0$$
$$\varphi_\nu = \sin\gamma + \frac{V}{U}\cos\gamma \qquad \text{on } \eta = -\frac{V}{U} + (\xi - 1)\tan\gamma$$
$$\varphi - (\xi\varphi_\xi + \eta\varphi_\eta) + \frac{1}{2}\left(\varphi_\xi^2 + \varphi_\eta^2\right) = 0 \quad \text{on } h(\xi,\eta) = 0$$
$$-(\xi h_\xi + \eta h_\eta) + (h_\xi\varphi_\xi + h_\eta\varphi_\eta) = 0 \quad \text{on } h(\xi,\eta) = 0$$
$$\varphi \to 0 \qquad \text{as } \xi^2 + \eta^2 \to \infty$$

where Ω is fluid domain, $h(\xi,\eta) = 0$ is the equation of the free surface and ν is the unit normal to the boundary, which is oriented inward the fluid domain.

As discussed in Iafrati and Korobkin (2004), the free surface conditions are strongly simplified by introducing a modified velocity potential defined as

$$S = \varphi - \frac{1}{2}\rho^2 \quad \rho = \sqrt{\xi^2 + \eta^2}$$

in terms of which the kinematic and dynamic boundary conditions become

$$S_n = 0 \quad S_{tau} = \pm\sqrt{-2S} \ , \tag{2}$$

respectively. In the above equation, τ denote the arclength along the free surface, which grows moving toward the positive ξ-axis. It can be shown that the sign in front of the dynamic boundary condition is always negative on the part of the free surface which is ahead of the leading edge whereas it change from negative to positive when moving along the free surface from $\xi = -\infty$ up to the trailing edge.

Additional conditions are enforced at the trailing edge of the plate, according to which the free surface is always attached at the edge of the plate and leaves the plate tangentially. These conditions are similar to the ones used for the plate entry problem (Iafrati and Korobkin, 2004; Iafrati, 2007). The conditions are expressed as:

$$h(1, -V/U) = 0 \quad h_\eta = -h_\xi\tan\gamma \ .$$

The first condition is enforced by assigning that the vertex of the first free surface panel one is at the trailing edge of the plate. The condition that the free surface leaves the plate tangentially is enforced by varying the point along the free surface where the sign in the dynamic boundary condition changes from negative to positive (see Iafrati and Korobkin, 2004).

In order to reduce the computational effort needed for the description of the solution within the thin jet layer, the thinnest part of the jet is described by a simplified shallow water model, similar to that used in Korobkin and Iafrati (2006).

In Fig. 5 the free surface profiles obtained at the same plate incidence, $\gamma = 10$ deg, and different horizontal velocity components $U = 30, 40$ and 50 m/s, are shown. Due to the different values of the ratio V/U, the plate is positioned at different heights. In terms of the non-dimensional variables, the root of the jet moves forward when reducing the horizontal velocity component. Note that, because of the difference in U, this does not reflect what occurs in physical variables. Behind the trailing edge of the plate there is a wake region and the free surface forms a corner with the angle between the two sides of the free surface of about 60 degrees.

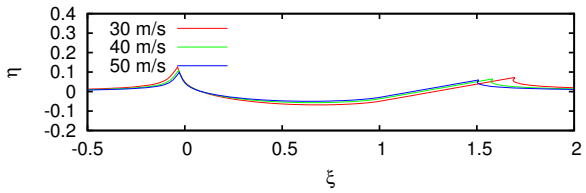

Figure 5: Free surface shapes obtained for a plate incidence $\gamma = 10$ at different horizontal velocities. For the sake of the clarity, on the right hand side of the plate, the thinnest part of the jet, described by the shallow water model, is not depicted.

The solutions for the thinnest part of the jet, described by the shallow water model, are plotted in Fig. 6. According to the definition of the self-similar variables, the position of a point in the self-similar plane gives an indication of the velocity of that point in the physical plane being $u = \xi U$ and $v = \eta U$. From the results presented it is found that the position of the tip is $\xi_T = 3.33, 3.11, 2.97$ for $U = 30, 40$ and 50 m/s, respectively. Hence, for the three cases in Fig. 6 the horizontal velocity of the tip is about 100, 124.4 and 148.5 m/s.

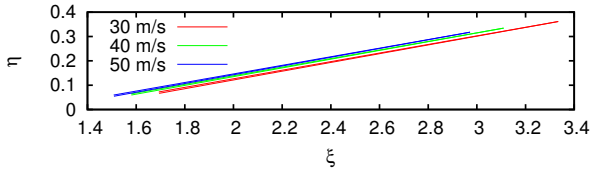

Figure 6: Free surface shapes of the jet regions obtained for a plate incidence $\gamma = 10$ at different horizontal velocities.

The most interesting aspect in terms of applications concerns the pressure distributions. For the three cases discussed above, the distributions of the self-similar pressure $\psi = p/(\varrho U^2)$, ϱ being the liquid density, are shown in Fig. 7.

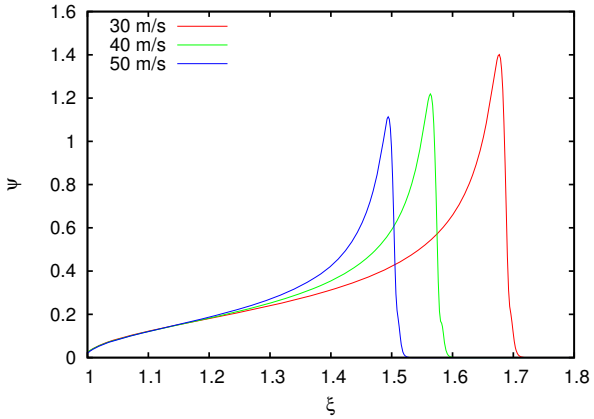

Figure 7: Pressure distributions for a plate incidence $\gamma = 10$ at different horizontal velocities.

It is seen that the non-dimensional pressure diminishes when increasing the horizontal velocity, with the peak values located at $\psi_p = 1.40, 1.22$ and 1.11 for $U = 30, 40$ and 50

m/s. However, the physical value of the pressure grows due to the quadratic term U^2.

In Fig. 8 and 9, the role played by the incidence of the plate on the free surface configuration and on the pressure distribution is shown for the case with $U = 30$ m/s. The results indicate that, when reducing the incidence of the plate, there is an increase of the wetted length as well as an increase in the intensity of the pressure peak.

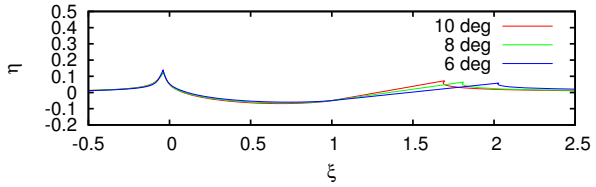

Figure 8: Free surface shape for $U = 30$ m/s, and different values of the plate incidence.

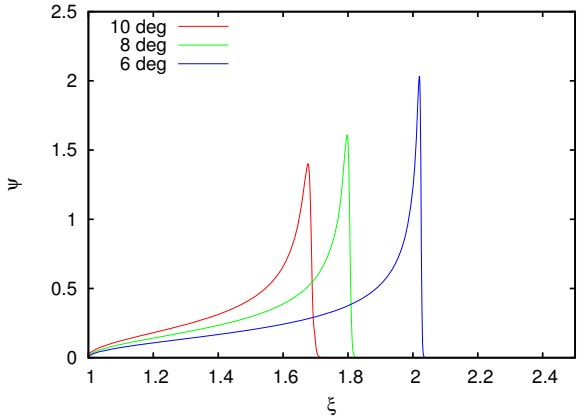

Figure 9: Pressure distributions for $U = 30$ m/s, and different values of the plate incidence.

The analysis of the solution is still in process and a much deeper discussion on the dependences will be presented at the Workshop. Hopefully, comparisons with experimental results will be established as well.

4. ACKNOWLEDGMENTS

This work has been partially funded by the Flagship Project RITMARE - The Italian Research for the Sea - coordinated by the Italian National Research Council and funded by the Italian Ministry of Education, University and Research within the National Research Program 2011-2013." Part of the work has been done in the framework of the SMAES-FP7 project (Grant Agreement N. 266172).

5. REFERENCES

H. Climent, L. Benitez, F. Rosich, F. Rueda and N. Pentecote (2006) *Aircraft Ditching Numerical Simulation*, 25th International Congress of the Aeronautical Sciences, Hamburg, Germany.

O.M. Faltinsen and Y.A. Semenov (2008) *Nonlinear problem of flat-plate entry into an incompressible liquid*, J. Fluid Mech. 611, 151-173.

A. Iafrati and Korobkin (2004) *Initial stage of flat plate impact onto liquid free surface*, Phys. Fluids 16, 2214-2227.

A. Iafrati and Korobkin (2005) *Self-similar solutions for porous/perforated wedge entry problem*, 20th IWWWFB, Longyearbyen, Norway.

A. Iafrati (2007) *Free surface flow generated by the water impact of a flat plate*, Proc. 9th Int. Conf. Num. Ship Hydrod., Ann Arbor (MI), USA.

C. Judge, A. Troesch and M. Perlin (2004) *Initial water impact of a wedge at vertical and oblique angles*, J. Engng. Math., 48, 279-303.

A. Korobkin and A. Iafrati Numerical study of jet flow generated by impact on weakly compressible liquid, *Phys. Fluids 18, 032108.*

R.F. Smiley (1951) An experimental study of water-pressure distributions during landings and planing of a heavily loaded rectangular flat-plate model *NACA TN 2453.*

Second-order resonance among an array of two rows of vertical circular cylinders

H. Kagemoto[1], M. Murai[2] and T. Fujii[3]
1: The University of Tokyo (presenting author)
5-1-5 Kashiwanoha, Kashiwa city, Chiba 277-8563, Japan
kagemoto@k.u-tokyo.ac.jp
2: Yokohama National University
79-1 Tokiwadai, Hodogaya-ku, Yokohama-city, Kanagawa 240-8501, Japan
m-murai@ynu.ac.jp
3: The University of Tokyo
5-1-5 Kashiwanoha, Kashiwa-city, Chiba 277-8563, Japan
fujii@geel.k.u-tokyo.ac.jp

1. Introduction

Wave trapping in an array of floating bodies has been one of the main topics in the recent workshops. It is a scientifically interesting phenomenon, but also it has practically important implications in that wave trapping could entail large free-surface displacement and/or large forces on the bodies.

Other than first-order wave trapping, some of the recent works are focusing on the second-order free-surface dynamic elevations, e.g. Murakami and Yoshida (1994), Sanada et. al (1997), Malenica et. al (1999), Wang and Wu (2008), Teng and Cong (2012). The arrays subjected to these works are mostly composed of 2~4 cylinders and they all conclude that second-order free-surface displacement could sometimes be relevant and could not be neglected in the design of corresponding structures such as TLPs. Some of the above mentioned works compare their theory with experimental results (Murakami and Yoshida (1994), Sanada et al. (1997)), but they do not necessarily refer to the results from the viewpoint of wave trapping.

On the other hand, in theoretical works (Malenica et. al (1999), Teng and Cong (2012)) it is suggested that second-order wave trapping takes place at half the wave frequency at which the corresponding linear near-trapped mode occurs.

In the present study, we show that the second-order resonance of dynamic free-surface displacement could in some cases be quite relevant among an array of two rows of vertical cylinders not only in theory but also in real phenomena. Discussion is also made if the second-order wave trapping is manifested at half the wave frequency at which the corresponding linear near-trapped mode occurs as suggested by the works mentioned above.

2. Experiment

Water-tank experiments were conducted using an array of two rows of vertical truncated circular cylinders as shown in Figure 1. Four kinds of cylinder arrangement, that is, 2 x 9 cylinders, 2 x 7 cylinders, 2 x 5 cylinders, 2 x 3 cylinders were used. (Figure 1 is the case of 2 x 9 cylinders.) The cylinders were fixed in regular head waves and the water-surface displacements at the origin of the coordinate system were measured.

3. Theory

The theory used in the present calculations is not a new one but that presented by Sanada et. al (1997), which extended the theory of Linton and Evans (1990) for the analysis of second-order wave diffraction. The theory is applicable only to bottom-mounted vertical cylinders and therefore, in a strict sense, can not be used for the present cases, in which the cylinders were truncated, but we confirmed through the comparison of first-order free-surface displacements obtained by the theory with those obtained by a theory applicable for truncated cylinders that the theory used in the present calculations give results with acceptable accuracy within the context of the present experiments.

4. Results and Discussion

Figures 2 show the experimental and theoretical results on the free-surface displacement at the origin of the coordinate system in 2 x 9, 2 x 7, 2 x 5, 2 x 3 arrays. The horizontal axes of the figures are the period of the incident wave. From these figures, the following facts are observed.

(1) Second-order free-surface displacement could be manifested significantly at certain wave frequency range.

(2) The theoretical results on the second-order surface elevation agree quite well with the experimental results. The second-order peak value can be really as high as that predicted by the theory.

(3) The peak value of the second-order free-surface displacement is enhanced as the number of the cylinders involved increases. It is also observed that the peak period of the second-order free-surface displacement becomes closer to one of the peak periods of the first-order free-surface displacement as the number of the cylinders increases.

In many of resonant phenomena, the peak value of the response could be quite large theoretically, while in reality the peak value is attenuated due to unaccounted damping forces, but in the present case it is surprising that the peak value in reality can be as high as that predicted theoretically, which only accounts for radiation damping as the damping.

As for the suggestion made by some of the former works that the second-order wave trapping is

manifested at half the wave frequency at which the corresponding linear near-trapped mode occurs, it seems that it is not the case in the present cases.

The free-surface displacement at two other places (at (-0.165, 0.0), (-0.165, 0.165)) were calculated for the case of 2 x 9 cylinders. The distinct differences from those shown in Figures 2 are:

1. The peak of the first-order free-surface displacement observed in Figures 2 at around T=0.6sec totally disappears at (-0.165, 0.0), (-0.165, 0.165).
2. Though the peak of the second-order displacement observed in Figures 2 also appears at (-0.165, 0.0) and (-0.165, 0.165), the peak values at these two points are not as distinct as that observed in Figures 2.

References

1. Linton, C.M. and D.V. Evans: The interaction of waves with arrays of vertical circular cylinders, *Journal of Fluid Mechanics*, Vol.215, 549-569, 1990

2. K. Murakami and A. Yoshida: Second-order wave interaction with arrays of vertical cylinders of arbitrary cross section, *Coastal Engineering Proceedings*, Vol.24, 1469-1483, 1994

3. T. Sanada, N. Mizutani and K. Iwata: Second-order approximate solution of nonlinear wave diffraction due to vertical cylinder array, *Intl. Journal of Offshore and Polar Engineering*, Vol.7, No.3, 1997

4. Malenica, S., Eatock Taylor R., Huang, J.B.: Second order water wave diffraction by an array of vertical cylinders, *Journal of Fluid Mechanics*, 390, 349-373, 1999

5. C.Z. Wang and G.X. Wu: Analysis of second-order resonance in wave interactions with floating bodies through a finite-element method, *Ocean Engineering*, 35, 717-726, 2008

6. B. Teng and P.W.Cong: Simulation of nonlinear wave elevation around a square array of truncated cylinders, Proc. 27th International Workshop on Water Waves and Floating Bodies, 2012

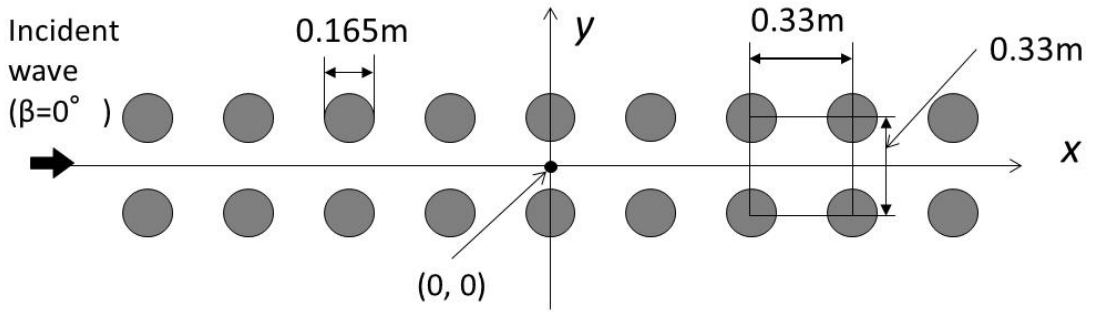

Figure 1 A 2 x 9 array of cylinders

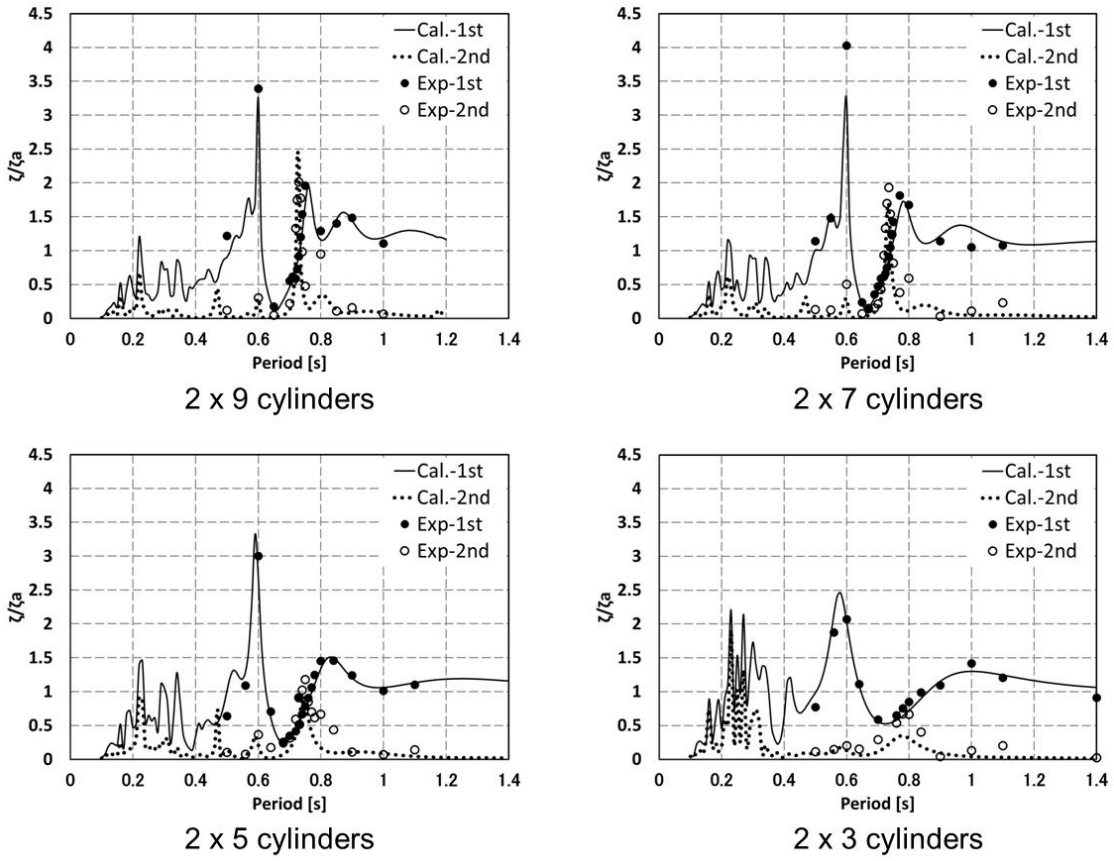

Figure 2 Numerical and experimental results on the 1-st and 2-nd order free-surface displacement among cylinder arrays at (0,0)

Abstract for 28th IWWWFB, Marseille, France, 2013

Time-domain Hydro-elastic dynamic analysis of a large floating body including second-order wave loads

H.Y. Kang and M.H. Kim
Ocean Engineering Program, Dept. of Civil Eng, Texas A&M University
College Station, Texas, USA
Email: hykang@tamu.edu and m-kim3@tamu.edu

INTRODUCTION

With increasing demands for energy and goods, various types of floating structures face expansion of scale and working environment, i.e. extended spar or TLP for ultra-deep water, various offshore platforms for arctic, very large container ships, multiply connected floating breakwaters and wave energy converters. Corresponding to the expansion of scale and environment, the floating structures are exposed to various problems including resonance, which is induced by deformation of the body and it's interaction with waves or any other offshore loadings such as iceberg impact.

To resolve the elastic floating body interaction, several methods were suggested: modal expansion method for linear waves and direct simulations using FEM-BEM or FEM-FEM combinations. Considering that resonance normally occurs at a couple of lowest elastic modes, second order analysis may be required to account for the resonance induced by sum-frequency wave force. Contrary to full coupling effect by direct simulation, the corresponding computing cost and accuracy issue could be drawbacks of the direct simulation.

As an initiating work to achieve complete second order hydroelastic analysis on time domain, a fully coupled time-domain hydro-elastic dynamic analysis is addressed, based on modal expansion method to couple with elasticity and Volterra series method to apply second order wave induced loading. The methodology can be extended to various applications for irregular waves such as additional coupling with mooring system or impact loadings, even with dramatically reduced computing cost. In addition, it can generate instantaneous irregular wave-induced loadings acting on the floating body as time series, which can be used for global and local stress analysis.

FORMULATION

To account for interactions of body deformation, a finite series of elastic modes is regards as sufficient basis to represent the deformation. In further, the elastic modes are applied to a general boundary value problem as additional modes to solve with rigid body's six degree of freedom. For the extended modes of elasticity, inertia and stiffness components can be obtained by modal analysis, based on diagonalization by eigenfunction.

Assuming a pontoon type floating body as Euler-Bernoulli Beam in Eq. 1, analytic solution of mode shapes is given and one can get diagonalized modal inertia, stiffness, and excitation for the modes. A few simple geometries have analytic solutions of mode shapes. For arbitrary body, one may get approximate modal results from a FEM program.

$$\frac{\partial}{\partial x^2}\left(EI\frac{\partial^2 w}{\partial x^2}\right)+m\frac{\partial^2 w}{\partial t^2}=q(x)r(t)$$

$$w(x,t)=\sum_{k=1}^{\infty}a_k(t)\varphi_k(x) \qquad where\ \ \varphi_k(x)\ \text{is}\ k^{th}\ \text{mode shape function.} \tag{1}$$

$$\int_x m\varphi_k{}^2(x)dx\cdot\ddot{a}_k(t)+\int_x EI\varphi_k''''(x)\varphi_k(x)dx\cdot a_k(t)=\int_x q(x)\varphi_k(x)dx\cdot r(t)\ \ where\ k=1,...,e$$

With the additional elastic modes, boundary value problem is extended for body surface boundary condition to the elastic modes e.

$$\nabla^2\phi^{(1)} = \nabla^2(\phi_D{}^{(1)} + \phi_R{}^{(1)}) = 0 \qquad \text{in fluid domain}$$

$$\text{where } \phi_D{}^{(1)} = \phi_I{}^{(1)} + \phi_S{}^{(1)}, \text{ and } \phi_R{}^{(1)} = \sum_{k=1}^{K} \zeta_k \phi_k{}^{(1)}, \; K = 6+e$$

$$\frac{\partial \phi^{(1)}}{\partial z} - \kappa\phi^{(1)} = 0 \quad \text{on } z = 0, \qquad \text{and } \frac{\partial \phi^{(1)}}{\partial z} = 0 \quad \text{on } z = -h, \tag{2}$$

$$\frac{\partial \phi_R{}^{(1)}}{\partial n} = i\omega n \cdot (\xi + \alpha \times r + \varphi), \quad \frac{\partial \phi_D{}^{(1)}}{\partial n} = 0 \quad \text{on } S_w$$

Based on the fully coupled hydro-elastic dynamic coefficients and hydrostatic revision due to elastic motions (Kang et al., 2012), time domain hydro-elastic dynamic analysis is developed from Kramers-Kronig relation.

$$(M_{ij} + \Delta M_{ij}^{\infty})\ddot{X}_j + (K_{ij}^E + K_{ij}^H)X_j = F_i^{(1)}(t) + F_i^{(2)}(t) + F_i^C(t) + F_i^D(t) \text{ where } i, j = 1,\ldots,6+e$$

$$\Delta M_{ij}^{\infty} = \Delta M_{ij}(\omega_{\max}) + \int_0^{\infty} R_{ij}(t)\frac{\sin(\omega_{\max}t)}{\omega_{\max}}dt \qquad \text{where} \quad R_{ij}(t) = \frac{2}{\pi}\int_0^{\infty} B_{ij}(\omega)\cos(\omega t)d\omega \tag{3}$$

$$F_i^C(t) = -\int_{-\infty}^{t} R_{ij}(t-\tau)\dot{X}_j(\tau)d\tau = -\int_{-t}^{\infty} R_{ij}(\tau)\dot{X}_j(t-\tau)d\tau = -\int_0^{\infty} R_{ij}(\tau)\dot{X}_j(t-\tau)d\tau$$

Comparing with rigid body time domain analysis, matrix size is extended to $6+e$, and coupling effects between elastic motions and rigid motions are given in terms of off-diagonal elements in inertia and hydrostatic matrices, and convolution integrals.

Considering that first several elastic modes normally have natural frequencies outside of linear wave spectrum but within range of sum-frequency excitations, it would be needed to apply second order wave induced loadings into the hydro-elastic analysis. Under an assumption of small wave slope, perturbation method is utilized to solve the second order wave-body interaction problem (Molin, 1979 and Kim and Yue, 1989 and 1990). The boundary value problem is given in Eq. 4, based on Kim and Yue 1990. Similarly to first order boundary value problem, main difference between rigid body analysis and elastic body analysis in second order is also body boundary condition.

$$\nabla^2\phi_D^{(2)} = 0 \qquad \text{in fluid domain,}$$

$$\left(\frac{\partial}{\partial t^2} + g\frac{\partial}{\partial z}\right)\phi_D^{(2)} = \left[\frac{1}{g}\frac{\partial \phi^{(1)}}{\partial t}\frac{\partial}{\partial z}\left(\frac{\partial^2\phi^{(1)}}{\partial t^2} + g\frac{\partial \phi^{(1)}}{\partial z}\right) - \frac{\partial}{\partial t}\left(\nabla\phi^{(1)}\right)^2\right]$$
$$-\left[\frac{1}{g}\frac{\partial \phi_I^{(1)}}{\partial t}\frac{\partial}{\partial z}\left(\frac{\partial^2\phi_I^{(1)}}{\partial t^2} + g\frac{\partial \phi_I^{(1)}}{\partial z}\right) - \frac{\partial}{\partial t}\left(\nabla\phi_I^{(1)}\right)^2\right] \quad \text{on free surface} \tag{4}$$

$\frac{\partial \phi_D^{(2)}}{\partial n} = -\frac{\partial \phi_I^{(2)}}{\partial n} + n \cdot B$, where B is second order body boundary velocity including elasticity.

Starting with second order radiation potential problem for elastic body by separation from combined body boundary condition above, one can find that the formulas for the radiation potential-induced hydro-elastic dynamic coefficients are identical between first and second order because of similar form of boundary condition. However, the relevant frequency $\omega^{(2)}$ is different and it presents sum and difference frequencies of bichromatic incident waves.

$$\frac{\partial \phi_R{}^{(2)}}{\partial n} = i\omega^{(2)} n \cdot (\xi^{(2)} + \alpha^{(2)} \times r + \varphi^{(2)}) \quad \text{on } S_w \tag{5}$$

Therefore, for the second order hydro-elastic dynamic analysis in time domain, added mass for infinite frequency and convolution integral terms are same as ones in linear order analysis.
Contrary to radiation problem, diffraction potential problem is quite complex to solve. First, correct second order body boundary velocity should be derived for the diffraction problem, including the elastic modes. In sequence, the fully coupled diffraction potential-induced pressures and excitations are achieved in the second order hydroelastic analysis. For example, Malenica and Hauteclocque (2012) addressed a fixed elastic cylinder case.
Following definition from Kim and Yue (1990), second order wave excitations are given as

$$F_{ex}^{(2)} = F_I^{(2)} + F_D^{(2)} + F_q^{(2)}, \tag{6}$$

which consists of second order potential-induced loading and first order potential-induced quadratic terms. Focusing on time-domain based second-order hydro-elastic analysis, among the two remaining terms in the second order loadings than the wave excitation, the second order hydrostatic loading, in particular, presents that hydrostatic restoring term in Eq. 3 is identical in both of linear and second order analyses.
Therefore, second order hydro-elastic dynamic analysis in time domain can be conducted for irregular waves by adopting the two-term Volterra series after obtaining fully coupled second order wave excitations.

$$F_h^{(1)}(t) = \mathrm{Re}\sum_a^N \left[A_a f_a^h e^{i\omega_a t} \right]$$
$$F_h^{(2)}(t) = \mathrm{Re}\sum_a^N \sum_b^N \left[A_a A_b^* f_{ab}^{h-} e^{i(\omega_a - \omega_b)t} + A_a A_b^* f_{ab}^{h+} e^{i(\omega_a + \omega_b)t} \right] \text{, where } h \text{ is index same as } i \text{ in Eq. 3.} \tag{7}$$

NUMERICAL RESULTS

Hydro-elastic dynamic analysis program for a large floating elastic body has been developed in both frequency and time domains (Kang et al. 2012). In particular, the calculations include shear forces and bending moments at specified sections of the body. The two independently developed programs are cross-checked to each other. For a case study, a simple pontoon-type elastic barge is investigated with 80 (L) x 10 (B) x 5 (D) m; four different bending stiffness cases of infinity, 2.56E10 Nm^2 (Full EI), 1.28E10 Nm^2 (Half EI) , and 6.4E09 Nm^2 (Quarter EI) are investigated with Euler-Bernoulli beam theory, and the most flexible two cases compared between linear and second order analyses. A JONSWAP spectrum with Hs=5, Tp=10.6, and Gamma=1.6 is used as an input wave spectrum.
For both of Half EI and Quarter EI cases, resonances occurred at the first elastic modes in second order analysis. In case of Quarter EI, it has resonance even in linear analysis due to its relatively low natural frequency, and that resonance get more amplified in second order analysis due to sum-frequency force; demonstrated in Fig. 2 ~ 4. The natural frequencies about 1.25 rad/sec and 1.77 rad/sec of Quarter EI and Half EI are for "dry-hull" natural frequency. After including hydrostatic-stiffness and added-mass effects, they changed to about 1.4 rad/sec and 1.68 rad/sec, respectively, as given in Fig. 2.

As a preliminary study, rigid body motion-induced second order excitations are only applied. This is practically acceptable unless high accuracy is needed since the elastic-response contribution in the body-boundary condition of the second-order problem is expected to be an order-of-magnitude smaller than that from rigid-body responses. After including the second-order sum-frequency wave loading, the elastic responses are significantly increased at the lowest-elastic-mode natural frequency, as can be seen in both spectral and time-series analyses. In further study, the complete solution of second order hydro-elastic dynamic analysis will be found, especially for the fully coupled second order excitations of a floating elastic body.

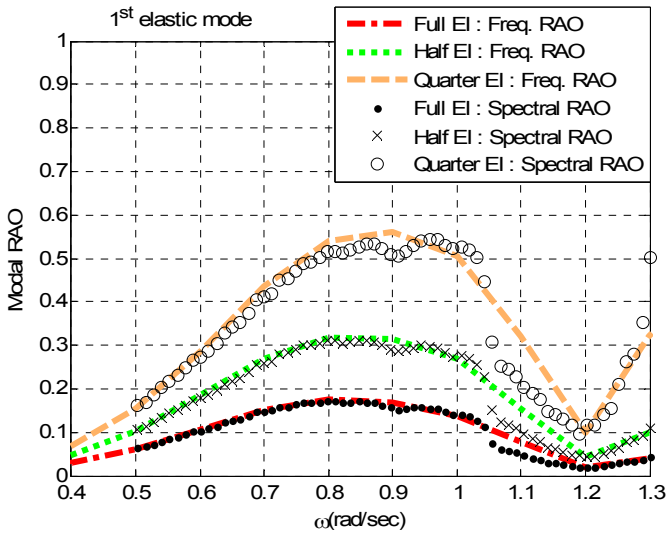

Figure 1 Confirmation by spectral RAO comparison in linear waves

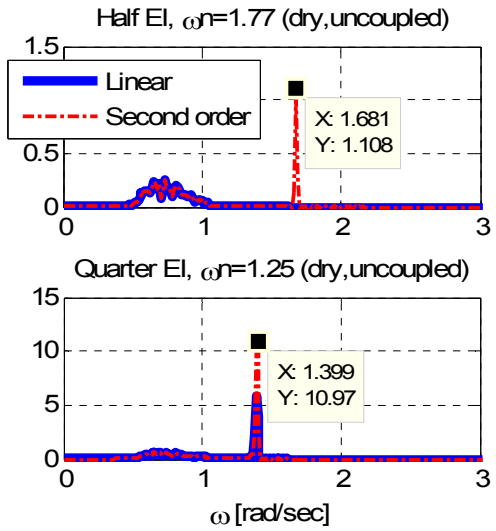

Figure 2 Spectral comparison between 1st and 2nd order for resonance

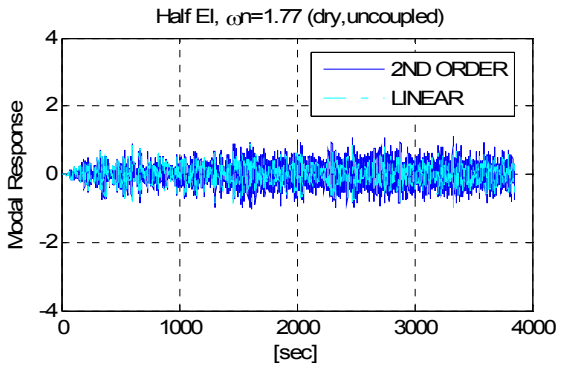

Figure 3 Time series comparison Half EI

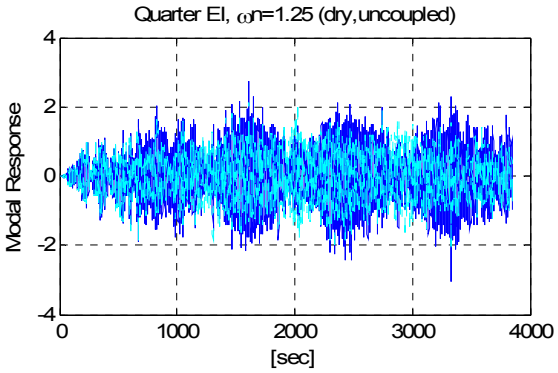

Figure 4 Time series comparison for Quarter EI

REFERENCES

Kang, HY, Kim, MH, Kim, MK, Cho, CY (2012). "Hydroelastic dynamic analysis of large-scale flexible offshore platforms," Proc 22nd ISOPE, Greece, Vol. 1, pp. 967-974.

Kim, MH and Yue, DKP (1989). "The complete second-order diffraction solution for an axisymmetric body. Part 1. Monochromatic incident waves," Journal of Fluid Mechanics, Vol. 200, pp. 235-264.

Kim, MH and Yue, DKP (1990). "The complete second-order diffraction solution for an axisymmetric body. Part 2. Bichromatic incident waves and body motions," Journal of Fluid Mechanics, Vol. 211, pp. 557-593.

Malenica, S. & De Hauteclocque G. (2012). "Second order hydroelastic response of the vertical circular cylinder to monochromatic water waves," 27thIWWWFB, Copenhagen, Denmark.

Molin, B (1979). "Second order diffraction loads upon three dimensional bodies," Applied Ocean Research, Vol. 1, pp. 197-202.

The 28th International Workshop on Water Waves and Floating Bodies
07-10 April, 2013
L'Isle sur la Sorgue, France

Multiple oblique impacts on thin liquid layer with restoring forces

T.I. Khabakhpasheva[1] **and A.A. Korobkin**[1,2]

[1] Lavrentyev Institute of Hydrodynamics, Novosibirsk, 630090, RUSSIA,
tana@hydro.nsc.ru
[2] University of East Anglia, Norwich, UK, a.korobkin@uea.ac.uk

Two-dimensional unsteady motion of a smooth body over a water surface with multiple collisions and subsequent rebounds from this surface is considered. This problem is studied in connection with landing of aircraft on the water and flights of wing-in-ground-effect vehicles (WIG) in close proximity to the water surface. In the present analysis, the water is of small depth and its flow caused by the impacts is described by the shallow water model. Free body motions with subsequent water impacts and the corresponding hydrodynamic loads are of primary interest. In the past only a single impact between the water surface and a smooth body was studied [1-8]. These investigations revealed that the landing of a smooth body with high horizontal speed on water typically leads to the rebound of the body followed by skipping along the water surface. It was shown that the body rotation plays an important role in impacts and rebounds of a free body. This regime of the body motion with multiple impacts on the water surface may cause vibrations of the fuselage with significant bending stresses or even lead to the overturning of aircraft. It is interesting to note that regimes of the landing of a free body with a single impact on the water surface and the subsequent smooth planing along the water were not detected in the calculations. Motions of a free body are determined by its orientation and speeds before the impact, and the hydrodynamic loads acting on the body surface during its contact with the water. Between the subsequent impact, it is assumed that the body motions are governed by gravity only. Aerodynamic forces are not included in the model.

To find regimes with smooth landing on water, it is suggested to include restoring forces which reduce the vertical motion of the body and also its rotation. In addition, damping forces are included. Parameters of the restoring and damping forces can be considered as control parameters which could be selected to achieve smooth landing. It can be expected that wrong choice of the parameters may lead to instability of the body motions with increasing amplitudes of its vertical displacement and rotation. If the parameters do not vary in time, the control system should be considered as passive. Active control assumes that there are time-varying external forces which are changed by the pilot.

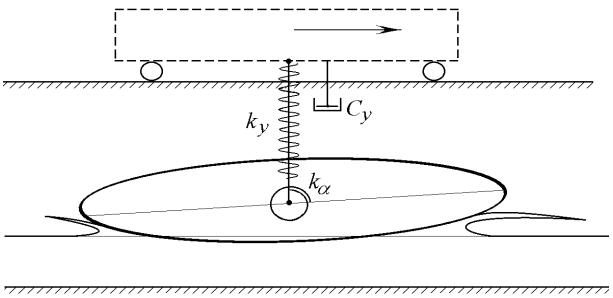

Fig. 1 Smooth body impact on a liquid layer with restoring forces and damping.

The configuration under investigation in this study is shown in Figure 1. A smooth body is represented by an elliptic cylinder which centre is connected by a vertical rod to the carriage of zero mass. The carriage can move only horizontally with the same horizontal speed as the speed of the body. The rod can move vertically with respect to the carriage. The distance between the carriage and the centre of mass of the body is controlled by a linear spring with the rigidity coefficient k_y. In the equilibrium, the centre of mass is at distance y_* from the bottom of the liquid layer and the weight of the body is balanced by the restoring force of the spring. During the body motion along the water surface, the vertical restoring force acting on the body is $-k_y(y_0(t)-y_*)$, where $y_0(t)$ is the current vertical coordinate of the centre of mass and t is time. In addition, a vertical damping force, $-c_y\dot{y}_0(t)$, is included. This damping force could be due to a viscous friction between the carriage and the vertical rod. The rod is pivoted at the centre of mass. The elliptic cylinder can rotate around this pivot with the angle between its axis and the horizontal being $\alpha(t)$. The axis of the cylinder is connected to the rod with a torsional spring of stiffness k_α and damping coefficient c_α. The spring force is given by $-k_\alpha(\alpha(t)-\alpha_*)-c_\alpha\dot{\alpha}(t)$, where α_* is an equilibrium inclination angle of the cylinder. Initially the carriage with the attached cylinder moves at a horizontal speed $\dot{x}_0(0)$ with the compressed vertical spring, $y_0 > y_*$, and equilibrium angle of inclination α_*. Then the vertical spring is released, the cylinder moves down towards the water surface and touches it tangentially at $t = 0$.

Note that a body landing on water without control of its vertical motion ($k_y = 0$, $c_y = 0$) but with the restoring moment, $k_\alpha > 0$, can be considered as a body with internal gyroscopic stabilizer. Such stabilizers can be also used to reduce roll motions of ship. Experiments showed that a stone skips successfully over water if the stone's rotational speed exceeds a certain value. The spinning stabilizes the stone much like an internal gyroscope stabilizes a body's landing on water.

The body motions are governed by the equations

$$m\ddot{y}_0 = F_y(t) - k_y(t)(y_0(t) - y_*(t)) - c_y(t)\dot{y}_0(t), \qquad m\ddot{x}_0 = F_x(t),$$

$$J\ddot{\alpha} = M(t) - k_\alpha(t)(\alpha(t) - \alpha_*(t)) - c_\alpha(t)\dot{\alpha}(t),$$

where m is the mass of the body, J is the moment of inertia, $F_x(t)$ and $F_y(t)$ are the horizontal and vertical components of the hydrodynamic force acting on the body surface in the contact region, $M(t)$ is the moment of the hydrodynamic force. Dot stands for the time derivative. Note that the gravity force is balanced by the vertical spring and does not appears in the equations. The hydrodynamic forces and moment are calculated by integrating the pressure distribution along the wetted part of the body surface [4,5]. The hydrodynamic pressure is calculated within the shallow water approximation when the cylinder is in contact with water.

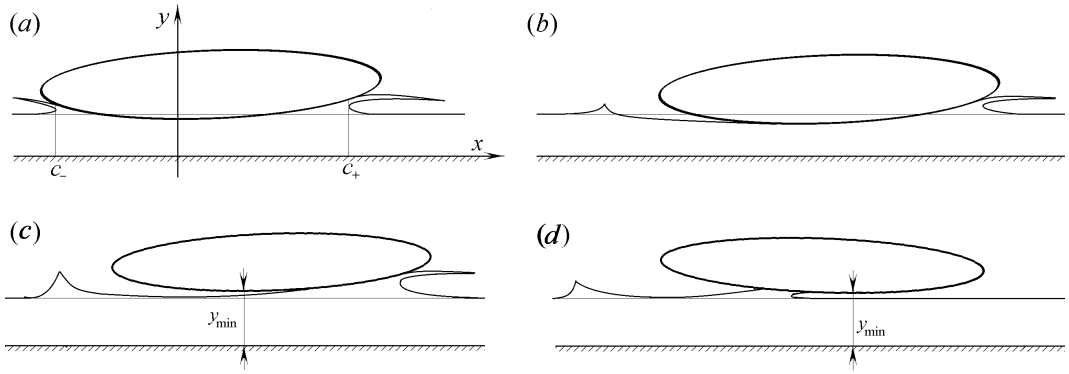

Fig. 2 Four typical positions of the body during its impact on shallow water with high horizontal speed.

Hydrodynamic loads are set zero during the time intervals when the body is above the water surface. Interaction stages are separated by these time intervals. It is assumed that each impact occurs on the undisturbed water surface. Each interaction stage is subdivided into the impact phase (Fig.2a), when the body enters the water layer and the wetted area expands in both directions with jetting at both edges of the wetted region [1], and the planing phase (Fig.2b-d), when the jetting occurs only at the leading edge and the water surface separates smoothly from the body surface at the trailing edge [5]. The position of the separation point is determined by using the Brillouin-Villat condition which requires that both the pressure and its tangential derivative are equal to zero at this point. The position of the leading edge is determined by using the matching conditions which come from the conditions of mass, momentum and energy conservations at this point [2-6]. The equations of the body motions, the conditions at both the leading and trailing edges of the wetted region and the equations of the shallow water flow are reduced to the system of nine nonlinear differential equations and one algebraic equation for the position of the separation point. These equations are integrated numerically in time with the initial conditions specifying the body motions before each impact.

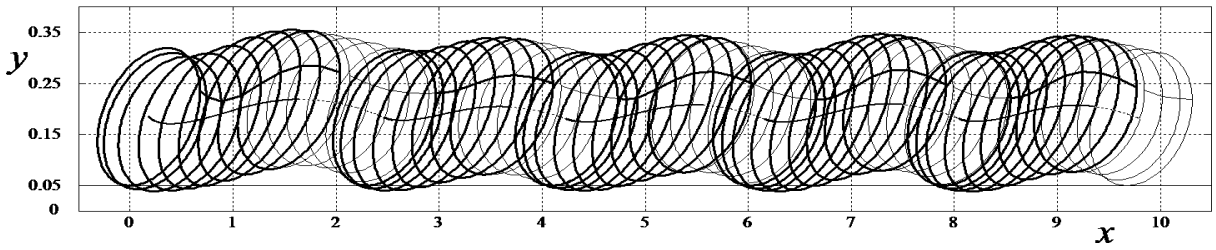

Fig. 3 Subsequent positions of the elliptic cylinder at different time instants are shown by thick lines when the cylinder is in contact with water and by thin lines when it is above water. The time step is 20ms.

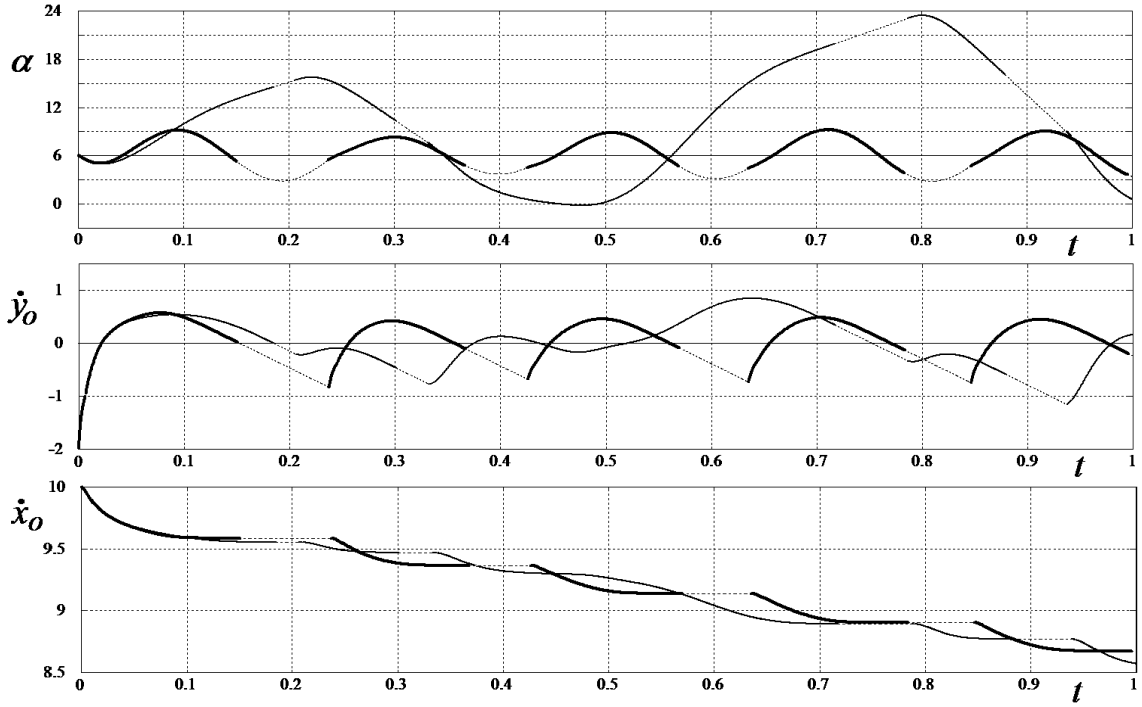

Fig. 4 Inclination angle $\alpha(t)$ of the elliptic cylinder (a), the vertical (b) and horizontal (c) components of the body velocity are shown as functions of time. The time is in seconds, the speed in m/s and the inclination angle is in degrees. Thick lines are for $\alpha_* = 6^o$, $k_\alpha = 10000$ N/rad and thin lines are for $k_\alpha = 0$. Dashed lines in both cases show motion of the cylinder without interaction with the fluid.

Calculations were performed in the dimensional variables for the elliptic cylinder with semi-axis $a = 0.5$m and $b = 0.125$m. The results of the calculations presented in Figures 3 and 4 are for the cylinder of mass 150 kg, water density $\rho = 1000$ kg/m^3 and the depth of the water layer $h = 0.05$m. The initial values of the vertical speed is -1 m/s, horizontal speed 10 m/s. The initial inclination angle of the cylinder is 6^o. The rigidity of the vertical spring k_y is zero, the coefficient of the torsional spring $k_\alpha = 10000$ N/rad, and the equilibrium inclination angle α_* of the cylinder is 6^o. The damping coefficients c_y and c_α are set zero. The time step of integration is 10^{-4} s. The calculations were performed for the time interval of 1s duration. During this short interval the cylinder impacts on water and bounces back five times. Positions of the body with time step 20 ms are shown in Figure 3. Note the different vertical and horizontal scales of the axis. In Figure 4, the results for the inclination angle, vertical speed of the body and its horizontal speed without the restoring moment are shown with thin lines, and with this moment by thick lines. It is seen that without the restoring moment the inclination angle changes significantly during the first second of the calculations varying from the initial 6^o to zero and then to 24^o. The restoring moment reduces the variation of the angle to 3^o around the equilibrium value. Note that the restoring moment does not change the motions of the body during initial 0.1s. The restoring moment makes the interaction stages shorter and the motions rather periodic with the period about 0.2 s. This implies that this moment governs the motions. The restoring moment does not change significantly the reduction rate of the horizontal speed of the body. This speed is reduced by 15% during the first second of the body interaction with the liquid layer.

The results of the calculations revealed that a smooth landing on water can be achieved by reducing both the horizontal and vertical speeds of the aircraft and keeping its inclination angle small. In the case of emergency landing the horizontal speed cannot be reduced but the vertical speed and the aircraft angle can be controlled. The horizontal speed can be as high as 50 m/s which makes the landing aircraft skip over the water surface. Hydrodynamic loads can be used to reduce the horizontal speed. To increase the horizontal component of the loads, the penetration depth should be big. This can be achieved by increasing the inclination angle and the time interval during which the fuselage is in contact with water. The rebound of the fuselage should be reduced by controlling the vertical motion and the inclination angle.

To gain the experience with effects of the control parameters on the aircraft emergency landing, a model of multiple impacts has been developed. This model can be used to find optimal control regimes of smooth landing. As a first attempt, it is suggested to determine the control parameters $k_y(t)$ and $k_\alpha(t)$ which maximize the duration of the first impact on water for a given set of landing conditions.

The work was supported in part by the FP7 project SMAES - Smart Aircraft in Emergency Situations 266172.

References

1. Batyaev E.A. & Khabakhpasheva T.I. 2013 Initial stage of inclined impact of a smooth body on a thin layer of liquid. *Fluid Dynamics*. 2. 68-80.

2. Hicks P.D. & Smith F.T. 2011 Skimming impacts and rebounds on shallow liquid layers. *Proc. R. Soc. A,* 467, 653-674.

3. Khabakhpasheva, T.I. 2009 Fluid-structure interaction during the impact of a cylindrical shell on a thin layer of water *J. Fluids and Structures.* 25(3), 431-444.

4. Khabakhpasheva, T.I. & Korobkin, A.A. 2012 Inclined impact of smooth body on thin liquid layer. In *Proc. 27-th IWWWFB*, Copenhagen, pp. 85-88.

5. Khabakhpasheva T.I., Korobkin A.A., Oblique impact of a smooth body on a thin layer of the inviscid liquid. *Proc. Royal Society (A)* 2013.

6. Korobkin, A.A. 1995 Impact of two bodies one of which is covered by a thin layer of liquid. *J. Fluid Mech. 300*, 43-58.

7. Reinhard, M., Korobkin, A.A. & Cooker, M.J. 2012 The bounce of a blunt body from a water surface at high horizontal speed. In: *Proc. 27-th IWWWFB*, Copenhagen, pp. 153-156.

8. Reinhard, M., Korobkin, A.A. & Cooker, M. 2012 Elastic plate impact into water at high speed with early water detachment. In *Proc. 6th ICHMT*, Tokyo, pp. 1-10.

The effect of a vertically sheared current on rogue wave properties.

C. Kharif[1], S. Viroulet[1],* and R. Thomas[1]
[1] *Aix-Marseille Univ., IRPHE CNRS: UMR 7342 - Aix-Marseille Universit - AMU - Ecole Centrale Marseille.*
(Dated: January 16, 2013)

Rogue waves are unexpected large and spontaneous waves that can occur on the surface of calm sea and during severe storm. In this study a nonlinear Schrodinger equation governing the complex envelope of a surface water wave train propagating on an uniform vertical shear current is used (Thomas R., Kharif C. & Manna M., 2012). As a result it is shown that the vorticity modifies significantly the properties of rogue wave, namely their lifetime and height. In the presence of a shear current co-flowing with the waves it is shown that the height of the rogue waves is increased whereas the lifetime is decreased. Just the opposite, for a counter-flowing current, the height and lifetime are reduced and increased, respectively.

I. INTRODUCTION

Rogue waves are among the wave naturally observed by people on the sea surface that represent an inseparable feature of the Ocean. Rogue waves appear from nowhere, cause danger, and disappear at once. They may occur on the surface of a relatively calm sea and not reach very high amplitudes, but still be fatal for ships and crew due to their unexpectedness and abnormal features. A wave is considered as a rogue wave if its height H_r is more than twice the significant height H_s. For a Gaussian sea and a narrow band spectrum, the significant height $H_s = 4\sigma$, where σ is the standard deviation of the elevation. Rogue wave can be generated by different mechanisms such as wave-current interaction, geometrical or dispersive focusing, modulation instability (the Benjamin-Feir instability), soliton collison, crossing seas, etc. In this study we consider rogue waves due to modulational instability. Several studies have been carried out on the propagation of surface water waves propagating steadily on a rotational current ([2, 5, 6]). Few papers have been published on the effect of a vertical shear current on the Benjamin-Feir instability of a Stokes' wave train in the presence of uniform vorticity. Johnson [3] studied the slow modulation of a harmonic wave on a two dimensional flow of arbitrary vorticity. Using the method of multiple scale he obtained the condition of linear stability for a plane nonlinear wave. This condition is verified if the product of the dispersive and nonlinear terms of the nonlinear Schrodinger equation (NLS equation) is negatif. The instability properties of weakly nonlinear wave packet to three dimensional perturbations have been studied by Oikawa *et al.* [4]. Their analysis were illustrated for the case of a linear shear. The Benjamin-Feir instability of a wave train propagating on positive and negative shear currents have been studied by Choi [1]. For a fixed steepness, he found that the envelope of the modulated wave train grows faster in a positive shear current and slower in a negative one. Thomas *et al.* [7] using the method of multiple scales derived a vor-NLS equation in finite depth when the vorticity is taken into account. They carried out a stability analysis of a weakly nonlinear wave train in the presence of uniform vorticity. They demonstrated that vorticity modifies significantly the modulational instability properties of weakly nonlinear plane waves, namely the growth rate and nabwidth. They shown that these plane wave solutions may be linearly stable to modulational instability independently of the dimensionless parameter kh. Using the Benjamin-Feir Index (BFI) concept, they demonstrated that the number of rogue waves increases in the presence of a shear current co-flowing with the wave whereas it is the opposite for a counter-flowing current. We consider the vor-NLS equation derived by Thomas *et al.* [7] to investigate the properties of rogue waves in the presence of vertical uniform shear current, namely their lifetime and amplification.

II. THE VOR-NLS EQUATION

Generally in coastal and ocean waters, the velocity profiles are varying with depth due to the bottom friction and surface wind stress. For example, tide currents may have an important effect on the propagation of waves and wave pack-

*Electronic address: viroulet@irphe.univ-mrs.fr

ets. Surface drift of the water induce by wind can also affect their propagation due to the velocity in the surface layer. The velocity field can be decomposed into a rotational term and an irrotational term which correspond to the induced wave velocity (the wave motion is assume to be potential). The fluid is inviscid and incompressible. Hence, the Kelvin-Lagrange theorem states that the vorticity is conserved.

$$\mathbf{V} = \Omega y \mathbf{i} + \nabla\phi(x, y, t) \tag{1}$$

The wave train move along the x axis, the y axis is oriented upward and gravity downward. The water depth h is constant and the bottom is located at $y = -h$. Ω represents the magnitude of the shear and ϕ the velocity potential due to the wave.

A. Governing equations

The governing equtions are :
$\nabla^2\phi = 0, -h < y < \eta(x,t)$
$\phi_y = 0, y = -h$
$\eta_t + (\Phi_x + \Omega\eta)\eta_x - \Phi_y = 0$
$\Phi_t + \frac{1}{2}\Phi_x^2 + \frac{1}{2}\Phi_y^2 + \Omega\eta\Phi_x + g\eta - \Omega\Psi = 0$

where Φ means that ϕ is calculated on the free surface and η the free surface elevation. Using the Cauchy-Riemann conditions, the dynamic boundary condition may be rewritten as follows :

$$\Phi_{tx} + \Phi_{ty}\eta_x + \Phi_x(\Phi_{xx} + \Phi_{xy}\eta_x) + \Phi_y(\Phi_{xy} + \Phi_{yy}\eta_x)$$
$$+\Omega\eta_x\Phi_x + \Omega\eta(\Phi_{xx} + \Phi_{xy}\eta_x) + g\eta_x + \Omega(\Phi_y - \Phi_x\eta x = 0$$

B. The multiple scale analysis

We present briefly the derivation of the NLS equation by using the method of multiple scales (for more details see Thomas & al. 2012 [7]).

$$\phi = \sum_{n=-\infty}^{+\infty} \phi_n exp[in(kx - \omega t)], \tag{2}$$

$$\eta = \sum_{n=-\infty}^{+\infty} \eta_n exp[in(kx - \omega t)], \tag{3}$$

where k is the wavenumber of the carrier and ω its frequency. Then ϕ_n and η_n are written in perturbation series

$$\phi_n = \sum_{j=n}^{+\infty} \epsilon^j \phi_{nj}, \tag{4}$$

$$\eta_n = \sum_{j=n}^{+\infty} \epsilon^j \eta_{nj}, \tag{5}$$

with ϵ the small parameter corresponding to the wave steepness of the carrier.

We seek a solution modulated on a slow time scale $\tau = \epsilon^2 t$ and slow space scale $\xi = \epsilon(x - c_g t)$

$$\eta(x,t) = \frac{1}{2}(\epsilon a(\xi,\tau)\exp[i(kx - \omega t)] + c.c) + \mathcal{O}(\epsilon^2) \tag{6}$$

With c_g the group velocity of the carrier wave. The new system of governing equations becomes :

$$\begin{aligned}
\epsilon^2\phi_{\xi\xi} + \phi_{yy} = 0, -h < y < \eta(x,t) \\
\phi_y = 0, y = -h \\
\epsilon^2\eta_\tau - \epsilon c_g\eta_\xi + \epsilon^2\Phi_\xi\eta_\xi + \epsilon\Omega\eta\eta_\xi - \Phi_y = 0 \\
\epsilon^3\Phi_{\xi\tau} - \epsilon^2 c_g\Phi_{\xi\xi} + \epsilon^3\Phi_{y\tau}\eta_\xi - \epsilon^2 c_g\Phi_{\xi y}\eta_\xi \\
+ \epsilon^3\Phi_\xi\Phi_{\xi\xi} + \epsilon^3\Phi_\xi\Phi_{\xi y}\eta_\xi + \epsilon\Phi_y\Phi_{\xi y} + \epsilon\Phi_y\Phi_{yy}\eta_\xi \\
+ \epsilon^2\Omega\eta_\xi\Phi_\xi + \epsilon^2\Omega\eta\Phi_{\xi\xi} + \epsilon^2\Omega\eta\Phi_{\xi y}\eta_\xi + \epsilon g\eta_\xi \\
+ \Omega\Phi_y - \epsilon^2\Omega\Phi_\xi\eta_\xi = 0
\end{aligned}$$

Substituing the expansion for the potential ϕ and the free surface elevation η lead to the nonlinear Schrodinger equation (after a tedious development to the third order) :

$$ia_\tau + La_{\xi\xi} + N|a|^2 a = 0 \tag{7}$$

where

$$\begin{aligned}
L &= \frac{\omega}{k^2\sigma(2+X)}\mu(1-\sigma^2)[1 - \mu\sigma + (1-\rho)X] - \sigma\rho^2 \\
M &= \frac{-\omega k^2(U + VW)}{8(1+X)(2+X)\sigma^4} \\
U &= 9 - 12\sigma^2 + 13\sigma^4 - 2\sigma^6 + (27 - 18\sigma^2 \\
&\quad + 15\sigma^4)X + (33 - 3\sigma^2 + 4\sigma^4)X^2 + (21 + 5\sigma^2)X^3 \\
&\quad + (7 + 2\sigma^2)X^4 + X^5 \\
V &= (1+X)^2(1 + \rho + \mu\overline{\Omega}) + 1 + X - \rho\sigma^2 - \mu\sigma X \\
W &= 2\sigma^3\frac{(1+X)(2+X) + \rho(1-\sigma^2)}{\sigma\rho(\rho + \mu\overline{\Omega}) - \mu(1+X)}
\end{aligned}$$

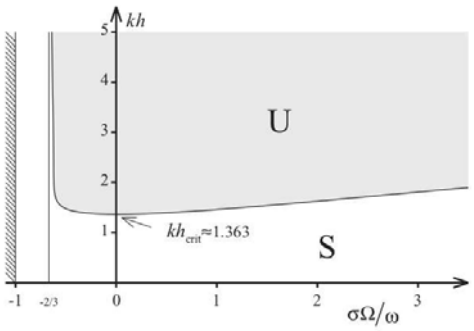

FIG. 1: *Stability diagram.* ***S****: stable,* ***U****: unstable. (Thomas et al. (2012) [7])*

with

$$\begin{aligned} \mu &= kh \\ \sigma &= \tanh(kh) \\ \rho &= \frac{c_g}{c_p} \\ \overline{\Omega} &= \frac{\Omega}{\omega} \\ X &= \sigma\overline{\Omega} \end{aligned}$$

III. STABILITY ANALYSIS

A solution of equation (7) can be expressed using a Stoke wave :

$$a = a_0 exp(iNa_0\tau) \tag{8}$$

A linear stability analysis gives the stability criterion for a Stoke's wave :

$$L(-2Na_0^2 + l^2L) \geq 0 \quad \text{stable} \tag{9}$$
$$L(-2Na_0^2 + l^2L) < 0 \quad \text{unstable} \tag{10}$$

The stability domain is plotted in figure 1 as a function of $\sigma\overline{\Omega}$ and kh.

There are two critical values as a function of the vorticity and the water depth. Indeed for a value of $\sigma\overline{\Omega} < -2/3$ which correspond to a vorticity $\Omega = -2\sqrt{\frac{kg}{3}}$, Stoke's waves are stable. When there is no vorticity ($\overline{\Omega} = 0$) Stoke's waves are stable for $kh < 1.363$. Note that for three dimensional motion there are oblique modulations even when $kh < 1.363$.

IV. APPLICATION TO ROGUE WAVES

In the previous section a development to third order and a stability analysis have been performed to investigate the influence of the vorticity on the Benjamin-Feir instability of Stoke's waves (see [7] for more details). In this section we consider the nonlinear evolution of the unstable infinitesimal perturbations within the framework of the vor-NLS equation. A series of numerical simulations of the vor-NLS equation is performed for different values of the wave steepness of the carrier wave, the water depth and the vorticity. The nonlinear stability analysis is developed for constant vorticity varying from -0.4 to 0.4 and for $kh = \infty$ or $kh = 2$. Due to the limitation of the NLS equation to weakly nonlinear wave trains we choose $ak = 0.05$ and $ak = 0.10$. The wave number of the carrier wave is $k = 10$ and that of the perturbation is $l = 1$.

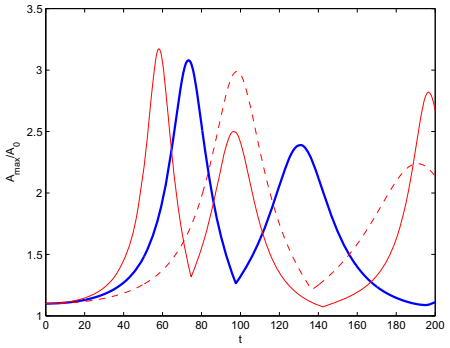

(a)

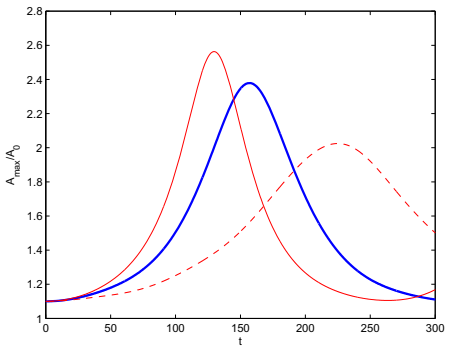

(b)

FIG. 2: *Evolution of the normalized maximum amplitude as a function of time. In infinite (a) and finite (b) depth. Thick continuous line corresponds to* 0 *vorticity, thin continuous one to* 0.2 *and thin dashed line to* -0.2.

The normalized maximum amplitude evolution as a function of time is shown in figure 2 for three different values of the vorticity (−0.2, 0 and 0.2). In both, finite and infinite depth, increasing the vorticity increases the maximum amplitude of the perturbation but decreases the width of the peak. To have a rogue wave event, the lifetime has been evaluated for a amplitude higher than two times the initial amplitude of the Stoke's wave.

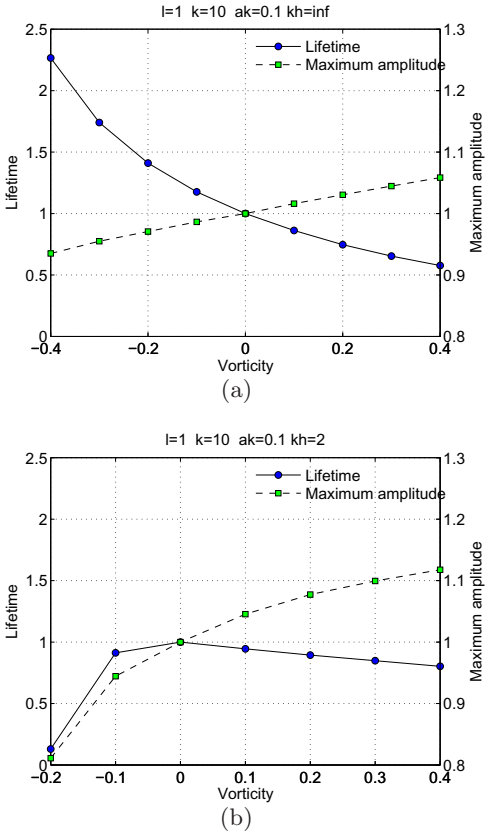

FIG. 3: *Evolution of the life time and the maximum amplitude as a function a vorticity in infinite (a) and finite (b) depth.*

Figure 3 shows the evolution of the lifetime and normalized maximum amplitude of the envelope as a function of the vorticity. In infinite (fig.3.a) and finite depth (fig.3.b) increasing the vorticity, increases the maximum amplitude but decreases the lifetime of the rogue wave. In figure 3.b the Stoke's wave is stable for values of vorticity lower than −0.2. This explain why the lifetime and maximum amplitude for negative values of vorticity are lower than those without vorticity, the instability is just high enough to be defined as a rogue wave.

V. CONCLUSION

Using a 1D nonlinear Schrodinger equation in the presence of a vertical shear current of non zero constant vorticity in finite and infinite depth, we have shown that the lifetime and maximum amplitude of rogue waves are significantly influenced by a vertical shear current. For a counter-flowing current the lifetime of a rogue is increased whereas the height is decreased. The opposite situation is observed for a co-flowing current. This study is still in progress, to take into account the influence of wind by introducing the Miles' mechanism.

[1] W. Choi. *Mathematics and Computers in Simulation*, 80:101–110, 2009.

[2] R. A. Dalrymple. *Journal of Geophysical Research*, 79:4498–4504, 1974.

[3] R. S. Johnson. *Proceeding of the Royal Society A.*, 347:537–546, 1976.

[4] M. Oikawa, K. Chow, and D. J. Benney. *Studies in Applied Mathematics*, 76:69–92, 1987.

[5] A. F. T. D. Silva and D. H. Peregrine. *Journal of Fluid Mechanics*, 195:281–302, 1988.

[6] J. A. Simmen and P. G. Saffman. *Studies in Applied Mathematics*, 73:35–57, 1985.

[7] R. Thomas, C. Kharif, and M. Manna. *Physics of Fluids*, 24, 2012.

Numerical Analysis of Floating-Body Motions in Arbitrary Bathymetric Domain

Taeyoung Kim, Yonghwan Kim*
Department of Naval Architecture and Ocean Engineering, Seoul National University
1, Gwanak-ro, Gwanak-gu, Seoul, Korea, (* yhwankim@snu.ac.kr)

1. INTRODUCTION

Recently, the installation of floating-type offshore structures in coastal area has been seriously considered. These offshore structures have drafts over 10 meters, and thus the shallowest conditions for operation are nearly 15~30 meters depth. For such finite water depth, the effect of bottom topology may be predominant to the wave propagation and motion responses of floating body.
One of concerns for finite depth is the nonlinear effect due to finite depth. To observe such effect, computational results based on the Boussinesq equation and Rankine panel method are compared for various bathymetry. The nonlinear solutions are obtained by the Boussinesq equation solver, while the Rankine panel method is applied for linear problems. The comparison is made for the two sets of computational result: wave propagation and wave-induced motion responses. In the both cases, the Boussinesq model does not show significantly different results from linear theory as long as water depth is not very shallow. Therefore, it can be found that a linear approach is useful for evaluating seakeeping performance of floating bodies in finite depth. Based on the linear regime, the motions responses of an LNG carrier at a port in Korea are computed.

2. BACKGROUND

2.1. Rankine Panel Method for Linear Problems

Laplace equation and linearized boundary conditions are applied to solve the boundary conditions for wave-body interaction. When sea bottom varies, the general solutions of incident waves, ϕI and ζI, are hard to find. In order to simulate incident wave adequately, wave making wall is implemented in incoming boundary surface (see Fig.1). Neumann-type boundary condition is applied at this boundary, as in Eq. (1). Furthermore, numerical damping zone is adopted on free surface, as in Eq (2), and the damping intensity, ν, is modified according to its proper behavior at the end of the computation domain.

$$\frac{\partial \phi}{\partial n} = \frac{\partial \phi_I}{\partial n} \tag{1}$$

$$\frac{d\zeta}{dt} = \frac{\partial \phi}{\partial z} - 2\nu(\zeta - \zeta_I) + \frac{\nu^2}{g}(\phi - \phi_I) \tag{2}$$

Rankine sources are distributed at boundary surfaces including sea bottom. Green's second identity can be used to compute the velocity potential, ϕ, as in Eq. (3). S_F, S_B, S_{BT} denote free surface, body, and bottom, respectively. All physical values are presented by applying bi-quadratic spline basis function.

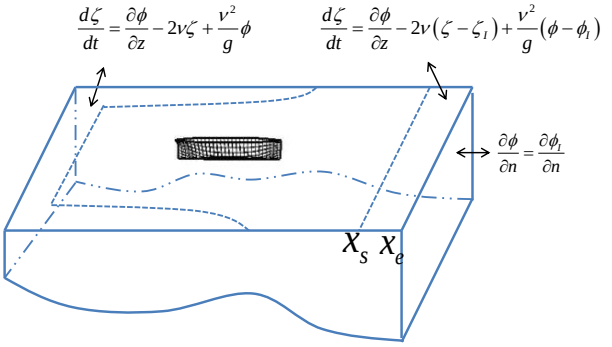

Fig. 1 Coordinate system

$$\phi + \iint_{S_F} \phi \frac{\partial}{\partial n}\left(\frac{1}{r}\right) ds + \iint_{S_B} \frac{1}{r}\frac{\partial \phi}{\partial n} ds + \iint_{S_{BT}} \frac{1}{r}\frac{\partial \phi}{\partial n} ds = \iint_{S_F} \frac{1}{r}\frac{\partial \phi}{\partial n} ds + \iint_{S_B} \phi \frac{\partial}{\partial n}\left(\frac{1}{r}\right) ds + \iint_{S_{BT}} \phi \frac{\partial}{\partial n}\left(\frac{1}{r}\right) ds \tag{3}$$

This Rankine panel method is applied in time domain to solve the prescribed boundary value problems. Wave loads are computed by integrating pressure on mean body, which is computed from Bernoulli equation. The fourth-order predictor-corrector method is applied for updating velocity potential and wave elevation. Radiation condition at far field is satisfied by applying damping zone, as similarly in Eq. (2).

2.2. Boussinesq Equation for Nonlinear Problems

Boussinesq equation approximates the velocities in fluid as a series form expanded from a reference location. In the present study, one of the state-of-the-art research is adopted which is developed by Madsen et al. (2006).

In this approach, the horizontal and vertical velocity of fluid can be represented as a series form of pseudo velocities, $\hat{\boldsymbol{u}}^*$ and $\hat{w}^*$, as in Eqs. (4) and (5). The infinite series of partial differential operators, J_I and J_{II}, include the differentiation up to fifth order.

$$\boldsymbol{u}(x,y,z,t) = J_I \hat{\boldsymbol{u}}^* + J_{II} \hat{w}^* \tag{4}$$

$$w(x,y,z,t) = J_I \hat{w}^* - J_{II} \hat{\boldsymbol{u}}^* \tag{5}$$

Pseudo velocities are computed by solving nonlinear boundary conditions with finite difference method. Then, horizontal and vertical velocities in the fluid can be calculated from Eqs. (4) and (5). Kinematic and dynamic free surface boundary conditions can update the velocities and wave elevation, by applying time-marching method.

3. NUMERICAL RESULTS

3.1. Comparison of Linear and Nonlinear Waves, and Motion Responses

Kinematic wave shapes are compared in two different depth conditions. At first, wave elevation is simulated in constant water depth by Rankine panel method and Boussinesq model. Because the modern ships have design draft around 10 meters, water depth is considered to be 15 meters to confirm the safety of under keel clearance. Fig. 2 shows the numerically generated waves in two different wave frequencies (ω), and those are compared to analytic solution of Stokes' linear wave. Longitudinal and vertical scales are normalized by wave length and a half of targeting wave height (H), respectively. In the Boussinesq model, two different wave heights, which are denoted in normalized from by water depth h, are selected to see the effect of nonlinearity. The nonlinear results in the Boussinesq model are not different significantly from the linear solution of the Rankine panel method. In addition, the results in both models are almost overlapped to the solution of Stokes' wave.

In next stage, wave elevation is simulated in sloped bottom. Sloped bottom is a useful example to describe the general shape of ocean bottom in near shore area. Many researchers have focused the effect of sloped bottom to dynamics of floating bodies (Buchner, 2006; Ferreira and Newman, 2009; Hauteclocque et al., 2009). Two different wave slopes are assumed, as in Fig. 3. h_0 and λ_0 denote water depth and wave length in inlet region. Wave elevations in both models show reasonable agreement to each other. Nonlinear effect is not dominant even at the higher wave amplitude in the Boussinesq model.

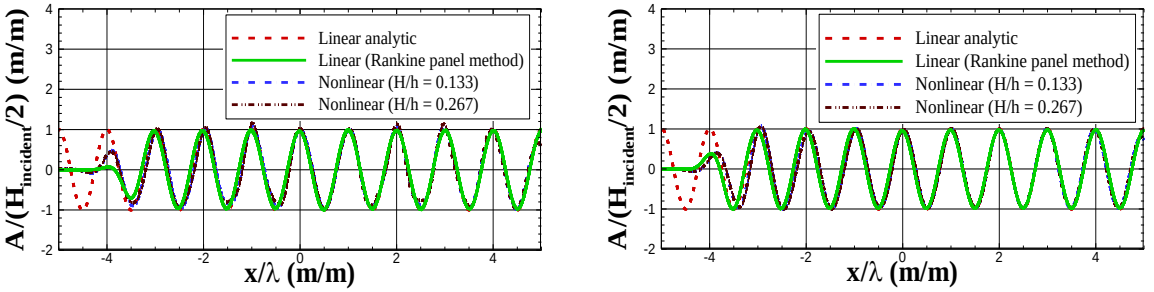

(a) Wave elevation ($\omega\sqrt{\lambda/g} = 1.509$, $h/\lambda = 0.060$) (b) Wave elevation ($\omega(\lambda/g)^{1/2}$=2.057, h/λ=0.130)

Fig. 2 Instantaneous wave elevation in constant water depth

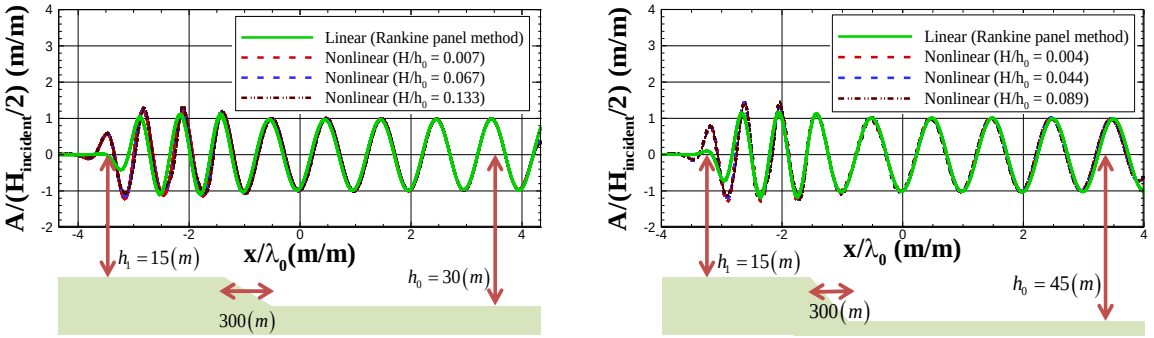

(a) Wave elevation ($\omega\sqrt{\lambda_0/g} = 1.773$, $h_0/\lambda_0 = 0.088$) (b) Wave elevation ($\omega(\lambda_0/g)^{1/2}$=1.939, h_0/λ_0=0.110)

Fig. 3 Instantaneous wave elevation in sloped bottom

Fig.4 shows the Froude-Krylov forces computed for the sloped bottom of Fig. 3(b). In this case, the ship model is an LNG carrier of 274m length and 11m draft. The LNG carrier is assumed to be located in the center of slopes, and bow towards to deeper region. The Froude-Krylov forces are only computed in the Boussinesq model. In three different wave heights, the Froude-Krylov heave force and pitch moment are not remarkably different, as shown in Fig. 4. This results implies that the nonlinearity is not significant in this water depth.
Fig.5 shows the heave and pitch motions in two different bottom changes. Particularly, the motion RAOs are compared with those for constant depths at the middle of slopes. It is interesting that the overall trends are similar between the results.
In this computational study, it is found that nonlinear effect is not significant in the moderate water depth where coastal LNG platforms can be installed. Therefore, a linear method can be useful in the analysis of wave loads and motion responses of ships and offshore structures in finite depth.

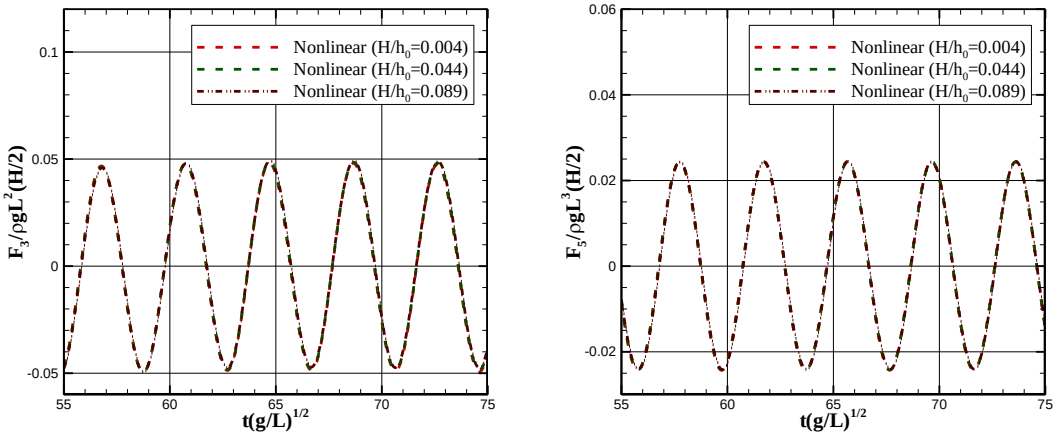

(a) Heave force (b) Pitch moment

Fig. 4 Froude-Krylov force and moment on LNG carrier (head sea, $\omega\sqrt{\lambda_0 / g} = 1.939$, $h_0 / \lambda_0 = 0.110$)

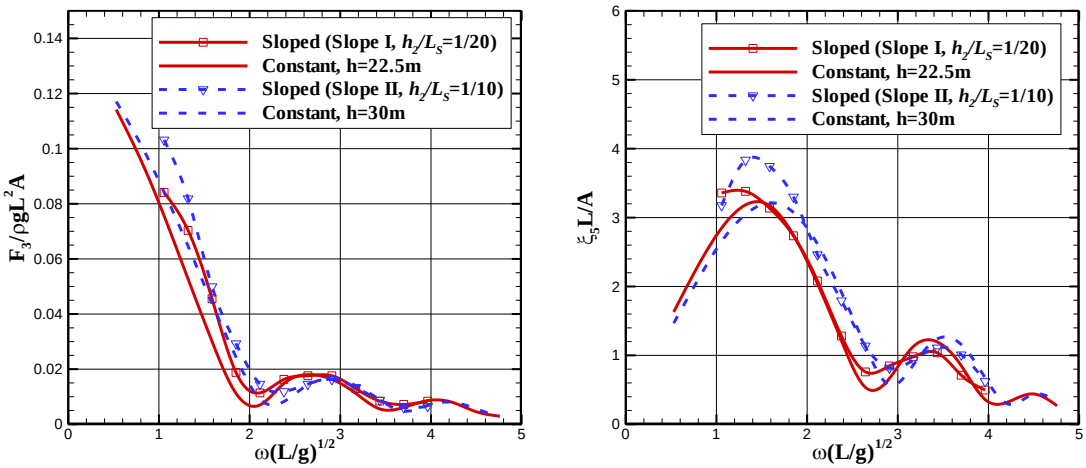

(a) Heave (b) Pitch

Fig. 5 Heave and pitch motions of LNG carrier: head sea, two bottom slopes (I: 15~30m, II: 15~45m)

3.2. Motion Responses of LNG Carrier in a Real Port

A real ocean seabed is modeled where the ship provides LNG to inland facility. The port is located at West Sea in South Korea. Fig. 6 shows the geometry around LNG terminal and representative wave flow in numerical computation. The mean depth near body is about 15 meters. Incident waves are assumed to propagate from open sea (left in figure) to narrow bay (right in figure). The direction of inflow changes due to the transversely varying bottom. In addition, the water depth also decreases as waves propagate along the bay. As a result, the shoaling effect usually increases wave amplitude in shallower region.

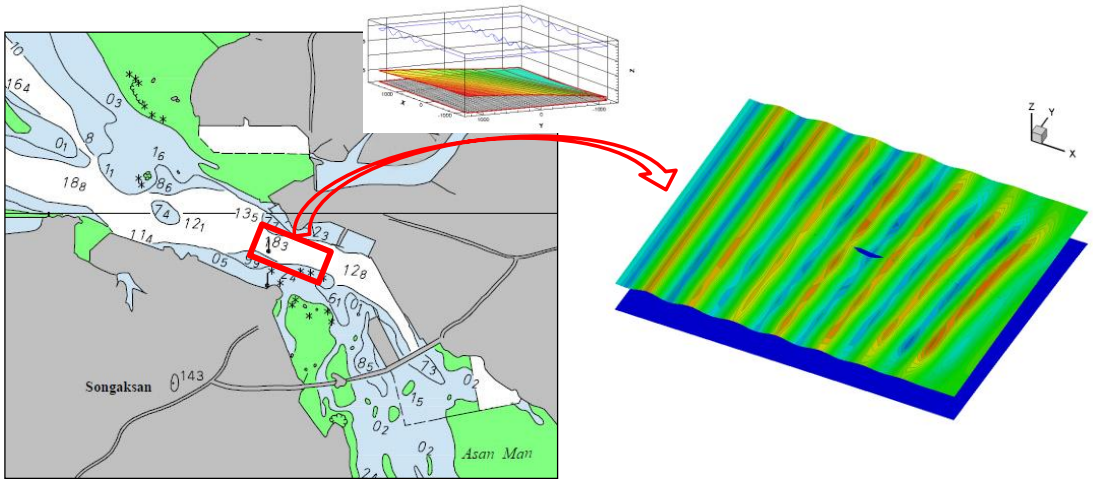

Fig. 6 Geometry of port in West Sea and representative wave around LNG carrier

Head and following waves are assumed at the inlet boundary to observe the body's responses. However, transverse flow is naturally generated due to the refraction of wave, as observed in Fig. 6. The direction is dependent on the depth variation and wave length. Fig. 7 shows the motion RAOs of the LNG carrier in regular wave. The magnitude of motion is normalized by amplitude of incident wave at inlet region. In this application, it is found that surge and heave responses are almost similar in both of head and following conditions. For pitch, the asymmetry of body and refracted waves around bow and stern regions cause different responses between head and following waves. To prevent transverse motion, position control is required according to the dominant wave component and its incident angle.

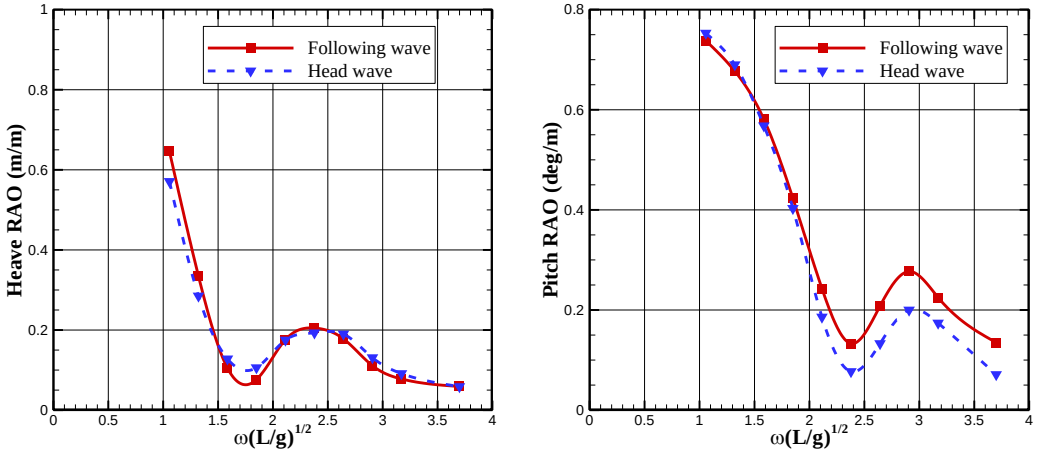

(a) Heave (b) Pitch

Fig. 7 Motion RAOs of LNG carrier around LNG terminal

REFERENCES

Belibassakis, K.A., 2008. , A boundary element method for the hydrodynamic analysis of floating bodies in variable bathymetry regions, Engineering Analysis with Boundary Elements, 32, 796– 810.

Buchner, B., 2006. The motions of a ship on a sloped seabed. In: Proceedings of 25th International Conference of Offshore Mechanics and Arctic Engineering. Hamburg, Germany.

Ferreira, MD., and Newman, JN., 2009. Diffraction effects and ship motions on an artificial seabed. In: Proceedings of 24th International Workshop on Water Waves and Floating Bodies. Zelenogorsk, Russia.

Hauteclocque, G., Rezende, F., Giorgiutti, Y., Chen, XB., 2009. Wave kinematics and seakeeping calculation with varying bathymetry. In: Proceedings of 28th International Conference of Offshore Mechanics and Arctic Engineering. Hawaii, USA.

Madsen, P., Fuhrman, R., Wang, B., 2006. A Boussinesq-type method for fully nonlinear waves interacting with a rapidly varying bathymetry. Coastal Eng. 53, 487-504.

Molin, B., Kimmoun, O., Remy, F. 2011, Slow-drift excitation in varying bathymetry, 26th IWWWFB, Athens, Greece.

HYDRODYNAMIC INTERACTIONS AMONG MULTIPLE CYLINDRICAL OWC' DEVICES RESTRAINED IN REGULAR WAVES

by

Dimitrios N. Konispoliatis dconispoliatis@yahoo.gr

Spyros A. Mavrakos mavrakos@naval.ntua.gr

National Technical University of Athens, School of Naval Architecture and Marine Engineering
9 Heroon Polytechniou Ave, GR 157-73, Athens, Greece

1 INTRODUCTION

In the present contribution, the diffraction and pressure-dependent-radiation problems for an array of OWC's devices restrained in regular waves with finite water depth is investigated in order to highlight the effect of the hydrodynamic interactions among the devices on the wave loading and wave energy extraction. The problem of the hydrodynamic interaction among neighbouring OWC devices may be important in evaluating the absorbed wave energy by each device in the array since the hydrodynamic characteristics of each member of a multi OWC's configuration may differ from the ones of a standalone, isolated device due to interaction phenomena. The latter are evaluated using the single OWC's hydrodynamic characteristics and the physical idea of method of multiple scattering (Twersky's [1952], Okhusu [1974], Mavrakos [1991]). Air volume flow rate, inner pressure and absorbed wave power are parametrically evaluated for several distances among devices in an array consisting of three devices.

2 FORMULATION OF THE HYDRODYNAMIC PROBLEM

We consider a stationary group of N rigid vertical axisymmetric oscillating water column devices excited by a plane periodic wave of amplitude $H/2$, frequency ω and wave number k propagating in water of finite water depth d. The outer and inner radii of each device q, q=1, 2,…, N, are a_q, b_q, respectively, whereas the distance between the bottom of the q device and sea bed is denoted by h_q and the distance between the devices by l (Figs. 1, 2). It is assumed small amplitude, inviscid, incompressible and irrotational flow so that linear potential theory can be employed. A global Cartiesian co–ordinate system O–XYZ with origin on the sea bed and its vertical axis OZ directed positive upwards is used. Moreover, N local cylindrical co-ordinate systems (r_q, θ_q, z_q), q = 1, 2, …, N are defined with origins on the sea bottom and their vertical axes pointing upwards and coinciding with the vertical axis of symmetry of the q device.

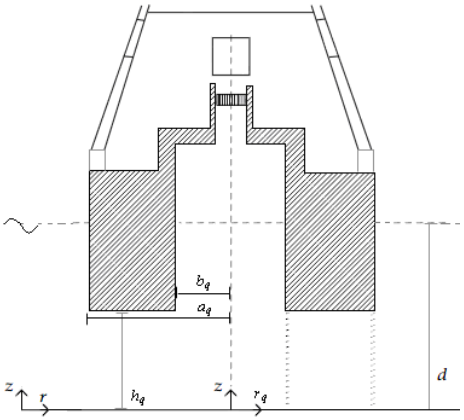

Fig.1. Schematic representation of a typical OWC device

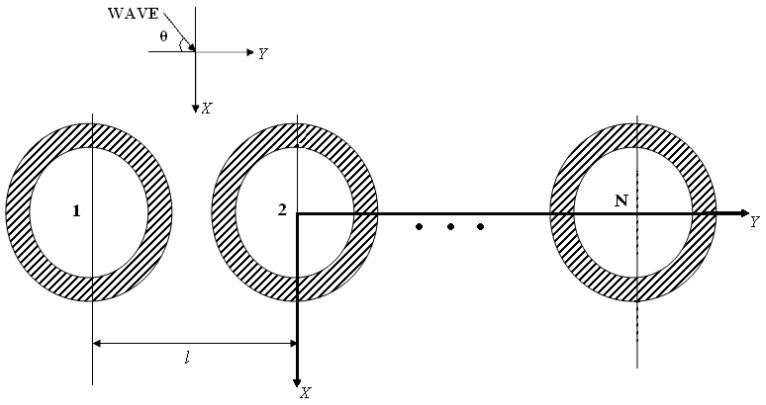

Fig.2. Stationary group of N identical OWC devices in a row

The fluid flow around the q=1,2,…,N device expressed in its own co-ordinate system can be described by the potential function: $\Phi^q(r_q, \theta_q, z_q; t) = \mathrm{Re}\left\{\phi^q(r_q, \theta_q, z_q) \cdot e^{-i\omega t}\right\}$ with

$$\phi^q(r_q,\theta_q,z_q)=\phi_0^q(r_q,\theta_q,z_q)+\phi_7^q(r_q,\theta_q,z_q)+\sum_{p=1}^{N}\phi_p^{qp}(r_q,\theta_q,z_q) \tag{1}$$

Here, ϕ_0^q is the undisturbed incident linear wave potential; ϕ_7^q is the scattered wave potential with the q device being considered fixed in the wave field with open duct and ϕ_p^{qp} is the radiation potential on body q due to time harmonic oscillating pressure head, $P_{in}^p=\mathrm{Re}\left\{p_{in0}^p\cdot e^{-i\omega t}\right\}$, in the chamber for the p device which is considered fixed in otherwise calm water.

The potentials φ_j^l ($l\equiv q$, qp ; j=0, 7, P; p=1, 2,…, N) are solutions of Laplace's equation in the entire fluid domain and satisfy, besides the zero normal fluid velocity on the sea bottom (z = 0) and on the mean body's wetted surface, S_0^q, the following boundary conditions on the inner and outer free surface, $z = d$:

$$\omega^2\varphi_j^l-g\frac{\partial\varphi_j^l}{\partial z}=\begin{Bmatrix}0 & \text{for} & r_q\ge a_q;\ l\equiv q \text{ or } qp;\ j=0,7,P\\ 0 & \text{for} & 0\le r_q\le b_q;\ l\equiv q;\ j=0,7\\ -\delta_{qp}i\omega p_{in0}^q/\rho & \text{for} & 0\le r_q\le b_q;\ l\equiv qp;\ j=P\end{Bmatrix} \tag{2}$$

Finally, a radiation condition for ϕ^q has to be imposed which ensures that propagating disturbances are outgoing.

As mentioned in the introduction, the method for evaluating the fluid flow around the q device in the array relies on single device hydrodynamic characteristics and accounts for the hydrodynamic interactions among the devices using the physical idea of multiple scattering. Each device of the configuration scatters / radiates waves towards the others, which in turn scatter waves contributing to the excitation of the initial device and so on. In this way, by superposing the incident wave potential and various orders of propagating and evanescent modes that are scattered and radiated by the cylindrical array elements, Fourier – Bessel series representations of the total wave field around each device q in the array may be obtained in its own cylindrical co-ordinate system. In doing so, use is made of the Bessel function addition theorem to express the radiated /scattered wave field from the pth device in the reference co–ordinate system (r_q,θ_q,z). By the way of example, the wave field around the body q of the arrangement due to inner pressure variation in p device, φ_P^{qp}, expressed in q-th body co-ordinate system is given by:

$$\varphi_P^{qp}(r_q,\theta_q,z)=\frac{p_{in0}^p}{i\omega\rho}\sum_{m=-\infty}^{\infty}\Psi_{Pm,j}^{qp}(r_q,z)e^{im\theta_q} \tag{3}$$

Where for the outer fluid domain, $r_{q\ge}a_q$, , $0\le z\le d$ the function $\Psi_{Pm,j}^{qp}$ is given by:

$$\Psi_{Pm,j}^{qp}(r_q,z)=\delta_{pq}\sum_{j=0}^{\infty}F_{Pm,j}^{qq}\frac{K_m(a_jr_q)}{K_m(a_ja_q)}Z_j(z)+\sum_{j=0}^{\infty}\left[G_{Pm,j}^{qp}\frac{I_m(a_jr_q)}{I_m(a_ja_q)}+F_{Pm,j}^{qp}\frac{K_m(a_jr_q)}{K_m(a_ja_q)}\right]Z_j(z) \tag{4}$$

The first term in (4) represents the isolated device wave field around the q body due to its own internal pressure variation, the second term denotes the incident wave fields on body q emanating from the scattered fields of the remaining devices considered open and the last term is the scattered wave filed around the q –th device. In (4) I_m and K_m denotes the mth order modified Bessel function of first and second kind, respectively; $F_{Pm,j}^{qq}$ are unknown Fourier coefficients for the radiated waves form the isolated body q with internal pressure head variation, $F_{Pm,j}^{pq}$ Fourier coefficients for the scattered waves from remaining open duct devices; $Z_j(z)=\left\{0.5\left[1+\sin(2a_jd)/(2a_jd)\right]\right\}^{-1/2}\cos(a_jd)$

Moreover, it holds:

$$G_{Pm,j}^{qp}=\sum_{l=1}^{N}(1-\delta_{lq})\sum_{v=-\infty}^{\infty}i^{m+v}\frac{K_{v-m}(a_j\ell_{qp})I_m(a_ja_q)}{K_v(a_ja_q)}F_{Pv,j}^{lp}e^{i(v-m)\theta_{\ell q}} \tag{5}$$

The time dependent volume flow produced by the oscillating internal water surface in q OWC device, q=1, 2,…, N, is denoted by $Q(r_q,\theta_q,z,t)=\mathrm{Re}\left[q^q(r_q,\theta_q,z)\cdot e^{-i\omega t}\right]$

where:

$$q^q=\iint_{S_i^q}u_z dS_i=\iint_{S_i^q}u(r_q,\theta_q,z=d)r_q dr_q d\theta_q=\iint_{S_i^q}\frac{\partial\phi^q}{\partial z}r_q dr_q d\theta_q \tag{6}$$

Here u_z denotes the vertical velocity of the water surface, S_i^q the inner water surface of the q device and ϕ^q the velocity potential in q device's chamber. It proves convenient to decompose the total volume flow, q^q into two terms associated with the diffraction, q_D^q, and the pressure–dependent radiation problem, q_P^q, as follows:

$$q^q = q_D^q + p_{in0}^q q_p^q = q_D^q - p_{in0}^q \left(B^q - iC^q\right) \tag{7}$$

where B^q and C^q are the corresponding radiation conductance and susceptance, respectively. Assuming uniform pressure distribution inside the chamber, it can be shown that, even though all *m*-modes terms affect the values of the diffraction and radiation potentials, by substituting those potentials in Equation (3) only the modes with $m=0$ contribute to q_P^q and q_D^q, as in an isolated device case [Mavrakos & Konispoliatis, 2011].

Assuming that the Wells turbine is placed in a duct between the chamber and the outer atmosphere, of the q device, and it is represented by a real valued pneumatic admittance g_T^q, then the total volume flow Q in q device, is equal to [Evans & Porter; 1997, Falnes; 2002, Falca˜o; 2002]:

$$Q(t) = g_T^q \cdot P_{in}^q(t) \tag{8}$$

The averaged value of the power absorbed from the waves over one wave period from the device q is obtained from [Evans & Porter; 1997]:

$$W^q = \frac{1}{2}\mathrm{Re}\left[\overline{q_D^q} \cdot p_{in0}^q\right] - \frac{1}{2}\overline{p_{in0}^q} \cdot B^q \cdot p_{in0}^q = \frac{1}{8}\overline{q_D^q}\left(B^q\right)^{-1} q_D^q \left\{1 - p_{in0}^q \left|g_T^q - \left(B^q + iC^q\right)\right|^2 \overline{p_{in0}^q} \Big/ p_{in0}^q \left|g_T^q + \left(B^q - iC^q\right)\right|^2 \overline{p_{in0}^q}\right\} \tag{9}$$

The capture width ℓ^q of the q device is the ratio of the power absorbed by the device to the available power per unit crest length of the incident wave [Martins-Rivas and Mei; 2009], i.e.

$$\ell^q = 2 \cdot W^q \Big/ \left(\rho g (H/2)^2 C_g\right) \tag{10}$$

C_g being the group velocity of the incident wave. The absorbed power (Eq.9) takes a maximum value of [Evans & Porter; 1997]:

$$W_{\max}^q = \overline{q_D^q}\left(B^q\right)^{-1} q_D^q / 8 \tag{11}$$

corresponding to an optimum inner pressure head $p_{in0_{optim}}^q = \left(B^q\right)^{-1} q_D^q / 2$.

If g_T^q, from Eq.8, reaches an optimum value, $g_{T_{optim}}^q = \left|B^q - iC^q\right|$ then the maximum value of the absorbed energy by device q, is:

$$W_{\max}^q = \frac{1}{8}\overline{q_D^q}\left(B^q\right)^{-1} q_D^q \left[1 - p_{in0}^q \left(2\left(g_{T_{optim}}^q\right)^2 + i\left(B^q C^q - C^q B^q\right) - 2 g_{T_{optim}}^q B^q\right)\overline{p_{in0}^q} \Big/ p_{in0}^q \left(2\left(g_{T_{optim}}^q\right)^2 + i\left(B^q C^q - C^q B^q\right) + 2 g_{T_{optim}}^q B^q\right)\overline{p_{in0}^q}\right] \tag{12}$$

The resulting maximum capture width is then given by [Evans & Porter; 1997]:

$$\ell_{\max}^q = 2 \cdot W_{\max}^q \Big/ \left(\rho g (H/2)^2 C_g\right) \tag{13}$$

3 NUMERICAL RESULTS

In figure 3 we examined an array of three same oscillating water column devices in a row. The variations of the value of the dimensionless parameter $v = \left|q_p^q\right|$, for $a_q / d = 1/2$, $b_q / a_q = 3/4$, $h_q / d = 3/4$, $l / a_q = 4$, 8, 12, for the middle device of the array, are being plotted. Next, we investigate how the direction of the wave propagation affects the value of the inner pressure in each of the above OWC devices. In figures 4 and 5 the dimensionless modulus of the inner air pressure is plotted in each device of the above configuration, $q = 1,2,3$, for incident wave angles $\theta = 0$, $\pi/2$, $l / a_q = 4$ and $g_T^q = 0.1 m^5/(Ns)$. Finally, in figure 6 the value of $\left(\ell_{\max}^1 + \ell_{\max}^2 + \ell_{\max}^3\right) / \left(3\ell_{\max}^{isolated}\right)$ for the three devices of the above configurations is presented, for $l / a_q = 4$, 8, 12. Here $\ell_{\max}^j$, j=1, 2, 3 denotes the maximum capture width in the j–th device for optimum inner pressure head, $p_{in0_{optim}}^q$, whereas $\ell_{\max}^{isolated}$ is its single device counterpart for optimum inner pressure value. From the depicted results the effect of the hydrodynamic interactions on the alteration of the single OWC device characteristics is shown.

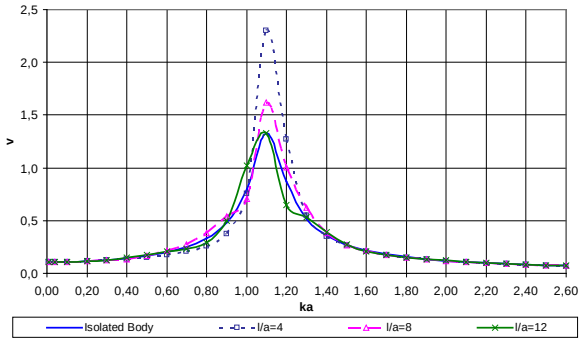

Fig.3. Modulus of $v = q_p^q / (10 \cdot \omega \cdot b_q^2 / (\rho \cdot g))$ versus $k \cdot a_q$, for $l = 4a_q, 8a_q, 12a_q$

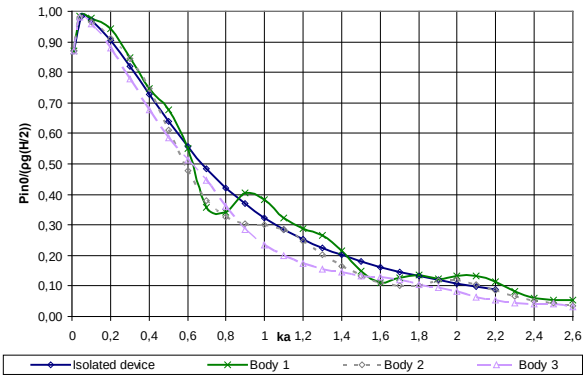

Fig.4. Modulus of inner air pressure versus $k \cdot a_q$, for θ=0

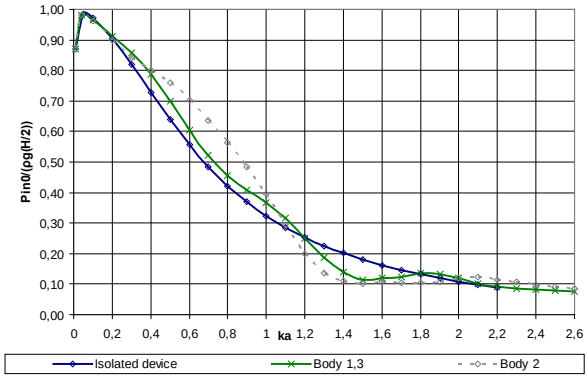

Fig.5. Modulus of inner air pressure versus $k \cdot a_q$, for θ=π/2

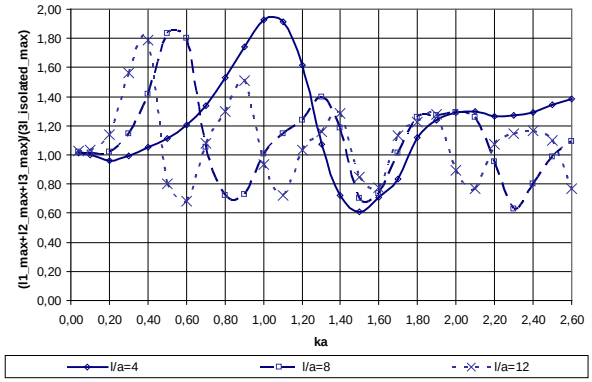

Fig.6. The value of $\left(\ell^1_{\max} + \ell^2_{\max} + \ell^3_{\max}\right) / \left(3\ell^{isolated}_{\max}\right)$ versus $k \cdot a$ for $l = 4a_q, 8a_q, 12a_q$ and $\theta = 0$ and optimum value of inner pressure head

4 ACKNOWLEDGEMENTS

This research has been co-financed by the European Union (European Social Fund – ESF) and Greek national funds through the Operational Program "Education and Lifelong Learning" of the National Strategic Reference Framework (NSRF) 2007 – 2013: Research Funding Program: ARISTEIA, Program POSEIDON (2041)

5 REFERENCES

Evans, D.V., Porter, R. 1997. Efficient calculation of hydrodynamic properties of OWC-type devices. *Journal of Offshore Mechanics and Arctic Engineering*, vol. 119, no. 4, pp. 210–218.

Falca˜o, A.F. de O. 2002. Wave-power absorption by a periodic linear array of oscillating water columns. *Ocean Engineering*, 29, pp.1163–1186.

Falnes, J. 2002. *Ocean waves and oscillating systems: linear interactions including wave-energy extraction*. Cambridge University Press.

Martins-rivas, H. & Mei, C.C. 2009. Wave power extraction from an oscillating water column at the tip of a breakwater. *Journal of Fluid Mechanics*, 626, pp.395–414.

Mavrakos, S.A. 1991. Hydrodynamic coefficients for groups of interacting vertical axisymmetric bodies, *Ocean Engineering*, 18(5), pp. 485 – 515.

Mavrakos, S.A. & Konispoliatis, D.N. 2011. Hydrodynamics of a floating oscillating water column device**.** *International Maritime Association of the Mediterranean* **(**IMAM 2011), Genoa, Italy.

Okhusu, M. 1974. Hydrodynamic forces on multiple cylinders in waves, Proceedings, *International Symposium on the Dynamics of Marine Vehicles and Structures in Waves*, University College London.

Twersky, V. 1952. Multiple scattering of radiation by an arbitrary configuration of parallel cylinders. *J. Acoustical Soc. of America*, 24 (1).

Wagner-type models of water impact with separation for a finite wedge

Alexander Korobkin

School of Mathematics, University of East Anglia, Norwich, UK
e-mail: a.korobkin@uea.ac.uk

Symmetric two-dimensional problem of a rigid wedge entering water at a constant speed is considered. The wedge is of finite height. The second stage of the flow, when the wedge is already completely wetted and a cavity is formed behind the wedge, is of concern. In particular, we need to calculate the hydrodynamic force acting on the wedge during this stage. It is known that the Wagner-type models quite well predict the force evolution during the impact stage, when the wedge is only partially wetted. The idea of the present approach is to introduce a fictitious body of infinite height, which consists of the wedge surface and the streamlines of the cavity behind the wedge computed for unbounded fluid region, and to calculate the hydrodynamic force by using the Wagner-type models applied to such a body.

1. Introduction

Wagner-type models include the Original Wagner Model (OWM), Modified Logvinovich Model (MLM) and the Generalised Wagner Model (GWM). There are also several other advanced models such as Second-order Wagner Model (Korobkin, 2007 and Oliver, 2007) and Combined Asymptotic Model, which are not considered in this study, thought they could be promising as it will be clear from the presented results.

Wagner-type models were derived for bodies with small deadrise angle. However, GWM and MLM can also predict the force $F(t)$ acting on entering bodies with moderate deadrise angles. Calculations by the Wagner-type models will be performed for the symmetric wedge with deadrise angle of 30 degrees. The wedge is of finite height with the upper base of length $B = 0.5$m. The wedge enters water of infinite depth at constant speed V. Gravity and surface tension are not included in the models. The results by the Wagner-type models are compared with the numerical results by S. Seng (2012) for the same wedge and conditions of the impact. Seng did his calculations by OpenFoam and presented the force coefficient $F_v = F/(\rho V^2)$ in terms of non-dimensional penetration depth h/H, where ρ is the water density, $h = Vt$ is the wedge displacement and $H = \frac{1}{2}B\tan(30^o)$ is the distance between the keel and the base of the wedge. It was known that the coefficient F_v is independent of the entry speed for the infinite wedge. The calculations by S. Seng showed that this coefficient is approximately independent of the wedge speed also during the stage with separation from the knuckles of the wedge. This result by Seng encouraged us to develop an approximate model of impact with separation where the body surface is continued with the cavity streamlines making a body of infinite length. The streamlines represent the free surface of the cavity behind a body placed in the uniform steady flow. These streamlines are treated as rigid within the present models.

2. Shape of the cavity behind symmetric wedge in uniform current

The analysis from the book by Gurevich (1978) was used to determine the shape of the cavity in the parametric form

$$x = \frac{B}{2} + \frac{B}{2\text{æ}(\gamma)} X(s), \quad y = H + \frac{B}{2\text{æ}(\gamma)} Y(s),$$

where s is the non-dimensional curvilinear coordinate along the free surface of the cavity, γ is the deadrise angle of the wedge and

$$\text{æ}(\gamma) = 8\cos\gamma \int_0^1 \frac{u^\sigma(1-u^2)\mathrm{d}u}{(1+u^2)^3}, \quad \sigma = \frac{2\gamma}{\pi}, \quad k = 1-\sigma.$$

The functions $X(s)$ and $Y(s)$ are obtained by integration of the following differential equations

$$\frac{\mathrm{d}X}{\mathrm{d}s} = \cos[k\phi(s)+\gamma], \qquad \frac{\mathrm{d}Y}{\mathrm{d}s} = \sin[k\phi(s)+\gamma], \quad \phi(s) = \arccos[(2s+1)^{-\frac{1}{2}}]$$

with the initial conditions $X(0) = 0$ and $Y(0) = 0$. The wedge and its continuation with the cavity surface are shown in Figure 1 for $x > 0$.

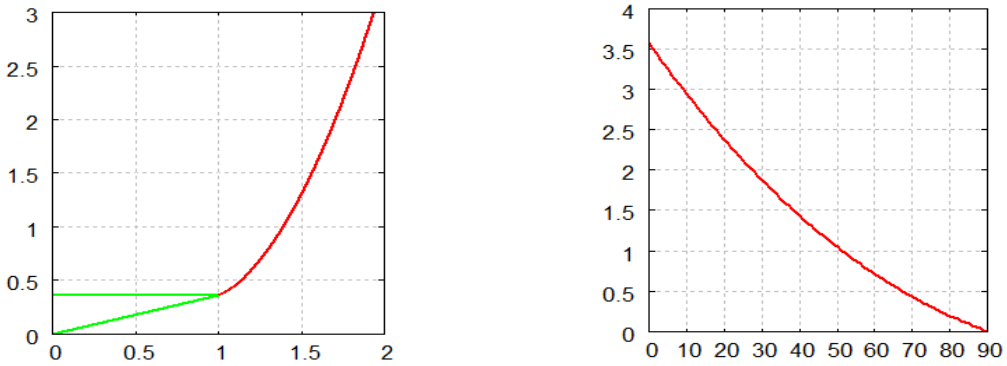

Figure 1. Shape of the wedge continued with the streamline in non-dimensional coordinates $x/(0.5B)$ and $y/(0.5B)$ (left) and the function æ(γ), where γ is in degrees (right).

The length of a small streamline element is $\delta l = B\delta s/(2\text{æ})$. Calculations of the streamline for the wedge with deadrise angle 30 degrees were done with $\delta s = 0.01$ which corresponds to the length δl of elements equal approximately to 1mm. Coordinates of the points on the wedge surface, where $x < 0.25$m, and on the streamline, where $0.25\text{m} < x < 0.389$m, with the distance between points about 1mm were saved in a data file which was used in the following calculations by the Wagner-type model representing a fictitious symmetric body with the equation $y = y_b(x)$, which penetrates water at a constant speed. In total, 500 elements represent the shape.

3. Original Wagner Model

In the OWM, the rigid shape $y = y_b(x)$ is in contact with water over the interval $|x| < c(t)$, where $c(t)$ and $\dot{c}/\dot{h}$ are computed by using the Wagner equation

$$\int_0^c \frac{y_b(x)\mathrm{d}x}{\sqrt{c^2-x^2}} = \frac{\pi}{2}h(t), \qquad \frac{\dot{c}}{\dot{h}} = \frac{\pi c}{2S(c)}, \quad S(c) = \int_0^c \frac{y_b'(x)x\mathrm{d}x}{\sqrt{c^2-x^2}}. \tag{1}$$

The integrals are evaluated by using linear approximation of the shape function $y_b(x)$ between nodes of the elements. This approach can be used for any $h(t)$. In the present calculations,

$h = Vt$. The hydrodynamic pressure in the wetted area of the fictitious body is given by the linearised Bernoulli equation

$$p(x,t) = \rho V^2 \frac{\dot{c}}{\dot{h}} \frac{c}{\sqrt{c^2 - x^2}}.$$

The pressure is integrated over the wetted area, if $c < B/2$, and over the wedge surface, if $c > B/2$, with the result

$$F_v = \frac{2c\dot{c}}{\dot{h}} K(c),$$

where $K(c) = \frac{\pi}{2}$ for $c < B/2$ and $K(c) = \arcsin(B/2c)$ for $c > B/2$. The calculated force coefficient F_v is shown in Figure 2 with respect to the non-dimensional penetration depth Vt/H by the solid line. The dashed line shows the result by OpenFoam (Seng, 2012). It is seen that the OWM overpredicts the force during the impact stage, which is well known drawback of this model. However, OWM predicts correctly the duration of the impact stage and the force evolution during the separation stage. The latter result is less obvious.

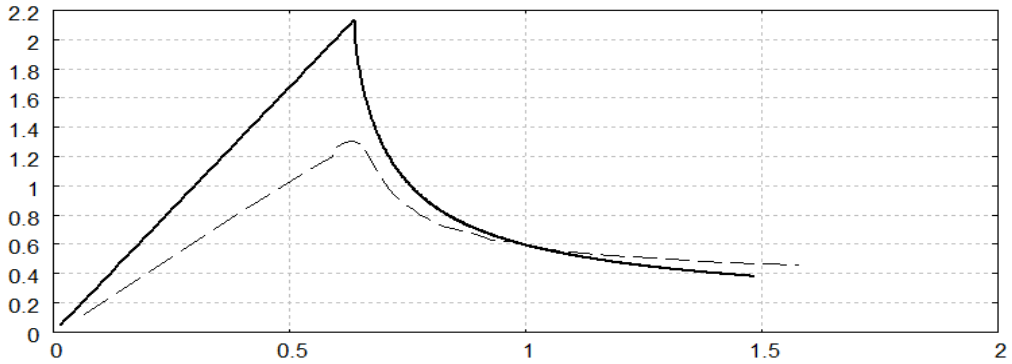

Figure 2. The force coefficient F_v as a function of non-dimensional penetration for the finite wedge of 30 degrees by the OWM (solid line) and by OpenFoam (dashed line).

4. Modified Logvinovich Model

Within MLM, we use the same shape of the fictitious body and equations (1) for the size of the wetted area and the speed of its expansion as in OWM. The force acting on the entering wedge is calculated by integrating the pressure only over the wedge surface. The formula for the force acting on an entering wedge by MLM was published by Korobkin (2004). This formula was updated to account for the cavity behind the wedge. First we calculate the coordinate $\tilde{x}(t)$ of the point on the wedge surface, at which the pressure is zero, if such a point exists. We introduce $\theta = \tilde{x}(t)/c(t)$ and χ such that $\theta = \sqrt{1-\chi^2}$. Then we consider the equation $\chi^2 \sin^2\gamma - 2\chi\dot{c}/\dot{h} + \cos^2\gamma = 0$ which is valid if the point $\tilde{x}(t)$ is on the wedge surface. If the latter equation has no real solution, it means that the point $\tilde{x}(t)$ is on the surface of the cavity behind the wedge. In this case we set $\tilde{x}(t) = B/2$. The force coefficient in MLM is given by

$$F_v = 2\frac{\dot{c}}{\dot{h}} \arcsin\theta - \frac{1}{2}\cos^2\gamma \log\left(\frac{1+\theta}{1-\theta}\right) - \theta\sin^2\gamma.$$

This force coefficient is shown in Figure 3 by the solid line. The dashed line shows the result by OpenFoam (Seng, 2012). It is seen that the MLM predicts the coefficient quite well during the impact stage but gives a wrong prediction at the separation stage. It is interesting to note that OWM predicts the force at the separation stage better than MLM.

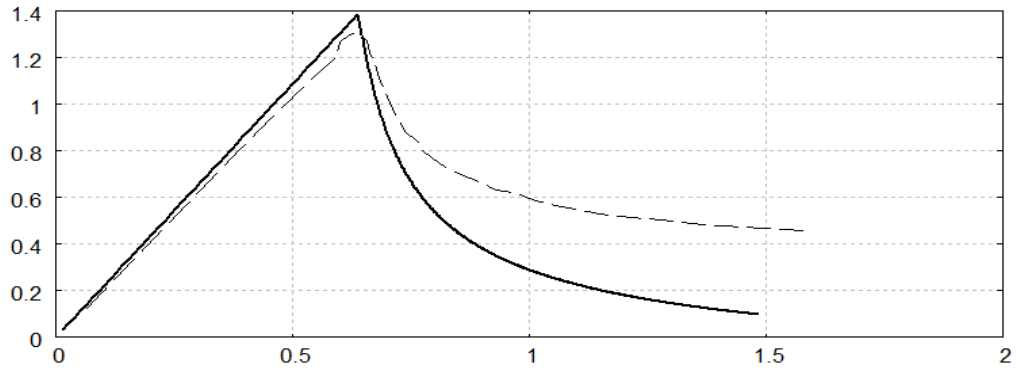

Figure 3. The force coefficient F_v as a function of non-dimensional penetration for the finite wedge of 30 degrees by the MLM (solid line) and by OpenFoam (dashed line).

5. Generalised Wagner Model

Calculations of the force acting on the wedge were performed by the GWM code (Korobkin, 2011) combined with the present model of separation (Figure 4).

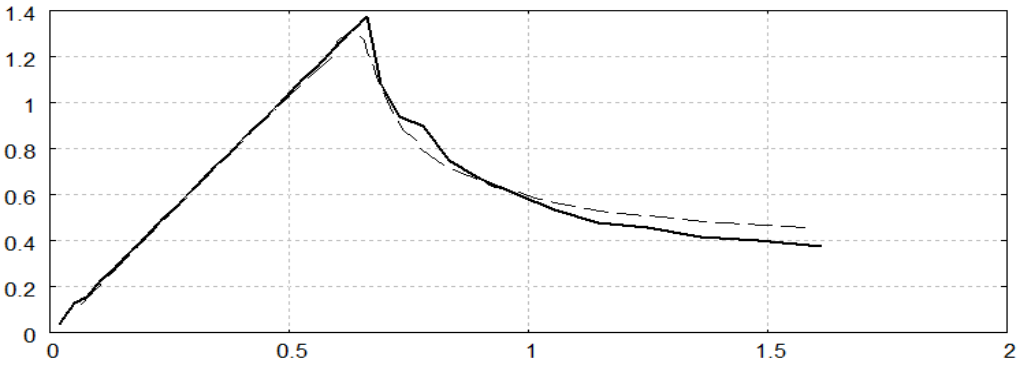

Figure 4. The force coefficient F_v as a function of non-dimensional penetration for the finite wedge of 30 degrees by the GWM (solid line) and by OpenFoam (dashed line).

It is seen that the GWM combined with the separation model suggested above predicts the force quite well during both the impact and separation stages. However, several problems with the GWM code were detected at the transition from the impact to separation stage.

This work is part of the project SMAES - Smart Aircraft in Emergency Situations - project number 266172 - of the Seventh Framework Programme (FP7).

References

Gurevich M.I. (1978) Theory of jets of ideal fluid. Nauka, Moscow, 536p. (in Russian)
Korobkin, A.A. (2004) Analytical models of water impact. European Journal of Applied Mathematics. Vol. 15, pp. 821-838.
Korobkin A.A. (2007) Second-order Wagner theory of wave impact. J. Eng. Math. Vol. 58, No. 1-4, pp 121-139.
Korobkin, A.A. (2011) Semi-analytical approach in generalised Wagner model. Proc. 26th Intern. Workshop on Water Waves and Floating Bodies, Athens, Greece, pp. 85-88.
Oliver J.M. (2007) Second-order Wagner theory for two-dimensional water-entry problems at small deadrise angles. J. Fluid Mech. 572, pp 59-85.
Seng S. (2012) On the approximation of the slamming force on 2D ship-like sections. 2nd Workshop on Springing and Whipping, November 2012, Split.

Trapping of time-harmonic waves by freely floating structures consisting of multiple bodies (motionless and/or heaving)

Nikolay Kuznetsov and Oleg Motygin

Laboratory for Mathematical Modelling of Wave Phenomena, Institute for Problems in Mechanical Engineering, Russian Academy of Sciences; V.O., Bol'shoy pr. 61, 199178 St Petersburg, RF
E-mail: Nikolay.G.Kuznetsov@gmail.com, O.V.Motygin@gmail.com

We study the coupled time-harmonic motion of the following mechanical system: infinitely deep water bounded above by a free surface and an immersed structure formed by a finite number $N \geqslant 2$ of surface-piercing bodies floating freely. The surface tension is neglected and the water motion is irrotational, whereas the motion of the whole system is of small amplitude near equilibrium. The latter assumption allows us to apply the linearized model proposed by John [1], which we write in the matrix form used in [3]. Our aim is to prove the existence of structures whose properties are as follows: (i) there exists a time-harmonic wave mode trapped by such a structure; (ii) some of the structure's bodies (may be none) are motionless, whereas the rest of the bodies (may be none) are heaving at the same frequency as water. Our construction is based on a generalization of the semi-inverse procedure (see [4] for a survey of this technique). The usual semi-inverse procedure was applied in [3] for obtaining infinitely many families such that every member of a certain family is a single *motionless* body floating freely; the corresponding trapped wave mode is common for each of these families. In the case of heaving bodies, a novel moment is that a subsidiary (with respect to the arising eigenvalue problem) condition guaranteeing the equilibrium is essential for verifying that the constructed structure floats freely.

1 Statement of the problem for multi-body structures

Let the Cartesian coordinates $(\boldsymbol{x},y)$, $\boldsymbol{x}=(x_1,x_2)$, be such that the y-axis is directed upwards, whereas the $\boldsymbol{x}$-plane coincides with the mean free surface of water. By $\widehat{B}_k$, $k=1,\dots,N$, we denote the domain occupied by the k-th body in its equilibrium position; its immersed part $B_k=\widehat{B}_k\cap\mathbb{R}^3_-\neq\emptyset$ can consist of several connected components (see fig. 1), $\mathbb{R}^3_-=\{\boldsymbol{x}\in\mathbb{R}^2,\,y<0\}$. Let $B=\cup_{k=1}^N B_k$ and $W=\mathbb{R}^3_-\setminus\overline{B}$ be the structure's submerged part and the water domain, respectively. The latter is supposed to be simply connected, but B has at least $N\geqslant 2$ connected components (see fig. 2); their number is greater than N if bodies like that shown in fig. 1 are present. Furthermore, $S_k=\partial B_k\cap\mathbb{R}^3_-$, $D_k=\widehat{B}_k\cap\{y=0\}$, $F=\{y=0\}\setminus(\cup_{k=1}^N\overline{D}_k)$ (see fig. 2), and $\boldsymbol{n}$ is the unit normal to ∂W directed to the exterior of W.

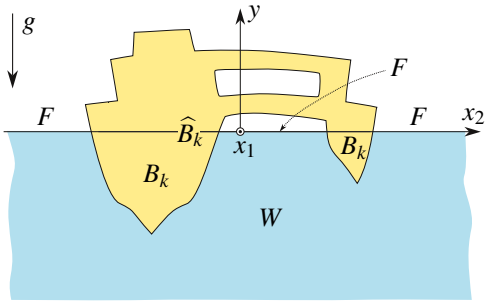

Figure 1: A body with two immersed parts.

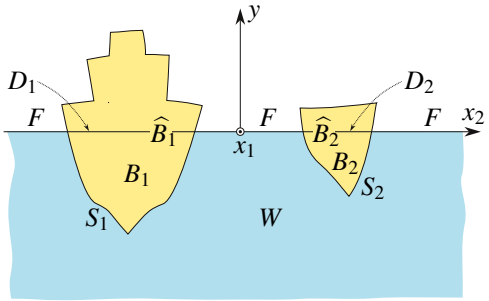

Figure 2: Definition sketch for two bodies.

The linearized time-dependent setting of the problem for $N=1$ was obtained in [1] (see [2] for its matrix form). In our case, the system's motion is described by the following first-order variables: the velocity potential $\Phi(\boldsymbol{x},y;t)$ and N vectors $\boldsymbol{q}^{(k)}(t)\in\mathbb{R}^6$. The latter characterize the motion of the centre of mass of the k-th body about its given rest position $\big(\boldsymbol{x}_0^{(k)},y_0^{(k)}\big)$; namely, the horizontal and vertical displacements are $q_1^{(k)}$, $q_2^{(k)}$ and $q_4^{(k)}$, respectively, whereas $q_3^{(k)}$ and $q_5^{(k)}$, $q_6^{(k)}$ are the angles of rotation about the axes that go through $\big(\boldsymbol{x}_0^{(k)},y_0^{(k)}\big)$ parallel to the y- and x_1-, x_2-axes, respectively. For studying time-harmonic oscillations of the radian frequency $\omega>0$ we put $\big(\Phi(\boldsymbol{x},y,t),\boldsymbol{q}^{(1)}(t),\dots,\boldsymbol{q}^{(N)}(t)\big)=\mathrm{Re}\big\{\mathrm{e}^{-\mathrm{i}\omega t}\big(\varphi(\boldsymbol{x},y),\mathrm{i}\boldsymbol{\chi}^{(1)},\dots,\mathrm{i}\boldsymbol{\chi}^{(N)}\big)\big\}$. Then the bounded complex-valued function φ and the vectors $\boldsymbol{\chi}^{(k)}\in\mathbb{C}^6$, $k=1,\dots,N$, must satisfy the following problem:

$$\nabla^2\varphi=0\ \text{ in } W;\quad \partial_y\varphi-\nu\varphi=0\ \text{ on } F;\quad \int_{W\cap\{|\boldsymbol{x}|=a\}}\big|\partial_{|\boldsymbol{x}|}\varphi-\mathrm{i}\nu\varphi\big|^2\,\mathrm{d}s=o(1)\ \text{ as }\ a\to\infty; \tag{1}$$

$$\partial_{\boldsymbol{n}}\varphi=\omega\,\boldsymbol{n}^{\mathsf{T}}\boldsymbol{D}_k\boldsymbol{\chi}^{(k)}\ \text{ on } S_k;\quad \omega^2\boldsymbol{E}_k\boldsymbol{\chi}^{(k)}=-\omega\int_{S_k}\varphi\boldsymbol{D}_k^{\mathsf{T}}\boldsymbol{n}\,\mathrm{d}s+g\,\boldsymbol{K}_k\boldsymbol{\chi}^{(k)}\quad\text{for every } k=1,\dots,N. \tag{2}$$

Here $\nabla = (\partial_{x_1}, \partial_{x_2}, \partial_y)$; $\nu = \omega^2/g$ and g is the acceleration due to gravity (see fig. 1); $^\mathsf{T}$ denotes the matrix transposition and $\boldsymbol{D}_k = \boldsymbol{D}\big(\boldsymbol{x} - \boldsymbol{x}_0^{(k)}, y - y_0^{(k)}\big)$, where $\boldsymbol{D}(\boldsymbol{x}, y) = \begin{bmatrix} 1 & 0 & x_2 & 0 & 0 & -y \\ 0 & 1 & -x_1 & 0 & y & 0 \\ 0 & 0 & 0 & 1 & -x_2 & x_1 \end{bmatrix}$. Two matrices in the equation of motion of the k-th body [the 2nd condition (2)] are as follows: $\boldsymbol{E}_k = \rho_0^{-1} \int_{\widehat{B}_k} \rho_k(\boldsymbol{x}, y)\, \boldsymbol{D}_k^\mathsf{T}(\boldsymbol{x}, y)\, \boldsymbol{D}_k(\boldsymbol{x}, y)\, \mathrm{d}\boldsymbol{x}\, \mathrm{d}y$;

$$\boldsymbol{K}_k = \begin{bmatrix} \mathbb{O}_3 & \mathbb{O}_3 \\ \mathbb{O}_3 & \boldsymbol{K}_k' \end{bmatrix}, \text{ where } \boldsymbol{K}_k' = \begin{bmatrix} I^{D_k} & I_2^{D_k} & -I_1^{D_k} \\ I_2^{D_k} & I_{22}^{D_k} + I_y^{B_k} & -I_{12}^{D_k} \\ -I_1^{D_k} & -I_{12}^{D_k} & I_{11}^{D_k} + I_y^{B_k} \end{bmatrix} \text{ and } \mathbb{O}_3 \text{ is the } 3\times 3 \text{ null matrix; } I^{D_k} = \int_{D_k} \mathrm{d}\boldsymbol{x},$$

$$I_i^{D_k} = \int_{D_k} \big(x_i - x_{0i}^{(k)}\big)\, \mathrm{d}\boldsymbol{x},\ I_{ij}^{D_k} = \int_{D_k} \big(x_i - x_{0i}^{(k)}\big)\, \big(x_j - x_{0j}^{(k)}\big)\, \mathrm{d}\boldsymbol{x},\ I_y^{B_k} = \int_{B_k} \big(y - y_0^{(k)}\big)\, \mathrm{d}\boldsymbol{x}\, \mathrm{d}y,\ \ i, j = 1, 2.$$

The elements of $\boldsymbol{E}_k$ are various moments of the whole body $\widehat{B}_k$ (see [3]); $\rho_k(\boldsymbol{x}, y) \geqslant 0$ is the distribution of density within the k-th body and $\rho_0 > 0$ is the constant density of water. All these 6×6 matrices are symmetric and positive definite. Every matrix $\boldsymbol{K}_k$ (it is related to buoyancy of the k-th body; see [1]) is symmetric as well.

Problem (1)–(2) must be augmented by conditions guaranteeing equilibrium for each of N floating bodies: • $I_\rho^{\widehat{B}_k} = \rho_0^{-1} \int_{\widehat{B}_k} \rho_k(\boldsymbol{x}, y)\, \mathrm{d}\boldsymbol{x}\, \mathrm{d}y = \int_{B_k} \mathrm{d}\boldsymbol{x}\, \mathrm{d}y$ (Archimedes' law for the k-th body); • $\int_{B_k} \big(x_i - x_{0i}^{(k)}\big)\, \mathrm{d}\boldsymbol{x}\, \mathrm{d}y = 0$, $i = 1, 2$ (the centre of buoyancy of the k-th body and that of its mass lie on the same vertical line); • $\boldsymbol{K}_k'$ is a positive definite matrix (this implies the stability of the equilibrium position for the k-th body; see [1, § 2.4]).

The boundedness of φ implies that $\nabla\varphi$ decays as $y \to -\infty$; the radiation condition [the 3rd condition (1)] means that waves are outgoing at infinity. In the same way as in [3], one proves the following assertion about the energy of the coupled system.

Let $(\varphi, \chi^{(1)}, \ldots, \chi^{(N)})$ satisfy problem (1)–(2). *Then φ belongs to the Sobolev space $H^1(W)$ and $\int_F |\varphi|^2\, \mathrm{d}\boldsymbol{x} < \infty$, that is, the kinetic and potential energy of the water motion is finite. Moreover, the equality*

$$\int_W |\nabla\varphi|^2\, \mathrm{d}\boldsymbol{x}\, \mathrm{d}y + \omega^2 \sum_{k=1}^N \overline{\boldsymbol{\chi}}^{(k)\mathsf{T}} \boldsymbol{E}_k \boldsymbol{\chi}^{(k)} = \nu \int_F |\varphi|^2\, \mathrm{d}\boldsymbol{x} + g \sum_{k=1}^N \overline{\boldsymbol{\chi}}^{(k)\mathsf{T}} \boldsymbol{K}_k \boldsymbol{\chi}^{(k)}$$

expresses the equipartition of energy of the system's motion.

In what follows, we suppose that φ is a real element of $H^1(W)$ and $\boldsymbol{\chi}^{(k)} \in \mathbb{R}^6$, $k = 1, \ldots, N$, because the real and imaginary part of any solution separately satisfy problem (1)–(2). Such a real solution $\big(\varphi, \boldsymbol{\chi}^{(1)}, \ldots, \boldsymbol{\chi}^{(N)}\big)$ is called a *trapped mode*, whereas the corresponding value of ω is called a *trapping frequency*.

2 Trapped modes with axisymmetric velocity fields

Since we are interested in trapped modes with axisymmetric velocity fields, we consider structures consisting of axisymmetric bodies (motionless and/or heaving). In order to find them we apply a modification of the semi-inverse procedure applied in [3]; this modification uses not only a special choice of the velocity potential, but also a particular form of the vectors $\boldsymbol{\chi}^{(k)}$. Namely, we fix $\omega > 0$ and seek a trapped mode in the form $\big(\omega\nu^{-2}\varphi_*, \boldsymbol{d}\boldsymbol{\chi}_*^{(1)}, \ldots, \boldsymbol{d}\boldsymbol{\chi}_*^{(N)}\big)$, where $\boldsymbol{d}$ is the diagonal matrix $\mathrm{diag}\{\nu^{-1}, \nu^{-1}, 1, \nu^{-1}, 1, 1\}$ and φ_*, $\boldsymbol{\chi}_*^{(k)}$ are dimensionless. We put

$$\varphi_*(\nu|\boldsymbol{x}|, \nu y) = 2\int_0^\infty (k\cos k\nu y + \sin k\nu y)\, P(k\nu|\boldsymbol{x}|)\, Q(k\nu r)\, \frac{k^2\, \mathrm{d}k}{k^2 + 1} - \pi^2 \mathrm{e}^{\nu y} L(\nu|\boldsymbol{x}|)\, M(\nu r), \quad y \leqslant 0. \tag{3}$$

Here $P = I_0$, $Q = K_1$, $L = J_0$ and $M = Y_1$ for $|\boldsymbol{x}| < r$, whereas $P = K_0$, $Q = I_1$, $L = Y_0$ and $M = J_1$ for $|\boldsymbol{x}| > r$. The value $r > 0$ is specified below; Y_0, Y_1 are the Neumann functions; J_0, J_1 and I_0, I_1, K_0, K_1 denote the standard and modified Bessel functions of the indicated orders, respectively. It is easy to check that φ_* is a non-dimensional harmonic function in $\mathbb{R}^3_-$. Moreover, the boundary condition $\partial_y\varphi_* - \nu\varphi_* = 0$ holds on $\partial\mathbb{R}^3_- \setminus \{|\boldsymbol{x}| = r, y = 0\}$, and φ_* has a singularity on the excluded circumference. Putting $r = r_m = \nu^{-1} j_{1,m}$, where $j_{1,m}$ is the m-th positive zero of J_1, we get that the last term in (3) vanishes for $|\boldsymbol{x}| > r$. We denote φ_* with $r = r_m$ by φ_m and see that $\varphi_m \in H^1(W)$ when W is a domain obtained by removing some neighbourhood of $\{|\boldsymbol{x}| = r_m, y = 0\}$ from $\mathbb{R}^3_-$. Therefore, φ_m can serve as the first component of a trapped mode provided m and a water domain are chosen properly. It is essential that the choice will also depend on the N-tuple $\big(\boldsymbol{\chi}_*^{(1)}, \ldots, \boldsymbol{\chi}_*^{(N)}\big)$. We take $\boldsymbol{\chi}_*^{(k)}$ in the form $(0, 0, 0, H_k, 0, 0)^\mathsf{T}$, and so $H_k = 0$ for a motionless body and $H_k > 0$ for a heaving body.

In order to define a water domain we use the Stokes stream function ψ_m corresponding to φ_m through the following relations:

$$\partial_{|\boldsymbol{x}|}\varphi_m = -(\nu|\boldsymbol{x}|)^{-1}\partial_y\psi_m, \quad \partial_y\varphi_m = (\nu|\boldsymbol{x}|)^{-1}\partial_{|\boldsymbol{x}|}\psi_m, \tag{4}$$

thus getting $\psi_m(\nu|\boldsymbol{x}|,\nu y) = -\pi^2\nu|\boldsymbol{x}|e^{\nu y}J_1(\nu|\boldsymbol{x}|)\,Y_1(j_{1,m}) - 2\nu|\boldsymbol{x}|\,\Psi(\nu|\boldsymbol{x}|,\nu r_m,\nu y)$, $|\boldsymbol{x}| < r_m$, $y \leqslant 0$, and

$$\psi_m(\nu|\boldsymbol{x}|,\nu y) = -2\nu|\boldsymbol{x}|\,\Psi(\nu r_m,\nu|\boldsymbol{x}|,\nu y), \quad |\boldsymbol{x}| > r_m,\ y \leqslant 0,$$

where $\Psi(\sigma,\tau,\eta) = \int_0^\infty (k\sin k\eta - \cos k\eta)\,I_1(k\sigma)\,K_1(k\tau)\,\dfrac{k^2\,\mathrm{d}k}{k^2+1}$ and the constant of integration is chosen so that $\psi_m(\nu|\boldsymbol{x}|,\nu y) \to 0$ as $\nu^2(|\boldsymbol{x}|^2+y^2) \to \infty$.

Relations (4) yield that $\partial_{\boldsymbol{n}}\varphi_m = 0$ on every surface in $\mathbb{R}^3_-$, where $\psi_m = \text{const}$. Some properties of streamlines $\psi_m(\nu|\boldsymbol{x}|,\nu y) = v$ for various values of v will be used below. In particular, all these lines are smooth in $\{|\boldsymbol{x}| > 0, y < 0\}$; if $v \neq 0$, then the line's end-points belong to the boundary of this quadrant, whereas one end can be at infinity when $v = 0$; a streamline emanates from every point on the half-axis $\{\nu|\boldsymbol{x}| > 0, \nu y = 0\}$ and the only exceptions are $(j_{1,m},0)$ and those points, where $\psi_m(\nu|\boldsymbol{x}|,0)$ attains its local extrema. Moreover, $\psi_m(\nu|\boldsymbol{x}|,\nu y) \to +\infty$ as $\nu^2[(|\boldsymbol{x}|-r_m)^2+y^2] \to 0$ and $y \leqslant 0$.

3 Construction of freely floating multi-body structures

3.1. Motionless structures. The above-listed properties of ψ_m, $m = 1,2,\ldots$, allow us to consider every bounded surface in $\mathbb{R}^3_-$ on which $\psi_m = \text{const}$ (the only exceptions are unbounded nodal surfaces) as the rigid wetted boundary of a motionless axisymmetric body semi-immersed into water (see [3] for details in the case $N = 1$). Fig. 3 (b) shows the vertical radial cross-section of 2 such bodies defined by $\psi_2(\nu|\boldsymbol{x}|,\nu y)$; this function can also be used for defining 3 bodies like that located in the middle below the body with 2 immersed parts. We even have $m < N$ in this example, but m must be sufficiently large for guaranteeing $N-1$ changes of sign for $\psi_m(\nu|\boldsymbol{x}|,0)$ when $0 < \nu|\boldsymbol{x}| < j_{1,N}$ (this yields the existence of N bodies).

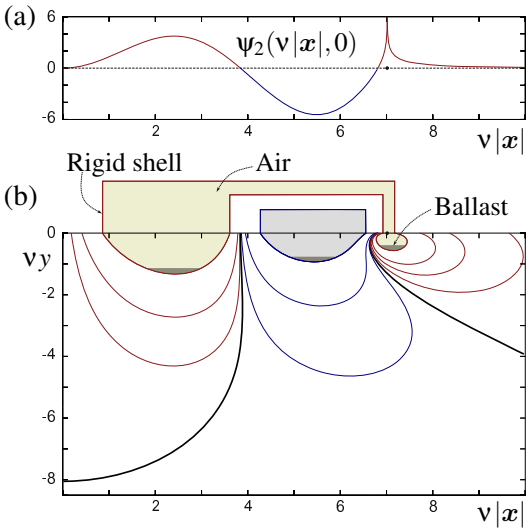

Figure 3: (a) The trace $\psi_2(\nu|\boldsymbol{x}|,0)$. (b) Streamlines $\psi_2(\nu|\boldsymbol{x}|,\nu y) = v$ for various values of v; nodal lines ($v = 0$) are bold. Straight segments show how wetted surfaces are connected above the free surface to form 2 bodies. Darkly shaded layers show the ballast guaranteeing that the bodies are in equilibrium.

Thus, using ψ_2 we defined a motionless structure and now it is necessary to check that it is freely floating. (In the general case, we have to show that $(\varphi_m, \mathbf{0}, \ldots, \mathbf{0})$, where $\mathbf{0}$ (the zero element of $\mathbb{R}^6$) is repeated N times, is a trapped mode for a structure of this type.) For this purpose it remains to verify that the following $6N$ equalities hold [see the 2nd equation (2)]: $\int_{S_k} \varphi\,\boldsymbol{D}_k^{\mathrm{T}}\boldsymbol{n}\,\mathrm{d}s = 0$, $k = 1,\ldots,N$. As in the case of a single body, $5N$ of these integrals vanish when all surfaces S_k are axisymmetric (see details in [3], Appendix). Therefore, it remains to show that $\int_{S_k}\varphi_m\partial_{\boldsymbol{n}}y\,\mathrm{d}s = 0$, $k = 1,\ldots,N$, when $\partial_{\boldsymbol{n}}\varphi_m = 0$ on S_k. Let the constructed bodies be numbered so that $\widehat{B}_N$ contains the singularity circumference $\{|\boldsymbol{x}| = r_m, y = 0\}$ inside. (It is the doubly immersed body in fig. 3.) First, we apply the method used in [3], Appendix, for proving that $\int_{S_N}\varphi_m\partial_{\boldsymbol{n}}y\,\mathrm{d}s = 0$. It involves the 2nd Green's formula written for the functions φ_m and $y+\nu^{-1}$ in the domain $(\mathbb{R}^3_- \setminus \overline{B}_N)\cap C_{\rho,\delta}$; here $C_{\rho,\delta} = \{|\boldsymbol{x}| < \rho\,,\ -\delta < y < 0\}$ and $\rho\,,\,\delta > 0$ are taken so that $B_N \subset C_{\rho,\delta}$. Then the required result follows from the boundary conditions, the behaviour of φ_m as $y \to -\infty$ and the Riemann–Lebesgue lemma applied as $\delta \to +\infty$. Then the same procedure yields the result for every $k = 1,\ldots,N-1$, but the domain must be changed to $(\mathbb{R}^3_- \setminus \overline{B_N \cup B_k})\cap C_{\rho,\delta}$ and the fact obtained on the previous step must be taken into account.

Of course, the ballast density within each body is to be chosen so that the conditions guaranteeing the body's equilibrium are fulfilled (see [3], § 3.3, for details).

3.2. Heaving structures. Let us turn to constructing N-body trapping structures heaving so that $H_k = H > 0$ in $\boldsymbol{\chi}_*^{(k)}$ for all k. For this purpose we modify our method outlined in sect. 3.1 as follows. We require a structure to be formed by bodies for which every S_k is a surface of constant level

$$\psi_m^{(H)}(\nu|\boldsymbol{x}|,\nu y) = \text{const}, \quad \text{where} \quad \psi_m^{(H)}(\nu|\boldsymbol{x}|,\nu y) = \psi_m(\nu|\boldsymbol{x}|,\nu y) - (\nu|\boldsymbol{x}|)^2 H/2\,. \tag{5}$$

If H is sufficiently small, then these level surfaces have properties similar to those listed at the end of sect. 2. Hence relations (4) imply that $\partial_{\boldsymbol{n}}(\varphi_m - H\nu y) = 0$ on every $S_k \subset \mathbb{R}^3_-$, $k = 1,\ldots,N$, and so the 1st condition (2) describes the heave motion of the whole structure. Again we choose S_N so that it separates the singularity of $\psi_m^{(H)}$ from infinity.

Fig. 4 (b) shows the vertical radial cross-section of 2 such bodies defined by $\psi_1^{(H)}(\nu|\boldsymbol{x}|,\nu y)$ with $H=0.1$. In this example of a heaving structure defined with the help of $\psi_1^{(H)}$, we have $m<N$ (cf. sect. 3.1); however, generally, m must be sufficiently large and H must be sufficiently small to guarantee the existence of N bodies.

It remains to verify the equations of motion [the 2nd condition (2)] for the constructed heaving structure which are as follows for axisymmetric bodies:

$$\nu H I_\rho^{\widehat{B}_k} = -\int_{S_k} \varphi_1 \partial_{\boldsymbol{n}} y \,\mathrm{d}s + H I^{D_k}, \quad k=1,2; \qquad (6)$$

we restrict ourselves by the case shown in fig. 4 (b). In order to check (6) we begin with applying the 2nd Green's formula to φ_1 and $y+\nu^{-1}$ in $(\mathbb{R}^3_- \setminus \overline{B}_2)\cap C_{\rho,\delta}$, where positive ρ, δ are taken so that $B_2 \subset C_{\rho,\delta}$. As in sect. 3.1, considerations based on the boundary conditions, the behaviour of φ_1 as $y\to-\infty$ and the Riemann–Lebesgue lemma with $\delta\to+\infty$ are applicable, but now we obtain that

$$\int_{S_2} \varphi_1 \partial_{\boldsymbol{n}} y \,\mathrm{d}s = H\nu \int_{S_2} (y+\nu^{-1})\,\partial_{\boldsymbol{n}} y \,\mathrm{d}s = -H\nu \int_{B_2} \mathrm{d}\boldsymbol{x}\mathrm{d}y + H I^{D_2}.$$

Substituting this into (6) with $k=2$, we see that (6) is true because it reduces to Archimedes' law for $\widehat{B}_2$. Then the same procedure yields the result for $k=1$, but the domain must be changed to $(\mathbb{R}^3_- \setminus \overline{B_1 \cup B_2})\cap C_{\rho,\delta}$ and the fact obtained on the previous step must be taken into account as well as Archimedes' law for $\widehat{B}_1$.

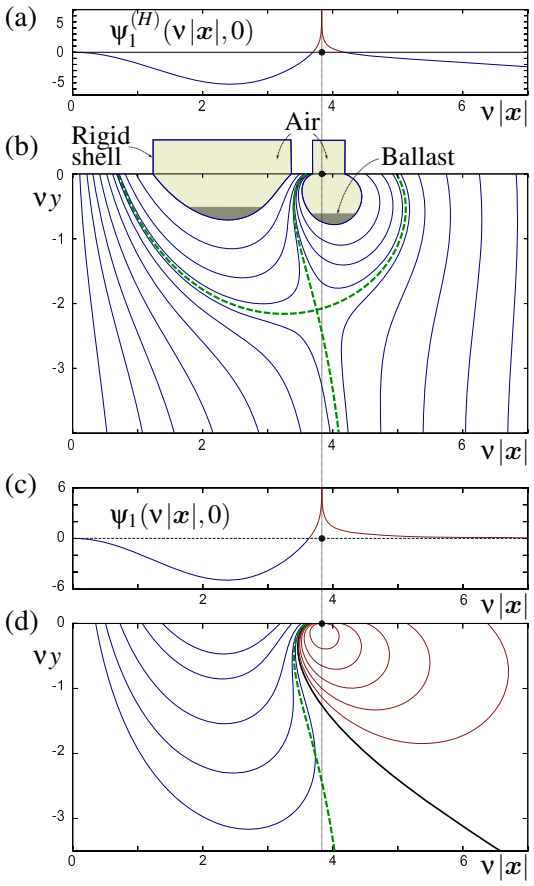

Figure 4: (a) The trace $\psi_1^{(H)}(\nu|\boldsymbol{x}|,0)$ with $H=0.1$. (b) Streamlines $\psi_1^{(H)}(\nu|\boldsymbol{x}|,\nu y)=v$ are plotted for $H=0.1$ and various $v\leqslant 0$; the nodal line ($v=0$) serves as S_2 (the wetted boundary of the right body); straight segments connect wetted surfaces above the free surface to form two bodies; two dashed lines ($v\approx -0.9464$) separate four different families of level lines. (c) The trace $\psi_1(\nu|\boldsymbol{x}|,0)$. (d) The dashed line is taken from (b); streamlines $\psi_1(\nu|\boldsymbol{x}|,\nu y)=v$ are plotted for various values of v; the nodal line ($v=0$) is bold.

3.3. Structures formed by motionless and heaving bodies. First, we consider $(\omega\nu^{-2}\varphi_1, \boldsymbol{0}, \boldsymbol{d}\boldsymbol{\chi}_2)$, where $\boldsymbol{\chi}_2 = (0,0,0,H,0,0)^{\mathsf{T}}$. It is clear that this triplet serves as a mode trapped by an axisymmetric structure formed by the heaving body $\widehat{B}_2$ defined in sect. 3.2 [the right body in fig. 4 (b)] and any motionless body obtained by rotation of the following domain: it is the union of the rectangle adjacent to the domain enclosed between the $\nu|\boldsymbol{x}|$-axis and a streamline of ψ_1 located to the left of the dashed curve in fig. 4 (d).

Now we take $(\omega\nu^{-2}\varphi_1, \boldsymbol{d}\boldsymbol{\chi}_1, \boldsymbol{0})$, where $\boldsymbol{\chi}_1$ is the same as $\boldsymbol{\chi}_2$ above. Hence this triplet serves as the mode trapped by an axisymmetric structure formed by the heaving body $\widehat{B}_1$ defined in sect. 3.2 [the left body in fig. 4 (b)] and any motionless body obtained by rotation of the following domain: it is the union of the rectangle adjacent to the domain enclosed between the $\nu|\boldsymbol{x}|$-axis and a streamline of ψ_1 located to the right of the dashed curve in fig. 4 (d).

4 Conclusion

Generalizing considerations of sect. 3, one obtains the following

Theorem. *For any $\omega>0$ and arbitrary integers $N\geqslant 2$ and n, $0\leqslant n\leqslant N$, there exists an axisymmetric trapping structure that consists of N bodies and has the following properties:* (i) $\left(\omega\nu^{-2}\varphi_m, \boldsymbol{d}\boldsymbol{\chi}_*^{(1)}, \dots, \boldsymbol{d}\boldsymbol{\chi}_*^{(N)}\right)$ *is the corresponding trapped mode (see its description in sect. 2), where m is sufficiently large and H_k in $\boldsymbol{\chi}_*^{(k)}$ is an arbitrary non-negative number lesser than $2\pi^2|Y_1(j_{1,m})J_1(j'_{1,N})|/j'_{1,N-1}$ ($j'_{1,\ell}$ is the ℓ-th positive zero of J'_1);* (ii) *all bodies float freely, n of them are motionless and described by properly chosen level lines of ψ_m, the remaining $N-n$ bodies are heaving and described by chosen in a special way level lines of functions* (5).

References:

[1] John, F. 1949 *Comm. Pure Appl. Math.* **2**, 13–57.

[2] Kuznetsov, N., Motygin, O. 2011 *J. Fluid Mech.* **679**, 616–627.

[3] Kuznetsov, N., Motygin, O. 2012 *J. Fluid Mech.* **703**, 142–162.

[4] Neményi, P. F. 1951 *Adv. Appl. Mech.* **2**, 123–148.

The 28th International Workshop on Water Waves and Floating Bodies
IWWWFB 2013
April 7-10, 2013, L'Isle sur la Sorgue, France

Towards Real Time Simulation of Ship-Ship Interaction - Part II: Double Body Flow Linearization and GPU Implementation*

Ole Lindberg †[1], Stefan L. Glimberg[2], Harry B. Bingham[3], Allan P. Engsig-Karup[2], and Peter J. Schjeldahl[1]

[1] *FORCE Technology, Department of Simulation, Training and Ports, DK-2800 Kgs. Lyngby, Denmark*
[2] *Technical University of Denmark, Department of Applied Mathematics and Computer Science, DK-2800 Kgs. Lyngby, Denmark*
[3] *Technical University of Denmark, Department of Mechanical Engineering, DK-2800 Kgs. Lyngby, Denmark*

The marine industry uses full mission marine simulators for training naval officers and as a tool in marine engineering. The quality of the training and the engineering assessments relies on the realism and visual presentation of the simulated ocean waves, ship waves and ship-ship interaction forces. Ambient ocean waves are often calculated by FFT's of a wave spectrum. Realistic real time calculation of ship waves are not available in ship simulators today. Ship-ship interaction forces are calculated using boundary element models or based on model experiments in towing tanks and precomputed force tables. The present work is motivated by 1) The need for ship wave calculation and more accurate and reliable ship-ship interaction force calculations in full mission marine simulators, 2) The development of new numerically accurate and computational efficient large scale ocean wave and ship wave models, and 3) The availability of affordable Graphical Processing Units (GPU's) ideal for high performance scientific computing. The main challenge is the real time constraint, which limits how complex the physical model can be and still have a computationally efficient and fast numerical solution. An ever changing simulated environment and human interaction are other challenges for the robustness and flexibility of the model. To meet these challenges, the physical model has to be simple, but still accurately representing the kinematic and dynamic effects of water waves and ship motions. The approach adopted is that described at last year's workshop Lindberg et al. [2012] and involves a simplified geometric representation of the ship hull by means of a dynamic pressure distribution applied on the free-surface; together with a GPU optimized fast Laplace solver based on high-order finite differences Engsig-Karup et al. [2009], Engsig-Karup et al. [2011].

Free Surface Flow and Ship Model

The mathematical model describing the flow around the ships and the wave motion is based on potential flow theory and the equations are presented in a ship fixed moving frame of reference

$$x = x_0 - Ut, \quad y = y_0, \quad z = z_0, \tag{1}$$

where (x_0, y_0, z_0) is the earth fixed frame of reference, t is time and U is the ship velocity positive x-direction. The water velocity is the gradient of the velocity potential $\boldsymbol{u} = (u, v, w)^T = \nabla\phi$. Continuity

*We wish to thank Maritime Development Center of Europe, FORCE Technology, DTU Mechanical Engineering and DTU Informatics for supporting this project and the Danish Center for Scientific Computing for providing supercomputing resources.
†Email: old@force.dk

requires the velocity potential to satisfy the Laplace equation

$$\nabla^2\phi = 0, \quad -h \le z \le \eta, \tag{2}$$

where $h = h(x, y)$ is the sea depth and $\eta = \eta(x, y)$ is the free surface elevation. The evolution of the free surface is described by the kinematic free surface boundary condition

$$\frac{\partial \eta}{\partial t} + (u - U)\frac{\partial \eta}{\partial x} + v\frac{\partial \eta}{\partial y}\phi = \frac{\partial \phi}{\partial z}, \quad z = \eta, \tag{3}$$

and the evolution of the free surface velocity potential is described by the dynamic free surface boundary condition

$$\frac{\partial \phi}{\partial t} - U\frac{\partial \phi}{\partial x} + \frac{1}{2}\boldsymbol{u}\cdot\boldsymbol{u} + g\eta + \frac{p}{\rho} = 0, \quad z = \eta, \tag{4}$$

where $g = 9.81 m/s^2$ is the gravitational acceleration, p is the pressure and $\rho \approx 1000 kg/m^3$ is the density. Note that the Bernoulli constant in the dynamic boundary condition is zero.

These equations comprise the fully nonlinear water wave problem and they are solved in a time dependent physical domain with a moving free surface boundary. Some complexity has to be removed to solve these equations in real time. The approximations start with perturbation expansions of the velocity potential and the free surface elevation

$$\phi = \phi_0 + \varepsilon\phi_1 + \varepsilon^2\phi_2 + \ldots, \quad \eta = \eta_0 + \varepsilon\eta_1 + \varepsilon^2\eta_2 + \ldots, \tag{5}$$

where the parameter ε is the ratio between the wave elevation and wave length $\varepsilon = H/\lambda$. The free surface velocity potential is further expanded in a Taylor series with respect to the still water level. The zero-order term is calculated either by a Neumann-Kelvin linearization $\phi_0 = Ux$ or a double body flow linearization

$$\begin{aligned}
\nabla^2\phi_0 &= 0, \quad -h \le z \le 0, & (6)\\
\boldsymbol{n}\cdot\nabla\phi_0 &= -n_x U, \quad (x, y) \in \Gamma_{ship}, & (7)\\
\frac{\partial \phi_0}{\partial z} &= 0, \quad (x, y) \notin \Gamma_{ship},\ z = 0, & (8)\\
\frac{\partial \phi_0}{\partial z} &= 0, \quad z = -h. & (9)
\end{aligned}$$

where $\boldsymbol{n} = (n_x, n_y, n_z)$ is the normal vector of the ship hull surface Γ_{ship}. Currently we are working with two approximations of the body boundary condition: a flat ship approximation and a pressure distribution representation. The first order solution is calculated from the kinematic and dynamic boundary conditions which are linearized around the steady solution

$$\begin{aligned}
\frac{\partial \eta}{\partial t} + \left(\frac{\partial \phi_0}{\partial x} - U\right)\frac{\partial \eta}{\partial x} + \frac{\partial \phi_0}{\partial y}\frac{\partial \eta}{\partial y} &= \eta\frac{\partial^2 \phi_0}{\partial z^2} + \frac{\partial \phi_1}{\partial z}, & (10)\\
\frac{\partial \phi_1}{\partial t} + \left(\frac{\partial \phi_0}{\partial x} - U\right)\frac{\partial \phi_1}{\partial x} + \frac{\partial \phi_0}{\partial y}\frac{\partial \phi_1}{\partial y} + g\eta + \frac{p}{\rho} &= 0, \quad z = 0, & (11)
\end{aligned}$$

where the pressure is zero on the free surface $(x, y) \in \Gamma_{FS}$ and determined by the following quasistatic approximation on the ship hull

$$p = -\rho\left(\left(\frac{\partial \phi_0}{\partial x} - U\right)\frac{\partial \phi_1}{\partial x} + \frac{\partial \phi_0}{\partial y}\frac{\partial \phi_1}{\partial y} + g\eta_0\right), \quad (x, y) \in \Gamma_{ship},\ z = 0. \tag{12}$$

Here it is assumed that the ship hull can be represented by a single valued function of the horizontal coordinates $\eta_0 = \eta_0(x, y)$.

Finally the radiation boundary condition

$$\phi = \begin{cases} \mathcal{O}\left((x^2 + y^2)^{-1/2}\right) \\ \mathcal{O}(1) \end{cases} \quad \text{as } x^2 + y^2 \to \infty \quad \text{for} \quad \begin{cases} x > 0 \\ x < 0 \end{cases} \tag{13}$$

is approximated by the zero'th order absorbing boundary condition

$$\frac{\partial \phi}{\partial t} + (Cn_x - U)\frac{\partial \phi}{\partial x} + Cn_y \frac{\partial \phi}{\partial y} = 0, \quad (x, y, z) \in \Gamma_A, \tag{14}$$

where $C = \sqrt{gh}$ is the wave celerity of absorbed wave component and Γ_A is the artificial physical domain boundary. This boundary condition is most efficient for shallow water waves and a wave direction normal to the boundary. Efficient absorbing boundary conditions for dispersive and possibly non-linear water waves at large angles is an advanced and open question for the water wave community.

Numerical Approximations and Solvers

The Laplace equation (2) for the potential is approximated by higher-order finite differences and solved by a multigrid preconditioned defect correction (PDC) method, Engsig-Karup et al. [2011]. The PDC enables efficient solution due to linear scaling in both computational work and memory. An explicit higher-order Runge-Kutta method is used for the temporal discretization of the linear kinematic free surface boundary condition (10) and dynamic free surface boundary condition (11) and the absorbing boundary condition (14). The functions for the free surface elevation η and the free surface potential ϕ have kinks at the waterlines of the ships and steep gradients in the vicinity of the ship hulls, which can give spurious oscillation in the numerical approximations of these functions and their derivatives. The derivatives are therefore approximated by the the higher-order Weighted Essentially Non-Oscillatory (WENO) method and the advective terms in the kinematic (10) and (11) are evaluated by the Hamilton-Jacobi WENO method with Lax-Friedrics flux Osher and Shu [1991].

Parallel GPU Implementation

The development of massively parallel GPUs within recent years has made GPUs attractive for a broad range of computationally intense applications within scientific computing and engineering. We find that GPUs are ideal for computing the ship wave and ship-ship interactions, not only because the numerical model fits the parallel architecture well, but also because the ocean waves should eventually be rendered in the marine simulator by the GPU itself. We have used an in-house developed library, based on the CUDA programming model, for assembling the solver. All finite difference operators are implemented as flexible-order matrix-free operators, in order to exploit that only a few different stencil coefficients are required. In this way we are able to keep memory consumption and memory access low, two important properties for obtaining good performance on GPU systems. Preliminary results indicate reasonable performance speedups compared to similar CPU-based implementations in the order of one to two magnitudes. Future work is still to prove if the real time calculations are possible given the currently proposed numerical model and hardware.

Tests, Validation and Applications

The model needs to calculate ship waves and ship forces and moments accurately. The kinematic and dynamic properties of the linearizations (Kelvin-Neumann and double body flow) and approximation of ship hull boundary conditions (flat ship and pressure distribution) are investigated. The convergence of the numerical approximations are tested to determine the optimal order of finite difference and WENO approximations and the required mesh resolution. Different types of finite difference meshes are investigated. In particular meshes with clustering of points close to the free surface, close to the ships and dynamic adaption based on error indicators.

An example of a convergence study is seen in figure 1 where the wave resistance is calculated on a Series 60 CB 0.6 model for Froude numbers in the range $Fr = 0.1, \ldots, 0.35$, Toda et al. [1992]. The number of points in the vertical direction are increased $N_z = 9, 10, 13, 17$ while the number of points in the horizontal directions are fixed at $(N_x, N_y) = (513, 385)$. Other numerical parameters are: 4th order finite difference, 2nd/4th order WENO and 4th order Runge-Kutta. The mesh points are clustered close to the free surface and around the ship. It is seen that at least 17 points are needed in the vertical direction and that the best agreement with the experimental data is found in the range $Fr = 0.1, \ldots, 0.25$. At the workshop more result on convergence and computational efficiency will be presented and most importantly a ship-ship interaction validation case with a tug besides a tanker Simonsen et al. [2012].

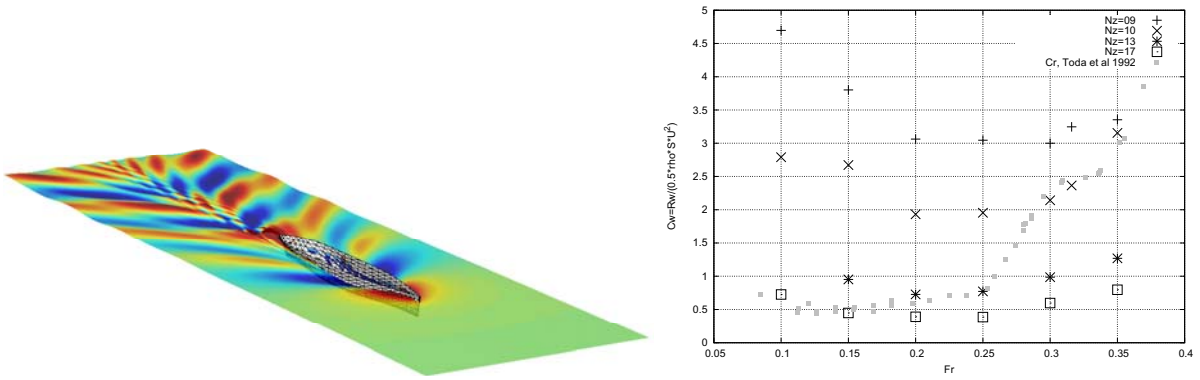

Figure 1: Left: A Series 60 CB 0.6 model at steady forward speed with $Fr = 0.316$. Right: Wave resistance for as a function of the Froude number and different N_z.

Conclusion

We have presented a linear free surface flow model for real time calculation of ship waves and ship-ship interaction in a full mission marine simulator. The model is currently being implemented for parallel excecution on GPU's. In the time ahead it will be verified, tested and optimized. Validation test on forward speed and ship-ship interaction cases are carried out to determine the required numerical resolution and the model accuracy. An example of a convergence study on Series 60 CB 0.6 has been presented and it is seen that at least $(Nx, Ny, Nz) = (513, 385, 17)$ points are required. At the workshop we will present more convergence and performance results along with a ship-ship interaction case between a tug and a tanker.

A. P. Engsig-Karup, H. B. Bingham, and O. Lindberg. An Efficient Flexible-Order Model for 3D Nonlinear Water Waves. *J. Comput. Phys.*, 228:2100–2118, 2009.

A. P. Engsig-Karup, M. G. Madsen, and S. L. Glimberg. A Massively Parallel GPU-Accelerated Model for Analysis of Fully Nonlinear Free Surface Waves. *Int. J. Num. Methods in Fluids*, 2011.

O. Lindberg, H. B. Bingham, A. P. Engsig-Karup, and P. A. Madsen. Towards Realtime Simulation of Ship-Ship Interaction. In *The 27th Int. Workshop on Water Waves and Floating Bodies*, 2012.

S. Osher and C. W. Shu. High-Order Essentially Nonoscillatory Schemes for Hamilton-Jacobi Equations. *Siam Journal on Numerical Analysis*, 28(4):907–922, 1991.

C. D. Simonsen, C. K. Nielsen, J. F. Otzen, and K. Agdrup. CFD Based Prediction of Ship-Ship Interaction Forces on a Tug Besides a Tanker. In *2nd International Conference on Ship Manoering in Shallow and Confined Water: Ship to Ship Interaction*, 2012.

Y. Toda, F. Stern, and J. Longo. Mean-Flow Measurements in the Boundary Layer and Wake and Wave Field of a Series 60 CB=0.6 Ship Model - Part 1: Froude Numbers 0.16 and 0.316. *J. Ship Res.*, 36: 360–378, 1992.

Dissipation around Rolling Boxes

Lin LU[1, 3], Xiaobo CHEN[2], Bin TENG[3], Ying GOU[3], Shengchao JIANG[3] and Xiaoling GUO[3]

[1]Center for Deepwater Engineering, Dalian University of Technology, Dalian 116024, China
LuLin@dlut.edu.cn
[2] Research Department, Bureau Veritas, Neuilly-Sur-Seine92570, France
[3] State Key Laboratory of Coastal and Offshore Engineering, Dalian University of Technology, Dalian 116024, China

Introduction

Potential flow theory is widely used in ocean hydrodynamics. With the great progress achieved so far, the weakness of the conventional potential flow model was also found for some special problems. One of the typical examples is the gap resonance, where the unexpected extremely large wave amplitude in the narrow gap, confined by the floating structures arranged side-by side, is predicted by the conventional potential flow model. The over-prediction of wave amplitude by the potential flow model near the resonant frequency is also observed for the liquid sloshing in a container. As far as ship motions in ocean wave are concerned, the rolling damping remains still great challenge for the potential flow theory. Empirical coefficients associated with the rolling damping are generally required in practical applications in order to make reasonable predictions of ship motions.

The gap resonance, sloshing and rolling problems mentioned above present a common characteristic, that is, the physical dissipation plays an important and critical role. However, *the conventional potential flow model is based on two basic assumptions of irrotational flow and inviscid fluid*, which means that the physical dissipation in the fluid flow has to be totally ignored. Therefore the conventional potential flow model becomes invalid for the cases with significant mechanical energy dissipation. In the context of viscous fluid flow with incompressibility, on the other hand, the mechanical energy dissipation can be described by the dissipation rate function from the energy equation,

$$\Psi = 2\mu s_{ij} s_{ij} \tag{1}$$

where μ stands for the fluid viscosity and s_{ij} = 0.5 $(\partial u_i/\partial x_j + \partial u_j/\partial x_i)$ for the strain rate tensor with u_i the flow velocity component. Eq. (1) denotes the work rate dissipated in unit volume, having a dimension of $[JS^{-1}L^{-3}]$. The dissipation function can be re-formulated by subtracting the continuity equation $2(\partial u_i/\partial x_j)^2 = 0$, which leads to[1]

$$\Psi = \mu\omega^2 + 4\mu\left(\frac{\partial u}{\partial y}\frac{\partial v}{\partial x} - \frac{\partial u}{\partial x}\frac{\partial v}{\partial y}\right) \tag{2}$$

for the two-dimensional situation, where ω is the vortice and u, v the velocity components in the 2-D case.

As for the potential flow, the vortices are definitely zero. Furthermore, if the fluid is ideal, no dissipation is produced since the viscosity is zero. However, if we consider the special case of irrotational (potential) flows of viscous fluids, that is, *the viscous potential flow*, the dissipation function might be not zero since the second term in the right hand of Eq. (2) has to be retained. Note that the viscous fluid flow can be irrotational flow [2]. Considering the Helmholtz Theorem, that is,

$$\mathbf{u} = \nabla\Phi + \mathbf{v} \tag{3}$$

where $\mathbf{u}$ is the velocity vector, Φ the velocity potential, giving $\nabla\Phi$ the irrotational velocity and $\mathbf{v}$ the rotational part of the velocity, Joseph et al (2006)[3] presented the integral dissipation function in space

$$\begin{aligned}\Theta = \int_V 2\mu s_{ij}s_{ij}dV &= 2\mu\int_V \frac{\partial^2\Phi}{\partial x_i\partial x_j}\frac{\partial^2\Phi}{\partial x_i\partial x_j}dV \\ &+ \frac{\mu}{2}\int_V\left(\frac{\partial v_i}{\partial x_j}+\frac{\partial v_j}{\partial x_i}\right)\left(\frac{\partial v_i}{\partial x_j}+\frac{\partial v_j}{\partial x_i}\right)dV \\ &+ 2\mu\int_V\left(\frac{\partial v_i}{\partial x_j}+\frac{\partial v_j}{\partial x_i}\right)\frac{\partial^2\Phi}{\partial x_j\partial x_j}dV\end{aligned} \tag{4}$$

The above dissipation function with Helmholtz decomposition shows that the energy dissipation is composed of three parts. The first one purely results from the potential flow (irrotational velocity components) $\Theta_p = 2\mu\int_\Omega \Phi_{,ij}\,\Phi_{,ij}\,d\Omega$ and the second part comes from the rotational velocity components, $\Theta_v = 0.5\mu\int_\Omega (v_{i,j}+v_{j,i})^2\,d\Omega$ while the third part due to the coupling effect of potential flow and rotational flow gives rise to $\Theta_{p\sim v} = 2\mu\int_\Omega (v_{i,j}+v_{j,i})\,\Phi_{i,j}\,d\Omega$. Eq. (4) indicates clearly that the potential flow of viscous fluid is able to partially consider the mechanical energy dissipation although the potential dissipation might be limited for the real-life problems.By using the Gauss theorem and considering the boundary conditions of potential flow of viscous fluids, the potential dissipation Θ_p can be transformed to the boundary integral[4],

$$\Theta_p = 2\mu\int_{Sf}\frac{\partial^2\Phi}{\partial\mathbf{n}^2}u_n ds + 2\mu\int_{Sf}\frac{\partial u_n}{\partial\boldsymbol{\tau}}u_\tau ds \tag{5}$$

Where $u_n = \partial\Phi/\partial\mathbf{n}$, $u_\tau = \partial\Phi/\partial\boldsymbol{\tau}$ with $\mathbf{n}$ and $\boldsymbol{\tau}$ the unit vectors in normal and tangent directions, respectively, and *sf* stands for the free surface boundary. Eq. (5) indicates that the energy dissipation of viscous potential flow appears along the free surface, which can be regarded as the theoretical foundation for our previous method by introducing damping term on the free surface for the gap resonance problem [5, 6]. It should be pointed out that the governing equations of mass conservation and momentum conservation are the same for the potential flows of both ideal fluid and viscous fluid, i.e., the Laplace equation and Bernoulli equation. The details of the viscous potential flow theory can be found in Ref. [4].

The introduction of the concept of viscous potential flow provides us a feasible approach to consider the dissipation in the frame of potential flow theory. However, the energy dissipation in realistic flows may involve significant vortical (rotational) contributions, and the dissipation will not be restricted to the free surface. Therefore, it is necessary to know well *where dissipation mainly appears and how much dissipation is for a special problem*. This is the main issue of the present work by examining the rolling dissipation in fluid. In the following section, the dissipation of a rotationally oscillating square box in viscous fluid will be examined by the CFD simulations. We consider one submerged box first and one floating box with free-surface effect as another case.

Submerged box rolling in closed container

The governing equation is the two-dimensional Navier-Stokes equations for incompressible viscous fluid in the Arbitrary- Lagrangian-Eulerian frame,

$$\frac{\partial u_i}{\partial x_i} = 0 \tag{6}$$

$$\frac{\partial u_i}{\partial t} + \left(u_j - c_j\right)\frac{\partial u_i}{\partial x_j} = -\frac{1}{\rho}\frac{\partial p}{\partial x_i} + \frac{\mu}{\rho}\frac{\partial}{\partial x_j}\frac{\partial u_i}{\partial x_j} \tag{7}$$

where u_i and c_j are the fluid velocity and mesh velocity components corresponding to the i-th Cartesian coordinate x_i (i=1, 2 for the present 2-D problem), p the pressure, t the time and the liquid density $\rho = 1000$ kg/m^3 is used in this work. For the purpose to understand well the influence of fluid viscosity the heavy dynamic viscosity $\mu = 10.0$ kg/m·s is adopted here. A rectangular box with square cross-section in *x-o-y* plan (with side length D =1.0 m) is placed in a closed square container fully filled with liquid. The rolling motion of the square cylinder is described by the forced rotational oscillation with respect to its centre, coinciding with the centre of the container.

$$\theta(t) = \theta_0 \sin\left(2\pi f t\right) \tag{8}$$

where θ is the time-dependent rotational angle in radian, θ_0 the amplitude and f the frequency in Hz. A sketch definition for the submerged square cylinder in a typical computational domain 40D×40D is shown in Fig. 1.

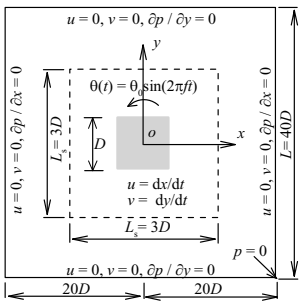

Fig. 1 Sketch definition of submerged rolling box

The no-slip boundary condition is applied on the solid wall, including the box surface and container boundary and a zero reference pressure is imposed at the down-right corner of the container.

The numerical model is firstly verified with different grid resolutions. It is confirmed that the computational meshes is fine enough, giving that the numerical results are free from the mesh density.That means the numerical dissipation is ignorable comparing with the physical dissipation. The influences of container size, fluid viscosity, rolling amplitude and frequency on the mean energy dissipation rate, denoted by Ξ, are concerned, which is evaluated as

$$\Xi = \frac{1}{T_2 - T_1}\int_{T_1}^{T_2} \Theta dt = \frac{1}{T_2 - T_1}\int_{T_1}^{T_2}\int_V 2\mu s_{ij} s_{ij} dV dt \tag{8}$$

where T_1 and T_2 is the integral time scale covering the stable state. Three different container sizes, measured by the container side length L = 20D, 40D and 60D, are examined with fixed rotation frequency f = 1.0 Hz and amplitudeθ_0 = 0.1 rad. The numerical results show that the mean energy dissipation rates in the whole fluid domain confined by the different container sizes hold the same value of 6.255 J/s. This suggests that wall effects from the container on the dissipation can be neglected for the present numerical set-up, in other words, the dissipation rate induced by the container boundaries approaches to zero, giving the reasonable assumption with infinite computational domain. Therefore, the medium container size L = 40D×40D is adopted as the benchmark for the following computations.

As mentioned previously, one of the concerned issues for the dissipation is to get know where the dissipation takes place. We evaluated the mean dissipation rate in several square regions with respect to the rotation centre, i.e., L_s = 1.0D, 1.6D, 2.0D, 3.0D, 4.0D, 10.0D, 20.0D, 30.0D and 40.0D, referring to the definition in Fig. 1. The other computational parameters include μ = 10 kg/m·s, ρ = 1000 kg/m^3, θ_0 = 0.1 rad and $f \in$ [0.1, 1.0] with an increment of 0.1 Hz. As shown in Fig. 2, the increase in the area of the sub-domain does not increases the dissipation rate significantly. That means the mechanical energy dissipation mainly happens in the near region of the rolling box. Careful examinations indicate that the area of 3.0D×3.0D may account for more than 90% dissipation of the whole fluid domain for the present cases. Fig. 2 suggests also that the dissipation rate increases approximately in parabolic with the rolling frequency at constant rolling amplitude, which means the higher frequency gives the larger dissipation.

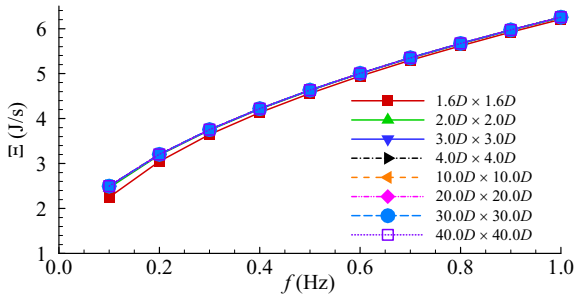

Fig. 2 Variation of mean dissipation rate with rolling frequency within different sub-domain size

Fig. 3 presents the comparisons of the dissipation rates under various rolling amplitudes. The mean dissipation rate is evaluated in the typical two sub-domains of $3.0D \times 3.0D$ and $20.0D \times 20.0D$. It can be seen that the rolling amplitude has significant influence on the mean dissipation rate. For a particular frequency, the larger rolling amplitude gives rise to the higher dissipation at a rate larger than linear increase.

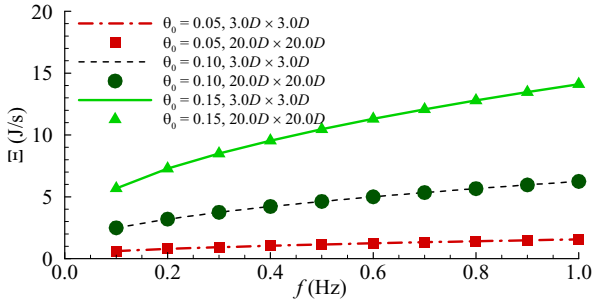

Fig. 3 Comparison of mean dissipation rate under different rotation amplitude

Fluid viscosity is expected to play important role in the mechanical energy dissipation, which is examined in Fig. 4 by considering the various viscosities at constant rolling amplitude $\theta_0 = 0.1$ rad and frequency $f = 0.4$ Hz. This figure shows that the total dissipation in the fluid domain does not behave a linear increase with the fluid viscosity although the viscosity in Eq. (1) presents in linearity. Fig. 4 implies the importance of velocity gradient (mainly accounted by the vortices).

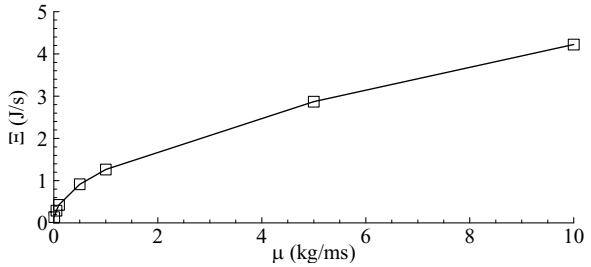

Fig. 4 Influence of fluid viscosity on dissipation

Based on the CFD numerical results the correlation between the dissipation and vortices are examined in Fig. 5 for typical $\theta_0 = 0.15$ rad and $f = 0.1$ Hz. It can be observed that the total dissipation shown in Fig. 5 (left), by using Eq. (1), mainly appears in the near region of the rolling box and the most significant energy dissipations appear around the sharp corners. The dissipation resulted from the vortex motion in Fig. 5 (middle), evaluated by the first term of the right hand of Eq. (2), presents the similar scenery to that of Fig. 5 (left). The further examination in quantity indicates that the vortices dissipation accounts for most of the total dissipation. From Fig. 5 (right), it is confirmed that the vortices mainly develop from the solid wall and the sharp corners. The numerical results shown in Fig. 5 suggest that the dissipation induced by the vortical flow has to be modeled in order to use the viscous potential flow theory to successfully describe the rolling damping. Two points should be addressed, 1) the physical dissipation should be introduced near to the rolling structure and 2) the appropriate dissipation amount should be used. One feasible method for the former topic might be the dissipative surface idea proposed by Chen et al (2011)[7] while the latter one can be estimated by using the CFD simulations as described in this work.

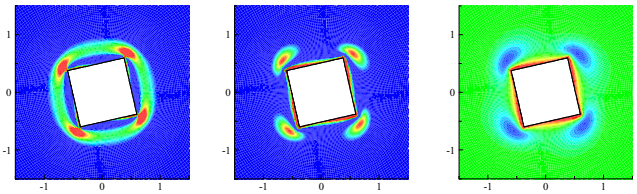

Fig. 5 Contours of dissipation rates and vortices

Floating box on free surface

By using the Navier-Stokes solver involving two-phase fluids, the rolling dissipation with free surface was simulated, where the liquid-gas interface is capture by the Volume of Fluid method. For the purpose of comparison, the computational domain, box size, rotationally oscillating amplitudes and frequencies are set to be as close as those in the previous section. The container is partially filled with liquid in a depth of $20D$, i.e., half of the vertical dimension. The viscosities and densities used in the computations for the liquid and gas phases are $\mu_L = 10.0$ kg/m·s, $\rho_L = 1000$ kg/m^3 and $\mu_A = 10^{-5}$ kg/m·s, $\rho_A = 1.0$ kg/m^3, respectively.

The time-series of wave elevations recorded at $x =$ 1.0m, 5.0m, 10.0m and 20.0m, respectively, are shown in Fig. 6 for the case with $f = 0.5$ Hz and $\theta_0 = 0.1$ rad. It shows that the wave amplitude decreases with the increase in the distance. At $x = 10$ m, the wave amplitude approaches to 1/6 of that at $x = 1.0$ m and the wave energy is totally damped out at $x = 20.0$ m. The further examinations show that the higher oscillating frequency leads to the faster decrease in the wave height with the distance.

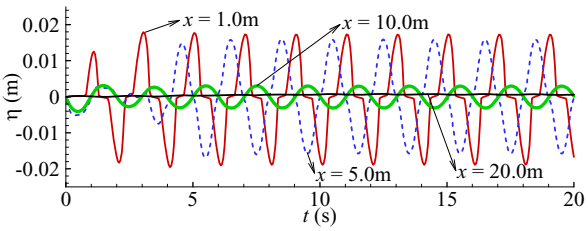

Fig. 6 Time series of wave elevation at different position

Eq. (2) suggests that the total dissipation rate consists of two parts, i.e., the first term and the second term on the right hand, which are denoted by the vortical dissipation rate and the other dissipation rate, respectively. The time evolutions of dissipation rates in the whole domain are examined in Fig. 7, for the case of $f = 1.0$ Hz and $\theta_0 = 0.1$ rad, where the space integral over both the liquid and gas phases are involved. Since the gas viscosity is much smaller than the liquid, it is confirmed to have rather limited contribution to the total dissipation. It can be seen that the total dissipation rate ($\int_\Omega \Psi d\Omega$) is

mainly resulted from the vortical flow ($\int_\Omega \mu\omega^2 d\Omega$). For the present case the dissipation rate induced by the second term of Eq. (2), i.e., $\int_\Omega 4\mu\,(u_y v_x - u_x v_y)\,d\Omega$, accounts for 10% of the total dissipation rate, in which both potential and vortical dissipations and their coupling effects are all involved according to the previous mentioned Helmholtz decomposition in Eq. (4).

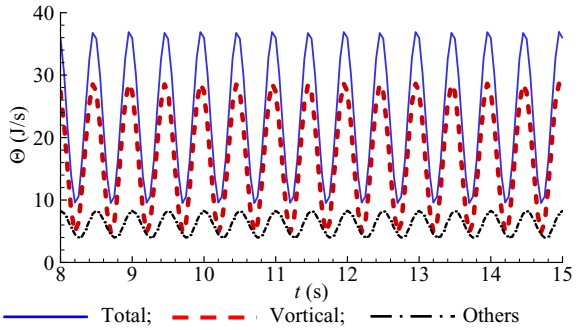

Fig. 7 Time series of dissipation rates in the whole domain

Following the previous examinations, the mean dissipation rates in various sub-domains with different square size are compared in Fig. 8, which is helpful to determine the most significantly dissipative region. The rotational amplitude and frequency considered here are 1.0 Hz and 0.1 rad, respectively. Note that the square sub-domains with side length L_s cover both of the liquid and gas regions and the three types of mean dissipation rate are considered. The numerical results show that the mean total dissipation, evaluated directly from Eq. (8), increases with the sub-domain size. However, as $L_s > 15$ m, that is, 15D in this work, the total mean dissipation rate approaches constant. That means the physical dissipation is mainly restricted in the scope of 15D×15D, which is much larger than the previous examined cases of submerged rolling box due to the presence of free surface. Again, the dissipation is observed to be mainly induced by the vortical flow. However, the mean vortical dissipation rate shows little dependence on the sub-domain size. As the sub-domain is large enough, the other dissipations account for nearly 25% of the total dissipation.

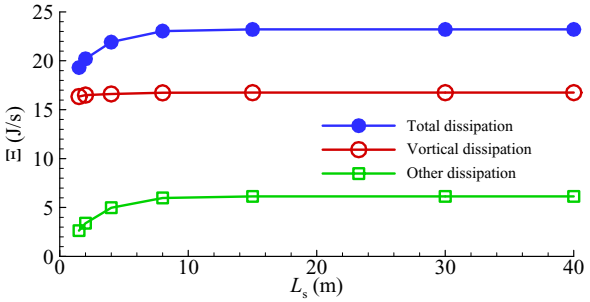

Fig. 8Mean dissipation rate in different sub-domain

The influence of rotational frequency on the mean dissipation rates in the whole domain are examined in Fig. 9 by considering the typical example with $\theta_0 = 0.1$ rad. It was found that at the lower frequencies the mean dissipation rate associated with the second term in Eq. (2) is very small while the total mean dissipation rate is almost the same as that from the vortical flow. With the increase in the frequency, the three dissipation rates increase gradually, and the difference between the total dissipation and the vortical dissipation becomes evident, which means the dissipation induced by the third term of Eq. (2) plays more and more important role at the higher oscillating frequencies.

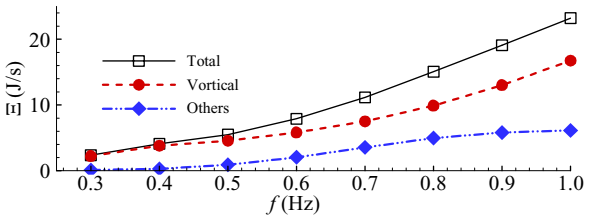

Fig. 9 Dependence of dissipation rate on rolling frequency

Conclusion

For the purpose to introduce dissipation in potential flows to deal with the near resonant problems in ocean engineering, we have performed analyses on the dissipation in viscous fluid and investigated quantitatively different components in the case of rolling boxes by using the CFD method. Two cases relative to one submerged box and one floating box at the free surface have been considered. The numerical results of dissipation rates associated with different components by varying rolling frequency and amplitude highlight that the major dissipation is contributed by fluid vortices in the region close to boxes. Further studies are needed to quantify the linear and quadratic coefficients of dissipation associated with rolling speed.

Acknowledgement

The finical supports from NSFC of China with granted Nos. 51279029and 51221961are acknowledged.

Reference

[1] Lamb H. 1945. *Hydrodynamics* (6th edition). Dover publication, New York, USA.

[2] Sirakov B T, Greitzer E M, Tan C S. 2005. A note on irrotational viscous flow.*Physics of Fluids*, 17, 108102.

[3] Joseph D. 2006. Helmholtz decomposition coupling rotational to irrotational flow of a viscous fluid.*PNAS*, 103 (39):14272-14277.

[4] Joseph D, Funada T, Wang J. 2008. *Potential Flows of Viscous and Viscoelastic Fluids*.Cambridge University Press.Cambridge, UK.

[5] Lu L, Teng B, Cheng L, Sun L, Chen XB. 2011a. Modelling of multi-bodies in close proximity under water waves — Fluid resonance in narrow gaps. *SCIENCE CHINA Physics, Mechanics & Astronomy*, 54 (1): 16-25.

[6]Lu L, Chen X B, TengB. 2012. Viscous dissipation and artificial damping for gap resonance problem.*Proceedings the 10th International Conference on Hydrodynamics (ICHD)*, Vol1, 257-262, October 1-4, St. Petersburg,

[7] Chen X B, Duan W Y, Liu H X. 2011. Dissipation effect in potential flows of fairly perfect fluid. *Proceedings of the 26th International Workshop on Water Waves and Floating Bodies (IWWWFB)*, 17-20 April, Athens, Greece.

Fluid-structure interaction during wave-impact with air-entrapment in a sloshing tank.

C. Lugni[*,**] claudio.lugni@cnr.it
A. Bardazzi[***] bardazzi.andrea@gmail.com
O. M. Faltinsen[**] oddfal@marin.ntnu.no
G. Graziani[***] g.graziani@uniroma1.it

$*$ CNR-INSEAN, National Research Council, Roma – Italy.
$**$ Centre for Autonomous Marine Operations and Systems, NTNU, Trondheim – Norway.
$***$ Dipartimento DIMA, Universita' degli studi di Roma 'Sapienza'.

The investigation carried out in the present research pursues the study started several years ago about the wave-impact phenomena in a sloshing tank relevant for a Liquefied Natural Gas ship at low filling depth. Depending on the local features of the wave approaching the tank wall, different impact phenomena may occur. When the angle between the liquid and the wall is small, a single gas bubble is entrapped during the impact; differently, for larger angle of impact, flip-through event or flat-impact may occur. Previous investigations for a fully 2D rigid tank [(1), (2), (3)], emphasized that the maximum pressure along the wall is not a reliable indicator of the maximum load, because of the stochastic nature of the local flow which characterizes the slamming phenomena. Further, when gas-entrapment matters making important the compressibility of the gas and its interaction with the free surface, Euler and Cavitation numbers, in addition to the traditional Froude scaling, should be taken into account for a proper scaling of the maximum loads [(2), (3)].

Based on the above results, in the last year new physical effects have been investigated by the present research group by means of a hydroelastic study. Hydroelasticity indeed, may be a crucial issue when slamming events occur in a LNG tank. Because of the low temperature inside the tank used to ensure the liquid state of the gas, the side walls, designed to realize a good thermal insulation, are not able to support the buffles traditionally installed in oil tankers to damp the sloshing phenomena. Then violent impacts may happen, especially in low filling conditions, when a travelling bore or an incipient breaking wave approaching the wall may characterize the sloshing flow inside the tank (4). These events, localized in space and time, may compromise the integrity of the structure when the time scales of the impacts are comparable to the highest natural vibration period of the structure. In this case hydroelasticity matters, as testified in previous experimental studies (5), (6) focused on the evolution of the flip-through event and an hybrid numerical-experimental hydroelastic model has been proposed to assess the relevance of hydroelasticity.

Here, an experimental investigation is presented to study the role of the hydroelasticity during the evolution of a slamming event with air-entrapment. The strain distribution along a deformable aluminum plate inserted in a rigid vertical wall of a sloshing tank has been measured to characterize the features of the local loads. Depressurized conditions have been realized to examine the relevance of the Euler and Cavitation numbers on the hydroelasticity of the deformable wall.

The same setup used in (5), (6) has been applied in the present experiments. A 2D plexiglas tank (LxHx$B = 1$ m x 1 m x 0.1 m) reinforced with steel and aluminum structure has been used to allow tests in depressurized conditions (see fig. 1). A filling depth $h/L = 0.122$ has been considered. An elastic aluminum plate, whose lowest natural wet frequency (in fully wet condition) has been Froude-scaled with respect to that of the typical panel used in a Mark III containment system (4), has been inserted in an extremely rigid stainless steel wall. The plate, 9 cm high, $2,5$ mm thick and located at 13 cm from the bottom of the tank, corresponds to a scale factor 30. It is clamped to the steel frame in correspondence to the vertical ends, while the lateral boundaries are left free. In this way, assuming a two-dimensional evolution of the hydrodynamic load, a double-clamped beam behaviour is realized. In depressurized conditions, in order to ensure the same ullage pressure on the rear (looking outside the tank, i.e. in air) and on the front (looking inside the tank, i.e. in water) side of the plate, an *ad hoc* small steel tank has been built (see bottom-left image on fig. 1) and fixed rigidly to the main sloshing tank. The small tank has been connected to the same vacuum pump used to realize the depressurized conditions in the main tank; in this way, ullage pressure has been decreased from atmospheric pressure down to 25 mbar. Finally, the hexapod system 'MISTRAL' (made by Symetrie) forced a pure sway sinusoidal motion of the tank. The measurement setup for the hydroelastic investigation was composed by two differential pressure probes along the rigid vertical wall below the elastic plate and five strain gauges along the deformable aluminum plate (see top panel on figure 1). Preliminarily, aiming to determine the dynamic response of the strain gauges, two miniaturized accelerometers have been mounted next to two strain gauges and the corresponding signals have been compared.

A second setup is used to ensure the repeatability of the flow conditions in the fully rigid case (no hydroelastic case). To the aim, the thin elastic plate is substituted with a rigid aluminum plate 20 mm thick. An accelerometer is put on the vertical rigid wall to check its rigidity as well as the global motion of the tank. Five differential pressure transducers were mounted along the rigid plate at the same positions of the strain gauges in the elastic case. The signals of the transducers were recorded through an acquisition system with a sample rate of 50 kHz. During the tests, visualizations of the local flow during the evolution of the phenomenon were performed through a high-speed digital video camera (with sample rate of 5 kHz), while a global view of the sloshing flow was recorded through two slow digital cameras (with a sample rate

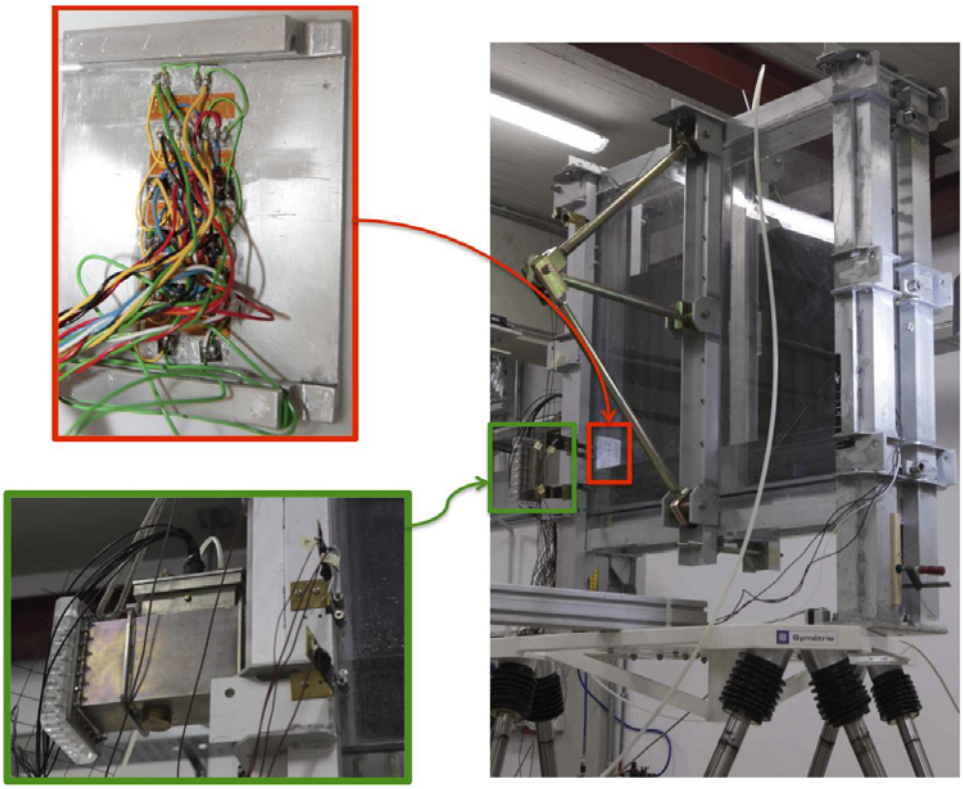

Figure 1:
Experimental set-up for the sloshing-tank experiments. Top-left panel: enlarged view of the rear part of the elastic plate with the strain gauges (top panel). Bottom-left panel: enlarged view of the small tank used to ensure the depressurized conditions on the external part of the elastic plate.

of 100 Hz). A common reference signal was used to synchronize the images with the analog signals of the transducers. Finally, an absolute pressure transducer measured the ullage pressure inside the tank.

Some preliminary results. The same impact scenario, that is a wave impact with air entrapped at the wall, is realized experimentally imposing a sinusoidal motion of the tank with period equal to 1.6 s. Three different sizes of the entrapped air-cavity, large (case a)), medium (case b)) and small (case c)), are investigated by changing the amplitude of the sinusoidal motion, i.e. 65 mm, 63 mm and 61.5 mm, respectively. The influence of the Euler number, i.e. of the ullage pressure inside the tank, has been investigated. In the following, some preliminary results will be discussed, postponing to the Workshop the complete analysis of the investigation.

Figures 2, 3 and 4 show the time history of the strain measured by the gauge placed in the centre of the elastic plate, for the large, medium and small air-cavity case, respectively. Each figure from left to right reports three different panels corresponding to three different values of the ullage pressure: 100 mbar, 400 mbar and 800 mbar, respectively. According to the study performed in (3) for a fully rigid tank, the oscillation frequency of the air-cavity depends on the Euler number, increasing with the ullage pressure of the tank. However, when an elastic plate is considered, the structural natural frequency may be excited as well. The last event depends on the time rise of the first peak of the hydrodynamic load. Of course, when the frequency of the bubble is close to the natural structural frequency, a resonance phenomenon is expected. Although a really small air-cavity has been obtained for the case c), its highest frequency of oscillation (occurring at atmospheric pressure) is still slightly smaller than the lowest natural frequency of the structure.

In correspondence of the lowest ullage pressure (see left panel of each figure), the two frequencies, i.e. that of the bubble and the lowest natural frequency of the structure, are expected to be quite far from each other. Indeed, the first one decreases with the Euler number, while the second one, though dependent on the wetted length of the deformable plate is practically Euler number independent (neglecting the small variation induced by the different wetted length due to the different size of the cavity with the Euler number). This mechanism justifies the strain time history observed on the left panel of the figures 2-3-4. More in detail, the time rise of the first peak is able to excite the hydroelastic behavior of the elastic plate, as highlighted by the vibration (around 1 kHz) occurring during the first 6 ms. However, for the case a) the larger time rise characterizing the first peak (about 2 ms) is not enough to excite a relevant hydroelastic phenomenon. Further, as expected for the lowest ullage pressure case, the hydroelastic frequency is much larger than the oscillation frequency of the air-cavity; this means that during the first oscillation of the bubble (i.e. 12 ms, 9 ms and 6 ms for the case a, b and c, respectively) the hydroelastic vibrations are completely damped out. When increasing the ullage pressure

(see middle and right panels of figures 2-3-4), the oscillation frequency of the air-cavity increases, approaching the lowest natural frequency. This phenomenon causes a different behavior for the case a), b) and c): while the maxima and minima of the strains are almost the same of the large bubble case, they vary consistently (but for the first peak) for the medium and small bubble cases. A possible reason of this behavior could be the interaction between the vibration of the structure and the oscillation of the bubble. However, at the moment it is premature to draw any definitive conclusion. Note, finally, that for each of the three cases considered, the value of the first peak of the strain remains almost unchanged with the Euler number. This suggests that this peak is not dominated by the compressibility of the air-cavity.

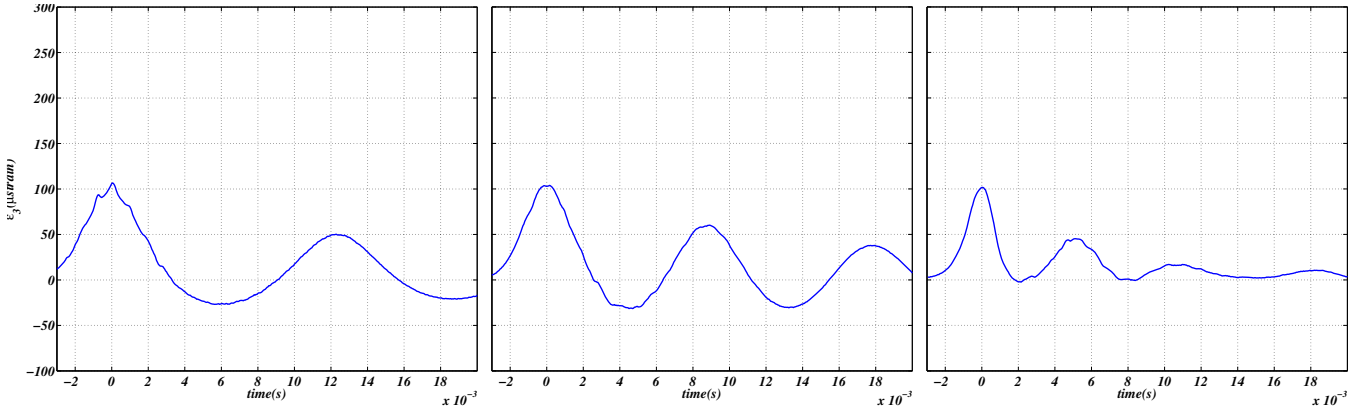

Figure 2: Case a. Large air-cavity entrapped. From left to right: time history of the strain measured at the centre of the elastic plate, for three different values of the ullage pressure (100 mbar, 400 mbar and 800 mbar, respectively).

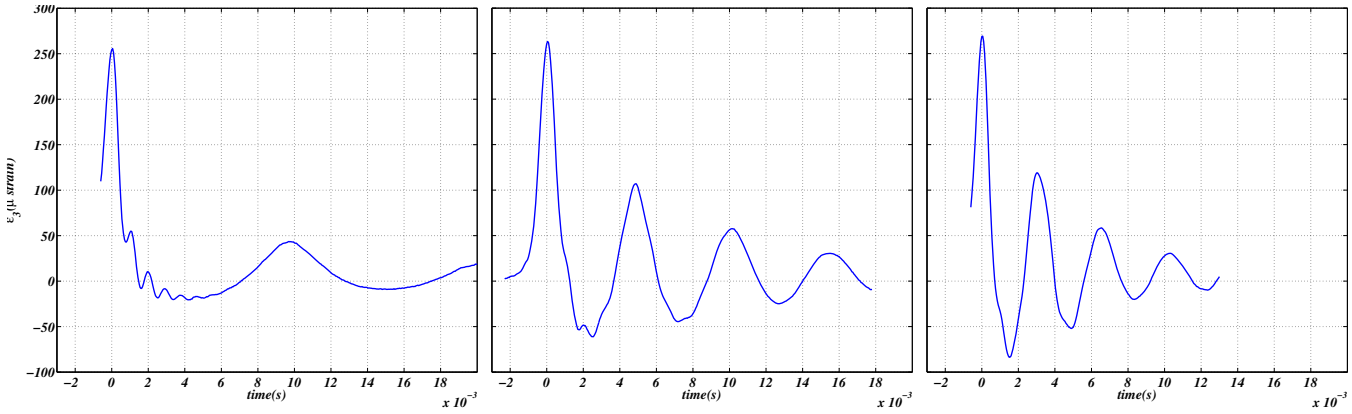

Figure 3: Case b. Medium air-cavity entrapped. From left to right: time history of the strain measured at the centre of the elastic plate, for three different values of the ullage pressure (100 mbar, 400 mbar and 800 mbar, respectively).

This research activity was partially supported by the Centre for Ships and Ocean Structures (CeSOS), NTNU, Trondheim, within the "Violent Water-Vessel Interactions and Related Structural Loads" project and presently ongoing within the new born Centre for Autonomous Marine Operations and Systems (AMOS), Trondheim, and partially funded by the Flagship Project RITMARE - The Italian Research for the Sea - coordinated by the Italian National Research Council and funded by the Italian Ministry of Education, University and Research within the National Research Program 2011-2013."

References

[1] C. Lugni, M. Brocchini, and O. M. Faltinsen, "Wave impact loads: The role of flip-through," *Physics of Fluids*, no. 18, p. 19, 2006.

[2] C. Lugni, M. Miozzi, M. Brocchini, and O. M. Faltinsen, "Evolution of the air cavity during a depressurized wave impact.i. the kinematic flow field," *Physics of Fluids*, no. 22, p. 16, 2010.

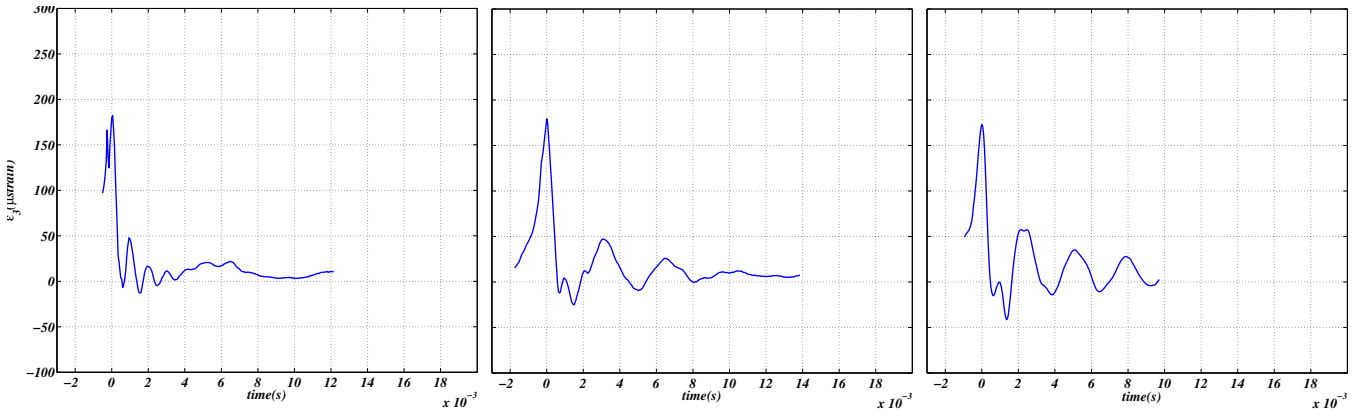

Figure 4: Case c. Small air-cavity entrapped. From left to right: time history of the strain measured at the centre of the elastic plate, for three different values of the ullage pressure (100 mbar, 400 mbar and 800 mbar, respectively).

[3] C.Lugni, M.Brocchini, and O. Faltinsen, "Evolution of the air cavity during a depressurized wave impact.ii. the dynamic field," *Physics of Fluids*, no. 22, p. 13, 2010.

[4] O. M. Faltinsen and A. N. Timokha, *Sloshing*. Cambridge, UK: Cambridge University Press, 2010.

[5] A. Bardazzi, C. Lugni, O. Faltinsen, M. Greco, G. Colicchio, and G. Graziani, "Wave-impact in a sloshing tank: hydroelastic challenges," *Proc. IWWWFB, Denmark*, 2012.

[6] A. Bardazzi, C. Lugni, O. Faltinsen, and G. Graziani, "Hydroelastic study of the impact phenomena in sloshing flow," *Hydroelasticity in Marine Technology, Tokyo*, 2012.

Shapes of Zero Wave Resistance and Trapped Modes

Michael V. Makasyeyev
Institute of Hydromechanics of Ukrainian National Academy of sciences,
8/4, Gelyabova str. 03056, Kyiv, Ukraine, M_Makasyeyev@ukr.net

1. Introduction

The energy reduction at the transportation on the water is an actual problem. The searching for vessel shapes with minimal and zero wave resistance is an important part of them. It is possible to search of shapes of zero wave resistance at least by two ways.
The first is a modification of the body shape so that the wave resistance is minimal. The other method is based on a bijection of shape and pressure distribution that is generated. It is the searching of pressure distribution which gives the optimal shape. The first method can be called a direct, the second - an inverse. It is possible to search for optimal shape by combination of these methods. The shapes of zero wave resistance are considered by inverse method for several types of pressure distribution in [1]. In the present work the inverse method on a base of generalized functions technique is developed and some theoretical aspects of this approach are examined. The relation with trapped modes is considered.

2. Conditions for existence of the shapes with zero wave resistance

We consider the motion of a body with constant speed V_0 on a surface of ideal and incompressible liquid in assumptions of the linear theory of waves. The coordinate system is associated to the body and the x axis is directed against the velocity of the inverse flow. The fluid motion is irrotational and the potential $-V_0 x+\varphi(X,y,t)$ exists, where φ is the potential of disturbance velocity, $X=x\in R^1$ in 2D-theory and $X=(x,z)\in R^2$ in 3D-theory, y is the vertical axis, t is a time. The free surface shape is described by the function $y=\eta(X,t)$, $X\in R^n\setminus S(t)$, $n=1,2$, $S(t)$ is the projection on R^n of a point set of free surface and body surface intersection..We consider the shapes, which we can describe by an unique function $y=f(X,t)$, $X\in S(t)$ to simplify the analysis.
The problem is formulated as unsteady in order to avoid the analysis of diffraction conditions on infinity. The required steady solution with correct conditions on infinity is easier obtained by limiting process at $t\to\infty$. In addition, at $V_0=0$ it is the problem about a floating body on a wave surface. In this case, the steady problem will be the problem of steady oscillations under wave action and a searching for body shape which does not make resistance to a breaking wave.
The boundary conditions on the border of fluid and solid body $\Gamma(t)$ include the Bernoulli integral

$$N\varphi+(\nabla\varphi)^2/2=-gf(X,t)-\overline{p}(X,y,t), \quad (1)$$

and kinematic condition

$$\nabla\varphi\cdot\nabla(y-f(X,t))=Nf(X,t),\ X\in S(t), \quad (2)$$

where $N=\frac{\partial}{\partial t}-V_0\frac{\partial}{\partial x}$, $\overline{p}(X,y,t)=\frac{p_a(X,y,t)-p_0}{\rho}$ is a relative pressure in the fluid, p_0 is an absolute pressure on the free surface, ρ is the density of fluid. The conditions on a free surface are the same but linearized and with zero pressure:

$$N\varphi=-g\eta(X,t),\quad y=-0,\ X\in R^n\setminus S(t), \quad (3)$$

$$\frac{\partial\varphi}{\partial y}=N\eta(X,t),\quad y=-0,\ X\in R^n\setminus S(t), \quad (4)$$

If the depth of fluid is h, then

$$\frac{\partial\varphi}{\partial y}=0,\ y=-h. \quad (5)$$

For infinity depth

$$|\nabla\varphi|=0,\ y\to-\infty. \quad (6)$$

The Initial conditions are

$$\varphi(X,y,0)=\varphi_0(X,y),\ \frac{\partial\varphi}{\partial t}(X,y,0)=\varphi_1(X,y), \quad (7)$$

where φ_0 and φ_1 are known functions.
For unique calculation of wave resistance the body mass and its distribution of body volume or the total mass and the center of mass position must be set.
If the relations (1) and (2) have the nonlinear terms, the numerical solution is only possible. It is obvious that it is useful to have all possible solutions of simpler problems to better understand the problem, to create a theoretical basis and benchmarks for the full nonlinear theory. For this purpose we consider the case when the conditions (1) and (2) are linearized. It is can be valid for weakly submerged hulls or for motion with a relatively high speed, when the immersion is reduced due to the dynamic overpressure.
The boundary conditions (1)—(2) on the solid boundaries after linearization and conditions on the free surface (3)—(4) can be combined, if we

introduce a function of the pressure distribution $p(X,t)$ on the entire plane $y=0$, which determines the pressure on the body at $X \in S(t)$ and is zero at the free surface. We will describe the form of fluid boundary by single function $\eta(X,t)$ also, and $\eta(X,t)=f(X,t)$ for $X \in S(t)$.

The new problem can be written as

$$\nabla^2\varphi = 0,\ -h < y < 0, \tag{8}$$

$$N\varphi = -gf(X,t) - p(X,t),\ \ y=-0, \tag{9}$$

$$\frac{\partial\varphi}{\partial y} = N\eta(X,t),\ y=-0. \tag{10}$$

We use the Fourier transform to analyze the problems (8)—(10) and (5)—(7).

First, we continue the function φ on the whole space R^{n+1}. We set $\varphi(X,y,t)=0$ for $y>0$ and $\varphi(X,y,t)=\varphi(X,-y-2h,t)$ for $y<-h$.

As a result, the function φ is defined on the whole space and it is continuous with their derivatives at $y=-h$ and it is discontinuous with their derivatives at $y=0$ and $y=-2h$. Then we introduce the generalized functions φ, p and η generated by a classical, over the space of tempered test functions [2]. In this case, the generalized Fourier transforms of these functions exist in the same space.

The generalized function φ obeys the equation

$$\nabla^2\varphi = -\varphi(X,-0,t)[\delta'(y)-\delta'(y+2h)] - \\ -\frac{\partial\varphi}{\partial y}(X,-0,t)[\delta(y)+\delta(y+2h)], \tag{11}$$

where $\delta(y)$ and $\delta'(y)$ are delta function and its derivative. We designate the generalized Fourier transform of function φ in R^n on X as $\Phi(\Lambda,y,t)$, where $\Lambda=(\lambda,\mu)$ in R^2 and $\Lambda=\lambda$ in R^1. We designate also the Fourier transforms of p and η as $P(\Lambda,t)$ and $H(\Lambda,t)$. We obtain

$$\Phi(\Lambda,y,t) = \frac{\cosh|\Lambda|(y+h)}{|\Lambda|\sinh|\Lambda|h}\overline{N}H(\Lambda,t) \tag{12}$$

and relation between $P(\Lambda,t)$ and $H(\Lambda,t)$

$$\left(\frac{1}{\zeta(\Lambda)}\overline{N}^2 + g\right)H(\Lambda,t) = -P(\Lambda,t), \tag{13}$$

by applying the Fourier transform to (11) and the method of fundamental solutions, and taking into account (9) and (10). There are $|\Lambda|=\sqrt{\lambda^2+\mu^2}$ in R^2 and $|\Lambda|=|\lambda|$ in R^1, $\overline{N}=\frac{\partial}{\partial t}+i\lambda V_0$, and $\zeta(\Lambda)=|\Lambda|\tanh|\Lambda|h$. At $h\to\infty$ we have $\zeta(\Lambda)=|\Lambda|$ and $\Phi(\Lambda,y,t)=e^{|\Lambda|y}\overline{N}H(\Lambda,t)/|\Lambda|$.

The general solution of (13) with initial conditions is

$$H(\Lambda,t) = \zeta(\Lambda)\int_0^t P(\Lambda,\tau)e^{i\lambda V_0(\tau-t)}D(\Lambda,\tau-t)d\tau + \\ + G_0(\Lambda,t)e^{-i\lambda V_0 t}, \tag{14}$$

where $D(\Lambda,t)=\left[\sin\sqrt{g\zeta(\Lambda)}t\right]/\sqrt{g\zeta(\Lambda)}$,

$$G_0(\Lambda,t) = H_0(\Lambda)\overline{N}D(\Lambda,t) + H_1(\Lambda)D(\Lambda,t),$$

and the functions $H_0(\Lambda)$ and $H_1(\Lambda)$ are Fourier transforms of functions $\eta_0(\Lambda)=\eta(\Lambda,0)$ and $\eta_1(\Lambda)=\frac{\partial\eta}{\partial t}(\Lambda,0)$ which are obtained from initial conditions. The inverse Fourier transform of (14) in R^n gives the formula for determination of time-dependent shape of the surface generated by the pressure $p(X,t)$ at arbitrary time dependence.

We obtain from (14) the formula for steady motion at a constant speed, assuming that the steady motion appears at larger times when there are no pressure perturbations, that is, when $P(\Lambda,t)\approx P(\Lambda)$. For large t the initial conditions can be set homogeneous and then

$$H(\Lambda,t) = -\frac{i}{2}\sqrt{\frac{\zeta(\Lambda)}{g}}P(\Lambda)\int_{-\infty}^{t}\theta(\tau)\left[e^{-i\tau\xi_1(\Lambda)} - \right. \\ \left. - e^{-i\tau\xi_2(\Lambda)}\right]d\tau,$$

where $\theta(t)$ is the Heaviside function, $\xi_1(\Lambda)=\lambda V_0-\sqrt{g\zeta(\Lambda)}$ and $\xi_2(\Lambda)=\lambda V_0+\sqrt{g\zeta(\Lambda)}$. At $t\to\infty$, the integral here is the sum of the Fourier transforms of Heaviside functions.

As a result, $H(\Lambda,t)$ will not depend on the time, $H(\Lambda,t)=H(\Lambda)$ and we obtain

$$H(\Lambda) = P(\Lambda)Q(\Lambda) \tag{15}$$

as in [4], where

$$Q(\Lambda) = reg\frac{\zeta(\Lambda)}{\lambda^2 V_0{}^2 - g\zeta(\Lambda)} + \\ + \frac{\pi i}{2}\sqrt{\frac{\zeta(\Lambda)}{g}}[\delta(\xi_1(\Lambda)) - \delta(\xi_2(\Lambda))],$$

and *reg* indicates a regularization, and delta functions support on a $(n-1)$-dimension surfaces $\xi_1(\Lambda)=0$ and $\xi_2(\Lambda)=0$.

The similar formulas for harmonic oscillations on the wave surface are obtained from (14) based on the assumptions that the pressure becomes harmonic under the action of an regular wave $H_0^*(\Lambda)e^{ikt}$ and $P(\Lambda,t)=P^*(\Lambda)e^{ikt}$, where k is the oscillation frequency, and $H_0^*(\Lambda)$ and $P^*(\Lambda)$ are amplitude functions. At $t\to\infty$, we obtain in analogous, that $H(\Lambda,t)=H^*(\Lambda)e^{ikt}$ and

$$H^*(\Lambda) = P^*(\Lambda)Q^*(\Lambda) + H_0^*(\Lambda). \tag{16}$$

The wave resistance is now

$$R_w(t) = -\int_{R^n} p(X)\cdot\frac{\partial\eta}{\partial x}(X)dX\,. \qquad (17)$$

We can show that, since the function $p(X)$ is square integrable and finite, and $\frac{\partial\eta}{\partial x}(X)$ is a sectionally continuous, then

$$\int_{R^n} p(X)\frac{\partial\eta}{\partial x}(X)dX = \frac{1}{(2\pi)^n}\int_{R^n}\overline{P(\Lambda)}(i\lambda)H(\Lambda)d\Lambda\,, \qquad (18)$$

where the overbar means the complex conjugate.
For the motion described by (15), we obtain

$$R_w = -\int_{R^n}|P(\Lambda)|^2(-i\lambda)Q(\Lambda)d\Lambda =$$

$$= -\frac{\pi}{2}\int_{R^n}\lambda\sqrt{\frac{\zeta(\Lambda)}{g}}|P(\Lambda)|^2\left[\delta(\xi_1(\Lambda))-\delta(\xi_2(\Lambda))\right]d\Lambda\,.$$

The products with the delta functions which support by $(n-1)$-dimensional surfaces are calculated by decomposition formulas of generalized functions.

As a result, R_w will depend on the value of $|P(\Lambda)|^2$, calculated at fixed values of Λ, giving the parameters of movement. The value of $|P(\Lambda)|^2$ determines the wave amplitude at infinity and depends on $p(X)$ and S. The minimization of R_w will consist in searching for optimal $p(X)$ and S. We have the analogous formulas in the case of harmonic oscillations in the wave surface.

3. The simple samples

We consider a simple example of 2D theory ($n=1$) of motion with speed V_0 at $h\to\infty$ [3].

Then $\Lambda=\lambda$ and $\xi_{1,2}(\lambda)=\lambda V_0 \mp\sqrt{g|\lambda|}$, $\delta(\xi_{1,2}(\lambda))=2\delta\left(\lambda\mp g/V_0^2\right)/V_0$, and we have in nondimesional values

$$R_x = \nu|P(\nu)|^2 = \nu A^2\,, \qquad (18)$$

where $\nu = ga/V_0^2$, a is a linear size, $A=\sqrt{{A_s}^2+{A_c}^2}$, $\tan\alpha = A_s/A_c$,

$$A_s = \int_{-\infty}^{\infty} p(x)\sin\nu x dx\,,\quad A_c = \int_{-\infty}^{\infty} p(x)\cos\nu x dx\,.$$

The conditions for mass and center of mass position are

$$\int_{-\infty}^{\infty} p(x)dx = \frac{\Delta_y}{\rho a^2 V_0^2} = \nu\,,\quad \int_{-\infty}^{\infty} xp(x)dx = x_c\nu\,, \qquad (19)$$

where Δ_y is the body weight, or displacement, and x_c is the center of mass axis, $a=\sqrt[3]{\Delta_y/\rho g}$.

There is the most easily to make a zero amplitude in (18) for symmetrical distribution of pressure at $x_c=0$.

The amplitude of the resulting wave at $p(x)=p_c=const$ on $[-1,1]$ is $A=A_c=p_c\int_{-1}^{1}\cos\nu x dx = 2p_c\frac{\sin\nu}{\nu}$, and wave resistance is $R_w=\nu{A_c}^2=\frac{2{p_c}^2}{\nu}\sin^2\nu$. It is equal to zero at $1=\frac{\pi n}{\nu}$, $n=\pm1,\pm2,\ldots$. Therefore, the length of the interval $l=2$ must satisfy the condition $l=2\pi n/\nu$, $n=1,2,\ldots$. Since the wavelength is $L=2\pi/\nu$, then this condition is $l=nL$. The length of the interval must be a multiple of the wavelength.

We consider the constant pressure distribution on the two symmetrical identical segments $[-1,-b]$ and $[b,1]$ as a

$$p(x)=p_1\vartheta([-1,-b];x)+p_2\vartheta([b,1];x),\ 0<b<1$$

where $\vartheta([c,d];x)$ is the characteristic function of interval which is 1 for $x\in[c,d]$ and is zero for $x\notin[c,d]$. It is ensue from (19) in the case of a symmetric distribution of pressure that must be $p_1=p_2=\frac{\nu}{2(1-b)}$, or

$$p(x)=\frac{\nu}{2(1-b)}\{\vartheta([-1,-b];x)+\vartheta([b,1];x)\}\,.$$

The calculations show that at $l=2$ the value l/L, giving $R_w=0$, tends to 1 at $b\to0$. It tends to 0.5 at $b\to1$. Indeed, at $b\to1$ we have

$$\lim_{b\to a}p(x)=\frac{\nu}{2}\left[\delta(x+1)+\delta(x-1)\right]. \qquad (20)$$

In this case $A_s=0$, and $A_c=\nu\cos\nu$. The wave resistance is zero at $1=(1/2+n)\pi/\nu$, $n=0,\pm1,\pm2,\ldots$ or $l=2=(1/2+n)L$, $n=0,1,2,\ldots$

The velocity potential for distribution (20) is

$$\varphi(x,y)=$$

$$=\frac{\nu}{2\pi}v.p.\int_0^{\infty}\frac{e^{\lambda y}}{\lambda-\nu}\left[\sin\lambda(1+x)-\sin\lambda(1-x)\right]d\lambda+$$

$$+\nu e^{\nu y}\cos\nu\cos\nu x\,. \qquad (21)$$

We consider also the harmonic oscillations on the wave $\eta_0(x,t)=\mathrm{Re}\,\eta_0^*(x)e^{ikt}$. Then

$$H_0^*(\lambda)=2\pi\left[A_0\delta(\lambda-\omega)+B_0\delta(\lambda+\omega)\right],$$

where A_0 and B_0 are complex constants that specify the wave amplitude, $\omega=ak^2/g$. In this case

$$H^*(\lambda)=reg\frac{P^*(\lambda)|\lambda|}{\omega-|\lambda|}+$$

$$+\pi i\omega\left[P^*(\omega)\delta(\lambda-\omega)+P^*(-\omega)\delta(\lambda+\omega)\right]+H_0^*(\lambda)$$

and wave resistance is

$$R^*_w = i\omega\left[A_0\overline{P^*(\omega)} - B_0\overline{P^*(-\omega)}\right].$$

If the wave is incident on the left then $B_0 = 0$ and

$$R^*_w = i\omega A_0\overline{P^*(\omega)}.$$

Then the modulus of wave resistance

$$\left|R^*_w\right| = \omega\left|A_0\right|\left|P^*(\omega)\right| = \left|A_0\right|^2 R,$$

where $R = \omega\left|P^*(\omega)\right|/\left|A_0\right|$ is the reflection coefficient.

We consider the pressure distribution

$$\mathrm{Re}\, p^*(x) = \frac{p_c}{2}\left[\delta(x+1)+\delta(x-1)\right],\ \mathrm{Im}\, p^*(x) = 0.$$

In this case $A_c = p_c\cos\omega$. The reflection coefficient is zero at $\omega = \pi/2 + n\pi$, $n = 0,\pm1,\pm2,...$

The velocity potential in this case is

$$\varphi^*(x,y) =$$

$$= \frac{\omega p_c}{2\pi} v.p.\int_0^\infty \frac{e^{\omega y}}{\lambda-\omega}\left[\cos\lambda(1+x)+\cos\lambda(1-x)\right]d\lambda -$$

$$-i\omega p_c e^{\omega y}\cos\omega\cos\omega x + \varphi_0^*(x,y). \quad (22)$$

Other examples will be shown in the report.

4. Relation with trapped modes

The potentials (21) and (22) for the pairs of symmetric point pressure are there actually limits of potentials of symmetric pairs bodies when they degenerate into points. At zero wave resistance the potentials (21) and (22) do not contain the second terms. The first terms coincide up to a constant factor with potentials that are among the known examples of potentials of trapped modes [4, 5] at $a = 1$.

Trapped modes are defined as modes on the surface of an ideal fluid with a finite energy that do not create waves on infinity, and therefore have zero wave resistance. In the examples these modes are generated by point sources located in a certain way.

Pressure points which we have considered make sense combinations of point sources also and generate waves of finite energy, too. However, the trapped modes [4, 5] have another important characteristic. They are the solutions of the homogeneous boundary value problems for the differences of two potentials and illustrate the examples of non-uniqueness of solutions.

The homogeneous condition on the free surface is also homogeneous in the original problem. In particular, for the problem of Neumann-Kelvin it has the form

$$V_0^2\frac{\partial^2\varphi}{\partial x^2}(x,-0) + g\frac{\partial\varphi}{\partial y}(x,-0) = 0. \quad (23)$$

This condition is also satisfied for the difference of potentials. The homogeneous condition on the solid body is $\partial\varphi/\partial n = 0$. However, in the case of degeneracy of the rigid body to the point this condition makes no sense in the classical meaning.

The contours of the streamlines covering the singularities, considered as the contours of bodies for constructing examples of trapped modes. The condition $\partial\varphi/\partial n = 0$ is satisfied on these contours due to the fact that they are free streamlines inside fluid and on which have no pressure drop.

In general, it is possible to build such kind of trapped modes for a given contour or configuration of bodies by a selection of parameters and geometry of singularities. However any condition for $\partial\varphi/\partial n$ does not make sense for the classical functions at points of non-smooth contact of body and fluid boundaries. We may notice that the condition (23) is satisfied on the boundary with zero pressure, and on the boundary with a nonzero constant pressure excepting the boundary points. This condition is also indefinite at the points of singularities location when they are distributed on the free surface. In all cases, the boundary conditions in the classical formulation of problems are satisfied everywhere except for a set of points of function discontinuities and their derivatives. The non-uniqueness of solutions of boundary value problems in the classical formulation may be a result of indefinite characteristics of singularities on these sets of breaks and their geometry.

The use of generalized functions eliminates the problem of non differentiability of classical functions. The correct interpretation in generalized functions of the physical meaning of discontinuities of functions is needed for studying and resolving the problem of non-uniqueness of solutions of boundary value problems in the linear wave theory.

References

1. Yeung R.W., Makasyeyev M.V., Matte C. On Wave Elevations under a Moving Pressure Distribution in Minimum-Resistance Conditions // Proc. of the 26th IWWWFB. April 17–20, 2011, Athense. Pp. 213–216.
2. Vladimirov V/S. Equations of Mathematical Physics. – Moscow. 1981. – 512 p. (In Russian)
3. Makasyeyev M.V. Unsteady planing on a surface of heave fluid // Visnyk Kharkivs'koho natsional'noho universytetu im. V. N. Karazina. 2009, № 863 . Pp. 169–178. (In Russian).
4. Kuznetsov N., Maz'ya V., Wainberg V. Linear water waves. A mathematical approach. – Cambrige University Press. 2002. – 532 p.
5. McIver M. An example of non-uniqueness in the two-dimensional linear water wave problem // J. Fluid Mech. V. 315. !996. Pp. 257-266.

Near Trapping and the Singularity Expansion Method

Michael H. Meylan[1] **Colm Fitzgerald**[2]

[1]School of Mathematical and Physical Sciences, The University of Newcastle, Australia

[2]Department of Engineering Science, The University of Oxford, Parks Road, Oxford, OX1 3PJ, UK

e-mail addresses: mike.meylan@newcastle.edu.au, colm.fitzgerald@eng.ox.ac.uk

1 Introduction

Trapped modes are very special solutions to the linear water wave problem in which a solution with finite energy but no decay in time decay exists (McIver, 1996). A near trapped mode is a wave which has a very slow decay in time (and correspondingly slow growth in distance) and they may be thought of as corresponding to slight perturbations of a trapping structure geometry, although they occur in many different situations (Evans & Porter, 1997; Meylan & Eatock Taylor, 2009) and are a feature of multiple scattering and resonance.

It is well known that strong connections exist between the frequency and time domain solutions and this connection is exploited in the Cummins method (Cummins, 1962), which is the standard solution method in the time-domain for determining body motions (it cannot be used to determine the fluid motion). However, a more direct connection between the frequency and time domain solution can be derived using the generalized eigenfunction method (Fitzgerald & Meylan, 2011). The singularity expansion method is a method for approximating time dependent wave problems by a deformation of the contour of integration which appears in the inverse Laplace transform (Hazard & Loret, 2007).

2 Mathematical Formulation

Positions are described in Cartesian coordinates $\boldsymbol{x} = (x, z)$ with z being directed vertically upwards. The fluid is two-dimensional with domain Ω of constant finite depth h_{-1} for $x < -l$ and h_1 for $x > l$. The sea bed is positioned at $z = -h(x)$, the free-surface is at $z = 0$, and the domain extends to infinity in the horizontal directions. The linearized boundary conditions can be adopted. The time-dependent motions are described by the velocity potential $\Phi(\boldsymbol{x}, t)$ which satisfies

$$\Delta\Phi(\boldsymbol{x}, t) = 0, \quad \boldsymbol{x} \in \Omega, \tag{1a}$$

$$\partial_n\Phi = 0, \quad \boldsymbol{x} \in \partial\Omega_B, \tag{1b}$$

$$\partial_n\Phi = 0, \quad z = -h(x), \tag{1c}$$

where ∂_n is the outward normal, $\partial\Omega_B$ is the wetted body surface and $z = h(x)$ is the sea floor. On the free-surface $\partial\Omega_F$

$$\partial_z\Phi = \partial_t\zeta, \quad \boldsymbol{x} \in \partial\Omega_F, \tag{1d}$$

$$\partial_t\Phi = -\zeta, \quad \boldsymbol{x} \in \partial\Omega_F, \tag{1e}$$

where ζ is the free surface displacement. These equations have been non-dimensionalized. An initial disturbance on the free-surface is given by

$$\zeta(\boldsymbol{x}, 0) = \zeta_0(x)|_{t=0}\,, \quad \boldsymbol{x} \in \partial\Omega_F. \tag{2}$$

We assume that $\Phi(\boldsymbol{x}, 0) = 0$. A finite energy condition must also be satisfied.

2.1 Frequency-domain solution

Given that the motions are assumed harmonic for all time we can write $\Phi = \mathrm{Re}\,\{\phi \mathrm{e}^{-i\omega t}\}$ and $\zeta = \mathrm{Re}\,\{\xi e^{-i\omega t}\}$ so that equations (1a-1e) become

$$\Delta\phi = 0, \quad \boldsymbol{x} \in \Omega, \tag{3a}$$

$$\partial_n\phi = 0, \quad \boldsymbol{x} \in \partial\Omega_B, \tag{3b}$$

$$\partial_n\phi = 0, \quad z = -h(x), \tag{3c}$$

$$-\mathrm{i}\omega\xi = \partial_z\phi, \quad \boldsymbol{x} \in \partial\Omega_F, \tag{3d}$$

$$\mathrm{i}\omega\phi = \xi, \quad \boldsymbol{x} \in \partial\Omega_F. \tag{3e}$$

In the frequency domain, the initial conditions given by equations (2) are replaced by conditions at infinity. We assume a wave of the form

$$\phi^I_\kappa(\boldsymbol{x}, k_\kappa) = \mathrm{e}^{-\mathrm{i}\kappa k_\kappa x}\frac{\cosh k_\kappa(z - h_\kappa)}{\cosh k_\kappa h_\kappa}, \tag{4}$$

is incident from negative infinity ($\kappa = -1$) or incident from positive infinite ($\kappa = 1$) where k_κ is the wavenumber given by the positive

real solution to the dispersion equation $\omega^2 = k_\kappa \tanh k_\kappa h_\kappa$. We decompose the total potential as the sum of an incident and scattered wave potential

$$\phi_\kappa(\boldsymbol{x}, k_\kappa) = \phi^I_\kappa(\boldsymbol{x}, k_\kappa) + \phi^S_\kappa(\boldsymbol{x}, k_\kappa), \tag{5}$$

where the scattering potential ϕ^S_κ must satisfy the radiation condition .

3 Solutions of the time-dependent problem.

We define the Dirichlet to Neumann operator $\partial_n \boldsymbol{G}$ by

$$\partial_n \boldsymbol{G}\psi = \partial_n \Phi|_{z=0}\,, \quad \boldsymbol{x} \in \partial\Omega_F, \tag{6}$$

where Φ is the solution to

$$\Delta\Phi = 0, \quad \boldsymbol{x} \in \Omega, \tag{7a}$$
$$\partial_n\Phi = 0, \quad \boldsymbol{x} \in \partial\Omega_B, \tag{7b}$$
$$\partial_n\Phi = 0, \quad z = -h(x), \tag{7c}$$
$$\Phi = \psi, \quad z = 0,\ \boldsymbol{x} \in \partial\Omega_F. \tag{7d}$$

Therefore, equations (1a-1e) can be written as

$$\partial_t^2\zeta + \partial_n \boldsymbol{G}\zeta = 0. \tag{8}$$

3.1 Generalized eigenfunction expansion method

The generalized eigenfunction method (GEM) presented here is a slight modification of that presented in Meylan (2009) to allow for non-constant depth and to include the possibility of a trapped mode. The evolution operator $\partial_n \boldsymbol{G}$ is self-adjoint in the Hilbert space given by the following inner product

$$\langle \zeta, \eta \rangle_{\mathcal{H}} = \int_{\partial\Omega_F} \zeta\eta^* \,\mathrm{d}x, \tag{9}$$

where * denotes complex conjugate. The eigenfunctions of $\partial_n \boldsymbol{G}$ satisfy

$$\partial_n \boldsymbol{G}\psi = \omega^2\psi. \tag{10}$$

Equation (10) is nothing more than equations (3). We define the eigenfunctions by restricting the frequency domain solution for an incident wave to the free surface, i.e.,

$$\psi_\kappa(x,k) = \phi_\kappa(\boldsymbol{x}, k_\kappa)|_{\boldsymbol{x}\in\Omega_F}\,. \tag{11}$$

It is possible for there to exist point spectra for this operator which correspond to the existence of a trapped mode. In this case

$$\partial_n \boldsymbol{G}\psi_p = \omega_p^2\psi, \tag{12}$$

but

$$\langle \psi_p, \psi_p \rangle_{\mathcal{H}} < \infty. \tag{13}$$

The GEM allows us to calculate the time-dependent solutions using these eigenfunctions as follows

$$\begin{aligned}\zeta(x,t) = \mathrm{Re}\Big\{ \int_0^\infty \sum_{\kappa\in\{-1,1\}} &\langle \zeta_0(x), \psi_\kappa(x,k)\rangle_{\mathcal{H}} \\ &\times \psi_\kappa(x,k)\, \frac{\mathrm{d}k}{\mathrm{d}\omega}\bigg|_{h=h_\kappa} e^{-\mathrm{i}\omega t}\,\mathrm{d}\omega\Big\} \\ + \mathrm{Re}\left\{ \sum_{p\in\Lambda} \frac{\langle \zeta_0(x), \psi_p(x)\rangle_{\mathcal{H}}}{\langle \psi_p(x), \psi_p(x)\rangle_{\mathcal{H}}} \psi_p(x) \mathrm{e}^{-\mathrm{i}\omega_p t} \right\},\end{aligned} \tag{14}$$

where Λ is the set of trapped mode points (which is the empty set in the case no trapped waves are present).

3.2 Fourier/Laplace transform solution of time-domain equations

The Fourier/Laplace transform and its inverse is given by

$$\hat{f}(\sigma) = \int_0^\infty f(t)e^{i\sigma t}\,\mathrm{d}t,\ f(t) = \frac{1}{2\pi} \fint_{-\infty}^{\infty} \hat{f}(\sigma)e^{-i\sigma t}\,d\sigma,$$

where the integration is taken above any poles on the real axis (which correspond to trapped modes in our case). The Fourier/Laplace transform of equation (8) and the initial condition (2) gives

$$-\sigma^2\hat{\zeta} + \partial_n \boldsymbol{G}\hat{\zeta} = -\mathrm{i}\sigma\zeta_0. \tag{15}$$

The solution for the displacement is given by

$$\begin{aligned}\zeta(x,t) &= \frac{1}{2\pi} \fint_{-\infty}^{\infty} -\left(\partial_n \boldsymbol{G} - \sigma^2\right)^{-1} \mathrm{i}\sigma\zeta_0 \mathrm{e}^{-\mathrm{i}\sigma t}\,\mathrm{d}\sigma \\ &= \mathrm{Re}\left\{ \frac{1}{\pi} \fint_0^\infty -\left(\partial_n \boldsymbol{G} - \sigma^2\right)^{-1} \mathrm{i}\sigma\zeta_0 \mathrm{e}^{-\mathrm{i}\sigma t}\,\mathrm{d}\sigma \right\}.\end{aligned} \tag{16}$$

3.3 Singularity expansion method

The singularity expansion method (SEM) is based on deforming the contour of integration and writing the integral (16) as a sum over the poles and ignoring the contribution from branch cuts or the integral at infinity. The poles are the solutions to

$$\left(\partial_n \boldsymbol{G} - \sigma^2\right) \chi_p = 0, \tag{17}$$

where we do not restrict χ_p to have finite energy and we consider complex σ. We also define the mode associated with the adjoint operator, $\bar{\chi}_p$, as

$$\left(\partial_n \boldsymbol{G} - \sigma^2\right)^* \bar{\chi}_p = 0, \tag{18}$$

where the star denotes the adjoint operator. If we approximate the solution to equation (16) by the contribution from the only the poles we obtain

$$\zeta(x,t) \approx \operatorname{Re}\left\{\sum_p \frac{\langle -2\sigma_p \zeta_0(x), \bar{\chi}_p(x)\rangle_{\mathcal{H}}}{\langle (\partial_n \boldsymbol{G} - \sigma^2)' \chi_p, \bar{\chi}_p\rangle_{\mathcal{H}}} \chi_p \mathrm{e}^{-\mathrm{i}\omega_p t}\right\}. \tag{19}$$

4 Numerical solution

We describe here a numerical method which allows us to solve for the the Fourier/Laplace solution even for complex frequency values and which we can use to calculate the SEM solution. We use a boundary element method combined with a matched vertical eigenfunction expansion. A finite domain $\bar{\Omega}$ is defined by restricting Ω to $|x| < l$. We discretize the boundary of Ω with a set of constant panels. Outside of the domain $\bar{\Omega}$, Ω consists of two semi-infinite domains containing no bodies where the fluid depth is constant where the solution can be found by an eigenfunction expansion. The method is described in detail in Wang & Meylan (2002) and is similar to the modified finite element method used in Hazard & Lenoir (1993).

The constant panel boundary element method gives the matrix equation

$$\frac{1}{2}\boldsymbol{\phi} = \boldsymbol{H_n}\boldsymbol{\phi} - \boldsymbol{H}\boldsymbol{\phi_n}, \tag{20}$$

where $\boldsymbol{\phi}$ ($\boldsymbol{\phi_n}$) is the vector of potential (derivative) values on the boundary panels and $\boldsymbol{H}$ ($\boldsymbol{H_n}$) is the matrix corresponding to the Green function (normal derivative of the Green function).

To solve equation (20) we need to find a relationship between the normal derivative and the potential on the boundary. The boundary is divided into four regions. $\partial\Omega_1$ is the body and sea floor, $\partial\Omega_2$ is the free surface, $\partial\Omega_3$ is the left hand vertical boundary, and $\partial\Omega_4$ is the right hand vertical boundary.

The boundary condition on $\partial\Omega_3$ and $\partial\Omega_4$ is the most complicated as it depends non-trivially on the frequency. We use an integral relation to expresses the normal outward derivative in terms of an expansion in the vertical eigenfunctions,

$$\partial_n \phi = \boldsymbol{Q_{-1}}\phi, \quad \text{on} \quad \partial\Omega_3. \tag{21}$$

where $\boldsymbol{Q_{-1}}$ is given in Wang & Meylan (2002). We apply a similar derivation on the boundary $\partial\Omega_4$. The normal derivatives can be expressed in terms of the potential on all four boundaries,

$$\partial_n \boldsymbol{\phi} = 0, \quad \text{on} \quad \partial\Omega_1, \tag{22a}$$
$$\partial_n \boldsymbol{\phi} = \sigma^2 \boldsymbol{\phi}, \quad \text{on} \quad \partial\Omega_2, \tag{22b}$$
$$\partial_n \boldsymbol{\phi} = \boldsymbol{Q_{-1}}\phi, \quad \text{on} \quad \partial\Omega_3, \tag{22c}$$
$$\partial_n \boldsymbol{\phi} = \boldsymbol{Q_1}\phi, \quad \text{on} \quad \partial\Omega_4. \tag{22d}$$

We write this condition as

$$\boldsymbol{\phi}_n = \boldsymbol{A}(\sigma)\boldsymbol{\phi}, \tag{23}$$

where we explicitly included the dependence of $\boldsymbol{A}$ on the parameter σ.

For the case of the Fourier/Laplace transform solution we have

$$\left(\frac{1}{2} - \boldsymbol{H_n} + \boldsymbol{H}\boldsymbol{A}\right)\boldsymbol{\phi} = \boldsymbol{H}\boldsymbol{f}_0, \tag{24}$$

where $\boldsymbol{f}_0 = 0$ on $\partial\Omega_i$ except

$$\boldsymbol{f}_0 = \zeta_0, \quad \text{on} \quad \partial\Omega_2. \tag{25}$$

We locate the poles and vector $\boldsymbol{\chi}_p$ by searching for the values σ_p for which

$$\left(\frac{1}{2} - \boldsymbol{H_n}\boldsymbol{\phi} + \boldsymbol{H}\boldsymbol{A}(\sigma_p)\right)\boldsymbol{\chi}_p = 0, \tag{26}$$

and we define the adjoint vector $\bar{\boldsymbol{\chi}}_p$ by

$$\left(\frac{1}{2} - \boldsymbol{H_n} + \boldsymbol{H}\boldsymbol{A}(\sigma_p)\right)^* \bar{\boldsymbol{\chi}}_p. \tag{27}$$

We can then express the SEM numerically using our matrix approximation of the operator as

$$\zeta(x,t) \approx \operatorname{Re}\left\{\sum_p \frac{\langle\, 2\sigma_p \boldsymbol{f}_0, \bar{\boldsymbol{\chi}}_p(x)\rangle \chi_p(x)}{\langle \left\{\boldsymbol{H}\left(\frac{1}{2} - \boldsymbol{H_n} + \boldsymbol{H}\boldsymbol{A}\right)\right\}' \boldsymbol{\chi}_p, \bar{\boldsymbol{\chi}}_p\rangle} \mathrm{e}^{-\mathrm{i}\omega_p t}\right\}, \tag{28}$$

where the inner product is the standard inner product for vectors. Note that by $\boldsymbol{\chi}_p$ we mean the vector defined on the boundary of $\bar{\Omega}$ while χ_p is the value restricted to the surface, and defined outside the region $\bar{\Omega}$ if needed. We require the region $|x| < l$ to enclose the initial condition. The derivative of the matrix is calculated numerically.

5 Results

We consider an initial surface displacement of the form

$$\zeta_0(x) = \mathrm{e}^{-20(x-0.2)^2}. \tag{29}$$

The exact solution is given by the solid line and is calculated using the GEM (equation (14)). The SEM solution (calculated using equation (28)) is given by the dashed line.

Figure 1 shows the exact and SEM solution for the case of two semi-circular fixed bodies with radius 0.1 centered at $(\pm 1, 0)$. The fluid depth is constant $h = 1$ and is not plotted but the circular bodies are plotted for illustration. Sixteen poles were used in the SEM approximation.

6 Summary

We have shown that the phenomena of trapping and near trapping in the time domain can be connected via the formula derived using the SEM. We have derived a practical method to implement the SEM and implemented it numerically.

References

Cummins, W. E. 1962 The impulse response function and ship motions. *Schiffstechnik* **9**, 101–109.

Evans, D. V. & Porter, R. 1997 Near-trapping of waves by circular arrays of vertical cylinders. *Appl. Ocean Res.* **19** (2), 83–99.

Fitzgerald, C. & Meylan, M. H 2011 Generalized eigenfunction method for floating bodies. *J. Fluid Mech.* **677**, 544–554.

Hazard, C. & Lenoir, M. 1993 Determination of scattering frequencies for an elastic floating body. *SIAM J. Math. Anal.* **24** (4), 1458–1514.

Hazard, C. & Loret, F. 2007 Generalized eigenfunction expansions for scattering problems with an application to water waves. *Proc. R. Soc. Edin. A* **137**, 995–1035.

McIver, M. 1996 An example of non-uniqueness in the two-dimensional water wave problem. *J. Fluid Mech.* **315**, 257–266.

Meylan, M. H. 2009 Generalized eigenfunction expansion for linear water-waves. *J. Fluid Mech.* **632**, 447–455.

Meylan, M. H. & Eatock Taylor, R. 2009 Time-dependent water-wave scattering by arrays of cylinders and the approximation of near trapping. *J. Fluid Mech.* **631**, 103–125.

Wang, Synthia D. & Meylan, M. H. 2002 The linear wave response of a floating thin plate on water of variable depth. *J. of Applied Ocean Res.* **24** (3), 163–174.

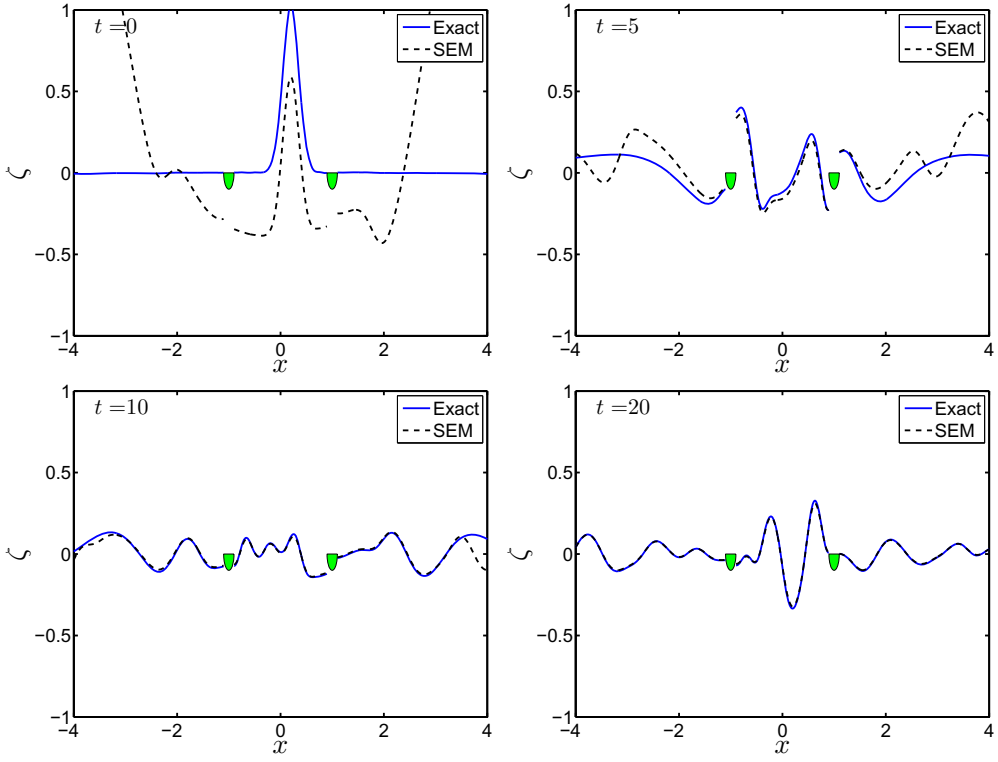

Figure 1: The exact (solid line) and SEM (dashed line) solution for the times shown. The scattering bodies are plotted for illustration.

External Dynamics System of Twin Floating Bodies for Perfect Wave Absorption

Munehiko Minoura, Chutatsu Hirao, Yuki Miyazaki, Masashi Kashiwagi
Department of Naval Architecture and Ocean Engineering, Osaka University
2-1 Yamada-oka, Suita, Osaka 565-0871, Japan
minoura@naoe.eng.osaka-u.ac.jp

INTRODUCTION

Regular waves propagating in a two-dimensional waterway can be absorbed perfectly by a single floating body which oscillate in two modes of motion such as a couple of heave and sway motions or heave and roll motions. It is naturally required the symmetrical and asymmetrical motions for the perfect wave absorption.

In a specific situation we can absorb waves perfectly by either motion only of the floating body. For an instance, the floating body placed at the end of the experimental towing tank without gaps between the floating body and the tank wall enables it by the heave motion only. That is the result of canceling another mode because of the symmetrical condition of the free surface at the end of the tank. The wave tank having wave-makers and active wave absorbers is generally designed based on this principle. However, the situation of the experiment and the experimental tank make it difficult to place the wave-makers and absorbers at the end of the tank. For the multiple application of the experimental tank, it is desired to place the wave-makers and absorbers at an arbitrary place and time.

Symmetrical and asymmetrical motions of the floating body provide symmetrical and asymmetrical waves propagating from the floating body. This wave condition can be generated by heave motion only of two floating bodies. The mechanism of the wave-maker allowing only heave motion is simpler and more practical than that of two modes of motion.

This paper addresses the problem of the wave absorption by the twin floating bodies with the external dynamics system. In the beginning, the wave condition for the perfect wave absorption by the twin floating bodies is described and formulated based on the theory of the mutual interaction of waves. As a solution of these formulae, the characteristics of the external dynamics system attached on the wedge-shaped floating body and block-shaped floating body are obtained. These results give us the possibility and problem of wave absorption of this system.

WAVE CONDITION FOR PERFECT ABSORPTION

The arrangement of the twin floating bodies is shown in Fig. 1. The geometry of floating bodies is symmetric and each body has geometry. The heave motion is allowed only for these floating bodies. The external dynamics system attached on the floating body is modeled with a spring and a dash pot. Changing the restoring and damping factors of a spring and a dash pot depending on a wave period, this system enables to absorb incident waves perfectly. In a real system a spring and a dash pot are replaced with a mechanical actuator controlled by the displacement and velocity of the motion of the floating body. The wave and wave force acting on the floating body assume to be obtained by the linear potential theory.

Let s, $d_j^{\pm}$ and $r_j^{\pm}$ denote the complex amplitude of incident waves, diffraction waves and radiation waves. The incident waves is naturally

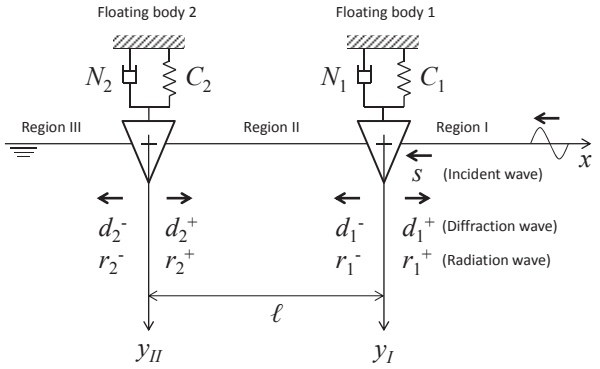

Fig. 1 Definition of waves and coordinate system.

expressed as

$$\zeta_a(x,t) = \mathrm{Re}\left[se^{i(kx+\omega t)}\right].$$

Where k is a wave number and ω is an angular frequency of waves.

The incident wave coming from a far field into the floating body 1 is completely absorbed in a steady condition, then the complex amplitude of waves in the region I and III is described as

$$d_1^+ + r_1^+ + L(d_2^+ + r_2^+) = 0, \tag{1}$$
$$d_2^- + r_2^- + L(d_1^- + r_1^-) + Ls = 0. \tag{2}$$

Where, L denotes the transfer function of the waves progressing the distance ℓ.

$$L = e^{-ik\ell}.$$

Relation of the mutual interaction regarding the diffraction waves is described as

$$d_1^+ = iH_{14}^- L(d_2^+ + r_2^+) + iH_{14}^+ s, \tag{3}$$
$$d_1^- = iH_{14}^+ L(d_2^+ + r_2^+) + iH_{14}^- s, \tag{4}$$
$$d_2^+ = iH_{24}^+ L(d_1^- + r_1^- + s), \tag{5}$$
$$d_2^- = iH_{24}^- L(d_1^- + r_1^- + s). \tag{6}$$

Where, $H_{j4}^{\pm}$ is the Kochin function of diffraction waves, H_{j4}^+ indicates the progressive wave from the floating body j toward the counter direction as the incident wave and H_{j4}^- indicates the progressive wave from the floating body j toward the same direction as the incident wave.

Regarding the radiation waves, due to the symmetrical geometry of the floating body, we can obtain $r_1^+ = r_1^- = r_1$ and $r_2^+ = r_2^- = r_2$. Then

the solution of the simultaneous equations 1-6 are shown as

$$d_1^+ = W^{-1}\left[sL^2(R_1 - T_1)(R_2 - T_2)(R_1 + Q_1) - sR_1\right], \quad (7)$$

$$d_1^- = W^{-1}\left[sL^2(R_1 - T_1)(R_2 - T_2)(R_1 + Q_1) - sQ_1\right], \quad (8)$$

$$d_2^+ = W^{-1}sLR_2(R_1 - T_1), \quad (9)$$

$$d_2^- = W^{-1}sLQ_2(R_1 - T_1), \quad (10)$$

$$r_1 = W^{-1}\left[-sL^2(R_1 - T_1)(R_2 - T_2)(R_1 + T_1) + sR_1\right], \quad (11)$$

$$r_2 = W^{-1}sLT_2(-R_1 + T_1). \quad (12)$$

Where W, R_j, Q_j, T_j are defined as

$$W = L^2(R_1 - T_1)(R_2 - T_2) - 1,$$
$$R_j = iH_{j4}^+,$$
$$Q_j = iH_{j4}^-.$$
$$T_j = 1 + Q_j.$$

MOTION OF FLOATING BODY

Let M_1 denote the total mass of the floating body and the external dynamics system. Let y_1 denote the displacement of the heave motion. The force acting on the floating body 1 consists of the mechanical force by the external dynamics system and the hydrodynamic force. Concerning the hydrodynamic force, we must take the exciting force induced by the reflected waves from the floating body 2. The linear equation of motion of the floating body 1 with respect to the angular frequency ω is given as

$$M_1\ddot{y}_1 = -N_1\dot{y}_1 - C_1y_1 - a_1\ddot{y}_1 - b_1\dot{y}_1 - c_1y_1 + \mathrm{Re}\left[\rho gH_{12}L(d_2^+ + r_2^+)e^{i\omega t}\right] + \mathrm{Re}\left[\rho gH_{12}se^{i\omega t}\right]. \quad (13)$$

Where, H_{12} is the Kochin function of the heave oscillation of the floating body 1. The symbols of a_1, b_1 and c_1 indicate the added mass, the wave damping coefficient and the restoring coefficient respectively. The complex amplitude of the heave oscillation expressed as Y_1 and A_1 is defined as

$$A_1 = -\omega^2(M_1 + a_1) + i\omega(N_1 + b_1) + C_1 + c_1, \quad (14)$$

then, the equation 13 is represented as

$$A_1Y_1 = \rho gH_2\left\{L(d_2^+ + r_2^+) + s\right\}. \quad (15)$$

The Kochin function gives the relation between r_1 and Y_1 as

$$r_1 = -ikH_{12}Y_1.$$

Applying this relation to the equation 15, we obtain

$$A_1 = \frac{-ik\rho g{H_{12}}^2}{r_1}\left\{L\left(d_2^+ + r_2^+\right) + s\right\}. \quad (16)$$

In a similar way, the equation for the floating body 2 is provided as

$$A_2 = \frac{-ik\rho g{H_{22}}^2}{r_2}L\left(d_1^- + r_1^- + s\right). \quad (17)$$

Where, H_{22} is the Kochin function of the heave oscillation of the floating body 2.

CHARACTERISTICS OF EXTERNAL DYNAMICS SYSTEMS

The characteristics of the external dynamics system is determined by substituting wave conditions for the equation of motion. Substituting Eqs. 8, 9, 11 and 12 for Eqs. 16 and 17, we obtain A_1 and A_2 for the perfect absorption. They are expressed as A_{p1}, A_{p2};

$$A_{p1} = ik\rho g{H_{12}}^2\frac{2L^2(R_1 - T_1)(R_2 - T_2) - 1}{L^2(R_1 - T_1)(R_2 - T_2)(R_1 + T_1) - R_1}, \quad (18)$$

$$A_{p2} = ik\rho g{H_{22}}^2\frac{1}{T_2}. \quad (19)$$

Using the relations regarding the Kochin function:

$$H_{j2} = \bar{H}_{j2}(R_j + T_j), \quad (20)$$

$$b_j = \rho\omega H_{j2}\bar{H}_{j2}. \quad (21)$$

and the dispersion relation of wave: $\omega^2 = kg$, we obtain

$$A_{p1} = i\omega b_1\frac{2L^2P - (R_1 + T_1)}{L^2P - R_1}, \quad (22)$$

$$A_{p2} = i\omega b_2\left(\frac{R_2}{T_2} + 1\right). \quad (23)$$

Where, $\bar{H}_{j2}$ is a conjugate of H_{j2} and

$$P = (R_1 + T_1)(R_1 - T_1)(R_2 - T_2).$$

The characteristics of the external dynamics system at this moment are described as C_{pj} and N_{pj}. They independently consist of the real and imaginary part of A_{pj} as shown in Eq. 14. Therefore, comparing the real and imaginary part of (22) and (23) gives the characteristics of the external dynamics system.

$$C_{p1} = \mathrm{Re}\left[A_{p1}\right] + \omega^2(M_1 + a_1) - c_1 \quad (24)$$

$$N_{p1} = \frac{1}{\omega}\mathrm{Im}\left[A_{p1}\right] - b_1 \quad (25)$$

$$C_{p2} = i\omega b_2\frac{R_2}{T_2} + \omega^2(M_2 + a_2) - c_2 \quad (26)$$

$$N_{p2} = 0 \quad (27)$$

Equations 26 and 27 are derived from the matter that R_j/T_j is a pure imaginary number. The wave power absorbed by each external dynamics system is expressed by

$$\text{Absorbed wave power} = \frac{1}{2}N_{pj}\omega^2\left|Y_j\right|^2.$$

The equation 27 naturally indicates that the external dynamics system of the floating body 2 does not absorb wave energy. Actually the characteristics expressed by Eq. 26 and 27 corresponds to the condition of the external dynamics system of a single floating body which perfectly reflects the incident waves. Namely, the wave energy is absorbed by the external dynamics system of the floating body 1 only. Moreover, this characteristics does not depend on the gap between the floating bodies.

Using a single symmetrical floating body with the external dynamics system, we can absorb a half of wave energy at a maximum efficiency. Then, the condition of the external dynamics system is well known as

$$C = \omega^2(M + a) - c, \quad (28)$$

$$N = b. \quad (29)$$

Equations 24-26 are regarded as the modified condition from Eqs. 28 and 29.

COMBINATION OF FLOATING BODY

The theoretical characteristics of the external dynamics system for the perfect absorption of incident waves are shown in several cases regarding the wedge-shaped and block-shape floating body and their combination.

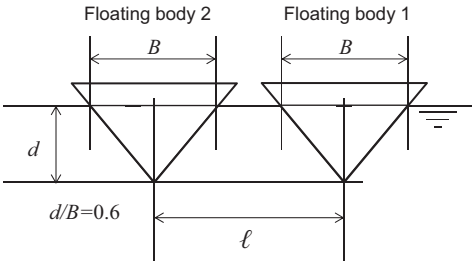

Fig. 2 Geometry of wedge-shaped floating bodies.

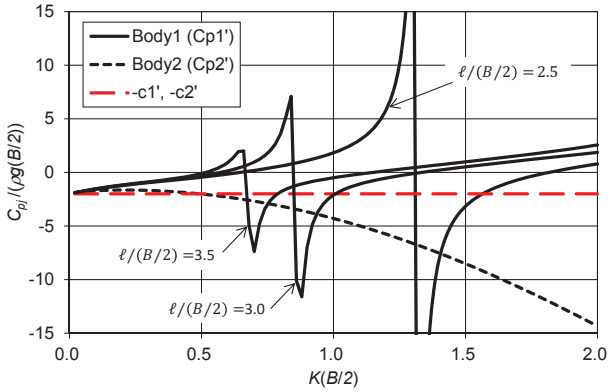

Fig. 3 Restoring coefficients of the external dynamic system of wedge-shaped floating bodies.

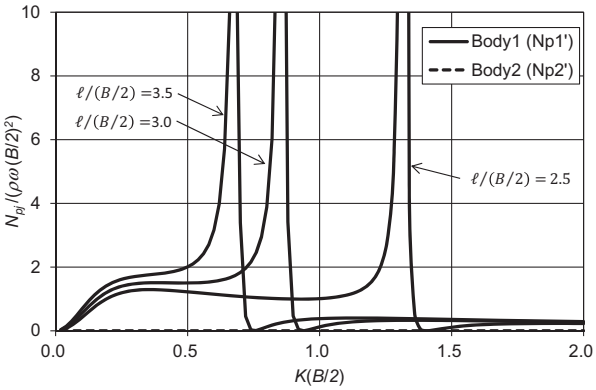

Fig. 4 Damping coefficients of the external dynamic system of wedge-shaped floating bodies.

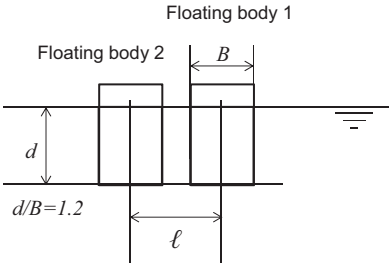

Fig. 5 Geometry of block-shaped floating bodies.

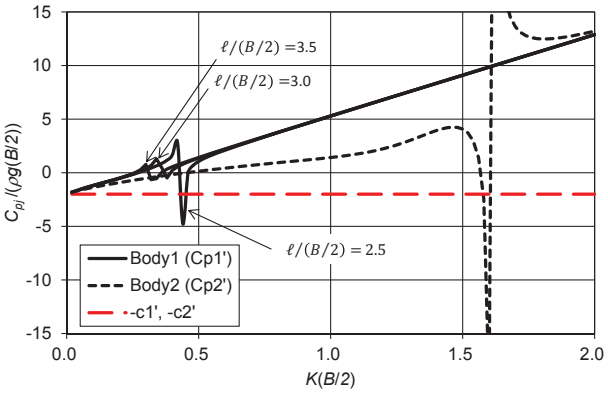

Fig. 6 Restoring coefficients of the external dynamic system of block-shaped floating bodies.

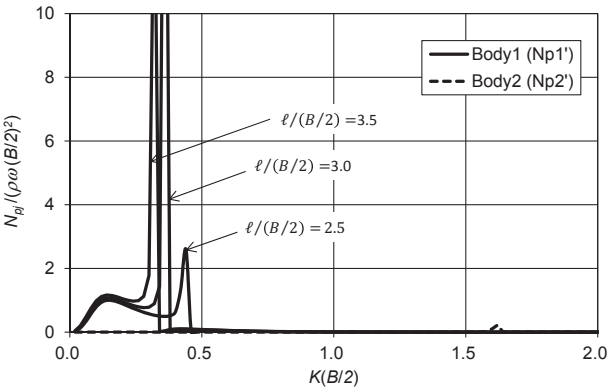

Fig. 7 Damping coefficients of the external dynamic system of block-shaped floating bodies.

The arrangement of the wedge-shaped floating body is shown in Fig. 2 and the theoretical characteristics of the external dynamics system are shown in Figs. 3 and 4. These were calculated by Eq. 24-27 and the Kochin functions were obtained by the boundary element method based on the linear potential theory. The aspect ratio of the draft:d and the breadth:B at the water line is $d/B = 0.6$. The gap between the floating bodies is changed from $\ell/(B/2) = 2.5$ to 3.5. The nondimensional frequency $K(B/2) < 2$ is appropriate for a real wave-maker and absorber of an experimental tank/basin. The mass inside the external dynamics system is disregarded in the calculation.

According to the motion of equation of the floating body, the total restoring coefficient must be positive in a steady oscillation. Its condition is provided as $C_{pj} + c_j > 0$. Therefore, the restoring coefficient of the external dynamics system must satisfy

$$C_{pj} > -c_j. \tag{30}$$

However, this condition is not applicable to C_{p2} in the wider range of wave frequency more than $K(B/2) > 0.5$. The snap point of C_{p1} depends on R_j, T_j and the gap between the floating bodies. In this point a steady oscillation is not obtained due to the condition of Eq. 30 and the wave absorption is impossible due to $N_{p1} = 0$ as shown in Fig. 4. As a result, the range of the wave frequency is quite restricted for the steady oscillation of this system.

The arrangement of the block-shaped floating body is shown in Fig. 5 and the theoretical characteristics of the external dynamics system are shown in Figs. 6 and 7. The restoring coefficients satisfy the condition Eq. 30 in the wider range of wave frequency than that of the wedge-shaped floating body as shown in Fig. 6. However, the damping coefficients are much less(not zero) in the range of $K(B/2) > 0.5$ as shown in Fig. 7. This matter indicates that a large amplitude of the heave motion

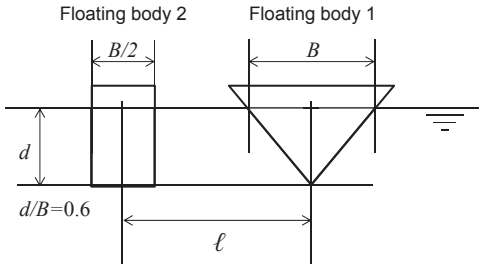

Fig. 8 Combination of wedge-shaped and block-shaped floating bodies.

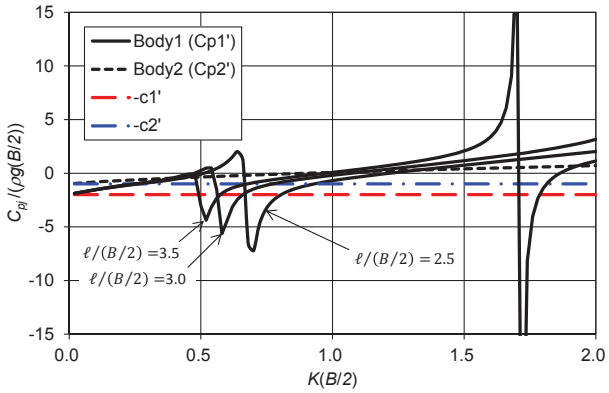

Fig. 9 Restoring coefficients of the external dynamic system of the combination of wedge-shaped and block-shaped floating bodies.

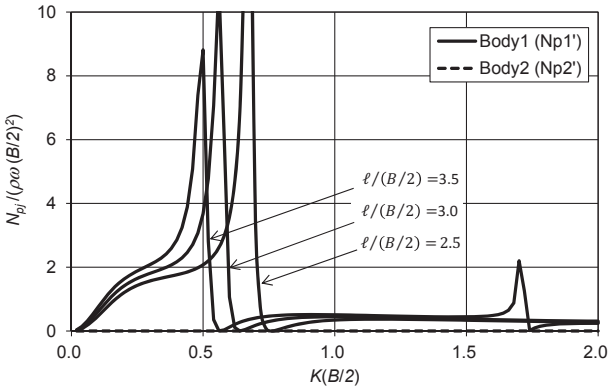

Fig. 10 Damping coefficients of the external dynamic system of the combination of wedge-shaped and block-shaped floating bodies.

of the floating body 1 appears for the wave energy absorption.

The combination of the wedge-shaped and block-shaped floating body is shown in Fig. 8 and the theoretical characteristics of the external dynamics system are shown in Figs. 9 and 10. The displacements of both floating bodies are same. The restoring coefficient C_{p2} satisfies the condition Eq. 30 in all range, however C_{p1} is not acceptable for this condition at the snap point. The snap points appear in the lower wave frequency: $0.5 < K(B/2) < 0.7$ than the combination of the wedge-shaped and wedge-shaped floating bodies because the gap between the floating bodies is relatively larger.

The combination of the block-shaped and block-shaped floating bodies seems to be the best for wave absorption, however the efficiency of wave generation of the block-shaped floating body is not higher. To apply the wedge-shaped floating body having the higher efficiency of wave generation, we need to avoid the snap point of C_{p1}. The relation between R_j, T_j and the gap of the floating bodies must be investigated because the snap point of C_{p1} is determined by the denominator of Eq. 23.

CONCLUSIONS

The characteristics of the external dynamics system attached on the twin floating bodies for the perfect wave absorption are shown theoretically with the mutual interaction theory of waves. The external dynamics system is modeled by a linear spring and dash pot. As a result, the following knowledge is obtained.

- The external dynamics system of the floating body located at the lee side for incident waves must reflect waves perfectly. The damping coefficient of this external dynamics system must be zero. All wave energy is consequently absorbed by the external dynamics system located at the weather side.
- The total of the mechanical and hydrodynamic restoring coefficients must be more than zero for the steady oscillation of the floating bodies. This condition is not satisfied in the wider wave frequency for the system of the wedge-shaped and wedge-shaped floating bodies. However, replacing the floating body by the block-shaped one, we can satisfy this condition.
- This system is also expected to have the function of a wavemaker, namely has to absorb and generate waves simultaneously. Considering the efficiency of wave generation, the wedge-shaped floating body is better at the weather side. The restoring coefficient of the external dynamics system attached on the wedge-shaped floating body snaps at a specific wave frequency. At this frequency, the condition for the steady oscillation is not satisfied. To apply the wedge-shaped floating body having the higher efficiency of wave generation, we need to avoid this snap point.

REFERENCES

Naito, S, Huang, J, Nagata, M and Nakamura, S (1987). "Research on Perfect Absorption of Regular Wave with the Terminal Device", *Journal of Kansai Society of Naval Architects, Japan*, No 205, pp29-32 (in Japanese).

Kagemoto, H and Yue, DKP (1986). "Interactions among multiple three-dimensional bodies in water waves: an exact algebraic method", *J. Fluid Mechanics*, Vol. 166, pp. 189-209.

Naito, S (2006). "Wave Generation And Absorption In Wave Basins: Theory And Application ", *International Journal of Offshore and Polar Engineering*, Vol. 16, No. 2, pp. 81-89.

Time dependent flexural gravity wavemaker problem

S. K. Mohanty, R. Mondal, T. Sahoo
Department of Ocean Engineering and Naval Architecture
Indian Institute of Technology, Kharagpur -721 302, India
sanjaymath@gmail.com, ramju08@yahoo.com, tsahoo1967@yahoo.com

1. Introduction

Currents with speeds exceeding 1m/s are observed in the near shore regions in many parts of the world and the mutual interaction between waves and the underlying currents alter the wave characteristics significantly. There is negligible progress in the literature to deal with wave structure interaction problems in the presence of current in time domain. Meylan et al. (2004) studied the wave interaction with a finite floating elastic plate in time domain using Laplace transform and Green's function technique. In the present paper, a class of initial boundary value problems associated with the time dependent flexural gravity wave maker problems are handled using Laplace transform method and Green's function technique in both the cases of finite and infinite water depths.

2. Mathematical formulation

In the present paper, the time dependent flexural gravity wavemaker problems are analyzed in two-dimensional cartesian co-ordinate system in both the cases of finite and infinite water depths assuming that a thin elastic plate of thickness d and density $\rho_i$is floating on the free surface of water. Assuming that the fluid is inviscid, incompressible of constant density ρ occupies the region $0 < x < \infty$, $0 < y < h$ in case of finite depth, ($0 < y < \infty$ in case of infinite depth). Further, it is assumed that the fluid motion is irrotational and there is a uniform current flowing with speed U along the direction of wave propagation. Thus, the total velocity potential $\oplus(x, y, t)$ is written as $\oplus(x, y, t) = Ux + \Phi(x, y, t)$ and the plate deflection is denoted as $\eta(x, t)$. Thus, the velocity potential $\Phi(x, y, t)$ satisfying the two dimensional Laplace equation is given by

$$\nabla^2\Phi = 0, \quad \text{in the fluid region,} \tag{1}$$

along with the bottom boundary condition

$$\partial_y\Phi = 0, \ \text{ on } y = h, \ \text{ and } \ \Phi, |\nabla\Phi| \to 0, \ \text{ as } \ y \to \infty, \tag{2}$$

in case of water of finite and infinite depths respectively. The linearized kinematic and dynamic conditions on the plate covered surface are given by

$$\partial_t\eta + U\partial_x\eta = \partial_y\Phi, \quad \text{on} \quad y = 0. \tag{3}$$

$$(D\partial_y^4 - Q\partial_y^2 + \gamma\partial_t^2 + g)\Phi_y = (\partial_t + U\partial_x)^2\Phi, \ \text{ on } \ y = 0, \tag{4}$$

where ∂ with suffix indicates the partial derivative with $D = EI/\rho$, $Q = N/\rho$, $\gamma = \rho_i d/\rho$, $I = d^3/(12(1-\nu^2))$, E is the Young's modulus, N is the compressive force, ν is the poison's ratio, and g is the acceleration due to gravity.

3. Green's function for flexural gravity waves

In this Section, the time dependent Green's functions $G(x, y; x_0, y_0, t)$ are derived for flexural gravity wave problems in case of finite and infinite water depths assuming that a point source of strength $m(t)$ is located at (x_0, y_0) in the fluid domain. The Green's function $G(x, y; x_0, y_0, t)$ satisfy the two dimensional Laplace equation as in Eq.(1) in the fluid domain except at (x_0, y_0), along with the boundary conditions as in Eqs. (2)–(4). In addition, the Green's function $G(x, y; x_0, y_0, t)$ satisfies the conditions

$$G \sim m(t)\ln r_1, \ \text{ as } \ r_1 \to 0, \quad \text{ and } \quad G, |\nabla G| \to 0, \quad \text{as} \quad r_1 \to \infty, \tag{5}$$

with $r_1 = \sqrt{(x-x_0)^2 + (y-y_0)^2}$. Further, the Green's function $G(x, y; x_0, y_0, t)$ satisfies the initial conditions

$$G, \partial_t G = 0, \quad \text{on } \ y = 0, \quad \text{at } \ t = 0. \tag{6}$$

In order to determine $G(x,y;x_0,y_0,t)$ associated with the aforementioned initial boundary value problem, the problem is transformed to a boundary value problem by using the Laplace transform in the time variable t. The transformed Green's function $\bar{G}(x,y;x_0,y_0,p)$ satisfies the two dimensional Laplace equation as in Eq. (1) in the fluid domain except at (x_0,y_0) along with the boundary conditions (2) and

$$(D\partial_y^5 - Q\partial_y^3 + g\partial_y^3 - p^2 - U^2\partial_x^2 - 2Up\partial_x)\bar{G} = 0 \ \text{ on } \ y = 0, \tag{7}$$

Finite water depth:
The transformed Green's function $\bar{G}(x,y;x_0,y_0,p)$ satisfying the governing Eq. (1) along with the boundary conditions (2) and (7) in case of finite water depth is given by

$$\bar{G} = \bar{m}(p)\Big[\ln\frac{r_1}{r_2} - \int_0^\infty \Big\{\frac{2e^{-kh}g_1(y,y_0)\cos k(x-x_0)}{k\cosh kh} + \sum_{m=I}^{II}\frac{\Omega_h^2 g_2(y,y_0)e^{i\epsilon_m k(x-x_0)}}{\{\Omega_h^2 + (p+i\epsilon_m Uk)^2\}g_3(k)}\Big\}dk\Big], \tag{8}$$

where $\Omega_h^2 = (Dk^4 - Qk^2 + g)k\tanh kh$, $r_2 = \sqrt{(x-x_0)^2 + (y+y_0)^2}$,

$$\left.\begin{aligned} g_1(y,y_0) &= \sinh ky \sinh ky_0, \quad g_3(k) = k\sinh kh\cosh kh, \\ g_2(y,y_0) &= \cosh k(h-y)\cosh k(h-y_0), \end{aligned}\right\}, \epsilon_m = \begin{cases} 1, & \text{for } m = I, \\ -1, & \text{for } m = II. \end{cases} \tag{9}$$

Using the inverse Laplace transform and convolution theorem, Eq. (8) yields

$$G(x,y,x_0,y_0,t) = m(t)\Big\{\ln\frac{r_1}{r_2} - 2\int_0^\infty \frac{e^{-kh}g_1(y,y_0)\cos k(x-x_0)}{k\cosh kh}dk\Big\}.$$
$$- 2\int_0^\infty \frac{\Omega_h g_2(y,y_0)}{g_3(k)}\Big\{\int_0^t m(\tau)\sin\Omega_h(t-\tau)\cos k\{(x-x_0) - U(t-\tau)\}d\tau\Big\}dk. \tag{10}$$

Assuming that the motion is simple harmonic in time with angular frequency ω, the associated Green's function is written in the form $G(x,y;x_0,y_0,t) = Re[\mathcal{G}(x,y;x_0,y_0)e^{-i\omega t}]$. Thus, the spatial Green's function $\mathcal{G}(x,y;x_0,y_0)$ satisfy Eq. (1) along with the boundary conditions (2) and (7). Hence, substituting $p^2 = -\omega^2$ and $\bar{m}(p) = 1/(2\pi)$, Eq. (8) yields

$$\mathcal{G} = \frac{1}{2\pi}\Big[\ln\frac{r_1}{r_2} - \int_0^\infty \Big\{\frac{2e^{-kh}g_1(y,y_0)\cos k(x-x_0)}{k\cosh kh} + \sum_{m=I}^{II}\frac{\Omega_h^2 g_2(y,y_0)e^{i\epsilon_m k(x-x_0)}}{\{\Omega_h^2 - (\omega+\epsilon_m Uk)^2\}g_3(k)}dk\Big\}\Big]. \tag{11}$$

Now, applying Cauchy residue theorem, $\mathcal{G}(x,y;x_0,y_0)$ is rewritten as

$$\mathcal{G} = \sum_{m=I}^{II}\Big[\sum_{n=0,I}^{II}\frac{\delta_{m,n}M_1(k_n)f_n(y)f_n(y_0)}{L'(k_n,\epsilon_m)}e^{i\epsilon_m k_n(x-x_0)} + \sum_{n=1}^{\infty}\frac{M_1(k_n)f_n(y)f_n(y_0)}{L'(k_n,\epsilon_m)}e^{-p_n|x-x_0|}\Big], \tag{12}$$

where $M_1(k_n) = -i\kappa_n(Dk_n^4 - Qk_n^2 + g)$, $f_n(y) = \cosh k_n(h-y)/\cosh k_n h$, with $L(k,\epsilon_m) = \Omega_h^2 - (\omega + \epsilon_m Uk)^2$, $\delta_{I,0} = \delta_{II,0} = \delta_{I,I} = \delta_{II,II} = 1$, $\delta_{I,II} = \delta_{II,I} = 0$, $\kappa_n = 1/2$ for $n = 0$ and one otherwise. The expansion formula in Eq. (12) reduces to the formula by Manam et al. (2006) in the absence of current.

Infinite water depth:
Proceeding in a similar manner as in case of finite depth, the transformed Green's function $\bar{G}(x,y;x_0,y_0,p)$ in case of infinite water depth is obtained as

$$\bar{G}(x,y;x_0,y_0,p) = \bar{m}(p)\Big\{\ln\frac{r_1}{r_2} - \sum_{m=I}^{II}\int_0^\infty \frac{\Omega^2 e^{i\epsilon_m k(x-x_0)-k(y+y_0)}}{k\{\Omega^2 + (p+i\epsilon_m Uk)^2\}}dk\Big\}. \tag{13}$$

where $\Omega^2 = (Dk^4 - Qk^2 + g)k$. Using inverse Laplace transform and convolution theorem from Eq. (13), the time dependent Green's function $G(x,y;x_0,y_0,t)$ is obtained as

$$G = m(t)\ln\frac{r_1}{r_2} - \int_0^\infty\int_0^t \frac{2\Omega e^{-k(y+y_0)}}{k}m(\tau)\sin\Omega(t-\tau)\cos k\{x - x_0 - U(t-\tau)\}d\tau dk. \tag{14}$$

In case of simple harmonic motion proceeding in a similar manner as in case of finite water depth the spatial Green's function $\mathcal{G}(x,y;x_0,y_0)$ is obtained as

$$\mathcal{G}(x,y;x_0,y_0)=\frac{1}{2\pi}\Big[\ln\frac{r_1}{r_2}+\int_0^\infty\frac{e^{-ky}}{2}\Big\{C^+(k)e^{ik(x-x_0)}+C^-(k)e^{-ik(x-x_0)}\Big\}dk\Big], \tag{15}$$

with $C^\pm=-\Omega^2e^{-ky_0}/[k\{\Omega^2-(\omega\pm Uk)^2\}]$. Applying Cauchy residue theorem, the Green's function $\mathcal{G}(x,y;x_0,y_0)$ can be rewritten as

$$\mathcal{G}=\sum_{m=I}^{II}\sum_{n=0,I}^{II}\frac{\delta_{m,n}M_1(k_n)e^{-k_n(y+y_0)}}{F_1(k_n,\epsilon_m)}e^{i\epsilon_mk_n(x-x_0)}-\int_0^\infty\frac{M(k,y)M(k,y_0)}{k\triangle(k)}e^{-k(x-x_0)}dk, \tag{16}$$

where $F_1(k,\epsilon_m)=5Dk^4-3Qk^2+g-2U(\omega+U\epsilon_mk)$, $M(k,y)=\Omega^2k\cos ky-(\omega+iUk)^2\sin ky$ and $\Delta(k)=\Omega^4k^2+(\omega+iUk)^4$. It can be easily proved that the series as in Eq.(12) and integral in Eq.(15) are absolutely convergent.

4. Flexural gravity wave-maker problem

In this Section, the Green's function derived in the aforementioned subsection will be used to find the expansion formulae for the velocity potentials associated with the flexural gravity wave maker problems in time domain in the presence of current in both the cases of finite and infinite water depths. Here, the velocity potential $\Phi(x,y,t)$ satisfies the governing Eq. (1), the initial conditions (6) along with the boundary conditions in Eqs. (2)–(4). Assuming that a wave maker located at $x=0$ is oscillating with velocity $U_1(y,t)$. Thus, the boundary condition on the wave maker is given by

$$\frac{\partial\Phi}{\partial x}=U_1(y,t)+U,\quad\text{on}\quad x=0. \tag{17}$$

In order to find the velocity potential $\Phi(x,y,t)$, the initial value problem is converted to a boundary value problem in $\bar\Phi(x,y,p)$ where $\bar\Phi(x,y,p)$ is the Laplace transform of $\Phi(x,y,t)$. Then, Green's identity is applied to the boundary value problem associated with the transformed functions $\bar\Phi(x,y,p)$ and a suitable chosen Green's function $\bar G^{mod}(x,y;x_0,y_0,p)$ defined by

$$\bar G^{mod}(x,y;x_0,y_0,p)=\bar G(x,y;x_0,y_0,p)+\bar G(x,y;-x_0,y_0,p), \tag{18}$$

where $\bar G(x,y;x_0,y_0,p)$ is the transformed Green's function as in Eqs. (8) and (13) in cases of finite and infinite water depths respectively. From Eq. (18), it is clear that $\bar G^{mod}_x(x,y;x_0,y_0,p)=0$. Applying Green's identity to the boundary value problem in $\bar\Phi(x,y,p)$ and $\bar G^{mod}(x,y;x_0,y_0,p)$ and proceeding in a similar manner as in Manam et al. (2006), the velocity potential $\bar\Phi(x_0,y_0,p)$ is obtained as

$$\bar\Phi(x_0,y_0,p)=A(p)-2\int_R\Big\{\bar U_1(y,p)+(U/p)\Big\}\bar G(0,y;x_0,y_0,p)dy, \tag{19}$$

$$A(p)=\int_0^\infty\Big[\frac{2U^2}{p^2}\Big(\bar\Phi_{xx}\bar G_y-\bar G_{xx}\bar\Phi_y\Big)-\frac{4U}{p}\Big(\bar G_x\bar\Phi_y-\bar\Phi_x\bar G_y\Big)\Big]_{y=0}dx$$
$$-\frac{2}{p^2}\Big\{D\Big(\bar\Phi_{yyyx}\bar G_y+\bar G_{yyy}\bar\Phi_{xy}\Big)-Q\bar\Phi_{xy}\bar G_y\Big\}_{(x,y)=(0,0)}, \tag{20}$$

where R varies from 0 to ∞ and 0 to h in the case of infinite and finite water depth respectively. Taking the inverse Laplace transform of Eq. (19) and using convolution theorem the velocity potential $\Phi(x_0,y_0,t)$ in case of finite water depth is obtained as

$$\Phi(x_0,y_0,t)=L^{-1}\{A(p)\}-2\int_0^h\int_0^t\{U_1(y,t-\tau)+U\}\Big[m(\tau)\Big\{\ln\frac{r_1}{r_2}$$
$$-2\int_0^\infty\Big(\frac{e^{-kh}g_1(y,y_0)\cos kx_0}{k\cosh kh}-\frac{\Omega_hg_2(y,y_0)F_h(\tau,x,x_0)}{g_3(k)}\Big)dk\Big\}\Big]d\tau dy. \tag{21}$$

Similarly, taking inverse Laplace transform of Eq. (19) and using convolution theorem the velocity potential $\Phi(x_0, y_0, t)$ in case of infinite water depth is obtained as

$$\Phi(x_0,y_0,t) = L^{-1}[A(p)] - 2\int_0^\infty \int_0^t \{U_1(y,t-\tau)+U\}\Big\{m(\tau)\ln\frac{r_1}{r_2} - 2\int_0^\infty \Omega e^{-k(y+y_0)}F(\tau,x,x_0)dk\Big\}d\tau dy, \tag{22}$$

where

$$F_h(t,x,x_0) = \int_0^t m(\tau)\sin\Omega_h(t-\tau)\cos k[x-x_0-U(t-\tau)]d\tau, \tag{23}$$

$$F(t,x,x_0) = \int_0^t m(\tau)\sin\Omega(t-\tau)\cos k[x-x_0-U(t-\tau)]d\tau. \tag{24}$$

In particular, for $p^2 = -\omega^2$ and $\bar{m}(p) = 1$, from Eqs. (8) and (13), the spatial velocity potential $\phi(x, y)$ associated with the time harmonic motion with angular frequency ω are derived as

$$\phi(x,y) = \sum_{m=I}^{II}\Big\{\sum_{n=0,I}^{II} A_{m,n}(k_n)f_n(y)e^{i\epsilon_m k_n x} + \sum_{n=1}^{\infty} B_{m,n}(k_n)f_n(y)e^{-k_n x}\Big\}, \text{ for finite depth,} \tag{25}$$

$$\phi(x,y) = \sum_{m=I}^{II}\sum_{n=0,I}^{II} A_{1m,n}(k_n)e^{-k_n y}(y)e^{i\epsilon_m k_n x} + \int_0^\infty \frac{\hat{T}(k)M(k,y)e^{-kx}dk}{\triangle(k)}, \text{ for infinite depth,} \tag{26}$$

where

$$\left.\begin{aligned}
A_{m,n}(k_n) &= \frac{2\delta_{m,n}M_1(k_n)}{L'(k_n,\epsilon_m)}\Big[\int_0^h \{U_1(y)+U/(i\omega)\}f_n(y)dy \\
&\quad - \int_0^\infty \Big\{\alpha(k_n)+\beta(k_n)\Big\}e^{i\epsilon_m k_n x}dx + \frac{k_n\tanh k_n h}{\omega^2}\{Q\beta_1 - Dk_n^2\beta_1 - D\beta_2\}\Big], \\
A_{1m,n}(k_n) &= \frac{\delta_{m,n}M_1(k_n)}{F(k_n,\epsilon_m)}\Big[\int_0^\infty \{U_1(y)+U/(i\omega)\}e^{-k_n y}dy \\
&\quad - \int_0^\infty \Big\{\alpha_1(k_n)+\beta_1(k_n)\Big\}e^{i\epsilon_m k_n x}dx + \frac{k_n}{\omega^2}\{Q\beta_1 - Dk_n^2\beta_1 - D\beta_2\}\Big], \\
\hat{T}(k) &= \Big[\frac{1}{k}\int_0^\infty \{U_1(y)+U/(i\omega)\}M(k,y)dy + \frac{(\omega+Uik)^2}{\omega^2}\{(Q-Dk^2)\beta_1 + D\beta_2\}\Big] \\
&\quad + \frac{2iU}{\omega^2}\int_0^\infty \Big\{(\omega+Uk)^2(iU\beta_4 - 2\omega\beta_5) - \Omega^2 k\beta_3(2\omega+iUk)\Big\}e^{-kx}dx,
\end{aligned}\right\} \tag{27}$$

with $B_{m,n}(k_n) = A_{m,n}(ik_n)$, $\beta_1 = \phi_{xy}(0,0)$, $\beta_2 = \phi_{yyyx}(0,0)$, $\beta_3 = \phi_y(x,0)$, $\beta_4 = \phi_{xx}(x,0)$, $\beta_5 = \phi_x(x,0)$, $\beta(k) = \frac{U^2k}{\omega^2}\{k\beta_3 - \beta_4\tanh kh\}$, $\alpha(k) = -\frac{2iUk}{\omega}\{i\epsilon_m\beta_3 + \beta_5\tanh kh\}$, $\alpha_1(k_n)$ and $\beta_1(k_n)$ can be obtained by taking $h \to \infty$. It is easy to check that in the absence of current the expansion formula for time harmonic velocity potential as in Eqs. (25) and (26) is same as in Manam et al. (2006). Particular cases with computational results associated with the initial value wavemaker problem will be presented in the workshop.

References

1. Meylan, M. H., Hazard, C. & Loret, F. (2004) Linear time dependent motion of two dimensional floating elastic plate in finite depth water using the Laplace transform. *IWWWFB 19*, Italy, http://www.iwwwfb.org/Abstracts/iwwwfb19/iwwwfb19-35.pdf.

2. Manam, S. R., Bhattacharjee, J. & Sahoo, T. (2006) Expansion formulae in wave structure interaction problems. *Proc. R. Soc. A*, **462**, 263–287.

Expansion formula for velocity potential for wave interaction with floating and submerged structures

S. C. Mohapatra and T. Sahoo
Department of Ocean Engineering and Naval Architecture
Indian Institute of Technology, Kharagpur -721 302, India
e-mail: saratiitkgp@gmail.com, tsahoo1967@gmail.com

1 Introduction

In recent decades, there is a significant study on surface wave interaction with very large floating structures for ocean space utilization. An interesting aspect of these class of problems is to reduce the structural response of very large floating structures (VLFS). One of the approaches for mitigating structural response of a very large floating structure under wave action is with the help of a submerged flexible structures (see Wang et al. (2010)). Hassan et al. (2009) analyzed the surface wave interaction with submerged flexible plates of finite and semi-infinite length in two-dimensional as well as the three-dimensional problem involving a circular plate by the matching method. In the present paper, Fourier type expansion formula for the velocity potentials and associated orthogonal mode-coupling relations are derived in water of finite depth to deal with wave interaction with floating flexible structures in the presence of submerged flexible structures. The expansion formula are also derived in an alternate manner using Green's function technique.

2 Expansion formula

Under the assumption of the linearized theory of water waves and small amplitude structural response, the problem is considered in the two-dimensional Cartesian co-ordinate system with x-axis being in the horizontal direction and y-axis in the vertically downward positive direction. An infinitely extended thin elastic plate is floating at the mean free surface $y = 0$ in an infinitely extended fluid and another infinitely extended submerged flexible plate is kept horizontally at $y = h$ in the fluid domain as in Figure 1. Assuming that the fluid is inviscid, incompressible and irrotational and simple harmonic in time with angular frequency ω, the fluid motion is described by the velocity potentials $\Phi_j(x, y, t) = \mathrm{Re}\{\phi_j(x, y)e^{-i\omega t}\}$ with subscript $j = 1$ referring to the fluid domain bounded by the floating and submerged plate and $j = 2$ referring to the fluid domain bounded by the submerged plate and bottom bed. Further, it is assumed that the deflection of the floating and submerged plates are of the forms $\zeta_j = \mathrm{Re}\{\zeta_j(x)e^{-i\omega t)}\}$ with $j = 1$ refers to the floating plate and $j = 2$ refers to the submerged plate. The spatial velocity potential $\phi_j(x, y, t)$ satisfies the Laplace equation as given by

$$\nabla^2\phi_j = 0, \quad \text{in the respective fluid domain.} \tag{2.1}$$

The rigid bottom boundary conditions are given by

$$\frac{\partial\phi_2}{\partial y} = 0 \quad \text{at} \quad y = H. \tag{2.2}$$

The linearized kinematic condition on the submerged plate surface at $y = h$ as given by

$$\left.\frac{\partial\phi_2}{\partial y}\right|_{y=h+} = \left.\frac{\partial\phi_1}{\partial y}\right|_{y=h-}. \tag{2.3}$$

Assuming $m_{pi}\omega^2 << 1$ (as in Schulkes et al. (1987)), the mean free surface at $y = 0$, ϕ_1 satisfies

$$D_1\frac{\partial^5\phi_1}{\partial y^5} - N_1\frac{\partial^3\phi_1}{\partial y^3} + \frac{\partial\phi_1}{\partial y} + K\phi_1 = 0 \quad \text{on y} = 0,\ 0 < \text{x} < \infty. \tag{2.4}$$

On the submerged flexible plate at $y = h$, ϕ_1 and ϕ_2 satisfy

$$D_2\frac{\partial^5\phi_2}{\partial y^5} - N_2\frac{\partial^3\phi_2}{\partial y^3} + K(\phi_2 - \phi_1) = 0, \quad \text{for} \quad y = h,\ 0 < x < \infty, \tag{2.5}$$

where $D_i = E_iI_i/\rho g$, $N_i = Q_i/\rho g$ and $K = \omega^2/g$. In addition, assuming that a vertical

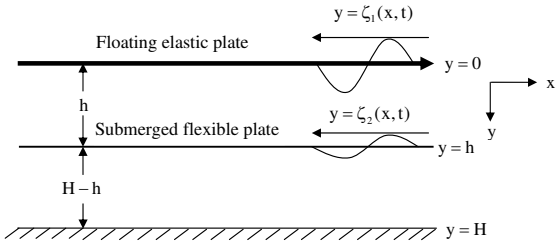

Figure 1: Schematic diagram of floating and submerged flexible plates in water of finite depth

wavemaker oscillates with frequency ω and amplitude $u(y)$ about its mean position on the wavemaker at $x = 0$, the spatial velocity potential ϕ satisfies

$$\frac{\partial\phi}{\partial x} = u(y) \quad \text{on} \quad x = 0, \tag{2.6}$$

for $0 < y < H$ except at $y = h$. Finally, the far field radiation condition is of the form given by

$$\phi(x, y) = \sum_{n=I}^{II} B_n g_n(y) e^{ip_n x} \quad \text{as} \quad x \to \infty, \tag{2.7}$$

where p_ns are the progressive flexural gravity wave modes generated due to the interaction of the surface gravity waves with the floating and the submerged flexible plates, $g_n(y)$ are the vertical eigenfunctions and B_n are associated with the unknown wave amplitude at far field.

2.1 Fourier type expansion formula

Using eigenfunction expansion method, the velocity potential $\phi(x, y)$ satisfying Eq.(2.1) along with the boundary conditions in Eqs.(2.2)-(2.5) in finite water depth is of the form

$$\phi(x, y) = \sum_{n=I,...,X,1}^{\infty} B_n\psi_n(y)e^{ip_n x}, \quad \text{for} \quad x > 0, \tag{2.8}$$

$$\text{with } \psi_n(y) = \begin{cases} \{(D_2p_n^4 - N_2p_n^2)p_n \tanh p_n(H-h) - K\}\dfrac{L_1(ip_n, y)}{L_1(ip_n, h)}, & \text{for } 0 < y < h, \\ -K\cosh p_n(H-y)/\cosh p_n(H-h), & \text{for } h < y < H, \end{cases} \tag{2.9}$$

and B_ns are the unknowns to be determined with $L_1(ip_n, y) = iK\{p_n(D_1p_n^4 - N_1p_n^2 + 1)\cosh p_n y - K\sinh p_n y\}$. The eigenvalues $p_n, n = I, II, ..., IX, X$ in Eq.(2.8) in p satisfy the dispersion relation

$$\mathcal{G}(p) \equiv K - \frac{p(1 + D_1p^4 - N_1p^2)}{\mu} = 0, \tag{2.10}$$

with $\mu = \dfrac{K\{1+\coth ph\coth p(H-h)\}-(D_2p^4-N_2p^2)p\coth ph}{K\{\coth ph+\coth p(H-h)\}-p(D_2p^4-N_2p^2)}$. Keeping the realistic nature of the physical problem, it is assumed that the dispersion relation in Eq.(2.10) has two distinct positive real roots $p_n,\ n=I,II$, eight complex roots $p_n,\ n=III,...,X$ of the form $a\pm ib$ and $-c\pm id$ and infinite number of purely imaginary roots $p_n,\ n=1,2,...$ of the form $p_n=i\nu_n$ (which can be easily observed for specific problems through contour plots). The bounded characteristics of the far field behavior of the velocity potential in Eq.(2.7) yields $B_{VII}=...=B_X=0$ in Eq.(2.8). Further, it can be easily derived that the eigenfunctions ψ_ns satisfy the orthogonal mode-coupling relation given by

$$\begin{aligned}
\langle\psi_m,\psi_n\rangle &= \langle\psi_m,\psi_n\rangle_1+\langle\psi_m,\psi_n\rangle_2=E_n\delta_{mn} \quad \text{for all} \quad m=n=I,...,VI,1,2,...\\
\text{with } \langle\psi_m,\psi_n\rangle_1 &= \int_0^h F_m(y)F_n(y)dy-\frac{N_1}{K}\psi_m'(0)\psi_n'(0)+\frac{D_1}{K}\{\psi_m'(0)\psi_n'''(0)+\psi_m'''(0)\psi_n'(0)\},\\
\langle\psi_m,\psi_n\rangle_2 &= \int_h^H \psi_m(y)\psi_n(y)dy-\frac{N_2}{K}\psi_m'(h)\psi_n'(h)+\frac{D_2}{K}\{\psi_m'(h)\psi_n'''(h)+\psi_m'''(h)\psi_n'(h)\},\\
E_n &= \frac{-\mathcal{D}(ip_n,h)\sinh p_nh[\psi_n'(0)]^2\mathcal{G}'(p_n)}{2K^2p_n^2},
\end{aligned}$$

where $\mathcal{D}(ip_n,h)=-\{p_n(D_1p_n^4-N_1p_n^2+1)\sinh p_nh-K\cosh p_nh\}$. The constants B_ns are given by

$$B_n=\frac{\langle u(y),\psi_n(y)\rangle}{ip_nE_n}. \tag{2.11}$$

Next, one of the important characteristics of the eigenfunctions $\psi_n(y)$s is mentioned without proof as a Theorem next.

Theorem. The eigenfunctions $\psi_n(y)$s in Eq.(2.9) are linearly dependent.

Proceeding in a similar manner as in Mondal and Sahoo (2012), the above theorem can be proved and details are deferred here.

2.2 Derivation of line source potentials

The symmetric wave source potential associated with surface gravity wave problems $G(x,y;x_0,y_0)$ (which is also referred as the Green's function) in the presence of floating and submerged elastic plates satisfies Laplace equation in the fluid region except at the structural boundaries and at the source point (x_0,y_0) along with the boundary conditions as in Eqs.(2.2)-(2.5). Near the source point (x_0,y_0), the Green's function behaves like

$$G\sim\frac{1}{2\pi}\ln(r) \quad \text{as} \quad r=\sqrt{(x-x_0)^2+(y-y_0)^2}\to 0. \tag{2.12}$$

Assuming the symmetric property of the fundamental wave source potential about $x=x_0$, condition (2.12) yields (as in Mohapatra et al. (2011))

$$\frac{\partial G}{\partial x}=\delta(y-y_0)/2 \quad \text{on} \quad x=x_0. \tag{2.13}$$

Using the generalized identity

$$\int_0^\infty \delta(y-y_0)F(y)dy=\begin{cases} F(y_0) & \text{if} \quad y_0>0,\\ F(y_0)/2 & \text{if} \quad y_0=0,\end{cases} \tag{2.14}$$

and the expansion formula as in the previous Section, the source potential $G(x,y;x_0,y_0)$ is obtained as

$$G(x,y;x_0,y_0)=\sum_{n=I}^{VI}B_n\psi_n(y)e^{ip_n(x-x_0)}+\sum_{n=1}^{\infty}B_n\psi_n(y)e^{-\nu_n(x-x_0)} \quad \text{for} \quad x>x_0, \tag{2.15}$$

where B_ns are given by

$$B_n = \begin{cases} \dfrac{-\delta_1 \sinh p_n(H-h) L_1(ip_n; y_0)}{2p_n E_n K \mathcal{D}(ip_n, h)} & \text{for } 0 \le y_0 < h, \\ \dfrac{-\sinh p_n(H-h) L_1(ip_n; h)}{2p_n E_n} - \dfrac{i \cosh p_n(H-h)}{2p_n E_n} & \text{for } y_0 = h, \\ \dfrac{-i\delta_1 \cosh p_n(H-y_0)}{2p_n E_n} & \text{for } h < y_0 \le H, \end{cases}$$

and $p_n = i\nu_n$ for $n = 1, 2, 3, ...$ with $\delta_1 = 1$ for $y_0 \in (0, h) \cup (h, H)$ and $\delta_1 = 1/2$ for $y_0 = 0, H$ and p_n, ν_n, $\psi_n(y)$, $L_1(ip_n; y_0)$, E_ns, $\mathcal{D}(ip_n, h)$ being the same as in previous Section.

2.3 Expansion formula based on Green's function technique

In this subsection, using the source potential $G(x, y, x_0, y_0)$ derived in the previous subsection and Green's identity, the expansion formula for the flexural gravity wavemaker problem in the presence of a horizontal flexible plate is derived. In this case, the spatial velocity potential $\phi(x, y)$ satisfies the Laplace equation as in Eq.(2.1), along with the bottom boundary condition as in Eqs.(2.2), the boundary conditions on the floating and submerged flexible plates as in Eqs.(2.4) and (2.5). In order to derive an integral representation of the velocity potential in terms of the Green's function $G(x, y; x_0, y_0)$ satisfying the condition on the wavemaker as in Eq. (2.6), set

$$G^{mod}(x, y; x_0, y_0) = G(x, y; x_0, y_0) + G(-x, y; x_0, y_0), \tag{2.16}$$

with zero normal velocity on the wavemaker, i.e., $G^{mod}_x(0, y; x_0, y_0) = 0$. Using Green's identity, the velocity potential $\phi(x_0, y_0)$ is obtained as

$$\phi(x_0, y_0) = -\Big[2\int_{\Re} G(0, y; x_0, y_0) u(y) dy + \frac{2}{K}\Big[D_1\{G_{1yyy}\phi_{1xy} + G_{1y}\phi_{1xyyy}\} - N_1 G_{1y}\phi_{1xy}\Big]_{(x,y)=(0,0)} + \frac{2}{K}\Big[D_2\{G_{2yyy}\phi_{2xy} + G_{2y}\phi_{2xyyy}\} - N_2 G_{2y}\phi_{2xy}\Big]_{(x,y)=(0,h)}\Big]. \tag{2.17}$$

The Green's function and velocity potential derived here can be used to deal with gravity wave interaction with floating structure in the presence of submerged flexible structure of various configurations in finite water depth. Expansion formulae for the same class of problems can be derived in case of infinite water depth with suitable utilisation of mixed type of Fourier transform as in Mondal and Sahoo (2012) and alternately using Green's function technique as discussed in case of finite water depth.

References

Hassan, U. L. M., Meylan, M. H. and Peter, M. A., 2009. Water wave scattering by submerged elastic plates, *Q. Jl Mech. Appl. Math.* 62(3), 245–253.

Wang, C. M., Tay, Z. Y., Takagi, K. and Utsunomiya, T., 2010. Literature review of methods for mitigating hydroelastic response of VLFS under wave action, *Applied Mechanics Review* 63, 030802-1–18.

Mondal, R. and Sahoo, T., 2012. Wave structure interaction problems for two-layer fluids in three dimensions, *Wave Motion* 49, 501–524.

Mohapatra, S. C., Karmakar, D. and Sahoo, T., 2011. On capillary-gravity wave motion in two layer fluids, *J. Engng Math.* 71(3), 253–277.

Schulkes, R. M. S. M., Hosking, R. J. and Sneyd, A. D., 1987. Waves due to a steadily moving source on a floating ice plate, Part 2. *J. Fluid Mech.* 180, 297–318.

Cloaking a circular cylinder in deep water

J. N. Newman
jnn@mit.edu

(Submitted to 28th IWWWFB – L'Isle sur la Sorgue, France – 7-10 April 2013)

1 Introduction

In the diffraction problem, where a fixed body scatters the incident waves, 'cloaking' refers to the condition where there is no scattering in the form of radial outgoing waves. The possibility of cloaking in the diffraction of water waves is of scientific interest, since it is not obvious that this condition can be achieved with a body of nonzero volume on or near the free surface. Cloaking may also have practical applications, such as reducing the mean drift force.

Porter [1] and Newman [2] have considered the possibility of cloaking a bottom-mounted circular cylinder, using an annular bed with variable depth in both the radial and azimuthal directions. Their computations show that near-zero values of the scattered energy can be achieved by optimizing the bathymetry of the bed. Subsequently, in response to a stimulating question at the last Workshop [3], axisymmetric beds have been discovered with equally small values of the scattered energy [4]. This surprising discovery contradicts the author's conjecture in the reply to [3].

The use of variable bathymetry may be impractical, especially in deep water. Thus the present work considers the possibility of cloaking a circular cylinder of finite draft in a fluid of infinite depth. Two types of surrounding structures are used to minimize the total scattered energy. The first is an array of smaller cylinders which surround the inner cylinder, as shown in Figure 1. This configuration was suggested by the work of Farhat et al [5]. The second type is an axisymmetric ring (toroid) with the cross-section represented by a Fourier series. In both cases it is shown that the scattered energy can be reduced to very small values by optimizing the dimensions and shape of the surrounding bodies.

As in [2], the approach is based on minimizing the scattered energy computed by WAMIT, using multi-variate optimization to search for the appropriate values of the geometrical parameters. The results are normalized based on unit values of the incident-wave amplitude, fluid density, and draft of the inner cylinder. The radius of the inner cylinder is 0.5 and the optimizations are performed at the wavenumber $K = 1$. The scattered energy is computed from the Kochin function, which represents the amplitude of the far-field radiating waves, using equation 7 of [2].

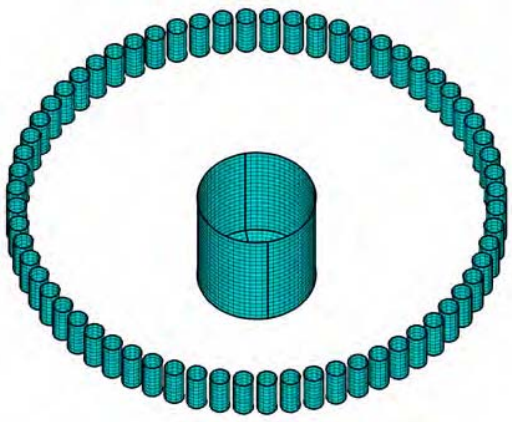

Figure 1: Perspective view of the optimized structure with $N = 64$ outer cylinders.

2 Arrays of circular cylinders

N circular cylinders with radius r and draft d are uniformly spaced around a circle of radius R_0, concentric with the inner cylinder. The entire structure is fixed on the free surface. Five different arrays are considered with N=(4,8,16,32,64), as shown in Figure 2. The incident waves propagate in the direction parallel to the horizontal axis in Figure 2. Optimum values of the parameters r, d and R_0 are computed to minimize the energy. Table 1 shows the values of these parameters with the corresponding minima of the scattered energy E and ratio E/E_0, where E_0 is the scattered energy of the inner cylinder by itself.

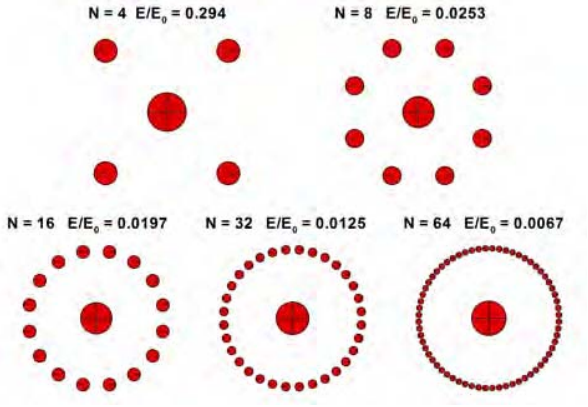

Figure 2: Plan view of the arrays N=4,8,16,32,64.

Figure 3 shows the scattered energy for a range of wavenumbers. The results for $N \geq 8$ are practically the same, with very small values at $K = 1$ and substantially less energy in the range $0.7 < K < 1.2$ compared to the inner cylinder by itself. From momentum conservation it follows that the mean drift force is small if the scattered energy is small. This is confirmed in Figure 4.

Since E decreases as N increases, and the array approximates an axisymmetric ring as $N \to \infty$, these results suggest the possibility of cloaking with an axisymmetric structure and motivate the alternative configuration in Section 3.

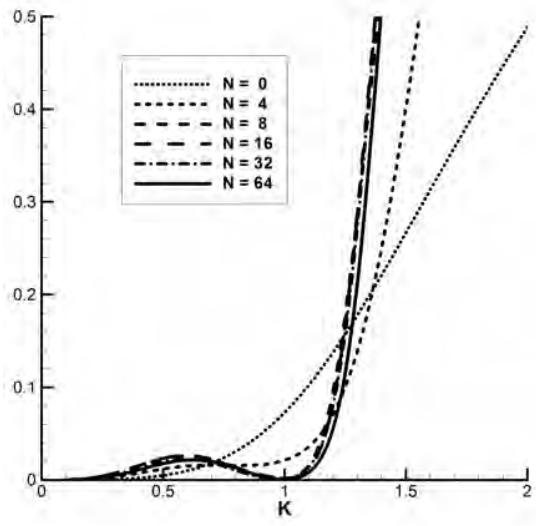

Figure 3: Scattered energy for the cylinder alone ($N = 0$) and five optimized structures shown in Figure 2.

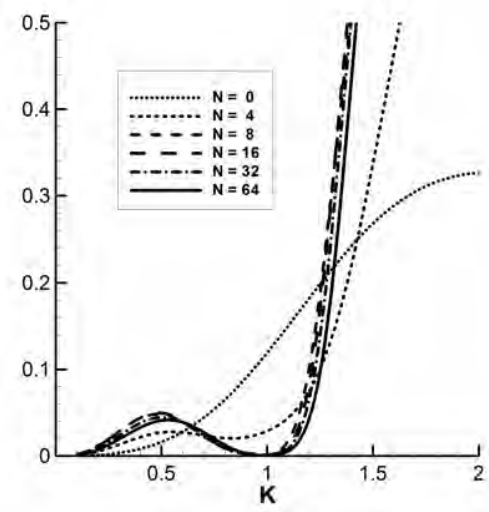

Figure 4: Mean drift force on the cylinder and five optimized structures.

N	r	d	R_0	E	E/E_0
4	0.2993	0.3434	2.2071	0.0214	0.2939
8	0.2933	0.4745	2.2031	0.0018	0.0253
16	0.1963	0.4785	2.1592	0.0014	0.0197
32	0.1309	0.4507	2.1003	0.0009	0.0125
64	0.0848	0.3606	2.0170	0.0005	0.0067

Table 1: Optimized parameters of the arrays.

3 Axisymmetric rings

In this configuration the surrounding structure is a toroid with its cross-section defined by

$$R = R_0 + \sum_{m=1}^{[(N-1)/2]} S_m \sin m\psi + \sum_{m=1}^{[(N-2)/2]} C_m \cos m\psi,$$

$$z = -d \cos \psi.$$

Here (R, z) are cylindrical coordinates with R the radius from the vertical $z-$axis, $z = 0$ the plane of the free surface and z positive upward. The parametric coordinate ψ varies between $-\pi/2$ on the inner waterline and $\pi/2$ on the outer waterline. The optimization parameters include R_0, d, and the Fourier coefficients S_m and C_m. In the simplest case $N = 3$ only S_1 is included and the cross-section is elliptical, as shown in Figure 5.

The minimum values of the energy ratio E/E_0 are shown in Figure 6 for $N \leq 16$. It is evident that ratios on the order of 10^{-4} represent the limit of what can be achieved using the single-precision code WAMIT. These values of the energy ratio are substantially smaller than the corresponding results in Section 2, providing numerical evidence

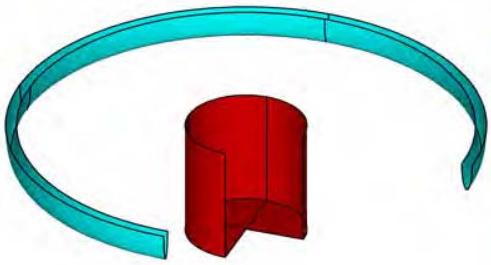

Figure 5: Perspective view of the cylinder and toroid with elliptical section (N=3). One quadrant is omitted to show the cross-section.

for the existence of axisymmetric cloaking structures. The optimized sections are shown in Figure 7. For $N \geq 12$ these are practically identical. The coefficients for $N \leq 8$ are listed in Table 2.

Figure 8 shows the mean drift force for the structure $N = 16$, including the separate components acting on the cylinder and toroid. It is interesting to note that both of these components have zero-crossings at $K = 1$. Thus the occurrence of near-zero mean drift force on the complete structure is not a consequence of cancellation between the two components. This is explained below.

If the incident-wave potential is the product of a real function and e^{-ikx}, the symmetric and anti-symmetric components of the scattered potential satisfy Neumann boundary conditions on the body where the normal derivatives are real and imaginary, respectively. If there is no scattered energy these potentials vanish at infinity faster than a radiated wave, and satisfy homogeneous boundary conditions on the free surface (and bottom). It follows that they are respectively real and imaginary throughout the fluid domain, assuming uniqueness. Thus there is no anti-symmetric component of the second-order mean pressure, and no drift force acting on sub-elements of the body which

	N= 3	4	5	6	7	8
R_0	1.926	1.656	1.654	1.481	1.466	1.450
d	0.241	0.245	0.258	0.253	0.252	0.259
S_1	0.046	0.054	0.051	0.058	0.060	0.060
C_1		-0.072	-0.074	-0.053	-0.056	-0.055
S_2			-0.014	-0.022	-0.024	-0.016
C_2				-0.039	-0.040	-0.036
S_3					0.002	-0.002
C_3						0.035

Table 2: Optimized parameters for toroids $N \leq 8$.

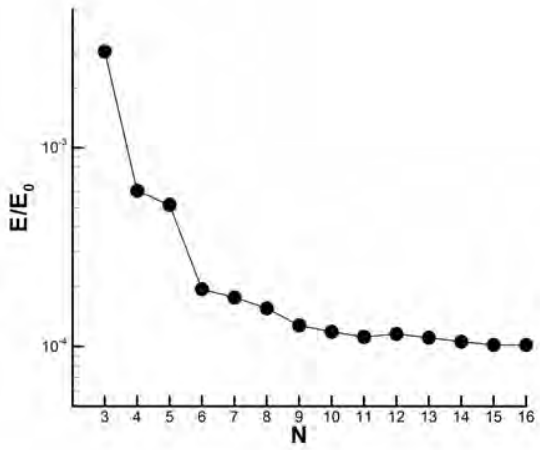

Figure 6: Energy ratio for toroids.

are symmetrical about $x = 0$. This explains the results for the separate components in Figure 8.

Figure 9 shows the scattered component of the free-surface elevation at $K = 1$ along radial lines at angles θ between zero and 90 degrees from the x-axis. Only one quadrant is shown since the real part is symmetric about $x = 0$ and the imaginary part is anti-symmetric. There is substantial angular variation of the elevation in the interior domain between the cylinder and torus. In the exterior domain outside the torus the elevation is relatively small, and attenuates rapidly with increasing radius as expected. The real part appears to be nearly axisymmetric. The amplitude of the scattered elevation for the cylinder alone is shown for comparison in the left-hand plot of Figure 9.

References

[1] Porter, R. 'Cloaking of a cylinder in waves,' IWWWFB26 (2011), Athens.

[2] Newman, J.N. 'Scattering by a cylinder with variable bathymetry,' IWWWFB27 (2012), Copenhagen.

[3] Bingham, H., (www.iwwwfb.org/Abstract/iwwwfb27/iwwwfb27_discussions.pdf, page 52)

[4] Newman, J.N., (www.wamit.com/Reports/2012ConsortiumReport.pdf, page 31)

[5] Farhat, M., Enoch, S., Guenneau, S. & Movchan, A.B. 'Broadband cylindrical acoustic cloak for linear surface waves in a fluid,' Physical Review Letters, **101**, 134501 (2008).

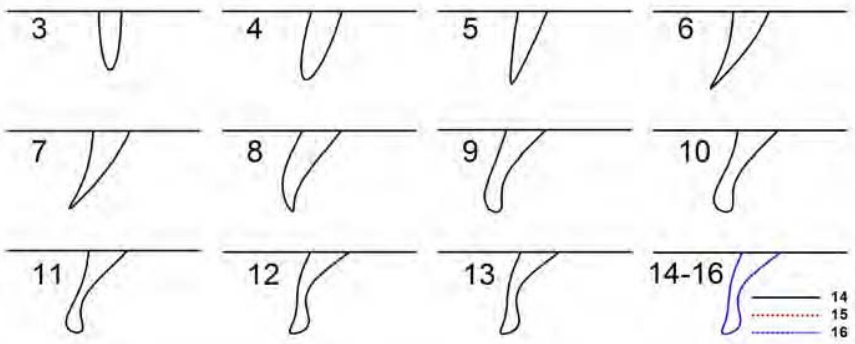

Figure 7: Cross-sections of the toroids. The sections $N = 14, 15, 16$ are superposed.

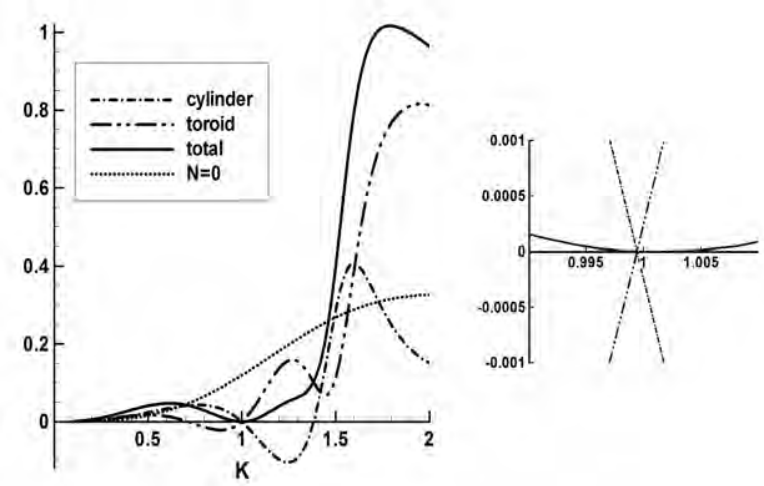

Figure 8: Total drift force on the configuration N=16 and separate components acting on the inner cylinder and toroid. The dashed line is the force on the inner cylinder alone (N=0). The small zoom figure on the right shows the zero-crossings of the components at K=1.

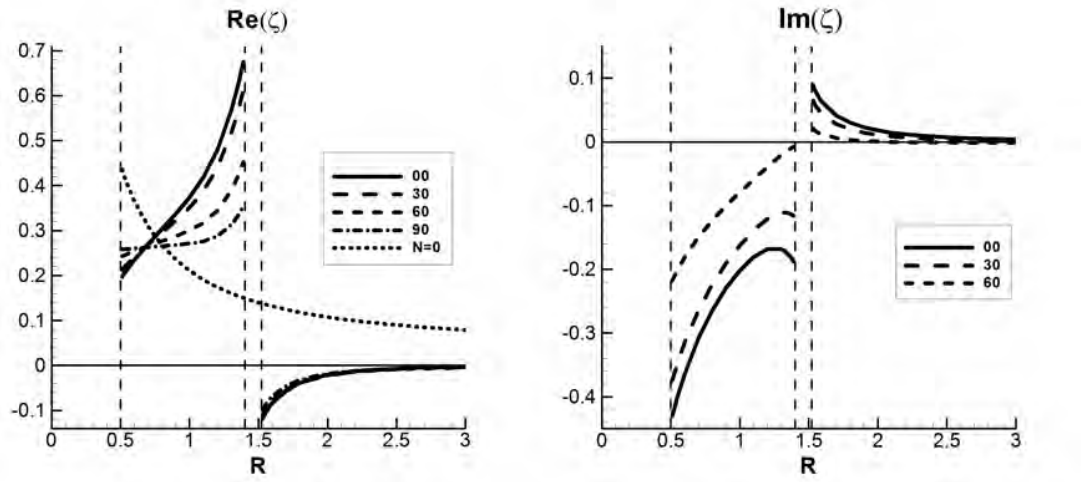

Figure 9: Real and imaginary parts of the free-surface elevation for the configuration N=16 at K=1, plotted vs the radius R at $\theta = (0, 30, 60, 90)$ degrees from the x-axis. The waterline radii of the bodies are indicated by vertical dashed lines. In the left-hand plot the line N=0 is the amplitude of the elevation for the cylinder alone, at θ=0.

Current effects on higher harmonic waves

De-zhi Ning, Hong-xing Lin, Bin Teng
Department of Hydraulic Engineering, Dalian University of Technology, Dalian, 116024,China
e-mail: dzning@dlut.edu.cn, sunwind920@126.com, bteng@dlut.edu.cn

INTRODUCTION

The problem of waves propagating over a submerged obstacle has been widely investigated during the past decades. Higher bound and free harmonic waves are generated in the process of wave transformation above the submerged obstacle. As the important issues, the physics of harmonics generation and the nonlinear interaction among these harmonics were studied by many researchers, such as Grue (1992), Brossard and Chagdali (2001), Liu et al. (2009), Teng et al.(2010) and Ning et al. (2012). Actually, waves and currents generally coexist and their interactions play important roles in most of the ocean dynamic processes. Although numerous works on wave-current interactions, such as Thomas (1981), Zaman et al.(2008) and Yoon & Liu(1989), have been conducted, the analysis of current effects on the higher harmonics scattering by a submerged body is still relatively scarce.

In this abstract, the monochromatic wave over a submerged obstacle in the presence of uniform current is investigated using a fully nonlinear numerical scheme based on a 2D boundary element method (BEM). The phase-locked and free higher harmonic modes downstream the structure are decomposed by means of a two-point method, and their characteristics under the influence of current are further studied.

NUMERICAL MODEL

For wave overtopping a submerged obstacle in the presence of a uniform current as shown in Fig. 1, a 2D Cartesian coordinate system *oxz* is defined with the origin *o* in the plane of the undisturbed free surface, x=0 is at the left end of the domain, z is positive upwards. Fluid is assumed to be ideal, so that the potential flow theory can be used inside the fluid domain Ω. Due to the presence of uniform current U_0, the total velocity potential can be described to consist of component related to the current xU_0 and the rest part of potential $\varphi(x, z, t)$. Both the total velocity potential and φ satisfy the Laplace equation.

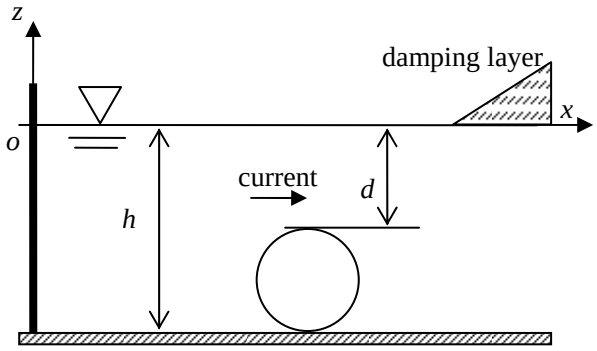

Fig.1 Sketch of the problem

On the instantaneous free surface, both the fully nonlinear kinematic and dynamic boundary conditions are satisfied and the mixed Eulerian-Lagrangian method is used to advance the time marching. On the bottom boundary, the rigid and impermeable condition is imposed. On the inflow boundary S_I, the fluid motion is generated by prescribing the second-order Stokes wave velocity. Due to the current effect, the input velocity potential can be written as follows

$$\varphi_I = \frac{gA_e}{\omega - kU_0}\frac{\cosh k(z+h)}{\cosh kh}\sin(kx-\omega t) + \frac{3}{8}A_e^2(\omega - kU_0)\frac{\cosh 2k(z+h)}{\sinh^4 kh}\sin 2(kx-\omega t) \quad (1)$$

where ω is angular frequency, h is the static water depth, A_e is a parameter related to the wave amplitude in the presence of current. Based on the conservation of wave action (Bretherton & Garrett ,1968), it satisfies the following relation

$$A_e = A_0\sqrt{\frac{\omega - kU_0}{\omega}\frac{C_{g0}}{C_g}} \quad (2)$$

in which A_0 and C_{g0} mean the wave amplitude and wave group velocity in quiescent water.

Towards the end of the computational domain, an

artificial damping beach is applied on the free surface so that the wave energy is gradually dissipated in the direction of wave propagation (Ning et al., 2009).

By using the second Green's theorem, the prescribed boundary value problem can be transformed to the following boundary integral equation:

$$C(p)\varphi(p)=\int_{\Gamma}(\varphi(q)\frac{\partial G(p,q)}{\partial n}-G(p,q)\frac{\partial \varphi(q)}{\partial n})d\Gamma \tag{3}$$

where p and q are source and field points, and C is the solid angle which can be conveniently and economically computed by an indirect method in the present study. Γ is liquid domain boundary including free surface boundary and solid boundary. G is a simple Green function written as follows:

$$G(p,q)=\frac{1}{2\pi}(\ln r_1+\ln r_2) \tag{4}$$

where $r_1=\sqrt{(x-x_0)^2+(z-z_0)^2}$,

$r_2=\sqrt{(x-x_0)^2+(z+z_0+2\mathrm{h})^2}$.

Then the boundary surface is discretized with a number of three-node line elements. The geometry of each element is represented by the quadratic shape functions, thus the entire curved boundary can be approximated by a number of higher-order elements. Within the boundary elements, physical variables are also interpolated by the same shape functions, i.e. the elements are isoparametric.

Since the discretized integral equation is always variant in time, all the boundary surfaces are regridded and updated at each time step using the mixed Eulerian-Lagrangian scheme and 4th-order Runga-Kutta approach. Once the Eq. (3) is solved, we can obtain the time series of surface elevation at any position.

When wave-current pass the submerged obstacle, higher harmonics generated by nonlinear wave-wave and wave-current interactions in the shallow water over the bar will leave the obstacle leeward as free waves. So the surface elevation at any point x in the lee side of the submerged body can be written as

$$\begin{aligned}\eta(t,x)=&\sum_{n=1}^{\infty}a_F^{(n)}\cos(k_n x-n\omega t+\psi_n(x))\\&+\sum_{n=2}^{\infty}a_L^{(n)}\cos(n(kx-\omega t+\psi_1(x)))\end{aligned} \tag{5}$$

where $a_F^{(n)}$ are the amplitudes of the free transmitted waves with frequencies of integer times of the incident wave frequency, $a_L^{(n)}$ are the amplitudes of the nth-order phase-locked waves, $\psi_1(x)$ is the initial phase angle of the fundamental wave and $\psi_n(x)$ ($n\geq 2$) the nth harmonic free waves, k and k_n are the wave number of the fundamental waves and the nth harmonic free waves, and satisfy the following dispersion relations

$$(\omega-kU_0)^2=gk\tanh kh \tag{6}$$

and

$$(n\omega-kU_0)^2=gk_n\tanh k_n h,\ \ n=2,3,\mathrm{L} \tag{7}$$

respectively. The fundamental wave amplitude, as well as the higher free and locked wave amplitudes, is obtained from the time histories of the surface elevation. The Fourier transform is introduced as follows

$$\eta_n(x)=\frac{1}{T}\int_0^T\eta(x,t)e^{-inwt}dt=A_n(x)+iB_n(x) \tag{8}$$

where $A_n(x)$ and $B_n(x)$ are the corresponding real and imaginary components, respectively. Then the two-point method (Grue, 1992, Teng et al., 2010) is used in the Eq.(8) and the unknowns in in Eq.(5) can be obtained.

NUMERICAL RESULTS

As a validation of the present model, the proposed numerical model is used to compute the combined wave-current field parameter in a domain with flat bottom, in which the input parameters static water depth h=0.6m, angular frequency ω=5.42rad/s, wave height H_0=0.06m are considered. The length of the corresponding computational domain is taken as 10λ($\lambda=2\pi/k$ denotes wave length), meshed with 200×10 cells in x and z directions after convergent tests, in which the last 1.5λ is used as the damping layer. Figs.2 and 3 show the comparisons of wave height and wave length in the presence of different current with other published numerical and experimental data, respectively. In the figure, the

symbol C_0 represents the current-free wave celerity. From the figures, it can be seen that a good match of the numerical results with experimental data is observed.

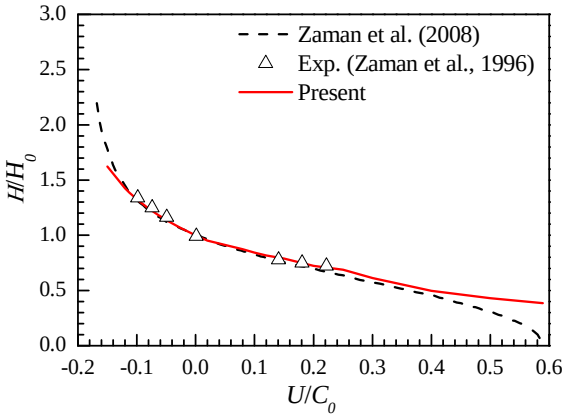

Fig.2 Comparisons of the wave height obtained by the present numerical model with Zaman et al.(2008) and experimental data (Zaman and Togashi, 1996).

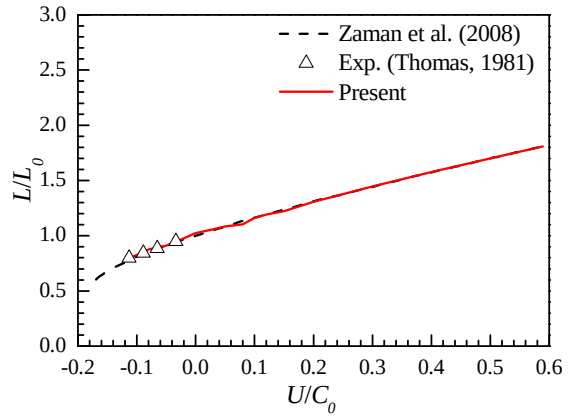

Fig.3 Comparisons of the wavelength obtained by the present numerical model with Zaman et al.(2008) and experimental data (Thomas, 1981).

To testify the two-point method for separating higher free harmonics from scattering waves, another case for monochromic wave propagating a submerged horizontal cylinder in quiescent water is considered as shown in Fig.1. Parameters including static water depth h=0.45m, cylinder radius R=0.1m, submerged depth d=0.1m are chosen. Fig.4 shows the distribution of the dimensionless fundamental and second-harmonic free wave amplitudes ($A_F^{(n)}/A_0$) with incident wave amplitude A_0. The comparisons between the present numerical results and experimental data (Grue, 1992) are also given here. From the figure, it can be seen that there are good agreements between numerical solutions and experimental data. The fundamental wave amplitude is always very close to the input one A_0, while the second-harmonic free amplitude is increased with the increasing of input wave amplitude A_0, and then reaches a maximum value at a critical input-amplitude.

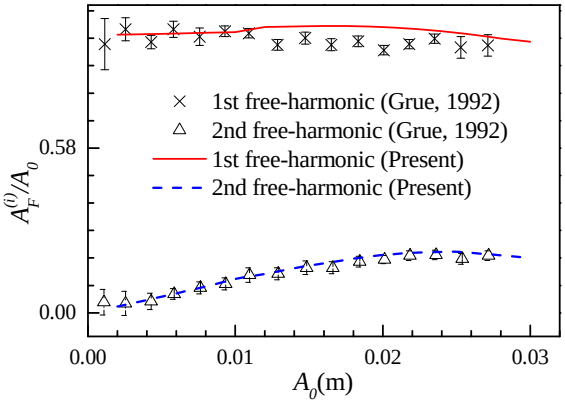

(a) wave period T=0.95s

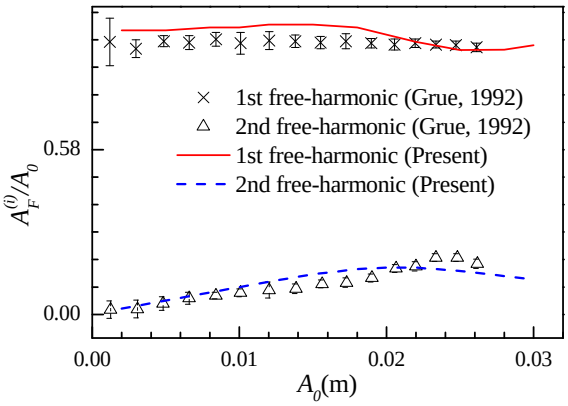

(b) wave period *T=0.82s*

Fig.4 Distribution of fundamental and 2nd-order free harmonic wave amplitudes with amplitude A_0.

Keeping the same wave parameters as those in Fig.4(a), three currents (i.e., U_0/C_{g0}=0, ±0.1) are introduced to the proposed numerical model. Fig.5 gives the distribution of the dimensionless fundamental, second- and third-harmonic free wave amplitudes with incident wave amplitude A_0. It can be seen that the portion of higher free harmonics becomes larger on the opposing current than that on zero current, but vice verse on the following current. Due to wave-current interactions, the maximum value of dimensionless higher free harmonic amplitude is upstream shifted for the opposing current relative to that for zero current. On the contrary, it is downstream shifted for the following current, as shown in Fig.5(b).

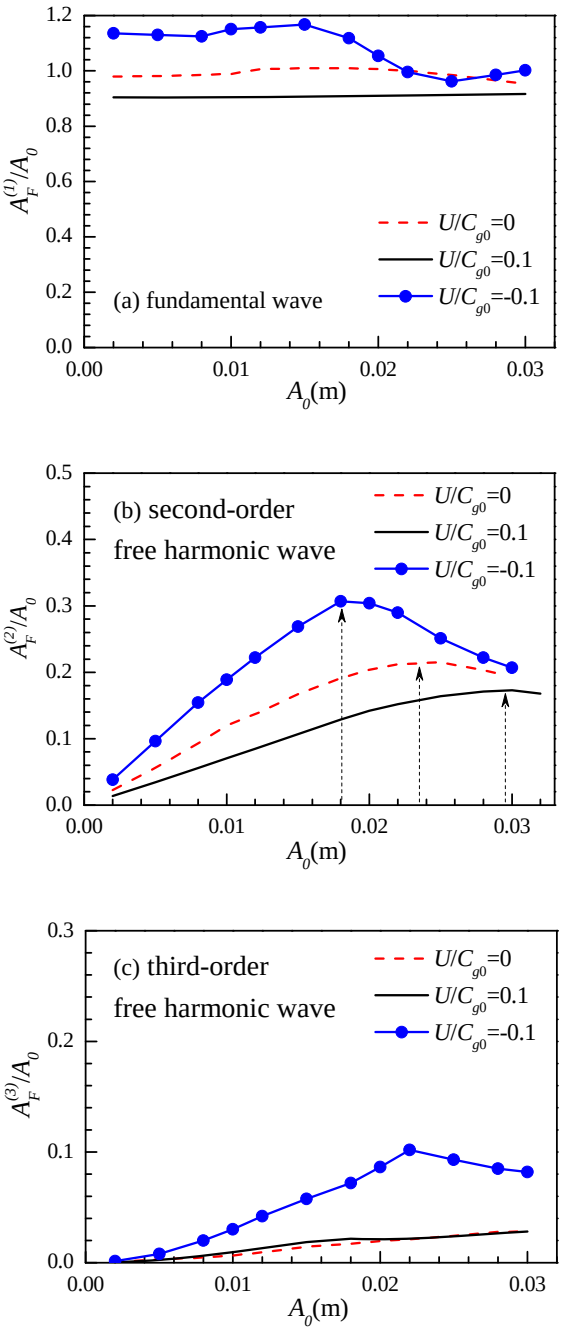

Fig.5 Distribution of harmonic amplitudes with A_0.

Numerical experiments of the effect of current velocity and input angular frequency on the higher harmonics are also carried out. The details will be shown in the workshop.

CONCLUSIONS

The phenomenon of wave propagation over a submerged obstacle in the presence of uniform current is examined by a powerful numerical model. The higher free harmonics are separated from the transmitted waves by using a two-point method. Good agreements of numerical results with the other published data are shown. The influence of the current on the characteristics of higher free harmonics are investigated.

ACKNOWLEDGEMENTS

The authors gratefully acknowledge the financial support from China NSFC (Grant Nos. 51179028, 51222902, 51221961).

REFERENCES

[1] Bretherton, FP and Garrett GJR (1968). "Wavetrains in inhomogeneous moving media." *Proceedings of the Royal Society of London*, 302, pp: 529-554.

[2] Brossard J and Chagdali M (2009). "Experimental investigation of the harmonic generation by waves over a submerged plate." *Coastal Engineering*, 42, pp: 277-290.

[3] Grue J (1992). "Nonlinear water waves at a submerged obstacle or bottom topography." *Journal of Fluid Mechanics*, 244, pp. 455-476

[4] Liu C R, Huang Z H, Tan S K(2009). "Nonlinear scattering of non-breaking waves by a submerged horizontal plate: Experiments and simulations" *Ocean Engineering*, 36, pp: 1332-1345.

[5] Ning D, Teng B, Zang J and Liu S(2009). "A fully nonlinear numerical model for focused wave groups." *Proceedings of 23rd IWWWFB*, Jeju, Korea

[6] Ning D, Zhuo X, Chen L and Teng B(2012). "Nonlinear numerical investigation on higher harmonics at lee side of a submerged bar." *Abstract and applied analysis*，doi: 10.1155/2012/214897

[7]Thomas G P(1981). "Wave-current interactions: an experimental and numerical study. Part 1. Linear waves. "*Journal of Fluid Mechanics*, 110, pp. 457-474.

[8] Teng B, Chen L, Ning D and Bai W(2010). "Study on the higher harmonic waves over a submerged bar." *Proceedings of 25th IWWWFB*, Harbin, China.

[9] Yoon S B and Liu PLF(1989). "Interactions of currents and weakly nonlinear water waves in shallow water." *Journal of fluid mechanics*, 250, pp:397-419.

[10] Zaman M H and Togashi H (1996). " Experimental study on interaction among waves, currents and bottom topography." *Proceedings of the Civil Engineering in the Ocean*, pp:49-54.

[11] Zaman M H, Togashi H and Baddour RE (2008). "Deformation of monochromatic water wave trains propagating over a submerged obstacle in the presence of uniform currents." *Ocean Engineering*, 35, pp:823-833.

Focused wave impact on a vertical cylinder: Experiment, numerical reproduction and a note on higher harmonics

B. T. Paulsen[*,1], H. Bredmose[†] and H. B. Bingham[*]

[*]**Technical University of Denmark, Department of Mechanical Engineering, Lyngby, Denmark**

[†] **Technical University of Denmark, Department of Wind Energy, Lyngby, Denmark**

E-mail address for correspondence: botp@mek.dtu.dk

Introduction

Wave impact from phase focused waves on a vertical cylinder is studied by means of laboratory experiments and numerical computations. The laboratory experiments were carried out at DHI, Denmark as a part of a Hydrolab project and have previously been presented here at the workshop [3, 5], where the focus was on higher-harmonic forces. Here we consider data from the same set of experiments but focus on numerical reproduction and the observed differences. Special attention is paid to the appearance of artificial higher harmonics in the measurements, which are shown to be a consequence of impulsive unset of structural vibrations.

The experimental and numerical setup

The laboratory experiments were carried out at DHI, Denmark and a detailed description can be found in [5, 6]. It shall be noticed that the force on the cylinder was measured by a force cell placed at the top of the cylinder. To ensure that the force on the cylinder was entirely captured by the force cell a small clearance between the cylinder and the basin floor existed. The force is thus really the reaction force between the test pile and its fixed mount. The natural frequency of the cylinder, when placed in the basin, was measured by a decay test and estimated to be $f_n = 3.8$ Hz.

For reproducing the experiments a numerical domain is setup. The numerical domain has a total length of 10 m and a width of 3 m corresponding to $12D$, where $D = 0.25$ m is the cylinder diameter. At the wave maker the water depth is $h_0 = 0.8$ m, which is then gradually reduced from $x = 2.0$ m by a bed slope of 1/20. The domain is enclosed by generation- and absorption zones at the inlet and outlet respectively. A two-dimensional sketch of the numerical domain is presented in figure 1.

For the numerical computations the incompressible Navier-Stokes equations for the two phase flow of water and air are solved in combination with a volume of fluid (VOF) scheme for tracking the free surface. The numerical model is established within the framework of the open-source CFD-toolbox OpenFOAM® in combination with the wave generation utility waves2Foam [4].

Impacts from a single phase focused wave group with an amplitude distribution given by a JONSWAP spectrum with $H_s = 0.40$ m and $T_p = 2.00$ s is considered. Since the exact paddle signal to the wave maker is unknown, a linear reconstruction of the incident wave group is carried out. The method follows the description in [1], and the wave reconstruction is based on measurements from a single wave gauge located at $x = 0.77$ m.

Results

In figure 2a the measured and computed free surface elevation at $\{x, y\} = \{7.20; 0.00\}$ m is presented in both time and frequency domains. In the time domain a fair agreement is seen until the passage of the two large waves which are both underestimated by the numerical model. Hereafter, the

[1]Presenting author

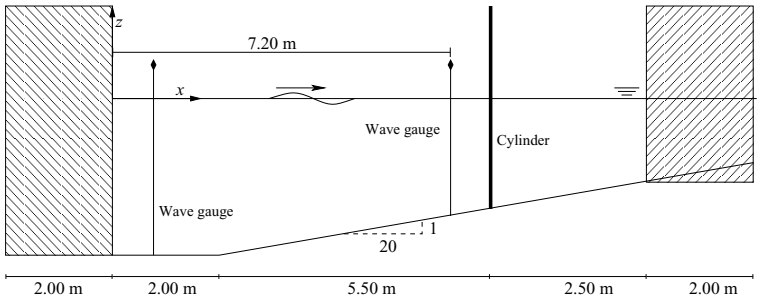

Figure 1: Two-dimensional sketch of the numerical domain. The generation and relaxation zone is indicated by oblique lines.

numerical model slightly underestimates the trough of the subsequent waves, whereas both the wave crest height and the phase is well captured. Considering the surface elevation in the frequency domain a good agreement is seen except for the second harmonic, which is slightly underestimated by the numerical model. The computations and experiments agree well for frequencies higher than the second harmonic.

In figure 2b the inline force on the cylinder is presented in both time and frequency domains. In the time domain the agreement between the measurements and the numerical computations is generally good. As seen from the figure, the experimentally measured inline force is occasionally traced by high frequency oscillations from the eigenmotion of the cylinder, excited by the two large waves. These oscillations are naturally not present in the computations where the cylinder is modelled as perfectly rigid. The peak force from the two largest waves seems to be underestimated by the numerical model. However, it is unclear to what extent the numerical model has underestimated the hydrodynamic force, as the eigenmotion of the cylinder also contributes to the large peak forces.

In the frequency domain a good agreement is seen for the first harmonic, whereas a fair agreement is seen for the second harmonic. For frequencies higher than the second harmonic, a substantial amount of higher harmonic forcing is observed in the measurements, which is not present in the numerical computations. It shall be noticed that a similar deviation for the higher harmonics was not observed in the Fourier transform of the free surface elevation.

Discussion

In general a good agreement between the numerical computations and the experiments is observed. The only exception is the substantial higher-harmonic forcing seen in the Fourier transform of the experimentally measured inline force. However, these higher-harmonic forces are not related to the hydrodynamic forcing but can be explained as an artefact of the intermittent eigenmotion of the cylinder.

The origin of the higher harmonics and why they are projected into the harmonics of the incident wave can be explained be considering the inline force on the cylinder written in the following form

$$f(t) = f_{hydro}(t) + \cos(\omega_n t)\,\chi(t) \tag{1}$$

where the first term is the hydrodynamic forcing and the last term is a simplified representation of the eigenmotion, with radian frequency $\omega_n = 2\pi f_n$. Since the eigenmotion of the cylinder is only present in finite time intervals this term is modulated by a characteristic function, χ, of the following form

$$\chi(t) = \begin{cases} 1 & : x \in \mathbb{I} \\ 0 & : x \notin \mathbb{I} \end{cases} . \tag{2}$$

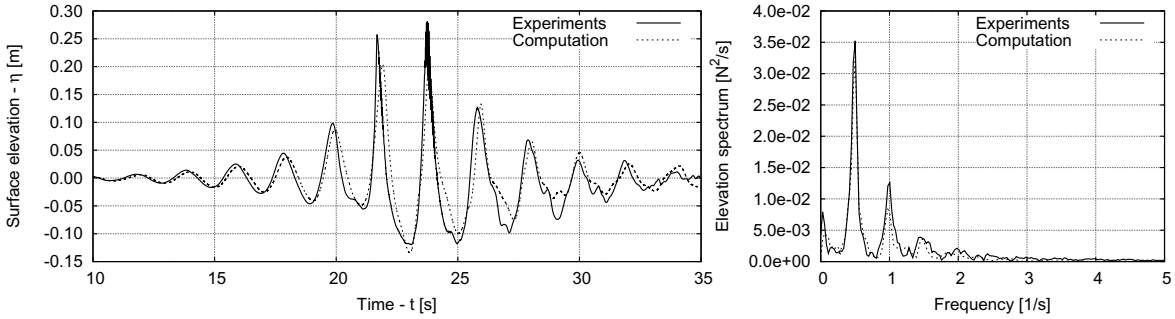

(a) Measured and computed surface elevation in front of the cylinder: $x = 7.2$m, $y = 0.0$m. Left panel; Time domain. Right panel; Frequency domain

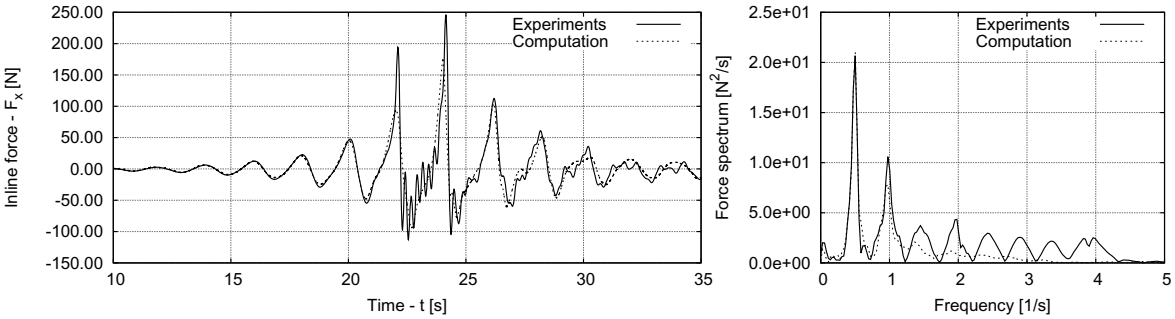

(b) Measured and computed inline force on the cylinder. Left panel; Time domain. Right panel; Frequency domain.

We now consider the Fourier transformation of the inline force, $(\mathcal{F}f)(\gamma)$, where γ is the frequency parameter in Fourier space. The characteristic function, χ, is assumed to be one in a finite interval of $I = [-a/2, a/2]$. The hydrodynamic force is in generally unknown, whereas the last term can be evaluated analytically. It follows from [2], that the Fourier transform of equation (1) is given by

$$(\mathcal{F}f)(\gamma) = (\mathcal{F}f_{hydro})(\gamma) + \frac{1}{2}\left(\frac{\sin \pi a (\gamma - \omega_n/2\pi)}{\pi(\gamma - \omega_n/2\pi)} + \frac{\sin \pi a (\gamma + \omega_n/2\pi)}{\pi(\gamma + \omega_n/2\pi)}\right) \tag{3}$$

From equation (3) it is seen that the characteristic function, χ, introduces harmonic oscillations in the Fourier transformed signal with a frequency proportional to the width of the characteristic function, a. In many cases it is reasonable to assume that the width, a, is related to the period of the incident waves. For instance, for the experimental measurements shown in figure 2b the typical duration is approximately $T/2$, where T is the wave period. So, since the eigenmotion of the cylinder is only present in finite time intervals the Fourier transform of this part of the signal could potentially introduce artificial higher harmonics.

For illustration purpose the following example is constructed (see, figure 2)

$$f(t) = [\sin \omega t + \cos(\omega_n t)\,\chi(t)]\,G(t) \tag{4}$$

Here the hydrodynamic forcing is assumed regular with radian frequency, ω, and the structure is assumed to oscillate with radian frequency ω_n. The characteristic function χ is equal to one in the time intervals $I \in \{[t_1, t_2]; [t_3, t_4]\}$, as indicated in figure 2, and with widths $a = \frac{2\pi}{\omega}\{0.57; 0.56\}$. Finally the signal is multiplied by a Gaussian, $G(t)$, to mimic the temporal behaviour of the phase focused group. Notice that the Gaussian modulation of the signal does not introduce any harmonic frequencies and only serves the purpose of increasing the visual similarity with the phase focused group. For the test function are the frequencies from the experiment, $\omega = \omega_{exp} = 2\pi 0.5$ rad/s and

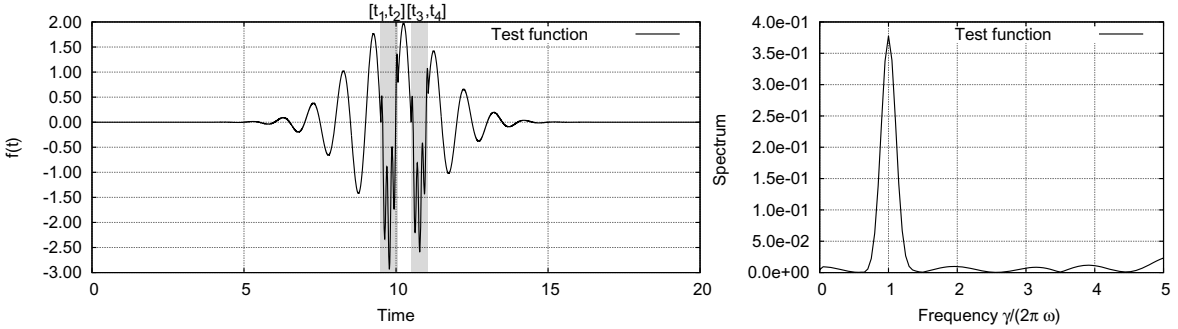

Figure 2: Time and frequency representation of test function. Areas of shaded grey indicates interavals where $\chi = 1$.

$\omega_n = 2\pi f_n$ rad/s, applied. In the Fourier transform of the test function artificial higher-harmonics, as the one observed in the experimental measurements, are clearly seen. Since the time intervals of $\chi = 1$ are not perfectly half the peak period is a perfect fit to the higher-harmonics not seen.

The example shows that the discontinuous onset of structural vibration can produce artificial higher harmonics over broad ranges of the spectrum.

From the analysis and the numerical example is it obvious that frequencies from the test setup are not easily filtered in Fourier space as a post process. The characteristic function, χ, and the time intervals a are in general unknown so there is no way of knowing at what frequencies energy from the structural motion has been project onto. A time domain filtering is not unproblematic either, as important details related to the hydrodynamic forcing is easily destroyed by the filtering process.

In the present work is numerical methods shown to be a vulnerable tool for investigating and understating experimental measurements and by that gaining further insight.

Acknowledgement

The Authors will like to thank professor Paul Taylor, from the University of Oxford and Jun Zang, from the University of Bath, for kindly sharing the experimental data. Further the authors will like to thank Jon Juel Thomsen, from the Technical University of Denmark, for fruitful discussion regarding the higher harmonics.

References

[1] H. Bredmose, a. Hunt-Raby, R. Jayaratne, and G. N. Bullock. The ideal flip-through impact: experimental and numerical investigation. *Journal of Engineering Mathematics*, 67(1-2):115–136, November 2009.

[2] O. Christensen. *Differentialligninger og uendelige rækker*. Institut for Matematik, DTU, Kgs. Lyngby, 2006.

[3] C. Fitzgerald, J. Grice, P. H. Taylor, R. E. Taylor, and J. Zang. Phase Manipulation And The Harmonic Components Of Ringing Froces On A Surface Piercing Column. *IWWWFB27*, 2012.

[4] N.G. Jacobsen, D.R. Fuhrman, and J. Fredsøe. A Wave Generation Toolbox For The Open-Source CFD Library: OpenFOAM. *International Journal for Numerical Methods in Fluids*, 2012.

[5] J. Zang, P. H. Taylor, and M. Tello. Steep Wave And Breaking Wave Impact On Offshore Wind Turbine Foundations - Ringing Re-visited. *IWWWFB25*, July 2010.

[6] J. Zang and P.H. Taylor. Steep and breaking wave impacts on offshore wind turbine columns. In *Proceedings on the Third International Conference on the Application of Physical Modelling to Port and Coastal Protection*, 2011.

A real-time simulation technique for ship-ship and ship-port interactions

J.A. Pinkster
PMH bv, Rotterdam
The Netherlands
jo.pinkster@gmail.com

Karan Bhawsinka
MARIN, Wageningen
The Netherlands
K.Bhawsinka@marin.nl

Introduction

Since the early 70's ship maneuvering simulators using fully equipped bridge structures are being used to study the real-time behavior of ships in open water and in ports and to train ships crews to carry out maneuvers safely and efficiently. The number of simulators in use bears testimony to the need for insight in ship behavior and the successes reached in training crews to sail ever larger ships in existing and new ports. Besides training of crew members, simulators are used to judge maneuvering characteristics of new, as yet unbuilt ships, efficiency and safety of new harbours and the effects of new propulsion systems and maneuvering aids. The basic process of a real-time maneuvering simulator is the mathematical model which represents the behaviour of a vessel sailing at variable speeds in deep or shallow water, in current, at high and at low speed without or with the effects of port structures, bottom irregularities and of other ships included. At the present, probably all simulators make use of mathematical models based on Newton's equations of motion for a body moving in the horizontal plane or , in some cases, in all 6 degrees of freedom. Hydrodynamic forces due to flow around the hull, rudder action and variations in propeller speeds are incorporated based on empirical data derived from model tests or from analysis of full scale data. An increasingly important effect on vessel moving in ports is due to ship-ship interactions or ship-port structure interactions, the last being, for instance, bank suction effects where banks can also be submerged structures or local water depth changes. It is common practice to include such effects based on tabulated interaction data derived from model tests or off-line computations using more or less complicated hydrodynamic models ranging from strip-theory-based interaction models to double-body potential flow using panel models or even full-blown CFD computations.

Real time computation of interaction forces

The present contribution concerns the development of a computational procedure for ship-ship and ship-port structure interaction using a double-body potential flow method and its real time application in a maneuvering simulator. The purpose is to be able to dispense with the need to generate interaction data bases and such an approach is expected to increase flexibility with respect to cases studied in the simulator. The method is applicable to multi-body cases involving ships and port structures. The flow equations are solved using standard zero-order panels and Rankine sources with or without the effect of restricted water depth (see ref. 1 and ref.2). A crucial aspect of the application of such computational methods in real time is the computational load, governed by the number of ships, port structure elements and the total number of unknowns (panels) that need to be solved at each time step. Until recently, the only way to directly influence the computation time was to decrease the number of panels in the problem, the lower limit being set by the required accuracy of the computed result. However, in recent years, the advent of inexpensive multi-core computers and parallelization of the codes has brought the possibility of real-time application for practical cases into view. Also a recent development concerns the application of Graphic Processing Units (GPU), originally developed for fast visualization of computer games, for which nowadays compilers are available making it relatively easy to program such codes for processing using these extremely fast and massively parallel devices. Such units are relatively inexpensive and can be added on to existing desk-top units. At present, top-of-the-line consumer units sport 1500 - 3000 parallel computing cores and can be truly called 'massively parallel' computers.

In order to illustrate the developments for the computation of the ship-ship interaction problem, an example is shown in the Figure below. This Figure shows the panel models of a container vessel sailing at 7 kn overtaking a container vessel sailing at 4 kn in a 600 m wide and 8000 m long channel section. The number of panels on each vessel amounted to 828 and 810 respectively and the on the channel sides 5840 panels. The water depth amounted to 19 m.

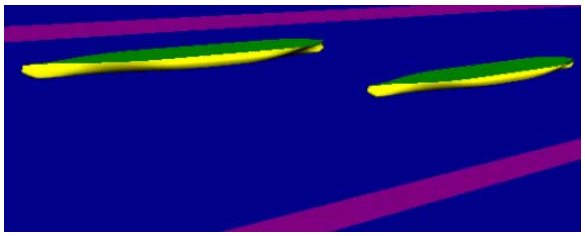

	Total No. of panels	I7, 1 core s/step	I7, OMP s/step	I7 , GPU s/step
Channel 1	7478	97	9.0	3.2
Channel 2	4558	30	4.5	1.3
Open water	1638	1.3	0.24	0.26

Computations were carried out for the vessels sailing in channel 1 (quays modeled using panels), channel 2 (one side modeled with panels, other quay through mirroring) and in open water for 3 cases: firstly, using a single core of an i7 processor, secondly, applying OpenMP and using all cores of the same i7 processor and lastly, applying a NVIDIA GTX690 GPU (using only one of the two processors on the board) attached to the i7 processor. The average time to compute each time step are given in the table. These results show that for the open water case even the single i7 core gives acceptable results. Applying OMP and the GPU result in about the same time per step. For the case of the vessels sailing in the channel considerable differences occur with the single core giving unacceptably long computation time. Applying OMP reduces the time considerably while the GPU results are again significantly lower. The question is what is an acceptable refresh rate? This depends, for instance, on the time scale of the maneuvers. An overtaking maneuver takes considerably more time, with lower rate of change of the forces, than a meeting maneuver, the former allowing a lower refresh rate than the latter. Careful study will determine which refresh rates are acceptable for real time simulation of maneuvering vessels.

The total number of panels on the ships and the port geometry is of great influence on the computational costs. Careful modeling of the port structures will be essential in order to achieve acceptable time step costs since it appears that computation times for the ship-ship interactions without presence of port structures are already useful. The particular case of a channel could also be modeled by double symmetry . The total number of panels would remain at 1638 and the computational costs reduced accordingly with some additional overheads for the mirroring operation. We have chosen to use panels to model the channel sides since in real cases the double symmetry technique would not always be applicable due to the irregular shape of real port geometries or due to sloping banks. In the presentation more details of the computational procedure will be given as well as correlations between computed and measured interaction forces.

Application in real time simulator

The real time simulator at MARIN uses a modular type mathematical maneuvering model. This means that total forces acting on ships are divided into different modules like hull forces, propeller forces, rudder forces and their interactions, environmental forces (caused by wind, wave, current), bank suction forces, ship-ship interaction forces, tug forces etc. Traditionally, bank suction and ship-ship interaction forces were calculated at every time step by interpolation from a predefined force database. Now, at every time step, these forces are calculated using a software developed by PMH called ‘Delpass’ here onwards. This software is running on a separate PC (called Delpass computer) to avoid influencing the real time simulation processes. The coupling of Delpass with MARIN’s real time simulator is described in the flowchart below. The Delpass computer, an i7-based machine, was running the OMP-version of the code. Before the start of simulations, Delpass reads one time inputs from an input file (called ‘manforc.inp’). This file contains information like number and names of data files to be used in the computations (containing panel description of concerned ship and port structures), water depth etc. At every time step,

Delpass reads velocity and position of all concerned structures from another input file (called 'moton.inp'). Delpass receiver updates motion.inp file every time simulator sends new velocity and position values (using simulator sender). Using data from these two input files (motions.inp and manforc.inp), Delpass calculates interaction forces and moments at every time step for the current relative position and velocity of concerned structures and writes them into an output file (called 'force.out'). Delpass sender passes this data to simulator receiver every time the output file is updated. Finally the simulator software receives interaction forces and moments through this receiver, adds them to total ship forces, solves the motion equations for the next time step and passes the results (new velocity and position values) to Delpass receiver using the simulator sender. This cycle is repeated at every time step to account for the effect of ship-ship or ship-port interaction in real-time. It should be noted that there are various time steps involved in the whole cycle (Delpass calculation time step, Simulator calculation time step, Simulator sender time step and Simulator receiver time step). Our analysis shows that simulator sender and receiver time steps can influence the interaction force results, hence care must be taken while deciding their values.

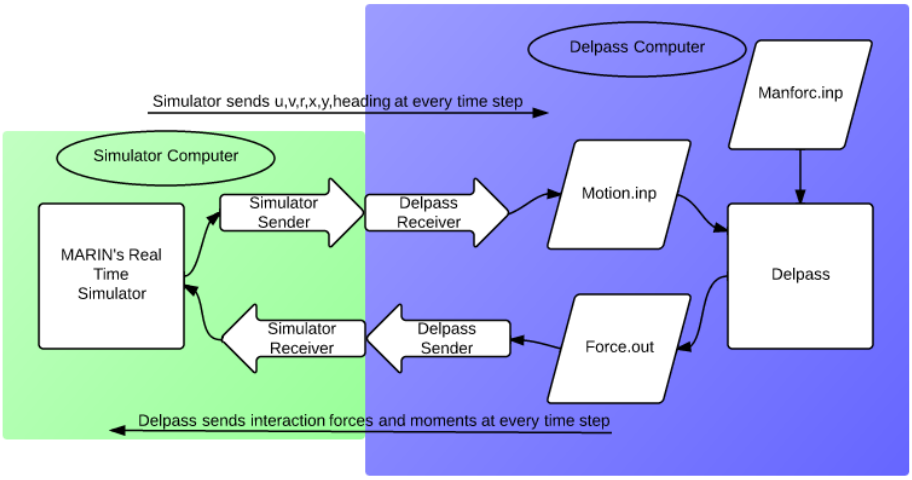

Figure: Flowchart detailing the coupling of Delpass with MARIN's real time simulator

Several cases have been tested with coupled Delpass at MARIN. In one test case, a Car Carrier is overtaking a Qmax LNG Carrier in Eemshaven fairway. The principle particulars of ships and number of panels on all the three structures are given in table below.

	Length (L_{PP})	Breadth (B)	Draught (T)	Displacement	Block Coefficient (C_b)	No. of Panels
Units	[m]	[m]	[m]	[m^3]	[-]	[-]
Car Carrier	225.0	32.2	9.0	42926.5	0.658	794
QMax LNG Carrier	345.0	55.0	12.0	167089	0.734	892
Eemshaven fairway	-	-	-	-	-	1010

The speeds at which the two ships were sailing and the distance between them is described in table below:

Ships	Velocity (kn)	Distance between ships (m)
Car Carrier	15	50
QMax LNG	9	

Note that both the ships were made very heavy during the run so that their trajectory is not influenced by the interaction forces. Hence both ships move in a straight line. This was done because the results from

standalone Delpass for a similar run were available to make a comparison (the plot below shows the comparison, OD = online Delpass, SD = standalone Delpass). In the presentation more test results will be discussed.

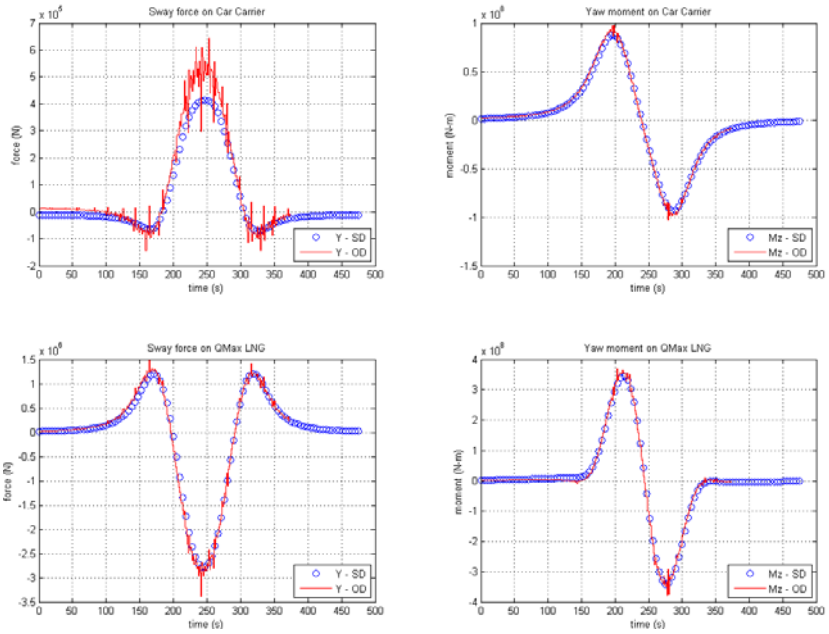

Figure: Interaction forces on Car Carrier and QMax from standalone and coupled Delpass

To obtain the results shown above, the simulator calculation time step was 0.2 s, the simulator sender time step was 1.3 s, the simulator receiver time step was 0.7 sec and the Delpass calculation time step varied from 0.6 to 1.3 s.

Conclusions

Delpass is a significant add-on to MARIN's real time maneuvering simulator. As it has been observed from various tests conducted at MARIN with coupled Delpass, the interaction forces calculated in real time are quite reliable. Implementing Delpass in a real time simulator reduces effort that was initially needed to create interaction forces databases and provides more flexibility to user in training scenarios where interaction forces play an important part. A real time simulator coupled with Delpass provides its users the freedom to simulate wider range of distances and speeds between passing structures.

Future Work

The GPU version of Delpass can be coupled with simulator for bulkier cases. This has not been tested at the moment. At present, Delpass assumes constant water depth. This feature can be enhanced in future to account for interaction forces caused due to changing bathymetry.

Acknowledgement

We would like to thank Freek Verkerk and Wendie Uitterhoeve for their help and guidance.

References

1. Pinkster, J.A. : ' The Influence of a Free Surface on Passing Ship Effects' , International Ship Building Progress, 2004.
2. Xu Xiang, Faltinsen,O.M.:' Maneuvering of Two Interacting Ships in Calm Water' , 11th International Symposium on Practical Design of Ships and Other Floating Structures, Rio de Janeiro, Brazil , 2010.

Whipping Response of a Box Barge in Oblique Seas

Dominic J. Piro[†] and Kevin J. Maki

Department of Naval Architecture and Marine Engineering
University of Michigan, Ann Arbor, MI, 48109 USA
[djpiro, kjmaki]@umich.edu

[†] Presenting Author

Introduction

The hydroelastic response of ships moving in waves has been studied for many years to understand and predict the structural failure of a vessel. Accurate prediction of stress is important for failure assessment, both from fatigue and extreme loading. Fatigue loading will cause cracks to form in high stress regions, especially in the deckhouse of naval combatants. Extreme loading can cause a vessel to break apart in heavy seas. This is a complicated problem that requires the combined analysis of the ship structure with the stochastic air-sea environment over the lifetime of a ship.

The goal of the present work is to numerically predict the non-linear response of a vessel in a seaway subject to loading from the wind-wave environment. In particular, the current work is focused on the challenges that arise in large amplitude waves where both global wave bending loads and local impacts are important. The method used in the current work combines a non-linear computational fluid dynamics solver with a modal structural dynamics solver. The two domains are combined in a tightly-coupled time-accurate algorithm. The method is described in Piro and Maki [2] and extended in this work to include rigid body motion in waves.

The motivation for using CFD for the fluid domain is the ability to implicitly capture non-linear free surface topology, specifically, breaking waves that occur during slamming. Furthermore, this method models viscosity and turbulence. Generally viscous damping is small, but can be important, such as in roll.

In this abstract, the method is validated using previous numerical and experimental work by Senjanović et al. [4]. Ongoing work is focused on using the method to analyze whipping response in large amplitude waves.

Methodology

The starting point of the present work is Piro and Maki [2]. The experimental model has a shear center far from the center of gravity to model a real containership. The finite element model for this case is comprised of Euler beam elements representing the backbone of the experimental model. The difference in position of the center of mass and shear center is achieved by adding stiff bar elements that lower the center of gravity. Finally the hull is represented by transfer shell elements that have no mass or stiffness. The beam and shell elements can be seen in Figure 1.

The displacements and rotations of the beam are linearly applied to shell elements as shown below:

$$\left\{ \begin{array}{c} d_x(x,y,z,t) \\ d_y(x,y,z,t) \\ d_z(x,y,z,t) \end{array} \right\} = \left\{ \begin{array}{c} -\frac{dv(x,t)}{dx}(y-y_b) - \frac{dw(x,t)}{dx}(z-z_b) \\ v(x,t) - \phi(x,t)(z-z_b) \\ w(x,t) + \phi(x,t)(y-y_b) \end{array} \right\}, \tag{1}$$

where d_x, d_y, and d_z are the shell displacements in the x, y, and z directions, $v(x,t)$ is the horizontal displacement of the beam, $w(x,t)$ is the vertical displacement of the beam, $\phi(x,t)$ is the torsional rotation of the beam, and y_b and z_b are the y and z locations of the beam. The x axis is along the vessel length and the z axis is defined positive up, opposite the direction of gravity.

The rigid body modes and elastic structure modes are solved separately. The rigid body motion is solved using symplectic integration, which conserves energy and is well suited for long-time integration. The discrete equations for translational motion are:

$$\vec{v}^n = \vec{v}^o + \Delta t \frac{\vec{F}^o}{m}, \tag{2}$$

$$\vec{x}^n = \vec{x}^o + \Delta t \vec{v}^n, \tag{3}$$

where o denotes a value at the old time step, n denotes a value at the new time step, $\vec{x}$ is the position, $\vec{v}$ is the velocity, $\vec{F}$ is the external force, and m is the mass. Underrelaxation and iteration are used to stabilize the equations of motion for vessel. This is necessary when the vessel has relatively large added mass.

An approximate body boundary condition is used on the structural boundary of the fluid domain. The fluid grid moves with the rigid body motion, and the velocity boundary condition contains both the rigid body and structural components. This process is similar to that described in [2]. Using this method, the fluid forces will not contain the hydrostatic stiffness force. Therefore, translational and rotational springs are added to the finite element model to represent the hydrostatic contribution. This procedure avoids the non-robust and expensive mesh deformation process.

Waves are generated using the `waves2Foam` toolkit developed for OpenFOAM by Jacobsen et al. [1]. The toolkit provides inlet wave boundary conditions for the velocity and volume-fraction variable. Also included are "relaxation zones" that help build the waves in the domain upstream of the vessel. These zones are also used to damp the waves downstream.

Results

In this work the hydroelastic response of a flexible box-barge in oblique seas (heading angle $\beta = 60°$) is studied. The barge is similar to the one studied by Š. Malenica et al. [5], Remy et al. [3], and Senjanović et al. [4], with length $L = 2.445$ m, beam $B = 0.6$ m, draft $T = 0.12$ m, and depth $D = 0.25$ m. Two structures are used, one for the RAO validation study, and one for the slamming study. The elasticity for the RAO comparison is provided by a 1 cm x 1 cm bar located 0.187 m above the waterline. For the slamming study, the size of the bar is increased to 1.8 cm square to be stiffer and more realistically represent a scaled vessel.

Validation of RAOs To properly generate the RAOs of rigid and elastic responses of the vessel, the correct wave amplitude must be known. Therefore, simulations are preformed where the wave field is propagated through the domain without the body. A probe is placed where the center of the body will be to generate a time series of wave elevation. The amplitude from this time series is used in the RAO calculation. A focus of ongoing work is to improve the generation, propagation, and damping of these waves.

Response amplitude operators of heave, pitch, roll, vertical bending, horizontal bending, and torsion are compared to the results presented in [4]. Preliminary results to show the capability of the method are shown with four wave periods, 0.8, 1.0, 1.2, and 1.4 s. Figure 2 shows the comparison between the present method and the previous results. The rigid body mode RAOs from the present method compare well with the previous experimental data, as do the RAOs for the bending modes. However, the torsion RAO shows larger differences with the previously published experimental and numerical results. This discrepancy is studied below, and will continue to be the subject of further analysis.

There are several possible explanations for the differences between the current torsion RAO and that of the previously published results. The first and most likely reason is the difference between the dry natural frequencies in the coupled horizontal-bending and torsion modes between the current work and that of Senjanović et al. [4]. The first five frequencies are 4.00, 4.84, 7.28, 9.51, and 12.35 rad/s in the current work while the previously reported values are 5.32, 7.92, 12.7, 15.56, and 21.56 rad/s. These lower frequencies are closer to the forcing frequency, which should yield a larger response. Different

modeling strategies are being examined to correct the natural frequencies. Another reason for discrepancy could be the flow between pontoons that is not modeled in the current simulations. This flow should add damping to the system, which would lower responses.

Non-linear effects and whipping Ongoing work is focused on understanding the effects of non-linearities and whipping response in large-amplitude waves. Presently simulations are being conducted for a range of wave amplitudes for a single wave length of 1.561 m ($T = 1.0$ s). The analysis will investigate the interaction between the wave bending and slamming responses.

Acknowledgements

The authors would like to gratefully acknowledge the support of a grant from the US Office of Naval Research, Award # N00014-10-1-0301 and # N00014-11-1-0846, under the technical direction of Ms. Kelly Cooper.

Bibliography

[1] N. G. Jacobsen, D. R. Fuhrman, and J. Fredsøe. A wave generation toolbox for the open-source cfd library: Openfoam®. *International Journal for Numerical Methods in Fluids*, 70(9):1073–1088, 2012. ISSN 1097-0363.

[2] D. J. Piro and K. J. Maki. Hydroelastic analysis of bodies that enter and exit water. *Journal of Fluids and Structures*, (0):–, 2012.

[3] F. Remy, B. Molin, and A. Ledoux. Experimental and numerical study of the wave response of a flexible barge. In *Fourth International Conference on Hydroelasticity in Marine Technology*. Wuxi, China, 2006.

[4] I. Senjanović, Šime Malenica, and S. Tomausević. Investigation of ship hydroelasticity. *Ocean Engineering*, 35(5-6):523 – 535, 2008. ISSN 0029-8018.

[5] Š. Malenica, B. Molin, F. Remy, and I. Senjanović. Hydroelastic response of a barge to impulsive and non-impulsive wave loads. In *Third International Conference on Hydroelasticity in Marine Technology*. Oxford, UK, 2003.

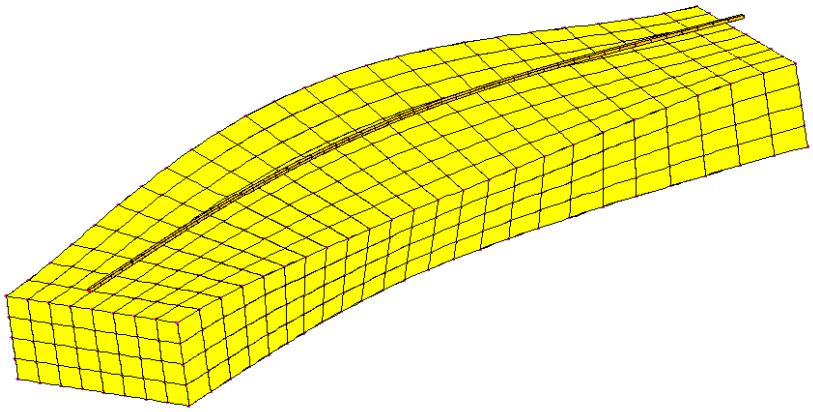

Figure 1: Structural model deformed with first horizontal bending-torsion mode.

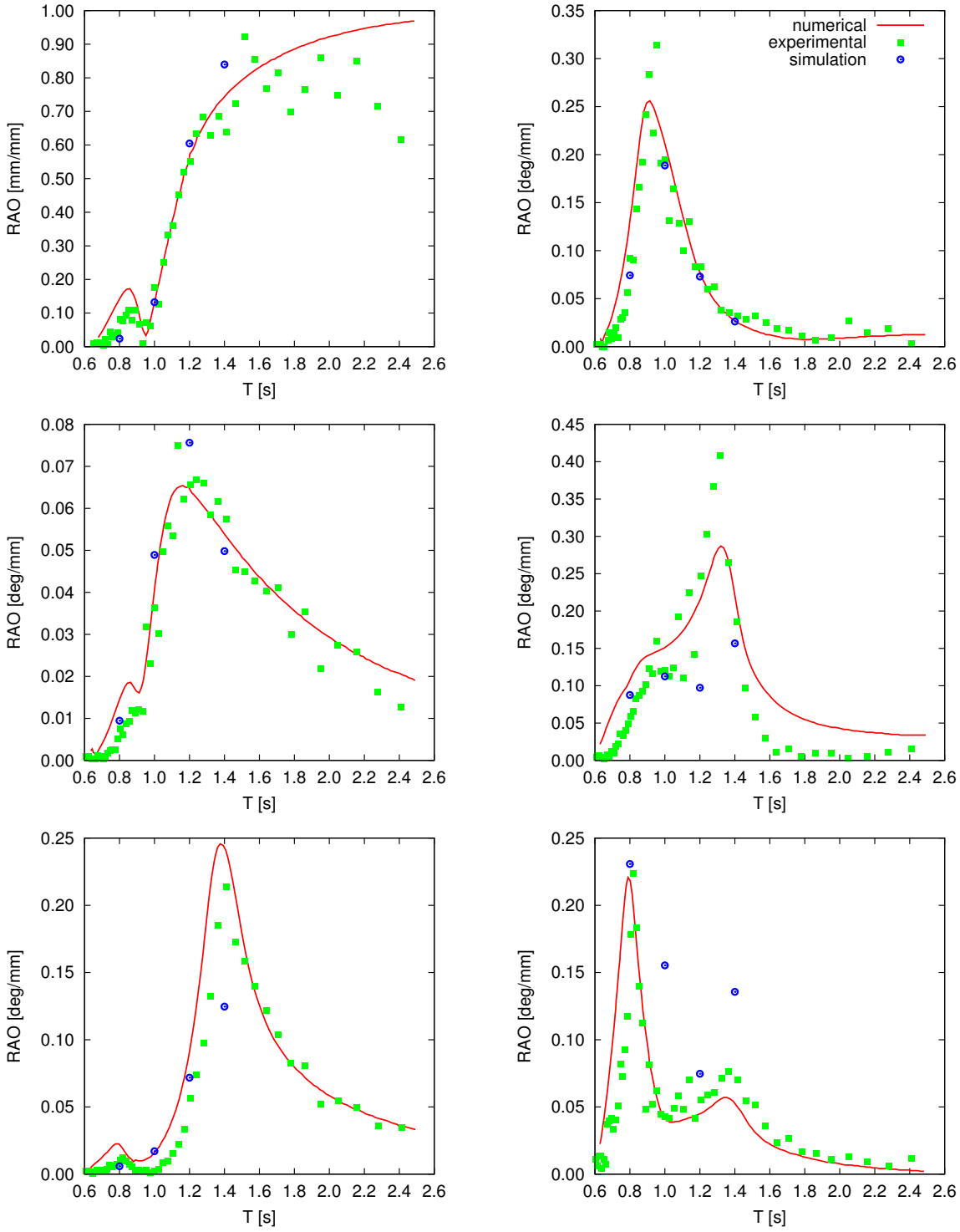

Figure 2: Comparison of RAOs between current simulations (open circles) and Senjanović et al. [4] (solid line and filled squares). The RAOs are of heave (top left), pitch (middle left), roll (bottom left), vertical bending (top right), horizontal bending (middle right), and torsion (bottom right)

A novel connection between the Ursell and Dean vertical barrier potentials

R. Porter & D. V. Evans,
School of Mathematics, University of Bristol, Bristol, BS8 1TW, UK

Abstract

This Abstract is dedicated to the memory of Professor Fritz Ursell whose influence continues to be reflected in contributions to the Workshop.

Fritz Ursell's first published paper in 1947 was on the scattering of an incident wave by a thin vertical barrier, aspects of which coincidentally also formed the basis of the first paper published by each of us, one or two generations later. This 1947 paper was remarkable in providing one of the few explicit solutions in linear water-wave theory, namely the potential everywhere in the fluid when an incident two-dimensional wave-train in deep water is scattered by a thin vertical rigid barrier immersed to a depth a. He also presented the solution to the complementary problem solved earlier by Dean (1945) who used complex function theory, in which the vertical barrier extends from infinity in the depths of the fluid to a point a distance a beneath the free surface.

In this paper we show that these distinct solutions and corresponding reflection coefficients can be related through two entirely new potentials which, given one of the above solutions enables the other to be determined. The results are a special case of a more general theory which can include finite depth, oblique incidence and different geometric configurations (Porter & Evans (2013, in preparation)).

1 The role of the new connection potentials

Cartesian coordinates are defined with the origin in the mean free surface and y pointing vertically downwards into the infinite depth fluid. A thin barrier occupies the interval $y \in B$ of the plane $x = 0$ and the gap in the barrier occupies the interval $y \in G$. In the Ursell and Dean problems B is the interval $(0, a)$ and (a, ∞) and G the interval (a, ∞) and $(0, a)$ respectively.

A plane two-dimensional monochromatic wave of radian frequency ω is incident from $x > 0$ on the barriers. Under the usual assumptions of linearised wave theory there exists a velocity potential $\Re\{\Phi(x, y)\mathrm{e}^{-\mathrm{i}\omega t}\}$ This complex-valued potential $\Phi(x, y)$ satisfies the equations

$$\Phi_{xx} + \Phi_{yy} = 0, \qquad y > 0, \tag{1}$$

with

$$K\Phi + \Phi_y = 0, \qquad \text{on } y = 0 \tag{2}$$

and $K = \omega^2/g$ where g is gravitational acceleration and

$$\nabla\Phi \to 0 \qquad y \to \infty. \tag{3}$$

We must also impose no-flow conditions on the barrier

$$\Phi_x(0^{\pm}, y) = 0, \qquad y \in B \tag{4}$$

and specify a radiation condition. We assume a wave incident from $x = \infty$ so that

$$\Phi(x, y) \sim \begin{cases} \mathrm{e}^{-\mathrm{i}Kx - Ky} + R\mathrm{e}^{\mathrm{i}Kx - Ky}, & x \to \infty \\ T\mathrm{e}^{-\mathrm{i}Kx - Ky}, & x \to -\infty \end{cases} \tag{5}$$

where R and T are the reflection and transmission coefficients. It can easily be shown that

$$\Phi(x, y) = \begin{cases} \mathrm{e}^{-\mathrm{i}Kx - Ky} + \mathrm{e}^{\mathrm{i}Kx - Ky} + \phi(x, y), & x > 0 \\ -\phi(-x, y), & x < 0 \end{cases} \tag{6}$$

where $\phi(x,y)$ is defined in $x>0$ and satisfies (1), (2) and (3) in addition to the boundary conditions

$$\phi_x(0,y)=0, \quad y\in B, \qquad \phi(0,y)+\mathrm{e}^{-Ky}=0, \quad y\in G \tag{7}$$

which results from imposing (4) on Φ and continuity of $\Phi(x,y)$ across $x=0$ when $y\in G$, based on the decomposition (6). Under this definition $\phi(x,y)\sim(R-1)\mathrm{e}^{\mathrm{i}Kx-Ky}$ as $x\to\infty$ with $T=R-1$. With r a local measure of the distance from any barrier edge immersed in the fluid, we also require $|\nabla\phi|\sim r^{-1/2}$ as $r\to 0$.

We label the Ursell and Dean potentials in (6) by $\phi^u(x,y)$ and $\phi^d(x,y)$ respectively, satisfying

$$\phi^{u/d}_x(0,y)=0, \quad y\in(0,a)/(a,\infty), \qquad \phi^{u/d}(0,y)+\mathrm{e}^{-Ky}=0, \quad y\in(a,\infty)/(0,a)$$
$$\phi^{u/d}(x,y)\sim(R^{u/d}-1)\mathrm{e}^{\mathrm{i}Kx-Ky} \quad \text{as } x\to\infty \tag{8}$$

Thus, from Ursell (1947) we have

$$\phi^u(x,y)+\mathrm{e}^{\mathrm{i}Kx-Ky}=C\left(\pi I_1(Ka)\mathrm{e}^{\mathrm{i}Kx-Ky}+\int_0^\infty\frac{L(k,y)J_1(ka)\mathrm{e}^{-kx}}{(k^2+K^2)}\mathrm{d}k\right) \tag{9}$$

where $C=(\pi I_1(Ka)+\mathrm{i}K_1(Ka))^{-1}$ and $R^u=\pi I_1(Ka)C$, and

$$\phi^d(x,y)+\mathrm{e}^{\mathrm{i}Kx-Ky}=B\left(K_0(Ka)\mathrm{e}^{\mathrm{i}Kx-Ky}-\int_0^\infty\frac{L(k,y)J_0(ka)\mathrm{e}^{-kx}}{(k^2+K^2)}dk\right) \tag{10}$$

where $B=(K_0(Ka)+\mathrm{i}\pi I_0(Ka))^{-1}$ and $R^d=K_0(Ka)B$. The above expressions involve Bessel functions whilst $L(k,y)=k\cos ky-K\sin ky$.

We now connect these potentials through the introduction of new potentials $\psi^{u/d}(x,y)$. Thus let

$$\phi^{u/d}(x,y)+\mathrm{e}^{\mathrm{i}Kx-Ky}=\mathrm{i}K^{-1}\left(\phi^{d/u}_x(x,y)+A^{d/u}\psi^{d/u}_x(x,y)\right). \tag{11}$$

Then from (8) we require

$$\psi^{u/d}_x(0,y)=0, \quad y\in(0,a)/(a,\infty), \qquad \psi^{u/d}_{yy}(0,y)=0, \quad y\in(a,\infty)/(0,a) \tag{12}$$

where the second condition arises from differentiating (11) with respect to x, using the Laplacian, and finally noting the relation $\phi^{u/d}_{yy}(0,y)=-K^2\mathrm{e}^{-Ky}$ for $y\in(a,\infty)/(0,a)$ from (8). We also assume

$$\psi^{u/d}(x,y)\sim\widetilde{R}^{u/d}\mathrm{e}^{\mathrm{i}Kx-Ky}, \qquad x\to\infty \tag{13}$$

where $\widetilde{R}^{u/d}\in\mathbb{C}$ is to be determined.

The constant $A^{d/u}$ is to be determined from the condition

$$\lim_{r\to0}r^{1/2}\left(\phi^{d/u}_x(x,y)+A^{d/u}\psi^{d/u}_x(x,y)\right)=0, \qquad \text{where } r=(x^2+(y-a)^2)^{1/2} \tag{14}$$

since $\phi^{u/d}$ is bounded near $r=0$.

The second condition in (12) may be integrated to give

$$\psi^d(0,y)=1-Ky, \quad y\in(0,a), \qquad \text{and} \qquad \psi^u(0,y)=1, \quad y\in(a,\infty) \tag{15}$$

to ensure that (2) is satisfied by $\psi^d(x,y)$ and (3) by $\psi^u(x,y)$.

Thus, we have shown in (11) that $\phi^{u/d}$ can be expressed in terms of the sum of the x-derivative of $\phi^{d/u}$ and a 'connection' potential $\psi^{d/u}(x,y)$ satisfying the same Neumann condition as $\phi^{d/u}(x,y)$ on the barrier but with different Dirichlet conditions described by (15). Using the far-field asymptotic form designated to each term in (11) and letting $x\to\infty$ gives

$$R^{u/d}=1-R^{d/u}-A^{d/u}\widetilde{R}^{d/u}. \tag{16}$$

2 Derivation of the connection potential $\psi^d(x,y)$.

As an illustration of the theory we shall derive the connection potential $\psi^d(x,y)$ from first principles and confirm that together with knowledge of the Dean potential and corresponding reflection coefficient it can be used through (11) and (16) to derive the Ursell potential and its reflection coefficient.

The most general potential satisfying (1), (2), (3) and (13) is written

$$\psi^d(x,y) = \widetilde{R}^d \mathrm{e}^{\mathrm{i}Kx-Ky} + \frac{2}{\pi}\int_0^\infty \frac{A(k)L(k,y)\mathrm{e}^{-kx}}{k(k^2+K^2)}\mathrm{d}k, \tag{17}$$

where $\widetilde{R}^d$ and $A(k)$ are unknowns. We define

$$U^d(y) \equiv \psi^d_x(0,y) = \mathrm{i}K\widetilde{R}^d\mathrm{e}^{-Ky} - \frac{2}{\pi}\int_0^\infty \frac{A(k)L(k,y)}{(k^2+K^2)}\mathrm{d}k \tag{18}$$

which is zero when $y > a$ on account of (12). Using Havelock's (1929) inversion theorem

$$\widetilde{R}^d = -2\mathrm{i}\int_0^a U^d(y)\mathrm{e}^{-Ky}\mathrm{d}y, \qquad \text{and} \qquad A(k) = -\int_0^a U^d(y)L(k,y)\mathrm{d}y \tag{19}$$

where use has been made of $U^d(y) = 0$ for $y > a$ to restrict the integration interval to $(0,a)$. It follows from substition of $A(k)$ from (19) into (17) and the imposition of (15) that

$$\int_0^a U^d(t)K(y,t)\mathrm{d}t = f(y), \quad y \in (0,a) \qquad \text{where } K(y,t) = \int_0^\infty \frac{L(k,t)L(k,y)}{k(k^2+K^2)}dk. \tag{20}$$

and with $f(y) = \frac{1}{2}\pi(\widetilde{R}^d\mathrm{e}^{-Ky} + Ky - 1)$. Ursell (1947) shows how this integral equation may be transformed after application of the differential operator $K + \partial/\partial y$ to become

$$\int_0^a \frac{V^d(t)}{y^2-t^2}\mathrm{d}t = -\left(f'(y) + Kf(y)\right)/y, \quad y \in (0,a) \qquad \text{where } V^d(y) = U^d(y) + K\int_a^y U^d(t)\mathrm{d}t. \tag{21}$$

Notice that $V^d(y)$ has the same singular behaviour as $U^d(y)$ near $y = a$ such that $\lim_{y\to a}(U^d(y) - V^d(y)) = 0$ and is bounded near $y = 0$.

For the particular $f(y)$ in this case $-(f'(y) + Kf(y))/y = -\frac{1}{2}\pi K^2$ so that $V^d(y)$ satisfies

$$\int_0^a \frac{V^d(t)}{y^2-t^2}\mathrm{d}t = -\tfrac{1}{2}\pi K^2, \qquad y \in (0,a). \tag{22}$$

There is a general formula for the inversion of integral equations of the type above with arbitrary right-hand sides and application of this for the particular right-hand side above gives

$$V^d(t) = \frac{D}{(a^2-t^2)^{1/2}} - K^2(a^2-t^2)^{1/2} \tag{23}$$

where D is a constant to be determined, whose origins can be traced back to transformation of the original integral equation (20) into (21). Thus, we substitute (23) back into (20) to determine D.

First we make use of an integral identity between $U^d(t)$ and $V^d(t)$, which is easily established from (21) and integration by parts, to obtain

$$\int_0^a L(k,t)U^d(t)\mathrm{d}t = k\int_0^a V^d(t)\cos ktdt = \tfrac{1}{2}\pi\left(kDJ_0(ka) - K^2aJ_1(ka)\right) \tag{24}$$

after using (23) and standard integral identities

$$\int_0^a \frac{\cos(ky)}{(a^2-y^2)^{1/2}}\mathrm{d}y = -\pi J_0(ka)/2 \qquad \text{and} \qquad \int_0^a (a^2-y^2)^{1/2}\cos(ky)\mathrm{d}y = \pi a J_1(ka)/2k. \tag{25}$$

It follows from using (24) in (20) that

$$\widetilde{R}^d \mathrm{e}^{-Ky} + Ky - 1 = D\int_0^\infty \frac{J_0(ka)L(k,y)}{(k^2+K^2)}\mathrm{d}k - K^2 a\int_0^\infty \frac{J_1(ka)L(k,y)}{k(k^2+K^2)}\mathrm{d}k, \qquad y\in(0,a). \tag{26}$$

With some effort, further integral relations can be established, in particular

$$\int_0^\infty \frac{J_0(ka)L(k,y)}{(k^2+K^2)}\mathrm{d}k = \mathrm{e}^{-Ky}K_0(Ka), \qquad \int_0^\infty \frac{J_1(ka)L(k,y)}{k(k^2+K^2)}\mathrm{d}k = \frac{(1-Ky)}{K^2a} - \frac{K_1(Ka)\mathrm{e}^{-Ky}}{K}. \tag{27}$$

Substituting these into (26) we find that the terms $1-Ky$ on each side of the equation cancel to leave

$$\widetilde{R}^d = DK_0(Ka) + KaK_1(Ka) \tag{28}$$

which determines D (in terms of $\widetilde{R}^d$). A relation for $\widetilde{R}^d$ follows from the first equation in (19) which can be written using the relation between U^d and V^d in (21) and integration by parts as

$$\widetilde{R}^d = -2\mathrm{i}\int_0^a U^d(y)\mathrm{e}^{-Ky}\mathrm{d}y = -2\mathrm{i}\int_0^a \cosh(Ky)V^d(y)\mathrm{d}y = -\mathrm{i}\pi\left(DI_0(Ka) - KaI_1(Ka)\right) \tag{29}$$

after susbtitution of (23) and using the results (25) with k replaced by $\mathrm{i}K$.

Equations (28) and (29) may be combined to give

$$\widetilde{R}^d = \mathrm{i}\pi B\left(I_0K_1 + I_1K_0\right)Ka, \quad D = \mathrm{i}BC^{-1}Ka, \quad \text{where} \quad B^{-1} = K_0 + \mathrm{i}\pi I_0, \quad C^{-1} = \pi I_1 + \mathrm{i}K_1 \tag{30}$$

are defined in (9) and (10) and where the argument of the Bessel functions is Ka throughout. We are nearly in a position to determine R^u from (16) but first need to determine A^d from (14). We have that $R^d = BK_0(Ka)$ and it can also be shown, en route to the derivation of the Dean potential, that $\phi_x^d(0,y) \sim B/(a^2-y^2)^{1/2}$. It follows from the comments after (21) and from (23) that we require $A^dD + B = 0$ and so (16) becomes

$$R^u = 1 - R^d + BD^{-1}\widetilde{R}^d = B(\mathrm{i}\pi I_0 + D^{-1}\widetilde{R}^d) = B\pi\left(\mathrm{i}I_0 + C(I_0K_1 + I_1K_0)\right) = \pi I_1(Ka)C \tag{31}$$

using (30), which is the Ursell result.

To derive the Ursell potential from (11) we first use (10) and (17), (19) and (24) to show that

$$\phi^d(x,y) + A^d\psi^d(x,y) = -\mathrm{e}^{\mathrm{i}Kx-Ky} + \left(BK_0(Ka) + A^d\widetilde{R}^d\right)\mathrm{e}^{\mathrm{i}Kx-Ky} + K^2aA^d\int_0^\infty \frac{L(k,y)J_1(ka)\mathrm{e}^{-kx}}{k(k^2+K^2)}\mathrm{d}k$$

where the resulting integral involving $J_0(ka)$ vanishes since $B + A^dD = 0$. Also it can be shown that $BK_0(Ka) + A^d\widetilde{R}^d = \mathrm{i}CK_1(Ka)$ so that from (11)

$$\begin{aligned}
\phi^u(x,y) + \mathrm{e}^{\mathrm{i}Kx-Ky} &= \mathrm{i}K^{-1}\frac{\partial}{\partial x}\left(\phi^d(x,y) + A^d\psi^d(x,y)\right) \\
&= \mathrm{e}^{\mathrm{i}Kx-Ky} - \mathrm{i}CK_1(Ka)\mathrm{e}^{\mathrm{i}Kx-Ky} - \mathrm{i}KaA^d\int_0^\infty \frac{L(k,y)J_1(ka)\mathrm{e}^{-kx}}{(k^2+K^2)}\mathrm{d}k \\
&= C\left(\pi I_1(Ka)\mathrm{e}^{\mathrm{i}Kx-Ky} + \int_0^\infty \frac{L(k,y)J_1(ka)\mathrm{e}^{-kx}}{(k^2+K^2)}dk\right)
\end{aligned} \tag{32}$$

since $-\mathrm{i}KaA^d = C$. This is precisely the Ursell potential given by (9). We could equally have derived the connection potential $\psi^u(x,y)$ and used it in conjunction with the Ursell potential to derive the Dean potential.

The connection potentials described here are of academic interest only in the present context as both the Ursell and Dean solutions are well-known. However it may transpire in more complicated problems that one of the problems is more difficult than the other in which case the connection potentials would provide the link between them.

References

[1] Ursell, F. Proc. Camb. Phil. Soc. **42** (1947), 374.

[2] Dean, W.R. Proc. Camb. Phil. Soc. **41** (1945), 231.

[3] Havelock T.H. Phil. Mag. **8** (1929), 569.

Two–dimensional and three–dimensional simulation of wave interaction with an Oscillating Wave Surge Converter

Ashkan Rafiee & Frederic Dias*
School of Mathematical Sciences
University College Dublin, Belfield Dublin 4, Ireland.
email: ashkan.rafiee@ucd.ie & frederic.dias@ucd.ie

Introduction and aim of the work

As the energy demand and the shortage in the world oil supplies are significantly increasing, new challenges arise in the current geopolitical situation. On the other hand, the global warming and economical situation of the world have significantly increased the need for a green energy generated from the renewable sources. Renewable sources such as wind and solar energies have been developed for the past few decades and there has been significant progress in harnessing energy from these sources. However, due to the importance of location on the power densities associated with these sources the demand for alternative renewable energy sources has increased.

During the 1970's global oil crisis, ocean waves were considered as a potential source of energy [1]. Nevertheless, due to the complicated nature of water wave interaction with floating/tethered bodies, the wave energy technology has not yet achieved a universal standard conceptual design similar to wind energy turbines. Therefore, various wave energy devices have been developed and deployed to harness the energy of water waves.

One of the most promising wave energy converter devices is the bottom hinged Oscillating Wave Surge Converter (OWSC). It has been known that bottom hinged OWSCs are an efficient way of extracting power from ocean waves [2]. OWSCs are in general large buoyant flaps, hinged at the bottom of ocean and oscillating back and forth under the action of incoming incident waves [3, 4]. The oscillating motion is converted into energy by pumping high pressure water to drive a hydro–electric turbine [5]. OWSCs are shallow water devices and hence the interacting waves have large horizontal velocity component. This results in a strong wave load on these devices. Therefore, large amplitude oscillations are expected. In some cases slamming can occur but this is the subject of work in progress. Hereby, the widely used potential flow theories are not sufficient to simulate wave interaction with OWSCs.

In this paper, the wave load on an OWSC will be studied using the Smoothed Particle Hydrodynamics (SPH) method. SPH method is a meshless, purely Lagrangian technique which was originally developed in 1977 by Lucy [6] and Monaghan and Gingold [7]. It has subsequently been successfully employed in a wide range of problems, e.g. astrophysics, fluid mechanics, solid mechanics, fluid–structure interaction and many more (see [8] for a recent review).

Mathematical model

The governing equations of transient compressible fluid flow include the conservation of mass and momentum equations. In this work, the governing equations are written in a Lagrangian framework as

$$\begin{aligned} &\frac{1}{\rho}\frac{\mathrm{d}\rho}{\mathrm{d}t} + \nabla\cdot\mathbf{v} = 0 \\ &\frac{\mathrm{d}\mathbf{v}}{\mathrm{d}t} = -\frac{1}{\rho}\nabla p + \nabla\cdot(\nu\nabla\mathbf{v}) + \mathbf{g} \end{aligned} \tag{1}$$

where ρ, t, $\mathbf{v}$, p, ν and $\mathbf{g}$ are density, time, velocity vector, pressure, kinematic viscosity and gravitational acceleration, respectively. The coordinates are X along the channel, Y along the vertical and Z across the channel.

In order to take into account the effects of turbulence on the flow, turbulent fluctuations are modelled through the concept of eddy viscosity estimated from the well-known and widely used $k-\epsilon$ model. The Lagrangian form of the Reynolds average Navier–Stokes (RANS) equations with $k-\epsilon$ turbulence model

*Presenting author

read [9]

$$\frac{\mathrm{d}\rho}{\mathrm{d}t} = -\rho\nabla\cdot\mathbf{v}$$

$$\frac{\mathrm{d}\mathbf{v}}{\mathrm{d}t} = -\frac{1}{\rho}\nabla\tilde{p} + \nabla\cdot\left[\left(\nu+\nu_T\right)\nabla\mathbf{v}\right] + \mathbf{g}$$

$$\frac{\mathrm{d}k}{\mathrm{d}t} = P - \epsilon + \nabla\cdot\left[\left(\nu+\frac{\nu_T}{\sigma_k}\right)\nabla k\right] \tag{2}$$

$$\frac{\mathrm{d}\epsilon}{\mathrm{d}t} = \frac{\epsilon}{k}\left(C_{\epsilon,1}P - C_{\epsilon,2}\,\epsilon\right) + \nabla\cdot\left[\left(\nu+\frac{\nu_T}{\sigma_\epsilon}\right)\nabla\epsilon\right]$$

$$\frac{\mathrm{d}\mathbf{r}}{\mathrm{d}t} = \mathbf{v}$$

where $\tilde{p} = p + 2/3\rho k$ is the modified pressure and $\nu_T = C_\mu k^2/\epsilon$ is the eddy viscosity. The production of turbulent energy P is given by

$$P = \nu_T\mathbf{S}:\mathbf{S} \tag{3}$$

where the rate–of–strain tensor $\mathbf{S}$ takes the form

$$\mathbf{S} = \frac{1}{2}\left[\nabla\mathbf{v} + (\nabla\mathbf{v})^T\right]. \tag{4}$$

The standard $k-\epsilon$ model constants are

$$\begin{gathered} C_\mu = 0.09; \quad C_{\epsilon,1} = 1.44; \quad C_{\epsilon,2} = 1.92; \\ \sigma_k = 1.0; \quad \sigma_\epsilon = 1.3. \end{gathered} \tag{5}$$

Results

The SPH simulations of OWSC were carried out in a 20 m long wave tank. The regular wave is modelled using a piston–type wave maker located at the left end of the tank. The displacement of the piston–type wavemaker is determined by the linear wavemaker theory [10]

$$X(t) = A_0\sin(\omega t) \tag{6}$$

where

$$A_0 = \frac{an_1}{\tanh(kh_0)}; \qquad n_1 = \frac{1}{2}\left(1+\frac{2kh_0}{\sinh(2kh_0)}\right). \tag{7}$$

Here, a, k, ω and h_0 are the wave amplitude, wave number, wave frequency and the initial water depth, respectively.

A dissipation zone is used for damping the wave amplitude at the right end of the tank. In this dissipation region, a friction source term is added to the vertical velocity component within the momentum equation. In order to avoid the velocity damping in the uniform horizontal flow, the damping force in the horizontal direction was not considered.

The dimensions of the OWSC model and the wave tank were similar to the ones described in [3] and a 2D schematic is shown in Fig. 1. The SPH particles were initially placed on a grid of squares with initial spacing of $l_0 = 0.022\ m$ and $l_0 = 0.033\ m$ for 2D and 3D simulations, respectively. In both cases the SPH smoothing length was set to $h = 1.5l_0$ and the boundary particles were placed with the spacing of $l_0/3$.

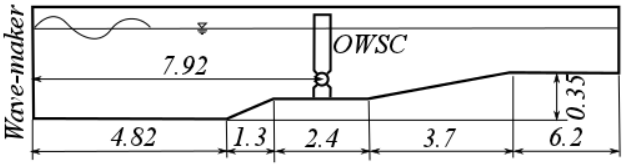

FIGURE 1: A two–dimensional schematic of the wave tank and the OWSC model. the dimensions are in meter.

The wavemaker was calibrated to produce regular waves with a 0.12 m wave height and a 2 s period. Figures 2 and 3 show snapshots of 2D and 3D SPH simulations at various times, respectively.

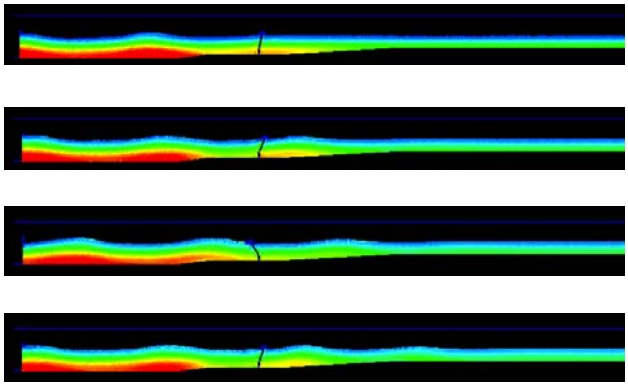

FIGURE 2: 2D SPH simulation of wave impact on an OWSC. Particles are coloured by their pressure.

By comparing Figs. 2 and 3 it can clearly be seen that after the incoming wave interacts with the OWSC, the flow is no longer 2D around the flap. Hence a 2D simulation is not sufficient to accurately predict the rotation of the flap. In order to scrutinise this further, the time variation of the flap angle is compared with experimental data obtained in the wave tank of Queen's University Belfast in Fig. 4.

As illustrated in Fig. 4, the maximum angle of rotation of the flap is under-estimated by 2D simulations whereas 3D simulations were able to capture

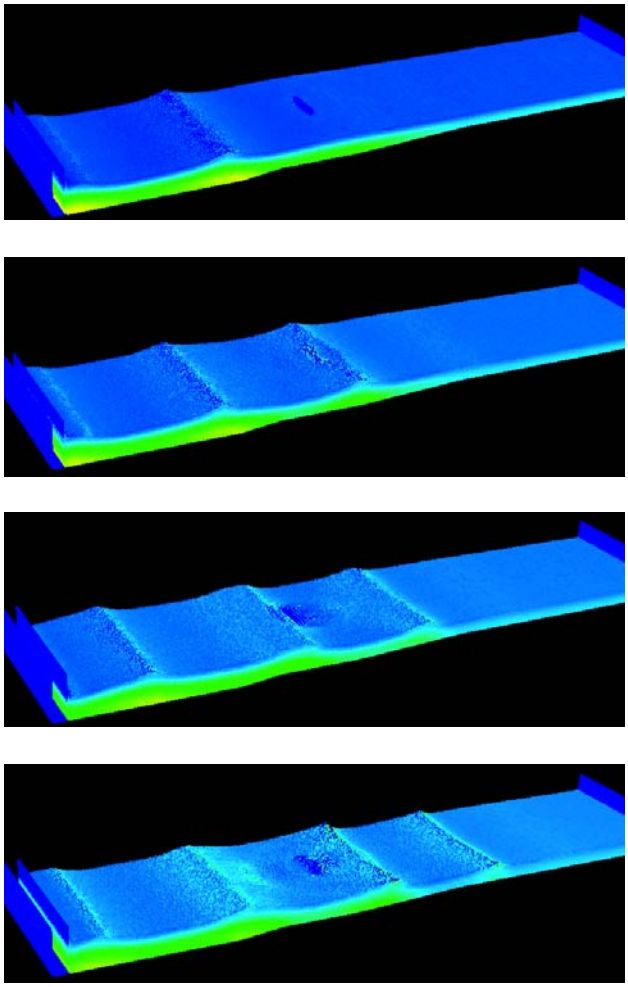

FIGURE 3: 3D SPH simulation of the interaction between incoming waves and an OWSC. Particles are coloured with their pressure.

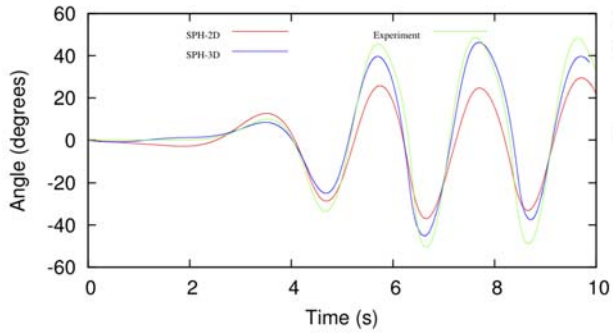

FIGURE 4: Comparison between angle of the flap from 2D and 3D simulations with experimental data.

the angle of flap more accurately.

In order to investigate the performance of OSWCs, it is crucial to understand and to accurately predict the wave loading on them. To do so, 13 pressure transducers were mounted on the front face (toward the wavemaker) of the device during the experiments. The initial locations of the transducers are given in Tab. 1. The position along the transverse Z axis is measured from the centre of the device.

TABLE 1: Initial position of the pressure transducers on the front side of the OWSC.

Pressure Transducer	pos Y [mm]	pos Z [mm]
PT1	0.6655	0.4680
PT2	0.4820	0.4680
PT3	0.7615	0.3640
PT4	0.6195	0.3640
PT5	0.4360	0.3640
PT6	0.6808	0.2600
PT7	0.5280	0.2600
PT8	0.7615	0.1560
PT9	0.6195	0.1560
PT10	0.4360	0.1560
PT11	0.7365	0.0520
PT12	0.6502	0.0520
PT13	0.4973	0.0520

Figures 5 and 6 show the time history of the pressure obtained with the 2D SPH simulations at the pressure transducer locations on the OWSC. Except at the pressure transducer 2 where both 2D and 3D simulations match, 3D results show very agreement with experimental data in all the other cases. The slight discrepancies between numerical estimations of the maximum pressure peaks and the experimental data are due to their stochastic nature and to the lack of exact repeatability of the experiments.

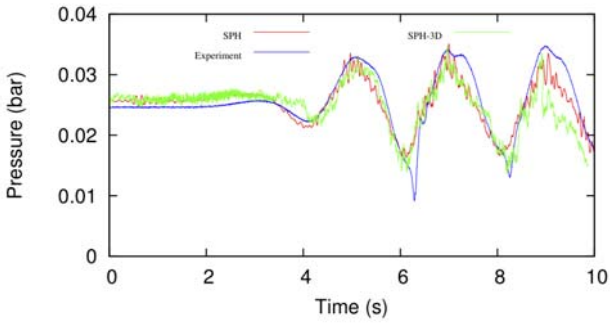

FIGURE 5: Time history of pressure variation at sensor $PT2$ in table 1.

Final Remarks

In this paper, a modified SPH method utilising a particle pair–wise Riemann solver in calculating density

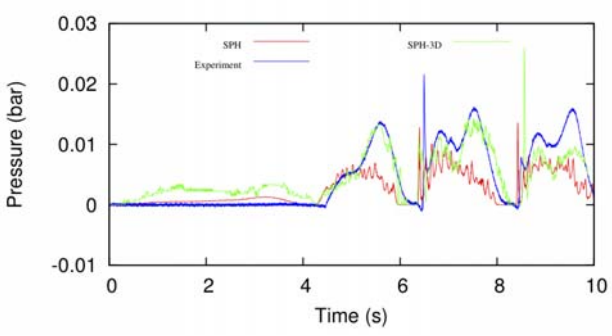

FIGURE 6: Time history of pressure variation on sensor $PT11$ in table 1.

filed was used to study the wave impact on an Oscillating Wave Surge Converter. In addition to capture the turbulent characteristics of the problem the Lagrangian form of the RANS $k-\epsilon$ model was included in the SPH equations. It was observed that the 3D SPH simulations resulted in a more accurate estimation of the pressure peaks on the OWSC. In addition, the time variation of the angle of rotation of the OWSC was in closer agreement with the experimental data for 3D simulations compared to the 2D simulations. The same comment applies for the total torque exerted on the flap around the hinged position (not shown here - see [11]). The main conclusion is that 3D simulations are essential to accurately estimate the loads on the OWSCs. 3D simulations with finer resolutions are currently being performed to study the effect of SPH particles size on the angle of rotation of the flap and the pressure exerted on the pressure sensors.

This work has been funded by Science Foundation Ireland (SFI) under the research project "High–end computational modelling for wave energy systems". The authors would like to thank Irish Centre for High-End Computing (ICHEC) for the provision of computational facilities and support. Also, this work was granted access to the HPC resources of Swiss National Supercomputing Centre (CSCS)/Mount Rosa – Cray XE6 cluster made available within the Distributed European Computing Initiative by the PRACE–2IP, receiving funding from the European Community's Seventh Framework Programme (FP7/2007-2013) under grant agreement n° RI–283493.

The experiments were performed at Queen's University of Belfast and the authors would like to extend their gratitude to Dr. Sylvain Bourdier and Prof. Trevor Whittaker for kindly sharing their experimental data.

References

[1] M. Folley, T. Whittaker, and M. Osterried, "The Oscillating Wave Surge Converter," in *The* 14^{th} *International Offshore and polar Engineering Conference (ISOPE)*, 2004.

[2] T. Whittaker, D. Collier, M. Folley, M. Osterried, A. Henry, and M. Crowley, "The development of Oyster – a shallow water surging wave energy converter," in 7^{th} *European Wave and Tidal Energy Conference*, Porto, Portugal, 2007.

[3] P. Schmitt, S. Bourdier, D. Sarkar, E. Renzi, F. Dias, K. Doherty, T. Whittaker, and J. Hoff, "Hydrodynamic loading on a bottom hinged oscillating wave surge converter," in *The* 22^{nd} *International Offshore and Polar Engineering Conference*, Rhodes, Greece, 2012.

[4] E. Renzi and F. Dias, "Resonant behavior of the oscillating wave surge converter in a channel," *Journal Fluid Mechanics*, vol. 701, pp. 482–510, 2012.

[5] L. Cameron, R. Doherty, A. Henry, K. Doherty, J. Hoff, D. Naylor, S. Bourdier, and T. Whittaker, "Design of the next generation of the Oyster wave energy converter," in 3^{rd} *International Conference on Ocean Energy*, 2010.

[6] L. B. Lucy, "A numerical approach to the testing of the fission hypothesis," *Astron. J.*, vol. 82, pp. 1013–1020, 1977.

[7] R. A. Gingold and J. J. Monaghan, "Smoothed particle hydrodnamics: Theory and application to nonspherical stars," *Mon. Not. Roy. Astr. Soc.*, vol. 181, pp. 375–389, 1977.

[8] J. J. Monaghan, "Smoothed Particle Hydrodynamics and its diverse applications," *Annu. Rev. Fluid. Mech.*, vol. 44, pp. 323–346, 2012.

[9] D. Violeau and R. Issa, "Numerical modelling of complex turbulent free–surface flows with the SPH method: an overview," *Int. J. Numer. Meth. Fluids*, vol. 53, pp. 277–304, 2007.

[10] R. G. Dean and R. A. Dalrymple, *Water wave mechanics for engineers and scientists.* Prentice–Hall, Englewood Cliffs, N.J., 1984.

[11] A. Rafiee and F. Dias, "Numerical simulation of wave interaction with an oscillating wave surge converter," in *Proceedings of OMAE 2013, ASME* 32^{nd} *International Conference on Offshore Mechanics and Arctic Engineering*, Nantes, France, 2013.

DEMONSTRATING THE FEASIBILITY OF A DISTENSIBLE-TUBE WEC WITH A DISTRIBUTED POWER TAKE-OFF

R.C.T.Rainey[1], Oil & Gas Division, Atkins Ltd., Euston Tower, 286 Euston Road, London NW1 3AT, UK *rod.rainey@atkinsglobal.com*

J.R.Chaplin, Energy and Climate Change Division, University of Southampton, Southampton SO17 1BJ, UK *j.r.chaplin@soton.ac.uk*

Background – Froude-Krylov theory

The operating principle of a distensible-tube WEC (wave energy converter) was first described at the 2006 Workshop [1], making the traditional Froude-Krylov assumption that the diffracted and radiated waves are negligible compared with the incident wave. An infinitely-long device, perpendicular to the wave crests, was assumed to have reached a steady state, and was analysed in the classical way ([2] Art.250) in a frame of reference moving with the water and bulge wave, in which the flow is steady. It was concluded that the pressure in the bulge wave became an increasingly large multiple of that in the water wave, as the water wave speed approached the free bulge wave speed. It is this resonant interaction which is exploited in a distensible-tube WEC, to concentrate water wave energy in a bulge wave. In the 2007 Workshop [3] experimental results were presented, confirming the operating principle, and investigating how the energy in the bulge wave might be extracted by means of a power take-off at the tail end of the device.

This Froude-Krylov analysis is extended in [4], by introducing a linear dissipation term in the elastic properties of the tube, intended to describe a power take-off distributed over the whole length of the device, rather than at the tail end of it. In this way the device can be made much longer – until the water wave energy starts to decay towards the tail of the device (i.e. the Froude-Krylov approximation breaks down – the threshold of this being established in [4]). See [5], figure13.

From an engineering point of view, it is highly advantageous to replace the linear dissipation term with a non-linear hysteresis loop, in which the pressure excursions are limited to a finite value, saving the tube from over-pressurisation in extreme conditions. See figure 1 below – the elliptic pressure-distension characteristic produced by a linear dissipation term becomes a parallelogram.

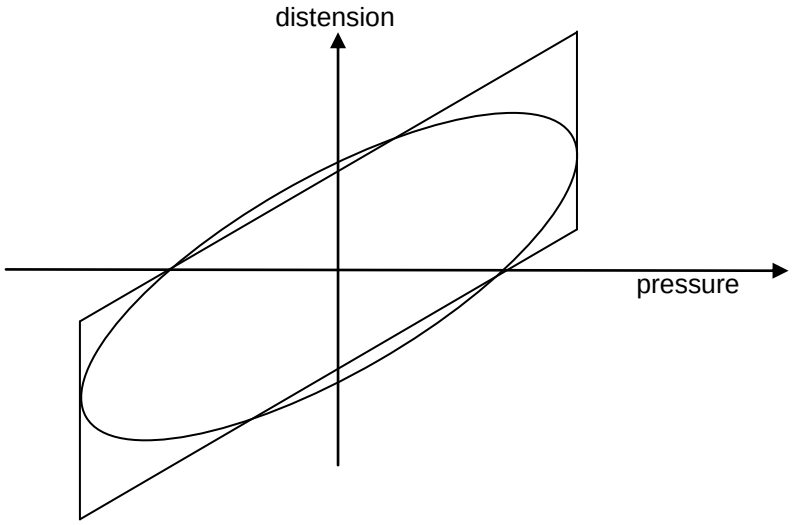

Figure 1. Linearising the pressure-distension characteristic

[1] Presenting author

In [4], an infinitely long device is considered in regular waves, and the linear dissipation is set so that the maximum pressure in the bulge wave is this pressure limit, as shown in figure 1. The power of the device can then be estimated as that dissipated by the linear dissipation term. In this way the power is obtained as a function of the pressure limit, and the water wave period and amplitude. It is then possible to consider irregular water waves on the narrow-bandwidth assumption, in which each individual wave is assumed to produce the same power as a member of a regular wave train of the same amplitude and period. The average power then follows from the Rayleigh distribution of wave amplitudes, and can be optimised by adjusting the pressure limit (up to a maximum value given by the strength of the tube). The result of this calculation is given in [4]: a 600m long device of $5m^2$ cross-section in the Benbecula wave climate produces an annual-average pneumatic power of 500kW. Maximum power, set by the strength of the tube (max bulge wave pressure = ±0.25bar), is 1200kW.

Device design

Two different designs for such a device are outlined in [4]. The simpler of these (although probably not the most economic) has a tube arranged with high-pressure pneumatic rams across it, as shown in figure 2 below.

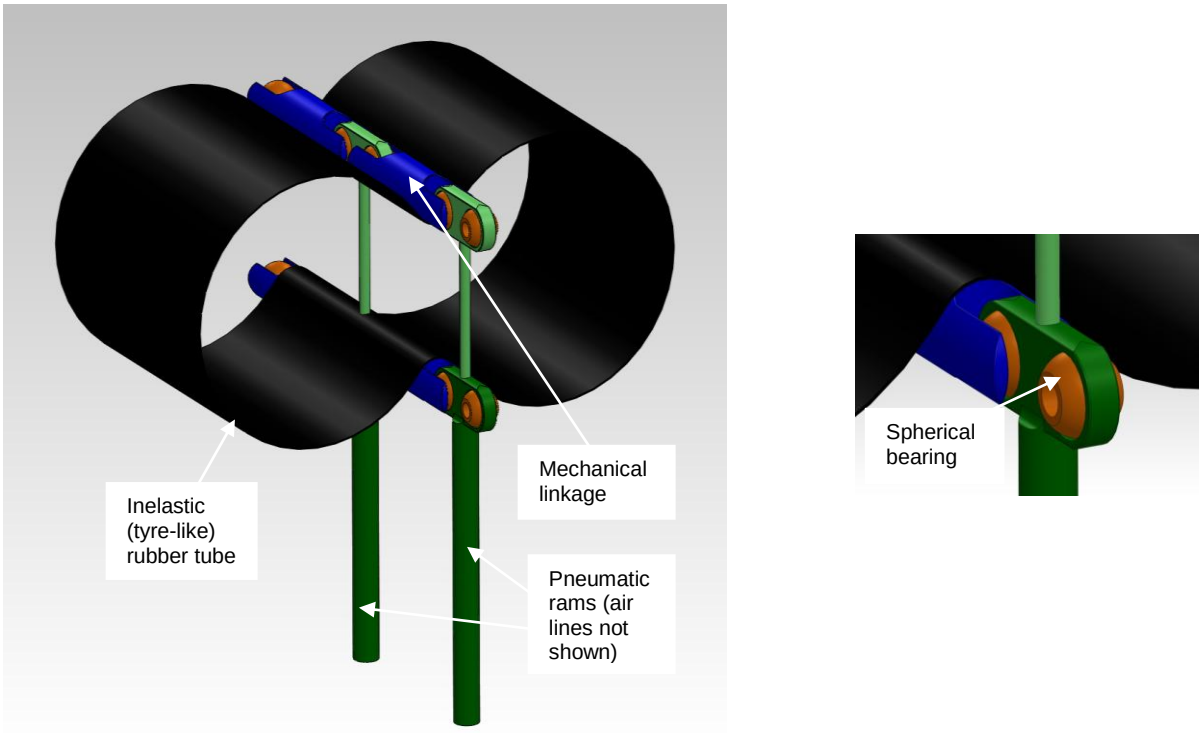

Figure 2. Section of distensible-tube WEC with distributed power take-off

The rubber tube is reinforced in the circumferential direction only, so the device can readily "snake" horizontally and vertically. Longitudinal pressure loads are carried by the mechanical linkage (0.3m diameter tubular steel members linked by spherical bearings, 1m between centres), which also transmits the circumferential pressure load in the tube to the pneumatic rams (maximum stroke ±0.9m, 1.4m between centres). It is these rams which provide the required distensibility of the tube, by virtue of the compressibility of the air in them. They have 7cm rod diameter and 17cm outer cylinder diameter (see [4], .IGS files – the bore diameter is 14cm), so their pressure amplification factor is $1.8\times1.4/\{\pi(0.14^2 - 0.07^2)/4\} = 220$. The required $0.0024kPa^{-1}$ tube distensibility (see (5)) implies that for each kPa increase in tube pressure (or 220kPa increase in air pressure), the fractional

increases in cross-sectional area is 0.0024, which is an increase in tube diameter of $1.8 \times 0.0024/2 = 0.0022$m. This corresponds to a ram stroke of 0.0022π, which gives a fractional decrease in air volume of $0.0022\pi/0.9 = 0.0077$, and thus a fractional increase in air pressure of $0.0077\gamma = 0.011$, assuming adiabatic air behaviour with $\gamma = 1.4$. The static air pressure must therefore be $220/0.011 = 20{,}000$kPa = 200 bar. It produces a static tube pressurisation of $20{,}000/220 = 90$kPa, which is rather greater than the 50kPa specified in [4], but this can be remedied by pressurising the lower compartments in the rams, and inter-connecting them with flexible air lines.

The air pressure in the upper compartments of the rams is limited by one-way valves, communicating (via short flexible jumper hoses) to low and high pressure flexible lines running the whole length of the device. These have sufficient internal diameter (10cm appears suitable) to limit flow losses, and also to enable them to act as pneumatic accumulators, smoothing the power flow. The whole device is single-point-moored from a small mooring buoy (conventional CALM type, or vertically-tethered), which also terminates the low and high pressure lines, just like the oil lines from a single-point-moored tanker. The air turbine between the two lines, like the control systems to regulate their pressure difference, is mounted on the buoy – the device itself is entirely passive, with no electrical systems.

Physical model testing

The concept of a distensible tube wave energy converter with a distributed power take-off is not one that seems to have been tested in the laboratory, although preliminary experiments have been carried out [6] with a view to using electro-active polymers. In this section we propose an experiment using a model which is designed to mimic the behaviour of the full-scale device described above, but which differs from it for various practical reasons. A scale model that incorporates a pneumatic system similar to that of the prototype is a feasible option, and would clearly have to feature in any subsequent programme of development. Careful design of the model rams could deliver both the appropriate static force across the tube, and the appropriate distensibility. But the purpose of the tests proposed here is to demonstrate feasibility in the simplest way (as in an earlier case [7]), without the complexity and expense of large numbers of inter-connected pneumatic rams operating at high pressure.

Accordingly, in the proposed model the rams are replaced by steel extension springs inside circular bellows. A sketch of one section of the laboratory model is shown in figure 3 below, with part of the bellows removed to reveal the tensioning spring inside. The longitudinal mechanical linkages of the full-scale device are replaced by upper and lower pipes which have sufficient bending stiffness to maintain the shape of the tube over the short gap between adjacent springs, while still allowing it to flex in the vertical and horizontal planes with the external wave motion. The bellows terminate internally with opposing one-way valves so that as the tube expands and contracts, they pump air (at a positive pressure relative to that of the water in the tube) through the same pipes, around a circuit which, as in the full-scale device, includes the power take-off (not shown here). In figure 3, arrows indicate the air flow in opposite directions in the two pipes. Outline calculations indicate that this arrangement is practicable at a scale of about 1:6.

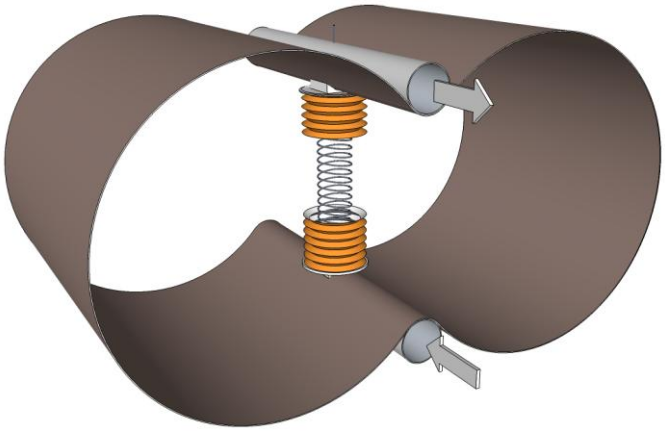

Figure 3. One section of the laboratory model of the device. Expansions and contractions of the tube cause the bellows to pump air along the pipes above and below, delivering a steady flow of air through the power take-off.

Full-scale demonstration

Because the device uses a conventional single-point mooring buoy (to which it is attached in the conventional way, with a nylon hawser), there is no need to demonstrate that part of the system. Instead, the device can be towed behind a small tug, or fishing trawler. This is much more convenient than installing it in a fixed test site, such as EMEC in Orkney. As well as the nylon hawser, the tug can take over the stern the low and high pressure pneumatic hoses. The turbine between them, and the electrical generator, can then be mounted on the tug, together with the control machinery.

In this way the performance of the device can be demonstrated in waves up to the highest from which power is required (viz. *Hs* = 10m, see [4]). Survivability in waves above that can be deduced from the physical model tests.

References

[1] Farley, F.J.M. & Rainey, R.C.T. Radical design options for wave-profiling wave energy converters. 21st IWWWFB, Loughborough, UK, 2006

[2] Lamb, H. Hydrodynamics. 6th Ed. Cambridge University Press 1932

[3] Chaplin, J.R., Farley, F.J.M. & Rainey, R.C.T. Power conversion in the Anaconda WEC. 22nd IWWWFB, Plitvice, Croatia, 2007.

[4] Rainey, R.C.T. Exploiting wave energy – why we shouldn't give up. Isaac Newton Institute, Cambridge, 2012. http://www.newton.ac.uk/programmes/INI/seminars/2012121716001.html

[5] Farley, F.J.M., Rainey, R.C.T. & Chaplin, J.R. Rubber tubes in the sea. Phil. Trans. R.Soc. A (2012) **370**, 381-403.

[6] Babarit, A., Gendron, B., Singh, J., Melis, C., & Jean, P. Modelisation numerique et experimentale d'un systeme houlomoteur electro-actif deformable. Available at http://website.ec-nantes.fr/actesjh/images/13JH/Articles/Babarit2_JH13.pdf

[7] Chaplin, J. R., Heller, V., Farley, F.J.M, Hearn, G.E. & Rainey, R.C.T., Laboratory testing the Anaconda. Phil. Trans. R. Soc. A (2012) **370**, 403-424

Wave-power extraction from a finite array of Oscillating Wave Surge Converters

E. Renzi*& F. Dias
UCD School of Mathematical Sciences
University College Dublin, Belfield Dublin 4, Ireland.
email: emiliano.renzi@ucd.ie & frederic.dias@ucd.ie

Introduction and aim of the work

Deployment of wave energy converters (WECs) in large arrays is envisaged as a fundamental market acceleration strategy towards the commmercialisation of wave energy systems. When working together in an array, WECs can interfere either in a constructive or a destructive manner, depending on the distance between the elements (Budal, 1977; Falnes, 1980; Thomas & Evans, 1981; Mavrakos & McIver, 1997; Thomas, 2008; Garnaud & Mei, 2009; Babarit, 2010; Falnes & Hals, 2012). In this paper we shall consider an array of large devices known as Oscillating Wave Surge Converters (OWSCs). The latter are flap-type WECs hinged on a bottom foundation and pitching under the actions of incident waves in the nearshore (Whittaker & Folley, 2012). In order to investigate the behaviour of an in-line array of many identical WECs, four quantities are essential: the incident wave amplitude and wavenumber, A and k respectively, the characteristic width of the elements w and the spacing a. Several parameters can be formed from those quantities which are fundamental in defining the regime of the system: A/w, kw, ka. First, in this paper we shall restrict our analysis to small-amplitude waves, for which $A/w \ll 1$. Within this assumption, the behaviour of the system can be described by recurring to the linearised versions of the inviscid-irrotational equations of motion (potential-flow model, see for example Mei *et al.*, 2005). This hypothesis rules out the occurrence of vortex-shedding and nonlinear diffraction effects, which are currently being investigated with the aid of computational fluid dynamic models (Rafiee & Dias, 2012). Yet the linearised potential-flow model encompasses a number of cases of practical interest (Mei *et al.*, 2005) and is worth investigating. Another fundamental parameter to characterise the system regime is the product kw between the wavenumber of the incident wave and the characteristic width of a single device. Several existing analytical models are indeed applicable to the OWSC in the limiting cases $kw \ll 1$ and $kw \gg 1$. The first case corresponds to the so-called "point-absorber" approximation (Budal, 1977; Falnes, 1980), while the second one refers to the "line-absorber" limit (Falnes & Hals, 2012). However, considering a characteristic OWSC width $w \simeq 30\,\mathrm{m}$ and a characteristic wavelength $\lambda = 2\pi/k \simeq 100\,\mathrm{m}$, yields $kw = O(1)$, which falls outside the limits of applicability of the aforementioned theories. Recently, new models have been generated to investigate the behaviour of an OWSC in a channel (Henry *et al.*, 2010; Renzi & Dias, 2012), an infinite array of OWSCs (Renzi & Dias, 2013a) and a single OWSC in the open ocean (Babarit *et al.*, 2012; Renzi & Dias, 2013b). However, the analysis of a finite array of OWSCs seems to not have been undertaken yet. Indeed several theoretical models are available concerning the interactions in an array of floating bodies (see for example Kagemoto & Yue, 1986; Mei *et al.*, 1994; Mavrakos & McIver, 1997; Newman, 2001; Adamo & Mei, 2005; Siddorn & Eatock Taylor, 2008), some of them relying on simplifying assumptions on the parameter ka. For $ka \ll 1$, the spacing between the elements can be neglected without appreciable consequences, as shown by Adamo & Mei (2005) for an array of closely-spaced flaps designed to protect Venice from flooding. On the other hand, when $ka \gg 1$ the wide-spacing approximation can be applied, for which radially outgoing waves are approximated as plane waves (Mavrakos & McIver, 1997). In the intermediate case $ka = O(1)$, which corresponds to the situation investigated here, interference effects between the elements of the array must be appropriately accounted for.

In this paper, we devise a new semi-analytical model for a finite array of OWSCs by extending the theory of Adamo & Mei (2005) to the case $ka = O(1)$ and combining it with the semi-analytical approach of Renzi & Dias (2013b). Applications will be shown for the case of two in-line converters; investigations of a larger number of converters is not shown here for the sake of brevity, but will be presented at the

*Presenting author

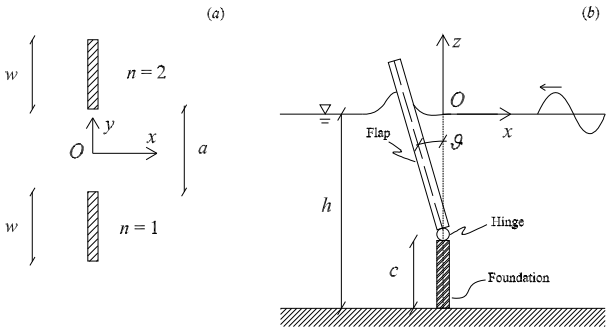

Figure 1: Geometry of the system.

Workshop.

Mathematical model

Referring to figure 1, consider a finite number N of OWSCs in an ocean of depth h, all aligned along the y axis. Each converter is modelled as a rectangular box of width w, pitching about a hinge at depth $z = -h + c$. Following Adamo & Mei (2005) and Renzi & Dias (2012, 2013a,b), the thickness of the flap is assumed to be immaterial. Let the x axis denote the offshore coordinate and the centre of the system O be on the axis of symmetry of the system. Assume that all the converters have identical geometry and are separated by the same distance a (see again figure 1). Incident waves of small amplitude $A \ll w$ are incoming from the right and set the converters into motion, which is then transformed into useful energy by means of generators linked to each OWSC. Within the limits of a linearised potential-flow theory, there exists a velocity potential $\Phi(x, y, z, t)$ which satisfies the Laplace equation:

$$\nabla^2 \Phi = 0 \tag{1}$$

in the fluid domain, being $\nabla f = (f_{,x}, f_{,y}, f_{,z})$, where subscripts with commas denote differentiation with respect to the relevant variable. On the free surface, the kinematic-boundary condition

$$\Phi_{,tt} + g\Phi_{,z} = 0, \quad z = 0 \tag{2}$$

is applied, g being the acceleration due to gravity. In addition, absence of vertical flux is required at the bottom:

$$\Phi_{,z} = 0, \quad z = -h. \tag{3}$$

Finally, let $\theta_n(t)$ be the angle of rotation of the nth converter, positive if anticlockwise; then the boundary condition on each OWSC writes:

$$\Phi_{,x} = -\theta_{n,t}(t)(z + h - c)H(z + h - c), \quad \text{on } \mathcal{L}_n. \tag{4}$$

In the latter expression, $\mathcal{L}_n$ indicates the contour of the nth flap and the Heaviside step function H is used to assure absence of flux through the bottom foundation. For time-harmonic oscillations, the boundary-value problem (1)–(4) is solved in terms of the velocity potential Φ by applying Green's integral theorem in the fluid domain and by expanding the unknown jumps in potential across the flaps in terms of the Chebyshev polynomials of the second kind. Such method is an extension of that applied by Renzi & Dias (2012, 2013a,b) and will not be detailed here for the sake of brevity. Once the potential is known, the motion of the bodies can be fully characterised. The equation of motion of the nth body in the frequency domain is

$$\left[-\omega^2(I + \mu_{nn}) + C - i\omega\left(\nu_{nn} + \nu_{pto}\right)\right]\Theta_n - \sum_{m=1}^{N}{}' \left(\omega^2\mu_{mn} + i\omega\nu_{mn}\right)\Theta_m = F_n. \tag{5}$$

In the latter, I is the flap moment of inertia, C the flap buoyancy torque, ν_{pto} the damping coefficient of the generators, μ_{mn} and ν_{mn} are, respectively, the added inertia and radiation damping of body n when body m is moving, F_n is the exciting torque on body n, and finally Θ_n is the complex amplitude of rotation of body n. The prime on the sum indicates exclusion of the term $m = n$. Expression (5) is a linear system of equations for the unknowns Θ_n, $n = 1, \ldots, N$. Once the Θ_n are all known, the total generated power is determined as

$$P = \sum_{n=0}^{N} \frac{\omega^2}{2}\nu_{pto}\left|\Theta_n^2\right|. \tag{6}$$

Finally, the performance of the system is measured with the interaction factor $q = P/(NP_{iso})$ which is the ratio between the total power captured by the array and the power captured by N isolated elements (Budal, 1977), for given period of the incident wave. Noting that q hides the real amount of absorbed power, Babarit (2010) introduced a modified performance evaluator, defined as $q_n^{mod} = (P_n - P_{iso})/\max_T(P_{iso})$, where P_n is the power output by the nth body in the array and the maximum is taken over the selected period interval. When $q_n^{mod} > 0$, interference effects increase the absorbed power by the nth element with respect to the isolated case. In the following, an application will be shown for the case of two in-line converters.

Results

In this section, results are shown for a system of two in-line OWSCs. Parameters are: $w = 26\,\text{m}$, $c = 4\,\text{m}$, $h = 13\,\text{m}$, $a = 30\,\text{m}$. The damping coefficient has been optimised to yield the maximum power possible

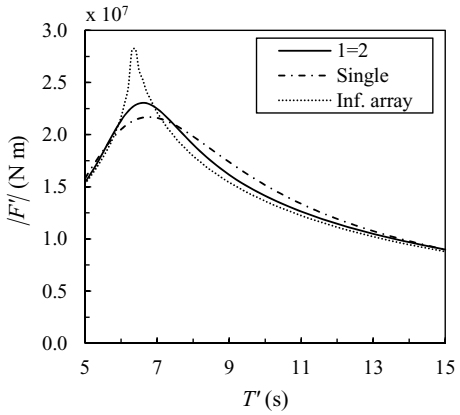

Figure 2: Exciting torque magnitude

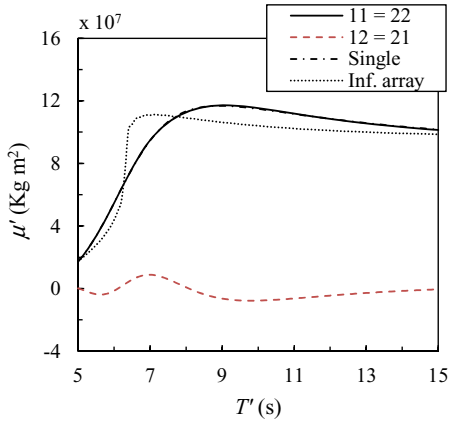

Figure 3: Reflexive ($\mu_{11} = \mu_{22}$) and mutual ($\mu_{12} = \mu_{21}$) added inertia torque.

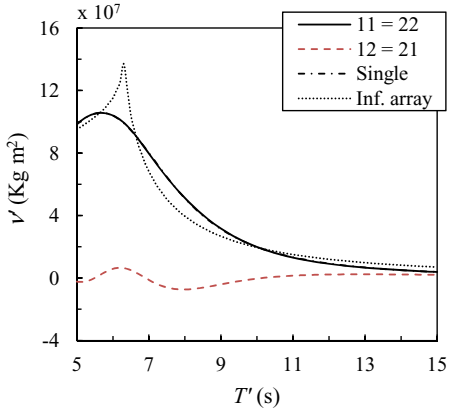

Figure 4: Reflexive ($\nu_{11} = \nu_{22}$) and mutual ($\nu_{12} = \nu_{21}$) radiation damping.

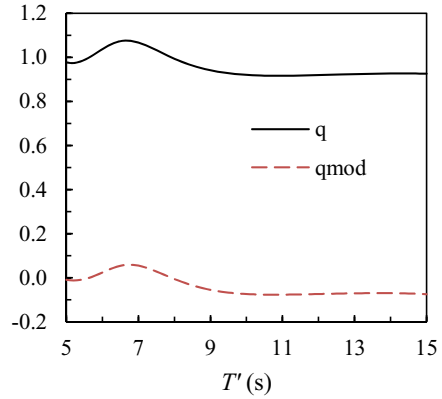

Figure 5: q and q_{mod} factors.

with given I and C (note that this does not correspond to body resonance). Normally incident sinusoidal waves are considered. Since the configuration is symmetric with respect to $y = 0$, both flaps have the same hydrodynamic parameters. In figures 2–5, the exciting torque, the added inertia torque, the radiation damping, the q and q^{mod} factors are shown versus the period of the incident wave, together with the relevant curves for an infinite array (Renzi & Dias, 2013a) and a single flap (Renzi & Dias, 2013b).

In addition to observing that, as expected, the values of the exciting torque are in between those of a single flap and an infinite array, the following comments can be made:

- A *near-resonant* mechanism is identified: F attains its maximum value near the first resonant period of the infinite array system (see Renzi & Dias, 2013a). Due to damping associated to wave spreading towards infinity, the peak exciting torque for the finite array is lowered and shifted towards larger periods (see also Sammarco & Renzi, 2007, for a similar mechanism).

- The curves of the reflexive added inertia and damping terms, μ_{nn} and ν_{nn} respectively, superimpose to those of a single flap in the open ocean. The mutual terms μ_{nm} and ν_{nm} are larger in short waves and decay in long waves (Babarit, 2010).

- As expected (Falnes, 1980; Mavrakos & McIver, 1997; Babarit, 2010), the q factor curve shows regions of constructive interaction ($q > 1$), as well as regions of destructive interaction ($q < 1$). The behaviour of the curve resembles that of the exciting torque. This shows that the OWSC hydrodynamics is governed by diffraction (Renzi & Dias, 2012, 2013a,b).

- Regions where $q > 1$ correspond to $q^{mod} > 0$. This means that for two in-line OWSCs, constructive interference is usually accompanied by an actual increase of absorbed power. Such result is not obvious and does not yield for systems of other converters (see Babarit, 2010).

- $\max q \simeq 10\%$ for $T \simeq 7\,\mathrm{s}$, indicating that the power output of each converter is $\simeq 10\%$ larger in the array then when acting isolated (i.e. "1+1 > 2").

Final Remarks

We provide a new semi-analytical solution for a finite array of in-line Oscillating Wave Surge Converters. Calculations for a system of two flaps show that constructive interference is possible for certain periods of the incident wave field. We also show that in an array of OWSCs the strongest constructive interaction is accompanied by the largest system efficiency. This does not yield in general for systems of other devices (see Babarit, 2010). Future applications will consider more populated systems and will aim to investigate the occurrence of trapped modes similar to those found by Mei *et al.* (1994) for a system of flap-type gates.

This work has been funded by Science Foundation Ireland (SFI) under the research project "High-end computational modelling for wave energy systems".

References

Adamo, A. & Mei, C.C. 2005 Linear response of Venice storm gates to incident waves. *Proc R Soc Lon A*, 461, 1711–1734.

Babarit, A. 2010 Impact of long separating distances on the energy production of two interacting wave energy converters. *Ocean Eng*, 37, 718–729.

Babarit, A., Hals, J., Muliawan, M.J., Kurniawan, A., Moan, T., Krokstad, J. 2012 Numerical benchmarking study of a selection of wave energy converters. *Ren Energy*, 41, 4463.

Budal, K. 1977 Theory for Absorption of Wave Power by a System of Interacting Bodies. *J. Ship Res.*, 21(4), 248–253.

Falnes, J. 1980 Radiation impedance matrix and optimum power absorption for interacting oscillators in surface waves. *Appl Ocean Res*, 2(2), 75–80.

Falnes, J. & Hals, J. 2012 Heaving buoys, point absorbers and arrays. *Phil Trans R Soc A*, 370, 246–277.

Henry, A., Doherty, K., Cameron, L., Whittaker, T. & Doherty, R. 2010 Advances in the design of the Oyster wave energy converter, *RINA Marine and Offshore Energy Conference*, London, UK.

Garnaud, X. & Mei, C.C. 2009 Bragg scattering and wave-power extraction by an array of small buoys. *Proc R Soc Lon A*, 466, 79–106.

Kagemoto, H. & Yue, D.K.P. 1986 Interactions among multiple three-dimensional bodies in water waves: an exact algebraic method. *J Fluid Mech*, 166, 189–209.

Mavrakos, S.A. & McIver, P. 1997 Comparison of methods for computing hydrodynamic characteristics of arrays of wave power devices. *Appl Ocean Res*, 19, 283–291.

Mei, C.C., Sammarco, P., Chan E.S. & Procaccini C. 1994 Subharmonic Resonance of Proposed Storm Gates for Venice Lagoon. *Proc R Soc Lon A*, 444, 257-265.

Mei, C.C., Stiassnie, M.& Yue, D. K.-P. 2005. Theory and applications of ocean surface waves. World Scientific, USA.

Newman, J.N. 2001 Wave Effects on Multiple Bodies. In: *Hydrodynamics in Ship and Ocean Engineering* (M. Kashiwagi editor), RIAM, Kyushu University ,Japan.

Rafiee, A. & Dias, F. 2012 Numerical simulation of wave impact on an oscillating wave surge converter. Proceedings of the 2nd International Conference on Violent Flows, Nantes (France), 157–163.

Renzi, E. & Dias, F. 2012. Resonant behaviour of the Oscillating Wave Surge Converter in a channel. *J Fluid Mech*, 701, 482–510.

Renzi, E. & Dias, F. 2013a Relations for a periodic array of flap-type wave energy converters. *Appl Ocean Res*, 39, 31–39.

Renzi, E. & Dias, F. 2013b Hydrodynamics of the Oscillating Wave Surge Converter in the open ocean. *Eur J Mech B/Flu*, in press.

Sammarco, P. & Renzi, E. 2007 Wave actions on the side caissons of the Venice gates. *Appl Ocean Res*, 29, 210–220.

Siddorn, P. & Eatock Taylor, R. 2008 Diffraction and independent radiation by an array of floating cylinders. *Ocean Eng*, 35, 1289–1303.

Thomas, G. 2008 The theory behind the conversion of ocean wave energy: a review. In: *Ocean Wave Energy* (J. Cruz editor). Springer, Germany.

Thomas, G.P. and Evans, D.V. 1981 Arrays of three-dimensional wave-energy absorbers. *J Fluid Mech*, 108, 67–88.

Whittaker, T. & Folley ,M. 2012 Nearshore oscillating wave surge converters and the development of Oyster. *Phil Tran R Soc A*,370, 345–364.

The Application of Velocity Decomposition to Airfoil Problems

William J. Rosemurgy†, Kevin J. Maki, and Robert F. Beck

Department of Naval Architecture and Marine Engineering
University of Michigan, Ann Arbor, MI, 48109 USA
[brosemu, kjmaki, rbeck]@umich.edu

† Presenting Author

Introduction

The work presented in this paper is the continuation of work previously presented at the IWWWFB by Edmund et al. (2011). The goal of this research is to find a method that provides the solution in the entire fluid domain of the Navier-Stokes problem, while being more computationally efficient than existing methods that require full field discretization. To achieve this goal, we use a velocity decomposition where the total velocity vector is expressed as the sum of an irrotational component and a vortical component. The majority of the flow in the fluid domain is irrotational and can be expressed as the gradient of a potential field. Rotational flow will be confined to the boundary layer near the body, the wake region downstream of the body, and the turbulent regions associated with breaking waves. It is well known that the potential which satisfies a zero-normal flow condition on the body (the *inviscid* potential) does not satisfy the real viscous flow problem even in the regions away from the body where the flow is essentially irrotational. This is almost entirely due to viscous effects near the body. Therefore, we seek a formulation for the *viscous* potential which incorporates the effects of viscosity in a general manner.

The work in Edmund (2012) applied velocity decomposition to the steady, non-lifting flow over deeply-submerged bodies at a wide range of Reynolds numbers. The ultimate goal of the current research is to apply our approach to free-surface problems. The flow over a body under a free surface is almost always asymmetrical which presents challenges for our approach. To address these issues we began by investigating the steady flow over a 2-dimensional, deeply-submerged NACA0012 airfoil which also has an asymmetrical velocity field around the body and in the wake. It is expected that the results presented at the Workshop will include a free surface, and a comparison to Duncan's experiments (1983) will be made.

Velocity Decomposition

We seek a velocity decomposition that provides a potential field which satisfies the real fluid problem in the region of space where the total velocity has no rotation. To arrive at a formulation for the viscous potential, we start with the decomposition of the total velocity vector, $\mathbf{u}$, as the sum of the gradient of the viscous potential, $\nabla\varphi$, and a vortical component, $\mathbf{w}$.

$$\mathbf{u} = \nabla\varphi + \mathbf{w} \tag{1}$$

If a viscous potential is found that delivers a vortical velocity field which vanishes with the vorticity vector, then the total velocity can be described completely by the gradient of the viscous potential outside of the vortical regions.

$$\mathbf{u} = \nabla\varphi \tag{2}$$

This opens the possibility to solve the governing equations for the viscous flow (Navier-Stokes, Reynolds-averaged Navier-Stokes, etc.) on a reduced fluid domain and to use the gradient of the viscous potential as a Dirichlet condition on the outer boundary of this reduced discretization. With this approach, the reduced fluid domain only needs to contain the regions where the vortical velocity is non-zero.

As mentioned in the introduction, the viscous potential, φ, is different from the inviscid potential, ϕ. The inviscid potential satisfies the kinematic condition of zero normal flow on the body, while the viscous potential will satisfy a modified Neumann boundary condition that is not necessarily zero on the body. To derive this condition we start with the no-slip body boundary condition that the total velocity vector must satisfy.

$$\mathbf{u} = 0 = \mathbf{w} + \nabla\varphi \qquad \text{on the body} \tag{3}$$

or

$$\nabla\varphi = -\mathbf{w} \qquad \text{on the body} \tag{4}$$

Dotting both sides with the body normal vector we obtain:

$$\frac{\partial \varphi}{\partial n} = -\mathbf{w} \cdot \mathbf{n} = -w_n \text{ on the body} \tag{5}$$

Following Morino (1986), we use the principle of conservation of mass to obtain an expression for the rotational contribution to the body boundary condition for the viscous potential. The divergence operator and the vortical velocity are expressed in a local coordinate system consisting of a normal vector $\mathbf{n}$ and two in-plane tangent vectors, $\mathbf{t}_1$ and $\mathbf{t}_2$. If the total velocity is solenoidal and the viscous potential satisfies the Laplace equation then the divergence of the vortical velocity must be zero:

$$\nabla \cdot \mathbf{u} = \nabla \cdot \mathbf{w} + \underbrace{\nabla^2 \varphi}_{=0} = \nabla \cdot \mathbf{w} = \frac{\partial w_n}{\partial n} + \frac{\partial w_{t_1}}{\partial t_1} + \frac{\partial w_{t_2}}{\partial t_2} = 0 \tag{6}$$

This equation is then integrated in the normal direction out to a distance δ.

$$w_n(0) = \int_0^\delta \left[\frac{\partial w_{t_1}}{\partial t_1} + \frac{\partial w_{t_2}}{\partial t_2} \right] dn + w_n(\delta) \tag{7}$$

The result is the expression for the normal component of the vortical velocity on the body surface. Combining Equations 5 and 7 results in the body boundary condition for the viscous potential.

$$\frac{\partial \varphi}{\partial n} = -\int_0^\delta \left[\frac{\partial w_{t_1}}{\partial t} + \frac{\partial w_{t_2}}{\partial t_2} \right] dn - w_n(\delta) \text{ on the body} \tag{8}$$

We seek a decomposition in which the vortical velocity vanishes with the vorticity as one moves away from the body (in a normal direction). This means that for a distance δ that lies far enough away from the body such that the vorticity is negligible, the decomposition will provide a vortical velocity which is zero at δ. Consequently, Equation 9 gives the body boundary condition for the viscous potential.

$$\frac{\partial \varphi}{\partial n} = -\int_0^\delta \left[\frac{\partial w_{t_1}}{\partial t} + \frac{\partial w_{t_2}}{\partial t_2} \right] dn \text{ on the body} \tag{9}$$

We use Equation 2 to specify the Dirichlet condition for the viscous flow on the inlet and lateral (far-field) boundaries of a reduced computational domain. However, from Equation 9 it is apparent that knowledge of the vortical velocity is required in order to calculate the body boundary condition. We approach this with an iterative strategy. The inviscid potential is initially used to set the Dirichlet condition for the viscous flow. Then the solver iterates between the viscous flow solver and the potential solver until a converged solution is reached. The vortical velocity at δ, $w_n(\delta)$, in Equation 8 is initially non-zero but is driven to zero as a consequence of the iterative scheme.

The vortical velocity evolves in the wake downstream of the body. A source distribution downstream of the body is used in order to include the effects of the vortical wake. The source distribution in the wake also satisfies Equation 9.

Potential Flow Solver

We solve the viscous potential problem using a boundary element method satisfying the body boundary condition for the viscous potential given in Equation 9 as well as the far-field radiation condition. We use a combination of flat, 2-dimensional source and vortex panels. The vortex panels have a linearly varying strength while the source panels have constant strength. The Kutta condition is met by requiring the vortex strength at the trailing edge to be zero. In the usual manner, a system of linear equations is developed to solve for the unknown vortex strengths by collocating at the center of each panel and satisfying the inviscid zero normal flow velocity condition. Similarly, the unknown source strengths are determined by forming a separate system of linear equations by collocating at the center of each panel and satisfying the body boundary condition for the viscous potential from Equation 9. The systems are directly solved using LAPACK, an open-source linear algebra package.

The lifting problem introduces a new challenge that we have not encountered before. In previous work we have only dealt with non-lifting bodies where the body is symmetric with respect to the onset flow which results in a symmetric flow around the body as well as a symmetric wake downstream. We include the vortical effects of the symmetric wake by placing a source distribution from the trailing edge to the end of the computational

domain. However, in a lifting problem the vortical wake is not symmetric and we must adjust our model to include this asymmetry. To do this we use two source distributions separated by a small distance, usually less than 1% of the chordlength which is illustrated in Figure 1. The boundary condition for the upper wake source distribution integrates the vortical velocity in the positive vertical direction while the boundary condition for the lower wake source distribution integrates the vortical velocity in the opposite direction. The non-physical source distributions in the wake region cause no difficulty because the velocities due to the viscous potential are only evaluated outside of the rotational region of the flow.

Viscous Flow Solver

The viscous fluid equations are solved using OpenFOAM, a finite-volume, open-source CFD package. The steady fluid equations are solved using the SIMPLE algorithm. The Spalart-Allmaras turbulence model with wall functions is used when needed. It is also important to mention that the potential flow panel method uses the same discretization of the body as the viscous flow solver.

Results

Results are computed for a deeply-submerged NACA0012 airfoil at $0-7^\circ$ angles of attack. Since a comparison with Duncan's experiments (1983) is the ultimate goal, we use a Reynolds number of 160,000 and a chordlength of 0.202 m. The velocity decomposition result is computed on a reduced size grid which has inlet and lateral (far-field) boundaries at 5 chordlengths from the body with 27k cells. For comparison, a conventional RANS result is computed on a grid with boundaries located at 100 chordlengths with 44k cells. To be consistent the two domains share the same geometry in overlapping regions and both have downstream boundaries located 250 chordlengths downstream. The surface of the airfoil is discretized into 100 flat panels. Velocity profiles at the quarter-chord, mid-chord, trailing edge and one chordlength downstream are shown in Figures 3 and Figures 4 for angles of attack of 3° and 7°, respectively. The velocity decomposition result has excellent agreement with the RANS calculation on the large domain. Figure 2 shows the lift coefficient calculated from the RANS result across a range of angles of attack. Experimental values from Jacobs and Sherman (1937) are included in Figure 2 for a slightly higher Reynolds number of 170,000. Again, the agreement between the large domain result and the velocity decomposition is very good, within 0.25%

Conclusion

Our velocity decomposition approach has been successfully applied to solve for the real viscous flow over a deeply submerged NACA0012 airfoil. The next step is to include free-surface effects. We expect to present results for the free-surface flow over a NACA0012 airfoil at the Workshop.

Acknowledgements

The authors would like to gratefully acknowledge the support of grants from the US Office of Naval Research, Award #N00014-10-1-0301 under the technical direction of Ms. Kelly Cooper, as well as Awards #N00014-11-1-0484 and #N00014-09-1-0978 under the technical direction of Dr. L. Patrick Purtell.

Bibliography

Duncan, J. The breaking and non-breaking wave resistance of a two-dimensional hydrofoil. *Journal of Fluid Mechanics*, 126:507–520, 1983.

Edmund, D. O., Maki, K. J., and Beck, R. F. An improved viscous / inviscid velocity decomposition method. In *International Workshop on Water Waves and Floating Bodies (IWWWFB)*, volume 26, 2011.

Edmund, D. *A Velocity Decomposition Method for Efficient Numerical Computation of Steady External Flows*. PhD thesis, University of Michigan, 2012.

Jacobs, E. N. and Sherman, A. Airfoil section characteristics as affected by variations of the Reynolds number. Technical Report 586, National Advisory Committee for Aeronautics, 1937.

Morino, L. Helmholtz decomposition revisited: vorticity generation and trailing edge condition. *Computational Mechanics*, 1(1):65–90, 1986.

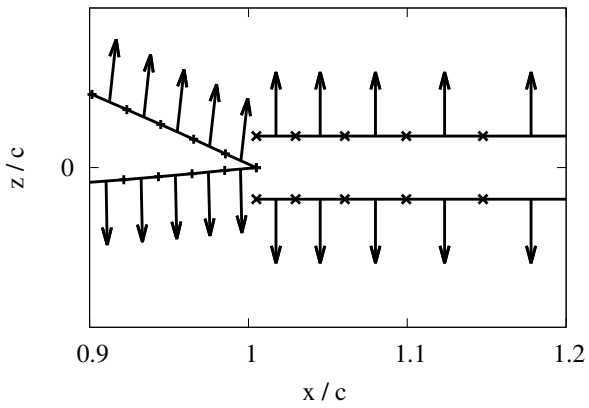

Figure 1: This figure shows the trailing edge region in order to describe the two wake surfaces.

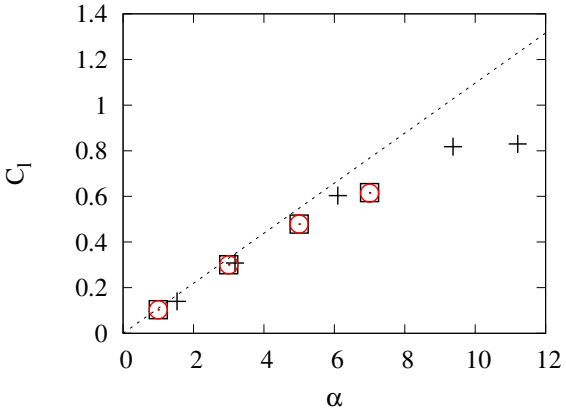

Figure 2: Lift coefficient vs. angle of attack. Thin wing theory (...), Experiments at Re = 170k by Jacobs and Sherman (1937) (+), Velocity decomposition (□), and Large domain RANS (○).

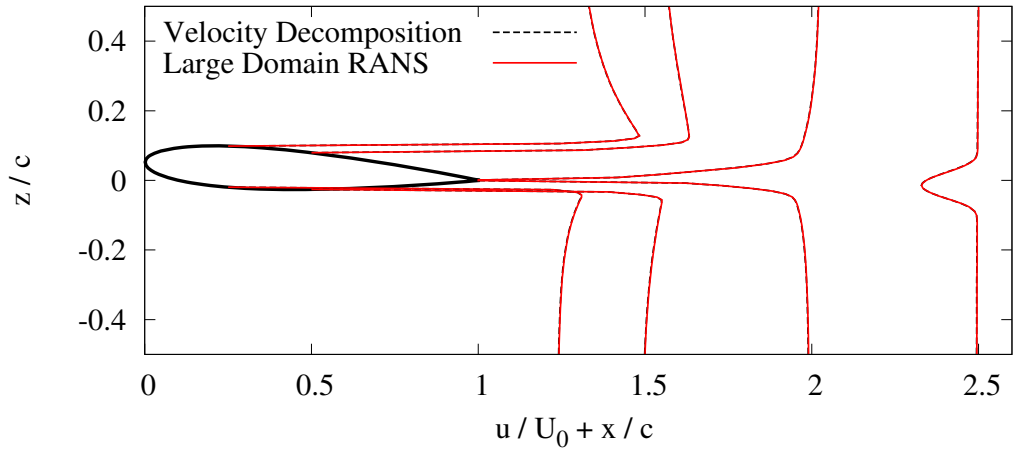

Figure 3: Velocity profiles calculated for a NACA0012 airfoil at 3° angle of attack computed using velocity decomposition, compared to the large domain (RANS) result.

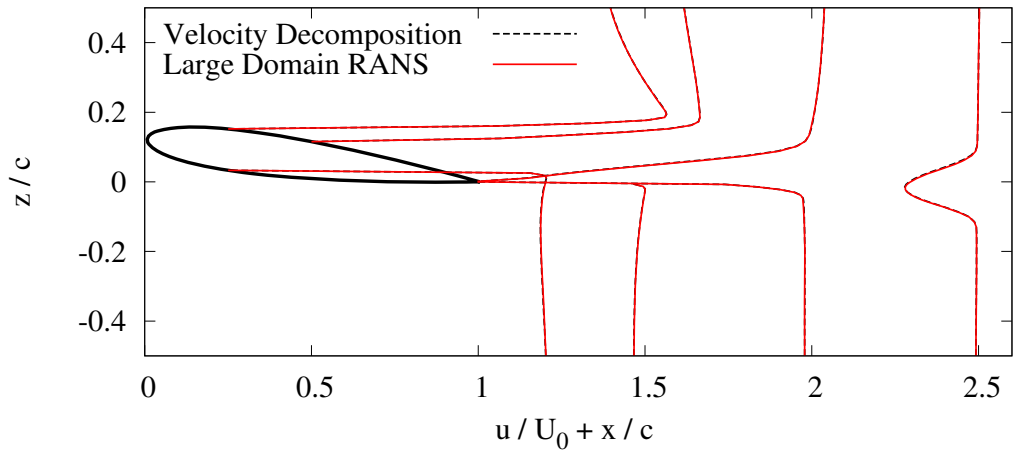

Figure 4: Velocity profiles calculated for a NACA0012 airfoil at 7° angle of attack computed using velocity decomposition, compared to the large domain (RANS) result.

Hydrodynamic impact of three-dimensional bodies on waves.

Y.-M. Scolan[*], **A. A. Korobkin**[**],
[*] ENSTA Bretagne, France, yves-marie.scolan@ensta-bretagne.fr
[**] University of East Anglia, England, a.korobkin@uea.ac.uk

1) Introduction

We consider a simple three-dimensional body entering vertically a liquid surface on which a regular wave propagates. As a simple body, an elliptic paraboloid is chosen. It is defined by two curvature radii at its initial contact point. The Wagner problem is posed in terms of the displacement potential and Galin's theorem is used to provide an analytical solution. Comparisons are done with experimental results.

2) Boundary value problem

The linearized boundary value problem (BVP) is formulated in terms of the displacement potential ϕ

$$\begin{cases} \Delta\phi = \phi_{,xx} + \phi_{,yy} + \phi_{,zz} = 0 & z < 0 \\ \phi = 0 & z = 0,\ (x,y) \in \mathrm{FS}(t) \\ \phi_{,z} = -h(t) + f(x,y) - \eta(y,t) & z = 0,\ (x,y) \in \mathrm{D}(t) \\ \phi \to 0 & (x^2+y^2+z^2) \to \infty, \end{cases} \tag{1}$$

where the regions $\mathrm{FS}(t)$ and $\mathrm{D}(t)$ are disconnected parts of the plane $z = 0$ and correspond to the free surface and the wetted area of the body, respectively. A closed curve, which separates the regions $\mathrm{FS}(t)$ and $\mathrm{D}(t)$, is denoted $\Gamma(t)$ and is referred to as the contact line. The body shape is represented by the equation $z = f(x,y)$, where $f(x,y)$ is a smooth positive shape function, $h(t)$ is the penetration depth of the body into the liquid and $\eta(y,t)$ represents the propagating wave along the y axis as illustrated below

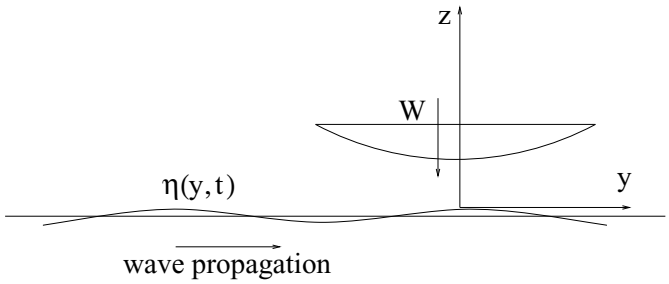

The draft of the elliptic paraboloid is H. Its equation in a local coordinate system (X,Y,Z) attached to the body is

$$f(X,Y) = \frac{X^2}{2R_x} + \frac{Y^2}{2R_y} \tag{2}$$

where (R_x, R_y) are the curvature radii at the initial contact point. The wave is described in a fixed coordinate system attached to earth

$$\eta(y,t) = C\left(\cos(\kappa y - \omega t + \theta) - 1\right) \tag{3}$$

This is an Airy wave of amplitude C propagating along the y axis. By tuning the phase θ, we can manage to get a crest at time $t = 0$ and at the origin $y = 0$. We consider the first instant of penetration and duration of penetration (until separation of the flow at the top of the shape) is much smaller than the period of the wave $T = \frac{2\pi}{\omega}$. The circular frequency ω is related to the wave number κ by using the dispersion relation in infinite depth $\omega^2 = g\kappa$, with $g = 9.81 m/s^2$. We first choose the phase $\theta = 0$ and we expand the shape of the wave for small time and around the origin of the coordinate system, yielding

$$\eta(y,t) = \frac{1}{2R_v}y^2 - \frac{V_\varphi}{R_v}ty + \frac{V_\varphi^2}{2R_v}t^2 + \textit{higher order terms} \tag{4}$$

where $R_v = \frac{1}{C\kappa^2}$ is the curvature radius of the wave and $V_\varphi = \frac{\omega}{\kappa}$ is the phase velocity. The Neumann condition of BVP (1) reduces to

$$\phi_{,z} = -h(t) + \frac{x^2}{2R_x} + \frac{y^2}{2R_y} + \frac{y^2}{2R_v} - \frac{V_\varphi}{R_v} ty + \frac{V_\varphi^2}{2R_v} t^2 \tag{5}$$

The equivalent curvature radius $\tilde{R}_y$ is introduced

$$\tilde{R}_y = \frac{R_v R_y}{R_v + R_y} \tag{6}$$

It is worth noting that new curvature radius might be smaller than R_x, even though the radius R_y is originally greater than R_x. As an example if $R_y = 2m$ and $R_x = 0.75m$, the inequality $\tilde{R}_y < R_x$ holds as soon as $R_v < 1.2m$. We use the following change of variables

$$\tilde{x} = x, \quad \tilde{y} = y - \frac{\tilde{R}_y V_\varphi t}{R_v}, \quad \tilde{h} = h - \frac{1}{2}\frac{V_\varphi^2}{R_v + R_y} t^2 \tag{7}$$

with the help of which the Neumann condition can be arranged as follows

$$\phi_{,z} = -\tilde{h}(t) + \frac{\tilde{x}^2}{2R_x} + \frac{\tilde{y}^2}{2\tilde{R}_y} \tag{8}$$

which is a canonical form in order to apply Galin's theorem as described in Scolan and Korobkin (2012). The boundary problem with the condition (8) is equivalent to the problem of impact of a fictitious elliptic paraboloid onto initially flat free surface without waves. The fictitious paraboloid is different from the original one by the radius of curvature in y-direction and increased vertical displacement of the body. It should be noted that $\tilde{h}(t)$ contains an additional contribution $-\frac{1}{2}\frac{V_\varphi^2}{R_v+R_y} t^2 = -\frac{1}{2} G t^2$ which decreases the vertical acceleration. The dissymmetry of the entry due to the propapating wave appears in the translational motion $\frac{\tilde{R}_y V_\varphi}{R_v} t = vt$.

3) Expansion of the wetted surface

The displacement potential reads

$$\phi(x, y, t) = -\frac{2\tilde{h} b}{3E(e)} \left(1 - \frac{\tilde{x}^2}{a^2} - \frac{\tilde{y}^2}{b^2}\right)^{3/2} \tag{9}$$

where implicitely the wetted surface is elliptic with aspect ratio k and (a, b) are the lengths of its major and minor semi axes respectively. The following identities are useful

$$2\tilde{h}\dot{b} = \dot{\tilde{h}} b, \qquad \frac{\dot{b}}{b} = \frac{\dot{a}}{a} \tag{10}$$

They follow from the application of Galin's theorem and the fact that $\frac{\tilde{R}_y}{R_x}$ is a constant in time. The relations between the sizes of the wetted surface and the data of the problem are the following

$$b = ka = \sqrt{2\tilde{R}_y \tilde{h} \left(2 - k^2 \frac{D}{E}\right)}, \quad a = \sqrt{2R_x \tilde{h} \left(1 + k^2 \frac{D}{E}\right)} = a_o \sqrt{\tilde{h}} \tag{11}$$

where $K(e)$, $E(e)$ and $D(e) = (K(e) - E(e))/e^2$ are the standard Elliptic Integrals. Those are functions of the eccentricity $e = \sqrt{1 - k^2}$ only. The aspect ratio k is given by

$$k_\gamma^2 = \sqrt{\frac{\tilde{R}_y}{R_x}} = k^2 \frac{1 + k^2 D/E}{2 - k^2 D/E} \tag{12}$$

In order to validate these results, we use the experimental data base obtained during the campaign described in Scolan (2012). A regular wave is generated with amplitude $C = 0.048m$ and period $T = 0.98s$. The curvature radius is $R_v = 1.186m$. The corrected curvature radius appearing after asymptotic expansion is $\tilde{R}_y \approx 0.745m$ quite similar to the curvature radius along the x direction which is $R_x \approx 0.75m$. We expect that the wetted surface in expansion is circular. Among the instrumentation used in the set-up, an immersed camera records the expansion of the wetted surface at the sampling frequency $200Hz$. The obtained pictures are shown below for the initial stage of penetration.

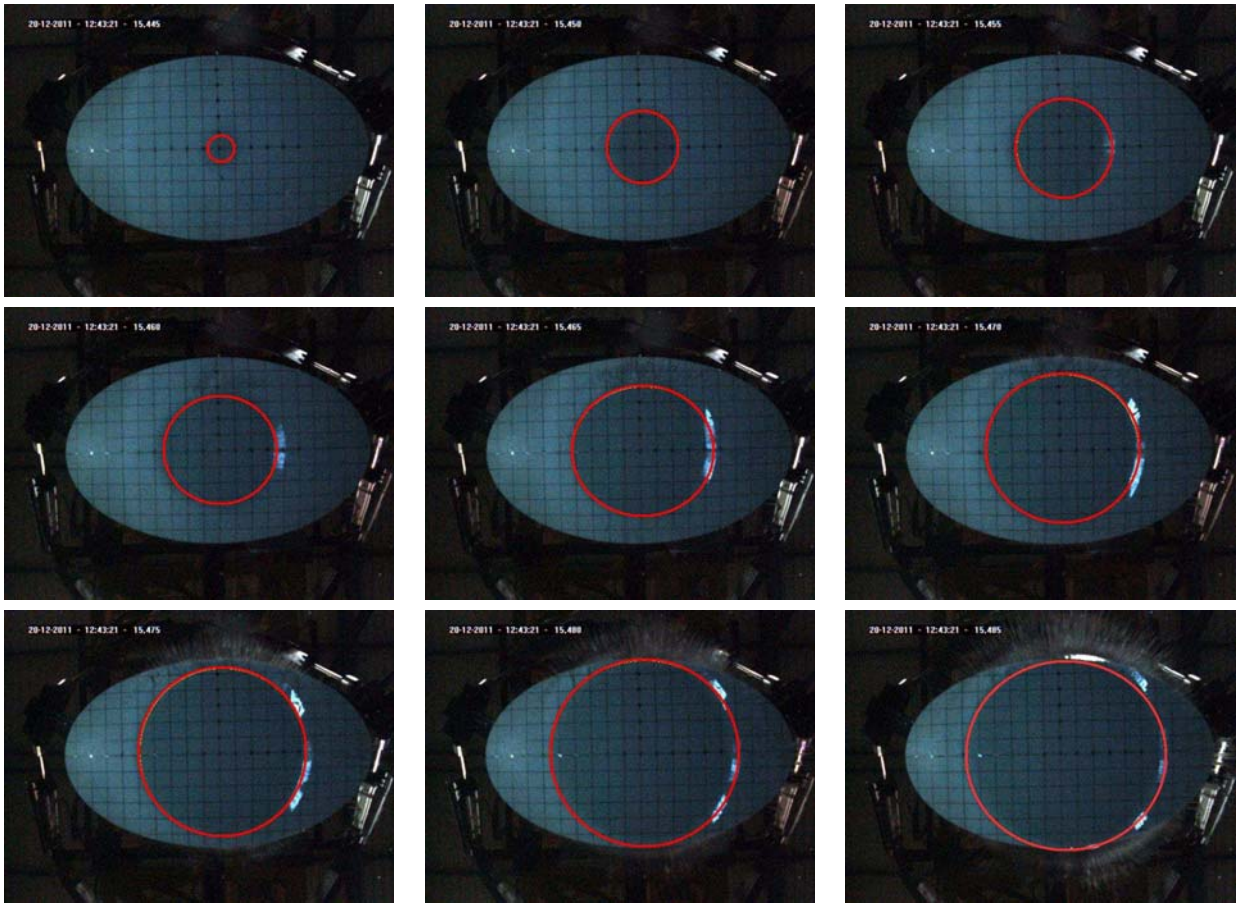

To sum up the results, we compare in the figure below the time variations of the length of the semi axes a and b given by equations (11).

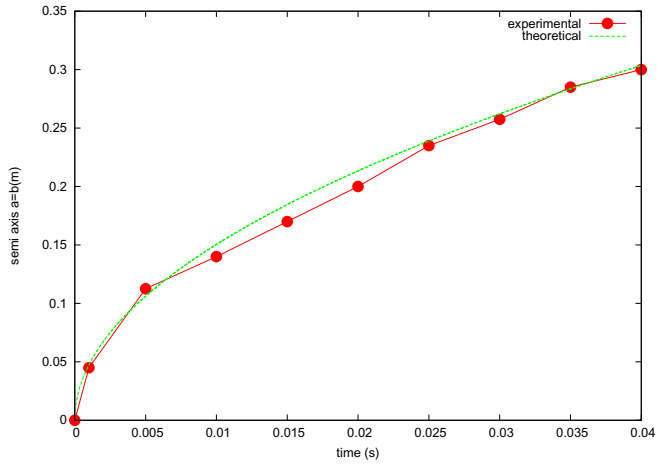

4) Local and global loads

The pressure is calculated from the second derivative in time of the displacement potential.

$$p = -\rho\phi_{,t^2} \tag{13}$$

After some algebra and by using the idendities (10), we arrive at

$$p = \frac{\rho}{E\sqrt{F}}\left(\dot{M}F + \frac{1}{2}M\dot{F}\right) \tag{14}$$

with

$$F = 1 - \frac{x^2}{a^2} - \frac{(y-vt)^2}{b^2}, \qquad M = 2\tilde{h}\left(\dot{b} + \frac{v(y-vt)}{b}\right) \tag{15}$$

The first order force follows from the integration of the pressure on the wetted surface. However the boundary condition on the free surface and the continuity of the displacement potential (and its derivatives) through the contact line, lead to the following expression of the vertical force

$$F_z = -\rho\frac{\mathrm{d}^2}{\mathrm{d}t^2}\int\int_{D(t)}\phi \mathrm{d}x\mathrm{d}y \tag{16}$$

By using (9), it is finally obtained

$$F_z = \frac{4\pi\rho}{15E}k^2 a_o^3 \frac{\mathrm{d}^2}{\mathrm{d}t^2}\left[\tilde{h}^{5/2}\right] \tag{17}$$

The time varitaion of F_z is plotted below.

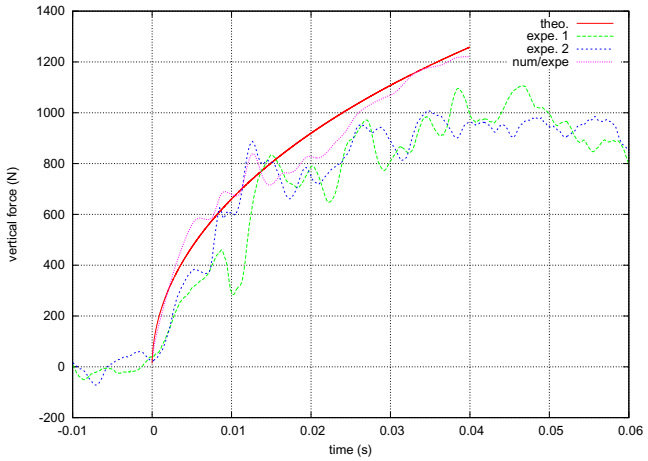

As usual the first order approximation overpredicts the force. If the experimental velocity and acceleration are introduced in the theoretical force formulation, it is observed the influence of the actual kinematics. Before separation occuring at $t \approx 0.04s$, the error is about 20 %. The Modified Logvinovich Model of the pressure must hence be used. Then the numerical integration of MLM pressure reduces the discrepancy.

5) References

1. Wagner, H. 1932 Über Stoss- und Gleitvorgänge an der Oberfläche von Flüssigkeiten. *ZAMM* **12**, pp. 193-215.

2. Scolan Y.-M. & Korobkin A. A., 2012, Hydrodynamic impact (Wagner) problem and Galin's theorem. 27^{th} International Workshop on Water Waves and Floating Bodies, Copenhagen, Denmark.

3. Scolan Y.-M., 2012, Hydrodynamic loads during impact of a three dimensional body with an arbitrary kinematics (in french). Proc. 13^{th} Journées de l'Hydrodynamique, Chatou, France.

COLLISION OF TWO LIQUID WEDGES

Y.A. Semenov[1], G.X. Wu[1], J.M. Oliver[2]

[1] Department of Mechanical Engineering University College London, London WC1E 7JE, UK
[2] Mathematical Institute, 24–29 St. Giles', Oxford OX1 3LB, UK
E-mail: semenov@a-teleport.com, g.wu@ucl.ac.uk, oliver@maths.ox.ac.uk

1. INTRODUCTION

Splashing following the collisions of liquids or granular materials is often observed in a variety of natural and engineering problems, such as plunging or breaking water waves, liquid droplets impacting on a free surface or a thin film of the same liquid, etc. Splashing leads to fluid fragmentation and the generation of drops and spray as well as fluid aeration. These phenomena involve the momentum and energy exchanges processes at the air-liquid interface, evaporation and air entrainment, cavity, bubbles, secondary drops, erosion, noise and sprays. A review of this of kind problem was presented by Yarin [1], which focused on drop impacts on thin liquid layers and dry surfaces. Kiger & Duncan [2] described the mechanism of air-entrainment, and Thoroddsen [3] centred the discussions on the initial stage of drop impact when liquid masses come into contact and coalesce. The current mathematical models may not be able to cover all the problems mentioned above. Nevertheless the formation of the splash jet and its effects on the main flow plays a major role in these phenomena. The present work aims to shed some light along this direction.

Much of the work on splashing jet has mostly been based on experimental observation. Although this has greatly improved our understanding, it is still far from giving a thorough insight into this phenomenon, especially at the initial stage of impacts when physical parameters change rapidly. .

Direct numerical simulations of splashing during droplets impacting on liquid layers were performed by Weiss [4] and Davidson [5] based on velocity potential theory with the boundary integral method and the surface tension was included. Their result showed that a splash jet might be formed, which moved close to the film, leading to the possibility of bubble entrapment. Incompressible Navier-Stokes equations with surface tension were solved numerically by Josserand & Zaleski [6]. The initial stage of a high speed droplet impact on a shallow water layer was investigated by Howison et al. [7] using the method of matched asymptotic expansions, with special attention given to the splash jet mechanics. A numerical investigation of splashing and wave breaking processes using the SPH method was performed by Landrini et al. [8]. Their numerical results reflected the experimental observations of breaking waves.

In this study, we investigate impact between two liquid wedges of the same density. It is assumed that the liquid is inviscid and incompressible, the flow is irrotational. When gravity and surface tension forces are neglected, the flow is self-similar. Such a formulation with fully nonlinear boundary conditions may be applicable to two sharp cornered wave crests colliding with each other at initial stage, and to other similar problems. The integral hodograph method [9, 10] is employed to derive analytical expressions for the complex-velocity potential, the complex-conjugate velocity, and the mapping function the physical plan and a parameter plan. The problem is reduced to a system of integro-differential equations in terms of the velocity magnitude and the velocity angle with the tangential direction of the liquid boundary. The results are presented as streamline patterns and the pressure distributions along the symmetry line of the wedge and near the root of the splash jet. It is found that the secondary impact could exist especially if the difference between the wedge angles is sufficiently large. The implications of such events are discussed.

2. THEORETICAL ANALYSIS AND NUMERICAL RSULTS

Two liquid wedges of half-angles α_+ and α_- move in the opposite directions with velocity V_O and V_D, respectively, and their apexes meet at point A right before the impact at time $t = 0$, where the origin of the Cartesian coordinate system xy is chosen. Dynamically, the problem depends on only the relative velocity $V_O + V_D$. Here we consider the case in which

we fix V_O and adjust V_D to ensure that A is the stagnation point. A sketch of the problem and the definitions of the geometric parameters are shown in figure 1*a*. The liquid wedges are assumed to be symmetric about the $y-$axis. For time $t>0$, a splash jet with the tip at point C appears, which is assumed to have evolved form A.

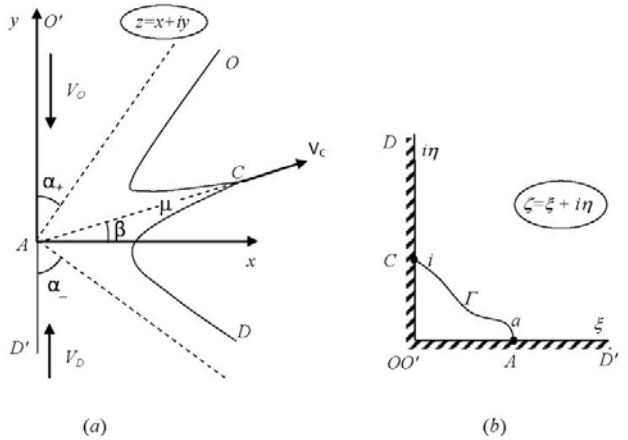

Figure 1. Sketch of the collision of two liquid wedges: (*a*) the stationary plane; (*b*) the parameter plane.

For a constant impact velocity of each liquid wedge, the time-dependent problem in the physical plane can be written in the stationary plane in terms of the self-similar variables $x=X/(V_O t)$, $y=Y/(V_O t)$. The complex velocity potential $W(Z,t)=\Phi(X,Y,t)+i\Psi(X,Y,t)$ for self-similar flows is written in the form

$$W(Z,t)=V_O^2 t w(z). \tag{1}$$

The problem is to determine the function $w(z)$ which conformally maps the stationary plane z onto the complex-velocity potential region w. We choose the first quadrant of the $\zeta-$plane as the parameter region to derive expressions for the nondimensional complex velocity, dw/dz, and for the derivative of the complex potential, $dw/d\zeta$, both as functions of the variable ζ. Once these functions are found, the velocity field and the mapping function $z=z(\zeta)$ can be determined [9].

Conformal mapping allows us to fix three arbitrary points in the parameter region, which are O, C, and D as shown in figure 1*b*. In this plane, the interval of the imaginary axis ($0<\eta<1, \xi=0$) corresponds to the free surface OC, and the interval ($1<\eta<\infty, \xi=0$) corresponds to the free surface CD. The positive real axis ($0<\xi<\infty, \eta=0$) corresponds to the symmetry line $O'D'$. The point $\zeta=a$ is the image of the stagnation point A in the stationary plane z. The parameter a is unknown and is to be determined as part of the solution.

The boundary-value problems for the complex-velocity function, dw/dz, and for the derivative of the complex potential, $dw/d\zeta$, can be formulated in the parameter plane. Then, applying the integral formulae determining an analytical function from its modulus and argument, and from its argument on the boundary of the first quadrant [9, 10], respectively, we obtain the following expression for the complex velocity and for the derivative of the complex potential:

$$\frac{dw}{dz}=v_0\left(\frac{\zeta-a}{\zeta+a}\right)\exp\left[-\frac{i}{\pi}\int_0^\infty \frac{d\ln v}{d\eta}\ln\left(\frac{i\eta-\zeta}{i\eta+\zeta}\right)d\eta+i\frac{\pi}{2}\right], \tag{2}$$

$$\frac{dw}{d\zeta}=K\zeta^{-1-2\alpha_+/\pi}\frac{\zeta^2-a^2}{(\zeta^2+1)^{1-\mu/\pi}}\exp\left[\frac{1}{\pi}\int_0^\infty \frac{d\lambda}{d\eta}\ln(\zeta^2+\eta^2)d\eta\right], \tag{3}$$

where K is a real scale factor, $v_0=v(0)=1$ is the nondimensionalized magnitude of the velocity at point O, $\lambda(\eta)=\theta(\eta)-\Delta_i$ is a continuous function in which $\theta(\eta)$ is the angle between the tangential direction of the free surface and the velocity vector on the free surface, and Δ_i are the jumps of the function $\theta(\eta)$ caused by corners of the flow boundary in the similarity plane.

Dividing Eq. (3) by Eq. (2), we can obtain the derivative of the mapping function

$$\frac{dz}{d\zeta}=\frac{dw}{d\zeta}\Big/\frac{dw}{dz} \tag{4}$$

whose integration along the imaginary axis in the parameter region provides the free boundaries OC and CD in the $z-$plane.

The parameters a and K are determined from the following physical consideration that the tip of the splash jet, point C, is evolved from point A at which the origin of the coordinate system ($Z=0$) is chosen. Denoting the coordinate of point C, $Z=Z_C$, the magnitude of the velocity V_C and the angle β with the $x-$axis, we can write the following equation in the similarity plane

$$z_C=v_C e^{i\beta}, \tag{5}$$

where $v_C = V_C / V_O = v(\eta)_{\eta=1}$, $\beta = -\arg(dw/dz)_{\zeta=i}$. $z_C = Z_C / (V_O t)$ can be obtained by integration of the mapping function (4) from point A to point C along an arbitrary contour Γ in the parameter region shown in figure 1*b*. This equation makes it possible to determine the parameters K and a , while the functions $v(\eta)$ and $\lambda(\eta)$ are determined from dynamic and kinematic boundary conditions which for the self-similar flow take the form [9]:

$$\frac{d\lambda}{d\eta} = \frac{v + s\cos\theta}{s\sin\theta}\frac{d\ln v}{d\eta}, \tag{6}$$

$$\frac{1}{\tan\theta}\frac{d\ln v}{d\eta} = \frac{d}{d\eta}\left[\arg\left(\frac{dw}{dz}\right)\right], \tag{7}$$

where $s = S/(V_O t)$ and $s = s(\eta)$ is the spatial length coordinate along the free surface in the similarity plane obtaining by integration of $ds/d\eta = \left|dz/d\zeta\right|_{\zeta=i\eta}$ with using Eq.(4).

By choosing in the Bernoulli equation the location of the reference point at the stagnation point A , putting there $S = 0$ and $W(Z_A, t) = 0$, and taking advantage of the self-similarity of the flow, we can determine the pressure at any point of the liquid region

$$c_p^* = \frac{2(P - P_A)}{\rho V_O^2} = \mathrm{Re}\left(-2w + 2z\frac{dw}{dz}\right) - \left|\frac{dw}{dz}\right|^2. \tag{8}$$

The method of successive approximations is used for solving the system of integro-differential equations.

In figure 2, streamline patterns are shown for an upper liquid wedge of $\alpha_+ = 10^\circ$ and different angles α_- of the lower liquid wedge. Here, the pressure coefficient along the line of symmetry $x = 0$ and the "zero" streamline passing through point A are also shown by dashed and dot-dashed lines, respectively. For the case shown in figure 2*a* the symmetry of the flow about the x axis, is clearly seen. The obtained value of the tip angle μ at point C shown in figure 1*a* for two identical wedges is $\mu = 9.47^\circ$ which is close to the value $\mu = 9.50^\circ$ obtained by Semenov & Wu [11] as the double contact angle for a liquid wedge impacting a solid wall.

The streamline patterns for an upper liquid wedge of $\alpha_+ = 10^\circ$ colliding with a lower wedge of $\alpha_- = 30^\circ, 70^\circ, 90^\circ$ respectively, are shown in figures 3*b* – 3*d*, respectively. For the case $\alpha_- = 30^\circ$, it can be seen that the splash jet is directed into the half-plane of the liquid wedge of smaller angle due to the larger momentum of the liquid wedge of larger angle.

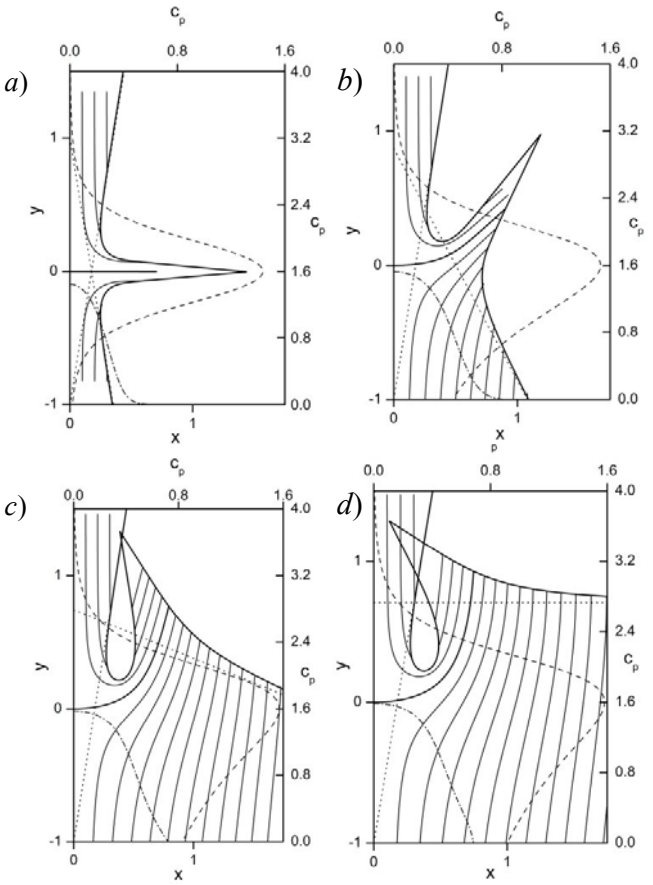

Figure 2. Streamline patterns (solid lines) and the pressure distribution along the $y-$axis (dashed line) and along the "zero" streamline starting at the origin (dot-dashed lines) for $\alpha_+ = 10^\circ$ and (*a*) $\alpha_- = 10^\circ$, (*b*) 30°, (*c*) 70° and (d) 90°. Here, $c_p = c_p^* - c_{pO}^*$, where c_{pO}^* is the pressure coefficient at point O or at any point on the free surface.

The dotted lines show the free surfaces of the undisturbed wedges at the same time point. It is seen that at some distance from the origin the dotted lines coincide with the free surfaces of the impacting liquid wedges. This distance corresponds to the region affected by the impact between the wedges. The $y-$ coordinate of the tip of the undisturbed upper wedge is its incoming velocity which is obviously $v_O = -y = 1$. Similar the y - coordinate of the tip of the lower wedge

is its incoming velocity. These figures show $v_D = y \le 1$ in these four cases.

The streamline pattern for $\alpha_- = 70°$ in figure 2*c* shows that the splash jet moves into the free surface of the upper liquid wedge forming a cavity. At the same time, the velocity direction of the liquid in the splash jet, which can be seen as the streamline slope, is almost parallel to the undisturbed free surface of the upper wedge. This secondary impact is not included in the present model and therefore the result does not fully reflect the real physics. Another issue is about the closed cavity. For the similarity solution to hold, the pressure of the trapped air inside the cavity has to be constant in the similarity coordinate system when the size of the cavity expands in the physical system. This is of course hardly the case in the real flow. From a mathematical point of view, the splash jet moves into the second sheet of the Riemann surface without interaction with the main flow.

The streamline pattern for $\alpha_- = 90°$ corresponding to a flat free surface is shown in figure 2*d*. The splash jet has moved further into the upper liquid wedge. In physical reality, the overlapping may lead to a bigger secondary impact between the splash jet and the wedge than in figure 2*c*. This could produce subsequent impacts and new splash jets. Such multi-impact processes with the formation of multiple cavities could produce a liquid/air mixture, liquid aeration, and the transformation of the splash jet into a spray, although it is speculative rather than conclusive at this stage. Similar situations occur for plunging breaking waves reviewed by Kiger & Duncan [2], in which the splash jet formed as a result of an impact between the wave crest and the free surface may be observed clearly in the case of oblique impacts or in the form of an air/liquid mixture in the case of nearly vertical impacts like a waterfall.

The numerical solutions are compared with asymptotic predictions based on the extended Wagner's theory in the small deadrise angle limit in which the half angle of both liquid wedges is close to $\pi/2$. In particular comparisons are made for the locations of the turning points (near the root of the splash jet); the splash jet thickness and length; and the pressure distribution on the line of symmetry of the wedge. The details will be presented in the workshop.

The first two authors gratefully acknowledge the Lloyd's Register Educational Trust (The LRET) for the support through the joint centre involving University College London, Shanghai Jiao Tong University and Harbin Engineering University. The LRET is an independent charity working to achieve advances in transportation, science, engineering and technology education, training and research worldwide for the benefit of all.

REFERENCES

1. Yarin, A.L. (2006) Drop Impact Dynamics: Splashing, Spreading, Receding, Bouncing. . . *Annu. Rev. Fluid Mech,*. **38**, p. 159 – 192.
2. Kiger, K.T. and Duncan, J.H. (2012) Air-Entrainment Mechanisms in Plunging Jets and Breaking Waves. *Annu. Rev. Fluid Mech.,* **44**, p. 563 – 596.
3. Thoroddsen, S.T., Etoh, T.G. and Takehara, K. (2008) High-Speed Imaging of Drops and Bubbles. *Annu. Rev. Fluid Mech.,* **40**, p. 257 – 285.
4. Weiss, D.A. and Yarin, A.L. (1999) Single drop impact onto liquid films: neck distortion, jetting, tiny bubble entrainment, and crown formation. *J. Fluid Mech.,* **385**, p. 229 – 254.
5. Davidson, M.R. (2002) Spreading of an inviscid drop impacting on a liquid film. *Chem. Eng. Sci.,* **57**, p. 3639 – 3647.
6. Josserand, C. and Zaleski, S. (2003) Droplet splashing on a thin liquid film. *Physics of Fluids,* **15**(6), p. 1650 – 1657.
7. Howison, S.D., Ockendon, J.R., Oliver, J.M., Purvis, R. and Smith, F.T. (2005) Droplet impact on a thin fluid layer. *J. Fluid Mech.,* **542**, p. 1 – 23.
8. Landrini, M., Colagrossi, A., Greco M., Tulin M.P. (2007). Gridless simulations of splashing processes and nearshore bore propagation. *J. Fluid Mech.,* **591**, p. 183 – 213.
9. Semenov, Y.A. and Iafrati, A. (2006) On the nonlinear water entry problem of asymmetric wedges. J. Fluid Mech., **547** , p. 231 – 256.
10. Semenov, Y.A. and Cummings, L.J. (2006) Free boundary Darcy flows with surface tension: analytical and numerical study. *Euro. J. Appl. Math*., **17**, p. 607 –631.
11. Semenov, Y.A. and Wu, G.X. (2013) Asymmetric impact between liquid and solid wedges. *Proc. R. Soc. A.* **469,** 2150 20120203; doi:10.1098/ rspa.2012.0203

Simplified Formulation for Parametric Roll in Regular and Irregular Waves

Kang-Hyen Song[(1)], **Yonghwan Kim**[(2)], **Dong-Min Park**[(3)]
Department of Naval Architecture and Ocean Engineering, Seoul National University
1, Gwanak-ro, Gwanak-gu, Seoul, Korea ([(1)] Currently in Korean Register of Shipping)
[(1)] khsong@krs.co.kr, [(2)] yhwankim@snu.ac.kr, [(3)] foster@snu.ac.kr

1. INTRODUCTION

The primary difficulty in quantifying parametric roll is that this phenomenon is a non-ergodic process. If the process is not ergodic, a large number of realizations are necessary to get a stable probability density function. Considering many sea states in wave scatter diagram, the total number of realizations to get a stable long-term prediction significantly increases. Therefore, very fast and effective numerical tool is needed for quantitative analysis under some simplification of real physics.

In most previous studies, the analytic or semi-analytic formulations have been developed to predict the occurrence of parametric roll. Particularly the formulations were based on 1-DOF Mathieu equation (e.g. Pauling, 1959) or approximated GZ variation with known pitch and/or heave-pitch motions. These studies were normally for regular excitation and they were limited to occurrence prediction, not suitable for quantitative analysis of nonlinear roll motion. Recently a few time-domain approaches such as panel, CFD, or impulse-response-function methods have been used to simulate nonlinear roll motions in regular and irregular waves. These can be used for quantitative analysis in irregular seaways, but a significant amount of computational effort is essential.

In this study, it is aimed to develop new formulae which are applicable to the quantitative analysis of parameters in irregular ways but heavy computation is not necessary. The primary idea of the study is to approximate the change of GM by using Fourier components and consider the first two components i.e. the mean and the first components, in the equation of roll motion. According to our study, the change of metacentre height GM, the main source of parametric roll, can be reasonably approximated as a linear system which is dictated by Gaussian distribution. In this study, new formulae are proposed for GZ variation and the equation of motion in regular and irregular waves.

2. APPROXIMATION OF GZ & GM

2.1 GZ Approximation

Let's consider the equation of motion s.t.

$$(I_{44}+A_{44})\ddot{\phi}+\delta_1\dot{\phi}+\delta_2\dot{\phi}\left|\dot{\phi}\right|+\Delta\cdot GZ(z,\phi,\theta)=0 \tag{1}$$

where $\Delta\cdot GZ(z,\phi,\theta)$ indicates the restoring term which is due to ship displacement Δ and nonlinear restoring arm $GZ(z,\phi,\theta)$. Belenky(2010) and Umeda(2010) proposed the approximated formulae of $GZ(z,\phi,\theta)$ as follows:

$$GZ(\phi,t)=\frac{GM(t)}{GM_{still}}GZ_{still}(\phi)\ \text{(Belenky)},\quad GZ(\phi,t)=(GM_{still}+GM_0)\cdot\phi+\{GM_1\cdot\cos(\omega t)\}\cdot\left\{1-\left(\frac{\phi}{\pi}\right)^2\right\}\cdot\phi\ \text{(Umeda)} \tag{2}$$

In this study, based on computational observation, $GZ(z,\phi,\theta)$ is approximated as follows:

$$GZ(\phi,t)=GZ_{still}(\phi)+\{GM(t)-GM_{still}\}\{\sin(\phi)-\sin^3(\phi)/\sin^2(\phi_{\max})\} \tag{3}$$

where subscript '*still*' indicates the values at still water. Fig.1 shows the GM variations for 65,000 and 8,000 TEU containerships when wave length and ship length are the same. Three approximated formulae are compared with the GZ variation obtained from direct computation. Better agreement of Eq.(3) is obvious.

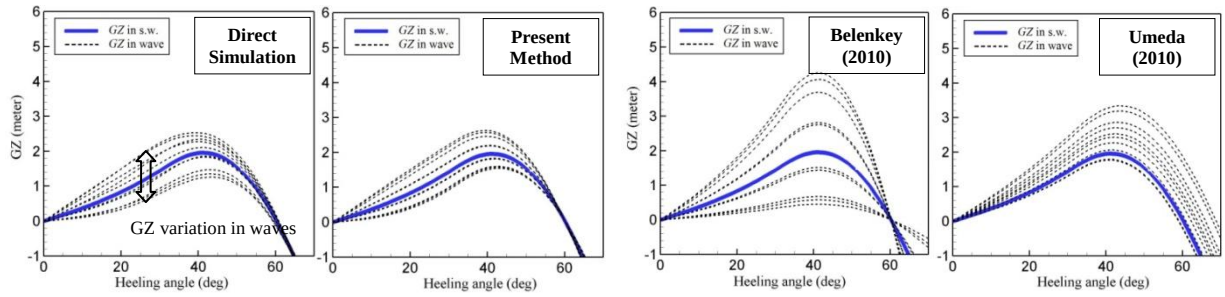

(a) 6,500 TEU containership

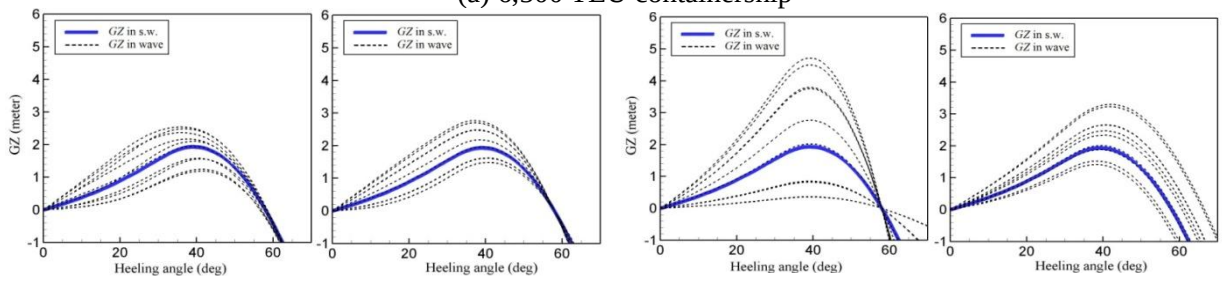

(a) 8,000 TEU containership

Fig.1 Comparison of GZ between direct computation and three approximated formulae for two containerships: $kA_w=0.1$, $\lambda = L$

Eq.(3) is nonlinear and GM is dependent on instantaneous displacement of ship motion. In the physical phenomenon of parametric roll, GM variation is a key mechanism. Therefore more simplification of Eq.(3) can be achieved when GM is properly approximated. In this study, GM is represented as a Fourier series.

$$GM(t) = GM_{still} + GM_f(t) = GM_{still} + GM_0 + \sum_{n=1}^{\infty} GM_n \cos(n\omega t + \alpha_n) \tag{4}$$

where GM_0 is the mean of *GM* and GM_n is the *n*-th component of Fourier component. According to our study, the followings are found:

(i) GM_0 is always positive.

(ii) The crests of GM_1 occurs every *1/n-th* of effective length.

(iii) GM_2 is too small to generate parametric roll.

Fig.2 shows GM_n of four commercial ships when $kA_w=0.1$ where A_w is wave amplitude. The three findings described above are clearly shown in these figures.

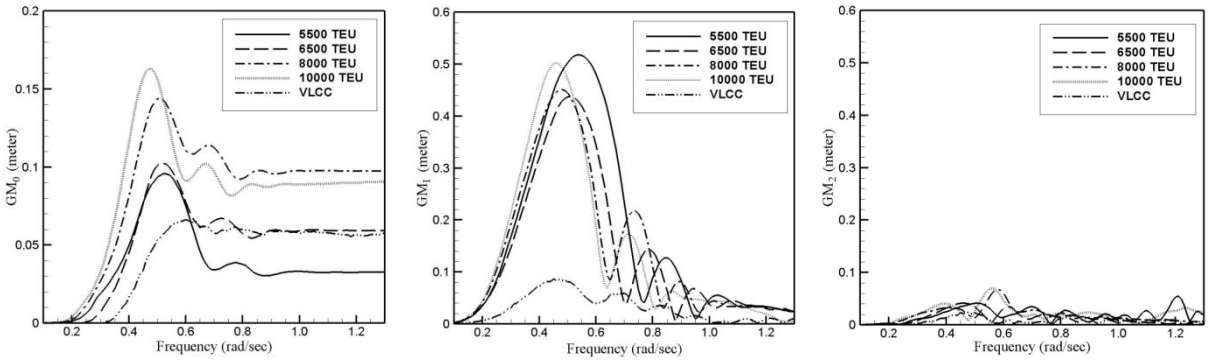

(a) GM_0 (b) GM_1 (c) GM_2

Fig.2 GM_n normalized with respect to wave amplitude: four commercial ships: $kA_w=0.1$

Fig.3 shows GM_0 and GM_1 for different wave amplitude. In this study, it is assumed that GM_0 and GM_1 are linearly varied with respect to wave amplitude. Particularly, as Fig.3 shows, this approximation is very reasonable for GM_1. In the case of GM_0, the linear variation seems to have some error. However, a linear approximation can provide the dominant component of GM_0. The linear

approximation of GM_n (n=0,1) is important particularly since the concept of response-amplitude-operator (RAO) is applicable for these components, i.e.

$$RAO \quad \text{of} \quad GM_n = \frac{GM_n}{A_w} \quad . \tag{5}$$

When this is the case, the following GM approximation can be proposed:

$$GM(t) = GM_{still} + a \cdot RAO_{GM_0}(\omega) + a \cdot RAO_{GM_1}(\omega) \cdot \cos(\omega t + \alpha) \quad \text{for regular waves} \tag{6}$$

$$GM(t) = GM_{still} + GM_0(Hs, Tz) + \sum A_{w,i} \cdot RAO_{GM_1}(\omega_i) \cdot \cos(\omega_i t + \alpha_i) \quad \text{for irregular waves} \tag{7}$$

$RAO_{GM_1}(\omega_i)$ indicates the RAO of GM_1, and

$$GM_0(Hs, Tz) = \sqrt{\int S(\omega) RAO_{GM_0}{}^2(\omega) d\omega} \, . \tag{8}$$

It should be mentioned that Eq.(8) is valid when Gaussian distribution is valid for GM_0.

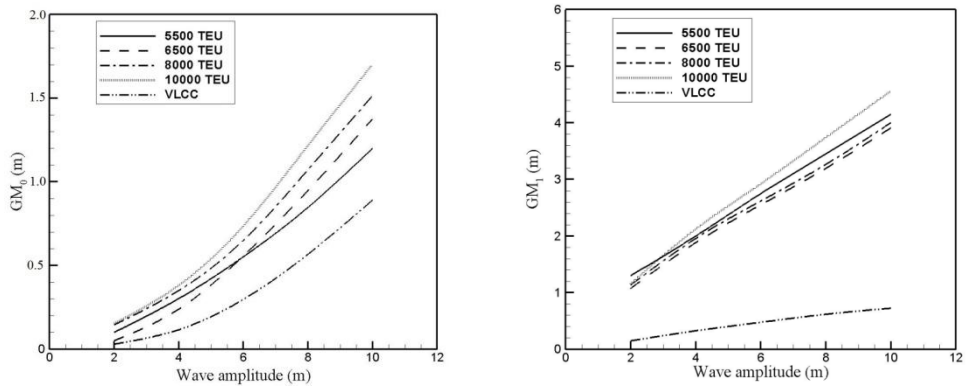

(a) GM_0 (b) GM_1

Fig.3 GM_0 and GM_1 for different wave amplitude: four commercial ships

Fig.4 shows the spectra of GM_1 of three large containerships which are under heave-pitch-roll motions in irregular wave conditions. The spectra of GM_1 are compared between direct numerical simulation and the approximated GM_1 by using Eq.(7). The overall agreement is very acceptable, proving the present approximation is quite reasonable.

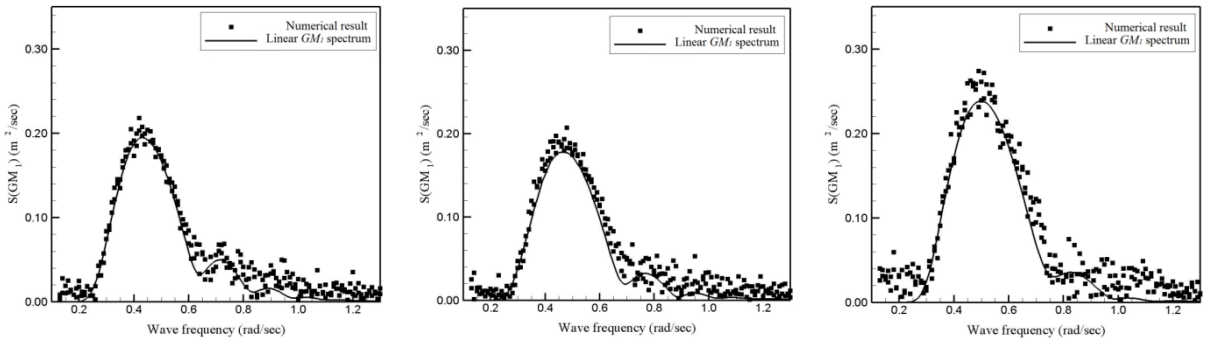

(a) 5,5000 TEU (b) 6,500 TEU (c) 8,000 TEU

Fig.4 Comparison of GM_1 spectra in irregular wave condition between direct computation and present approximation for three containerships: $Hs = 6m$, $\lambda_{modal} / L = 1.0$

3. APPROXIMATED ROLL EQUATION FOR PARAMETRIC ROLL

Adopting the approximated GZ and GM, the following formulae are proposed for parametric roll in

regular and irregular waves:

$$(I_{44}+A_{44})\ddot{\phi}+\delta_1\dot{\phi}+\delta_2\dot{\phi}|\dot{\phi}|+\Delta\cdot[GZ_{still}(\phi)+A_w\cdot\{RAO_{GM_0}(\omega) + RAO_{GM_1}(\omega)\cdot\cos(\omega t+\alpha)\}\cdot\{\sin(\phi)-\sin^3(\phi)/\sin^2(\phi_{\max})\}]=0 \quad \text{for regular waves} \tag{9}$$

$$(I_{44}+A_{44})\ddot{\phi}+\delta_1\dot{\phi}+\delta_2\dot{\phi}|\dot{\phi}|+\Delta\cdot[GZ_{still}(\phi)+\{GM_0(Hs,Tz) + \sum A_{w,i}\cdot RAO_{GM_1}(\omega_i)\cdot\cos(\omega_i t+\alpha_i)\}\cdot\{\sin(\phi)-\sin^3(\phi)/\sin^2(\phi_{\max})\}]=0 \quad \text{for irregular waves} \tag{10}$$

These equations are much more practical than formulae based on Mathieu equation, since these are applicable for quantitative analysis of parameter roll, particularly including in irregular waves. In the case of Mathieu-equation-based formulae, those are not appropriate for quantitative analysis and valid for only for regular waves. Furthermore, Eqs.(9) and (10) are much more efficient compared with direct simulation programs with compatible solution accuracy.

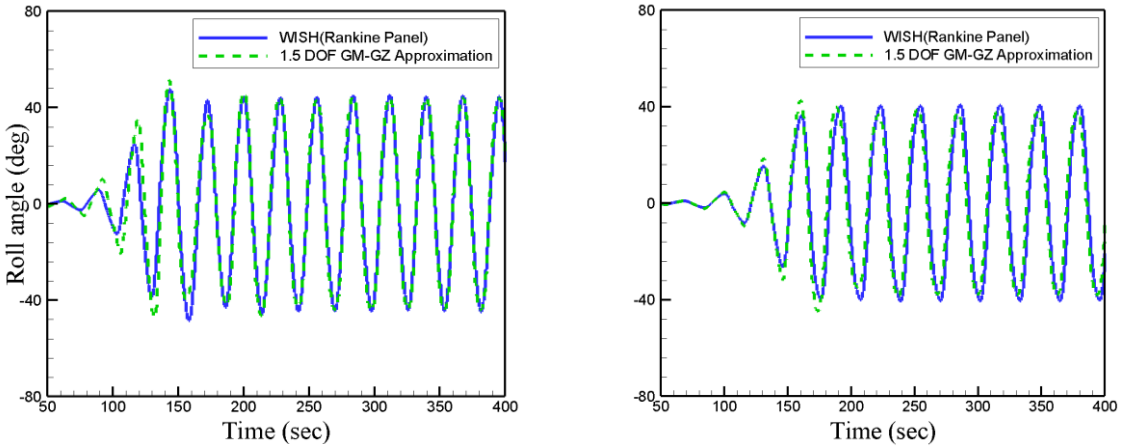

(a) $\lambda/L=0.8$ (b) $\lambda/L=1.0$

Fig.5 Comparison of roll motion between 3D panel method and present approximation: 6,500 TEU containership: $kA_w=0.1$

Fig.5 shows the comparison of roll motion in two regular wave cases between WISH, a 3D panel method program, and the present approximation, i.e. Eq.(9). The agreement between two solutions is excellent.

References

Belenky V.L., 2003, "Prababilistic analysis of roll parametric resonance in head seas", Proc. 8th International Conference on the Stability of Ships and Ocean Vehicles, Madrid

Dunwoody, A.B., 1989, "Roll of a ship in astern Seas – Metacentric height spectra," Journal of Ship Research, Vol 33, No 3, pp 221-228

Gabriele Bulian, 2006, "Theoretical, numerical and experimental study on the problem of ergodicity and 'practical ergodicity' with an application to parametric roll", Ocean Engineering 33, , pp. 1007-1043

IMO SLF 52/INF.2 and 52/WP.1, 2010, "Development of New Generation Intact Stability Criteria", IMO document, London.

Kim, Y., 2011, "Time-domain analysis of nonlinear motion responses and structural loads on ships and offshore structures: development of WISH programs", International Journal of Naval Architecture and Ocean Engineering, Vol 3, No1, pp 37-52.

Pauling, JR. & Rosenberg, RM. On Unstable Ship motions Resulting from Nonlinear Coupling, Journal of Ship Research 1959, 3, 36-46.

Spanos, D., 2007, "Numerical simulation of parametric roll in head seas," International Shipbuilding Progress 54, pp 249-267

Vidic-Perunovic, 2011, "Influence of the GZ calculation method on parametric roll prediction", Ocean Engineering 38, pp. 295-303.

WAVE FORCES ON OSCILLATING HORIZONTAL CYLINDER SUBMERGED UNDER NON-HOMOGENEOUS SURFACE

I.V. Sturova

Lavrentyev Institute of Hydrodynamics of SB RAS
pr. Lavrentyeva 15, Novosibirsk, 630090, RUSSIA
E-mail: sturova@hydro.nsc.ru

1. Introduction

In a linear treatment, the problem of oscillations of a submerged body under a free surface and the resulting hydrodynamic loads have been thoroughly studied. A wide range of mathematical techniques was given by Linton & McIver (2001) for the solution of problems involving the interaction of waves with structure. Extensive bibliographical notes were made in this book. However, to the author's knowledge, there is no study on wave structure interaction problems in fluid having mixed boundary conditions on the upper surface.

In this paper, the linear 2-D water-wave problem describing small oscillations of a horizontal cylinder is considered. The surface of an ideal and incompressible fluid of finite depth is partly covered by a semi-infinite thin elastic plate with a free edge. The solution is written as a distribution of mass sources over the surface of the cylinder and an integral equation is applied for the unknown source strength. Appropriate Green's function is introduced using the method of matched eigenfunction expansions in much the same manner as in paper by Sahoo *et al.* (2001). Generation of flexural gravity waves by a submerged cylinder under infinite elastic plate was considered by Sturova (2011).

2. Statement of the problem

Let a Cartesian coordinate system be taken with the x-axis directed along the undisturbed upper boundary of the fluid perpendicular to the cylinder axis, and the y-axis pointing vertically upwards. The fluid is assumed to be inviscid and incompressible; its motion is irrotational. A semi-infinite elastic plate floats on the surface of the fluid (Figure 1). The surface of the fluid that is not covered with the plate is free. The plate draft is ignored. The fluid depth is equal to H. The wave motions are generated in the fluid by the small oscillations of submerged rigid body with wetted surface S at a frequency ω with amplitudes ζ_j $(j = 1, 2, 3)$ for the sway, heave and roll problems, respectively.

Under the usual assumptions of linear theory, the time-dependent velocity potential can be written as

$$\Phi(x, y, t) = \Re\Big[i\omega \sum_{j=1}^{3} \zeta_j \varphi_j(x, y) \exp(i\omega t)\Big],$$

where $\varphi_j(x, y)$ are complex valued functions and t is time. The radiation potentials $\varphi_j(x, y)$ satisfy the Laplace equation in the fluid domain

$$\nabla^2 \varphi_j = 0 \quad (-\infty < x < \infty,\ -H < y < 0) \quad (1)$$

except in the region occupied by the cylinder.

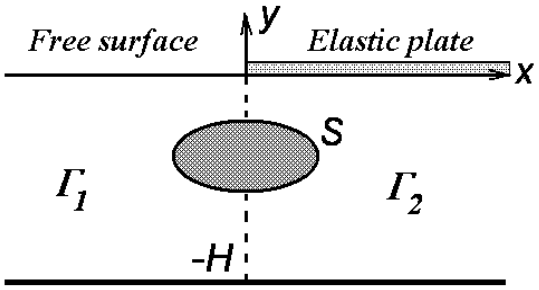

Figure 1: Schematic diagram.

The free surface condition in the open water region is given by

$$g\partial\varphi_j/\partial y - \omega^2 \varphi_j = 0 \quad (-\infty < x < 0,\ y = 0), \quad (2)$$

where g is the acceleration due to gravity. It is assumed that the plate is a thin homogeneous elastic material with uniform mass density ρ_s and thickness d. The plate is in contact with the water at all points for all time. On the elastic covered surface, the radiation potentials $\varphi_j(x, y)$ satisfy the boundary condition in the form

$$\left(D\frac{\partial^4}{\partial x^4} - \omega^2 M + g\rho\right)\frac{\partial \varphi_j}{\partial y} - \rho\omega^2 \varphi_j = 0 \quad (3)$$

$$(0 < x < \infty,\ y = 0),$$

where $D = Ed^3/[12(1 - \nu^2)]$, $M = \rho_s d$, E is the Young's modulus for the elastic plate, ν is its Poisson's ratio, ρ is the fluid density. At the plate

edge, free edge boundary conditions require vanishing bending moment and shear force:

$$\frac{\partial^3\phi_j}{\partial x^2\partial y} = \frac{\partial^4\phi_j}{\partial x^3\partial y} = 0 \quad (x = 0+,\ y = 0). \qquad (4)$$

The boundary condition on the closed smooth contour of the submerged body S has the form:

$$\partial\varphi_j/\partial n = n_j \quad (x, y \in S). \qquad (5)$$

Here, $\mathbf{n} = (n_x, n_y)$ is the inward normal to the contour S. The notations

$$n_1 = n_x, \quad n_2 = n_y, \quad n_3 = (y-y_0)n_1 - (x-x_0)n_2$$

are used where $x_0,\ y_0$ are the coordinates of the center of the roll oscillations.

The boundary condition at the bottom is

$$\partial\varphi_j/\partial y = 0 \quad (-\infty < x < \infty,\ y = -H). \qquad (6)$$

In the far field a radiation condition should be imposed that requires the radiated waves to be outgoing.

3. Method of solution

In order to solve the boundary-value problem (1)-(6), we introduce an unknown mass-source distribution $\sigma_j(x, y)$ over the contour S. We can now represent the radiation potentials at any point of the fluid in the form

$$\varphi_j(x, y) = \int_S \sigma_j(\xi, \eta) G(x, y; \xi, \eta) ds. \qquad (7)$$

Here, $G(x, y; \xi, \eta)$ is the Green function of the problem, which determines the velocity potential initiated by an oscillating mass source with unit strength, where (x, y) is the field point and (ξ, η) is the source point. The Green function must satisfy the following equation

$$\nabla^2 G = 2\pi\delta(x-\xi)\delta(y-\eta)$$

with the boundary conditions analogous to (2)-(4), (6) and the radiation condition in the far field, and δ is the Dirac delta-function.

In order to obtain the solution for the Green function, the eigenfunction expansion-matching method is employed. The fluid domain is divided into two regions: the downstream open region Γ_1 $(-\infty < x < 0,\ -H < y < 0)$ and the upstream plate-covered region Γ_2 $(0 < x < \infty,\ -H < y < 0)$. The solution for the Green function depends significantly on the position of the source point.

Case 1: source in Γ_1 $(\xi < 0)$.

In this case the value of $G(x, y; \xi, \eta)$ in Γ_i is denoted by $G_i^{(1)}(x, y; \xi, \eta)$ $(i = 1, 2)$. These functions will be sought as expansions in terms of eigenfunctions of corresponding boundary value problems:

$$G_1^{(1)} = G_0^{(1)} + R_0^{(1)} e^{ik_0 x}\psi_0(y) + \sum_{m=1}^{\infty} R_m^{(1)} e^{k_m x}\psi_m(y) \quad (x < 0), \qquad (8)$$

$$G_2^{(1)} = T_0^{(1)} e^{-ip_0 x} f_0(y) + \sum_{\substack{n=-2 \\ n\neq 0}}^{\infty} T_n^{(1)} e^{-p_n x} f_n(y) \quad (x > 0), \qquad (9)$$

where

$$\psi_0 = \cosh k_0(y+H)/\cosh k_0 H,$$

$$\psi_m = \cos k_m(y+H)/\cos k_m H \ (m = 1, 2, 3, ...),$$

$$f_0 = \cosh p_0(y+H)/\cosh p_0 H,$$

$$f_n = \cos p_n(y+H)/\cos p_n H \ (n = -2, -1, 1, 2, 3, ...).$$

The constants k_m's satisfy the dispersion relations

$$\mathcal{K} = k_0 \tanh k_0 H = -k_m \tan k_m H \quad (m = 1, 2, 3, ...), \quad \mathcal{K} = \omega^2/g$$

with $(m-1)\pi/H < k_m < m\pi/H$ $(m = 1, 2, 3, ...)$. The constants p_n's satisfy the dispersion relations

$$K = p_0(1 + Lp_0^4)\tanh p_0 H = -p_n(1 + Lp_n^4)\tan p_n H \ (n = -2, -1, 1, 2, 3, ...)$$

with $L = D/(g\rho - \omega^2 M)$ and $K = \rho\omega^2/(g\rho - \omega^2 M)$. It should be noted that p_{-2} and p_{-1} are complex conjugates with positive real parts, p_n's are positive and real with $(n-1)\pi/H < p_n < n\pi/H$ $(n = 1, 2, 3, ...)$, and $R_m^{(1)}$, $T_n^{(1)}$ are unknown constants to be determined to obtain the Green function completely. The function $G_0^{(1)}(x, y; \xi, \eta)$ is a velocity potential due to a source submerged under infinite free surface

$$G_0^{(1)} = \ln\frac{r}{r_1} + pv\int_0^{\infty} F_1(y, \eta; k)\frac{\cos k(x-\xi)}{Z_1(k)}dk - i\pi F_1(y, \eta; k_0)\frac{\cos k_0(x-\xi)}{Z_1'(k_0)}, \qquad (10)$$

where pv indicates the principal-value integration,

$$r^2 = (x-\xi)^2 + (y-\eta)^2, \quad r_1^2 = (x-\xi)^2 + (y+\eta)^2,$$

$$F_1 = \frac{2}{k(1+e^{-2kH})}\{[(k\cosh k\eta + \mathcal{K}\sinh k\eta)e^{-ky} -$$

$$(\mathcal{K}+k)e^{ky}\sinh k\eta]e^{-2kH} + ke^{k(y+\eta)}\},$$

$$Z_1(k) = \mathcal{K} - k\tanh kH, \quad Z_1'(k_0) \equiv dZ_1/dk|_{k=k_0}.$$

Because the velocity and pressure are continuous across the boundary between the regions Γ_1 and Γ_2, the full solution is obtained from matching conditions

$$\partial G_1^{(1)}/\partial x|_{x=0-} = \partial G_2^{(1)}/\partial x|_{x=0+},$$

$$G_1^{(1)}|_{x=0-} = G_2^{(1)}|_{x=0+} \quad (-H < y < 0).$$

Truncating the infinite series in (8), (9) and using the inner products as in the paper by Sahoo *et al.* (2001), unknown constants $R_m^{(1)}$ and $T_n^{(1)}$ can be determined.

Case 2: source in Γ_2 $(\xi > 0)$.

The Green function $G(x,y;\xi,\eta)$ in Γ_i is denoted by $G_i^{(2)}(x,y;\xi,\eta)$ and in the corresponding regions is expressed as

$$G_1^{(2)} = R_0^{(2)}e^{ik_0x}\psi_o(y) + \sum_{m=1}^{\infty} R_m^{(2)}e^{k_mx}\psi_m(y) \ (x<0),$$

$$G_2^{(2)} = G_0^{(2)} + T_0^{(2)}e^{-ip_0x}f_0(y) +$$

$$\sum_{\substack{n=-2\\ n\neq 0}}^{\infty} T_n^{(2)}e^{-p_nx}f_n(y) \quad (x>0), \qquad (11)$$

where the function $G_0^{(2)}(x,y;\xi,\eta)$ is a velocity potential due to a source submerged under infinite elastic plate

$$G_0^{(2)} = \ln\frac{r}{r_1} + pv\int_0^{\infty} F_2(y,\eta;p)\frac{\cos p(x-\xi)}{Z_2(p)}dp -$$

$$i\pi F_2(y,\eta;p_0)\frac{\cos p_0(x-\xi)}{Z_2'(p_0)}, \qquad (12)$$

where

$$F_2 = \frac{2}{p(1+e^{-2pH})}\{(p(Lp^4+1)\times$$

$$[(e^{-py}\cosh p\eta - e^{py}\sinh p\eta)e^{-2pH} + e^{p(y+\eta)}] -$$

$$2Ke^{-2pH}\sinh p\eta\sinh py\},$$

$$Z_2(p) = K - p(1+Lp^4)\tanh pH,$$

$$Z_2'(p_0) \equiv dZ_2/dp|_{p=p_0}.$$

Using boundary condition (5) on the body surface S, we obtain the integral equation for the functions $\sigma_j(x,y)$

$$\pi\sigma_j(x,y) - \int_S \sigma_j(\xi,\eta)\frac{\partial G}{\partial n}ds = n_j.$$

Once the distribution of the singularities $\sigma_j(x,y)$ has been calculated, we can determine the radiation potentials (7).

The radiation load acting on the oscillating body is determined by the force $\mathbf{F} = (F_1, F_2)$ and the moment F_3 which, without account for the hydrostatic term, have the form

$$F_k = \sum_{j=1}^{3}\zeta_j\tau_{kj} \quad (k=1,2,3),$$

$$\tau_{kj} = \rho\omega^2\int_S \varphi_j n_k ds = \omega^2\mu_{kj} - i\omega\lambda_{kj},$$

where μ_{kj} and λ_{kj} are the added mass and damping coefficients, respectively. There is the symmetry condition $\tau_{kj} = \tau_{jk}$.

4. Numerical results

Let us consider the most simple particular case of the problem when the elastic plate is substituted for the grid lid. In this case, boundary condition (4) is replaced by non-flow condition

$$\partial\varphi/\partial y = 0 \quad (0 < x < \infty, \ y = 0).$$

The solution for the Green's function $G_0^{(2)}$ can be obtained from (10) putting $\mathcal{K} = 0$. In addition the integral in (12) is taken in the ordinary sense and there is no term due to residue. The terms with p_{-2}, p_{-1}, p_0 are lacking in series (9), (11) and $p_n = n\pi/H$ $(n = 1,2,3,...)$. The calculations are performed for the circular contour S : $(x-c)^2 + (y+h)^2 = a^2$, where a is the radius of the circle and the coordinates of its center are equal to $x = c$, $y = -h$ $(h > 0)$.

It is well known, that non-zero values of the wave forces have only τ_{11} and τ_{22} for radiation by a submerged circular cylinder under infinite free surface. At the oscillations of the circular cylinder under infinite grid lid, non-zero values have only μ_{11} and μ_{22} and these values do not depend on frequency ω.

However, more complicated behavior of the wave forces takes place at mixed boundary conditions. Figures 2 and 3 give respectively dimensionless values of added mass and damping coefficients: $\bar{\mu}_{ij} = \mu_{ij}/(\pi\rho a^2)$, $\bar{\lambda}_{ij} = \lambda_{ij}/(\pi\rho a^2\omega)$ for the circular cylinder as functions of dimensionless frequency parameter $\bar{\omega}^2 = \omega^2 a/g$.

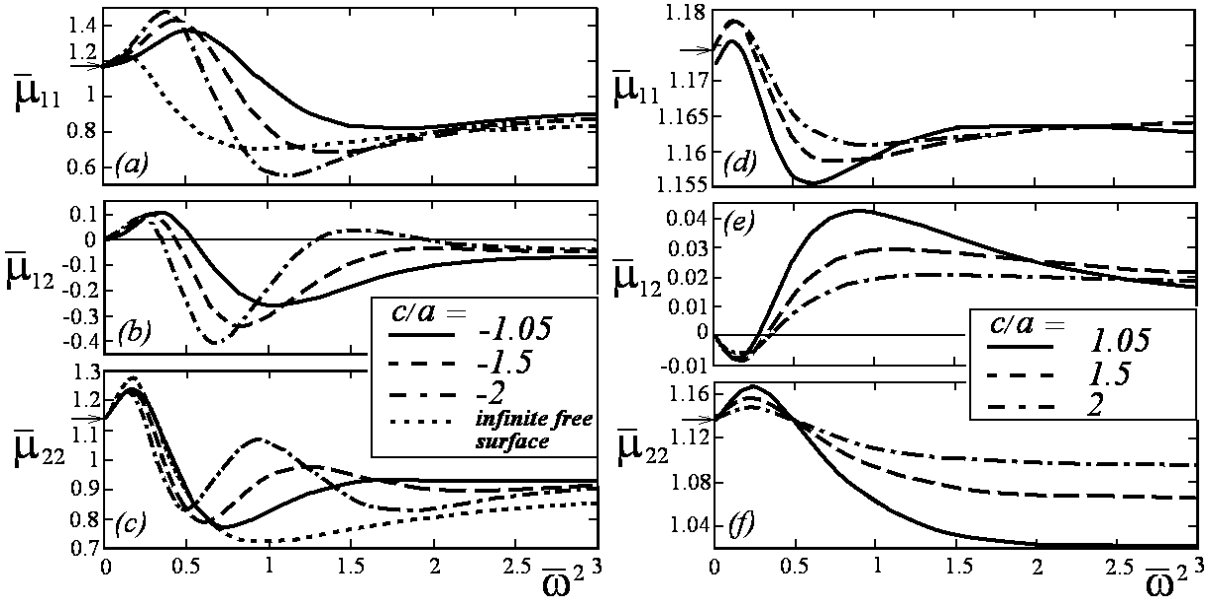

Figure 2: The added mass coefficients of a circular cylinder.

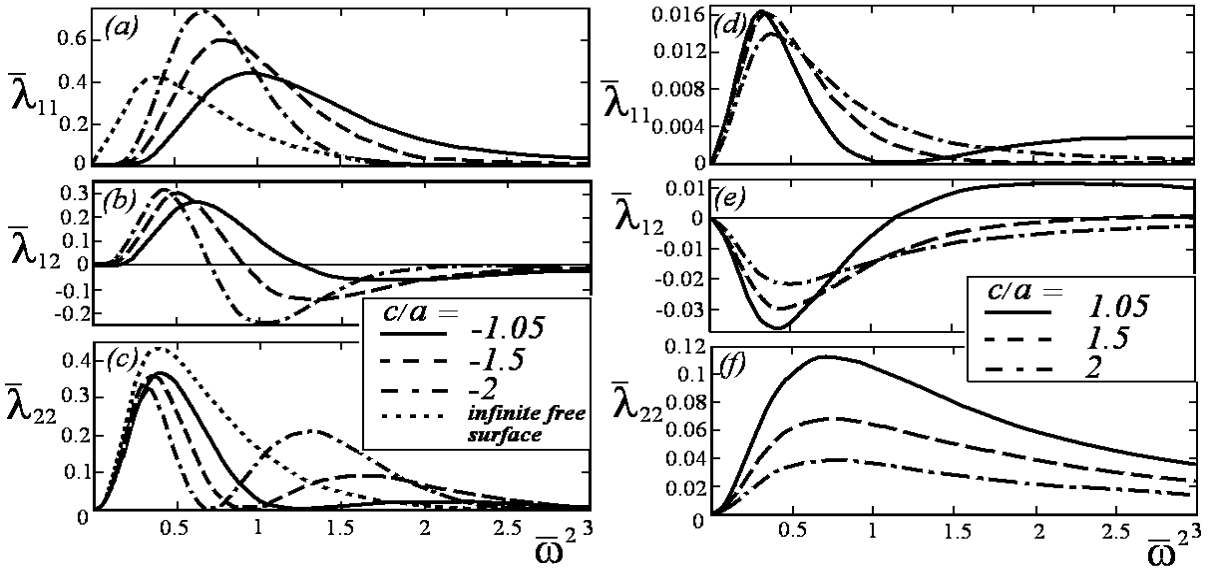

Figure 3: The damping coefficients of a circular cylinder.

The cylinder is submerged at $h = 2a$ and the depth of fluid is equal to $H = 10a$. Figures $2a, b, c$ and $3a, b, c$ give the values of wave forces for the cylinder submerged under the free surface, whereas figures $2d, e, f$ and $3d, e, f$ correspond to the position of cylinder under the grid lid. In figures $2a, c, d, f$, the horizontal arrows indicate the values of the added mass coefficients $\bar{\mu}_{11} \approx 1.1743$ and $\bar{\mu}_{22} \approx 1.1361$ for infinite grid lid. The dotted lines in figures $2a, c$ and $3a, c$ represent the values of added mass and damping coefficients for the circular cylinder submerged under infinite free surface, respectively.

More detailed results for the hydrodynamic load on the cylinder will be presented at the Workshop.

References

Linton, C.M., McIver, P., 2001, *Handbook of Mathematical Techniques for Wave/Structure Interactions*, Chapman & Hall/CRC Press, London/ Boca Raton, FL.

Sahoo, T., Yip, T.L., Chwang, A.T., 2001, Scattering of surface waves by a semi-infinite floating elastic plate, *Phys. Fluids*, 13(11), 3215-3222.

Sturova, I.V., 2011, Hydrodynamic loads acting on an oscillating cylinder submerged in a stratified fluid with ice cover, *J. Appl. Mech. Tech. Phys.*, 52(3), 415-426.

Stokes drift and net transport for two-dimensional wave groups in deep water

T.S. van den Bremer & P.H. Taylor
Department of Engineering Science, University of Oxford
ton.vandenbremer@eng.ox.ac.uk, paul.taylor@eng.ox.ac.uk

Introduction

This paper explores Stokes drift and net subsurface transport by non-linear two-dimensional wave groups with realistic underlying frequency spectra in deep water. It combines analytical expressions from second-order random wave theory with higher order approximate solutions from Creamer et al (1989) to give accurate subsurface kinematics using the H-operator of Bateman, Swan & Taylor (2003). This class of Fourier series based numerical methods is extended by proposing an M-operator, which enables direct evaluation of the net transport underneath a wave group, and a new conformal mapping primer with remarkable properties that removes the persistent problem of high-frequency contamination for such calculations.

Although the literature has examined Stokes drift in regular waves in great detail since its first systematic study by Stokes (1847), the motion of fluid particles transported by a (focussed) wave group has received considerably less attention. Focussed wave groups are relevant, because they can be used to describe the average shape of an extreme wave crest in a random sea (Tromans, Anaturk & Hagemeijer 1991). In practice, the wave field on the open sea often has a group-like structure.

From mass conservation it is clear that Stokes drift by a wave group and Stokes drift by regular waves behave in a fundamentally different way. In fact, the wave-induced Stokes drift and its associated return flow at depth should be locally confined to the wave group and only regular waves (infinite wave trains) can transport mass and momentum indefinitely (McIntyre 1981). Second-order wave theories (e.g. Dalzell 1999) based on the interaction between waves of different frequencies (cf. Longuet-Higgins 1962), predict an irrotational return flow at depth that is equal and opposite to the flow associated with Stokes drift at the surface, as illustrated in figure 1. We show that these results can be extended to higher order by retaining more of the non-linearity of the underlying equations using the results of Creamer et al (1989) with significant additional drift near the focus point.

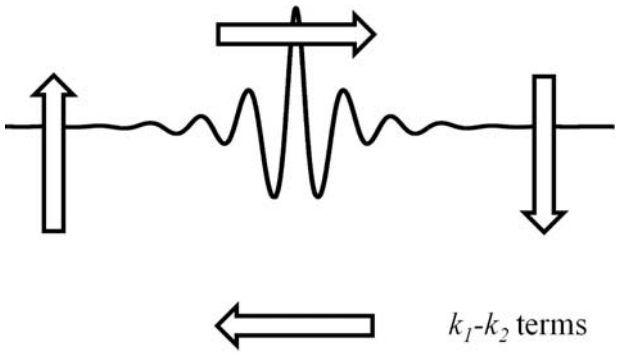

Figure 1: Illustration of the localized irrotational mass circulation moving with the passing wave group. The four fluxes, the Stokes transport in the near surface region and in the direction of wave propagation (left to right); the return flow in the direction opposite to that of wave propagation (right to left); the downflow to the right of the wave group; and the upflow to the left of the wave group, are equal.

Non-linear wave kinematics model

A two-dimensional body of water of infinite depth and indefinite lateral extent is assumed with a coordinate system (x,y), where x denotes the horizontal coordinate and y the vertical coordinate measured from the undisturbed water level upwards. Inviscid, incompressible and irrotational flow is assumed and the usual boundary conditions (kinematic and dynamic at the free surface and a no flow boundary condition at infinite depth) apply. In order to study the drift beneath large waves, we adopt the NewWave wave group of Tromans et al (1991) and set each amplitude term to be proportional to its share in the total discretized wave energy spectrum $S(\omega)$:

$$a_n = a_L \frac{S(\omega_n)}{\sum_{n=1}^{N} S(\omega_n)}, \tag{1}$$

so that the total maximum amplitude is a_L and the shape is that of the auto-correlation function for the sea state. In particular, we consider a (discretized) Jonswap spectrum for fetch-limited seas (Hasselmann, Dunckel

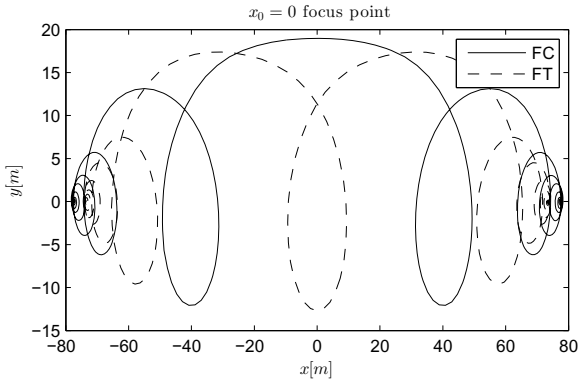

Figure 2: Particles trajectories at the free surface for a focussed wave crest (FC) and a focussed wave trough (FT) with a linear maximum wave amplitude $a_L = 15m$. The particles are at $x_0 = 0$ at the time of focus.

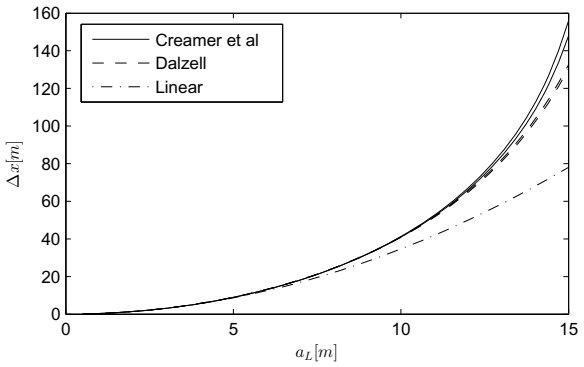

Figure 3: Net horizontal displacement $\Delta x = x(t = -\infty) - x(t = \infty)$ by a wave group travelling past as a function of the maximum linear wave amplitude a_L (i.e. increasing steepness) for focussed crests (top line) and focussed troughs (bottom line).

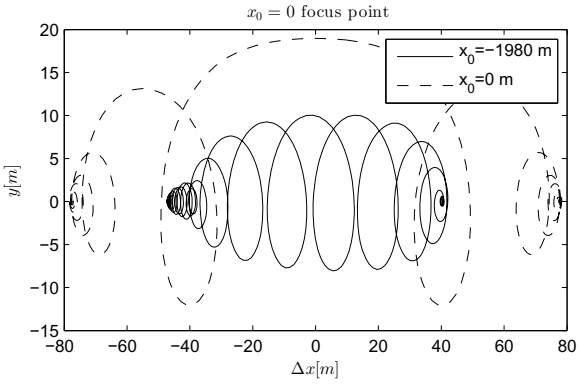

Figure 4: Particles trajectories at the free surface for a focussed wave crest (FC) with a linear wave amplitude $a_L = 15m$ for two different particles located at $x_0 = -1980$ m and $x_0 = 0$ m (focus point) at the time of focus.

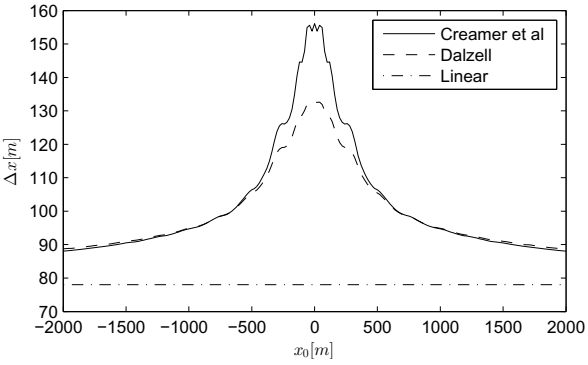

Figure 5: Net horizontal displacement $\Delta x = x(t = -\infty) - x(t = \infty)$ by a wave group with a linear maximum wave amplitude $a_L = 15$ m of particles at the free surface as a function of their location at the time of focus $x_0 = x(t = 0)$.

& Ewing 1980) and we set $T_p = 12.4$ and the peak-enhancement factor $\gamma = 3.3$. A random wave solution to the governing equation and the boundary conditions that is linear in wave steepness ($O(k\eta)$) takes the form:

$$\begin{aligned} \eta_L(x,t) &= \sum_{n=1}^{N} a_n \cos(k_n x - \omega_n t + \mu_n) \\ \phi_L(x,y,t) &= \sum_{n=1}^{N} a_n \omega_n e^{k_n y} \sin(k_n x - \omega_n t + \mu_n), \end{aligned} \tag{2}$$

To include non-linear effects, we rely on the formulation of Creamer et al (1989), who transform the surface elevation η and the surface potential ϕ_s, the two canonical variables that capture the (Hamiltonian) dynamics of the entire problem, into a new set of canonical variables. These new variables exactly reproduce the second-order non-linear behaviour of surface waves and provide a remarkably good approximation to higher-order non-linearity. The nth Fourier component of the transformations of surface elevation η_n and the surface potential $\phi_{s,n}$ on this non-linear free surface are given by (Creamer et al 1989):

$$\begin{aligned} \eta_n &= \frac{1}{|k_n|} \int_{-\infty}^{\infty} \left(e^{ik_n \tilde{\eta}_L(x)} - 1\right) e^{-ik_n x} dx, \\ \phi_n &= \frac{1}{|k_n|} \int_{-\infty}^{\infty} e^{ik_n \tilde{\eta}_L(x)} \tilde{\phi}'_L(x) e^{-ik_n x} dx, \end{aligned} \tag{3}$$

where $\tilde{\eta}_L(x)$ is the Hilbert transform of the linear free surface signal $\eta_L(x)$ and $\tilde{\phi}'_L$ is the Hilbert transform of the spatial gradient of the linear velocity potential.

Conformal mapping

We introduce the following conformal mapping to reduce the steepness of the surface profile to in turn improve the convergence behaviour of the H-operator of Bateman, Swan & Taylor (2003) to calculate subsurface kinematics and eliminate persistent high-frequency contamination

without having to resort to filtering:

$$\xi = z + iA - i\sum_{n=0}^{n=N} a_n e^{-i(k_n z - \omega_n t + \mu_n)}, \qquad (4)$$

where $z = x + iy$ are the complex coordinates in real space and $\xi = \alpha + i\beta$ are the complex coordinates in transformed space. The coefficients a_n and k_n are, respectively, the wave amplitude and the wave number of the first N components of the underlying linear signal. We demonstrate that (4), when applied inversely, for regular waves almost exactly maps a straight line in ξ-space ($\beta = 0$) to the free surface corresponding to a fifth-order Stokes expansion (cf. Fenton 1985) in z-space. For wave groups, the mapping (4) applied inversely maps a straight line into a wavy surface which exactly reproduces the features of a second-order free surface (e.g. Dalzell 1999) excluding the rather small effect of the frequency difference terms.

From the definition of the complex potential $\Psi = \phi + i\psi$, a relationship between the velocities in z and ξ-space can be found:

$$u - iv = \frac{d\Psi}{dz} = \frac{d\Psi}{d\xi}\frac{d\xi}{dz} = \big(u_\alpha - iu_\beta\big)\frac{d\xi}{dz}. \qquad (5)$$

By first mapping to a reduced steepness surface, applying the operators in this space and then mapping back, the persistent problem of high-frequency contamination is effectively eliminated removing the need for inevitably arbitrary numerical filtering.

The M(ass flux)-operator

To directly evaluate the mass flux beneath a given wave profile, we propose a new operator based on the principle of the H-operator of Bateman, Swan & Taylor (2003), which we term the M-operator. The general solution for the velocity potential as a solution to the governing Laplace equation $\nabla^2\phi = 0$ can be given by the sum of N Fourier components (cf. equation 2). From the Cauchy-Riemann equations for an irrotational and incompressible two-dimensional flow field, we have $\partial\phi/\partial x = \partial\psi/\partial y$. The partial derivative of the velocity potential $\partial\phi/\partial x$ can be evaluated from (2) to give a solution for the stream function ψ expressed as an indefinite integral:

$$\psi(x,y,t) = \sum_n^N A_n e^{k_n y}\cos(k_n x - \omega_n t + \mu_n) + f(x,t), \quad (6)$$

where the stream function (6) is now defined up to an arbitrary function of x and t, $f(x,t)$. We can define $\psi_s(x,t) = \psi(x,\eta(x),t) - \psi(x,-\infty,t)$ as the total mass flux (per unit width and with unit density) below the free surface:

$$\psi_s(x,t) = \sum_n^N A_n e^{k_n\eta(x,t)}\cos(k_n x - \omega_n t + \mu_n). \qquad (7)$$

The coefficients A_n and hence the value of the volume flux $\psi_s(x,t)$ can now be obtained from a procedure (the M-operator) similar to the H-operator of Bateman, Swan & Taylor (2003). Making use of the properties of the complex potential across conformally mappable spaces, the M-operator can be applied in ξ-space to avoid high-frequency contamination and ensure convergence.

Result 1: Stokes drift

As the particles undergoes its otherwise circular motion, two factors contribute to Stokes drift at the free surface: deviation from the still water level $z = 0$ and deviation from the initial horizontal position x_0. Using linear kinematics, the net horizontal displacement by a passing wave group $\Delta x = x(t = \infty) - x(-\infty)$ of a particle at the surface can thus be obtained by integrating the horizontal velocity $u(x, \eta(x,t), t)$ with respect to time:

$$\Delta x = \int_{-\infty}^{\infty}\frac{dx}{dt}dt = \sum_{n=1}^{N}\frac{a_n^2\omega_n k_n}{2}T^* + O(\epsilon^3), \qquad (8)$$

where $T^* = 2\pi/\Delta\omega$ is the repeat period of the discretized (with intervals $\Delta\omega$) frequency spectrum [1] and only up to second-order in wave steepness are included.

By numerically solving the two simultaneous differential equations for the position of a particle that is initially at the surface (and thus stays there):

$$\frac{dx}{dt} = u(x,y,t), \quad \frac{dy}{dt} = w(x,y,t), \qquad (9)$$

we also evaluate the Stokes drift in a framework in which kinematics are described by Dalzell's (1999) second-order wave theory and the Creamer transform. Figure 2 traces out the orbital paths that are described by a particle that is located at the focus point at the time of focus $t = 0$ for a focussed crest and a focussed trough based on the non-linear kinematics obtained from the Creamer transform. A large part of the transport is performed by just a few large orbits close to the focus point, where the surface elevation is large and the waves are at their most non-linear.

Figure 3 then compares the net horizontal displacement by a passing wave group Δx of a particle at the surface located at the focus point at the time of focus calculated by three different methods: the analytical expression based on linear wave theory (8) and the numerical solutions based on Dalzell's (1999) second-order random wave theory and the Creamer transform. It is evident from this figure that the horizontal displacement in-

[1] Note that (8) is not a function of the number of components N as N becomes large. To see this, note $a_n \sim N^{-1}$ and $T^* \sim N$ resulting in the individual terms in the sum (8) to behave as N^{-1}. Summing over all the N terms then cancels the dependency on N.

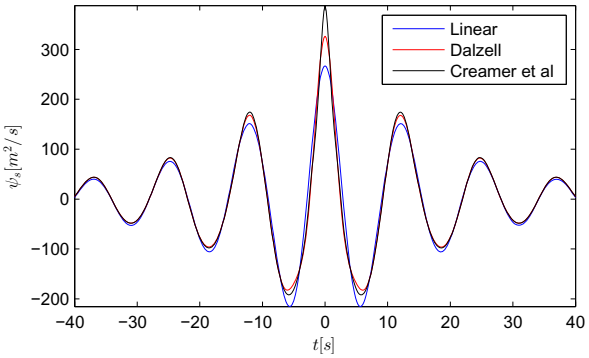

Figure 6: Net depth-integrated mass flux at the focus point as a function of time evaluated from linear theory, using the second-order random wave theory of Dalzell(1999) and the M-operator applied to the more non-linear signal obtained from the Creamer transform ($a_L = 15$ m).

creases with increasing wave amplitude and hence, keeping the other parameters of the spectrum fixed, increasing wave steepness and that non-linear effects are important.

It is evident from (8) that displacement predicted based on linear theory is not a function of the initial position of the particle. Close to the focus point, the net displacement will be produced by a few large orbits, whereas away from the focus point, where the wave group is dispersed, the equivalent net displacement is produced by a large number of small orbits. Comparing, on the other hand, the trajectories of two particles, one located at the focus point at the time of focus and one very far away from it, obtained from the non-linear kinematics and surface elevation through the Creamer transform, figure 4 shows very different behaviour. Clearly, a particle at the focus point at the time of focus is transported further mainly by one or two large orbits corresponding to the highest few peak of the wave group. Figure 5 shows the net displacement Δx as a function of the position of the particle at the time of focus x_0 confirming an additional drift effect for particles within $\sim \pm 2\lambda_p$ of the focus point at the time of focus, where here $\lambda_p \approx 240$ m. For a relatively steep wave considered herein (cf. $k_p a_L \approx 0.39$), the net displacement Δx in this region is approximately two times the net displacement predicted by linear theory.

Result 2: Return flow and net transport

One of the fundamental properties of wave groups is that the surface elevation returns to the still water $\eta(x) \to 0$ as $x \to \pm\infty$. The same applies to the kinematics. In fact, close to focus, non-zero surface elevation and kinematics are confined to $\approx \pm 4\lambda_p$ of the focus point. The transport of fluid in the direction of wave propagation by Stokes drift at and near the surface must therefore be compensated by a return flow at depth in the opposite direction to ensure conservation of mass. Creamer et al (1989), albeit only for a narrow-banded wave group, show that this is indeed the case for the non-linear wave profile obtained using their transform. For second-order random wave theories, the frequency difference terms $(k_1 - k_2)$ of the horizontal velocity are responsible for this return flow. These terms have a repeat period of $(2\pi/\Delta\omega)$, where $\Delta\omega$ is the interval of the discrete frequency spectrum. In the limit $\omega \to 0$, which corresponds to an infinite number of representative Fourier components $N \to \infty$ and the limit in which the wave group is truly localized and not periodic with a very long repeat period, these terms therefore correspond to a net flow, which only decays very slowly with depth (cf. $exp(|k_1 - k_2|y)$).

The M-operator is applied in figure 6 showing the zero-mean depth-integrated mass flux underneath a focussed crest from linear theory, Dalzell (1999) second-order random wave theory and the Creamer transform as a function of time. It is evident from this figure that non-linear effects account for a larger local transport of mass by the largest crest, which is compensated by a greater return flow underneath the troughs. A second feature is that the time integral of the depth-integrated flux for all cases is zero, to within the numerical accuracy of the computations, as would be expected from continuity.

References

Bateman, W.J.D., Swan, C. & Taylor, P.H., 2003. On the calculation of the water particle kinematics arising in a directionally spread wavefield. *J. Comput. Phys.* **186**, 70-92.

Creamer, D.B., Henyey F., Schult, R. & Wright, J., 1989. Improved linear representation of ocean surface waves. *J. Fluid Mech.* **205**, 135-161.

Dalzell, J.R., 1999. A note on finite depth second-order wave-wave interactions. *Appl. Ocean Res.* **21**, 3, 105-111.

Fenton, J.D., 1985. A fifth-order Stokes theory for steady waves. *J. Waterway Port Coastal and Ocean Engineering*, **111**, 216-234.

Hasselmann, D.E., Dunckel, M., Ewing, J.A., 1980. Directional Wave Spectra Observed during JONSWAP 1973. *J. Phys. Oceanogr.*, **10**, 1264-1280.

Longuet-Higgins, M.S., 1962. Resonant interaction between two trains of gravity waves. *J. Fluid Mech.*, **12**, 321-332.

Mcintyre, M.E., 1981. On the 'wave momentum' myth. *J. Fluid Mech.*, **106**, 331-347.

Stokes, G.G., 1847. On the theory of oscillatory waves. *Trans. Camb. Philos. Soc.* **8**, 441-455. Reprinted in: Stokes, G.G. (1880). Mathematical and Physical Papers, Volume I, Cambridge University Press. 197-229.

Taylor, P.H., 1992. On the kinematics of large ocean waves. *Proceedings 6th International Conference of the Behaviour of Offshore Structures (BOSS.)* **1**, 134-145.

Tromans, P.S., Anaturk, A.H.R., Hagemeijer, P.M., 1991. New model for the kinematics of large ocean waves - application as a design wave. *Proceedings of the 1st International Offshore and Polar Engineering Conference*, 64–71.

Evolution of water waves generated by subaerial deformable landslide

S. Viroulet, O. Kimmoun & C. Kharif

Aix-Marseille Univ., IRPHE CNRS: UMR 7342
Aix-Marseille Universit - AMU - Ecole Centrale Marseille.
viroulet@irphe.univ-mrs.fr

January 15, 2013

Abstract

We consider experimentally the waves generated by subaerial granular landslide. A set of experiments are performed in a $2.20 \times 0.40 \times 0.2$m wave tank to characterize the behavior of the granular flow as well as its influence on the generated wave. A PIV method is used to capture the evolution of the velocity field in the water. From these experiments several observations are presented on both the generation of the wave and the evolution of the granular during the collapse.

1 Introduction

Predicting the dynamics of granular flow plays an important role in geophysical and industrial applications. Since the seminal work of Bagnold in 1954 [1], a huge number of studies have considered the dynamics of dry granular media in various geometry such as on an inclined plane or in a rotating drum (for a review, see e.g. [3]). Most of these studies focused on dry granular flow as the situation is already complicated to describe. In particular, there is still a lack of constitutive laws to explain and predict the experimental observations. For a dense and dry granular flow, the $\mu(I)-$rheology seems to be the only model which allows a successful continuum description of the flow [5]. This rheology is purely phenomenological but has shown good agreement with experiments and numerical simulations in various situation (see [6]).

However, the situation becomes more complicated for underwater granular flow where the presence of the surrounding fluid modifies the rheology of the flow. Recently, Cassar & al. [2] adapted the $\mu(I)-$rheology to submarine flow by replacing the inertial time scale with a viscous time scale in order to take into account the presence and influence of the surrounding fluid. Numerically, Topin & al. [8] have performed numerical simulations on submarine granular collapse by coupling a contact dynamics method and a fluid dynamics method.

Whereas this last problem is already complicated to quantify, it becomes even more challenging to predict the impact of a granular media from the air into the water and the wave generated by this impact. This situation is a model for subaerial deformable landslide and would have many important implications to forecast the subsequent generation of tsunamis. Based on numerous experiments, Mohammed & Fritz [7] have studied the generation of impulse wave by subaerial landslides with a Froude number ($V_{slide}/\sqrt{gH}$) at the impact larger than one. From these experimental studies, they provided a predictive equation on wave amplitude, period and length.

Despite these studies, the dynamics of a dry granular flow during the collapse into water remains largely unknown, especially at Froude number smaller than unity. In this work, we study such a situation in an experimental setup designed to characterize both the wave generated by the impact but also the flow of the granular media after its penetration into the water. By performing systematic experimental studies and obtaining relevant scaling laws, we aim to estimate the potential tsunami which would be generated after an impact of granular flow into water in various geophysical events.

2 Experimental set-up and data acquisition

A schematic view of the experimental set-up is presented in figure 1. It consists in a wave tank of 2.20 m

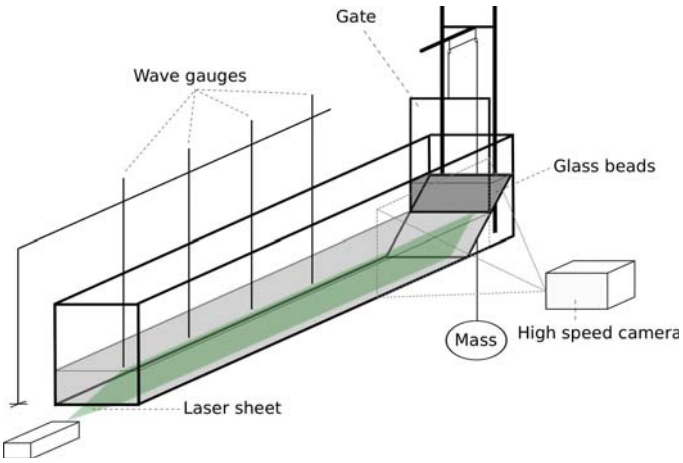

Figure 1: *Schematic view of the experimental set-up*

long, 0.40 m high and 0.195 m wide. The slope is made of a polyvinyl plate with glass beads stuck on it to take into account the friction and suppress slipping of particles on the surface. The initial water depth in the tank remains constant for all the experiments and equal to $H = 14.8$ cm. A vertical gate is used to delimitate the initial reservoir of granular materials located just above the undisturbed free surface. The gate is opened vertically using a 20 kg mass and pulley. The velocity of the gate reaches a value of 5 m.s^{-1} which is sufficient to ensure a granular front almost vertical at the initial time. The particles used are glass beads of diameter $d = 1.5$ mm and density $\rho_s = 2500$ kg.m^{-3}. It has been shown that the initial compaction of the material is an important parameter for the later granular flow [4]. Therefore, to ensure a good reproducibility of our experiments, the edge of the wave tank is hit a sufficient number of time with a hammer the same way for each experiment.

Then, the evolutions of the generated wave and of the granular flow are recorded with a high speed camera at 200 fps. The propagation of the generated wave is also measured with 4 resistive gauges located at 0.59 m, 1.052 m, 1.402 m and 2.019 m from the right side of the tank. (In some experiments we have also performed PIV measurement to estimate the velocity field in the water. The water was seeded with 8 μm diameter silver coated hollow glass spheres with a density of 1.1 g.cm^{-1}. Then, an intercorrelation window technique with several loops is performed to obtain the velocity field from the recorded movies.

Experiment	slope angle (°)	Initial mass (kg)
1	60	3.566
2	45	3.566
3	45	3.000
4	45	2.75
5	45	2.50
6	45	2.25
7	45	2.0

Table 1:

3 Experimental results

Several experiments were performed varying the initial mass of the landslide and the slope angle. This study is in progress, additional results will be presented during the conference. The range of parameters is summarized in table 1.

The first and second experiments in table 1 were both conducted three times to ensure the reproducibility of it. The evolution of the free surface at the first probe is represented in figure 2 for both configurations. The reproducibility of the experiment is excellent. We can also note that the maximum amplitude of the generated wave is larger for a higher slope angle. This observation was quite intuitive, the granular flow impact the undisturbed free surface stronger than in the case of a gentle slope.

The evolution of both the free surface and the granular media is represented on figure 3a) for a slope angle of 45°. For convenience, only 1 curve of 4 is displayed (we used more curves for the study).

The time evolution of the granular front position and its velocity are represented in figure 3b). The velocity of the granular remains constant during the collapse and is larger for a higher slope angle. This was quite unexpected, it seems that the slide reaches a terminal velocity very quickly. The evolution of the free surface during the generation is represented in figure 4.a for three differents experiments (tests 1, 2 and 5 in table 1). As expected increasing the slope angle and/or the initial mass of the granular, increase the maximum amplitude of the generated wave. Figure 4b) shows the evolution of the thickness of the granular slide during the collapse for these three experiments. Here again, the thickness increases with the slope angle but does not seems to depend of the initial mass of granular. Indeed for tests 2 and 5 the thickness is quite the same wherase the initial mass is about 30% less in one case.

The influence of the initial mass of granular is represented on figure 5 for a slope angle of 45°. The

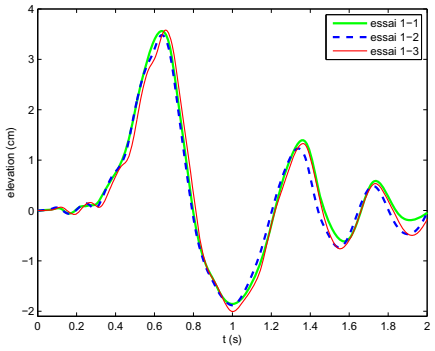

(a)

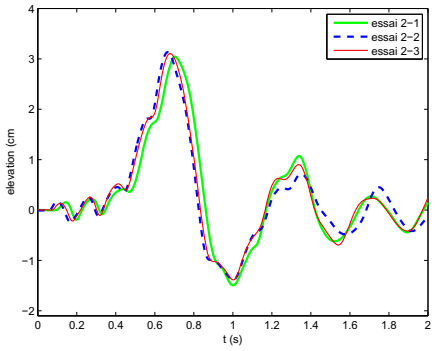

(b)

Figure 2: *Time evolution of the free surface at the first probe locates at* 0.59 *m from the right side of the tank. (a) slope angle of* 60°*, (b)* 45°*.*

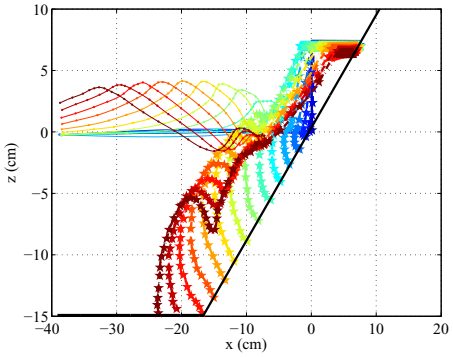

(a)

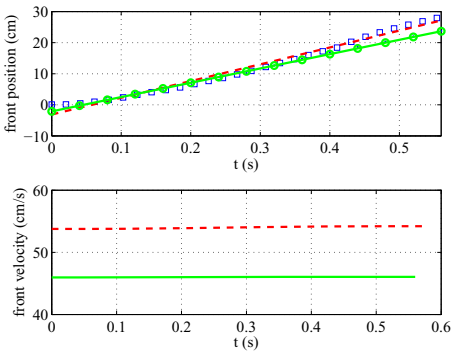

(b)

Figure 3: *(a) Evolution of the free surface and the granular media (time between two curve is* 1/50 *s. (b) Evolution of the front position and its velocity during the collpase for a slope angle of* 45° *continous line and* 60° *dashed line.*

maximum amplitude of the leading wave is represented at each gauge as a function of the initial mass of the slide. Has expected and already observed in previous figure (fig.4a) the amplitude of the generated wave increase with the mass of the slide.

The field velocity in the water during the collapse is represented in figure 6. We can observe the formation of a vortex at the head of the granular flow which may explain its constant velocity during the collpase (see fig. 6b). The leading beads reach their terminal velocity (which is about 0.20 m.s^{-1}) but the top of the intial amount of granular is still dry and pushes it. This generates an instability giving rise to the vortex. Figure 6c) shows that the vortex generated during the collapses induces a reverse current in the water, this current stops the granular flow for some instant and then finishes to slide down along the slope.

4 Discusion

From all these experiments we observed expected results on the generation of the wave. The amplitude increases with the slope angle and the initial mass of the slide. More suprising results were observed for the granular flow. One of the less intuitive is the velocity of the flow during the collpase. Indeed, the velocity increases with the slope angle but keeps a constant value during the collapse. Evaluating the terminal velocity of a single bead for a slope angle of 45° gives a value of 0.20 m.s^{-1} which is near twice less than the observed velocity. The other new observation is about the evolution of the thickness of the slide. It reaches a constant value, which can be explained by the generation of the vortex and the induced circulation but does not seem to depend on the initial mass of the slide. This study is still in progress. We are performing several experiments varying the slope angle, the water depth and the diameter of the beads to confirm these first observations and develop a scaling law on the evolution of the amplitude of the generated wave. A numerical study is also conducted using the approximation of a Bingham fluid to model the granular flow.

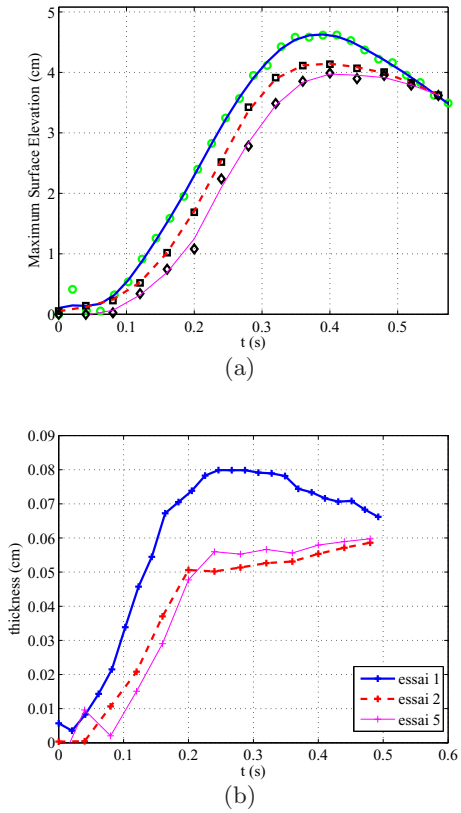

Figure 4: *(a) Elevation of the free surface as a function of time. (b) Evolution of the thickness of the granular flow during the collapse. Thick solid line essai 1 (see table 1), dashed line essai 2 and thin solid line essai 5. Markers represent the measurement from the camera.*

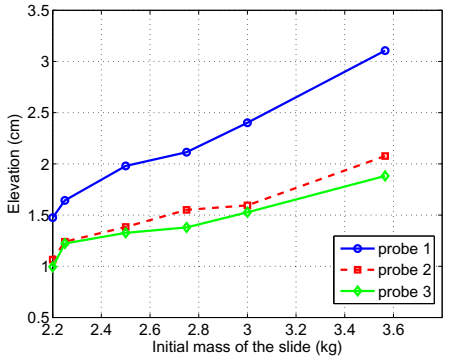

Figure 5: *Maximum elevation of the free surface at each probe as a function of the initial slide mass.*

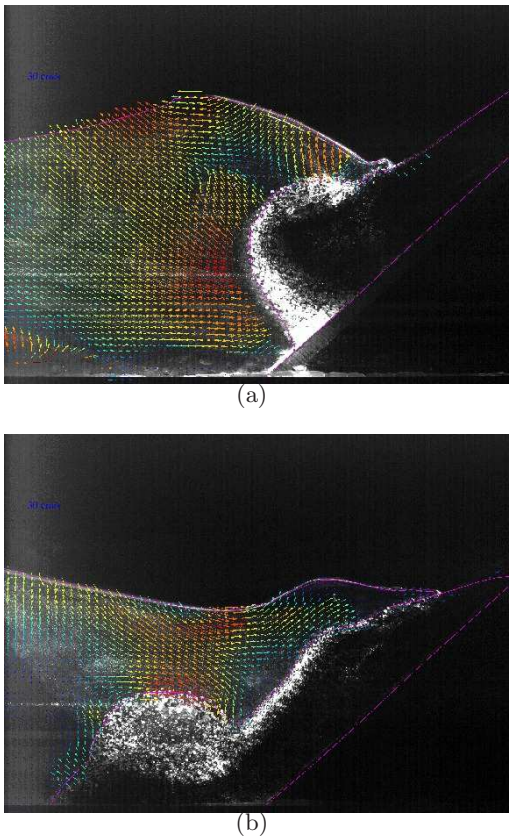

Figure 6: *PIV measurement for a slope angle of* 45°.

References

[1] R. A. Bagnold. *Proc. Roy. Soc. A*, 225:49–63, 1954.

[2] C. Cassar, M. Nicolas, and O. Pouliquen. *Phys. Fluids*, 17:103301, 2005.

[3] Y. Forterre and O. Pouliquen. *Ann. rev. mechanics*, 40:1–24, 2008.

[4] R. M. Iverson, M. E. Reid, N. R. Iverson, R. G. LaHussen, M. Logan, J. E. Mann, and D. L. Brien. *Sciences*, 290:513–516, 2000.

[5] P. Jop, Y. Forterre, and O. Pouliquen. *Nature*, 441:727–730, 2006.

[6] P.-Y. Lagrée, L. Staron, and S. Popinet. *J. Fluid Mech.*, 686:378–408, 2011.

[7] F. Mohammed and H. M. Fritz. *J. Geo. Res.*, page doi:10.1029/2011JC007850, 2012.

[8] V. Topin, Y. Monerie, F. Perales, and F. Radja. *Phys. Rev. L.*, 109:188001, november 2012.

Radiation and trapping behaviour of arrays of truncated cylinders

H. Wolgamot **R. Eatock Taylor** **P. H. Taylor**
hugh.wolgamot@eng.ox.ac.uk **r.eatocktaylor@eng.ox.ac.uk** **paul.taylor@eng.ox.ac.uk**

Department of Engineering Science, University of Oxford,
Parks Road, Oxford OX1 3PJ, United Kingdom

1 Introduction

Trapped modes and the associated trapping structures are a topic which has excited some interest in hydrodynamics over the past two decades. The first trapped modes identified were local oscillations in the vicinity of fixed structures, now called sloshing trapped modes and sloshing trapping structures respectively. McIver and McIver [2006] describe such a trapped mode as 'a free oscillation of an unbounded fluid with a free surface that has finite energy, does not radiate waves to infinity, and in the absence of viscosity will persist for all time.' Sloshing trapping structures discovered include toroidal shapes derived using an indirect procedure and infinite arrays of bottom-mounted cylinders - or the equivalent case of a cylinder in a channel. True trapped modes cannot be excited by an incident wave but near-trapped modes, in which radiation (and hence decay rates) are low but non-zero, may be excited by incident waves. Finite arrays of bottom mounted cylinders in linear and circular configurations have been found to support near-trapped modes.

More recently the term motion-trapping structure has been introduced by McIver and McIver [2006] to describe structures which can support a local bounded oscillation (at the appropriate frequency) in the vicinity of the structure while the structure is free to move, with no radiation to infinity. Such a structure must, in addition to possessing a wave-free frequency, satisfy a resonance condition requiring the structural and fluid inertia terms to balance any restoring force terms at that frequency. Given an initial displacement from equilibrium, such a structure would eventually reach simple harmonic motion at the trapped mode frequency (Porter and Evans [2008]). The stiffness terms in the resonance condition could be hydrostatic and/or mooring terms and examples of each case have been studied. Once mooring terms are introduced, any wave-free structure can become a motion-trapping structure, so the more limited class of structure may be that in which only hydrostatic restoring forces are present. Motion-trapping structures without moooring forces were considered by McIver and McIver [2006], who constructed 2-dimensional motion trapping structures, while McIver and McIver [2007] extended this approach to 3-dimensions and Porter and Evans [2008] started with a pair of rectangular cylinders or a thick-walled cylindrical shell (in 2- and 3-dimensions respectively) and varied the geometry to find motion trapping structures. Motion-trapping structures with mooring restraints were studied by Evans and Porter [2007] who found that a moored submerged circular cylinder moving in heave or sway could be a motion trapping structure and Newman [2008] who analysed mooring stiffnesses on the continuum from $-\infty$ to ∞.

A third class at the intersection of these two, described by Fitzgerald and McIver [2010], is passive trapping structures, which are sloshing trapped modes which exert no force on the body, thereby allowing the body to be freely floating without any associated energy loss through radiation. These modes are not considered here.

Arrays of truncated cylinders are also able to support (sloshing) near-trapped modes; such a mode was identified in the array of four truncated cylinders investigated using a semi-analytical method by Siddorn and Eatock Taylor [2008] - the array is shown in Figure 1. In this study the cylinders were also allowed to move independently and the condition number of the damping matrix used to identify frequencies where almost-wave-free modes could occur. A paper presented by the current authors at an earlier work-

shop (Wolgamot et al. [2011]) dealt with the directionality of optimum power absorption from arrays of independently moving bodies. In that work radiation from the array and the inverse of the damping matrix for the array were of great importance. The condition number of the damping matrix is closely related, and in this paper we start by studying the modes that may be identified using this method.

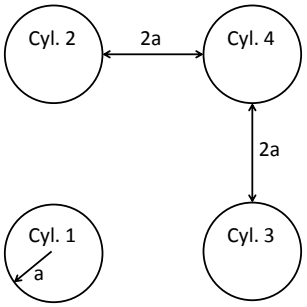

Figure 1: Plan view of four cylinder layout. Cylinders draft $d = 2a$, water depth $h = 4a$.

2 Four cylinders

The heave damping condition number plot of Siddorn and Eatock Taylor [2008] is shown in Figure 2. Also shown in this figure are results from the boundary element code DIFFRACT for the same array of independently moving cylinders and the condition number of the damping matrix when a small-body approximation is made; that is, the devices radiate but do not scatter. This latter information is interesting in assessing the importance of scattering on the behaviour of the radiating bodies.

It appears that in heave there are two frequencies in the range shown at which near-wave-free modes occur - in fact, the plot for surge (not shown here) is very similar, except that the frequencies of each mode are slightly higher. The second (higher frequency) mode corresponds approximately to the sloshing near-trapping wavenumber of the array.

To determine the body motion modes corresponding to the respective peaks in the condition number plot the following method was employed, based on a similar application in Meylan and Eatock Taylor [2009]. Consider the radiation damping matrix $\boldsymbol{B}(k)$, a real, symmetric n x n matrix, and an associated vector of cylinder displacements, $\boldsymbol{z}$. An approximation to the wavenumber of peak condition number may be denoted k_0, and we seek to solve the problem $\boldsymbol{B}(k)\boldsymbol{z} = 0$ near this wavenumber. If we let the desired wavenumber $k = k_0 + \sigma$ then, using a Taylor series expansion, we may write:

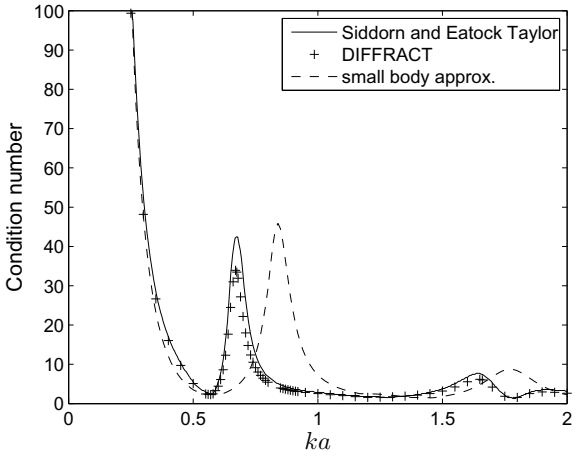

Figure 2: Condition number of heave damping matrix.

$$(\boldsymbol{B}(k_0) + \sigma \frac{\mathrm{d}\boldsymbol{B}}{\mathrm{d}k})\boldsymbol{z} = 0 \qquad (1)$$

which may be written as a generalised eigenvalue problem and solved for eigenvalue σ and corresponding eigenvector $\boldsymbol{z}$. Because DIFFRACT was used to calculate hydrodynamic coefficients we were unable to consider complex wavenumbers, but assume that the imaginary part of the wavenumber is small at the near-wave-free frequencies.

Using this method, the lowest-wavenumber peaks in the condition number plot for heave and surge radiation are found to give mode shapes with all bodies oscillating in phase; i.e. $z = [1, 1, 1, 1]$. The higher frequency peaks in heave and surge correspond to different modes, which will be discussed at the workshop. Thus the first peaks in each case correspond to a minimum of radiation from an oscillation of all cylinders as a single rigid body. Damping coefficients for the cylinder array heaving as a single body were calculated using DIFFRACT, and are shown in Figure 3, where a minimum may be observed at the expected frequency. In this Figure the damping of the multi-column structure is compared to four times the damping of a single heaving cylinder. This minimum damping frequency has been published previously in the results of Mavrakos [1991] and Kagemoto and Yue [1986], although no comment was made on the results. The minimum in

damping is quite significant, with a reduction in damping from the reference case of four isolated cylinders by a factor of about 30. As identified by Siddorn and Eatock Taylor [2008], this motion is an almost-wave-free mode. Attaching a spring of the appropriate stiffness would make the structure a 'near-motion-trapping' structure, which would eventually experience a slowly decaying oscillation at this frequency if given an initial displacement. Surge results are similar and will be presented at the workshop.

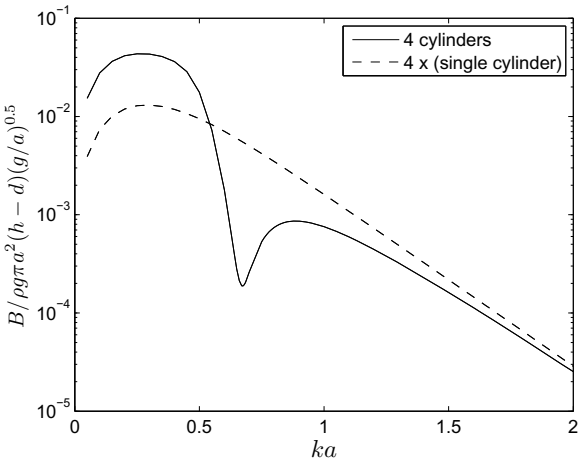

Figure 3: Heave damping of four rigidly connected cylinders.

The damping coefficient for the four heaving cylinders moving in a rigid body mode may be expressed as a combination of the elements of the heave damping matrix for the array, according to:

$$B = 4(B_{11} + 2B_{21} + B_{41}) \qquad (2)$$

using the symmetry of this problem. Some insight into what is occurring at the near-wave-free frequency may then be provided by using the small body approximation, in which damping coefficients are proportional to $J_0(ks)$ where J_0 is a Bessel function of the first kind and s is the spacing. Using this approximation, terms B_{21} and B_{41} will become negative when the s_{21} and s_{41} separations ($4a$ and $4\sqrt{2}a$) cause the argument ks of the Bessel function to pass beyond the first zero at $ks = 2.4048$ and into the negative region. The B_{41} term will become negative first, followed by the B_{21} term. At some middle point corresponding to optimum cancellation of the radiated waves from the respective cylinders the overall heave damping will reach its minimum. The effect of scattering shifts these behaviours in frequency, so that the minimum for the full problem occurs at lower frequency than the small body case.

The free surface elevations for the heave mode show that the mode is a pumping mode, where the free surface inside the array is displaced in the opposite direction to the cylinders. A transition from preferential radiation along the diagonals of the square array at frequencies below the near-wave-free frequency, to radiation perpendicular to the faces of the square at higher frequencies is observed, with minimum radiation at some optimum intermediate frequency. The free surface at this near-wave-free frequency is shown in Figure 4 and the radiation pattern may be readily identified as intermediate between the two cases discussed above.

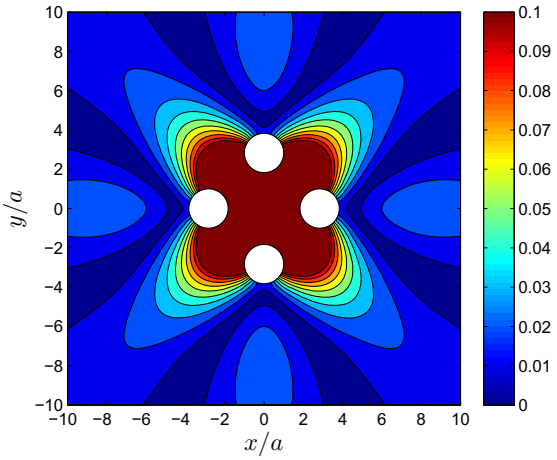

Figure 4: Free surface amplitudes at the first near-wave-free frequency around four rigidly connected cylinders oscillating in heave with unit amplitude. The colour axis is limited such that the radiation pattern external to the array may be seen.

This near-wave-free frequency has some interesting consequences. The Haskind relations relate the directionally averaged exciting forces to the damping coefficients. Therefore, a non-axisymmetric structure such as this will have different ratios of exciting force to damping (i.e. resonant response) at different incoming wave directions. For an optimum incoming wave direction this may lead to a very large resonant response, should the conditions for resonance be satisfied.

3 Eight cylinders

Porter and Evans [2008] found motion-trapping modes in axisymmetric shells of rectangular cross-section and many wave-free structures with an internal free surface have been reported. The simple array of four cylinders considered above is a poor

approximation to a shell-like structure, but exhibits a near-wave-free mode. This suggests that a symmetric array with more cylinders could more closely approximate a shell structure, and exhibit more complete wave-free behaviour. To this end, an array of 8 cylinders, moving as a rigid body, was analysed using DIFFRACT. The cylinders, of the same radius and draft as those considered in Section 2, were placed with centres evenly distributed around the circumference of a circle of radius $5a$. Note that this geometry falls outside the range considered by Porter and Evans, but was considered a convenient starting point. The heave damping coefficient for this structure, plotted on a logarithmic scale, is shown in Figure 5 and it is evident that there is strong wave-free behaviour at a frequency of around $ka = 0.42$. Indeed, the damping coefficients calculated by DIFFRACT at frequencies around the minimum (more accurately located at $ka = 0.4216$) were very small negative numbers, though monotonically increasing toward zero with increasing mesh refinement. (Such very small negative damping at a wave-free frequency was also observed by Newman [2008] where calculations were performed using WAMIT. These results would appear to be an artefact of the boundary element approximation in both codes.)

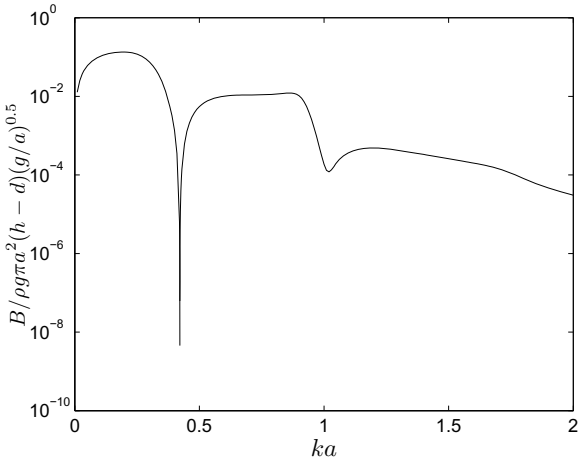

Figure 5: Heave damping of 8 rigidly connected cylinders, water depth $h = 4a$ as above.

This structure does not satisfy the resonance condition necessary for motion trapping in the geometry given, but the position of the resonance can be adjusted by changing the draft of the cylinders. Calculations indicate that an increase in draft of approximately 3.5% is sufficient to cause the resonance condition to be satisfied at the wave-free frequency. To the accuracy of the method used, the structure with the adjusted draft appears to be a motion-trapping structure, and can be constructed quite simply using this approach. The difficulty emphasised by Porter and Evans [2008] in finding a motion-trapping frequency due to the blow-up of the hydrodynamic coefficients at frequencies surrounding the wave-free frequency was not encountered, and may be due to their motion trapping being associated with higher modes than the pumping mode considered here.

Further comparisons of this structure with other known motion-trapping structures and related observations will be presented at the workshop.

Acknowledgement

H. Wolgamot was supported by a University of Oxford Clarendon Fund Scholarship.

References

DV Evans and R. Porter. Wave-free motions of isolated bodies and the existence of motion-trapped modes. *Journal of Fluid Mechanics*, 584(1):225–234, 2007.

CJ Fitzgerald and P. McIver. Passive trapped modes in the water-wave problem for a floating structure. *Journal of Fluid Mechanics*, 657:456–477, 2010.

H. Kagemoto and D.K.P Yue. Interactions among multiple three-dimensional bodies in water waves: an exact algebraic method. *Journal of Fluid Mechanics*, 166:189–209, 1986.

S.A. Mavrakos. Hydrodynamic coefficients for groups of interacting vertical axisymmetric bodies. *Ocean Engineering*, 18(5):485–515, 1991.

P. McIver and M. McIver. Trapped modes in the water-wave problem for a freely floating structure. *Journal of Fluid Mechanics*, 558(1):53–67, 2006.

P. McIver and M. McIver. Motion trapping structures in the three-dimensional water-wave problem. *Journal of Engineering Mathematics*, 58(1):67–75, 2007.

M.H. Meylan and R. Eatock Taylor. Time-dependent water-wave scattering by arrays of cylinders and the approximation of near trapping. *Journal of Fluid Mechanics*, 631:103, 2009.

JN Newman. Trapping of water waves by moored bodies. *Journal of Engineering Mathematics*, 62(4):303–314, 2008.

R. Porter and DV Evans. Examples of trapped modes in the presence of freely floating structures. *Journal of Fluid Mechanics*, 606:189–208, 2008.

P. Siddorn and R. Eatock Taylor. Diffraction and independent radiation by an array of floating cylinders. *Ocean Engineering*, 35:1289–1303, 2008.

H. Wolgamot, R. Eatock Taylor, P.H. Taylor, and C.J. Fitzgerald. The interaction factor for wave power in arrays. In *Proceedings of the 26th International Workshop on Water Waves and Floating Bodies*, 2011.

(*Abstract submitted to the 28th IWWWFB, Marseille, France, 7-10 April, 2013*)

Wave simulation in a 3D coupled numerical and physical wave basin

Z.W. Yang[1], H.B. Bingham[2], S.X. Liu[1]

[1] State Key Laboratory of Coastal and Offshore Engineering, Dalian University of Technology, China

[2] Department of Mechanical Engineering, Technical University of Denmark

E-mail: ouyangzhiwen@gmail.com, hbb@mek.dtu.dk, liusx@dlut.edu.cn

1. Introduction

The combination of numerical and physical models has increasingly been used for coastal or offshore water wave problems (Gierlevsen et al., 2003; Kofoed-Hansen et al., 2003). This approach allows the numerical model to focus on wave propagation in the offshore region and the physical model to treat the wave transformation in the near-shore region. The primary goal is to exploits the advantages of numerical and physical model to provide an improved description of full-scale, realistic engineering problems. However, the data transfer between the numerical and physical model is only on a stochastic level through bulk parameters, such as the significant wave height and spectral peak frequency.

Zhang et al. (2005, 2007) initially devised an ad hoc unified 3D wave generation theory to deterministically couple the numerical and physical wave basin. This theory accounts for shallow water wave generation theory and dispersive compensates based on the linear assumption. To improve the coupling accuracy, Yang et al. (2013) has extended the exiting model correct to second order, but only for wave flume. A range of stream function simulation tests has confirmed the accuracy and efficiency of this model.

This paper presents recent and preliminary work towards the extension of coupling theory of numerical and physical models to account for 3D coupled wave basin. The derivation of this new model is based on the second-order coupling model (Yang et al., 2013) and the ad hoc unified 3D wave generation theory (Zhang et al., 2007). Using a well-established 3D flexible-order, finite-difference-based fully nonlinear potential flow model (OceanWave 3D) devised by Engsig-Karup et al. (2009) for the numerical wave calculation and a 2D piston-type wavemaker for the physical wave generation, practical applications on unidirectional and multidirectional, regular and irregular, wave cases are presented.

2. Formulation and solution

A Cartesian coordinates (x, y, z) is adopted with xy-plane cincident with the undisturbed free surface and the z-axis directed upwards. The whole simulation domain is divided into a numerical region and a physical region. At the boundary between the two regions, the following condition must be satisfied,

$$U_N(x_0, y, t) = U_P(x_0, y, t) \tag{1-a}$$

$$V_N(x_0, y, t) = V_P(x_0, y, t) \tag{1-b}$$

where, (U_N, V_N) denotes the numerical depth-averaged velocity at x- and y-axis, respectively, which can be obtained from a suitable numerical model, or even any nonlinear wave theory. (U_P, V_P) represent the equivalents for physical model which is mainly used to determine the motion of wave paddle, x_0 the mean position between two models, t the time variable.

Considering the physical region, under the assumption of an inviscid, incompressible fluid undergoing irrotational motion, we can define the velocity potential, $\phi(x, z, t)$. The free-slip condition on the wavemaker reads

$$X_{0t} = \phi_x - \nabla\phi \cdot \nabla X_0 \qquad \text{on } x=X_0 \tag{2}$$

where $X_0=X_0(y, z, t)$ is wave paddle position , and ∇ denotes the vertical gradient $\nabla=(\partial y, \partial z)$. The previously defined (ϕ, $\tilde{U}$, X_0) can be further expanded in a perturbation series as

$$\phi = \varepsilon\phi^{(1)} + \varepsilon^2\phi^{(2)} + \ldots \tag{3-a}$$

$$\tilde{U} = \varepsilon\tilde{U}^{(1)} + \varepsilon^2\tilde{U}^{(2)} + \ldots \tag{3-b}$$

$$X_0 = \varepsilon X_0^{(1)} + \varepsilon^2 X_0^{(2)} + \ldots \tag{3-c}$$

where $\tilde{U}=(U, V)$, ε is a small ordering parameter proportional to the wave steepness H/L, with H being the wave height and L the wavelength. Combining Eqs. (2) with (3a) and (3c) yields

$$\varepsilon^1: \qquad \phi_x^{(1)} = \frac{\partial X_0^{(1)}(y,t)}{\partial t} \tag{4-a}$$

$$\varepsilon^2: \qquad \phi_x^{(2)} + \frac{\partial X_0^{(1)}(y,t)}{\partial y}\phi_y^{(1)} = \frac{\partial X_0^{(2)}(y,t)}{\partial t} \tag{4-b}$$

where we have considered a piston wavemaker such that the wave paddle position is rewritten as $X_0(y, z)$. Applying the shallow water assumption and considering the boundary condition of (1), Eq. (4) can be rewritten as

$$\varepsilon^1: \qquad \frac{\partial X_{0,sw}^{(1)}(y,t)}{\partial t} = U_N^{(1)}(X_{0,sw}^{(1)}(y,t),\, y,\, t) \tag{5-a}$$

$$\varepsilon^2: \qquad \frac{\partial X_{0,sw}^{(2)}(y,t)}{\partial t} + \frac{\partial X_{0,sw}^{(1)}(y,t)}{\partial y} V_N^{(1)}(X_{0,sw}^{(1)}(y,t),\, y,\, t) = U_N^{(2)}(X_{0,sw}^{(2)}(y,t),\, y,\, t) \tag{5-b}$$

where superscript "*sw*" indicates the use of shallow water theory for obtaining the paddle position from the depth-averaged particle velocity at the mean paddle position. One can note that this latter equation has the same form as that of Zhang et al. (2007), except that we respectively treat the first- and second-order solution. As the same manner with Zhang et al. (2007), the final paddle position should be corrected by wave dispersivity,

$$X_0^{(1)}(y,t) = F^{-1}\left[\Lambda_1 \cdot F\left[X_{0,sw}^{(1)}(y,t)\right]\right] \tag{6-a}$$

$$X_0^{(2)}(y,t) = F^{-1}\left[\Lambda_2 \cdot F\left[X_{0,sw}^{(2)}(y,t)\right]\right] \tag{6-b}$$

where Λ_1 and Λ_2 are the first- and second-order coupling coefficients, which can be found in Yang et al. (2013). F and F^{-1} represent the forward and inverse Fourier transform, respectively. Eqs. (6a) and (6b) give the dispersion correction needed when deviating from the shallow water limit.

To solve Eqs. (5a) and (5b), five points Lagrange interpolation method and fourth-order Runge-Kutta scheme are used to smooth the nonlinear distribution of velocity around the moving paddle and treat the time discretization, respectively. Finally, the combined wave paddle position can be given by

$$X_0(y,t) = X_0^{(1)}(y,t) + X_0^{(2)}(y,t) \tag{7}$$

3. Experimental validation and conclusions

To verify the new model, some unidirectional and multidirectional regular waves and irregular wave experiments has so far been tested in a 3D coupled numerical and physical wave basin. OceanWave3D model of Engsig-Karup et al. (2009) was used to simulate the numerical waves. The physical experiments were carried out in the multifunction wave basin of the Dalian University of Technology. The proposed coupling model is applied as the link between the numerical and the physical model. See Fig. 1 for the sketch. Several tests are presented below. In all tests, the numerical model is run beyond the wavemaker to provide the numerical wave information for obtaining the coupling wavemaker signals and comparing the resulting waves. For regular waves, a periodic stream function theory (Fenton, 1988) is applied to provide the depth-averaged velocity. For irregular waves, a standard *JONSWAP* spectrum was used. Various wave periods and heights are chosen for considering the dimensionless water depth kh and nonlinearity H/L_0, where L_0 is the wavelength in deep water according to linear theory.

Figure 2 shows regular wave results from the steepest-shallowest (where H/L_0=0.064, kh=0.63) and deepest water wave cases (where H/L_0=0.125, kh=5.59), respectively, and compares measured time series of surface elevation at three selected positions (Ref. point 8, 11 and 13, see Figure 1, right panel) in the wave basin, where the wave direction is α=15^o. On both plots the measurements generally agree with theoretical profiles though some instability can also been found in the left panel of Figure 2.

Figure 3 shows a unidirectional irregular wave case, with the wave direction is 30^o and a significant wave height is H_{m0}=0.12m, a peak period of T_p=1.2s, and the relevant shape parameter, γ=3.36, σ_a=0.07, σ_b=0.09. Comparisons of wave profiles are made on the same reference points. Figure 4 shows the similar comparison with that of Figure 3, except that the wave case chosen is multidirectional irregular waves, with the mean wave direction is 30^o. A good agreement is observed with the experimental data.

Conclusion from a larger set of experimental data is that the proposed coupled numerical and physical model is generally reliable for deterministically combining 3D wave simulation. Comparisons of the proposed model with the previous method and relevant parametric analysis are not included here for lack of paper space, but will be presented at the Workshop.

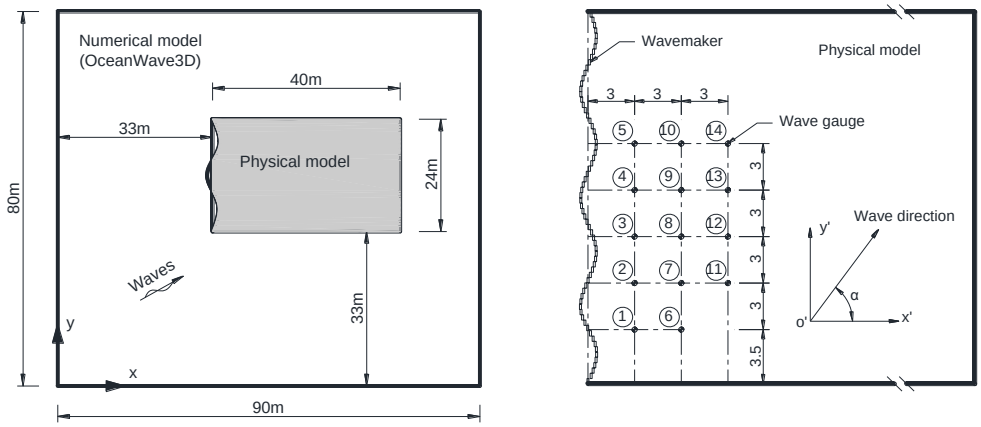

Figure 1. *Sketch of the coupled numerical and physical wave basin (left panel), and the layout of the physical basin (right panel).*

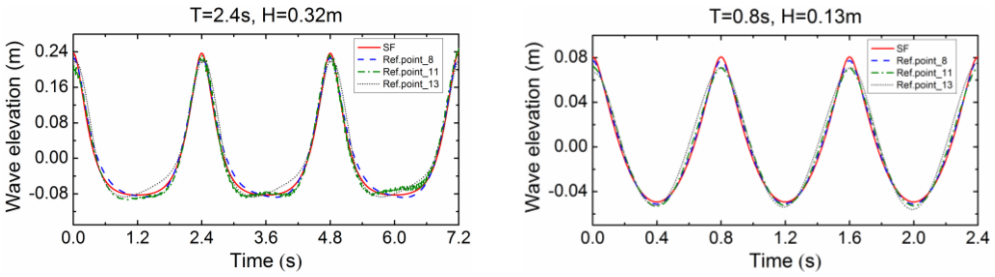

Figure 2. *Time series of surface elevations measured at different gauges for unidirectional regular waves, compared with the theoretical stream function theory (SF).*

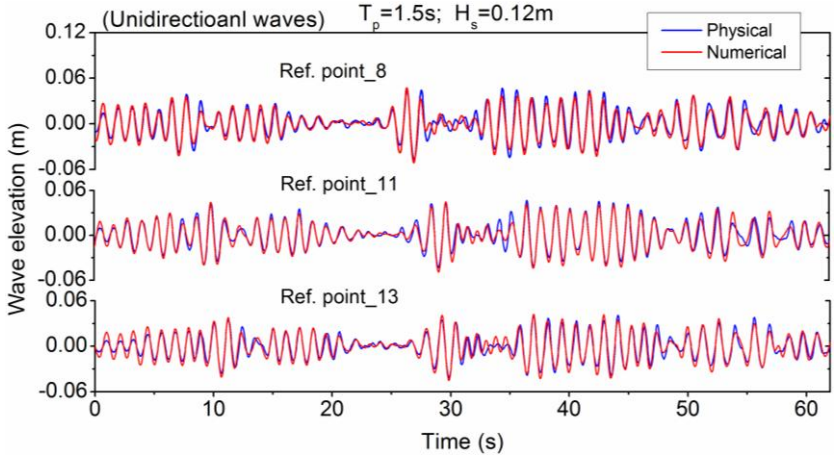

Figure 3. *Time series of surface elevations measured at different gauges for unidirectional irregular waves, compared with the numerical results.*

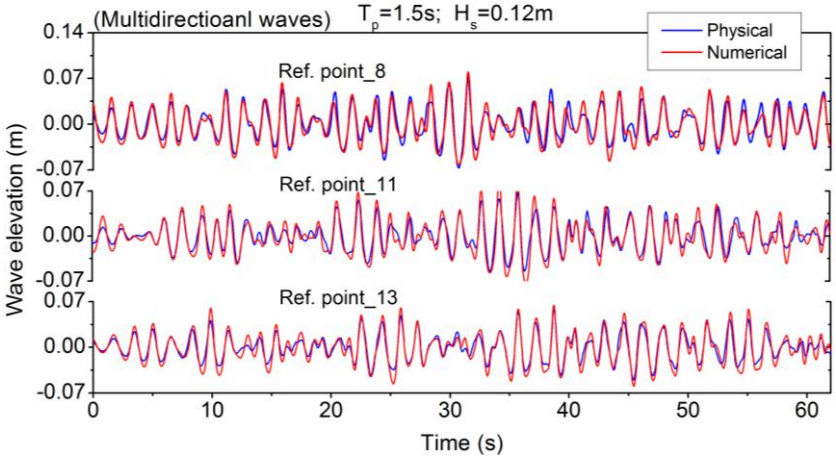

Figure 4. *Time series of surface elevations measured at different gauges for multidirectional irregular waves, compared with the numerical results.*

References

Engsig-Karup, A.P., Bingham, H.B., Lindberg, O., 2009. An efficient flexible-order model for 3D nonlinear water waves. Journal of Computational Physics 228, 2100–2118.

Fenton, J.D., 1988. The numerical solution of steady water wave problems. Computers and Geosciences 14(3), 357–368.

Gierlevsen, T., Vargas, B.M., Pires, V.P.L., Acetta, D., 2003. Numerical and physical modelling of storm at Rio Janeiro yacht club. COPEDEC VI, Colombo, Sri Lanka, 15-19 Sept. 2003.

Kofoed-Hansen, H., Sloth, P., Sørensen, O. R., et al. 2003. Combined numerical and physical modelling of seiching in exposed new marina. Proceedings of the 27th International Conference on Coastal Engineering, Sydney, Australia, 2000. 3601-3614.

Yang, Z., Liu, S., Bingham, H.B., Li, J., 2013. Second-order theory for coupling numerical and physical wave tanks: Derivation, evaluation and experimental validation. Coastal Engineering 71, 37-51.

Zhang, H., Schäffer, H.A., Jakobsen, K.P., 2007. Deterministic combination of numerical and physical coastal wave models. Coastal Engineering 54, 171-186.

Zhang, H., Schäffer, H.A., 2005. Waves in numerical and physical wave basins—a deterministic combination. Proceedings of Waves 2005, Madrid, Spain, July, 2005.

Hypersingular integral-equation solution for a finite-draft surface-piercing cylindrical shell at high- and low-frequency

Ronald W. Yeung* and Mohamed Hariri Nokob†
Department of Mechanical Engineering
University of California at Berkeley
Berkeley, CA 94720-1740, USA
* Correspondence author: rwyeung@berkeley.edu
† Presenter: mhariri@berkeley.edu

1. Background

A monocolumn structure, with a circular moonpool and internal dock to act as a so-called HUB, is considered as an intermediate station for transporting people to offshore locations in the Santos Oilfield in Brazil [1]. Such designs are promising and considered to be built. A split opening in the design allows marine vehicles in and out, thus acting as a floating harbor. In this work, we present a simplified model of such a harbor and develop the numerics to analyze the problem eventually. The body S considered is a floating bottomless harbor of circular cylindrical shape of radius a and draft d floating in deep water (see Fig.1). Modeling of similar problems using eigen-function expansion method (EEM) gained interest in the 80's (see, e.g. Yeung [2]).

We consider a general point $P=(x,y,z)$ in the fluid domain and another point $Q=(\xi,\eta,\zeta)$ on the surface of S. The coordinate system is taken to be on the still free surface with the y axis pointing upwards. We can state the "standard" problem as follows:

$$\nabla^2\phi = 0 \tag{1}$$

$$\phi_y - \nu\phi = 0,\ y = 0;\quad \nabla\phi = 0,\ y \to -\infty \tag{2}$$

$$\phi_n = \vec{V} \bullet \vec{n}(P),\ \vec{V} = (U_1, 0, U_2),\quad \text{for } P \text{ on } S \tag{3}$$

Here, the velocity potential is $\Phi = \mathrm{Re}\{\phi e^{-i\omega t}\}$ and (U_1, U_2) are the surge and sway velocities of S. The frequency factor $\nu = \omega^2/g$ is either zero or infinite in this work. The thickness of the boundary wall is infinitely thin and accordingly, special treatment is required as compared to bodies of finite thickness. The BIM is known to have difficulties dealing with this kind of problems. Hence we will use a special formulation for such thin-body geometry. The general integral equation over a three dimensional environment is given by:

$$4\pi\phi(P) = -\iint_S \phi(Q)\frac{\partial G(P,Q)}{\partial n_Q} - G(P,Q)\frac{\partial \phi(Q)}{\partial n_Q} dS_Q \tag{4}$$

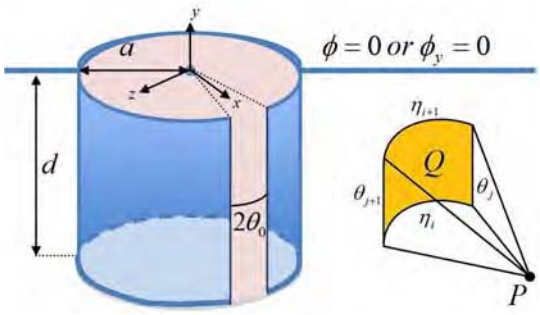

Figure 1: Sketch of the shell S and an arc-surface panel

where G is a suitable Green's function. In this work, we consider the following form of G:

$$G = \frac{1}{r_1} \pm \frac{1}{r_2} + H \tag{5}$$

$$r_{1,2} = \sqrt{(x-\xi)^2 + (y \mp \eta)^2 + (z-\varsigma)^2} \tag{6}$$

The $+(-)$ sign in (5) is chosen if the zero- (or infinite-) frequency case is considered. r_1 and r_2 correspond to the usual singular source and image reflection about $y=0$, respectively. We take $H=0$ here as it is regular when $P \to Q$ and can be handled relatively easily compared with the singular term r_1. For the thin shell case, only the dipole term remains, thus (4) reduces to

$$4\pi\phi(P) = -\iint_S [\phi(Q)]\frac{\partial G(P,Q)}{\partial n_Q} dS_Q \tag{7}$$

Here, $[\phi(Q)] \equiv \phi(a^+) - \phi(a^-)$ is the jump of ϕ across S and the integration is over the outside S only. Differentiation of (7) in the normal direction gives:

$$4\pi\frac{\partial\phi(P)}{\partial n_P} = \frac{-\partial}{\partial n_P}\iint_S [\phi(Q)]\frac{\partial\, G(P,Q)}{\partial n_Q} dS_Q \tag{8}$$

In (8), this normal velocity is explicitly given by (3) with a highly singular kernel. Only one function ϕ is present in this formulation. In fact, ϕ is proportional to the pressure difference across S and its solution is sufficient to compute the forces acting on the body.

The derivative in (8) can be taken under the integral sign on the condition that the integral be interpreted as a Hadamard finite part integral [3][4]. These integrals are usually difficult to compute and cannot be treated using standard quadrature method. The safest way to deal with them is by analytical integration when possible. This is the case in [5] and [6] for a flat surface (contour). The integral can also be treated by a process of regularization where the equation is written in terms of the unknown and its tangential derivative [3]. This procedure reduces the singularity of the integrand but leads to tangential derivatives, which are not needed for the problem and suffer from their own computational errors. By some transformations and Fourier expansions, the authors in [7] were successful in transforming the hypersingular equation to a one dimensional standard integral equation for the case of a flat disc. In this work, we tackle the problem hypersingularity using a combination of analytical integration and singularity separation.

2. Analytical Integration of the Kernel

The crux of the issue is to be able to evaluate the singular integrand of the integral equation (8):

$$\int_{\theta_0}^{2\pi-\theta_0}\int_{-d}^{0} a[\phi(Q)]\frac{\partial^2 1/r}{\partial n_P \partial n_Q}\,d\eta d\theta \tag{9}$$

This applies for both r_1 and r_2 in (5). In practice, this integral will be discretized and only the integral over a circular-arc panel quad of $(\eta_i,\eta_{i+1},\theta_j,\theta_{j+1})$ is needed, where i and j denote the vertical and circumferential grid index (Fig. 1). The potential jump is assumed constant over each panel. The normal to the solid boundary in this case is given by:

$$\vec{n}=[\cos\theta,0,\sin\theta] \tag{10}$$

on the outer side and the negative of that on the inner side. Defining α so that over the surface of the body $[x,z]=a[\cos\alpha,\sin\alpha]$ and noting that $[\xi,\zeta]=a[\cos\theta,\sin\theta]$, we get, with some effort:

$$\frac{\partial^2 1/r}{\partial n_P \partial n_Q}=\frac{\cos\delta}{(2a^2(1-\cos\delta)+K^2)^{3/2}} + \frac{3a^2(1-\cos\delta)^2}{(2a^2(1-\cos\delta)+K^2)^{5/2}} \tag{11}$$

with the definitions $\delta=\theta-\alpha$ and $K=\eta\pm y$ depending on whether r_1 or r_2 is used. The integration limits K_i and δ_j are defined in an obvious manner. Analytical integration in the vertical direction over the panel surface leads to:

$$\left[\frac{K}{2a^2(1-\cos\delta)\sqrt{2a^2(1-\cos\delta)+K^2}} + \frac{K(1-\cos\delta)}{2(2a^2(1-\cos\delta)+K^2)^{3/2}}\right]_{K_i}^{K_{i+1}} \tag{12}$$

The case when $\delta=0$ has a different result but is insignificant for the final evaluation. The expression of (12) has to be integrated circumferentially next over δ on the panel. The second term integral is regular with no singular points and can be integrated numerically with ease. The first integral is singular at *δ=0*. Using trigonometric identity, we can write the $\delta-$integral as:

$$\int_{\delta_j}^{\delta_{j+1}}\frac{1}{4a^2\sin^2\frac{\delta}{2}}\left[\frac{K}{\sqrt{4a^2\sin^2\frac{\delta}{2}+K^2}}\right]_{K_i}^{K_{i+1}}d\delta \tag{13}$$

Three cases arise: $K_i<K_{i+1}<0$, $0<K_i<K_{i+1}$, and $K_i<0<K_{i+1}$. The first 2 cases are treated the same way and the integral (13) is made regular as follows:

$$\pm\int_{\delta_j}^{\delta_{j+1}}\frac{1}{4a^2\sin^2\frac{\delta}{2}}\Big(f(\delta,K_{i+1})-f(\delta,K_i)\Big)d\delta \tag{14}$$

$$f(\delta,K)=\frac{|K|-\sqrt{4a^2\sin^2\frac{\delta}{2}+|K|^2}}{\sqrt{4a^2\sin^2\frac{\delta}{2}+|K|^2}} \tag{15}$$

The + (−) sign in (14) is used for the first (second) case. The absolute values are merely enforced to make the correct Taylor series expansion in what follows. The fact that this integral is *regular* can be better seen from its Taylor series near $\delta=0$:

$$\frac{f(\delta,K)}{4a^2\sin^2\frac{\delta}{2}}=\frac{1-\sqrt{4S+1}}{4K^2S\sqrt{4S+1}} =\frac{1-3S+10S^2-35S^3}{2K^2}+O(\frac{S^4}{K^2}) \tag{16}$$

with $S\equiv\left(a^2\sin^2\frac{\delta}{2}\right)\Big/K^2$. (17)

This expansion can also be used for the numerical integration when variable S is sufficiently small (<0.01). For the third case ($K_i<0<K_{i+1}$), (13) becomes:

$$\int_{\delta_j}^{\delta_{j+1}}\frac{1}{4a^2\sin^2\frac{\delta}{2}}\Big(f(\delta,K_{i+1})+f(\delta,K_i)\Big)\,d\delta + \int_{\delta_j}^{\delta_{j+1}}\frac{1}{2a^2\sin^2\frac{\delta}{2}}d\delta \tag{18}$$

The second integral in (18) is indeed the singular part and can be integrated analytically as follows:

$$\int_{\delta_j}^{\delta_{j+1}}\frac{1}{2a^2\sin^2\frac{\delta}{2}}d\delta=-\frac{1}{a^2}(\cot\frac{\delta_{j+1}}{2}-\cot\frac{\delta_j}{2}) \tag{19}$$

while the first integral is regular as for the previous cases.

In this work, we are mainly interested in the added mass of the body. That is given by (surge and sway alike). In the present notations:

$$\mu_{11} = \frac{M_{11}}{2\rho\pi a^2 d}$$

$$= \frac{1}{2\pi a^2 d U_1} \int_{\theta_0}^{2\pi-\theta_0} \int_{-d}^{0} a[\phi_1(Q)]\cos\theta d\eta d\theta \qquad (20)$$

$$= \frac{1}{2\pi a d U_1} \sum_{j=0}^{N_2} \sum_{i=0}^{N_1} [\phi_1(Q)]_{ij} \cos\theta_j \Delta\eta \Delta\theta$$

Here ρ is the fluid density. The case for roll and pitch is very similar and the results are expected to be so as well and thus will not be shown here for brevity.

3. Computational Results

The hypersingular integral(-equatiuon) method (HIM) is verified by comparing the results to those from an alternative treatment using an eigenfunction expansion method that follows the work of [8]. Unlike the case of [2] or [8], there is a significant increase in the number of unknowns with the open slit, since the vertical and circumferential eigenfunctions are fully coupled. A circumferential uniform grid is used for the HIM, as this will allow the use of rules of repetition to allow efficient computations of the influence coefficients of the integral equation (8). In fact, a grid with a cosine distribution was found to produce only a slight improvement. The EEM coded was designed for finite water depth and finite frequency, while ideally, for comparison, we would like to use a method designed for infinite depth. Nevertheless, by taking the frequency of the EEM code very low and very large, the limiting behavior of the potentials can be obtained. Naturally, numerical difficulties result in these extreme frequency limits and we only expect the EEM results to be sufficiently close to the real solutions. The HIM has the advantage that a geometry with a slit opening requires the same computation time as for the closed body, contrary to the EEM which suffers from long computation times with an open body because of the large number of modal functions required for convergence.

Table 1 (page 4) shows the surge added-mass results for the closed column ($\theta_o = 0$) using the current method and the EEM, with the conditions of the latter taken close to their maximum allowed condition of the code. We consider 3 cases of mesh sizes of ($N_1 \times N_2$) in Eqn. (20): 20x20, 30x30, and 40x40 panels for the HIM and 800 terms for the vertical modes of the EEM. Successive columns of the table corresponds to the normalized surge added mass for increasing values of d/a, at zero frequency. Results for the three mesh sizes, are listed, with errors from the HIM computations compared to the EEM solution, which is highly accurate for the closed slit geometry (h: domain depth/a, K: wave-number). It is clear from this table that the results match quite well. The results compare well for the case of a nonzero slit opening as well, but are not shown here for brevity. For these open-slit cases, the HIM computes much faster than the EEM. Figs. 2 and 3 show the distribution of the jump in the potential (hence the pressure difference on the shell) for the surge and sway motion as indicated in the caption. The slit has a 60-degree opening. The fact that the body acts as a doublet in the far field is clear from the positive pressure on one side and negative on the other. This is not symmetric about the *Oyz* plane because of the nonzero opening. Surging in the direction of the slit lead to a large negative pressure at these sharp edges, where flow separation would be expected in a real fluid. Swaying in the direction normal perpendicular to the slit-opening leads to a solution similar to the closed cylinder. The drop in pressure at the bottom rim of the shell is also evident. Figs. 4 and 5 are plots of the surge and sway added masses as a function of the draft/radius ratio for several slit openings at these limiting frequencies. The coupling added masses $\mu_{12} = \mu_{21}$ are zero by symmetry. Results for added mass in direction $m(=1,2)$ for a body moving in an arbitrary direction β, with respect to the x–axis, can be obtained as a linear combination of the surge and sway results in that direction as follows:

$$\mu_{\beta m} = \mu_{1m}\cos\beta + \mu_{2m}\sin\beta \qquad (21)$$

We note that the added masses (20) approach a fraction of 2 times the mass of the fluid in the cylinder when the draft increases to a large value. The fraction depends on θ_o. The zero-frequency limit solutions approach these limits faster than the infinite-frequency case. In the meeting, the complex behavior of the results with the wave effects *H* in Eqn. (5) will be shown.

5. Acknowledgement. The authors would like to thank Prof. Sergio Sphaier of UFRJ, Brazil, for bringing attention of this design in OMAE-2012. We also acknowledge the American Bureau of Shiping for partial support of this work.

6. References

[1] M. B. A. Moreira, M. Ferreira, and S. H. Sphaier, "Monocolumn hull with internal dock: an alternative for offshore transport of people," in *Proceedings of OMAE 2012*, Rio de Janeiro, Brazil, 2012.

[2] R. W. Yeung, "Added mass and damping of a vertical cylinder in finite-depth waters," *Applied Ocean Research*, vol. 3, no. 3, pp. 119–133, Jul. 1981.

[3] P. A. Martin and F. J. Rizzo, "On Boundary Integral Equations for Crack Problems," *Proceedings of the Royal Society of London. Series A, Mathematical and Physical Sciences*, vol. 421, no. 1861, pp. 341–355, Feb. 1989.

[4] G. Krishnasamy, L. W. Schmerr, T. J. Rudolphi, and F. J. Rizzo, "Hypersingular Boundary Integral Equations: Some Applications in Acoustic and Elastic Wave Scattering," *Journal of Applied Mechanics*, vol. 57, no. 2, p. 404, 1990.

[5] N. F. Parsons and P. A. Martin, "Scattering of water waves by submerged plates using hypersingular integral equations," *Applied Ocean Research*, vol. 14, no. 5, pp. 313–321, 1992.

[6] L. Farina and P. A. Martin, "Scattering of water waves by a submerged disc using a hypersingular integral equation," *Applied Ocean Research*, vol. 20, no. 3, pp. 121–134, Jun. 1998.

[7] P. A. Martin and L. Farina, "Radiation of water waves by a heaving submerged horizontal disc," *Journal of Fluid Mechanics*, vol. 337, pp. 365–379, 1997.

[8] C. J. R. Garrett, "Bottomless harbours," *Journal of Fluid Mechanics*, vol. 43, no. 03, pp. 433–449, 1970.

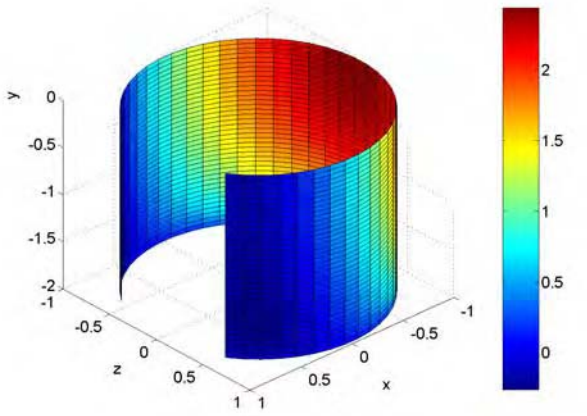

Figure 2: Potential jump over the surface of a surging shell with $d/a = 2, \theta_0 = \pi/6$

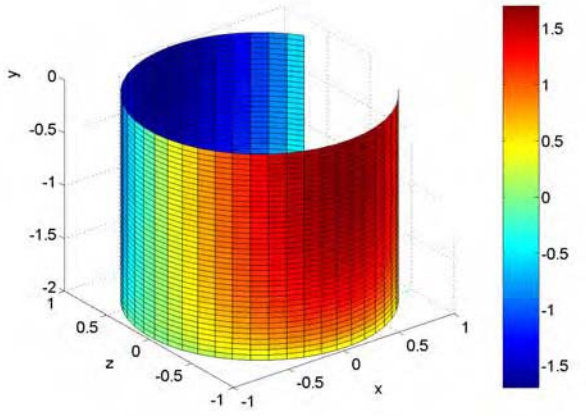

Figure 3: Potential jump over the surface of a swaying shell with $d/a = 2, \theta_0 = \pi/6$

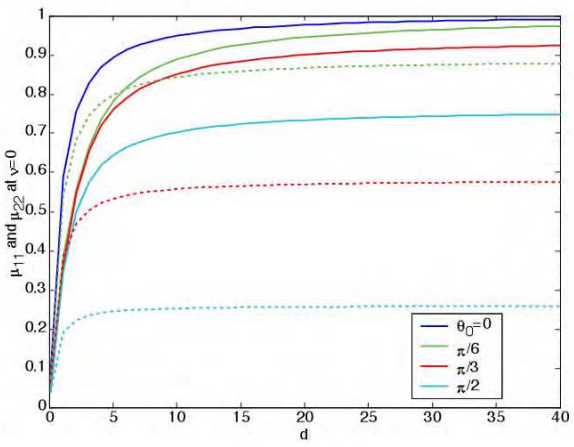

Figure 4: Added mass μ_{11} (solid) and μ_{22} (dashed) at zero frequency versus d/a for various slit opening

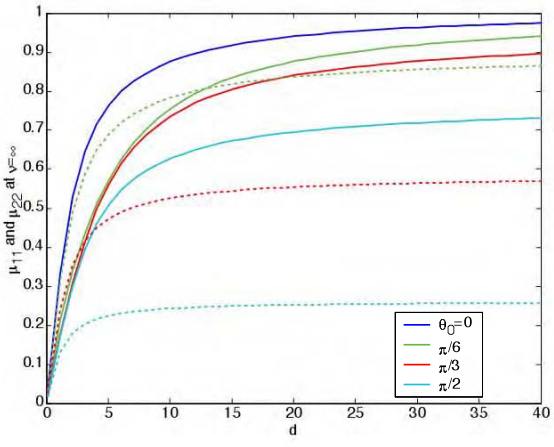

Figure 5: Added mass μ_{11} (solid) and μ_{22} (dashed) at infinite frequency vs. d/a for various slit opening

Table 1: Convergence of the HIM and comparison to EEM for zero-frequency case (see text for details)

d/a	1	2	5	10	20	40
HIM results						
HIM20 (20-20)	0.5680	0.7545	0.9018	0.9571	0.9850	0.9975
HIM30 (30-30)	0.5634	0.7490	0.8959	0.9513	0.9797	0.9935
HIM40 (40-40)	0.5612	0.7464	0.8932	0.9486	0.9772	0.9914
error 20-40* (%)	-1.2195	-1.0821	-0.9636	-0.8909	-0.7928	-0.6151
error 30-40* (%)	-0.3885	-0.3401	-0.3011	-0.2795	-0.2533	-0.2066
EEM results (800-1)	0.5597	0.7396	0.8880	0.9446	0.9721	0.9869
parameters	h=10,K=0.001	h=10,K=0.001	h=20,K=0.001	h=30,K=0.001	h=50,K=0.001	h=100,K=0.001
error HIM20-EEM* (%)	-1.4930	-2.0131	-1.5517	-1.3198	-1.3306	-1.0788
error HIM30-EEM* (%)	-0.6597	-1.2643	-0.8854	-0.7058	-0.7882	-0.6683
error HIM40-EEM* (%)	-0.2702	-0.9210	-0.5825	-0.4251	-0.5335	-0.4608

GN equations to describe internal solitary waves in two-layer fluid

B.B. Zhao and **W.Y. Duan**

College of Shipbuilding Engineering, HEU, 150001 Harbin (China)
Email: zhaobin_1984@yahoo.com.cn

Green-Naghdi (GN) equations in two-layer fluid are derived and used to describe internal solitary waves. Two methods to generate internal waves are studied here. The first method is to set an initial wave profile and velocity given by KdV theory. This method can not be used to generate internal solitary wave of large amplitude. Gravity collapse is used as the second method to generate internal solitary wave of large amplitude. The second method is similar to that in the experiment of Grue *et al.* (1999). The results by GN theory are in good agreement with those by the fully nonlinear model developed in Grue *et al.* (1999).

1 Introduction

In GN theory, nonlinear boundary conditions are satisfied on the instantaneous free surface. Demirbilek and Webster (1992) applied level-2 GN theory to shallow-water 2D problems. Zhao *et al.* (2010) applied the GN level-2 theory to 3D case. Zhao *et al.* (2009) applied the GN level-3 theory to 2D water wave simulations. Furthermore, Zhao and Duan (2012) applied higher level (level-5 and level-7) to 2D shallow-water wave problems and get fully satisfactory results. They achieved that the converged GN results are in excellent agreement with experimental results. Duan and Zhao (2012) applied GN theory to underwater landslide-induced tsunamis.

To authors' knowledge, GN theory has not been applied to flows in two-layer fluid before. For internal solitary waves, Grue *et al.* (1999) made experiments and introduced a fully nonlinear model. Their numerical procedure is started by prescribing a small amplitude and solving the equations iteratively. Then, they solve equations using Newton-Raphson's method with initial guess extrapolated from the previous solution. In this paper, we simulate internal solitary waves by using GN theory in two-layer fluid in time domain.

2 GN Theory

The GN equations for one-layer flow in Webster *et al.* (2011) are given by :

$$\frac{\partial \beta}{\partial t} = \sum_{n=0}^{K} \beta^n \left(w_n - \frac{\partial \beta}{\partial x} u_n \right) \tag{1}$$

$$\frac{\partial}{\partial x}\left(G_n + gS_n\right) + nE_{n-1} - \alpha^n \frac{\partial}{\partial x}\left(G_0 + gS_0\right) + \left(\beta^n - \alpha^n\right)\frac{\partial}{\partial x}\left(\frac{\hat{p}}{\rho}\right) = 0 \quad \text{for} \quad n = 1, 2, \cdots, K \tag{2}$$

where K stands for the level of GN theory, $z = \beta$ for the free surface, $z = \alpha$ for the bottom, expressions of E_n, S_n and G_n can be found in Webster *et al.* (2011).

For two-layer problems, we set the bottom as $z = \alpha(x,t)$, the interface as $z = \beta(x,t)$ and the free surface as $z = \gamma(x,t)$. The GN equations in two-layer fluid are then for upper layer :

$$\frac{\partial \gamma}{\partial t} = \sum_{n=0}^{K^U} \gamma^n \left(w_n^U - \frac{\partial \gamma}{\partial x} u_n^U \right) \tag{3}$$

$$\frac{\partial}{\partial x}\left(G_n^U + gS_n^U\right) + nE_{n-1}^U - \beta^n \frac{\partial}{\partial x}\left(G_0^U + gS_0^U\right) + \left(\gamma^n - \beta^n\right)\frac{\partial}{\partial x}\left(\frac{\hat{p}^U}{\rho^U}\right) = 0 \tag{4}$$

for $n = 1, 2, \cdots, K^U$ with K^U as the GN level in upper layer, and for lower layer :

$$\frac{\partial \beta}{\partial t} = \sum_{n=0}^{K^L} \beta^n \left(w_n^L - \frac{\partial \beta}{\partial x} u_n^L \right) \tag{5}$$

$$\frac{\partial}{\partial x}\left(G_n^L + gS_n^L\right) + nE_{n-1}^L - \alpha^n \frac{\partial}{\partial x}\left(G_0^L + gS_0^L\right) + \left(\beta^n - \alpha^n\right)\frac{\partial}{\partial x}\left(\frac{\hat{p}^L}{\rho^L}\right) = 0 \tag{6}$$

for $n = 1, 2, \cdots, K^L$ with K^L as the GN level in the lower layer.

The dynamic boundary conditions are

$$\hat{p}^L = p|_{z=\beta} = \bar{p}^U = \rho^U G_0^U + \rho^U g S_0^U + \hat{p}^U \tag{7}$$

$$\hat{p}^U = p|_{z=\gamma} = 0 \tag{8}$$

ensuring the continuity of pressure through the interface and pressure at the free surface.

3 Numerical algorithm

The equations (4) and (6) make a system of $(K^U + K^L)$ coupled, quasi-linear partial differential equations for the $(K^U + K^L)$ unknowns. The unknowns are expressed here as a $(K^U + K^L)$-dimensioned vector, $\boldsymbol{\xi}(x,t)$ and the equations are rewritten in the form as :

$$\tilde{\mathbf{A}}\dot{\boldsymbol{\xi}}_{,xx} + \tilde{\mathbf{B}}\dot{\boldsymbol{\xi}}_{,x} + \tilde{\mathbf{C}}\dot{\boldsymbol{\xi}} = \tilde{\mathbf{f}} \tag{9}$$

where,

$$\dot{\boldsymbol{\xi}} = [\dot{u}_0^U, \quad \dot{u}_1^U, \quad \cdots, \quad \dot{u}_{K^U-1}^U, \quad \dot{u}_0^L, \quad \dot{u}_1^L, \quad \cdots, \quad \dot{u}_{K^L-1}^L]^T \tag{10a}$$

$$\dot{\boldsymbol{\xi}}_{,x} = [\dot{u}_{0,x}^U, \quad \dot{u}_{1,x}^U, \quad \cdots, \quad \dot{u}_{K^U-1,x}^U, \quad \dot{u}_{0,x}^L, \quad \dot{u}_{1,x}^L, \quad \cdots, \quad \dot{u}_{K^L-1,x}^L]^T \tag{10b}$$

$$\dot{\boldsymbol{\xi}}_{,xx} = [\dot{u}_{0,xx}^U, \quad \dot{u}_{1,xx}^U, \quad \cdots, \quad \dot{u}_{K^U-1,xx}^U, \quad \dot{u}_{0,xx}^L, \quad \dot{u}_{1,xx}^L, \quad \cdots, \quad \dot{u}_{K^L-1,xx}^L]^T \tag{10c}$$

and $\tilde{\mathbf{A}}$, $\tilde{\mathbf{B}}$, $\tilde{\mathbf{C}}$ and $\tilde{\mathbf{f}}$ are functions of x and $\boldsymbol{\xi}$ and its spatial derivatives which are not given here for the sake of simplicity. This system can be easily solved by Thomas algorithm used in Demirbilek & Webster (1992). This algorithm is further improved in Zhao & Duan (2012).

4 Test cases

In this section, we will give some numerical simulations of internal solitary waves. The first method we used here is to set an initial wave shape on the interface. The initial shape and velocity are from the KdV Theory given in Long (1956) and in Grue *et al.* (1999).

We want to reproduce the same solitary wave generated by Grue *et al.* (1999). Their physical experiment are calibrated with a layer of fresh water above a layer of brine. The depth of the brine is $h_1 = 62$cm and the depth of the fresh water is $h_2 = 15$cm. The density of brine is 1.022g/cm^3 and the density of fresh water is 0.999g/cm^3.

On Figure 7 in their paper, the wave profile is given at a fixed position. Five wave profiles with $a/h_2 = 0.22$, 0.36, 0.91, 1.23 and 1.51 with a as the internal solitary amplitude, are shown. The cases with $a/h_2 = 0.22$ and $a/h_2 = 0.91$ are simulated here by using GN theory.

For $a/h_2 = 0.22$, the initial shape with amplitude $a = 0.22h_2 = 0.33$m is shown on the left of Figure 1. After 600 seconds propagation, an internal solitary wave of amplitude = 0.0351m is shown in the middle of Figure 1 (Note that the initial solitary wave amplitude is 0.033m). The KdV results with amplitude = 0.0351m is shown on the right of Figure 1.

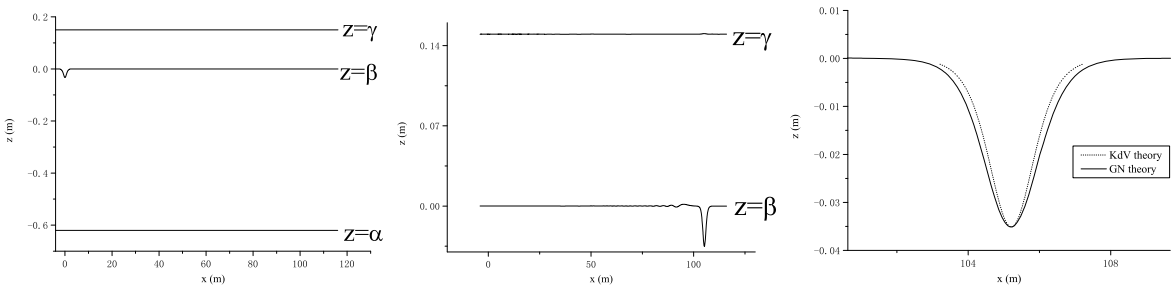

Figure 1: Initial wave profile with $a = 0.22h_2$ from KdV theory (left), snapshot at $t = 600$s (middle) and comparison with KdV results (right)

For $a/h_2 = 0.91$, we use the same method to simulate internal waves. The amplitude of initial wave is $a = 0.91h_2 = 0.1365$m at $t = 0$s. At $t = 550$s, the snapshot of wave train is shown on the left of Figure 2. We found that the amplitude of the leading internal solitary wave is only 0.09358m. Then, we calculate the profile of internal solitary wave with $a = 0.09358m$ from KdV theory. we compared GN results with the KdV theory, which is shown on the right of Figure 2.

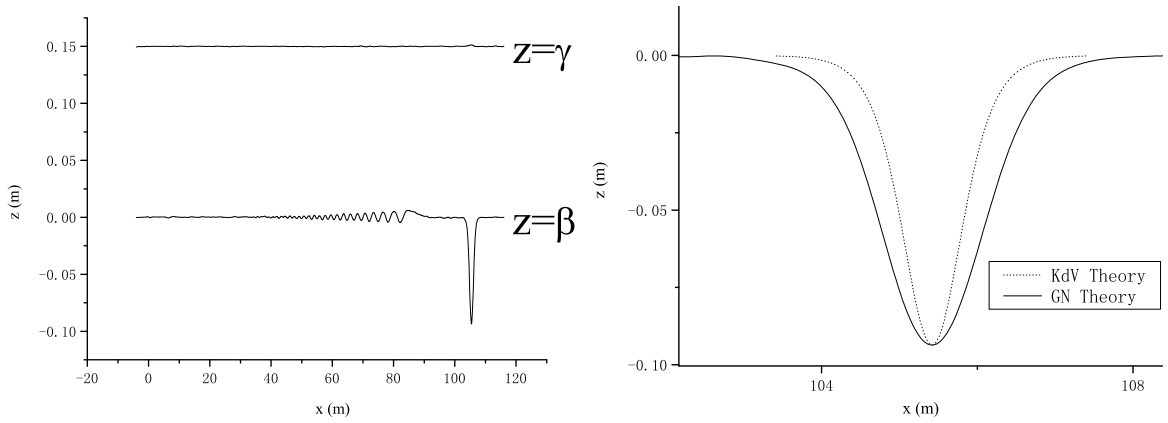

Figure 2: Snapshot at $t = 550$s with initial amplitude $a = 0.91h_2$ (left), comparison with KdV results (right)

We can see there are much difference between them. We tried to increase the amplitude of initial wave at $t = 0$, and we want to get a steady internal solitary wave with $a = 0.91h_2 = 0.1365$m. But, we failed. Because we use the KdV theory as the initial shape and velocity. As we know, the KdV theory can not predict large internal wave accurately.

We use another method to generate a solitary wave with amplitude $= 0.91h_2$. This method is similar to the physical experiment by Grue *et al.* (1999). The initial shape is shown on Figure 3. Here, the internal solitary wave is generated by gravity collapse. At $t = 0$s, the velocity is zero at everywhere. By careful changing the initial shape, finally we get a internal solitary wave with amplitude $a = 0.135$m.

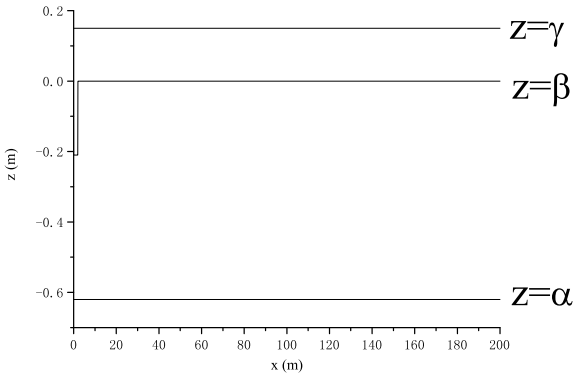

Figure 3: Initial wave profile similar to the physical experiment by Grue *et al.* (1999)

At $t = 355$s, the snapshot of the wave train is shown on the left of Figure 4. The amplitude of the leading solitary wave is 0.135m. Grue *et al.* (1999) gives the wave profile with amplitude $= 0.1365$m. The comparison between GN results and their fully nonlinear results is shown on the right of Figure 4.

We can see that the GN results are almost the same as the fully nonlinear model results by Grue *et al.* (1999). It should be noted that all cases here are simulated with $K^U = 1$ and $K^L = 1$. Higher level results will be presented at the workshop.

5 Conclusions

In this paper, the GN equations for two-layer fluid are given. The GN equations for two-layer flow has the similar form with one-layer case. We give some numerical results by using GN theory with $K^U = 1$ and

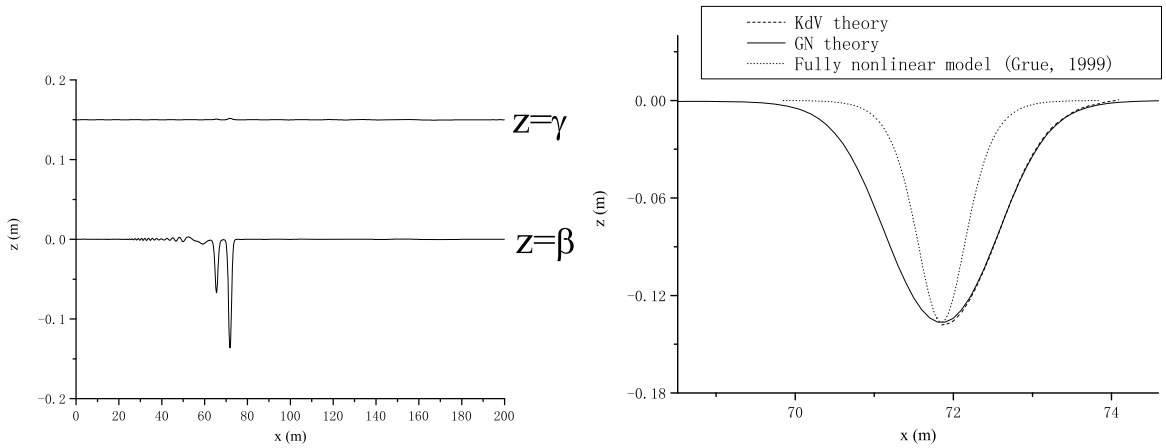

Figure 4: Snapshot at $t = 355s$ (left) and comparison with fully nonlinear model (right)

$K^L = 1$. For small amplitude internal solitary wave, the initial shape and velocity from KdV theory can be used as the incoming boundary condition in GN model. But, for large amplitude case, we need to find another method instead of the KdV theory. We use the similar method used by Grue *et al.* (1999) in their physical experiments. The internal solitary wave is generated by gravity collapse. For internal solitary wave amplitude $= 0.91h_2$, the GN theory gives the rather good results comparing with those by the fully nonlinear model in Grue *et al.* (1999).

Acknowledgments

On the GN theory, we get a lot of help from Profs. W.C. Webster, X.B. Chen and Z. Demirbilek, to which the authors are most grateful. The work is supported by the National Natural Science Foundation of China (No. 11102049), National Ministry of Science and Technology (International Science and technology cooperation project, No. 2012DFA70420), the Specialized Research Fund for the Doctoral Program of Higher Education of China (SRFDP, No. 20112304120021), the special Fund for Basic Scientific Research of Central Colleges, HEU. This work is also support by The LRET through the joint centre involving University College London, Shanghai Jiaotong University and Harbin Engineering University.

Reference

[1] Demirbilek, Z. & Webster, W.C., 1992. Application of the Green-Naghdi Theory of Fluid Sheets to Shallow-Water Waves: Report 1. Model formulation. US Army Wat. Exp. Sta., Coastal Engng. Res. Cntr. Tech Rep. No. CERC-92-11, Vicksburg, MS, 45pp.

[2] Grue J., Jensen A., Rusås P.-O., Sveen J.K., 1999. Properties of large-amplitude internal waves. J. Fluid Mech., vol. 380, pp. 257-278.

[3] Long, R. R. 1956. Solitary waves in one and two fluid systems. Tellus 8, 460.

[4] Webster W.C., Duan W.Y., and Zhao B.B., 2011. Green-Naghdi theory, part A: Green-Naghdi (GN) equations for shallow water waves. J. Marine Sci. Appl., 10 (3), 253-258.

[5] Duan W.Y., Zhao B.B., 2012. Simulation on Two-Dimensional Underwater Landslides-Induced Tsunamis by Using GN Theory. BICTAM First Workshop on Natural Hazards-Tsunami in conjunction with SCSTW5. Beijing, China.

[6] Zhao B.B., Duan W.Y., and Webster W.C., 2010. A Note on Three-Dimensional Green-Naghdi Theory. Proc. 25th IWWWFB, Harbin (China).

[7] Zhao B.B. and Duan W.Y., 2012. Application of the High Level GN Theory to Shallow-Water Wave Problems. Proc. 27th IWWWFB, Copenhagen (Denmark).